NASA Conference Publication 2462

Proceedings of the 1985 NASA Ames Research Center's Ground-Effects Workshop

Proceedings of NASA meeting held at
Ames Research Center
Moffett Field, California
August 20, 1985

NASA

NASA Conference Publication 2462

Proceedings of the 1985 NASA Ames Research Center's Ground-Effects Workshop

Edited by
Kerry Mitchell
Ames Research Center
Moffett Field, California

Proceedings of NASA meeting held at
Ames Research Center
Moffett Field, California
August 20, 1985

NASA
National Aeronautics
and Space Administration
Scientific and Technical
Information Branch
1987

EXECUTIVE SUMMARY

The NASA Ames Research Center's Ground-Effects Workshop was held on August 20-21, 1985; the proceedings are contained in this publication. The workshop was sponsored by the Powered-Lift Group of the Fixed-Wing Aerodynamics Branch at Ames Research Center.

The purpose of the workshop was to discuss the current technology base for aerodynamic ground effects and to establish directions for further research of advanced, high-performance aircraft designs, particularly those concepts utilizing powered-lift systems; e.g., V/STOL, ASTOVL, and STOL aircraft. To that end, 14 papers were presented in the following areas: suckdown and fountain effects in hover; STOL ground vortex and hot-gas ingestion; and vortex lift and jet flaps in ground effect. These subject areas were chosen with regard to current activities in the field of aircraft ground-effects research.

CONTENTS

THE ORGANIZING COMMITTEE

The papers presented at the Symposium were solicited and reviewed by the Organizing Committee. Authors are responsible for the content and the technical accuracy of their respective papers. The committee was composed of the following personnel:

Cochairman	David G. Koenig NASA Ames Research Center
Cochairman	Richard E. Kuhn STOVL Consultant
Member	Richard S. Christiansen NASA Ames Research Center
Member	James E. Eshleman NASA Ames Research Center

NASA AMES RESEARCH CENTER GROUND EFFECTS WORKSHOP PROGRAM
August 20, 1985

8:30	WELCOME: James A. Albers (Aerospace Systems Directorate)	
8:45	OVERVIEW: David G. Koenig (Powered-Lift Aerodynamics Group)	
	INTRODUCTION	
9:00	Ground Proximity Flow Fields	Kuhn (Consultant)
	SUCKDOWN AND FOUNTAIN EFFECTS IN HOVER	
9:30	Recent Large Scale Results	Christiansen (NASA Ames Research Center)
10:00	Investigation of Scale Effect on Single Jet Operation in Ground Effect for a Turbojet Engine	Benepe (General Dynamics) Lummus (General Dynamics)
10:30	BREAK	
11:00	Multiple Jet Impingement	Krothapalli (Florida State University)
11:30	Laser Doppler Velocimeter Measurements in a Three-Dimensional Fountain Upwash	Saripalli (McDonnell Douglas)
12:00	LUNCH	
1:00	Numerical Investigation of VTOL Jet-Induced Interactions	Rizk (Flow Industries) Menon (Flow Industries)
1:30	A Study of Impinging Jets via Numerical Simulation	Childs (Nielsen Engineering and Research)
2:00	BREAK	
	STOL--GROUND VORTEX AND HOT GAS INGESTION	
2:30	Investigation of the Formation Location and Strength of the STOL Ground Vortex	Billet (Pennsylvania State University)
3:00	Effects of Thrust Reversing in Ground Proximity	Joshi (Northrop) Hughes (Northrop)

3:30	STOL Landing-Thrust Reverser Jet Flow Fields	Kotansky (McDonnell Douglas) Glaze (McDonnell Douglas)

August 21, 1985

STOL--GROUND VORTEX AND HOT GAS INGESTION (CONTINUED)

9:00	Hot Gas Ingestion Scaling (Harrier/PCB)	Penrose (Rolls Royce, United Kingdom)
9:30	Hot Gas Ingestion: From Model Results to Full Scale Engine Testing	Johns (NASA Lewis Research Center) Biesiadny (NASA Lewis Research Center)

VORTEX LIFT GROUND EFFECT

10:00	An Experimental Investigation of Dynamic Ground Effect on Delta Wings	Muirhead (University of Kansas)

10:30 BREAK

JET FLAP

11:00	Flight Test Results	Stevens (NASA Ames Research Center)
11:30	Effects of Ground Proximity on a Low Aspect Ratio Propulsive Wing/Canard Configuration	Stewart (Rockwell) Kemmerly (NASA Langley Research Center)

12:30 LUNCH

1:30 PANEL DISCUSSION OF RESEARCH NEEDS: Chaired by Koenig

Recommendations and panel discussion
Panel members: Kuhn (Consultant), Hackett (Lockheed), Penrose (Rolls Royce, United Kingdom), Joshi (Northrop), and Hill (Grumman)

Richard Kuhn presented his recommendations followed by panel discussion on each of the following:

- Single-Jet Suckdown
- Multijet Hover
- Ground Vortex
- Jet-Flap Ground Effect
- Downwash at Tail
- Hot-Gas Ingestion
- Summary of Revised recommendations and priorities

3:00 ADJOURNMENT

V/STOL AND STOL GROUND EFFECTS AND TESTING TECHNIQUES

by R. E. Kuhn

PREFACE

The contract under which this report was prepared is a part of the NASA Ames Research Center effort to improve our understanding of the ground effects associated with V/STOL operation and to develop the equipment and testing techniques needed for this effort. Primary emphasis is on future experimental programs in the 40 by 80 and the 80 by 120 foot test sections and in the outdoor static test stand associated with these facilities.

Task I of the present contract covers a review of the commonly used experimental techniques and a comparison of data obtained by various techniques with each other and with available estimating methods. These reviews and comparisons provide insight into the limitations of past studies and the testing techniques used and identify areas where additional work is needed.

Task II will examine and recommend testing methods appropriate to the 40 by 80, 80 by 120 and static test stand facilities.

This contract work is being conducted under guidance of James Eshleman (contract monitor), David Koenig and Richard Christiansen of the 40 by 80 staff. Their help and advice is gratefully acknowledged.

SYMBOLS

A	Aspect ratio
A_j	Jet area, m^2
b	Wing span, m
c	Wing chord, m
C_L	Lift coefficient
ΔC_L	Lift coefficient increment
ΔC_m	Pitching moment coefficient increment
C_p	Pressure coefficient
D	Plate diameter, m
$\overline{D}$	Planform angular mean diameter, m
d	Jet diameter, m
d_e	Equivalent single jet diameter, m
e	Jet spacing, m
h	Height, m
L	Lift, N
ΔL	Induced lift increment, N
ΔL_f	Fountain induced lift increment, N
NPR	Nozzle pressure ratio
P_T	Total pressure, N/m^2
P_a	Ambient pressure, N/m^2
ΔP	Pressure increment, N/m^2
q_∞	Free stream dynamic pressure, N/m^2
q_n	Jet dynamic pressure at nozzle, N/m^2

$q_{w,max}$	Maximum dynamic pressure in wall jet at a radial station, N/m^2
R	Radius of plate, m
R_G	Radius of ground board, m
r	Radial distance or corner radius, m
S	Total planform area, m^2
S_L	Area contained within LIDs, m^2
T	Thrust, N
t	Time, sec
ΔT	Inlet temperature rise, deg
T_a	Ambient temperature, deg
T_j	Jet temperature at nozzle, deg
u	Vertical velocity in fountain, m/sec
V	Velocity, m/sec
V_e	Effective velocity ratio $V\tilde{e}\sqrt{q_\infty/q_n}$
V_j	Jet velocity at nozzle, m/sec
V_w	Velocity in wall jet, m/sec
$V_{w,max}$	Maximum velocity in wall jet at a radial station, m/sec
x	Longitudinal distance, m
X	Distance to leading edge of ground vortex flow field, m
X_V	Distance to ground vortex, m
X_0	Distance to zero pressure point, m
z	Vertical distance, m
Z	Depth of ground vortex flow field, m
α	Angle of attack, deg
ε	Downwash angle, deg
δ_j	Jet or jet sheet deflection

INTRODUCTION

The development of equipment and testing techniques for investigating the ground effects of V/STOL aircraft must be based on the available understanding of the flow phenomena involved. Our current understanding of the flow mechanisms involved in hovering and in transition in and out of ground effect is discussed under several categories in the main body of this report. The paragraphs that follow give a brief overview in an attempt to put the flow mechanisms in broad perspective.

The basic flow fields associated with hovering, transition and STOL operation of jet powered V/STOL aircraft are depicted in figure 1. The flow fields induce forces and moments on the aircraft which must be known in order to make accurate predictions of the performance and stability and control characteristics of the aircraft.

When hovering out of ground effect (upper left hand corner of fig. 1), the jet streams that support the aircraft entrain air and induce suction pressures on the lower surfaces. These pressures produce a small download, usually about 1 to 2 percent or less of the jet thrust. Because these downloads are small, the available empirical methods for estimating them (ref. 1) are adequate.

As the hovering aircraft descends into ground effect, the jet stream (or streams) impinge on the ground and form a radial wall jet flowing outward from the inpingement point(s). These wall jets also entrain air and significantly increase the induced suction pressures and the resulting down load as the configuration approaches the ground. There have been many investigations of the jet induced suckdown for single jet configurations, and while the basic phenomena is well understood, there are significant differences in the results obtained by various investigators. These will be presented and discussed in later sections.

With multiple jet configurations, the radial wall jets flowing outward from their respective impingement points meet and form an upflow or "fountain". The impingement of the fountain on the aircraft produces an upload which usually partially offsets the suckdown created by the entrainment action of the wall jets. Unfortunatly, the fountain flow also induces higher suction pressures between the jets and the fountains. The mechanisms involved are poorly understood and the present method for estimating the jet induced ground effects on multiple jet configurations are inadequate.

In the transition between hover and conventional flight, there are several flow mechanisms that induce forces and moments on the aircraft. The flow into the inlet produces an inlet momentum drag force and usually a nose up pitching moment. The exiting jet flow is deflected rearward by the free stream and rolls up into a pair of vorticies. These vorticies plus the blockage and entrainment action of the jets induce suction pressures behind and beside the jets and positive pressures ahead of the jets. The net effect for most jet V/STOL configurations is usually a loss in lift and a nose up pitching moment. However if the jets are at or near the trailing edge of the wing (particularly if they have appreciable spanwise extent as in a jet flap configuration) they induce positive lift and a nose down moment. The jet wake system also induces significant increases in the downwash at the tail.

In ground effect at transition speeds (STOL operation) all the above flow phenomena are present, but modified by the presence of the ground. In addition a ground vortex is formed by the action of the free stream in opposing the wall jet flowing forward from the impingement point(s) of the front jet(s). This ground vortex creates and defines the dust cloud produced when operating over loose terrain. It is also one of the hot gas ingestion mechanisms and it induces an additional lift loss and associated moment. Our knowledge of the factors that control the position and strength, and therefore the effects, of the ground vortex is incomplete at this time.

Both the ground vortex and the fountain flow are invloved in hot gas reingestion. In hover the fountain flow provides a direct path to bring hot gasses into the vicinity of the inlet where they can be inhaled. The severity of this part of the hot gas problem can be controlled to some extent by the placement of the inlet, by the arrangement of the jets and by the use of suitable flow deflectors. At forward speed the ground vortex provides an additional path to bring the hot gas in the forward flowing wall jet back to the vicinity of the inlet. Our ability to design for minimum ingestion is compromised by our limitied understanding of both the fountain flows and ground vortex.

The following sections will review each of these flow phenomena in more detail, present and compare the results of key investigations and make recommendations for the next steps in improving our understanding of the factors involved and in improving our ability to predict the aerodynamic and stability and control characteristics of V/STOL aircraft.

SINGLE JET SUCKDOWN

DATA BASE:

The first definitive work on jet induced suckdown in ground effect was done by Wyatt (ref. 2). He showed (fig. 2) that when the suckdown for plates of different sizes was plotted against the height divided by the plate diameter minus the jet diameter all the data would fall on a single curve. He also showed that the suckdown for noncircular plates would follow the same curve when the effective angular mean diameter, $\overline{D}$, of the planform is used.

A few years later Hall used a J-85 engine in a setup to measure the jet induced suckdown at large scale (ref. 3). His results (fig. 3) are in good agreement with the estimate based on Wyatt's work and appeared to indicate that any scale or real jet effects were negligible. However, the small scale results of reference 4 indicated somewhat more suckdown than either Wyatt's or Hall's work. There is considerable scatter in the data of reference 4 and most of the data were taken at higher nozzle pressure ratios than those for Wyatt's (ref. 2) data.

Other data also showed departures from Wyatt's and there have been several attempts to resolve these differences. One of these is presented in reference 1 (section 2.2.1) and attempted to examine the effects of pressure ratio by reanalysing available data. Excerpts from that study are presented in figures 4 and 5. In figure 4 Wyatt's data are compared with other data taken at low nozzle pressure ratios. There is considerable scatter in the data but it was found that if the exponent and the intercept value in Wyatt's expression are changed slightly most of the data falls within $\pm$ 1 percent of the new correlation line. Similar correlations at other nozzle pressure ratios showed that the effects of pressure ratio could be accounted for (within the data scatter) by making the exponent in Wyatt's expression a function of nozzle pressure ratio (fig. 5).

More recently Christiansen (ref. 7) conducted another large scale investigation. He used a J-97 engine to cover a wider range of nozzle pressure ratios than Hall's work. His results (fig. 6) show considerably higher values of suckdown at low heights than are predicted by any of the available modifications of Wyatt's method for estimating suckdown. They also show no effect of nozzle

pressure ratio (fig. 7). Clearly there are factors at work than have not been identified.

DISCUSSION:

There are several factors that could contribute to the differences shown in the results presented above. These include jet turbulence and the temperature, exit velocity distribution, cross gusts in the room in which the tests were conducted and the effects of ground board size. Few of the reports on jet suckdown give information on any of these factors. All of these and perhaps others need to be investigated. The following discussion is offered in hopes of providing some guidance for future investigations of these factors.

It should be useful to examine some of the basic mechanisms of jet induced suckdown. Figure 8 shows a pictorial sketch of the flow between the planform and the ground and some pressure distributions measured on the lower surface of the planform. The suckdown is created by the entrainment action of the vertical part of the jet and of the wall jet on the ground. This entrainment action draws air into the space between the planform and the ground and lowers the pressures on the lower surface of the planform. As long as the planform is above the critical height the pumping action should be relatively constant and the velocity of the entrained air must increase as the height is reduced. If the height is reduced by half, the velocity will be doubled. The suction pressures and therefore the download should be a function of the square of the height. In practice the exponent is a little over two because the gap is in reality the distance between the planform and the effective upper edge of the wall jet; not the distance to the ground.

When the planform is lowered to the height where it intersects the upper edge of the wall, jet entrained air can no longer be drawn in from around the planform but must be drawn from the wall jet itself. A trapped vortex condition is created and the pressure distribution is radically altered. The data of figure 8 are for a very large ratio of plate area to jet area and, fortunately, the "below critical height"condition is not encountered in practical aircraft configurations.

Under normal operating conditions, the flow field corresponds to the "above critical height" depiction shown at the right on figure 8. In this region both the wall jet and the vertical jet are entraining air. The amount of entrainment

should be proportional to the surface area of these surfaces. Figure 9 shows that at low heights where the suckdown is most serious the vertical surface area is small compared to the surface areas of the wall jet under the planform. Attention should, therefore, be focused on the characteristics of the wall jet and its effects on the suckdown. There have been numerous studies of the wall jet but none on the effect of the proximity of the planform on the wall jet or of the effects of the characteristics of the vertical jet before impingement on the characteristics, entrainment (pumping) ability or decay rate of the wall jet in the presence of the planform. This is where future work should be focused.

Reference 9 presents some data that indicate that the characteristics of the vertical portion of the jet may not have much effect on the wall jet characteristics (fig. 10). Reference 9 was concerned with the dust and debris problems of hovering helicopters and effect of the roughly triangular velocity distribution found in the slipstreams of these configurations on the development of the wall jet. Figure 10 compares the velocity decay and growth in thickness of the wall jet with distance from the impingement point for uniform and nonuniform nozzle exit velocity distributions. With the nonuniform velocity distribution, a trapped "doughnut shaped" vortex was generated centered on the impingement point. This trapped vortex flow was absent with the uniform velocity distribution. Beyond a radial station of about 2 exit diameters, the growth in thickness and decay in velocity in the wall jet created by the two exit velocity distributions were essentially the same indicating no difference in their entrainment action. This, however, leaves unanswered the questions of the effects of the changes in the velocities and shape in the region of the conversion from vertical to wall jet and the possible effect of planform proximity.

The effect of ground board size should also be investigated. The data of reference 7 were obtained with a ground board that was only about 50 percent greater in diameter than the planform. The earlier discussion has assumed that only the wall jet directly under the planform is important in determining the entrainment and suckdown. However, when the wall jet reaches the edge of the ground board, it suddenly has a mixing and entrainment surface on both the top and bottom (fig. 11). It will decay much faster and this decay will be felt upstream, perhaps thickening the wall jet under the planform. A rough estimate indicates that the wall jet would have to be thickened by about 50 percent to account for the higher suckdown exhibited at low heights by the configuration of reference 7. The effect of ground board size should be investigated.

Most of the data on single jet suckdown has been taken indoors but few of the reports indicate the size of the room in which the tests were run. Nor do they say anything about any obstructions that may have been near the experimental setup. One case in which the chamber where the static suckdown data were taken was clearly of inadequate size is reported in reference 10. The tests were run in a wind tunnel because the primary purpose was to investigate STOL ground effects. Two of the static "end points" taken at zero tunnel speed are presented in figure 12. The model in this case consisted of a 2 inch diameter nozzle to which various size planforms could be attached. The model was mounted at the center of an approximately 14 by 16 foot test section with a ground board that spanned the tunnel and could be raised and lowered to vary the height above the ground.

The experimental data presented in figure 12 show greater suckdown than the estimates, particularly for the larger plate. It was possible to enter the test chamber while the static tests were in progress and it was observed that the wall jet on the ground board flowed up the side wall of the test secton and across the ceiling. In addition, and more importantly, there were strong and random gusts throughout the chamber and in the vicinity of the model. It is these gusts that are believed to be responsible for the larger than expected measured suckdown.

The data of reference 4 were taken using a 1 inch diameter jet in a room that was 18.5 feet wide by 10 feet high and 42.5 feet long. It was, therefore, relatively larger than the test chamber of reference 10 but was it large enough? Figures 13 and 14 were prepared to offer some perspective on the problem.

Figure 13 presents the decay in the velocity of the wall jet with distance from the impingement point. If the path from the nozzle to the ground, across the floor, up the wall, across the ceiling and back to the model were "unrolled" the distance for the tests of reference 10 would be 195 diameters. If this distance were traversed on a flat surface, the downward velocity at the model would be less than 1 percent of the jet velocity. However it is not the down flow depicted in the sketch on figure 13 that is important but the random gusts. It is probable that these gusts are much stronger than the velocity the wall jet would have at a radial distance of 195 diameters (or 450 diameters for the configuration of reference 4).

Figure 14 presents the effect of a small crossflow velocity on the suckdown (estimated by the method of reference 10). It can be seen that it takes a cross flow velocity of only about 1 percent of the nozzle velocity to produce incremental changes in apparent suckdown of the magnitude seen in figure 3 for example. These estimates are for a steady crossflow. Gusts would produce an unsteady increment but there is no compensating effect. A gust from any direction will increase the download and the average of the unsteady readings will be higher than the suckdown would be if there were no crossflow gusts. These observations suggest that some of the differences between the suckdown data obtained by different investigators could be due to the inadequate size of the room in which the tests were made. The effects of test chamber size should be investigated.

RECOMMENDATIONS:

It is doubtful that additional force tests could uncover the reasons for the differences in suckdown discussed above. What is needed are investigations to probe the fundaments of the flow. Two investigations are recommended, one related to test chamber size and the other to study the effects of various factors on the development of the wall jet and in turn the effects on the suckdown.

1) A schematic of the test chamber size investigation is shown in figure 15. It would have to be conducted in a large high-bay area with a small model to obtain "gust free" data as the anchor point. The dimensions in figure 15 assume a 1 inch diameter jet. A jet/plate combination would be mounted so that the height could be varied and the suckdown force and pressure distribution measured on several plate sizes. The set up would be surrounded with strategically located hot wires to measure the gust velocities. Care would have to be taken to fair and streamline the mounting struts so that they did not reflect any of the wall jet to create gusts.

Following tests in the large room, chambers of succeedingly smaller sizes would be constructed around the test setup using plywood and 2 by 4's and the tests repeated to determine the effect of chamber size on the gust environment and suckdown.

If the tests show, as expected, that the gusts in the small chambers are the problem, studies of the use of strategically located damping "screens" and/

or venting would be used to see if they can reduce the gust effects to an acceptable level. It would be extremely helpful if such a "fix" could be found that would permit static tests in wind tunnel test sections so that hovering "end point" data could be obtained for configurations being tested in the STOL mode.

2) A schematic of the wall jet effects investigation is presented in figure 16. The heart of the investigation would be measurements of the growth in thickness and the velocity decay in the wall jet for various jet exit conditions and planform heights and the correlation of the suckdown with the observed changes in wall jet characteristics. The investigation should be run in a very large high-bay area to minimize gust effects due to chamber size. The jet size would have to be chosen to provide a thick enough wall jet for acceptable measurements, probably about a 4 inch diameter jet would be adequate but this would require a very large room. Tests should cover a range of ground board sizes and jets of varying pressure ratio, turbulence and exit distribution.

Because the ground effect suckdown is a fundamental problem for most jet VTOL configurations and the estimate of the single jet suckdown is the starting point or a significant factor in the estimation of more complex ground effects, a resolution of these problem areas is very important.

MULTIPLE JET GROUND EFFECTS

DATA BASE AND DISCUSSION:

Fountain Lift and Additional Suckdown:

When the wall jets from two jets of equal size and thrust meet, a fan shaped upwash or "fountain" is formed between the jets as shown in figure 17. If there are more than two jets, a fan shaped fountain is formed between each pair and a fountain "core" is formed where the fountain fans meet. The impingement of the fountain flow on the configuration produces an upload which partially offsets the suckdown induced by the wall jet entrainment action.

The result is not always a reduction in suckdown as shown in figure 18. Lummus (ref. 11) ran a two jet configuration and measured a suckdown greater than expected for a single jet configuration of the same planform to jet area ratio. He then ran a single jet with half the planform (thus maintaining the same planform to jet area ratio and nearly the same planform aspect ratio) and found less suckdown than for the two jet case. Thus the fountain lift increment ΔL_F is negative. He ran similar tests with other jet spacings and with 3 and 4 jet configurations (fig.19) and found negative fountain lift increments for the other two jet configurations and nearly zero fountain lift for 3 jet configurations.

The probable cause of this additional suckdown is shown in figures 20 and 21 (from ref. 12). A vortex-like flow is formed between the fountain flow and each of the adjacent jets (fig. 20). Figure 21 shows that, as expected, the impingement of the fountain flow produces high lifting pressures on the center region of the plate between the jets, but the vortex-like flows between the fountain and the jets induce equally strong suction pressures. The estimated suckdown for a single jet configuration with the same planform to jet area ratio would correspond to an average suction pressure coefficient about equal to the outer contour line shown in figure 21 (C_p = -0.004). Thus both the lifting pressures and the additional suckdown pressures are much greater than the pressures induced on a single jet configuration and the question of whether there is a net lift gain or loss depend on which predominates. Unfortunately there is no other pressure data of the type shown in figure 21 on which a method for estimating multiple jet ground effects can be based.

Yen, in reference 13, developed a theoretical framework for estimating the fountain lift contribution and recognized the additional suckdown term but offered no method to estimate it. Kuhn in reference 14 used Yen's fountain jet contribution and the estimated suckdown from an equivalent single jet configuration to back the additional suckdown contribution out of the available experimental data and developed an empirical method for estimating multiple jet ground effects. The method works reasonably well for configurations similar to those in the data base on which it was derived (fig. 22), but badly misses on some other configurations (fig. 23).

Additional pressure distribution data of the type shown in figure 21 are needed to more fully explain the effects of multiple jet interactions. Such pressure distributuion data appear at this time to provide the best hope of developing a reasonable method for estimating multiple jet ground effects.

Turbulence:

Lummus, in reference 11, also investigated the effect of jet turbulence. A grid of wires was placed in the nozzle slightly upstream of the exit to change the turbulence of the jet stream. The turbulence intensity was defined as the RMS values of the fluctuating total pressures (fig. 24) as measured by a total pressure survey across the exit divided by the average gage total pressure. The turbulence intensity for the base line nozzles, as well as the nozzles with turbulence genterators, were found to decrease with nozzle pressure ratio (fig. 25).

The effect of turbulence and pressure ratio for a two jet configuration is presented in figure 26. The suckdown is shown to increase with turbulence level. However, there is no way of knowing whether this increase is due to turbulence increasing the entrainment action of the wall jet or the strength of the fountain itself. Carefully controlled single jet tests as discussed above could provide a partial answer to this question and are needed.

Foley, in reference 16, investigated the turbulence in the fountain between two jets and it's sensitivity to "trips" on the stagnation line where the wall jets meet to form the fountain. Unfortunately the study did not include measurement of the effects on the suckdown (the setup did not include a plate or planform on which suckdown could be measured). The study showed that the upward velocity in the fountain was increased and the turbulence in the fountain

decreased (fig.27) by obstructions at the stagnation line. Even a 1/8 inch "trip" (about the thickness of the boundary layer under the wall jet) had a noticeable effect. These results suggest that there is an appreciable energy exchange between the wall jet flows across the stagnation line and that turbulence in the main jets may be affecting the fountain and its associated vortex flows more than the wall jet flowing outward away from the fountain. These effects need further investigation.

Other Configuration Variables:

The previous discussion has concerned only flat plate configurations. The fountain and additional suckdown effects on these simple cases must be understood to provide a solid base for isolating the other effects of real airplance configurations such as wing height, fuselage lower surface contour and devices to increase the fountain lift (LIDs). An attempt was made in reference 14 to develop methods for estimating some of these effects.

Figure 28 presents some data on the effect of fuselage contour on the fountain lift contribution. If the fuselage lower surface is flat with sharp corners and wide enough to intercept all of the fountain flow, all the fountains vertical momentum will be coverted to lift. If, however the fuselage lower surface has rounded corners, some of the fountain flow will adhere to this curved surface, retain some of its vertical momentum and less than full fountain lift will be realized. Three sets of data were found for the case of two jets, one on either side of a body with a longitudinal fountain between them. The reduction in fountain lift was found to correlate reasonably well with the ratio of the fuselage corner radius to the jet spacing. However, there is no data on fore and aft jet arrangements and little on 3 and 4 jet configurations. Additional work is needed in this area.

Reference 14 also attempted to develop a method for estimating the additional lift contributed by LIDs (lift improvement devices). An example is shown in figure 29 for a Harrier-type configuration (one of the configurations used in developing the method). LIDs attempt to "trap" some of the fountain flow and turn it downward to increase the lift. The LID contribution is therefore assumed to be some fraction of the fountain life that would be achieved on a flat plate and should be proportional to the area contained within the LIDs, S_L. This was found to be the case at intermediate heights but at the lowest

heights an expression using the inverse of the square root of the LIDs area (which appears illogical) had to be used.

Other configuration variables that will affect the fountain formation and the ground effect of multiple jet configurations include non-circular jets, jets canted inward or outward, jet deflection fore and aft, differential jet size and thrust and model attitude. There is some specific configuration data on some of these and the work of Kotansky and associates at McDonnell Douglas has provided a solid data base on the wall jets and fountains produced by vertical and deflected noncircular jets. The related data on the additional suckdown pressures induced by the vortex-like flows between the jets and the fountain are needed to provide a good foundation for developing estimating methods.

Pitching Moments:

The ground effect induced pitching moments have not received any attention. With practical aircraft configurations, such as that sketched in figure 30, a nose up moment will be experienced as the aircraft settles into ground effect. The positive pressures induced by the fountain flow will be experienced between the lifting jets and negative or suckdown pressures will be experienced on most of the rest of the lower surface area. A large part of the area subject to download will be aft of the center of gravity thus contributing a nose up moment. It should be possible to estimate these moments if the distribution of induced pressures are known. The fountain flow induced pressure distribution investigaton recommended above could and should be structured to include some nonsymmetrical flat plate configurations which would provide pressure as well as force data on which to begin building a method for estimating pitching moments.

RECOMMENDATIONS:

The recommendations with respect to multiple jet suckdown can be divided into four areas.

1) The most important investigation in the multiple jet ground effects area is a study to better understand the effects of the flow field between the jets, including the fountain and the associated vortex type flows between the fountain and the jets. This investigation should start with two jet configurations investigating the effects of height and jet spacing on the suckdown and

pressure distribution of selected flat plates. The study should include flow visualization to better understand the flow fields involved.

A proposed method for isolating the fountain and additional suckdown terms is shown on figure 31. The pressure distribution measured on a plate for a given jet spacing and height would be compared with the pressure distribution measured at the same height with single jet. Integration of the single jet pressures would be the single jet suckdown and should be equal to the measured suckdown. The fountain lift would be determined by integrating the portion of the distribution that shows a positive increment relative to the single jet case and the additional suckdown would be determined by integrating the excess negative pressures.

The flat plates used would have to be heavily instrumented with pressure taps, particularly between the jets (fig. 32), where the pressure gradients are steep. Only one quadrant of the plate would have to be fully instrumented for those configurations with a symmetry about two axes but a couple extra rows of pressure taps should be included in the other quadrants of the plate to ensure symmetry.

The study should investigate the effects of:

- Jet spacing
- Height
- Planform size and shape
- Jet pressure ratio and turbulence
- Wall Jet and fountain characteristics

The study should begin with two jet configurations and be extended to 3 and 4 jet configurations after the experimental techniques have been developed with the two jet configurations.

2) A revised method for estimating the ground effects of multiple jet configurations, including the fountain term and the additional suckdown term should be developed from the data obtained from the above study.

3) A method for estimating the pitching moments of multiple jet configurations hovering in gound effect should be developed. This will require including planforms that are nonsymmetrical fore and aft in the fashion of aircraft planforms in the pressure distribution studies of the first investigation.

4) Work should be extended to the items listed below after the first three studies are completed:

- Body contour
- LIDs
- Noncircular jets
- Canted jets
- Jets deflected fore and aft
- Differential jets size
- Differential jet thrust
- Wing height
- Model attitude

There is some data in the literature on most of these items and these data should be reexmined in the light of the findings of the above three studies to see if and where additional work is needed before embarking on new studies.

GROUND VORTEX IN STOL OPERATIONS

DATA BASE AND DISCUSSION:

In STOL operation the wall jet flowing forward ahead of the configuration is opposed by the free stream and rolled up into a horseshoe shaped ground vortex as depicted in figure 33. When operating over loose terrain this ground vortex creates and defines the dust cloud that can reduce visibility and damage engines. It is also one of the primary mechanisms of hot gas ingestion and can cause lift loss and pitching moments.

The ground vortex contribution is most significant at low speeds and heights and its significance decreases rapidly with increasing height and speed (fig. 34). Reference 10 presents the most complete database on these effects available at this time.

A ground vortex type of flow is also associated with jet flap configurations. Williams and Wood, in reference 20, found a trapped vortex under the high aspect ratio full span flap configuration when they approached the ground (fig. 35). The problems of the ground board boundary layer and jet flap configuration testing will be discussed in a later section.

Vortex Strength:

The ground vortex associated with jet impingement has been studied in several investigations (refs. 10 and 21-24). Two of these (ref. 10 and 24) measured the pressure distribution induced on the ground board by the ground vortex. Figure 36 illustrates a typical distribution on the center line through the impingement point. The jet is swept aft by the free stream and produces high positive pressures in the impingement region. The pressure decreases rapidly under the wall jet flowing forward from the impingement point and reaches a maximum negative pressure under the vortex. Ahead of the vortex the pressure rises and there should be a stagnation point where the wall jet and free stream are in balance. However the pressure coefficient never reaches a value of 1.0, probably because of unsteady mixing in this region. In reference 10 the point at which the pressure coefficient was zero was used as an indication of the effective leading edge of the vortex flow field.

The effect of jet exit height on the ground board pressure distributions along the center line through the jet impingement point is presented in figure 37. The data are from reference 10 at a velocity ratio of $V_e = 0.1$. The first clear evidence of the ground vortex occurs at a height of 15 jet diameters. At this height the jet impinges on the ground about 5 diameters behind the projected jet center and the maximum negative pressure, indicating the approximate position of the ground vortex, also occurs behind the projected jet centerline. As the height is reduced the ground vortex moves forward as expected and the increasing magnitude of the negative pressure coefficients indicates the vortex is gaining strength. The forward movement stops at a height of about 4 diameters (probably when the jet potential core reaches the ground) and the maximum negative pressure appears to have stabilized at a value of almost -3.0.

Figure 38 presents similar data from reference 24 on the effect of forward velocity on the ground vortex prssure distribution with the nozzle at a height of 4 diameters. At the highest velocity ratio (free stream almost half of the jet velocity) the pressure coefficients are small and the ground vortex is close to the jet centerline. As the velocity ratio decreases the ground vortex moves upstream as expected and the maximum negative pressure coeficient again stabilizes. However in this investigation the maximum negative value is only about -1.7.

The vortex strength in the investigation of reference 10 appears to be greatly different than that in the investigation of reference 24. At a height of 4 diameters and a velocity ratio of 0.1, the maximum negative pressure ratio coefficient has stabilized in both investigations but at a level of -1.7 in reference 24 and almost -3.0 in reference 10. The difference is believed to be associated with the nozzle pressure ratios at which the tests were conducted. The data of figure 37 (ref. 10) were taken at a nozzle pressure ratio of about 1.8 whereas a jet velocity of only about 80 meters per second (indicating a nozzle pressure ratio of less than 1.05) was used in reference 24. An investigation to study the effects of pressure ratio at several constant levels of velocity ratio is needed.

Vortex Position:

The five investigations of the ground vortex show a wide variation in the forward projection of the ground vortex flow field (fig. 39). Some of this variation may be due to the manner in which the forward edge of the flow field was defined (some measured the leading edge from photographs of dust clouds and some, like reference 10, used the position of the zero pressure coefficient (fig. 36). Also they were run at different pressure ratios. However, it is believed that the boundary layer on the ground board may be the biggest factor. With a boundary layer the high velocities in the wall jet, which are very close to the ground (fig.40), can penetrate further against the relatively lower velocities in the ground board bounday layer than they would be able to penetrate against the free stream. The investigation of reference 21 set out to simulate the boundary layer of the atmosphere and thus had a thick boundary layer. It is seen to indicate the most forward penetration (fig. 39). Reference 22, on the other hand, used the moving model technique and thus there was no boundary layer. It shows the smallest penetration. Little is know about the boundary layer in the other investigations other than that the investigation of reference 24 was made at a relativeley low Reynolds number and thus probably had a relatively thick boundary layer. Because of the importance of the ground vortex to both the aerodynamic characteristics and hot gas ingestion, a special investigation to determine the independent effect of the ground board boundary layer and pressure ratio is needed.

Thrust Reversers and the Effects of Jet Deflection:

Up to this point the illustrations used have considered vertical jets. The thickness of the wall jets and the strength and position of the ground vortex are strongly influenced by jet inclination (ref. 10). If the jet is inclined aft, more of the mass flow is directed aft and the wall jet flowing forward is thinner and the ground vortex is closer to the impingement point. Thrust reversers direct more of the flow forward, thicken the wall jet, move the ground vortex forward and increase its strength. Reference 25 shows that large lift losses and pitching moments can be generated (fig. 41).

The work reported in reference 25 also encountered a phenomena which may indicate a serious problem for thrust reverser equipped fighter aircraft. Close

to the ground the model experienced a severe rolling oscillation. Flow studies indicated that the ground vortex flow field was not fixed but moving rapidly fore and aft when these roll oscillations were encountered and that the forcing frequency full scale would be about 2 hertz. The stability and control implications for operational aircraft are unclear but these results suggest that investigations of the ground vortex should include instrumentation to study the dynamics of the wall-jet/free-stream interaction and the formation of the ground vortex.

RECOMMENDATIONS:

Because of the importance of the ground vortex effects on STOL performance, stability and control and hot gas ingestion the uncertanties and discrepencies discussed above must be resolved. The primary need at this time is to determine the effects of jet pressure ratio and the ground board boundary layer on the position, depth, strength and dynamic motion of the ground vortex flow field at various velocity ratios.

Figure 42 illustrates the key elements that should be included in this investigation. A body-jet combination that can be tested at various heights, pressure ratios and free stream velocities should be tested over a fixed and a moving ground board. Pressure distributions should be measured on the fixed ground board to correlate with previous studies and on the body to determine the effects of the ground board boundary layer and correlate with the flow field surveys. Some dynamic flow survey and high response pressure intrumentation measurements should be included to determine the dynamic movement of the ground vortex and the stagnation flow region.

JET FLAP GROUND EFFECTS STUDIES

DATA BASE AND DISCUSSION:

Ground Board Boundary Layer Effects:

Jet flap configurations operating at very high lift coefficients suffer a lift loss when operating within ground effect. Williams et al. (ref. 20) showed that when the jet sheet from the jet flap impinges on the ground a ground vortex-like flow was generated between the wing and the ground plane (fig.35). Turner, in reference 26, showed that the lift loss measured in a wind tunnel with a fixed ground board (with a bounday layer on the ground board) was considerably greater than the lift loss measured on the same model using the moving model technique (no boundary layer). And Werle', in reference 27, using the ONERA water tunnel to show the flow, demonstrated (fig. 43) that the interaction of the boundary layer with the wall jet flowing forward from the point where the jet sheet impinges on the ground caused a major alteration in the flow under the model.

These results lead to the development of several moving-belt ground-board installations, first in England and later in the United States and elsewhere. The installation shown in figure 44 illustrates the principal features. A slot is installed ahead of the belt to remove the boundary layer up to that point and the belt, by running at the same speed as the air in the test section, prevents the regeneration of the boundary layer. Turner, in references 28 and 29, showed that this technique gave essentially the same result as the moving model technique used earlier (fig. 45).

Alternate Ground Board Concepts:

The use of a moving belt ground board in the 40 by 80 and 80 by 120 foot test sections is impractical on two counts. First the development and installation of a large enough belt system would be excessively complex, time consuming and costly and second, belt materials compatible with the exhaust temperatures of the jet engines that are frequently used are not readily available.

The use of suction and/or blowing on the ground board has been suggested but the problem is where and how much to suck or blow. Hackett (refs. 30 and

31) investigated a blowing BLC system on the ground board using both a jet flap and vertical lifting jet model. He used measurements of pressures on the lower surface to determine the amount and location of blowing required with similar data measured over a moving belt as the control. He developed a criteria for blowing that would work well for most conditions tested. Figure 46 presents the blowing BLC design he proposed for the 40 by 80 test section.

A concern with blowing is the possibility of over blowing. Turner, in reference 29, investigated belt over-speed conditions and showed that if the belt was run faster than the air velocity a "negative" boundary layer was created and the lift continued to increase (fig. 47). With a blowing BLC system, the blowing slot must be ahead of the location of the model, a small boundary layer will be developed under the blowing air and an over velocity will be present above it to provide the overall momentum balance.

The French claim to have minimized this problem by using two blowing slots (ref. 32). Both slots ahead of the model with the first slot providing the bulk of the BLC flow required and the second providing a trimming flow to produce a nearly planer velocity distribution at the model station. The operating conditions are determined by adjusting the flow from each slot to achieve as near a planer velocity distribution at the model station with the model out (or at zero lift) and holding this BLC flow throughout the test program. The system was stated to work well for jet flap models but has not been used with jet lift models.

Hacket points out (ref. 31) that some over blowing is desired. With a belt ground board, the air at the surface of the belt is carried with the belt as show in figure 48. That is, the air in the boundary layer of the forward flowing wall jet is retarded and the wall jet boundary layer is thickened. (In the case of the aircraft moving forward over the fixed ground the air at the surface is retarded by the surface with the same result, the wall jet boundary layer is thickened and the wall jet loses energy). With a fixed model and fixed ground, this extra energy loss in the wall jet is not experienced and some over blowing is needed to compensate and achieve the correct ground vortex flow field. The question is how to determine where and how much to blow. Hackett used skin friction gages to set up the condition of zero skin friction under the model.

A major concern is the proper location of the BLC slot. Obviously the BLC slot, either suction or blowing, should not be placed under or aft of the ground

vortex location where it would do violence to the wall jet and the generation of the ground vortex that should be there. Figures 49 and 50 present estimates of the position of the leading edge of the ground vortex flow field with and without the ground board boundary layer. In order to cover a wide range of operating conditions, it would be desirable to be able to move the BLC slot location in accord with the operating conditions.

Figure 51 presents a schematic of a method that could be used to position the BLC slot (blowing or suction). The ground board would be raised above the tunnel flow to avoid the larger boundary layer on the floor and minimize the BLC requirements. The entire ground board would be translated fore and aft to position the BLC slot. Thus it should be possible to cover a wide range of operating conditions.

It is suggested that the ground vortex pressure distribution could be used as a "signature" to position the ground board (fig.52). As indicated above, the BLC slot must be kept ahead of the ground vortex flow field but there is no data to tell us how to locate it. An experimental program to investigate the feasibility of this approach is recommended.

Jet Flap and Direct Jet Lift Ground Effects Comparison:

If vertical jets are placed at or near the wing trailing edge, they induce a favorable lift out of ground effect similar to that produced by a jet flap. In reference 10 the effect of ground proximity on the induced lift produced by a jet flap configuration and a direct jet lift configuration were measured on the same wing-body configuration. A comparison of the results is presented in figure 53. The round jet and the slot jet had different areas and pressure ratios so a direct comparison is difficult but the conditions chosen in figure 53 were those that give about the same induced lift/thrust ratio out of ground effect. The resulting comparison is interesting in that the round jets show a favorable ground effect whereas the slot jets show the expected adverse ground effect associated with jet flap configurations. The reason for the different behavior appears to be associated with the differences in the ground vortex position and probably strength. The ground vorticies, as determined from the ground board pressure distributions, were much further forward and had a much greater spanwise extent for the slot jets (jet flap) than for the round jets.

The large favorable ground effect for the round jets is not very helpful (the configuration still has to fly out of ground effect) but the adverse behavior shown by the slot jet configuration is to be avoided. Some place between these configurations, a better compromise should be possible. An investigation of the effects of jet size, shape and spanwise extent should be initiated.

Dynamic Ground Effects:

The preceding discussion has assumed steady state operation in ground effect. In practice, an aircraft does not fly at a constant height but is either descending during landing or climbing after take-off. The ground effects are, therefore, transient. Stevens and Wingrove, in reference 33, present the lift history during a landing approach and wave-off of the augmentor wing aircraft (fig. 54). In this case the lift coefficient out of ground effect was only about 2.5 and ground effects are favorable. The data show a significant hysteresis with lower lift during the climbout after wave-off indicating a lag in the development of the effects of ground proximity.

Turner, in reference 26, investigated this lag using the moving model technique. The model was suspended from a carriage and brought up to speed before reaching the platform which represented the ground. Figure 55 shows that, for the flat ground board, the lift loss started to develop at the edge of the ground board but did not develop fully until it had traversed the ground board a distance of 4 or 5 chords. In a second series of tests, the forward edge of the ground board was inclined at an angle to represent a landing approach. A comparison of the lift measured with that expected for steady operation at each height shows a lag in the development of the lift corresponding to a flight distance of about 3 chords.

Techniques for investigating these rate-of-height change effects on the ground effects are needed. Conceptually, it might at first be thought possible to insert rapid actuators into a conventional support system to produce the dynamic height and angle of attack changes needed to simulate a landing approach and touchdown. However, a review of reference 34 suggests that achieving adequate stiffness in a conventional support system to ensure position accuracy while keeping them light enough to permit the rapid movements required will be extremely difficult. On the other hand, the support system shown in figure 56

(from ref. 34) places the support strut in the ground effect flow field and may compromise the results aerodynamically. It may be necessary to invert the entire system; mount the dynamic support drive on a solid foundation as shown in figure 56 but turn the model over and bring the support into the model from the top. This would require mounting the ground board above the model. The entire area of dynamic testing and the needed support system must be subject to more study.

RECOMMENDATIONS:

There are three recommendations with regard to jet flap research and testing techniques.

1) The moving belt ground board is not practical for the 40 by 80 and 80 by 120 foot test sections and an alternative must be developed. Boundary layer control, either blowing or suction, will have to be used. The problem is how to position the BLC slot for the relatively wide range of possible test conditions. It is recommended that the possibility of using the ground vortex pressure distribution signature to locate the BLC slot be investigated.

A sketch of the principal features to be included in such an investigation is presented in figure 57. A body containing a 1 inch diameter nozzle (one twelfth scale of the J-97 engine exhaust in the 80 by 120 foot test section) would be mounted over a ground board that is raised above the floor of the test section to avoid the floor boundary layer. A row of pressure orifices on the ground board centerline would be used to measure the pressure distribution generated by the ground vortex created by the flow from the 1 inch nozzle. The ground board would be translated fore and aft to determine the effect of BLC slot location on the ground vortex pressure signature and determine the sensitivity of the ground vortex flow field to BLC slot location. The model would first be tested over a moving belt ground board and the pressure distribution of the body measured so that it could be used for evaluation of the BLC ground board effectiveness. If initial tests with a simple jet model were successful, the program should be repeated with a jet flap wing configuration with pressures measured on the wing to ensure adequacy of the concept.

Consideration should be given to combining this investigation with the investigation suggested in the previous section to determine the effects of pressure ratio and ground board boundary layer on the ground vortex strength and

position. Or at least the two investigations should be coordinated so that they support each other.

2) An investigation of the effects of jet configuration bridging the gap between the jet flap and the direct lift jet at the wing trailing edge should be undertaken. Figure 58 presents the principal elements. A common wing body should be designed to incorporate full span and half span jet flaps and a series of jet shapes ranging from circular to very high aspect ratio slots as shown in figure 58 so that the effects of jet configuration can be fully explored. A range of jet and jet sheet deflection angles, from 90 degrees to about 45 degrees should be covered as well as a full range of momentum coefficients and velocity ratios.

3) It appears doubtful that the model support system that would be chosen for standard research investigations could be made suitable for the studies of transient ground effects. Also a support system that uses a strut from below the model will adversely affect the flow under the model and the ground effects experienced. The possibility of inverting the entire set-up for transient tests so that the model could be supported from its top rather than the bottom should be considered.

DOWNWASH AT THE TAIL

DATA BASE AND DISCUSSION:

Jet Flap Configurations:

Lift is produced by deflecting the flow around the aircraft downward. The slower the flight speed, the greater the deflection of the flow. Powered lift systems are designed to achieve this high deflection of the flow and, as a consequence, produce high downwash angles behind the wing (for example, fig. 59). The presence of the ground interrupts this downward deflection of the flow and, therefore, would be expected to affect not only the lift, but also the downwash behind the wing.

There is a useful data base on the downwash behind the wing of jet flap configurations out of ground effect, but there is relatively little data on the effects of ground proximity. Stewart, in reference 10, presents a curve for the ratio of the downwash in ground effect to the out-of-ground-effect downwash (fig. 60). Unfortunately, the curve is based on only two sets of data. Additional data are needed to determine the range of its validity.

Jet Lift Configurations:

There is even less data on the downwash behind direct jet lift configurations either in or out of ground effect. Figure 61 presents out-of-ground-effect downwash for a two jet configuration for three tail heights. As expected the downwash is seen to increase as the velocity ratio is reduced (as the dynamic pressure of the jet increases relative to the free stream dynamic pressure) and to decrease as the position of the tail is raised. On the other hand, much of the data for a Harrier-type configuration (fig. 62) show the opposite trend; the downwash decreases with decreasing velocity ratio. It is speculated in reference 10 that this trend reversal is due to the fact that the lift loss induced on the wing is increasing as the velocity ratio decreases and that this changes the spanwise load distribution on the wing in a manner so that the wing contribution to downwash overpowers the direct jet effect.

Figure 63 presents the effect of ground proximity on the downwash for the Harrier-type model of reference 39. The data indicate the surprising result

that at low speed, high power conditions (V_e = 0.1, fig. 63b), the downwash is negative; that is, an upwash is experienced close to the ground. Again the reason is not known but it is speculated in reference 10 that this upwash may be due to the fountain flow generated by the rear pair of jets on the configuration. Additional data are needed to clarify these data and to provide a better data base estimating downwash both in and out of ground effect.

RECOMMENDATIONS:

Specific investigations to study the downwash of powered lift configurations in ground effect could be developed, but in view of the large number of other ground effect studies that need attention, it is recommended that additional data in this area be obtained by seizing every opportunity presented by tests of complete configurations to extend them to obtain downwash data.

Care must be taken to see that the proper runs are included in the test program. Too often the basic data needed to extract downwash data are not obtained in test programs on complete configurations. Emphasis must be placed on obtaining both tail-on and tail-off data as well as stabilizer effectiveness data for each power and flap configuration tested. And, of course, these data should be obtained out of ground effect and at as many heights as practical.

HOT GAS INGESTION

DATA BASE AND DISCUSSION

The ingestion of hot gases into the engine inlet depends on the flow field under and around the aircraft. There are three basic mechanisms involved. Far field ingestion is illustrated in figure 64. The wall jet flowing outward from the impingement point under a single jet decreased in velocity with distance. Eventually the velocity has decreased to the point where the wall jet separates from the ground under the influence of buoyancy. The entrainment action of the wall jet causes an induced downward and inward flow that carries hot gases back to the vicinity of the inlet. The inlet temperature rise associated with the far field flow is small because there is considerable mixing before the flow reaches the inlet and the time required for the flow field to develop is such that this mechanism is seldom a problem in normal operations.

The fountain flow (fig. 65) is a more serious hot gas ingestion mechanism. When the wall jets flowing outward from the impingement points of adjacent jets meet, they are projected upward in a fountain flow. This flow can bring hot gases into the vicinity of the inlet. The path from the jet exit is short and the velocities are high, therefore, high temperatures can be brought to the vicinity of the inlet very quickly. The factors involved in determining the temperature rise from this source and what can be done to minimize it will be discussed further in later sections.

The ground vortex flow field (fig. 66) is the third basic mechanism. In STOL operation the wall jet flowing forward from the front jets is opposed by the free stream and rolled up into a horseshoe shaped ground vortex. This flow field transports the hot gases back to the vicinity of the inlet and can increase the inlet temperature.

Effect of Inlet Flow:

The inlet is a sink and in hovering draws air in from all directions. The extent to which this sink action influences the ingestion of hot gasses depends on the direction and energy of the hot flow. Hall, in reference 12, measured the effect of inlet flow on the temperature rise for two isolated lift engine simulators (fig. 67). In this case the fountain transports hot gases upward

between the simulated engines, but the temperature at the inlet face is not changed by the inlet flow. The air above and between the inlets is heated by mixing with the fountain flow and brought back to the inlet face by the induced downflow. Apparently, the sink effect of the inlet is not strong enough or close enough to the fountain to draw fountain air directly into the inlet.

Figure 68 on the other hand shows a case where the inlet flow is significant. In this case, the fountain flow impinges on the bottom of the configuration. Some hot air flows upward around the body and is in turn stopped and redirected by the wing and/or cannard. Boundary layers are generated on the various surfaces over which the fountain flows and leaves low energy hot air in the vicinity of the inlet where the sink effect can draw it in. In this case, the inlet flow is very important but the full mass flow does not have to be simulated.

Flow Control Devices:

Hall, in reference 40, investigated the effectiveness of various devices to control the flow and minimize hot gas ingestion. The most significant result of that work is shown in figures 69 and 70. The basic approach was to try to intercept the fountain flow and keep it from getting near the inlets. Flow diverters or "shields" were tried at the top of the body near the inlets and at the bottom of the body between the jets. Figure 69 shows that shields placed at the bottom of the body in the plane of the jet exits almost eliminated ingestion. On the other hand, shields at the inlet plane had almost no effect. The inlet temperature rise is the same as with the shields off. Apparently, the flow loses a lot of energy in flowing up around the sides of the body and there is a significant amount of dead hot air near the top of the body that the inlets can draw in.

With exit plane shields, however, the fountain flow is redirected before significant energy is lost and the laterally deflected flow (the "deflected upwash boundary" in fig. 69) carries the hot fountain flow away laterally. It also appears to contain sufficient energy to act as an entrainment mechanism and draw ambient air down from above, thus, insulating the inlet from the hot fountain flow. The inlet temperature rise shown with shield on in figure 69 is probably due to far field ingestion.

Tolhurst and Kelly show similar results in reference 41. Time histories of the operating conditions and inlet temperature for a six engine (J-85 engines) configuration are shown in figures 71 and 72. With the wing in the high position, low energy hot gas can easily be sucked into the "cruise engine" inlets and apparently large quantities of hot air find their way to the lift engine inlets. The time histories are for engine no. 3 and show very high and rapidly varying inlet temperatures that lead to compressor stall a few seconds after the jets are deflected to the vertical (fig. 71). With the wing in the low position, the fountain is apparently intercepted and redirected before it loses significant energy and low energy hot air is not left where it can be drawn into the inlets.

Kaemming and Smith in reference 42 present related results. In their flow visualization tests of a four jet configuration, they found that the impingment of the forward flowing wall jet on the nose gear created a nearly stagnant bubble of hot air immediately under the inlet from where it was drawn, by the sink effect, into the inlet.

From an aircraft design point of view, the lesson from the the above findings is to design the configuration so that the fountain is intercepted and redirected in a harmless direction before significant pockets of low energy hot air, that can be drawn into the inlets, are created.

From a testing point of view the lesson is that the space below and around the model must be kept clear of everything except legitimate parts of the model. The support system must be designed so that it does not affect the flow field under and near the model.

Effect of Forward Speed or Wind:

The ground vortex flow field is the principal additional mechanism that comes into play at forward speeds. The free stream that opposes the forward flowing wall jet and rolls it up into the ground vortex also carries hot gases from the top of the wall jet back to the inlet (fig. 73). As the speed is increased the distance from the impingement point back to the inlet and the time for mixing with the ambient air are reduced and the inlet temperature rises. Eventually a speed is reached where the ground vortex has been blown behind the inlet or has been reduced in depth so that all the hot flow is below the inlet and there is no temperature rise.

These trends are shown for a two-jet configuration in figures 74 and 75. With the jets in line with the free stream direction only the wall jet from the front jet is projected forward. Both the shields on and shields off cases show about a 5 or 6 degree increase in inlet temperature rise in the 5 to 8 knot speed range due to the free stream bringing heated air back to the inlet. At a speed of about 25 knots the ground vortex flow is blown aft and reduced in depth to the point that all the hot air is below the inlet.

However, with the jets side by side (fig. 75), the fountain flow between them is projected forward and upward and much more hot gas is available to be transported back to the inlet. The temperature is still rising at a speed of 25 knots, the highest speed investigated.

In this case the shields have no effect at forward speed, probably because part of the fountain flow the shields have deflected is projected directly into the oncoming free stream which carries it back to the inlet. Clearly the design of flow control devices must avoid this situtation.

This problem of minimizing the forward projection of hot gas flow has been addressed in the development of the AV-8B Harrier (ref. 43) by incorporating a spanwise fence at the forward end of the LIDs installation (fig. 76). Figure 77 shows that this fence greatly reduced the inlet temperature rise at low heights relative to that on the AV-8A (which uses the same engine/nozzle arrangement) but which did not have the spanwise fence. The higher rise experienced by the AV-8B model at intermediate heights is not explained.

Kuhn, in references 44 and 45, made an attempt at correlating the maximum inlet temperature rise experienced at forward speed. Figure 78 presents data for the four-jet, in-line configuration of reference 46. This model was designed so that either top or side inlets could be used and the wing could be placed in either a high or low position. The correlation (right side of figure 78) shows that the inlet temperature rise can be correlated with the inlet height for all four configurations. For the side inlets the height is measured to the lowest point on the inlet.

In reference 45 an attempt was made to correlate the inlet temperature rise data taken from several sources for configurations with side-by-side front jets (fig. 79). There is considerable scatter in hot gas ingestion data but the bulk of these data follow the same trend as the in-line configuration data of figure 78. However, because of the forward projecting fountain flow, these data show

maximum temperatures about four times as high as the configurations of figure 78 which had only a simple wall jet projected forward.

The DO-31 configuration (ref. 48) experienced a much higher inlet temperature rise than the other configurations including the XV-6A (ref. 47) which used the same engine. On the XV-6A (predecessor to the Harrier), the inlet temperature rise is dictated by the fan flow from the front nozzles. The rear nozzles are canted outward about 7 degrees more than the front nozzles so that the relatively cool fan air from the front nozzles shields the inlet from the hot rear exhaust. The cruise engines on the DO-31 are the same as the engine used in the XV-6A but the DO-31 also used the lift engine pods at each wing tip. These lift engines were canted aft to facilitate transition. As a result the nozzles of the lift cruise engines had to be deflected forward of the vertical in hovering to balance the thrust component of the lift engines. It is believed that this forward deflection of the cruise engine nozzles brought some of the hot rear exhaust forward where it could be ingested and caused the very high inlet temperature rises shown in figure 79. A more complete discussion of the DO-31 data is presented in references 45 and 49.

Additional data on a configuration with a forward projected fountain and with four inlet/wing-height combinations is presented in figure 80. The bulk of the data follow the trend presented in figure 79 (the side inlet high wing data are also used in figure 80) but the data for the top inlets with the high wing show considerably higher inlet temperature rises at the higher height than the rest of the data. It is speculated that the low energy hot air associated with the fountain flow up around the body may be responsible for these higher temperatures.

The Speed Required to Avoid Ingestion:

To avoid ingestion the inlet must be ahead of or above the hot gas cloud created by the interaction of the free stream with the wall jet and/or fountain flow projected ahead of the aircraft. Data on the forward projection of the ground vortex flow, which creates and defines the hot gas cloud, are presented in figure 39. These data are repeated in figure 80 along with the corresponding data on the depth of the cloud. All the investigations which attempted to determine the depth of the ground vortex flow field indicate the depth to be about half the forward projection. As with the forward projection Abbott's

moving model data (ref. 22) (no ground board boundary layer) showed the least depth. Th Schwantes investigation (ref. 24), which set out to simulate the boundary layer that would be present with atmospheric winds, showed the greatest depth. One can consider two boundaries then, one for hovering in a wind ($z/d = .45/V_e$) and one for STOL operation with no wind ($z/d = .27/V_e$). These boundaries are for single jet or in-line jet configurations.

The data from reference 46 on the speed at which the inlet temperature rise went to zero for the configuration with four jets in line are compared with these boundaries in figure 82. Because the data were taken in the wind tunnel with a ground board boundary layer they should correlate with the "wind" boundary. The estimated boundary appears to be about right but the investigation was not carried to high enough speeds or heights to be conclusive.

With two jets side by side a fountain flow will be projected forward and upward ahead of the configuration. This will increase the depth of the ground vortex flow field. Abbott, in reference 22, found that the depth was about doubled for the spacing he used. Unfortunately, there is no data on the effect of spacing ratio. (For very closely spaced jets it would be expected that the flow would approach that of a single jet of twice the area and the depth would only be increased by $\sqrt{2}$. Similarly, if the jets are very widely spaced they would be expected to produce two isolated flow fields with no increase in depth). More study of this area is needed.

The reference 46 data for the speed at which the inlet temperature rise went to zero for the configuration with two side-by-side jets forward are presented in figure 83 and compared with the estimated boundary for hovering in a wind (the data were taken in a wind tunnel with a boundary layer on the ground board). Again the estimated speeds appear about right, but the investigation was not carried to high enough speeds to be conclusive.

Time and Temperature Scaling:

The preceding discussion has considered mostly steady state data. In practice it takes some time for the flow field to develop. McLemore, in reference 50, presented a sequence of photographs (fig. 84) showing the development of the hot gas cloud. The model is a J-85 powered rig with a top inlet and at an exit height of two jet diameters in an outdoor facility. The concrete ground plane had a radius of 25 feet or about 25 jet diameters. A deflector was

attached to the exit so that the engine could be started and brought up to speed with the exhaust deflected aft of the vertical to avoid ingestion. At time zero the deflector was removed to bring the exhaust to the vertical. Simultaneously, at time zero a pulse of smoke was injected into the upward side of the jet and photographs were taken at .2 second intervals to record the development of the hot gas cloud. About 1 second was required for the cloud to develop to the point that smoke is brought back to the vicinity of the inlet and at this point the temperature was observed to begin to increase.

The photographs of figure 84 indicate that at 1 second the hot gas cloud had grown to a radius of about 25 diameters. The data of figure 80 would indicate that the fully developed hot gas cloud should have a radius of over 50 diameters with the stated cross wind condition. Apparently hot gas ingestion begins long before the hot gas cloud is fully developed.

Figure 85 presents a sketch of the developing hot gas cloud and a plot of the radius/diameter ratio as a function of time as measured from the photographs of figure 84. Abbott measured a similar time history of the hot gas cloud development for a 1 inch jet (ref. 22) but at about twice the effective velocity ratio. At one second Abbott's cloud had almost reached steady state size. This is to be expected because for the same exit velocity the distances involved in a scale model are reduced by the scale and the relative growth would be increased by the scale.

Although the hot gas cloud has reached a radius of 25 feet by the time ingestion starts, the ingestion apparently does not arise from the hot gases flowing out to the ground vortex and then being transported back to the inlet. The flow from the ground vortex back to the inlet should be moving at about the free stream velocity and it would take about 2 seconds (at 13 fps) for the hot gases to traverse the 25 feet back to the inlet even if they got to the ground vortex instantaneously. The time required is probably related to the height of the inlet and the speed at which the air mixing with the top edge of the wall jet rises to the height at which it can be blown back to the inlet. This appears to be an area where our basic understanding of the flow mechanisms is very weak and additional research is required.

Some observations with regard to time scaling in large and small scale hot gas testing are presented in figure 86. Two ingestion paths are considered. Path I involves fountain flow and Path II the hot gas cloud blown back at forward speeds or by winds. For Path I the distance from the exit to the inlet

is short, perhaps 8 to 12 feet for a 1 foot diameter nozzle. The velocity of the hot gases over most of this distance is large, approaching jet velocity in the wall jet before it enters the fountain, and the time required for the hot gases to reach the vicinity of the inlet is very short even at full scale. Hot gas ingestion will be almost instantaneous, or put another way, the inlet temperature should follow the build up of thrust and exit temperature with negligible delay. Measuring the time delays in this class of flow at small scale would require very high response instrumentation.

For Path II the velocities vary from almost jet velocity in the wall jet near the inpingement point to free stream velocity in the return path to the inlet. The data of figures 84 and 85 indicate that the path effective length must be about 10 to 15 feet. At one-tenth scale time lag in the build-up of the hot gas cloud would be one-tenth of those full scale and if the conditions involved in a landing approach representing, say 3 fps sink speed, at full scale are to be duplicated the model sink rate must be 30 fps (assuming full scale exhaust velocity and temperature). This results in the incremental angle of attack at the wing due to sink speed being 10 times that full scale! This indicates the problems of simultaneously matching the hot gas flow fields and those for lift development. Small scale testing requires scaling velocities, temperatures and times in combinations dictated by the importance of the parameters to be matched. The British (ref. 51) are wrestling with these problems and have developed sophisticated test apparatus (fig. 87) to study these areas.

Bore, ref. 51, has also pointed out that the temperature scaling law used until recently needs to be revised. It has generally been assumed that the inlet temperature rise is proportional to the excess of exit temperture over ambient temperature. And this assumption has been used in the present paper. Milford (refs. 53 and 54) has postulated that the temperature rise should be related to the heat flux and developed the revised expression for inlet temperature rise shown at the top of figure 88 (from ref. 51). The experimental data appear to confirm that the temperature rise is a function of the jet to ambient temperature ratio, but Bore suggests that the exponent may be different. Again the British are working on this problem.

Thrust Reversers:

Thrust reversing probably creates the most difficult hot gas ingestion control problem. In order to develop a high deceleration force, the flow from the engine exhaust must be deflected forward as much as possible. This increases the forward projection of the hot gas cloud and increases the speed at which the thrust reverser must be turned off to avoid ingestion.

Amin and Richards investigated the hot gas ingestion problem for a fighter-type aircraft (ref. 55) and found that the lateral cant (outward splay) angle of the reverser flow was an important parameter. Without cant their results indicated that ingestion would occur at about touchdown speed. By canting the flow out 40 degrees, the speed for ingestion was almost halved (fig. 89).

RECOMMENDATIONS:

The recommendations with respect to hot gas ingestion research can be grouped into three areas, hot gas cloud development at forward speeds, fountain control and time and temperature scaling problems.

1) Primary emphasis should be placed on the rate of growth and the character of the hot gas cloud to develop a better understanding of the mechanisms that bring hot gases to the inlet. Figure 90 illustrates the key elements to be included in the study. Time histories of the temperature and velocity distribution in the developing hot gas cloud should be made for single and side-by-side jet arrangements through a range of jet pressure ratios, effective velocity ratios and heights. Jet deflection angles and outward cant angles should also be included to cover thrust reverser configurations. Accurate determination of the character of the developing hot gas cloud will require tests at moderate to large scale.

The flow surveys should be supplemented by inlet temperature measurements for various inlet locations and inlet flow rates. The free stream velocities should be chosen to accurately determine the speed needed to avoid hot gas ingestion.

2) A separate program to expand the data base and understanding of the fountain flow and means of its control (LIDs, shields, etc.) in hover flight should be undertaken. This program should also contain both flow field studies and inlet temperature rise measurements.

3) The problems of dynamic testing and temperature scaling are being studied by the British. It is recommended that the possibility of a cooperative program with them to continue the work in this area be explored.

PROPULSION SYSTEM SIMULATION

A variety of techniques have and are being used for simulating the jet exhaust and inlet flow of the propulsion system in model testing. These range from simple high pressure jets through ejectors to the use of small jet engines. There are advantages and disadvantages connected with each. Koenig, in reference 56, presents an excellent review of the equipment and techniques available and the pros and cons of their use. There is no need to duplicate that review here. Instead this section will draw on that review and present some suggestions and observations on the equipment that should be used in connection with the investigations recommended above.

Single Jet Suckdown Investigation:

The direct use of high pressure air will be the best way to simulate the jet for the two investigations (figs. 15 and 16) recommended with respect to single jet suckdown. Typically the air supply at most facilities is stored at pressures of from 20 to 300 atmospheres and the pressure must be reduced to the nozzle pressures of 1.5 to 4 needed for the tests. Usually, a series of perforated plates and screens are used to reach the desired pressure and achieve good quality nozzle flow. Typical designs are shown in figure 91. Where space is available, as it is for the single jet suckdown investigations being considered here, the concept shown in figure 91-b will be preferred (but without the jet deflection and tunnel floor).

The "turbulence screens" shown in figure 91-b should be of fine mesh and chosen to achieve a uniform velocity distribution at the nozzle, as well as to achieve as low a turbulence at the nozzle as possible. For the investigations of the effect of turbulence and non-uniform exit distribution, the nozzle should be designed so that grids to produce the desired turbulence and the "screens" of non-uniform density, or similar device, to produce the desired changes in exit velocity profile can be inserted a short distance upstream of the nozzle exit. Devices similar to those used in the investigation of reference 11 may be suitable. The schedule of the investigation must include adequate time for the development and documentation of the desired jet characteristics.

Multiple Jet Ground Effect Investigation:

The direct use of high pressure air is also recommended for the multiple jet investigation suggested in figures 31 and 32. And again the large plenum chamber design of figure 91-b should be used, this time with provision to interchangeably mount twin and other multiple nozzle configurations with various spacings on the basic chamber.

Ground Vortex Investigation:

High pressure air is also preferred for the ground vortex (fig. 42) investigation. In this case, however, the nozzle should be installed in a body so that the body pressures can be used to evaluate the effects of the ground board boundary layer (tests with belt running and stopped). In order to install the nozzle in the body a design of the type shown in figure 91-a will be needed. A certain amount of 'cut and try' is required to get such a nozzle assembly to give a good flow particularly for several jet deflections. Again the schedule must provide adequate time for the development and documentation of the nozzle flow.

BLC Ground Board Development:

The same body/nozzle model (or a similar model) could be used to produce the ground vortex flow field needed in the development of the boundary layer control ground board concept suggested in figures 49 and 57. The 7 by 10 foot tunnel could be used as a 1/12 scale model of the 80 by 120 foot test section and this would indicate a nozzle diameter on the model of about 1 inch to represent a single J-97 exhaust in the big tunnel.

Jet Configuration Effects Investigation:

A different model would be required for this study which is sketched in figure 58. Again direct use of high pressure air would be the choice and the nozzles would have to be of the type shown in figure 91-a and very carefully designed and developed.

Downwash Investigation:

In as much as it is suggested that down wash data should be obtained by taking advantage of and expanding slightly complete model tests that come available for other purposes, special development of propulsion simulators for this purpose is not required. The characteristics of the flow from the propulsion units used should, however, be carefully documented including, if possible, the trajectory that the jets take under the influence of the free stream because the position of the jet wake is important to the downwash.

Hot Gas Ingestion Study:

This investigation requires heated exhaust flow, and for part of the study a sucking inlet is needed. In order to be able to vary the inlet and exit locations, a remote source of hot flow and a remote pump to power the inlet are desirable. Also the accuracy of the flow field studies will be improved if the nozzles, and, therefore, the associated wall jet flow is not too small. These considerations suggest that jet engines such as the J-97's should be used - one to power the exit(s) and one to pump the inlet.

Tests of Specific Aircraft Configuratons:

The previous sections have discussed the propulsion units needed for the several general research investigations recommended above. As such they are concerned only with improving our understanding of the ground effect flow fields and some of the considerations of testing complete models of specific configurations could be ignored. Notably the inlet flow need not be simulated in any of the above investigations except the hot gas ingestion study.

The inlet flow imposes forces and moments on the configuration due to the momentum of the inlet mass flow. If the inlet is on the axis through the center of gravity and the model is at zero side slip, only a drag force is generated. In the more general case the inlet flow can contribute force and moment increments on all three axes. However, there is no evidence nor any reason to believe that ground proximity will change these inlet effects.

Ejectors and high pressure air driven fans have been used to power complete models in small scale testing but corrections have to be made for the fact that

the inlet mass flow was less than it should be and the nozzle pressure ratios are often not duplicated. At large scale, small jet engines are often used but the engines are often larger than a scale model of the full scale engine would be with the result that the aerodynamic lines of the configuration are often violated.

Figure 92 presents the results of a preliminary examination of the possibility of powering a complete model with remotely mounted jet engines. In this case the aerodynamic line of the Kestrel (predecessor to the Harrier V/STOL aircraft) were used and it was assumed that two J-97 engines would be employed - one to pump the inlet and one to supply hot exhaust to the exits. As can be seen the hot ducting takes up all the available space in the fuselage in the vicinity of the wing and nozzles and it would be necessary to duct the inlet flow out the top of the fuselage ahead of the wing. Thus the aerodynamic lines of the top of the fuselage from ahead of the wing aft are violated and the vertical tail is eliminated. Some jet induced interference investigations in and out of ground effect might be attempted with this type of model but it could not be used for any lateral/directional investigations and even the downwash at the tail would be affected. Another problem with the concept shown in figure 92 is that all the jets would operate at the same temperature and pressure ratio. Many aircraft configurations have mixed propulsion systems with part of the thrust from the hot exhaust and part from fan flow or a remotely mounted auxillary unit. A more versatile propulsion simulation system is rquired for large subscale models.

The Compact Multimission Aircraft Propulsion Simulator (CMAPS) (fig. 93) is being developed to fill part of this role. The concept and characteristics of CMAPS are reviewed in reference 57. Four of these units could be used to power the model show in figure 92 and the inlet flow and nozzle pressure ratios could probably be matched. However, there is no provision for heating the exhaust and, therefore, a CMAPS powered model could not be used for hot gas ingestion studies.

Another possibility that should be investigated is the use of ejectors with provision to add heat to the exhaust flow. It would not be possible to simulate the full inlet flow but the available data (fig. 67 and 68) suggests that full inlet flow is not required. Part of the hot gas ingestion investigation recommended above should be designed to further explore the level of inlet flow required to obtain reliable inlet temperature rise data.

MODEL SUPPORT SYSTEM CONSIDERATIONS

The primary consideration with regard to the support system is to prevent the support system from altering the flow under and around the model. This suggests that the model should be supported from above and behind as sketched in figure 49.

The presence of obstructions under the model can alter the flow. Two extreme examples are shown in figures 93 and 94 (refs. 58 and 59). In reference 58 the upwash velocities in the fountain between two jets was measured with and without a reflection plate at the "plane of symmetry". With the reflection plate installed the flow adheres to the reflection plate and reaches higher values near the plane of symmetry than when the reflection plate is removed (fig. 94). Apparently the reflection plate prevents the exchange of energy across the plane of symmetry that is normally present. The same result was observed by Folley (ref. 16) who found that a vertical trip only as high as the thickness of the wall jet flowing outward from the impingement point of the jet would produce the same result.

In reference 59 the inlet temperature rise due to fountain flow was measured with and without a reflection plate at the plane of symmetry between two jets. The results (fig. 95) are dramatically different. Without the reflection plate the temperatures are very high with the jets close to the ground but drop off rapidly and go to zero when the inlets are raised above the top of the fountain flow. With a reflection plate the inlet temperature rise is much smaller at the low heights but increases as the height is increased. Apparently, the fountain flow adheres to the plate and is carried to much higher heights.

Obviously, struts or obstructions on the plane of symmetry between jets are to be avoided. Nothing is known about the effects of struts or obstructions at other points in the flow but, in general, obstructions to the wall jets flowing outward from the impingment points should be avoided or faired to minimize their effect on the flow. A useful addition to the multiple jet fountain investigation and to the hot gas ingestions suggested above would be to investigate the effects of realistically located model support struts.

CONCLUDING REMARKS

The basic flow mechanisms that produce the ground effects experienced by V/STOL and STOL aircraft are known but there are apparently details of the mechanisms that are not adequately understood. Even for the simplest case, the suckdown on a single centrally located jet, there are differences in the data from various investigators that cannot be explained. In other areas such as the ground vortex and hot gas cloud formation experienced in STOL operation there is circumstantial evidence to indicate that parameters such as pressure ratio and the ground board boundary layer have a major impact on the result but there is no data base for quantifying these effects.

It is doubtful that additional force tests alone will be of much help in clarifying the picture in most areas. A more fundamental approach is needed. Carefully structured investigations to isolate and document the effects of key parameters on the flow field under and around the configuration as well as on the forces amd moments induced are required. Additional comments on a few of the most important of the several areas discussed above are given below.

1) Resolution of the anomolies in the single jet suckdown area should be given first priority because the factors involved are fundamental to some of the other more complex areas. Both of the investigations sketched in figures 15 and 16 and discussed on page 8 should receive high priority.

2) The fountain flow produced by multiple jet configurations in hover and how to control it and its attendant side effects, are important because of the effects they have on lift and hot gas ingestion. The problem is complicated by the myriad of variables, jet arrangement and spacing, body contour, LIDS, etc. There are scraps of data on the effect of most of these variables but before these data can be put togetheer to form a good basis for estimating the multiple jet induced lift and moments, a better understanding of the flow field between the jets and the fountain is needed. The approach sketched in figures 31 and 32 and discussed under item 1 on page 13 is the recommended next step in this area.

3) The ground vortex flow field is important to jet lift V/STOL and jet flap configurations as well as thrust reverser operation on conventional aircraft and STOL fighters. It also creates a problem in STOL testing if precautions are not taken to remove the boundary layer on the ground board. There is some evidence to indicate that interaction of the ground vortex flow, the approaching boundary layer on the ground board and the flow around the wing

can lead to fluctuating rolling moments with thrust reversers activated. A fundamental investigation such as that sketched in figure 42 and discussed on page 19 is needed to better understand the factors involved.

4) A moving belt ground board, such as is used in small wind tunnels is not practical for the 40 by 80 and 80 by 120 foot test sections because of size and because of the hot exhaust from the jet engines used in these facilities. A boundary layer removal system will be required. It is suggested that the ground vortex signature could be used to position the BLC slot for varying test conditions. The general concept is illustrated in figure 51 and discussed on pages 20-21. An experimental setup to investigate and develop the concept is sketched in figure 57 and discussed on page 24.

5) The ground vortex flow field is also one of the primary mechanisms involved in hot gas ingestion. A better understanding of the development of the hot gas cloud created by the ground vortex flow field is needed. A sketch showing the elements and features of a recommended investigation of developing hot gas cloud is presented in figure 90 and discussed on page 36.

REFERENCES

1. Henderson, C., Clark, J. and Walters, M., V/STOL Aerodynamics and Stability and Control Manual", NADC-80017-60, Jan. 1980.
2. Wyatt, L. A., "Static Tests of Ground Effect on Planforms Fitted With a Centrally-Located Round Lifting Jet", Ministry of Aviation CP749, June 1962.
3. Hall, G. R., "Scaling of VTOL Aerodynamic Suck-down Forces", AIAA Journal of Aircraft, July-August 1967, pp. 393-394.
4. Spreeman, K. P. and Sherman, I. R., "Effects of Ground Proximity on the Thrust of a Simple Downward-Directed Jet Beneath a Flat Surface", NACA TN 4407, Sept. 1958.
5. Gentry, G. L. and Margason, R. J., "Jet-Induced Lift Losses on VTOL Configurations Hovering In and Out-of-Ground Effect", NASA TN D-3166, Feb. 1966.
6. Vogler, R. D., "Interference Effect of Single and Multiple Round and Slotted Jets on a VTOL Model in Transition", NASA TN D-2380, Aug. 1964.
7. Christiansen, R. S., "A Large Scale Investigation of VSTOL Ground Effects", AIAA-84-0366, Jan. 1984.
8. Yen, K. T., "An analytical Solution of Lift Loss for a Round Planform with a Central Lifting Jet", AIAA-81-0011, 1981.
9. Ludwig, G. R., "An Investigation of the Flow in Uniform and Nonuniform Jets Impinging Normally on a Flat Surface", AIAA-ICAS-64-796, AIAA-CASI Joint Meeting, Ottawa, Canada, Oct. 1964.
10. Stewart, V. R. and Kuhn, R. E., "A Method for Estimating the Propulsion Induced Aerodynamic Characteristics of STOL Aircraft in Ground Effect", NADC-80226-60, Aug. 1983.
11. Lummus, J. R. and Smith, E. W., "Flow-Field Characteristics and the Effect of Jet-Exhaust Simulation for V/STOL Vehicles Near the Ground", Proceedings of the NADC V/STOL Aircraft Aerodynamics Symposium, Naval Postgraduate School, Monterey Calif., May 1979, pp. 293-313.
12. Hall, G. R. and Rogers, K. H., "Recirculation Effects Produced by a Pair of Heated Jets Impinging on a Ground Plane", NASA CR-1307, May 1969.
13. Yen, K. T., "On the Vertical Momentum of the Fountain Produced by Multi-Jet Vertical Impingement on a Flat Ground Plane", NADC-79273-60, Nov. 1979.

14. Kuhn, R. E., "An Engineering Method for Estimating the Induced Lift on V/STOL Aircraft Hovering in and out of Ground Effect", NADC-80246-60, Jan. 1981.
15. Foley, W. H. and Sansone, J. A., "V/STOL Propulsion-Induced Aerodynamic Hover Calculation Method", NADC-78242-60, Feb. 1980.
16. Foley, W. H. and Finley, D. B., "Fountain Jet Turbulence", AIAA-81-1293, June 1981.
17. Spong, E. D. et al., "V/STOL Jet-Induced Interactions", Proceedings of NADC Workshop on V/STOL Aerodynamics, Naval Post Graduate School, Monterey, Calif., May 1979, pp. 440-508.
18. Wohllebe, F. A. and Migdal, D., "Some Basic Test Results of V/STOL Jet-Induced Lift Effects in Hover", AIAA-79-0339, Jan. 1979.
19. Johnson, D. B. et al., "Powered Wind Tunnel Testing of the AV-8B: A Straightforward Approach Pays Off", AIAA-79-0333, Jan. 1979.
20. Williams, J., Butler, S. F. J. and Wood, M. N., "The Aerodynamics of Jet Flaps", RAE R & M No. 3304, Jan. 1961.
21. Schwantes, E., "The Recirculation Flow Field of a VTOL Lifting Engine", NASA TT F-14912, June 1973.
22. Abbott, W. A., "Studies of Flow Fields Created by Vertical and Inclined Jet When Stationary or Moving Over a Horizontal Surface", RAE CP No. 911, 1967.
23. Weber, H. A. and Gay, A., "VTOL Reingestion Mocel Testing of Fountain Control and Wind Effects", Prediction Methods for V/STOL Propulsion Aerodynamics, Vol. 1, Naval Air Systems Command, pp. 358-380, 1975.
24. Colin, P. E. and Olivari, D. "The Impingement of a Circular Jet Normal to a Flat Surface with and without Cross Flow", AD688953 European Research Office, United States Army, Jan. 1969.
25. Joshi, P. B., "Generic Thrust Reverser Technology for Near Term Application", Northrop Study for the USAF, to be published.
26. Turner, R. T., "Ground Influence on a Model Airfoil with a Jet-Augmented Flap as Determined by Two Techniques", NASA TN D-658, Feb. 1961.
27. Werle', Henri, "Simulation de L'Effet de Sol au Tunnel Hydrodynamique (Ground Effect Simulation at the Water-Tunnel)", La. Rech. Aérospatiale, no. 95, July-Aug. 1963, pp. 7-15.

28. Turner, T. R., "A Moving-Belt Ground Plane for Wind-Tunnel Ground Simulation and Results for Two Jet-Flap Configurations", NASA TN D-4228, Nov. 1967.

29. Turner, T. R., "Endless-Belt Technique for Ground Simulation", NASA SP-116, April 1966, pp. 435-446.

30. Hackett, J. E. and Boles, R. A., "High Lift Testing in Closed Wind Tunnels", Proceedings of the AIAA 8th Aerodynamic Testing Conference, Bethesda, Md., AIAA 74-641, July 8-10, 1974.

31. Hackett, J. E. et al., "Ground Simulation and Tunnel Blockage for a Jet-Flapped Basic STOL Model Tested at Very High Lift Coefficients", NASA CR-137857, March 1976.

32. Private discussions with Ph. Poisson-Quinton.

33. Stevens, V. C. and Wingrove, R. C., "STOL Ground Effect Determined from Flight Data", AIAA-77-576, June 1977.

34. Crowder, J. P., Goldhammer, M. T. and Smyth, D. N., "STOL Aircraft Transient Ground Effects. Pt. II. Experimental Techniques Feasibility Study", NASA CR-137,767, Nov. 1975.

35. Lowry, J. G., Riebe, J. M. and Campbell, J. P., "The Jet Augmented Flap", IAS Preprint No. 715, Jan. 1957.

36. McCormick, B. W., "Aerodynamics of V/STOL Flight", Academic Press, 1967.

37. Vogler, R. D., "Wind Tunnel Investigation of a Four Engine Externally Blowing Jet-Flap STOL Airplane Model", NASA TN D-7034, Dec. 1970.

38. Mineck, R. E. and Schwendamann, M. F., "Aerodynamic Characteristics of a Vectored-Thrust V/STOL Fighter in the Transition-Speed Range", NASA TN D-7191, May 1973.

39. Margason, R. J. et al., "Wind-Tunnel Investigation at Low Speed of a Model of the Kestrel (XV-6A) Vectored-Thrust V/STOL Airplane", NASA TN D-6826, July 1972.

40. Hall, G. R., "Model Tests of Concepts to Reduce Hot Gas Ingestion in VTOL Lift Engines", NASA CR-1863, July 1971.

41. Tolhurst, W. H., Jr. and Kelly, M. W., "Characteristics of Two Large-Scale Jet-Lift Propulsion Systems", NASA SP-116, April 1966, pp. 205-228.

42. Kaemming, T. A. and Smith, K. C., "Techniques to Reduce Exhaust Gas Ingestion for Vectored-Thrust V/STOL Aircraft", AIAA-84-2398, Oct. 1984.

43. Clark, R. S. and Vasta, S. K., "Development of the AV-8B Propulsion System", AIAA-84-2426, Oct. 1984.

44. Kuhn, R. E., "Design Concepts for Minimizing Hot-Gas Ingestion in V/STOL Aircraft", Journal of Aircraft, Vol. 19, Oct. 1982, pp. 845-850.

45. Kuhn, R. E., "Hot Gas Ingestion and the Speed Needed to Avoid Ingestion for Transport Type STO/VL and STOL Configurations," AIAA-84-2530, Oct. 1984.

46. McLemore, H. c. and Smith, C. C., Jr., "Hot-Gas Ingestion Investigation of Large-Scale Jet VTOL Fighter Models", NASA TN D-4609, 1969.

47. McKinzie, G. A. et al., "P-1127 (XV-6A) VSTOL Handling Qualities Evaluation", Air Force Flight Test Center FTC-TR-68-10, Aug. 1968.

48. Holzhauser, C. A. et al., "A Flight Evauation of a VTOL Jet Transport Under Visual and Simulated Instrument Conditions", NASA TN D-6754, March 1972.

49. Gittner, U. et al., "Interaction Between Airframe Powerplant Integration and Hot Gas Ingestion for Jet-Lift V/STOL Transport Aircraft", AGARD 31st Flight Mechanics Panel Meeting on Integration of Propulsion System in Airframe, Sept. 1967.

50. McLemore, H. C., "Considerations of Hot-Gas Ingestion for Jet V/STOL Aircraft", NASA SP-116, April 1966, pp. 191-204.

51. Bore, C. L., "Ground Based Testing Without Wind Tunnels", AGARD Report No. R-710, Special Course on V/STOL Aerodynamics, May-June 1984.

52. Abbott, W. A., "Estimation of Intake Temperature During V/STOL Operation from Model Tests." NGTE Note NT.600, March 1966.

53. Milford, C. M., "Scaling Factors for Hot Gas Recirculation", BAe-KAD-N-GEN-2787, Aug. 1981.

54. Milford, C. M., "Further Consideration of Recirculation Temperature Scaling Laws", BAe-KAD-N-GEN-2844, June 1982.

55. Amin, N. F. and Richards, C. J., "Thrust Reverser Exhaust Plume Reingestion Model Tests", Journal of Aircraft, Vol. 21, June 1984, pp. 401-407.

56. Koenig, D. G., "V/STOL Wind Tunnel Testing", AGARD-R-710, Special Short Course on V/STOL Aerodynamics, May-June 1984, pp. 9-1 to 9-71.

57. Fearn, R. L. and Weston, K. P., "Induced Velocity Field of a Jet in a Cross Flow", NASA TP-1087, 1978.

58. Hertel, H., "Wandstromungen und Aufstrome aus der Umlenkung von Freistrahlgruppen (Wall Flows and Up-Streams Due to the Diversion of Free Jet Groups)", Fortschritt Berichte VDI Zeitschrift Fortschr, Vol. 12, No. 11, pp. 1-72, June 1966.

59. Ryan, P. E. et al., "A Generalized Experimental Investigation of Hot-Gas Recirculation and Ingestion for Jet VTOL Aircraft", NASA CR-1147, 1968.

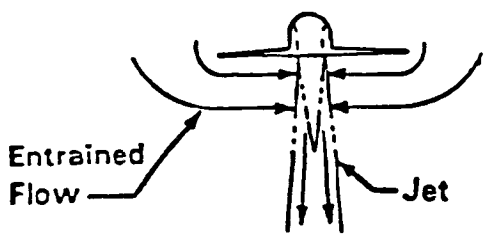

Hover

Out-of-Ground-Effect

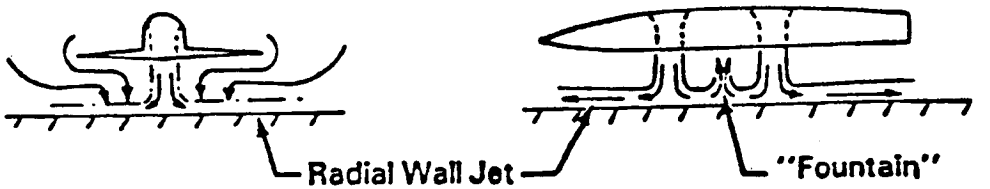

Single Jet

Multiple Jets

Hover In-Ground-Effect

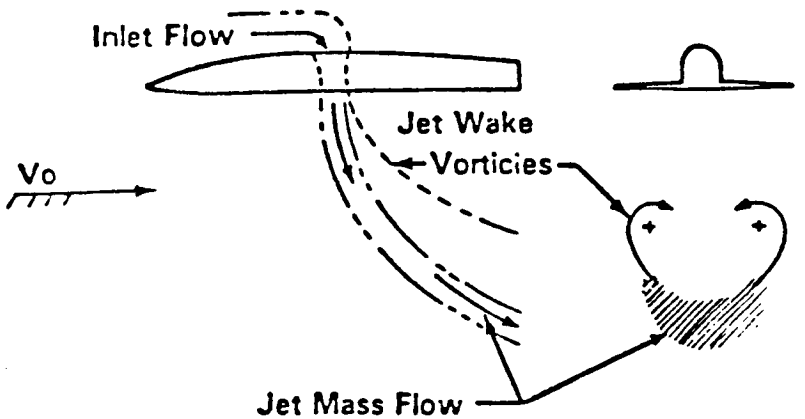

Transition Out-of-Ground-Effect

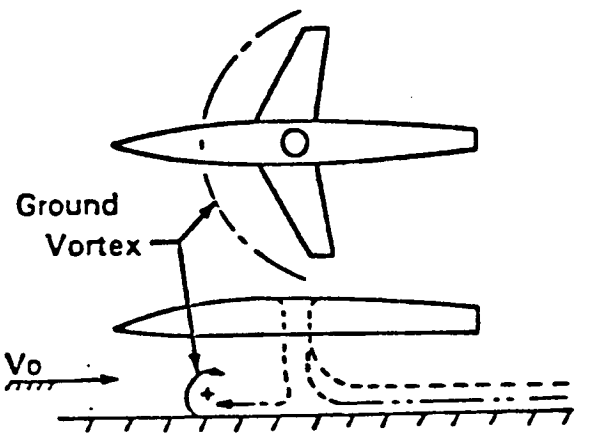

Transition In-Ground-Effect
(STOL Operation)

Figure 1.- Basic Flow Fields.

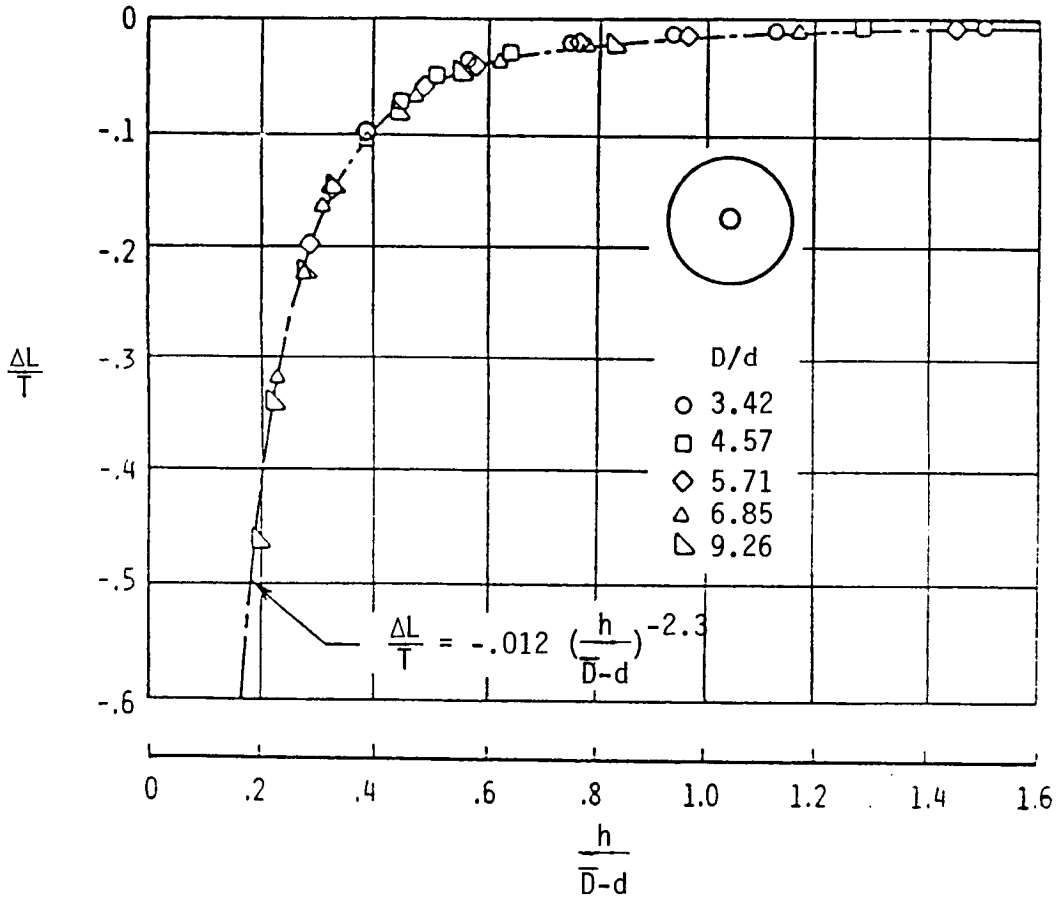

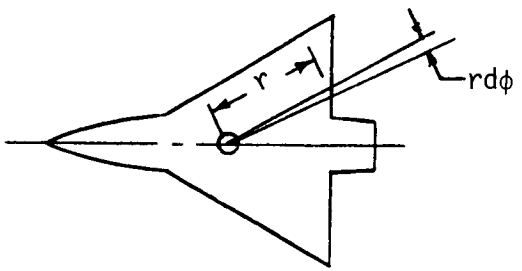

Definition of Planform
"Effective" Diameter

Figure 2.- Data of Reference 2 (Wyatt) NPR = 1.5

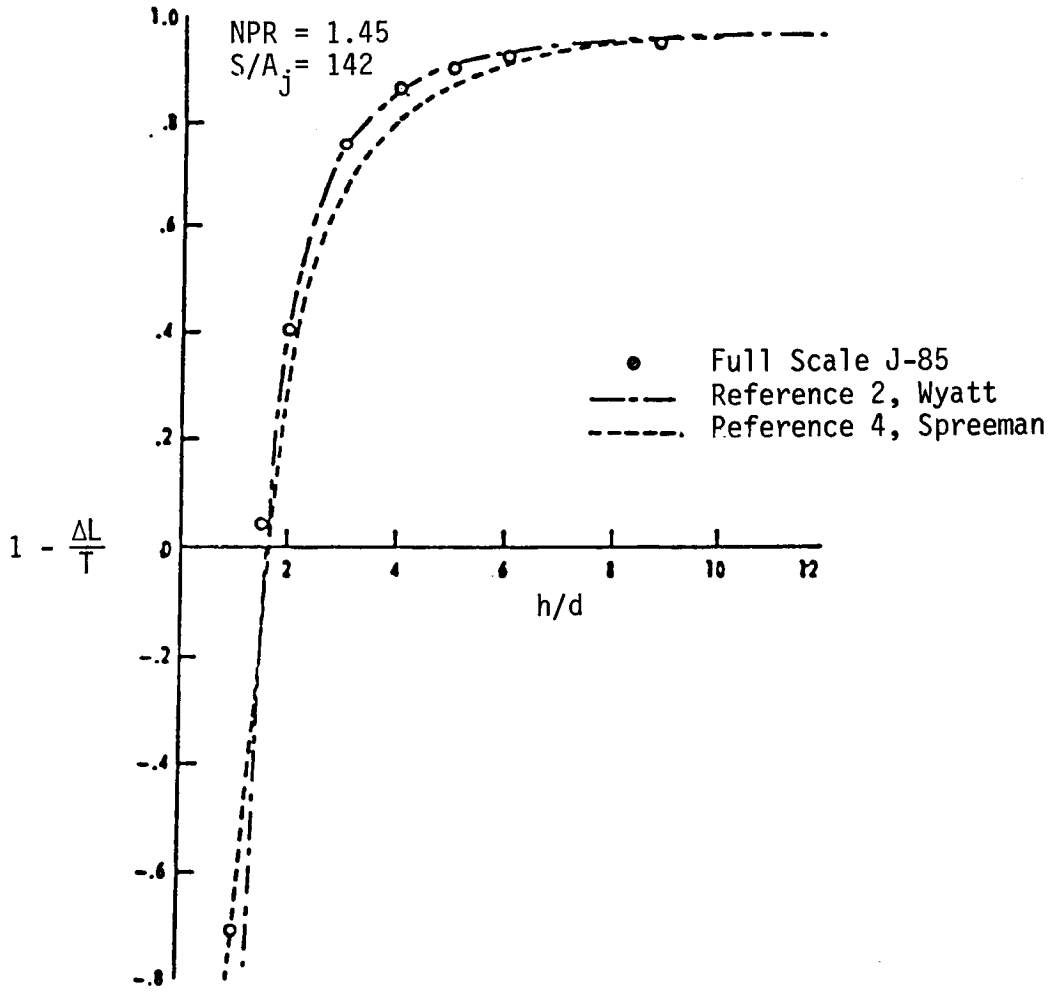

Figure 3.- Comparison of suckdown measured at large scale (Ref. 3) with results from two small scale tests.

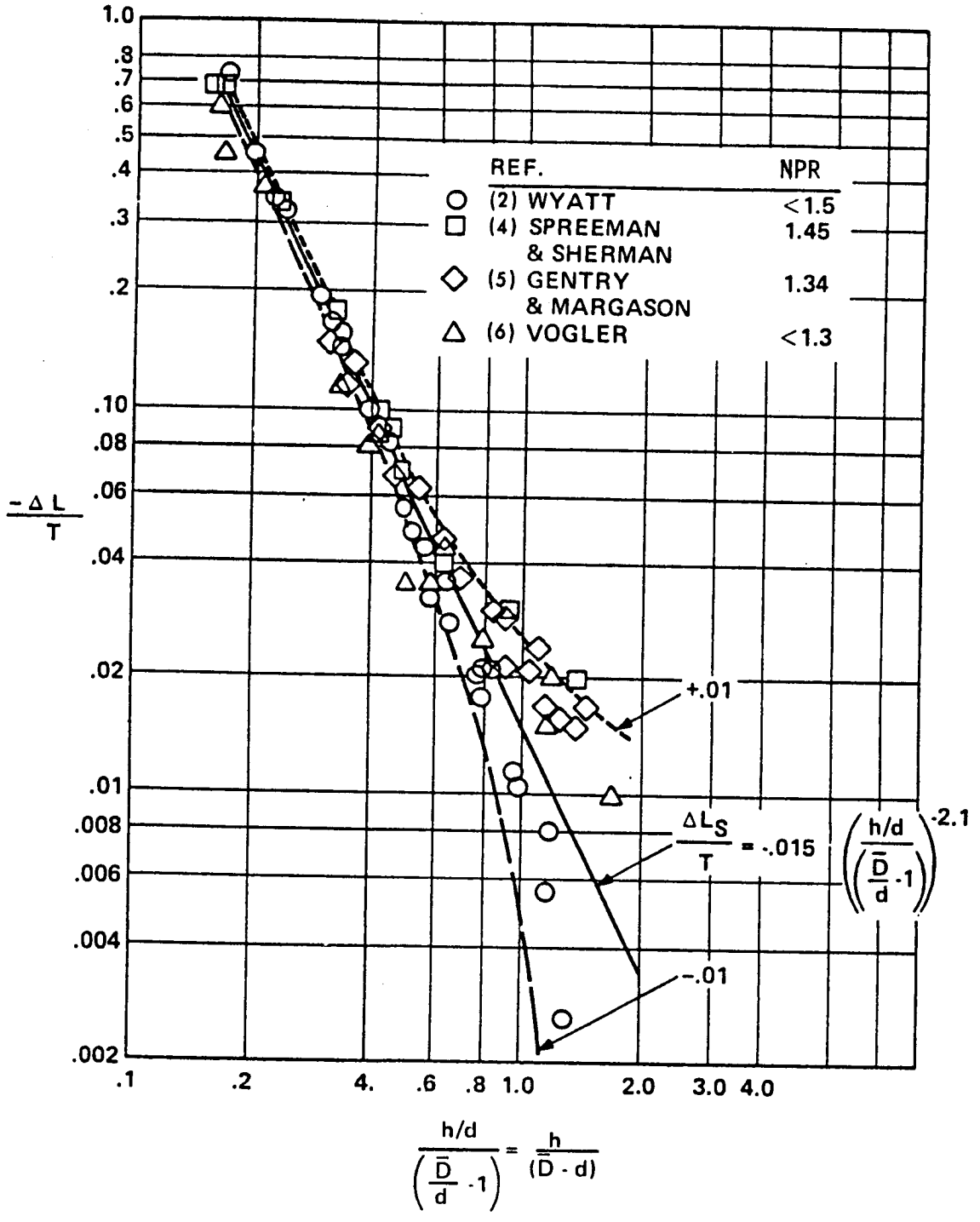

Figure 4.- Ground-induced lift loss on single jet configuration at low pressure ratios. (Ref. 1)

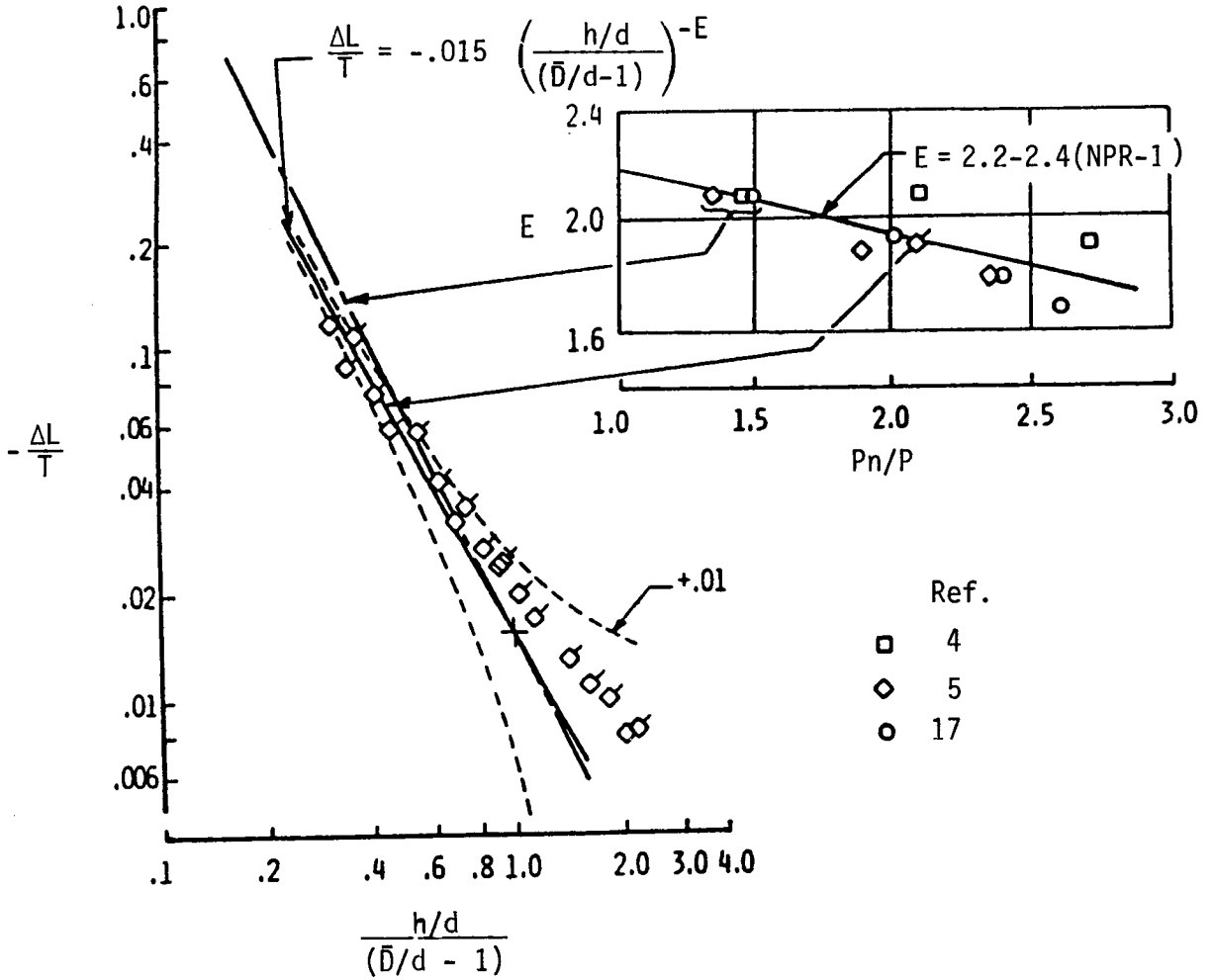

Figure 5.- Effect of pressure ratio on single-jet configuration lift loss in ground effect. (Ref. 1)

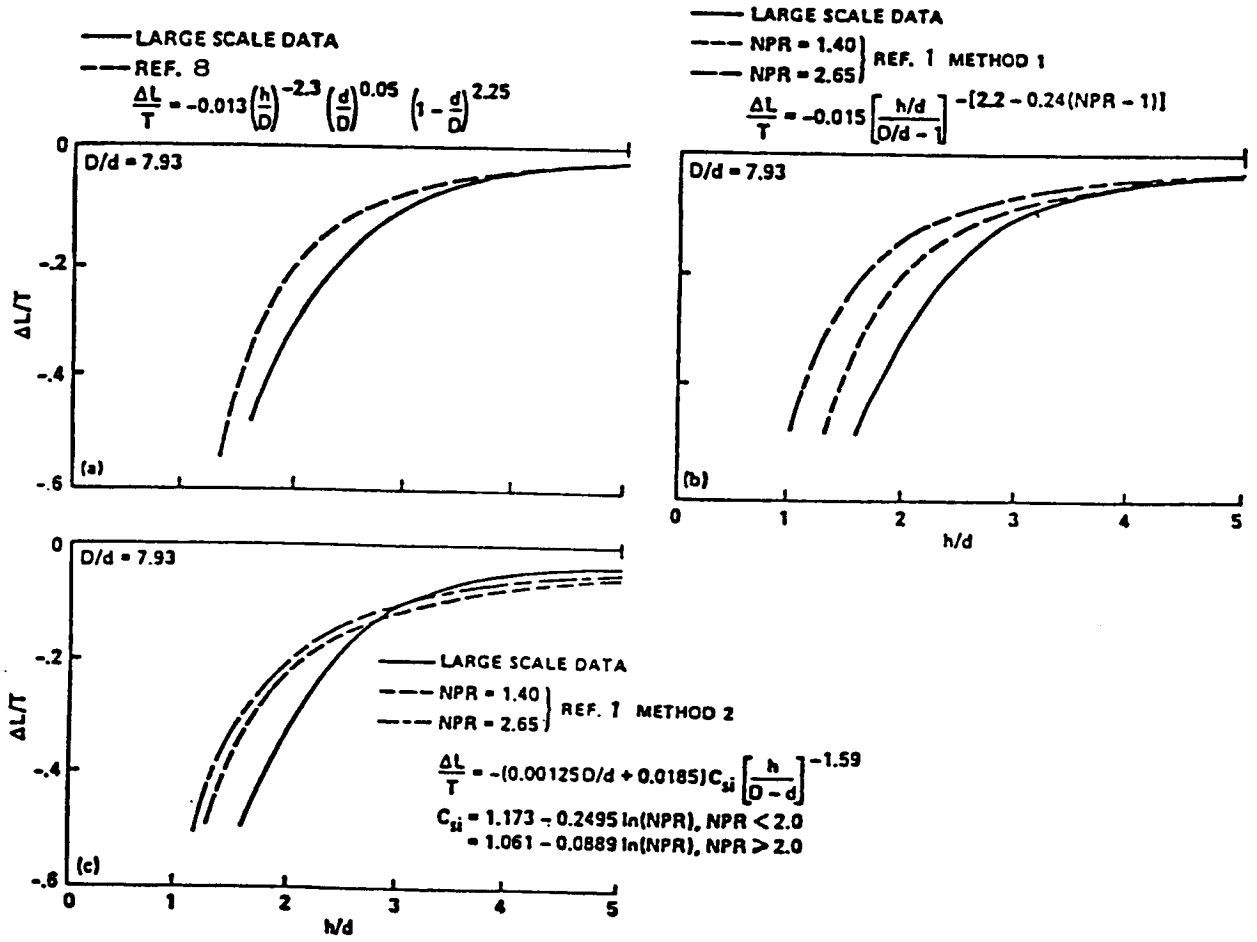

Figure 6.- Comparison of large-scale data with predicted lift losses. (a) Analytical solution; (b) empirical solution I; (c) empirical solution II. (Ref. 7)

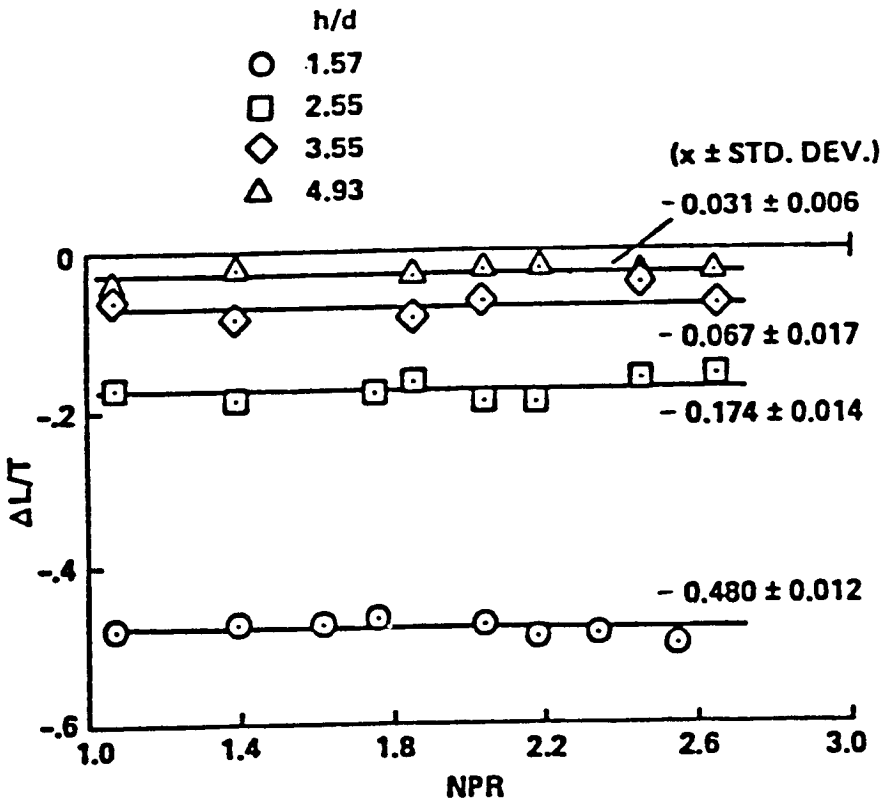

Figure 7.- Effects of pressure ratio on lift loss. (Ref. 7)

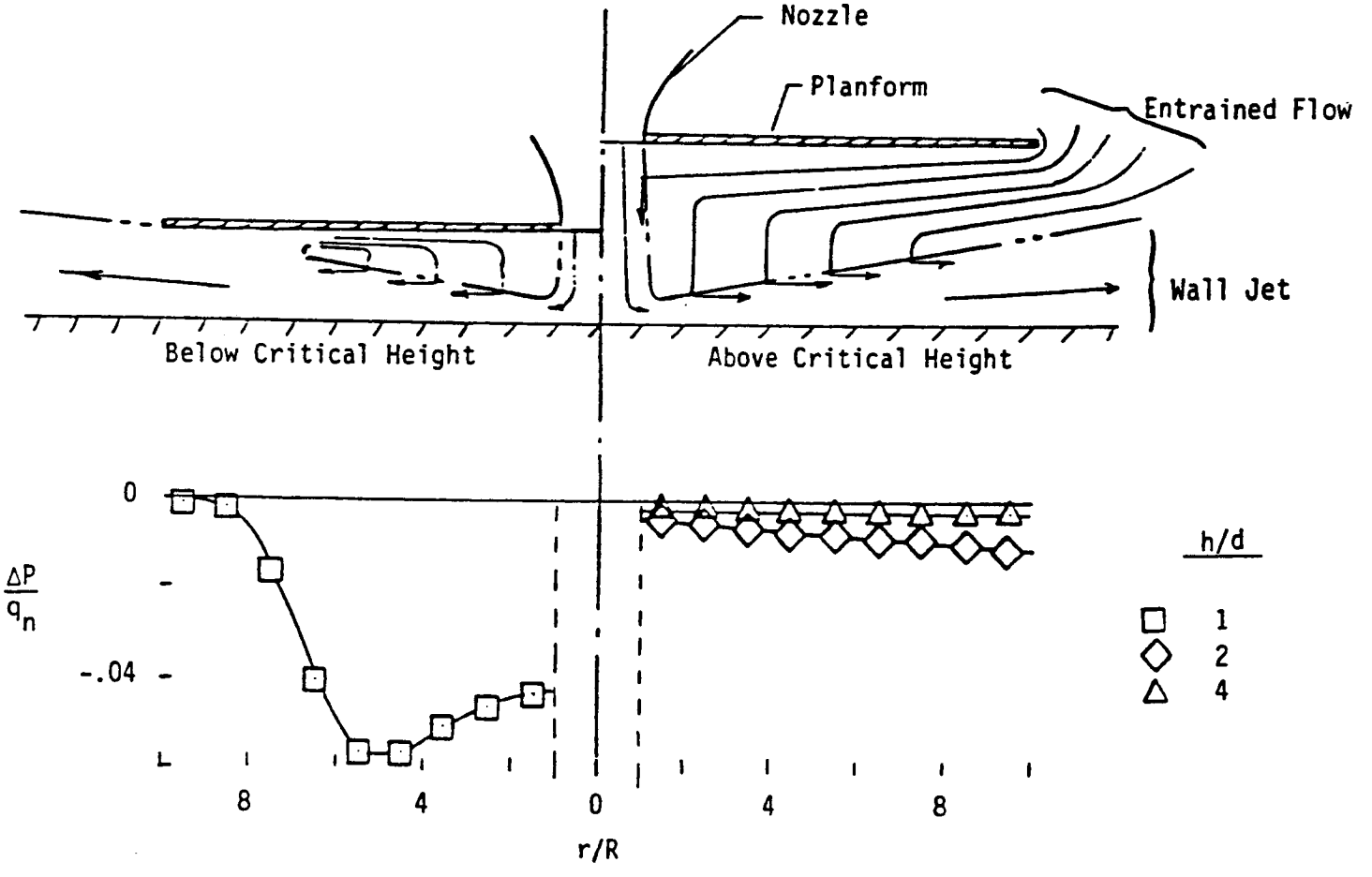

Figure 8.- Pressure on Plate in Hover, (Ref. 4).

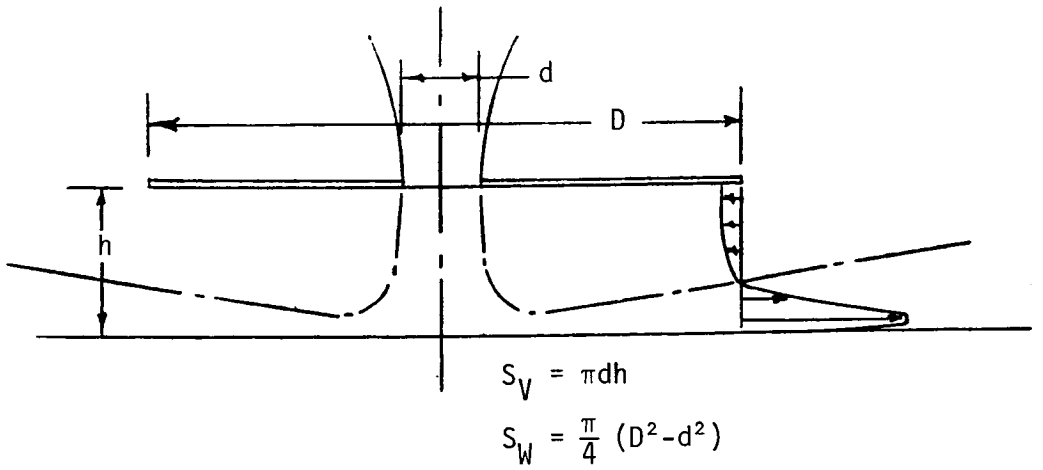

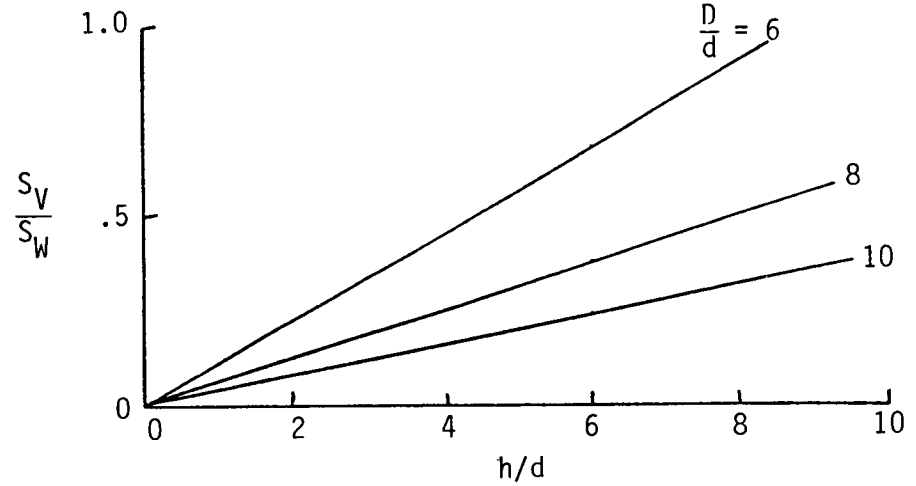

Figure 9.- At Low Operating Heights the Wall Jet is the Primary Entrainment Surface.

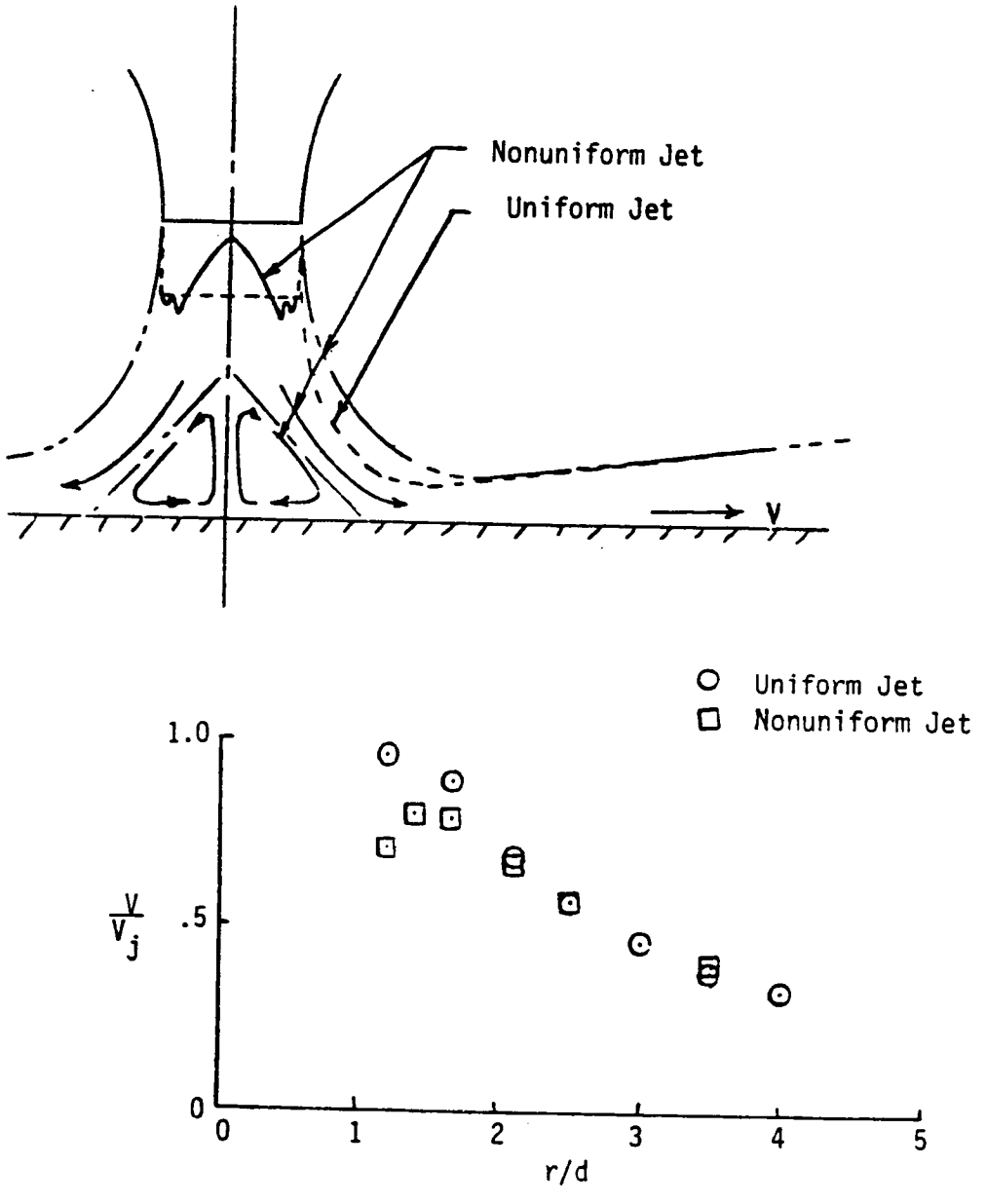

Figure 10.- Effect of exit velocity distribution on wall jet and flow in inpingement region. (Ref. 9)

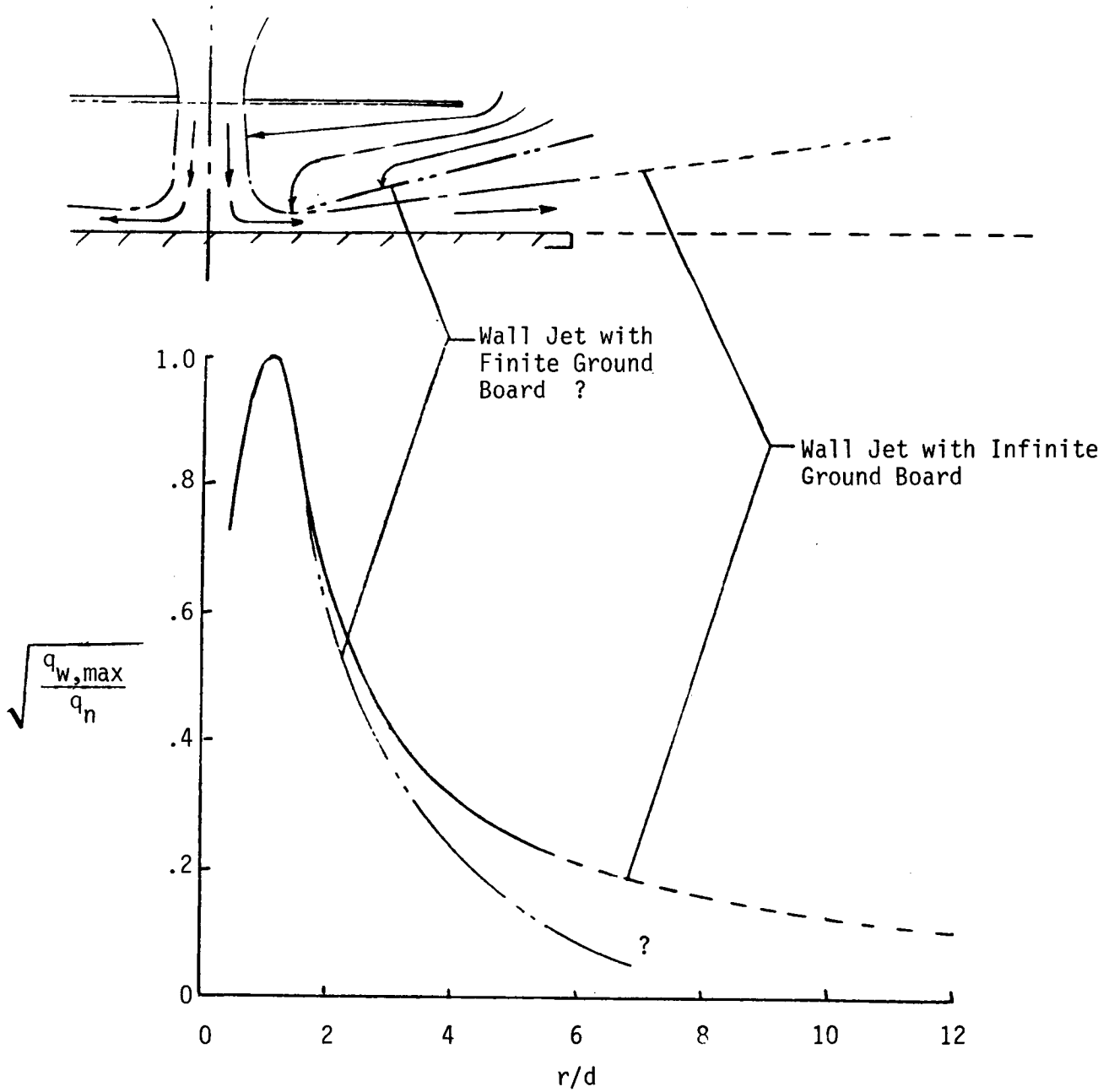

Figure 11.- Is there a significant effect of finite ground board size?

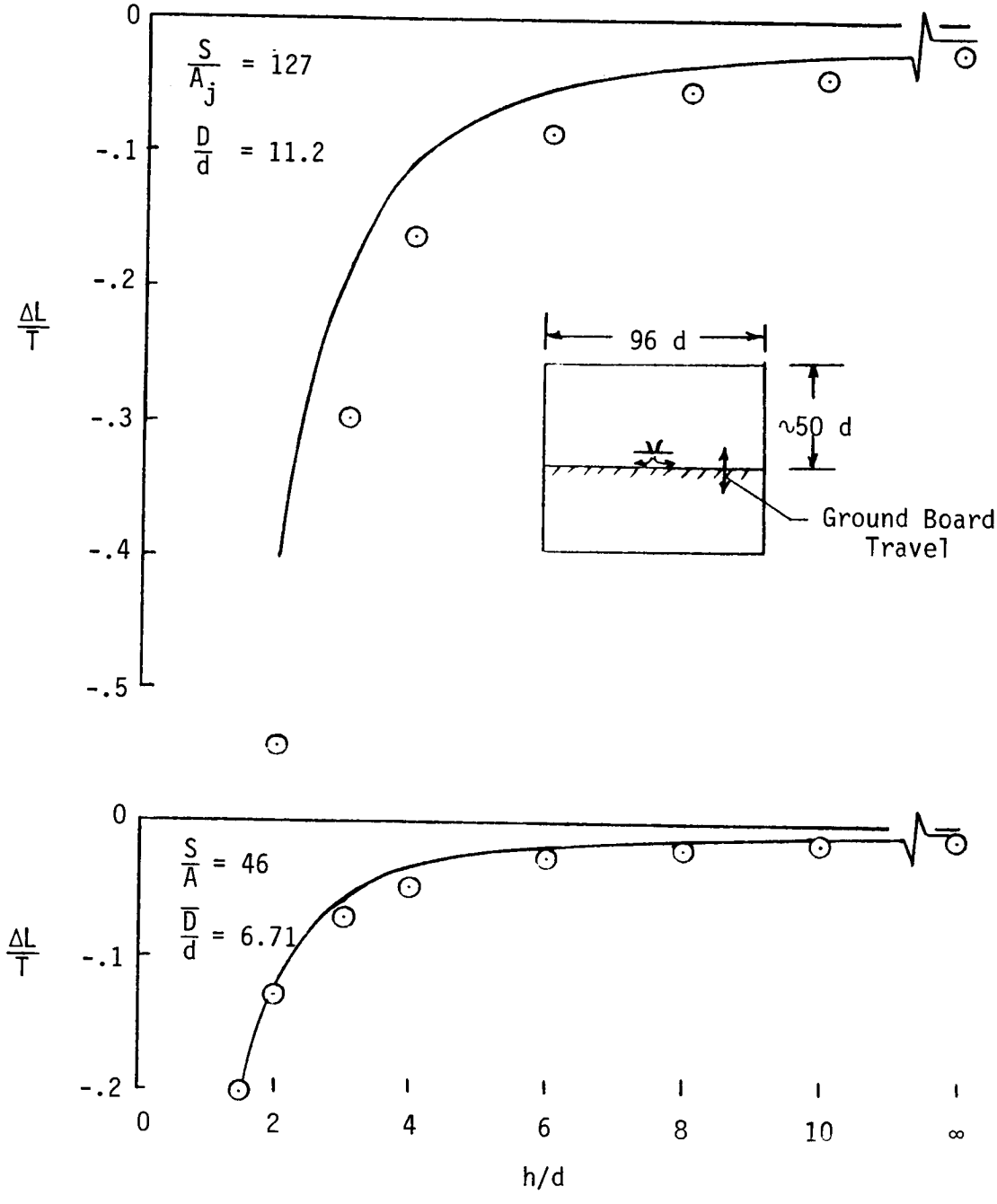

Figure 12.- Data taken in inadequate size test chamber. (Ref. 10)

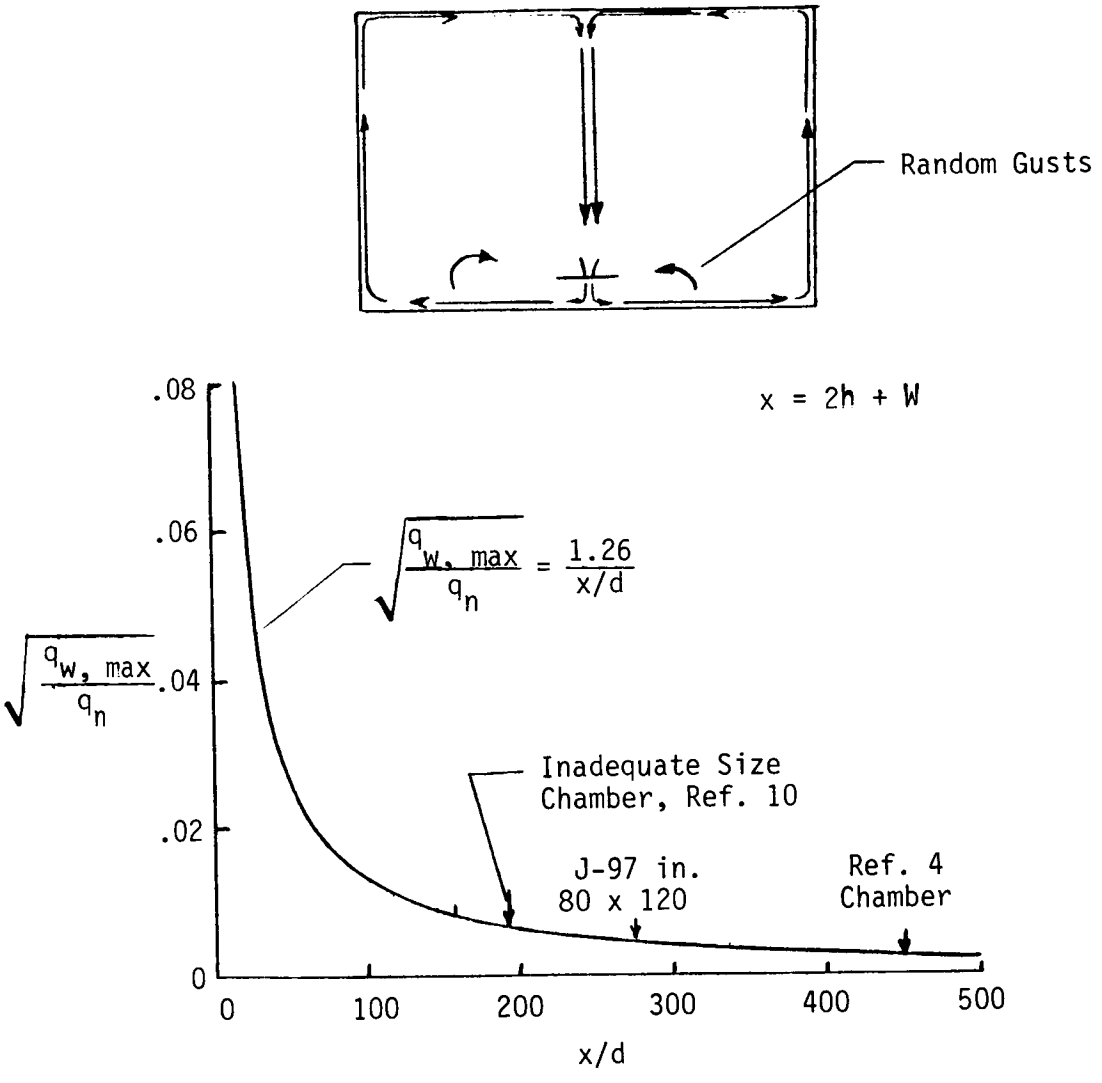

Figure 13.- Decay of velocity with distance from impingement point.

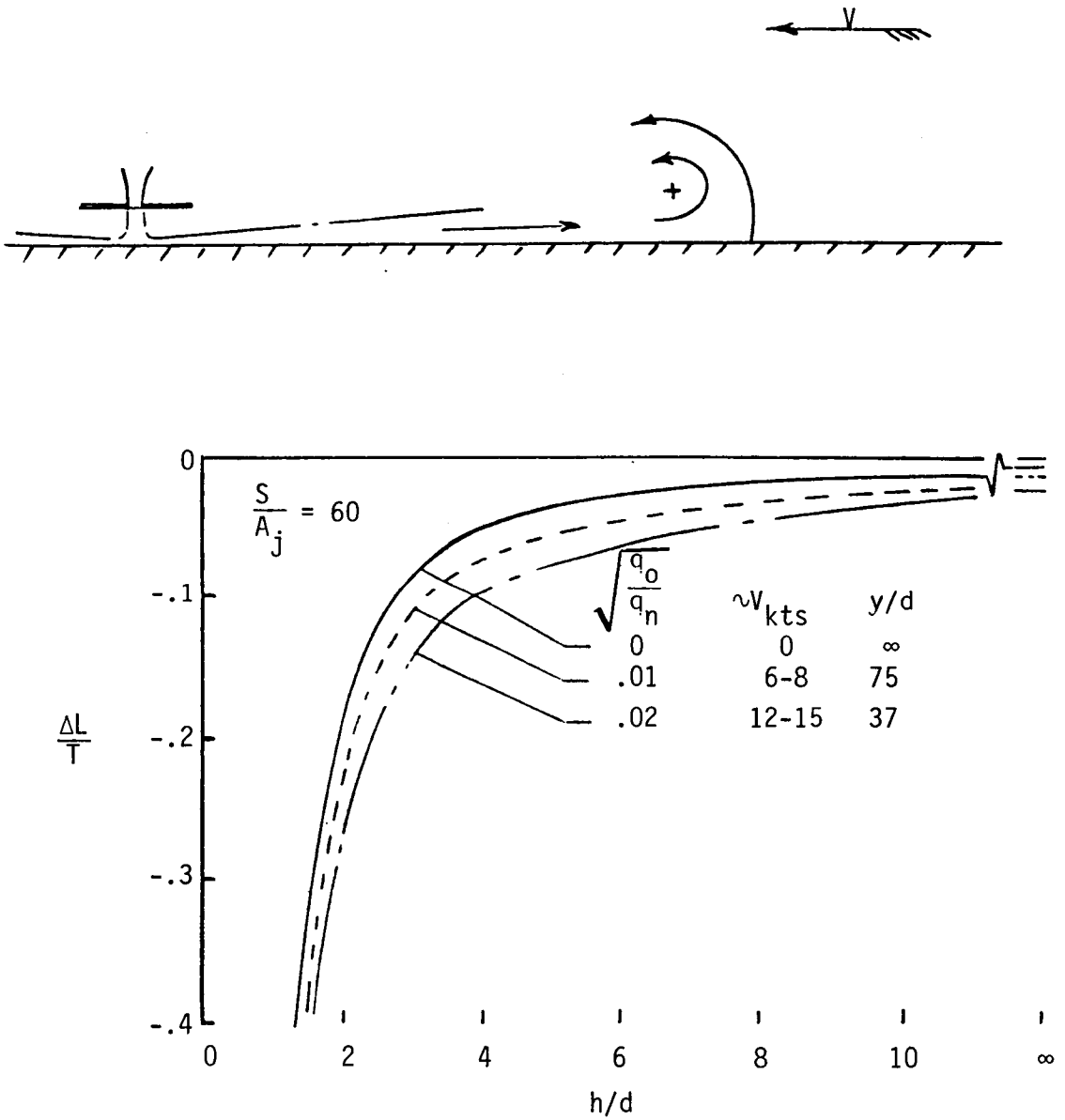

Figure 14.- Effect of Crossflow. (Ref. 10)

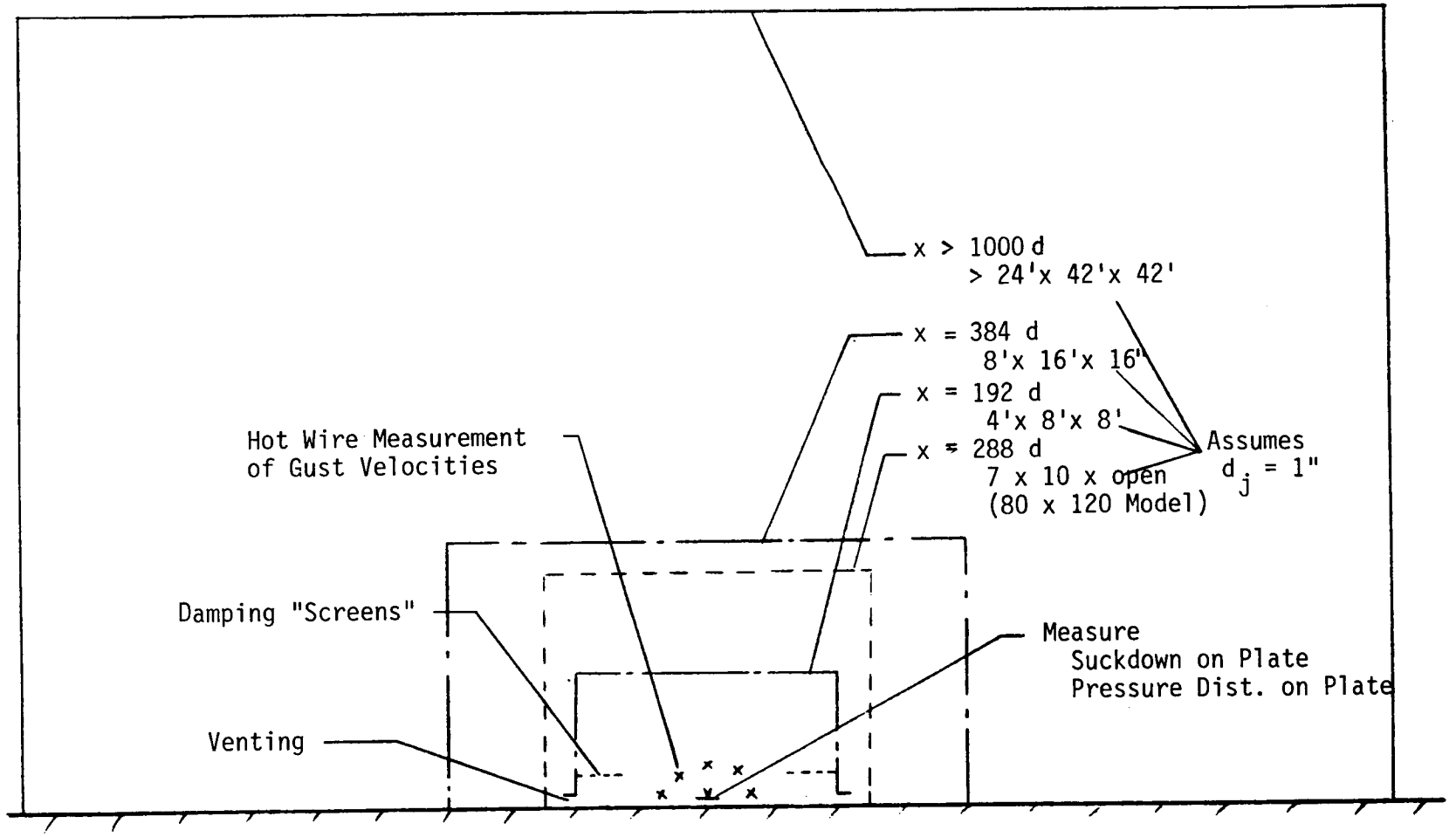

Figure 15.- Test Chamber Size Investigation.

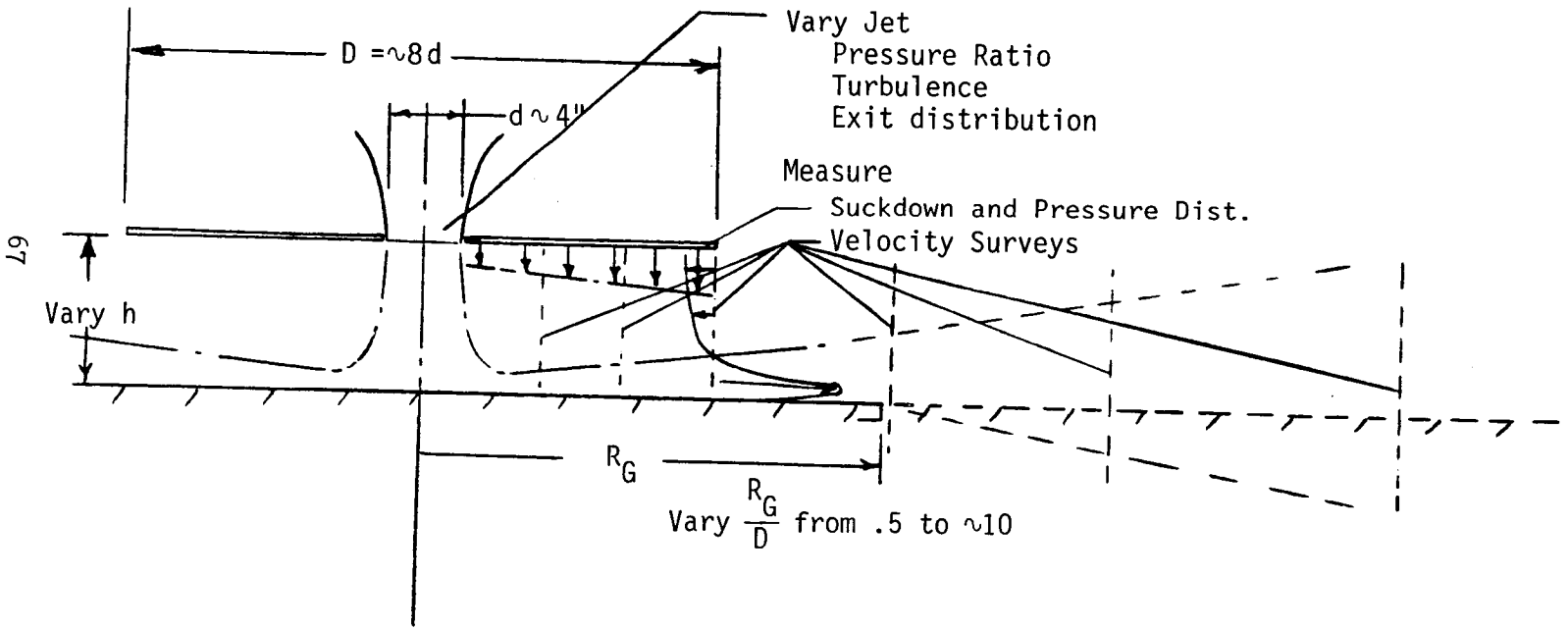

Figure 16.- Investigate Effects on and of Wall Jet Characteristics.

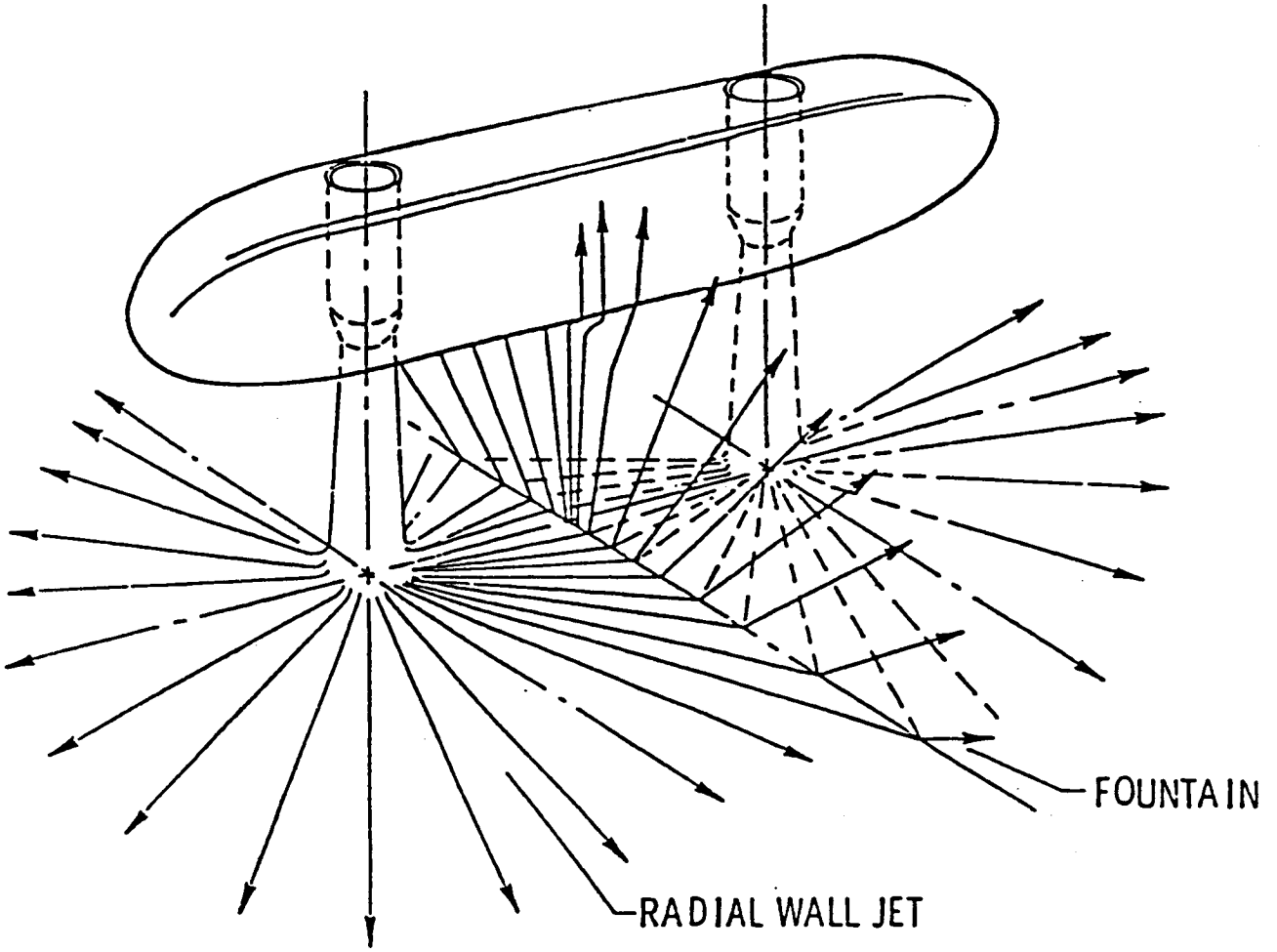

Figure 17.- Fountain flow generated between a pair of jets.

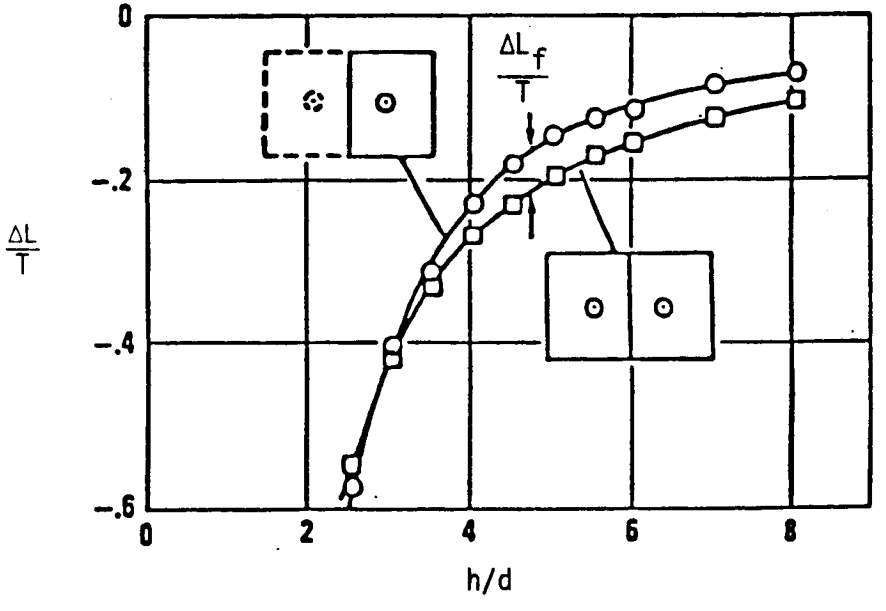

Figure 18.- Isolation of the incremental fountain effect for two nozzles. (Ref. 11)

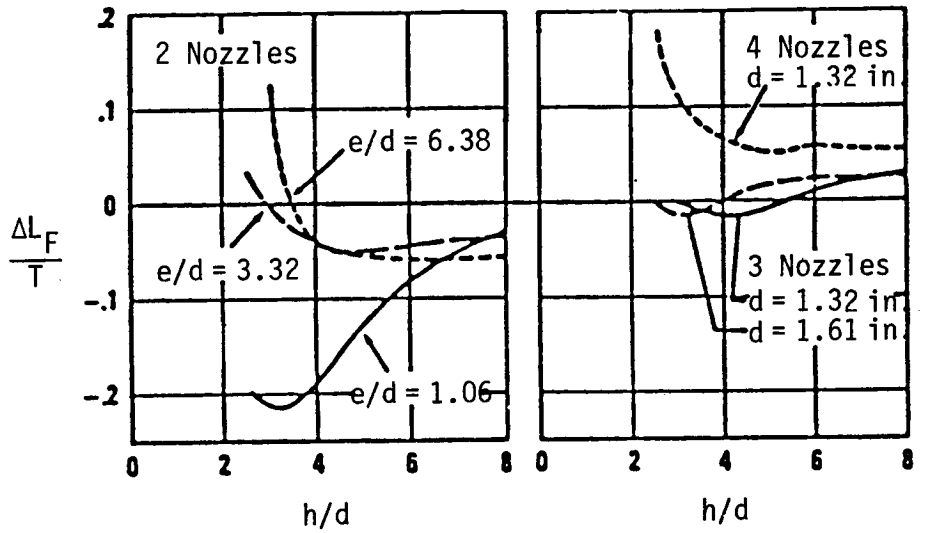

Figure 19.- Incremental fountain lift for two, three and four nozzles.
(Ref. 11)

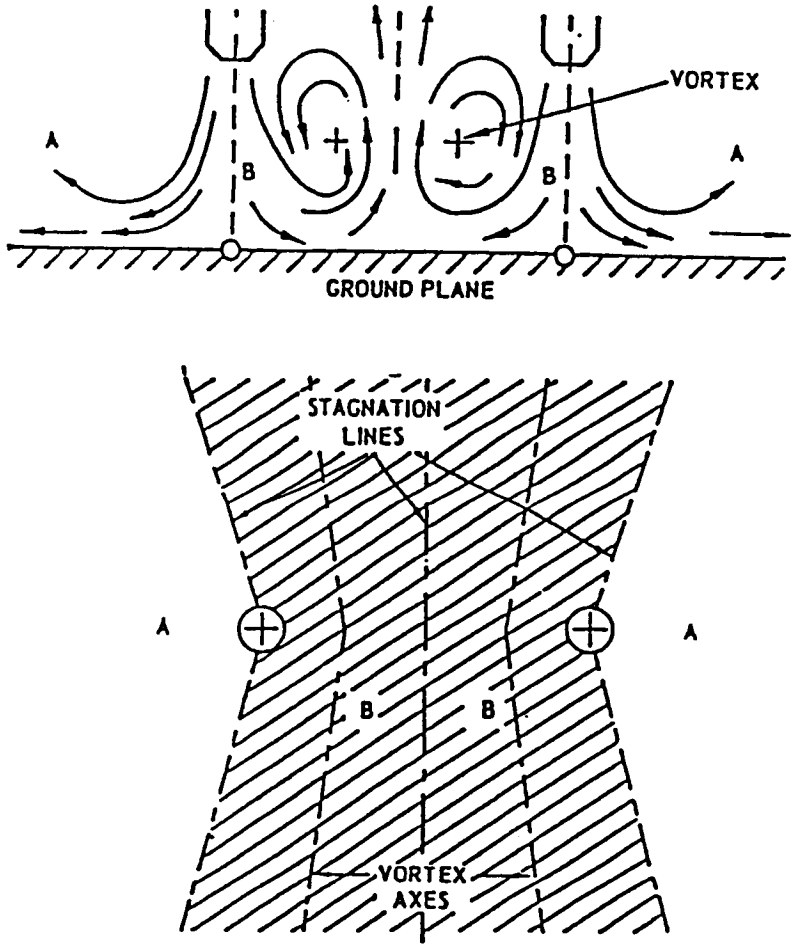

Figure 20.- Flow field between two jets hovering in ground effect. (Ref. 12)

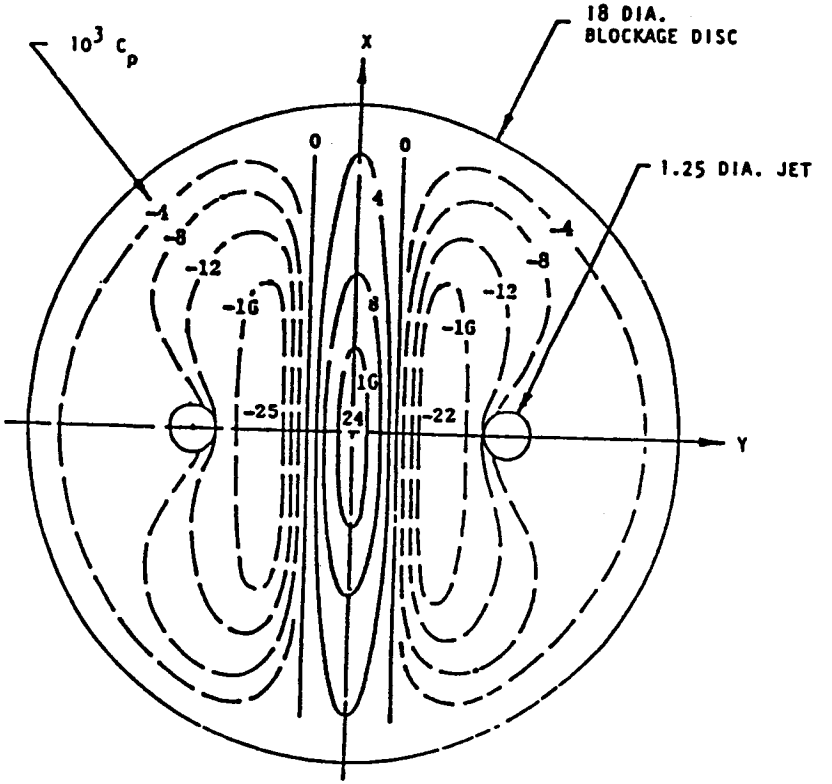

Figure 21.- Pressure distribution due to fountain flow from two jets in ground effect. (Ref. 12)

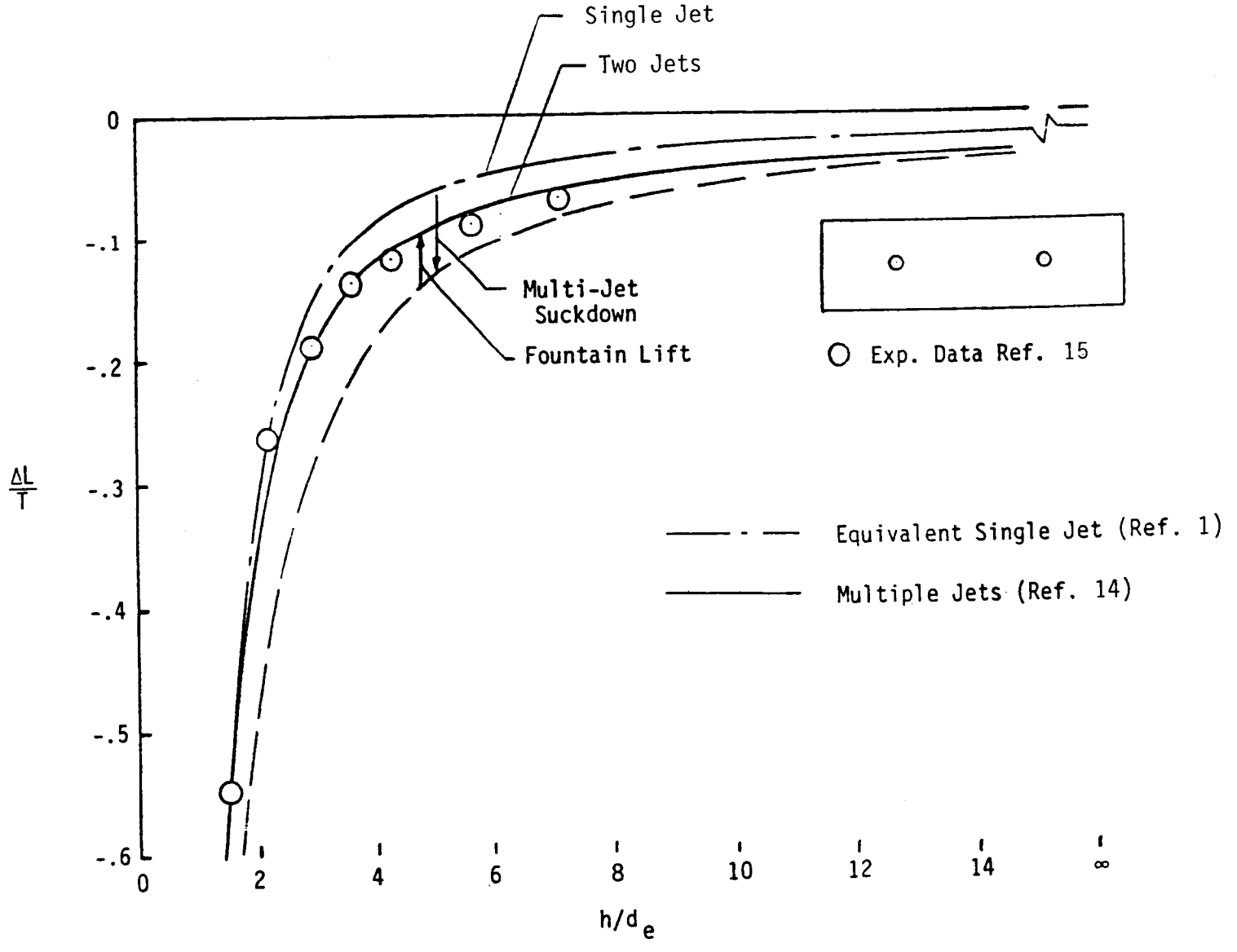

Figure 22.- Fountain lift and the additional multi-jet suckdown generated on a simple two-jet configuration.

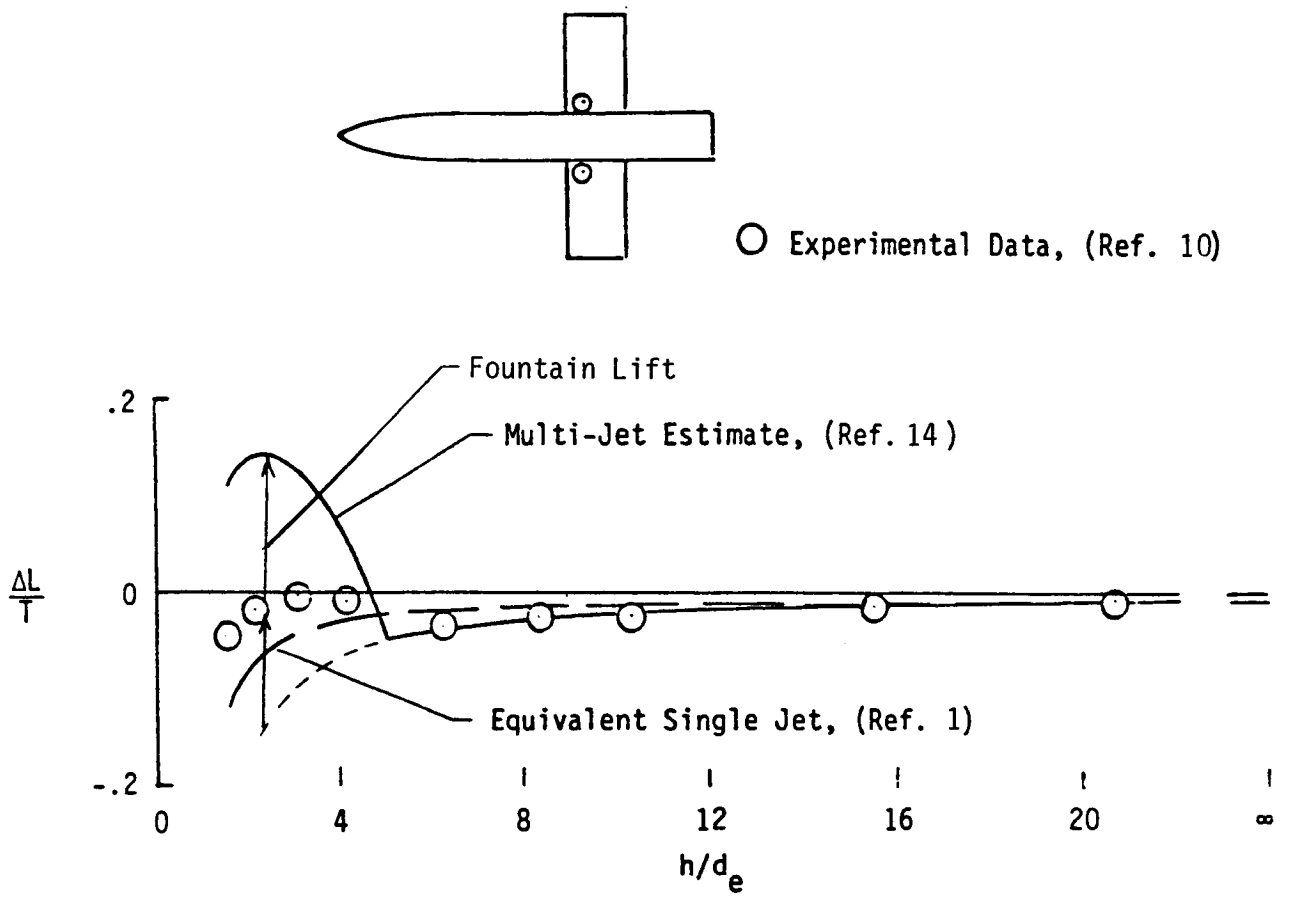

Figure 23.- Lift induced on simple 2-jet high wing configuration hovering in ground effect.

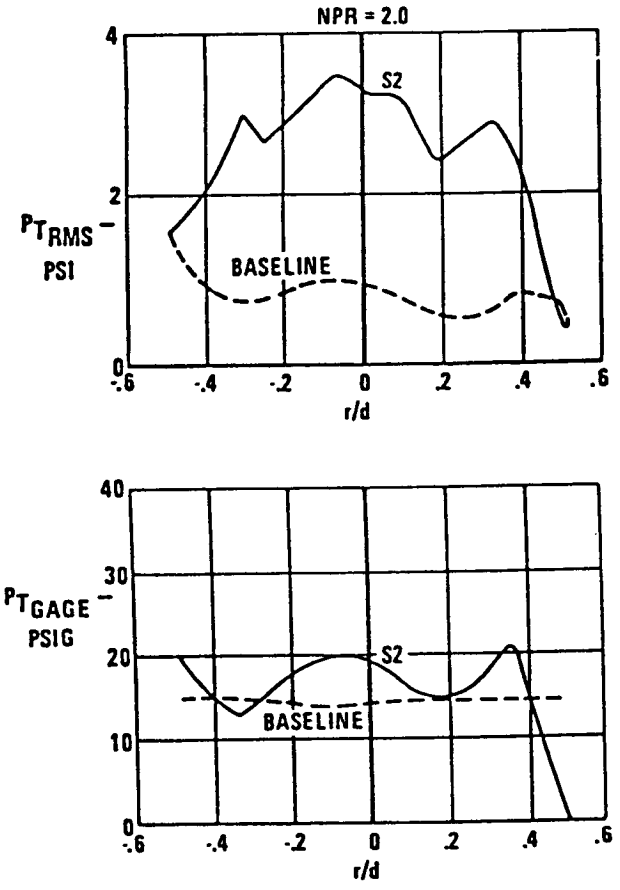

Figure 24.- Typical total pressure and $P_{T_{RMS}}$ surveys of nozzle exit for baseline nozzle and S2. (Ref. 11)

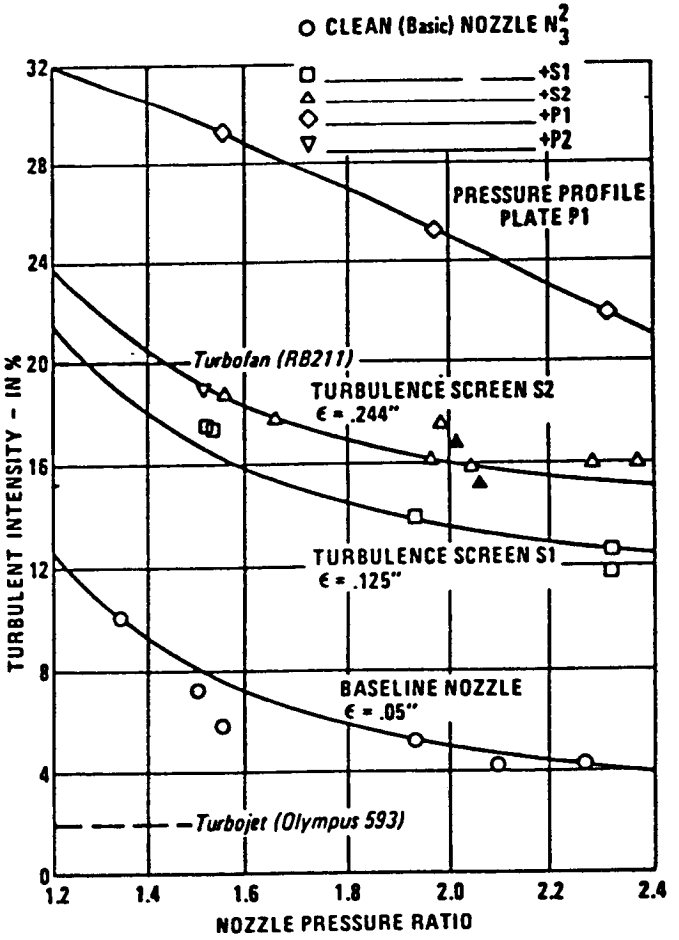

Figure 25.- Turbulent intensity vs. NPR for screens and plates. (Ref. 11)

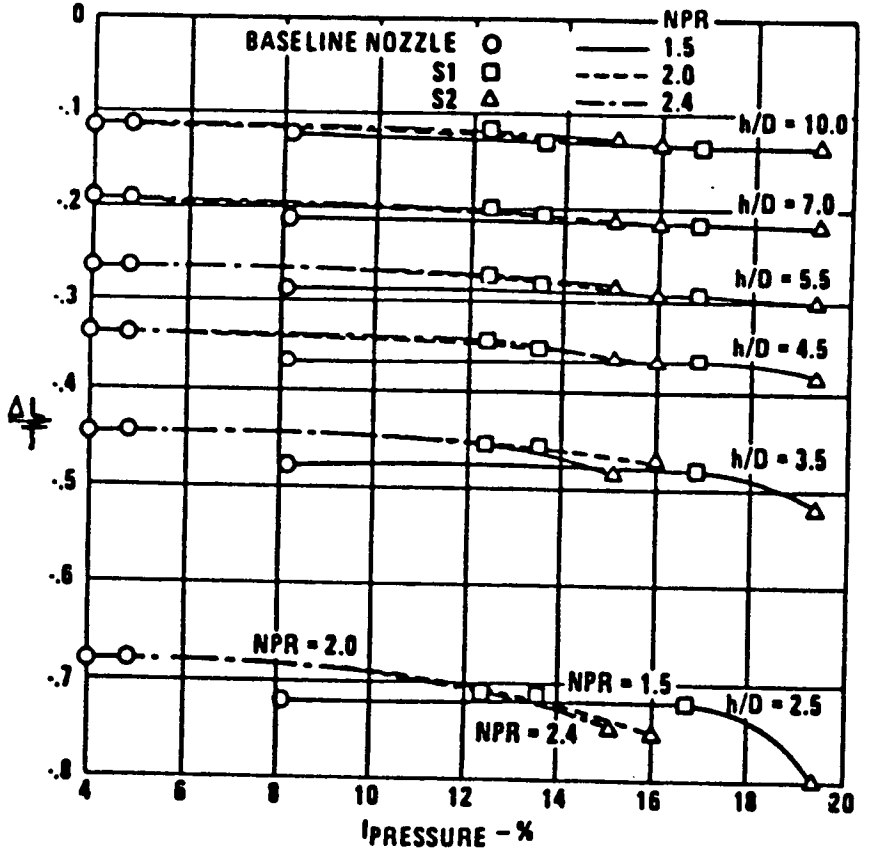

Figure 26.- Turbulence screens and NPR effects on net induced force coefficient for two nozzle configuration. (Ref. 11)

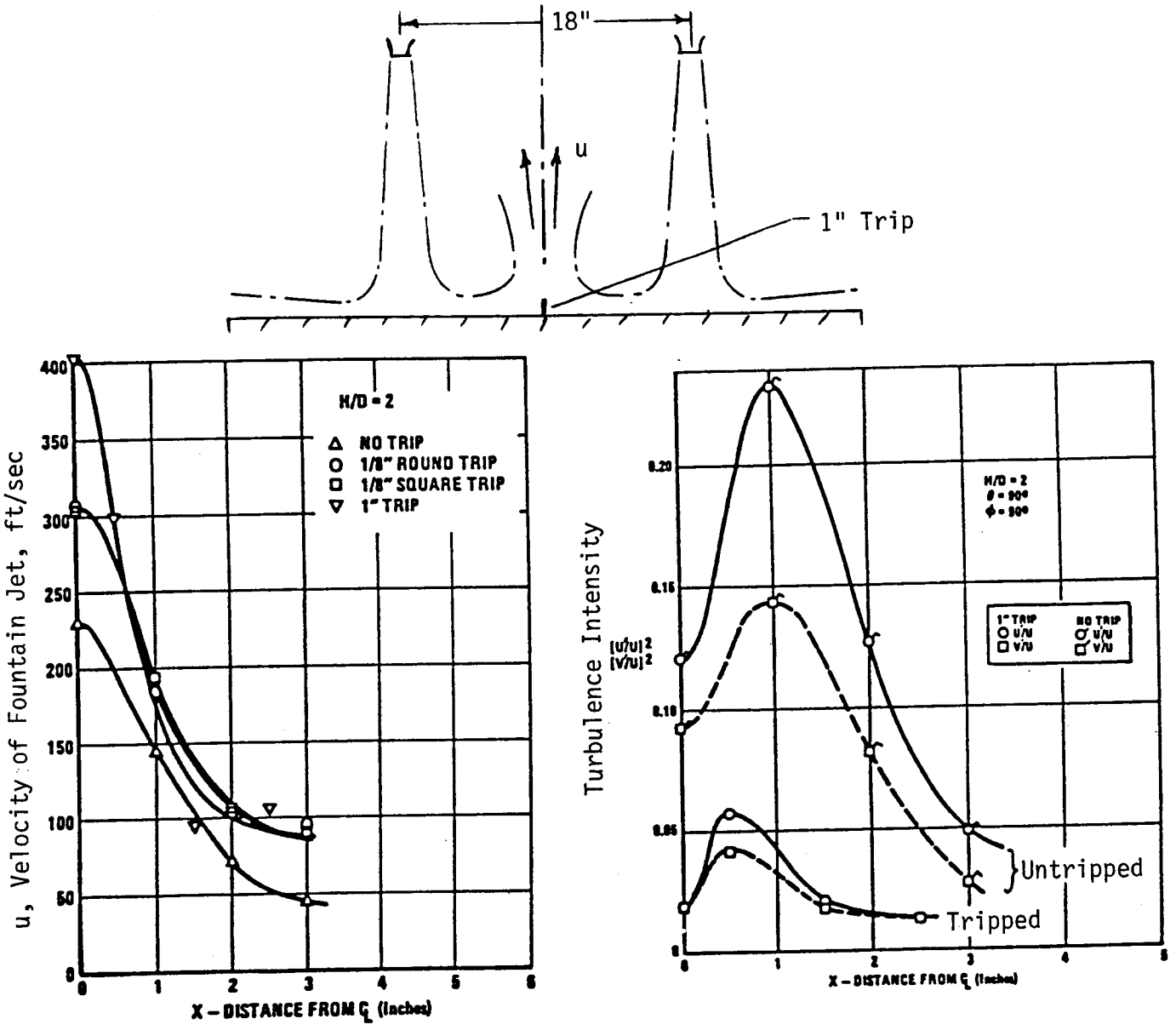

Figure 27.- Fountain turbulence. (Ref. 16)

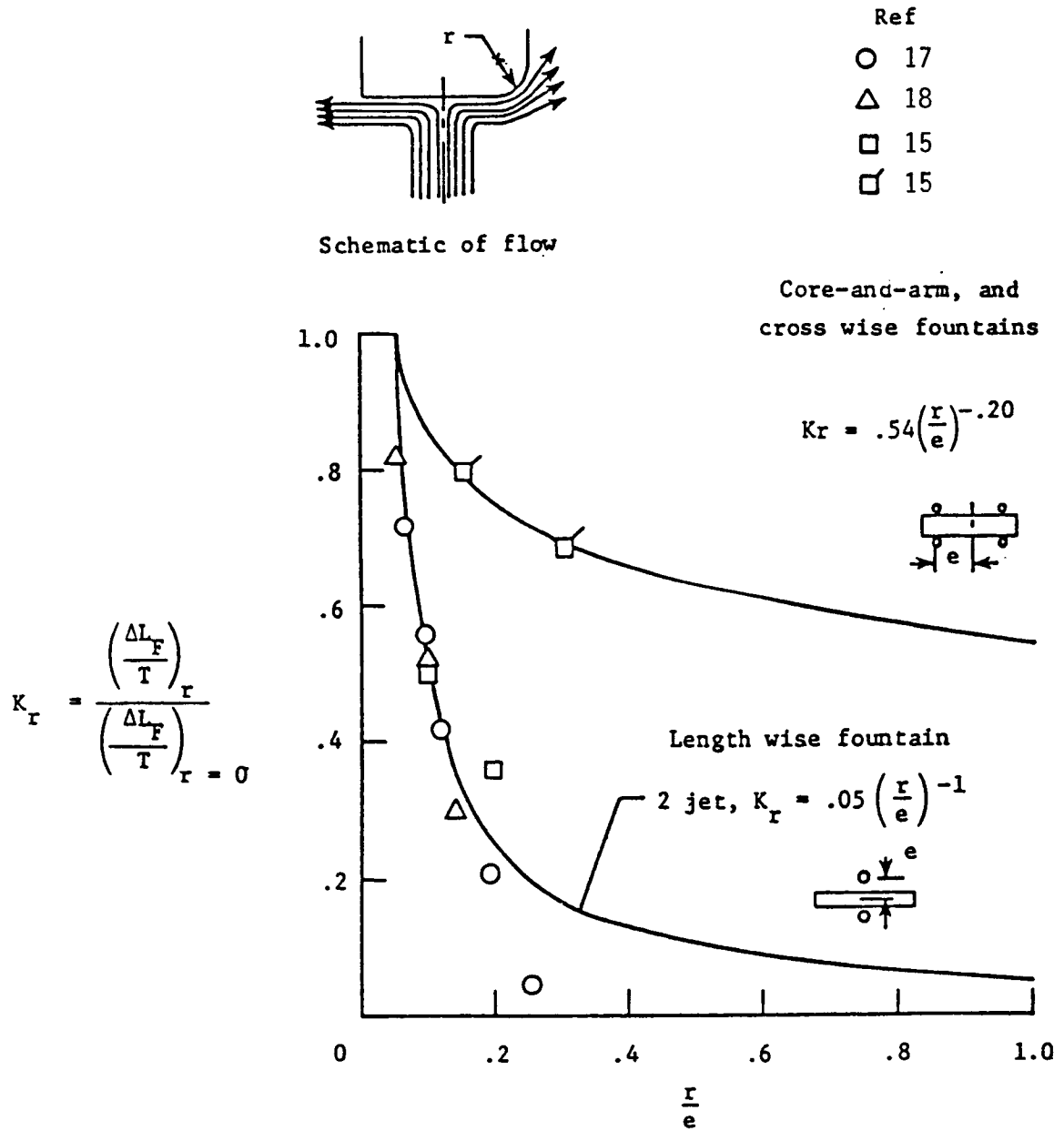

Figure 28.- Effect of lower surface contour. (Ref. 14)

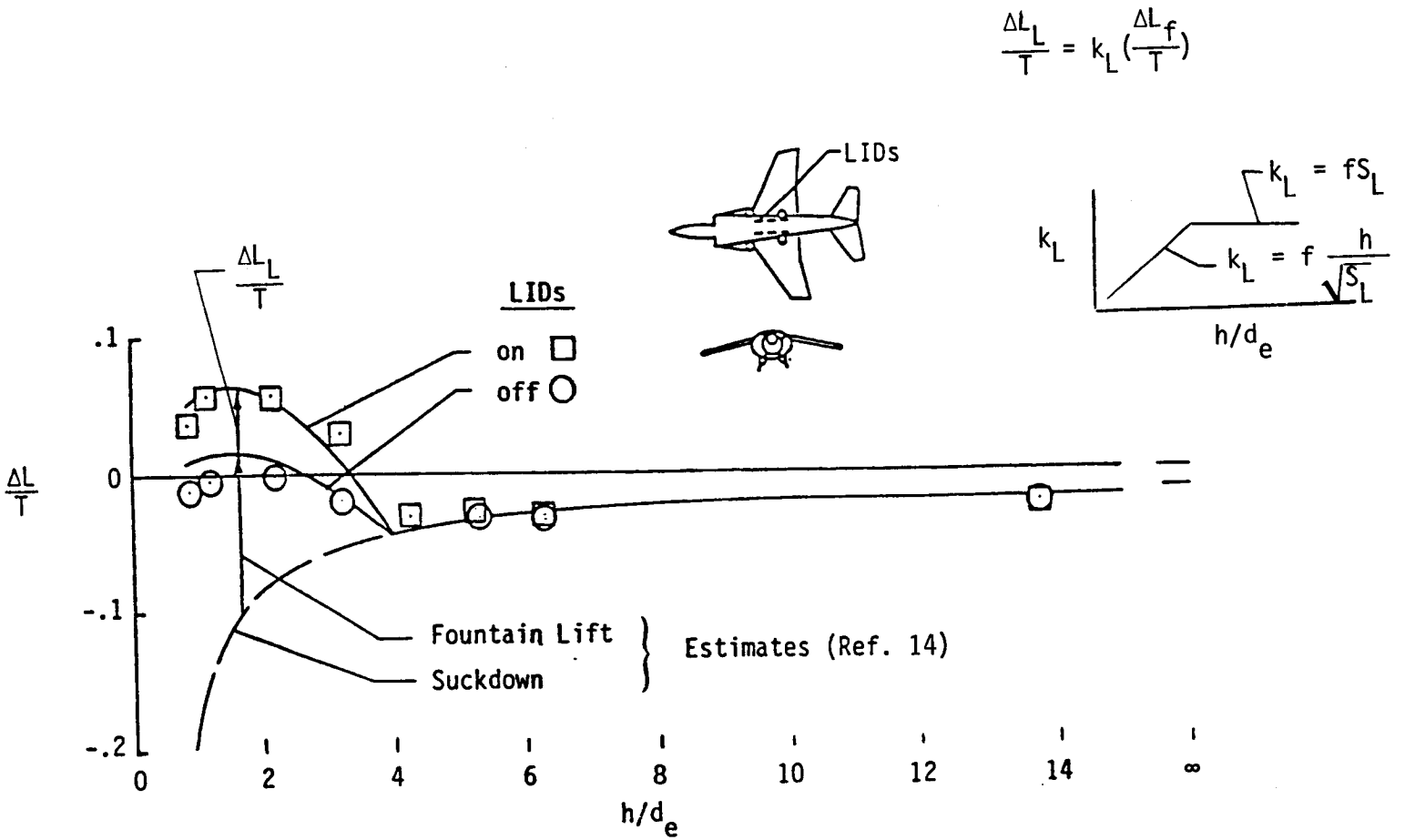

Figure 29.- Lift induced on Harrier configuration hovering in ground effect. (Ref. 19)

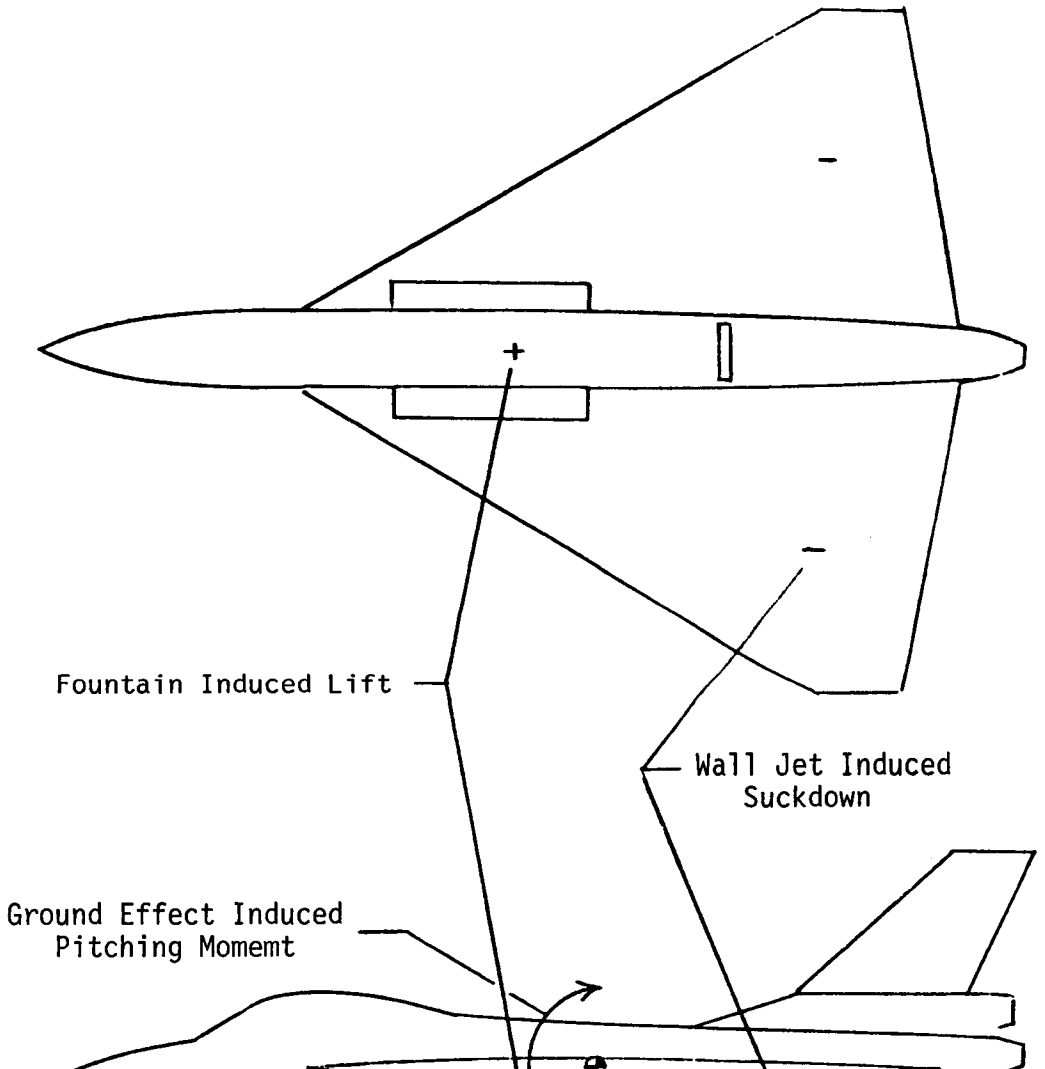

Figure 30.- Ground effect induced pitching moment.

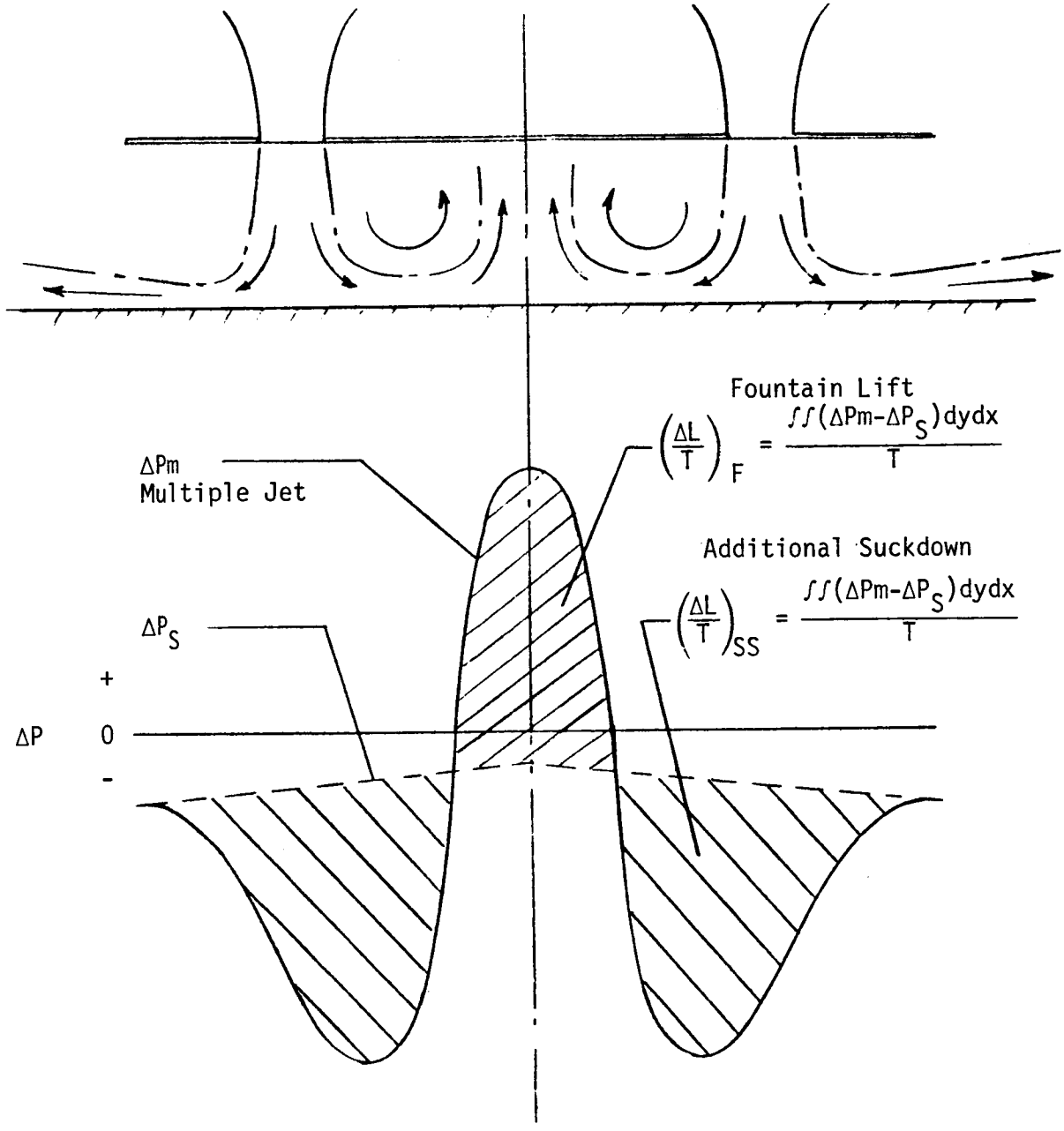

Figure 31.- Proposed method for determining fountain lift and additional suckdown.

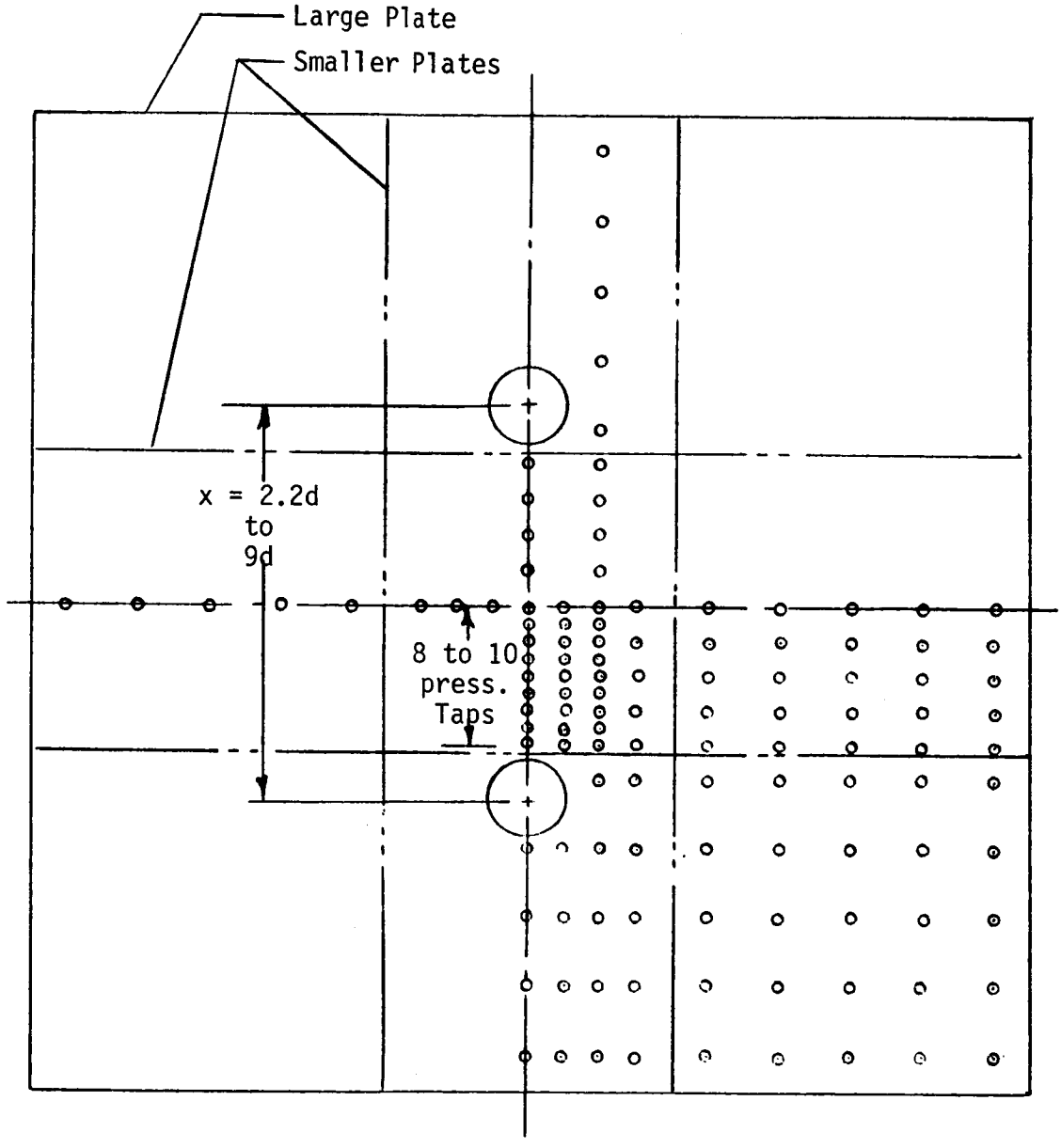

Figure 32.- Typical distribution of pressure taps.

THE GROUND VORTEX

- Creats and Defines Dust Cloud
- One of Primary Mechanisms in Hot Gas Ingestion
- Causes Lift Loss

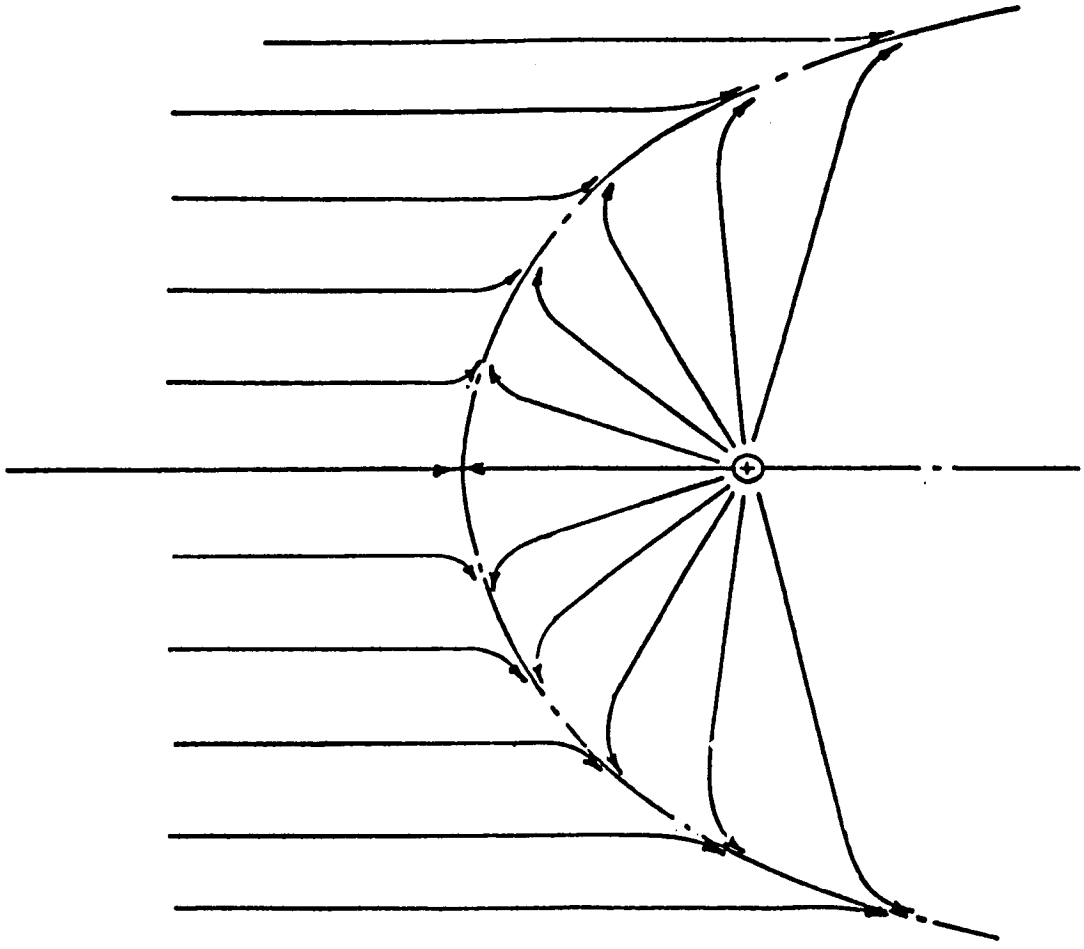

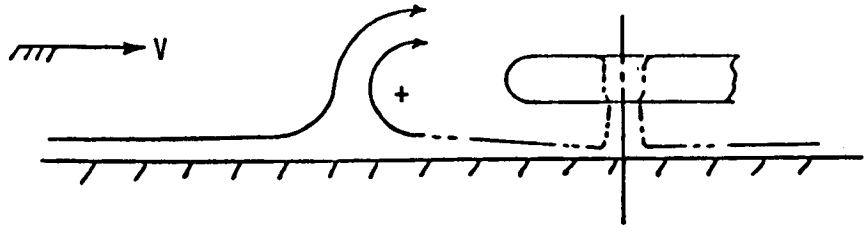

Figure 33.- Formation of ground vortex.

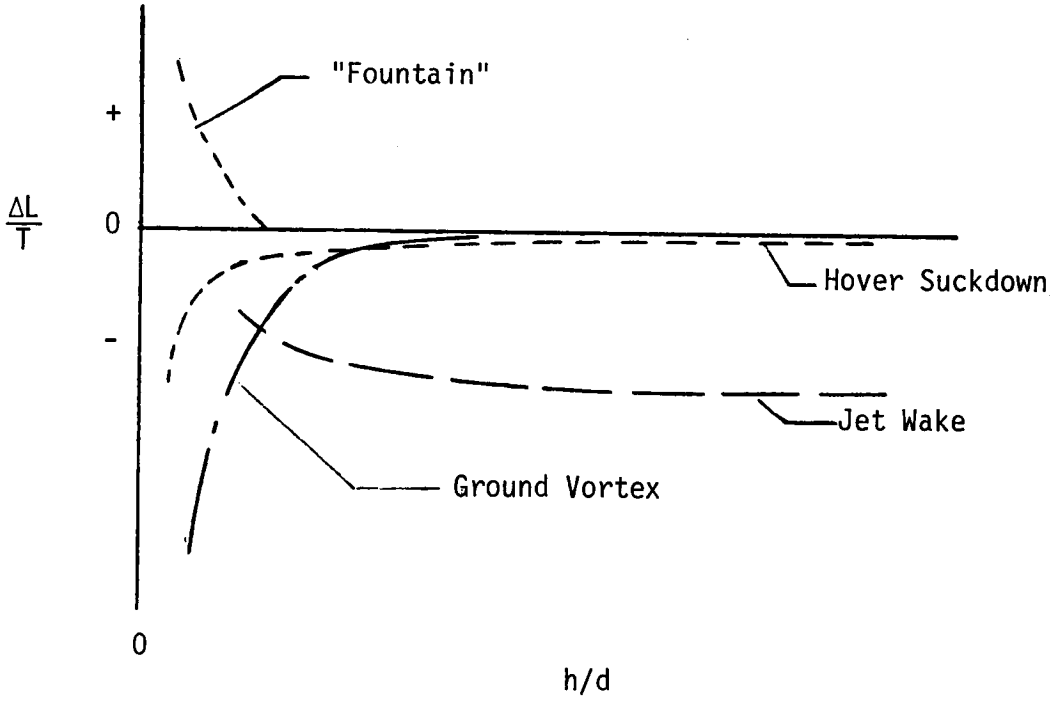

Figure 34.- STOL ground effect induced lift increments.

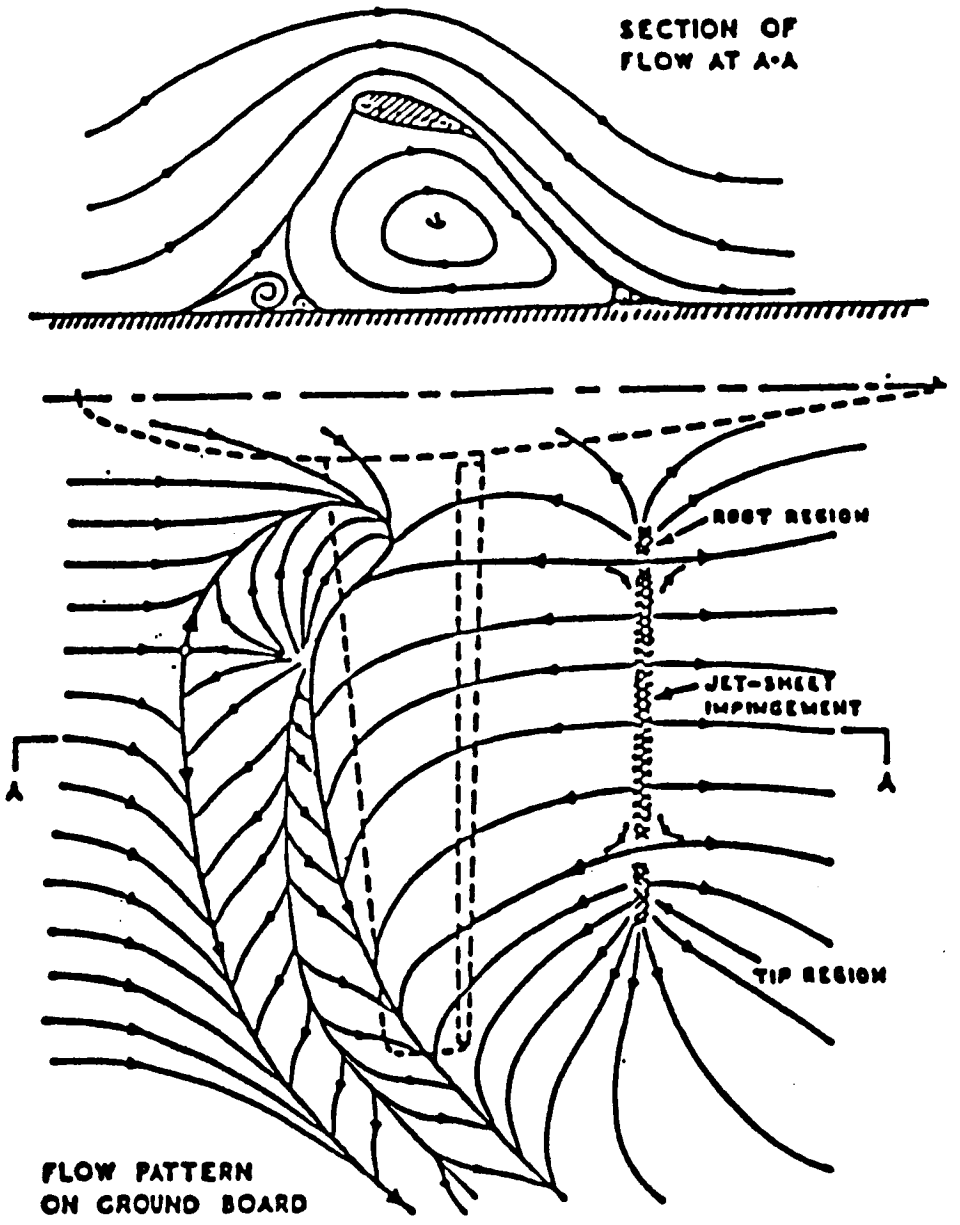

Figure 35.- Flow field under jet flap model with jet impingement on ground. (Ref. 20)
$\alpha = 15°$, $C_\mu = 2.1$, $H/\bar{c} = 1.5$, $\delta \sim 50°$.

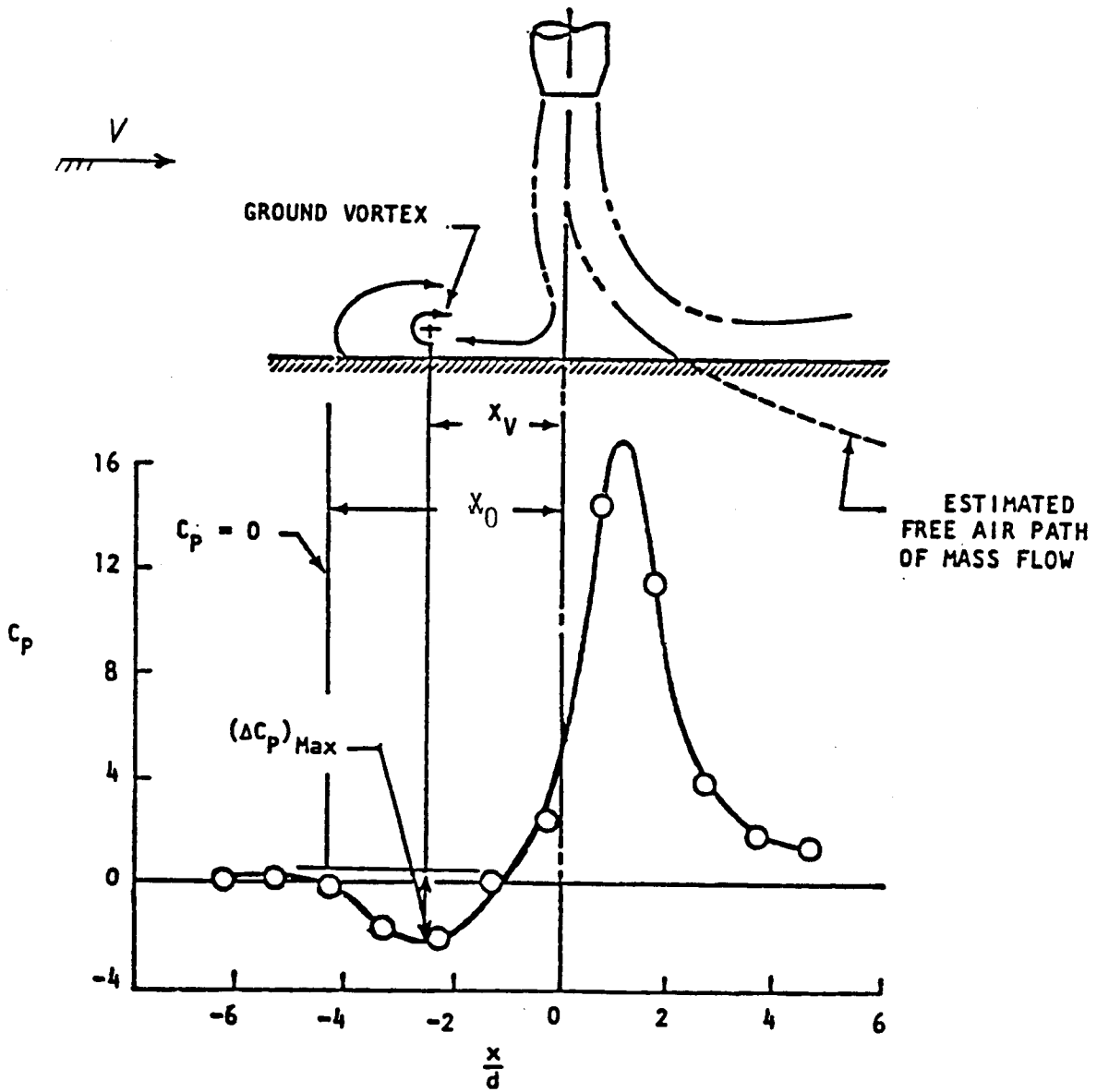

Figure 36.- Typical pressure distribution on ground board with definition of terms.

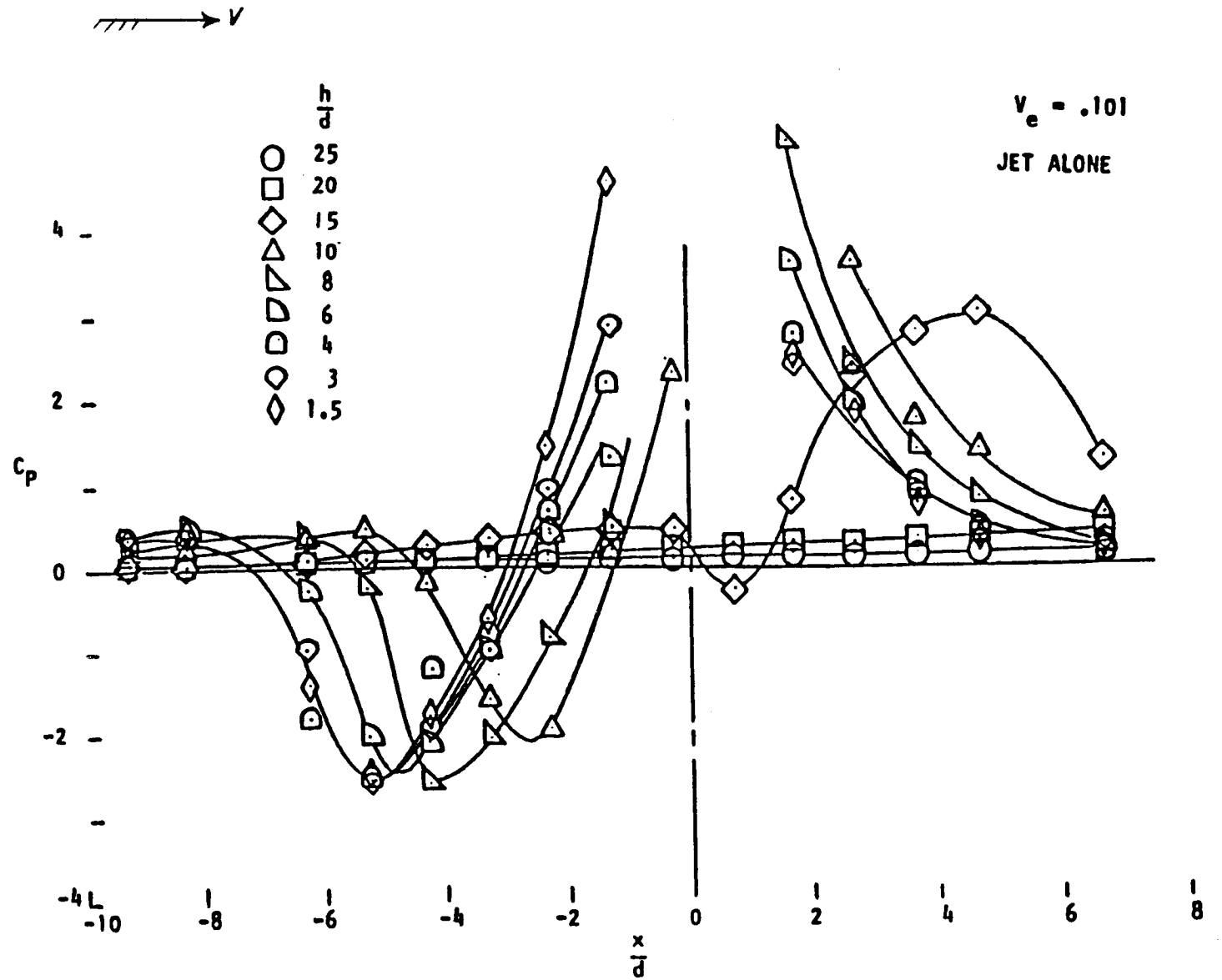

Figure 37.- Effect of height on pressure distribution measured on ground board jet alone, V_e=.101. (Ref.10)

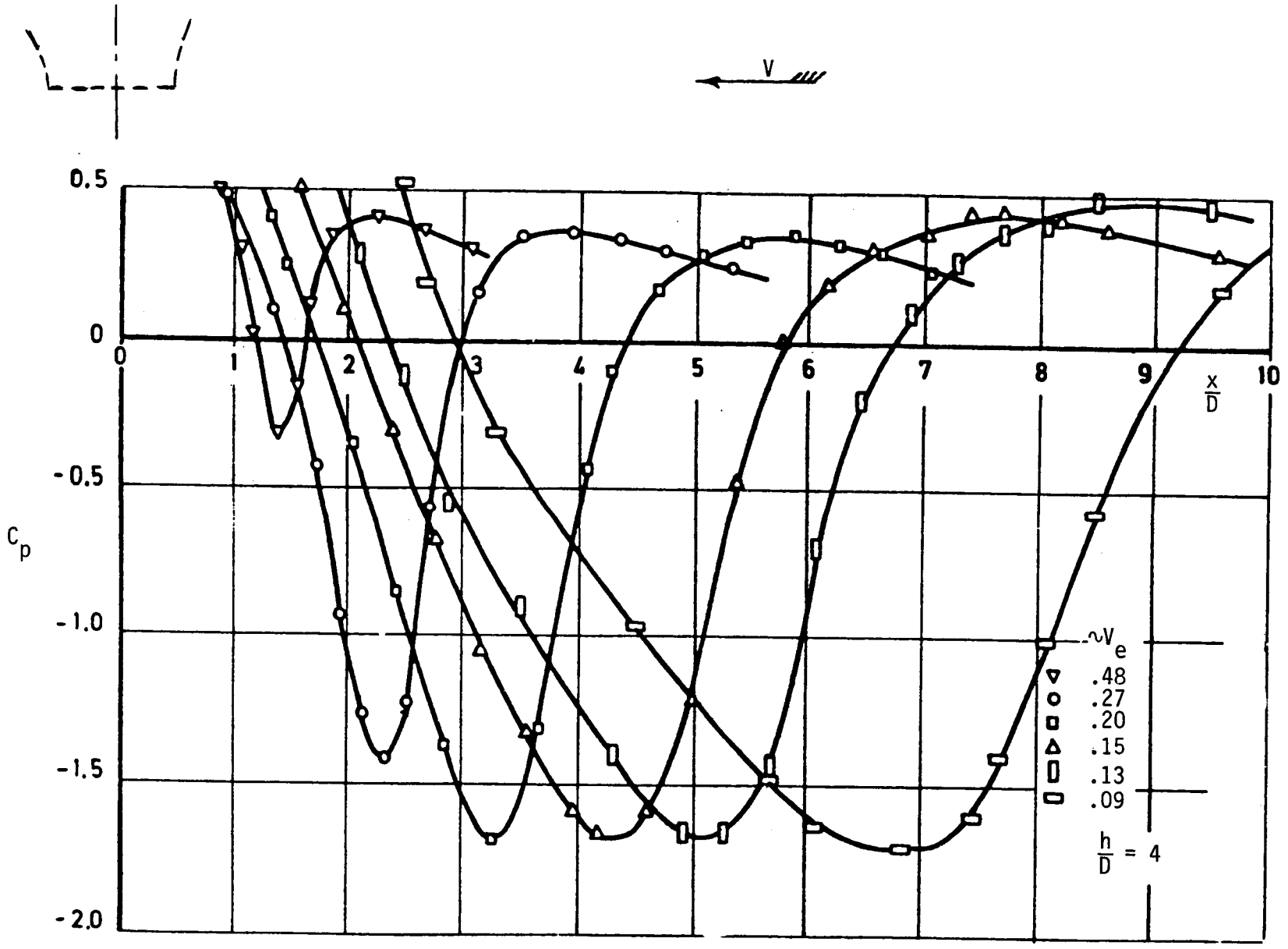

Figure 38.- Wall static pressure distribution under ground vortex. (Ref. 24)

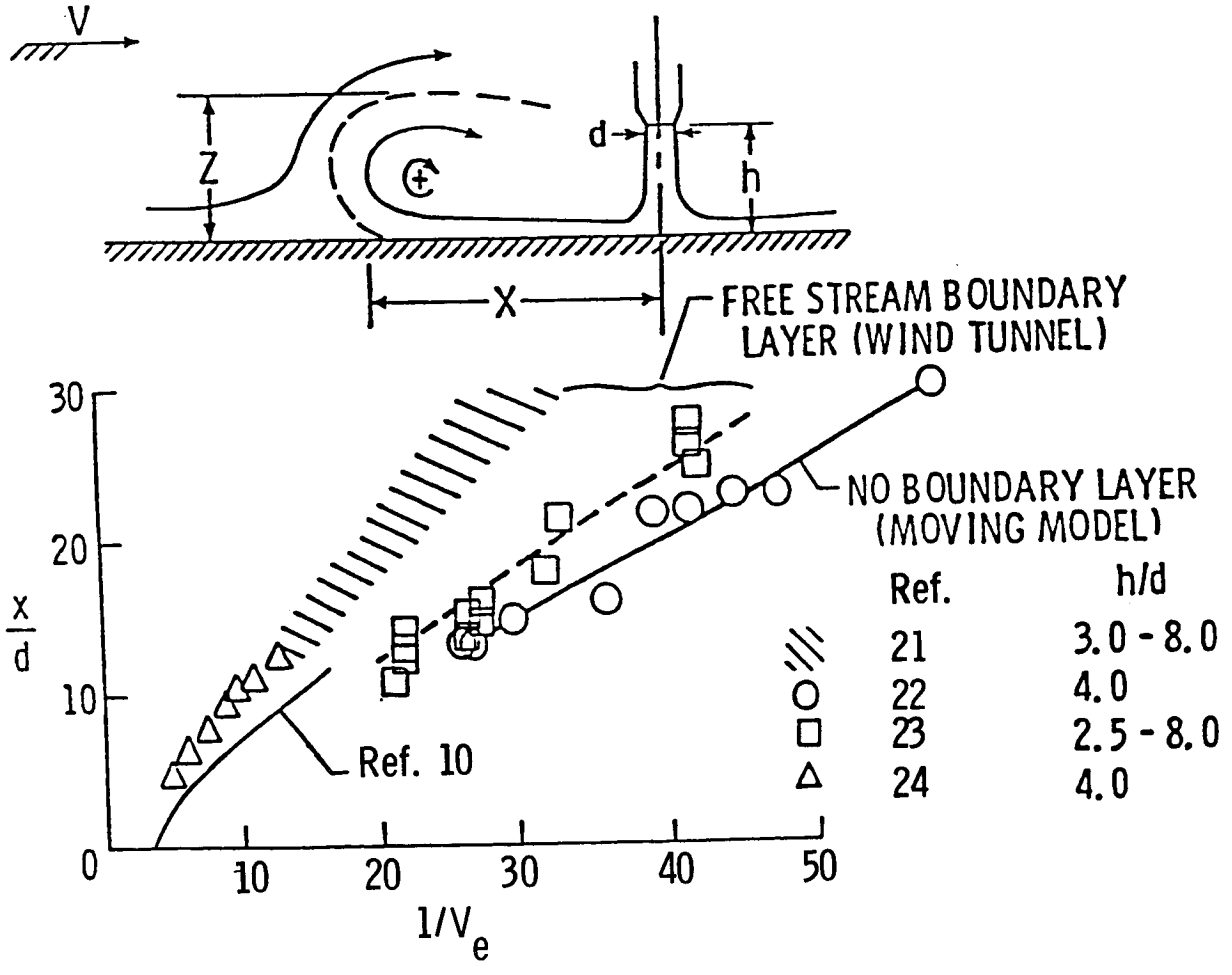

Figure 39.- Effect of ground boundary layer on foward extent of ground vortex.

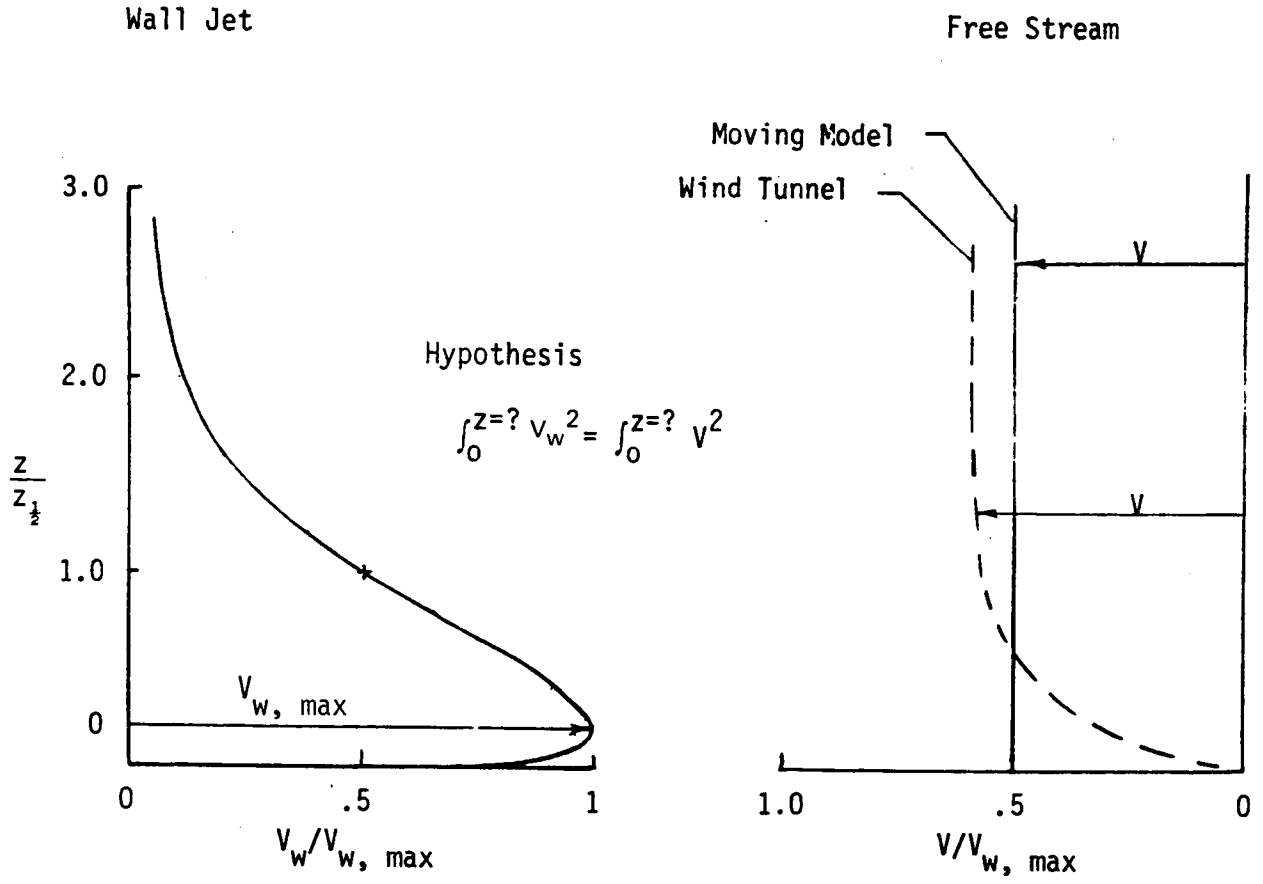

Figure 40.- At the point of maximun forward penetration the maximum velocity in the wall jet is twice the free stream velocity (without boundary layer). (Ref. 22)

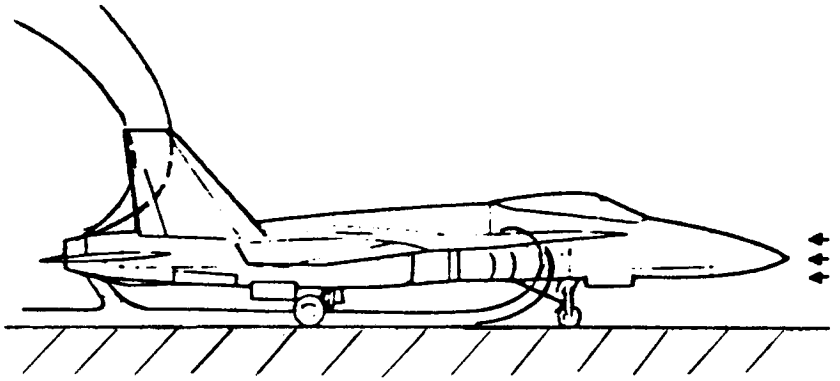

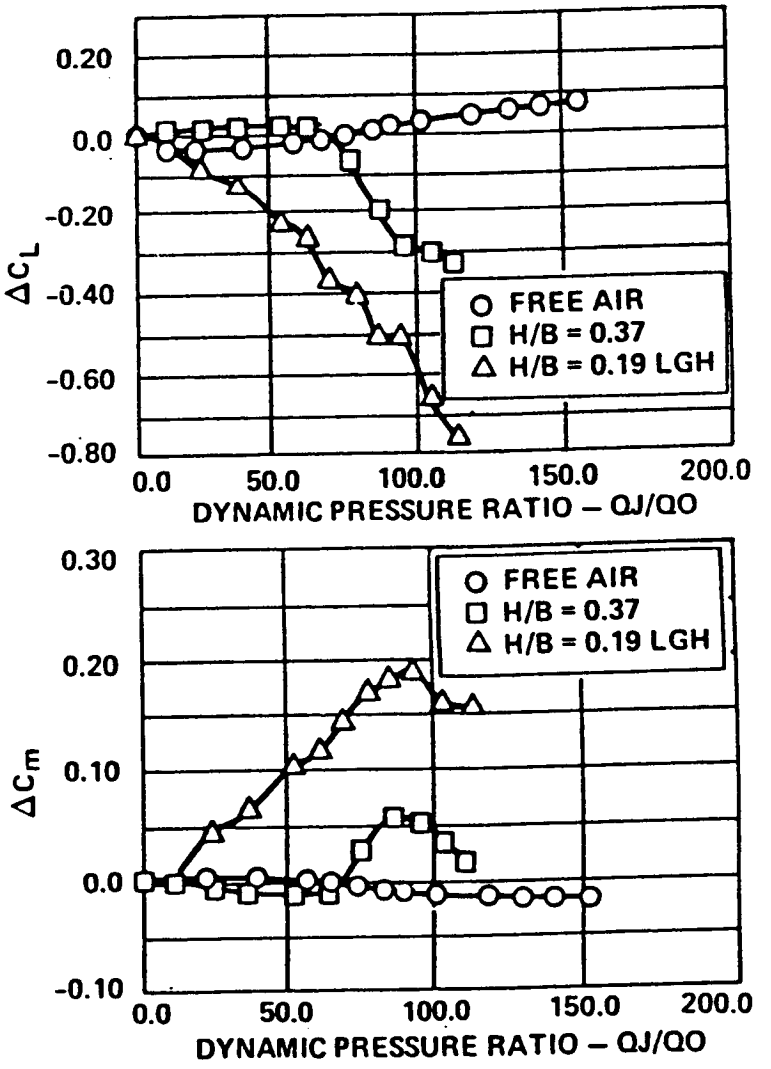

Figure 41.- Lift and moment induced by thrust reverser generated wall jet and ground vortex. (Ref. 25)

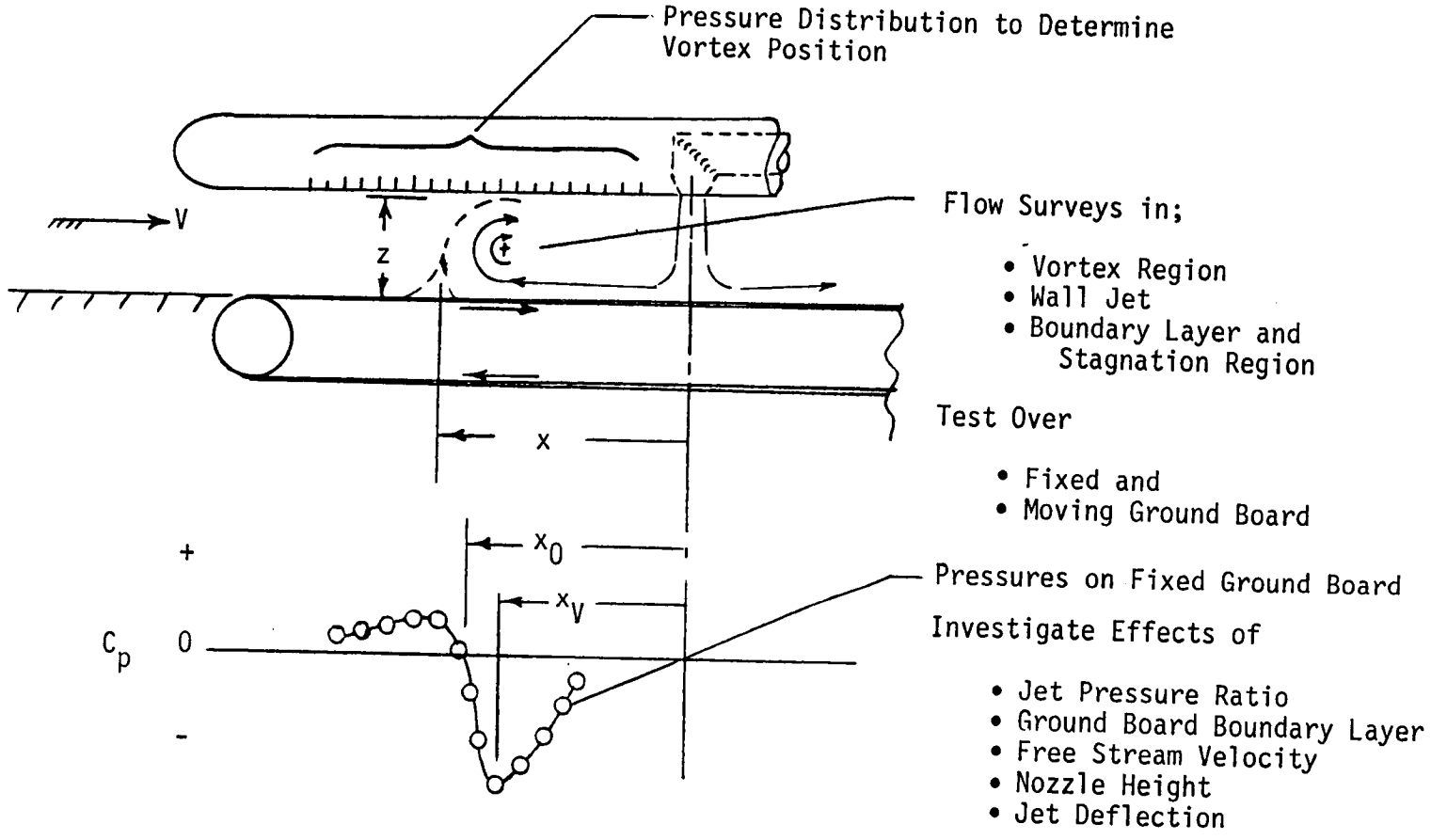

Figure 42.- Recommended ground vortex investigation.

FLOW STUDIES OVER FIXED AND MOVING GROUND PLANES

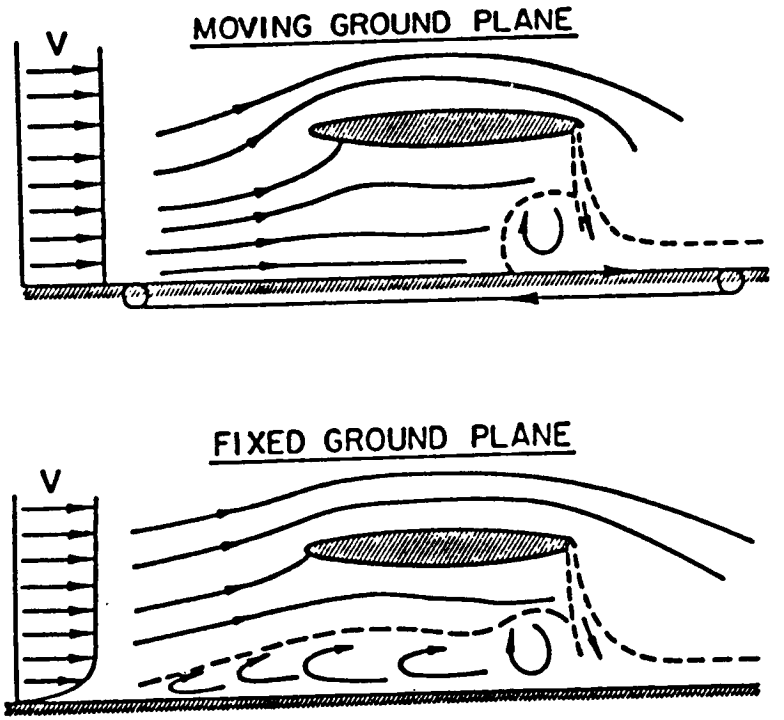

Figure 43.- Jet induced flow over fixed and moving ground planes. (Ref. 27)

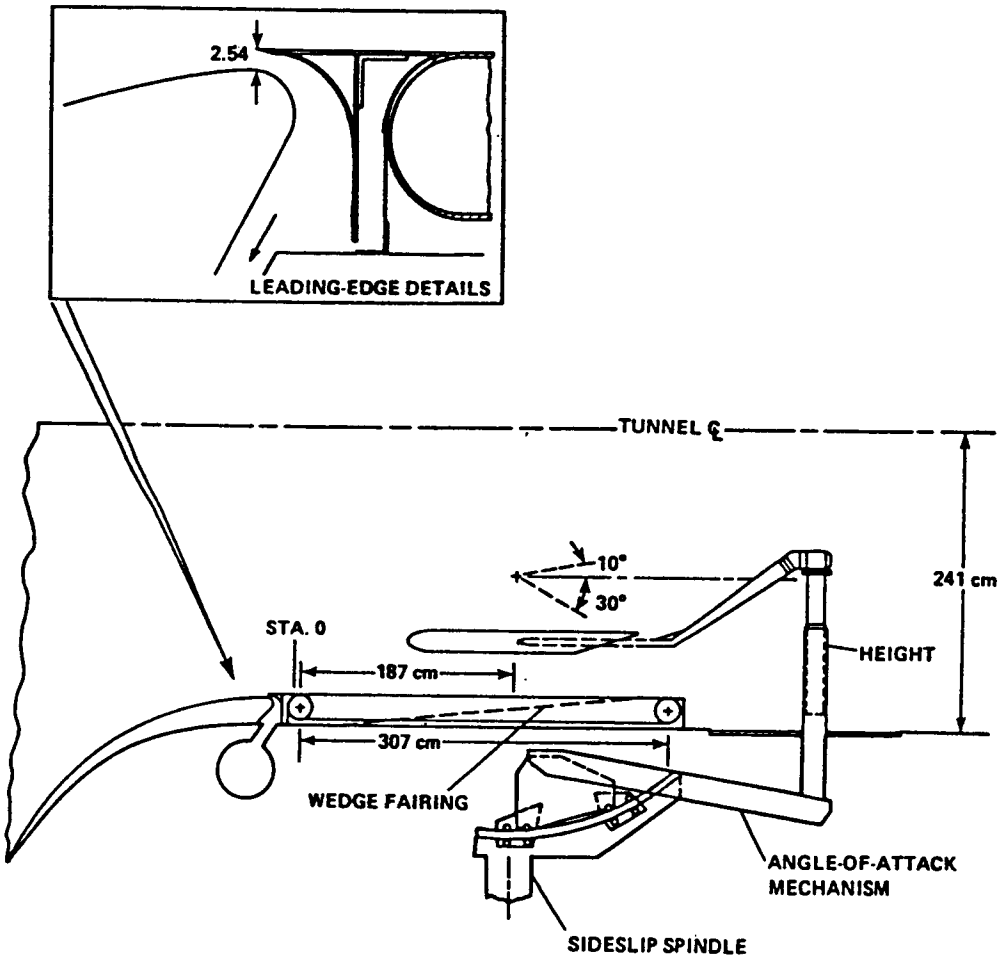

Figure 44.- Turner's moving-belt installation. (Ref. 28)

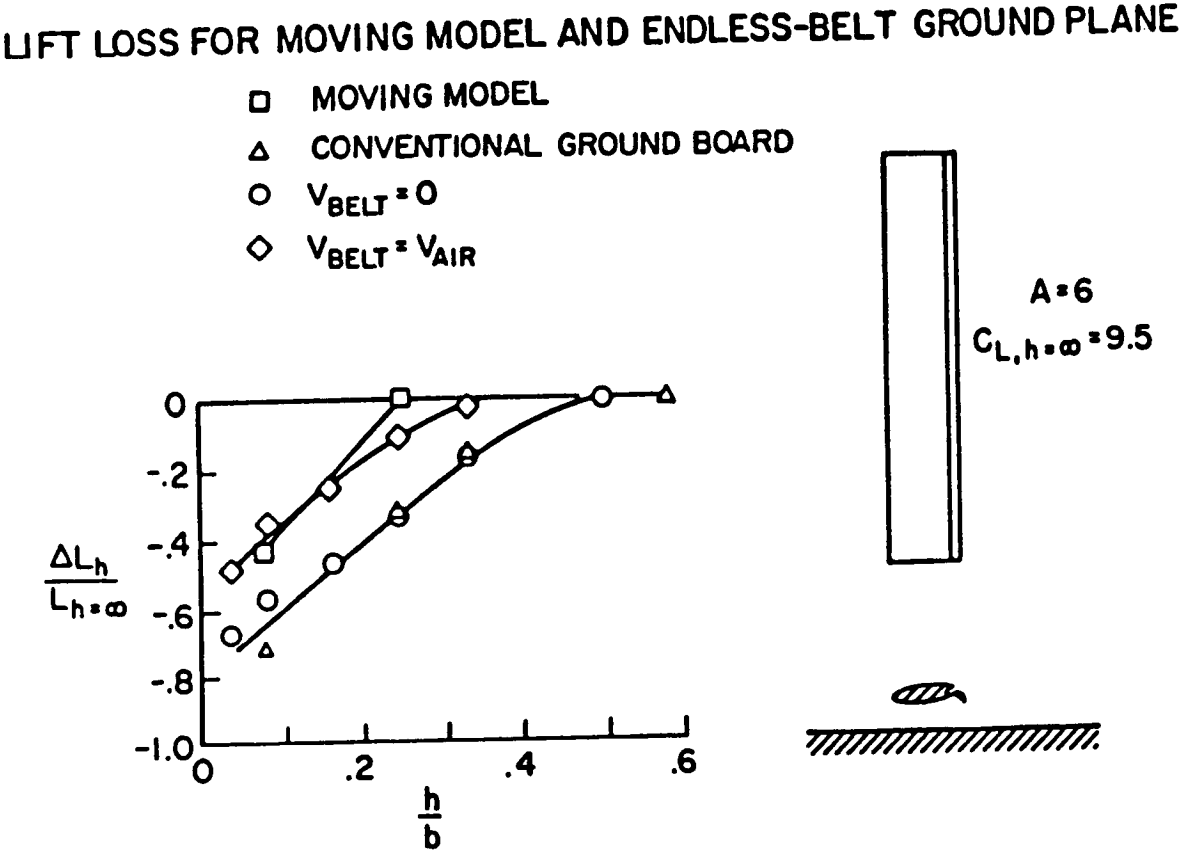

Figure 45.- Lift loss for jet flap model as determined by several testing techniques. (Refs. 28 and 29)

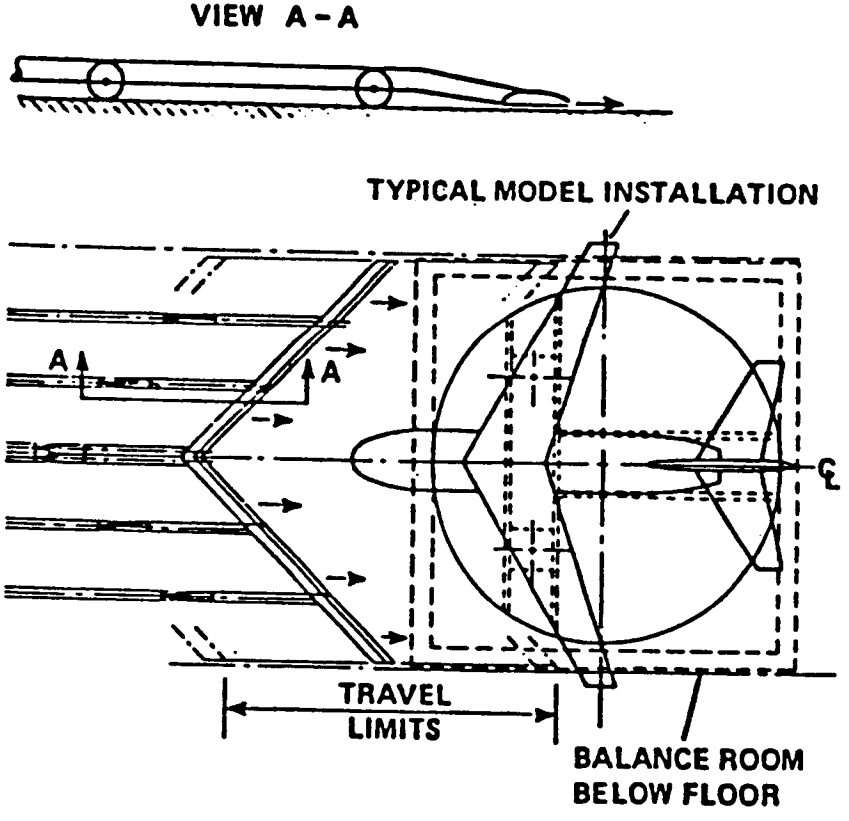

Figure 46.- Ames 40 by 80 proposed floor BLC design. (Ref. 30)

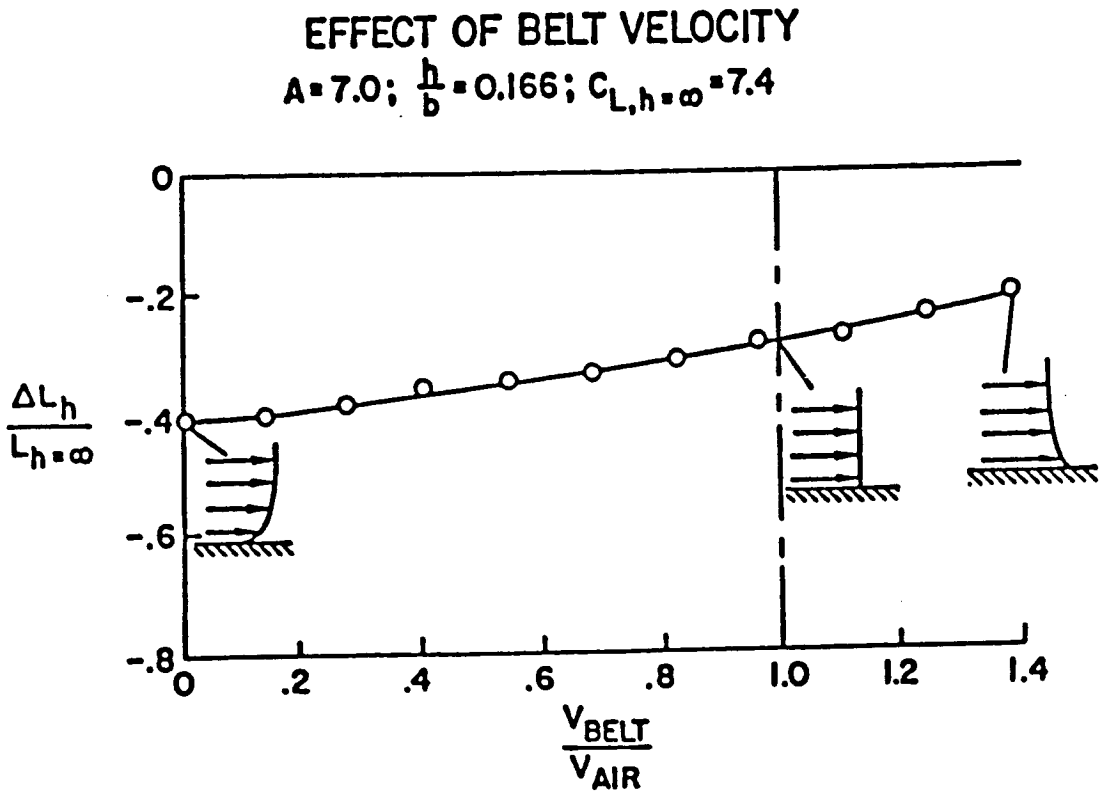

Figure 47.- A "negative" boundary layer may artificially increase lift. (Ref. 29)

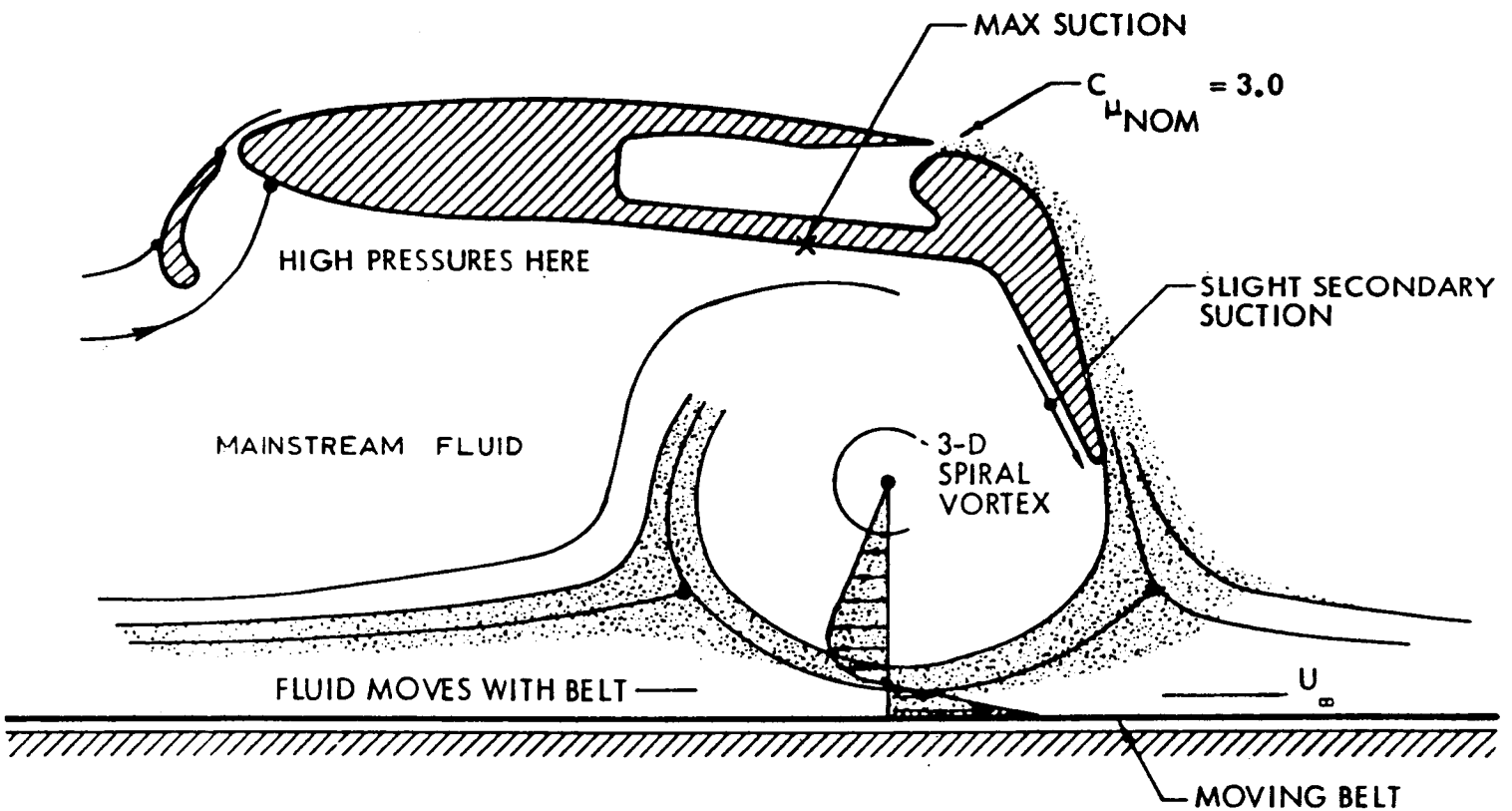

Figure 48.- Formation of trapped, underwing vortex at low altitude and high jet momentum. (Ref. 31)

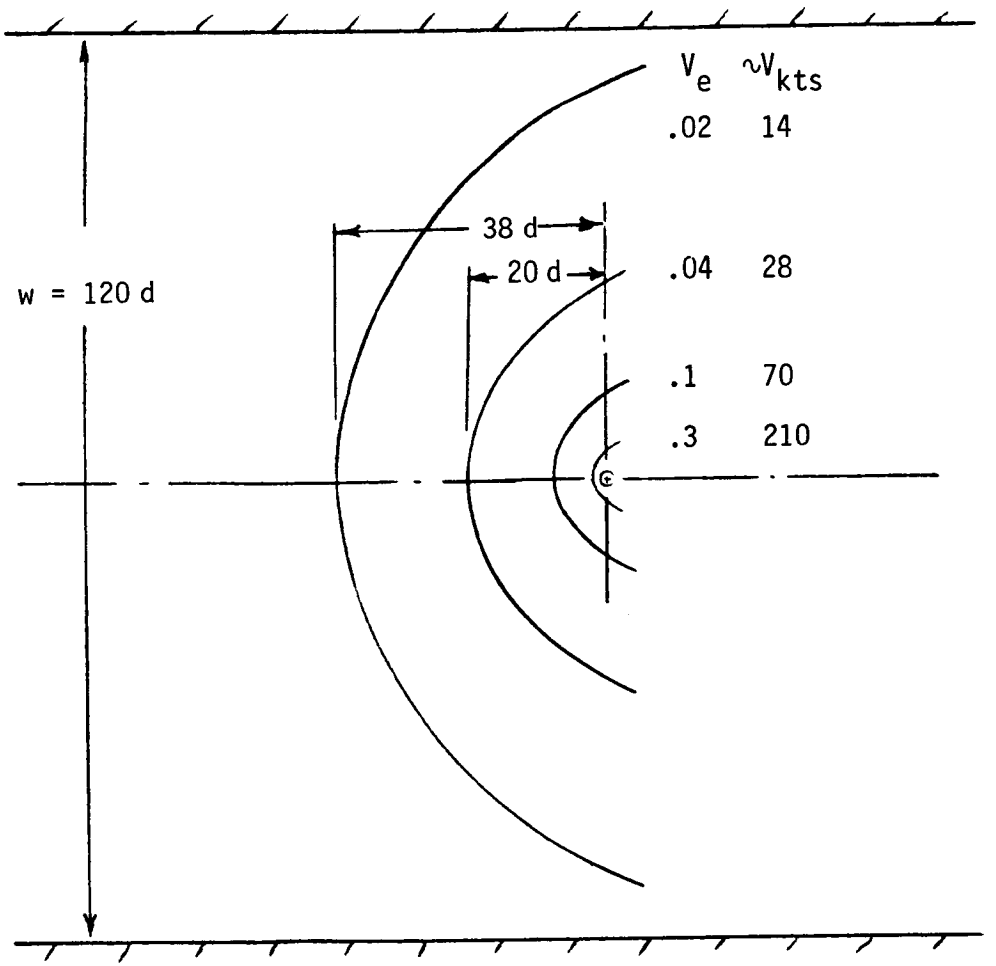

Figure 49.- Approximate leading edge of ground vortex flow, h/d = 1.0 without boundary layer removal.

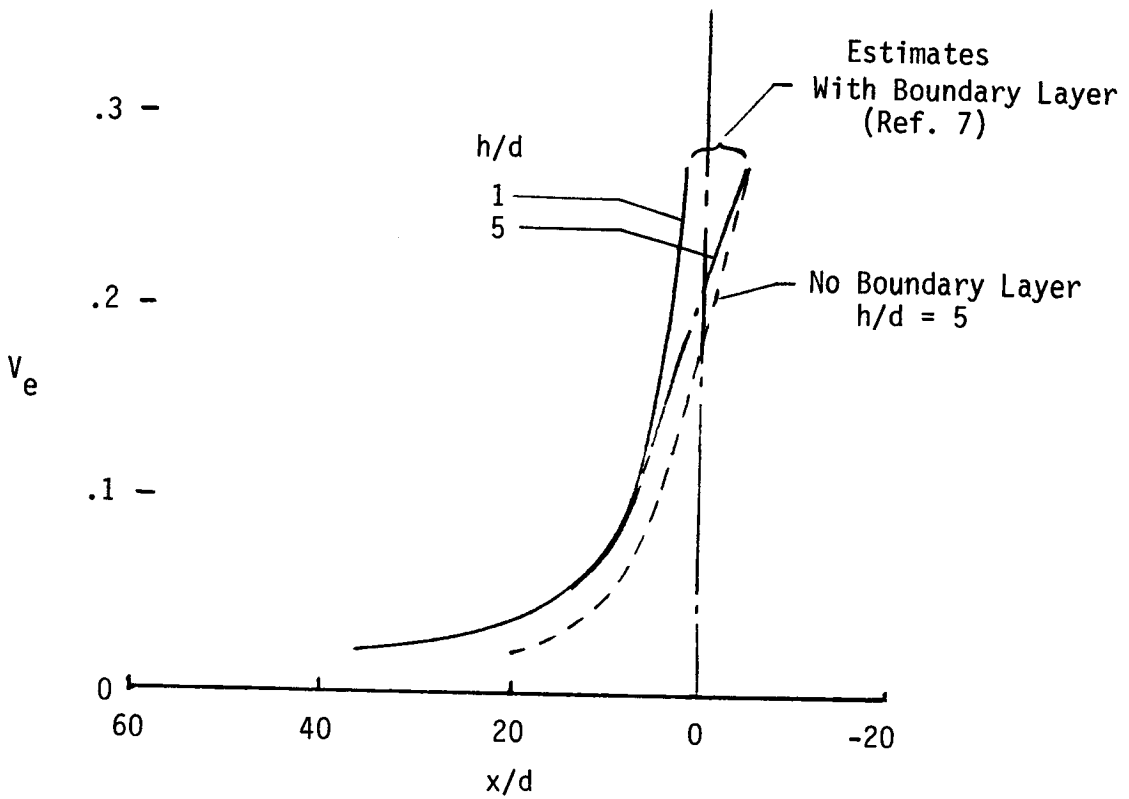

Figure 50.- Estimated position of leading edge of ground vortex flow at centerline.

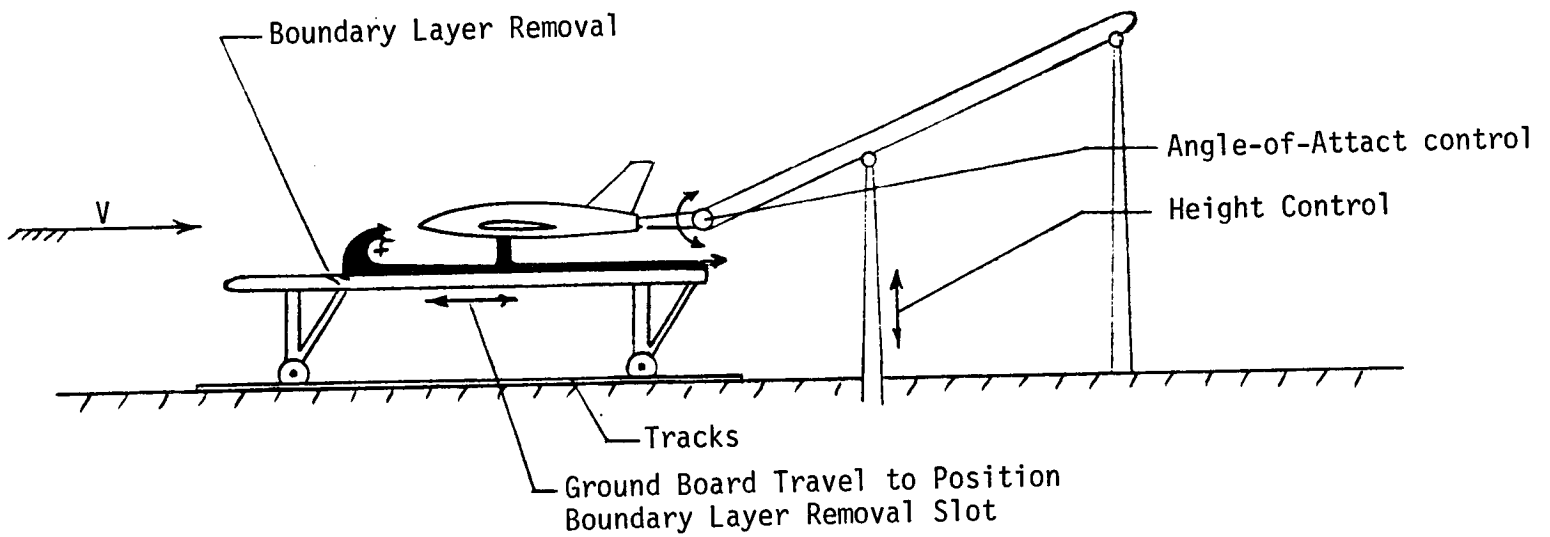

Figure 51.- Schematic of Proposed Ground Board Arrangement.

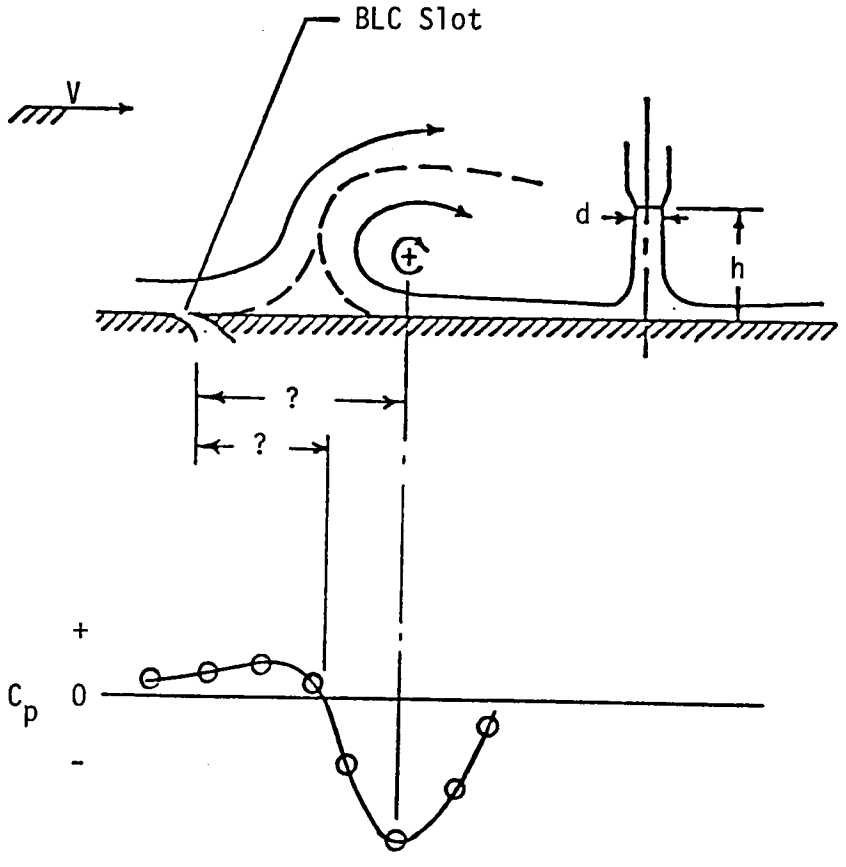

Figure 52.- The ground vortex pressure signature could be used to locate the BLC slot.

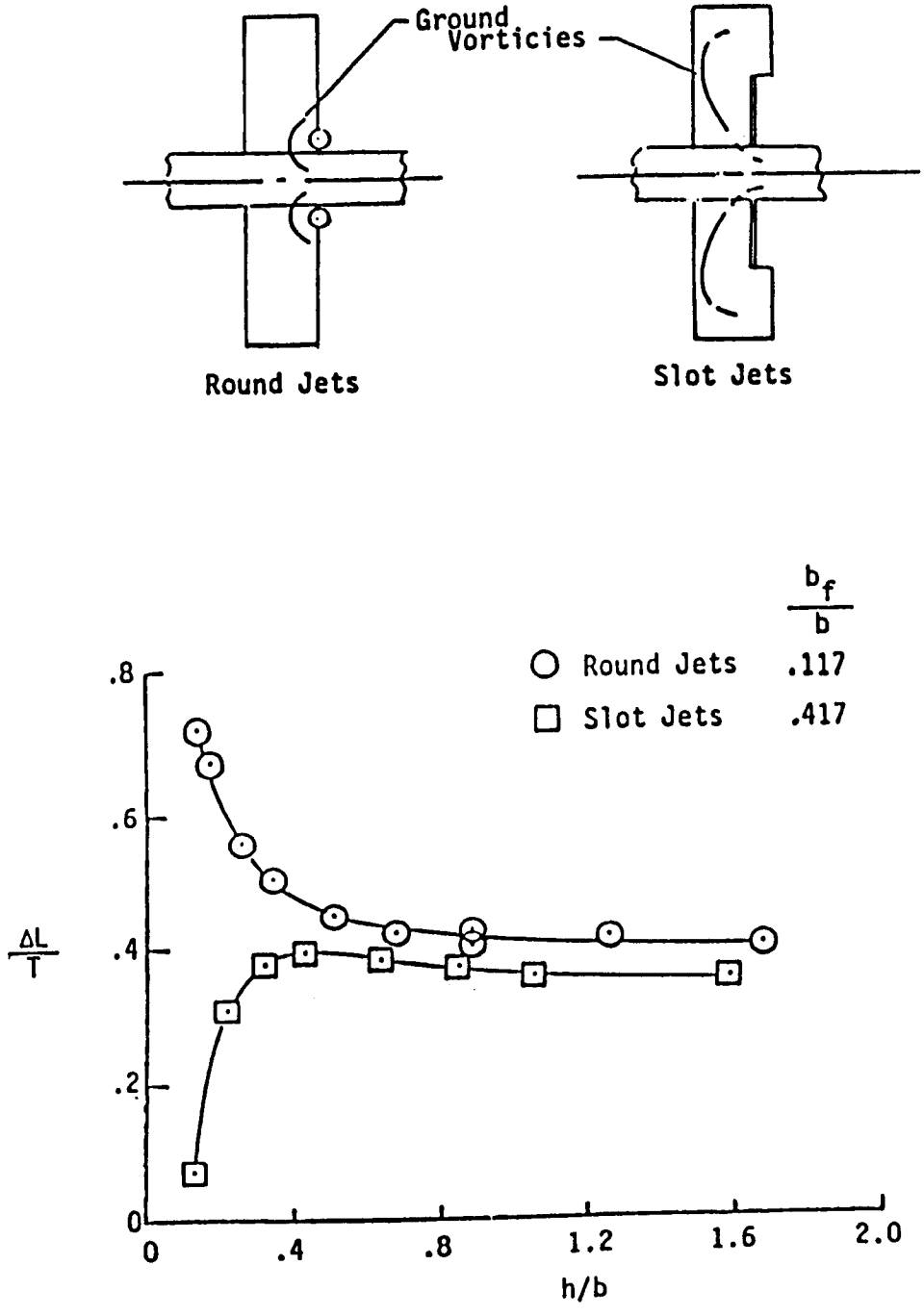

Figure 53.- Comparison of ground effects on circular (direct thrust) and slot jet (jet flap) configuration. (Ref. 10)

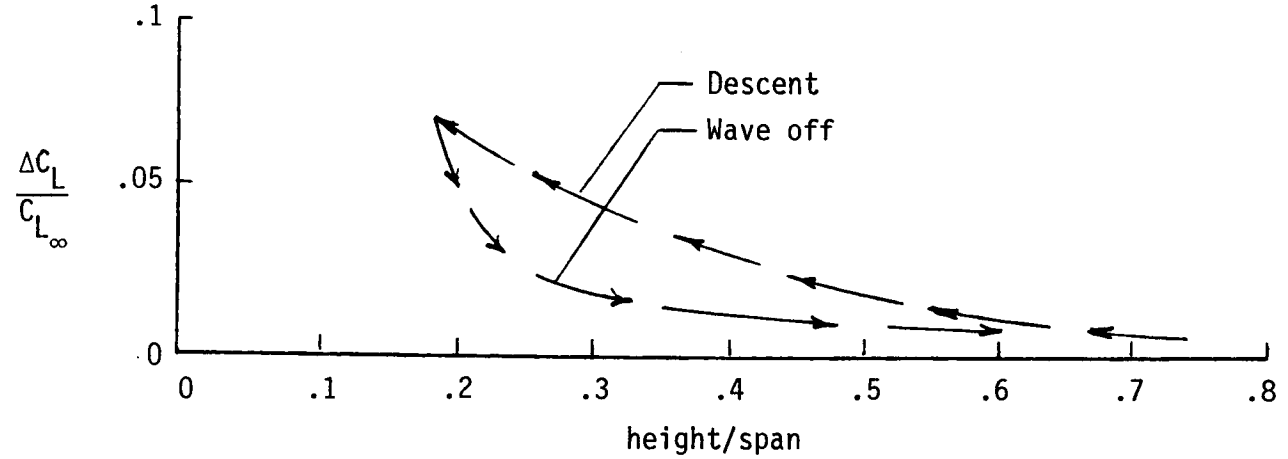

Figure 54.- Touch-and-Go landings show ground effect hysteresis. $C_{L_\infty} \sim 2.5$, (Ref. 33)

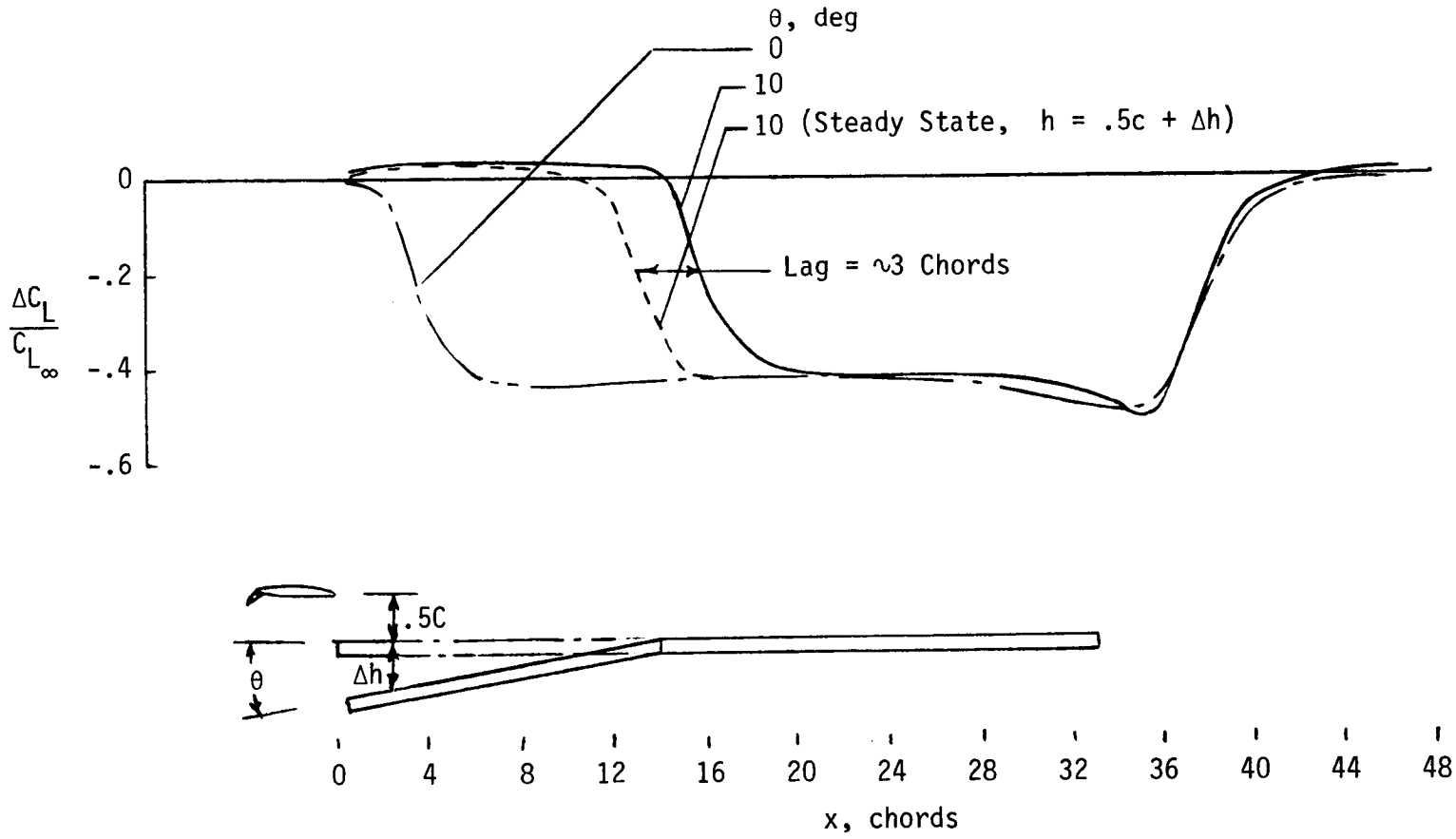

Figure 55.- Moving model tests show lag in development of jet flap ground effects. C_{L_∞} = 9.5, (Ref.26)

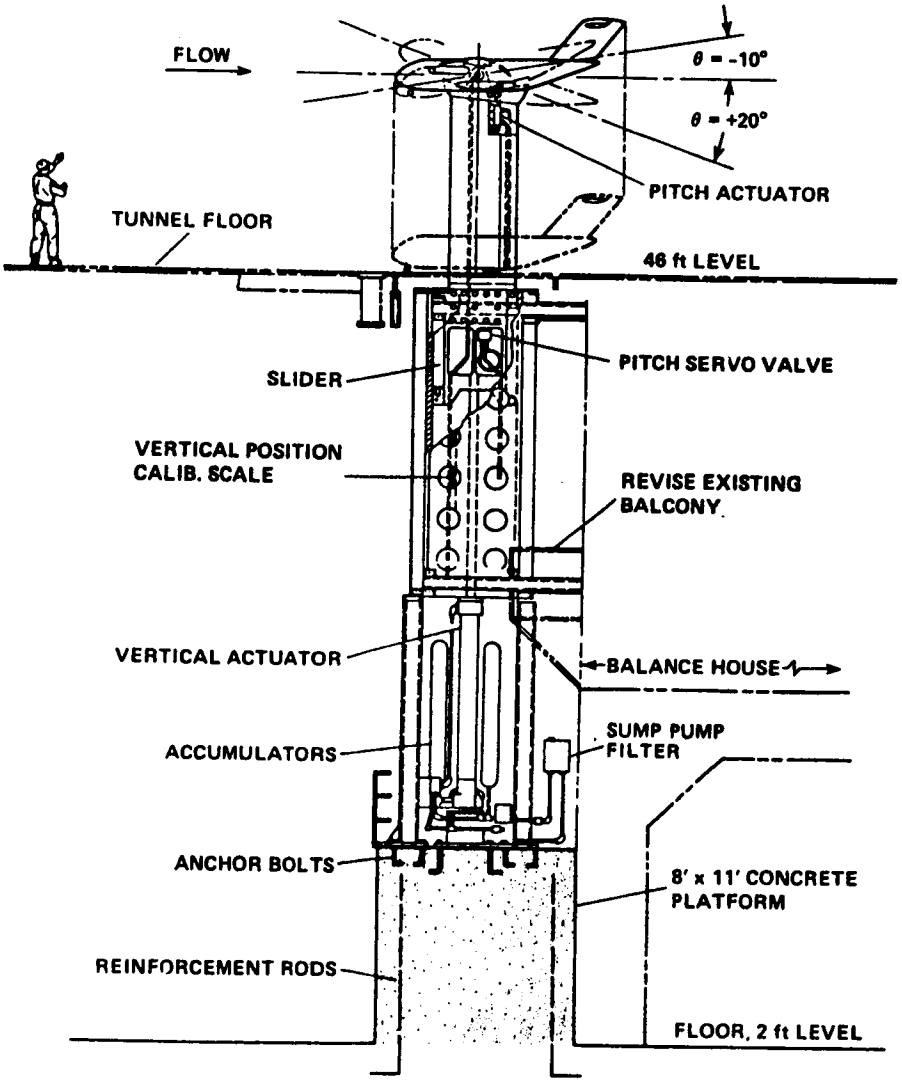

Figure 56.- Transient ground-effect support design for the Ames 40 by 80. (Ref. 34)

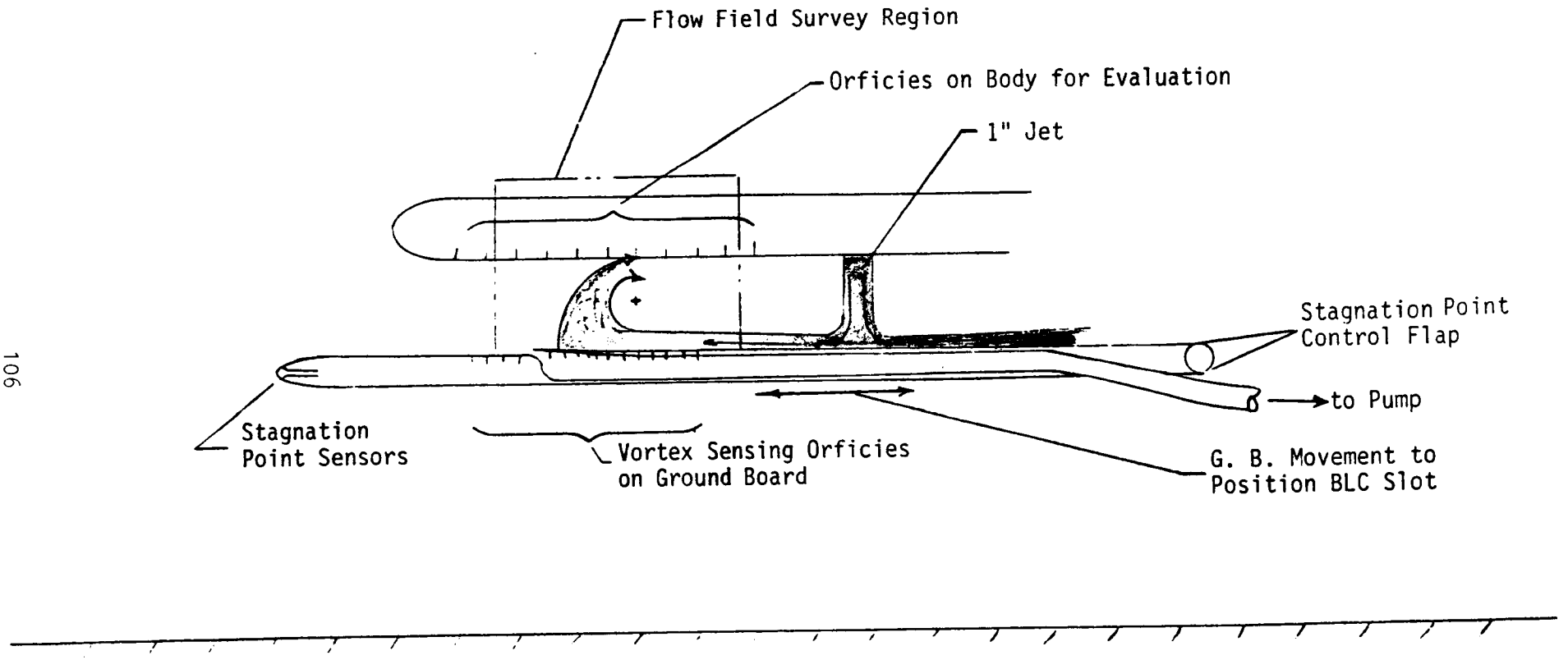

Figure 57.- Ground-vortex-signature controlled translating ground board concept.

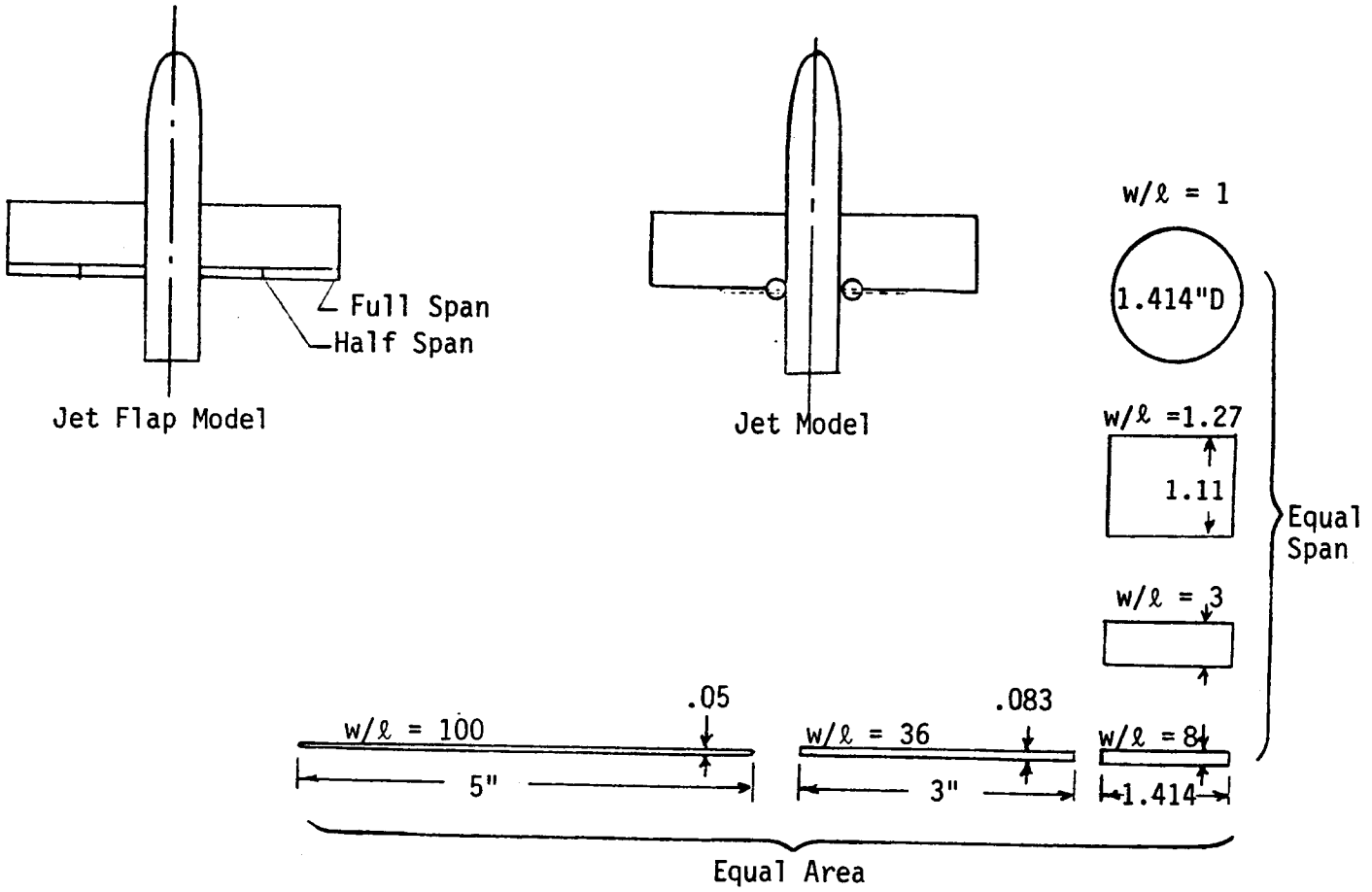

Figure 58.- Suggested model configurations for jet configuration effects investigation.

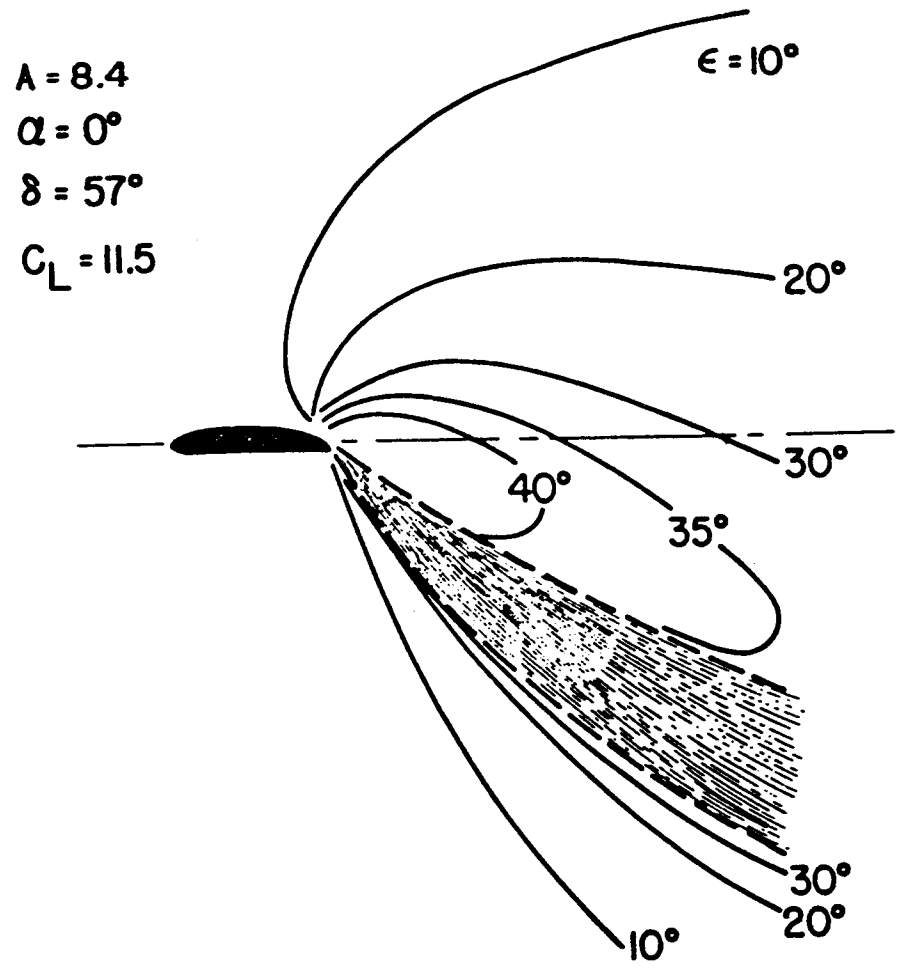

Figure 59.- Downwash field behind a jet-augmented flap at the midsemispan station. (Ref. 35)

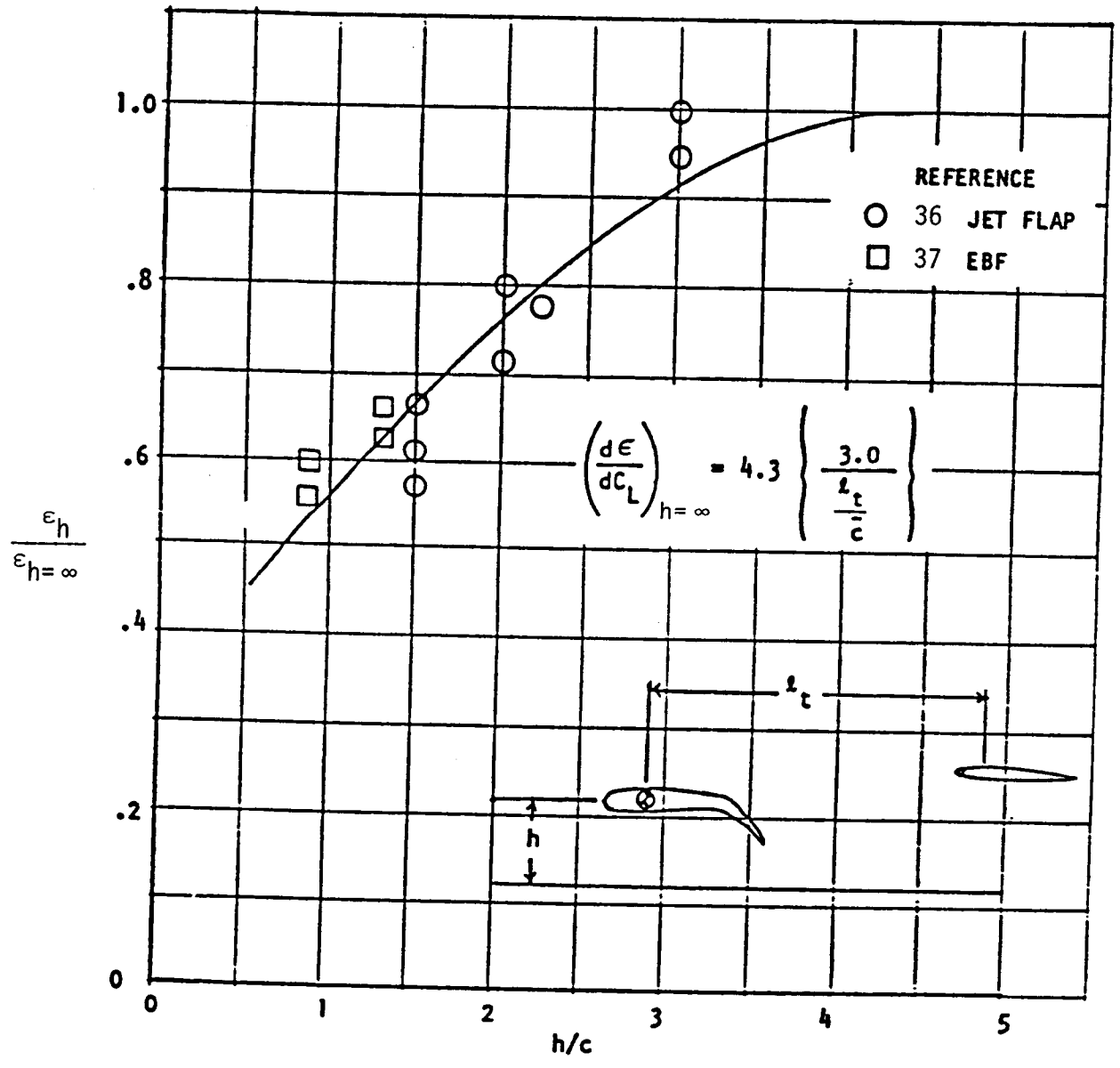

Figure 60.- Effect of ground proximity on downwash. (Ref. 10)

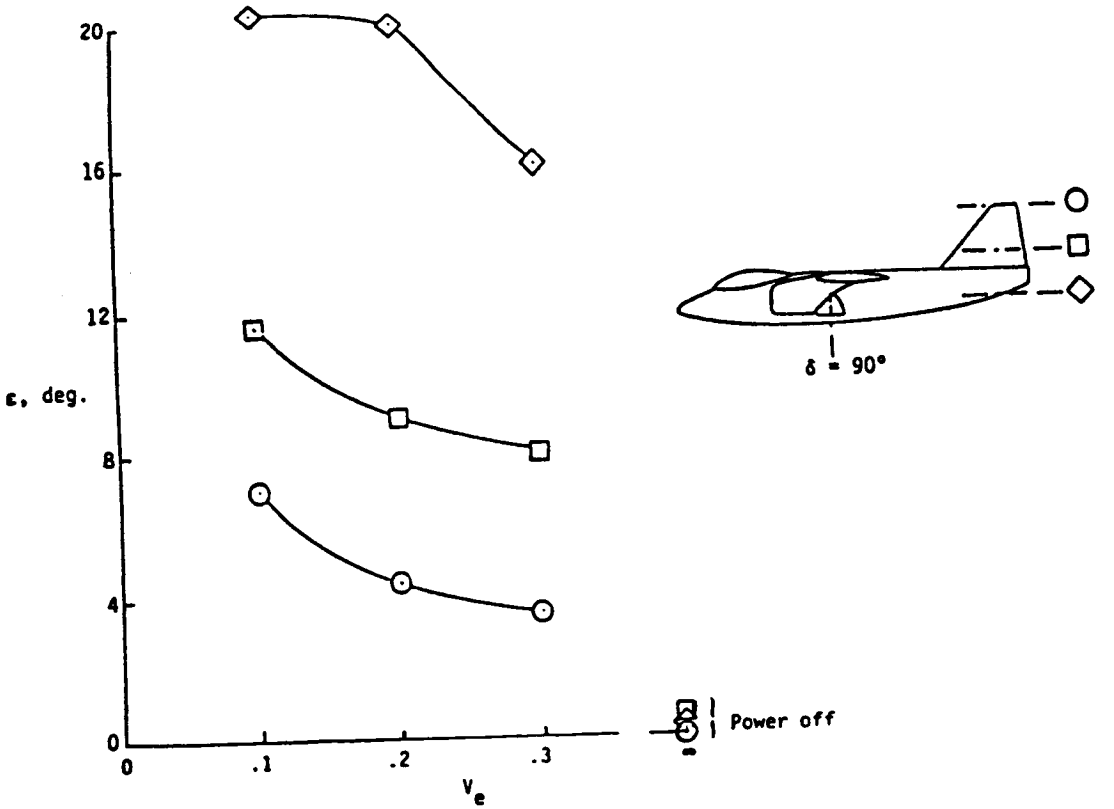

Figure 61.- Jet induced downwash for configuration of Ref. 38 showing effect of tail height.

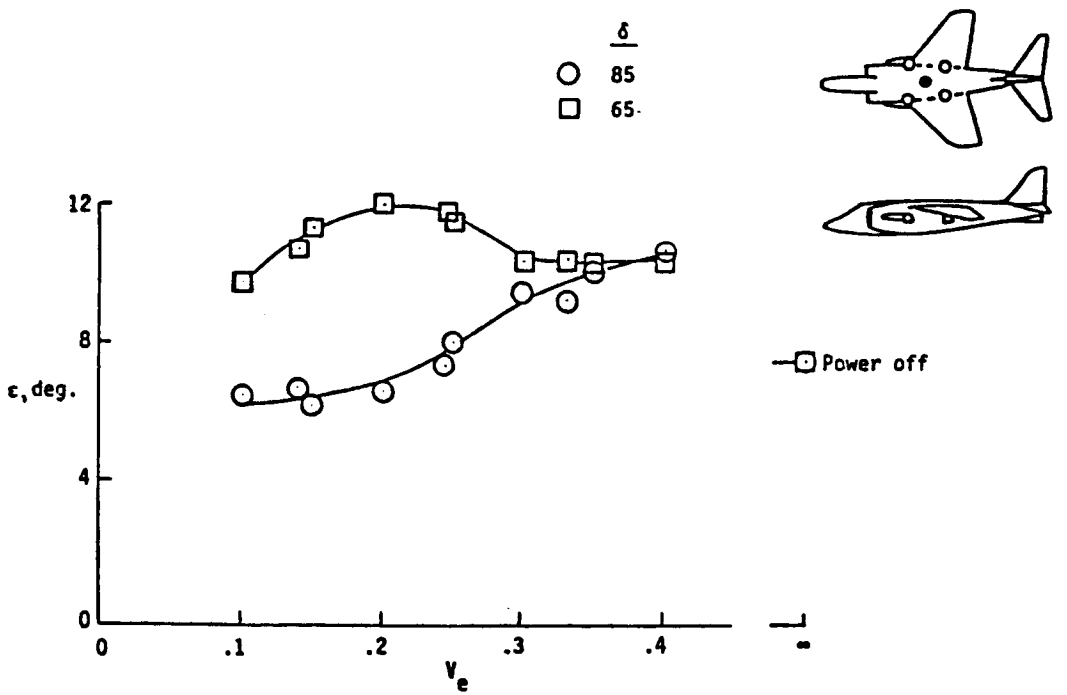

Figure 62.- Jet induced downwash for configuration of Ref. 39.

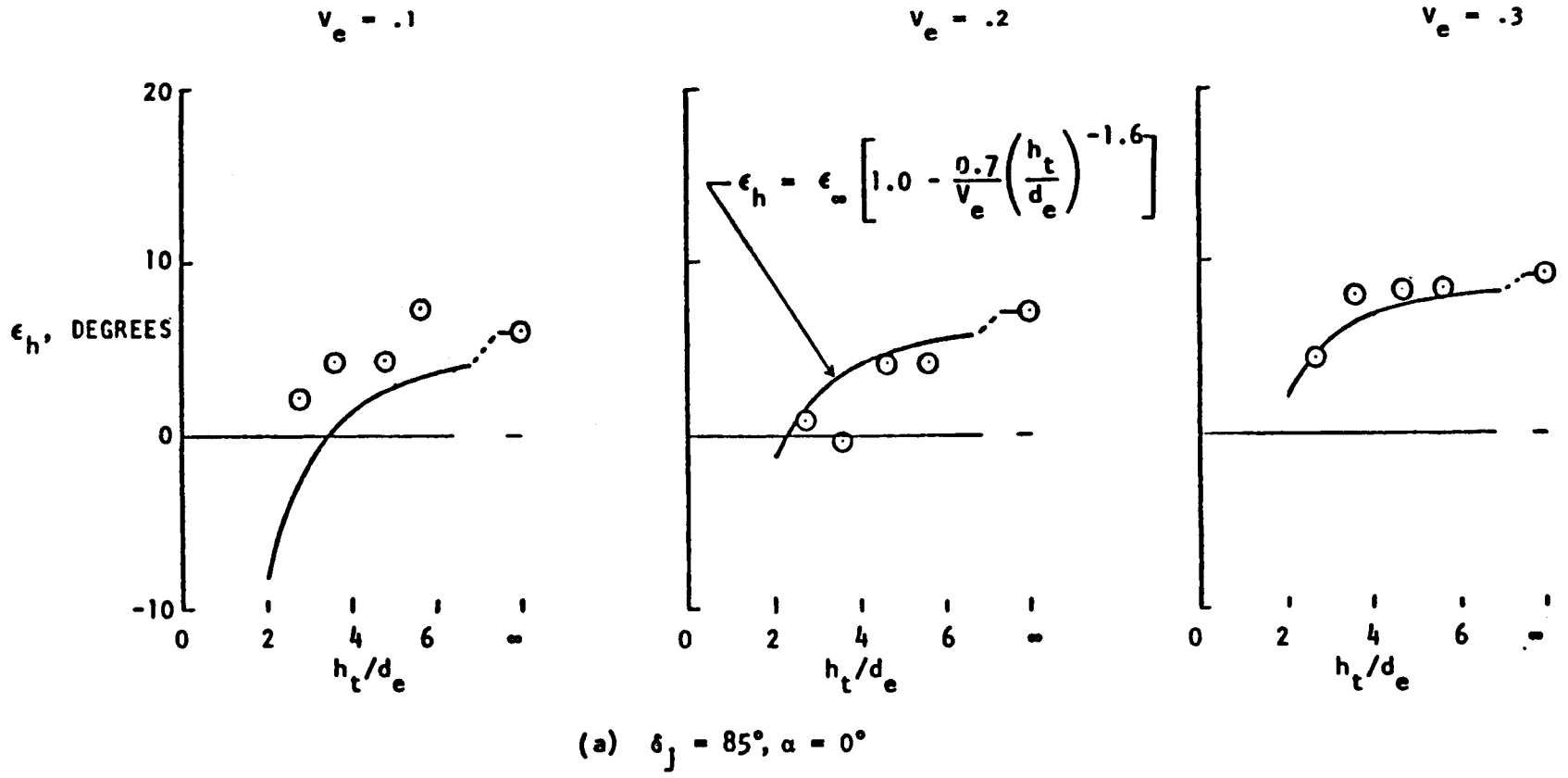

Figure 63.- Effect of ground proximity on downwash at tail of configuration of Ref. 39.

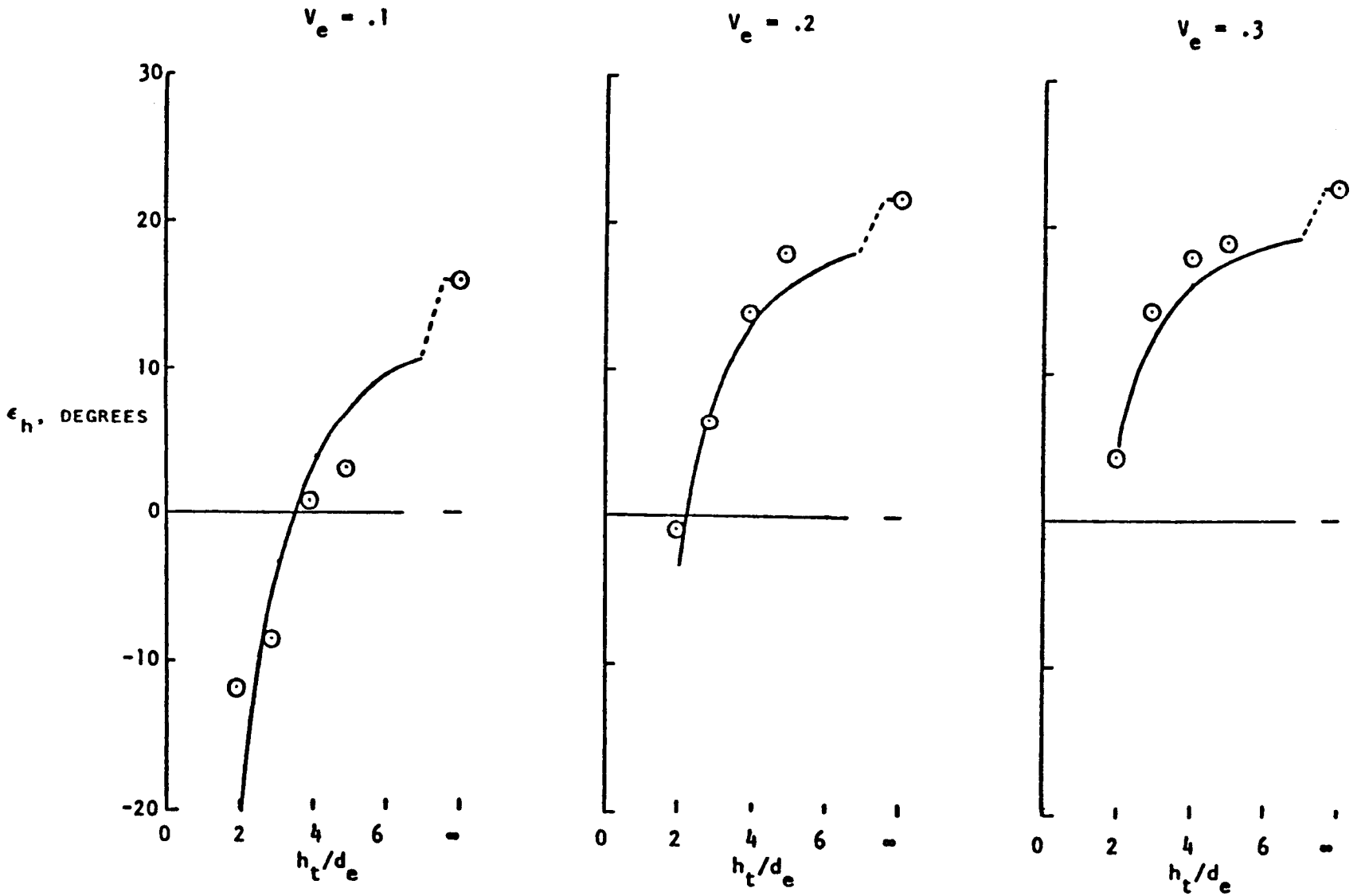

(d) $\delta_j = 65°$, $\alpha = 9°$

Figure 63.- (Concluded).

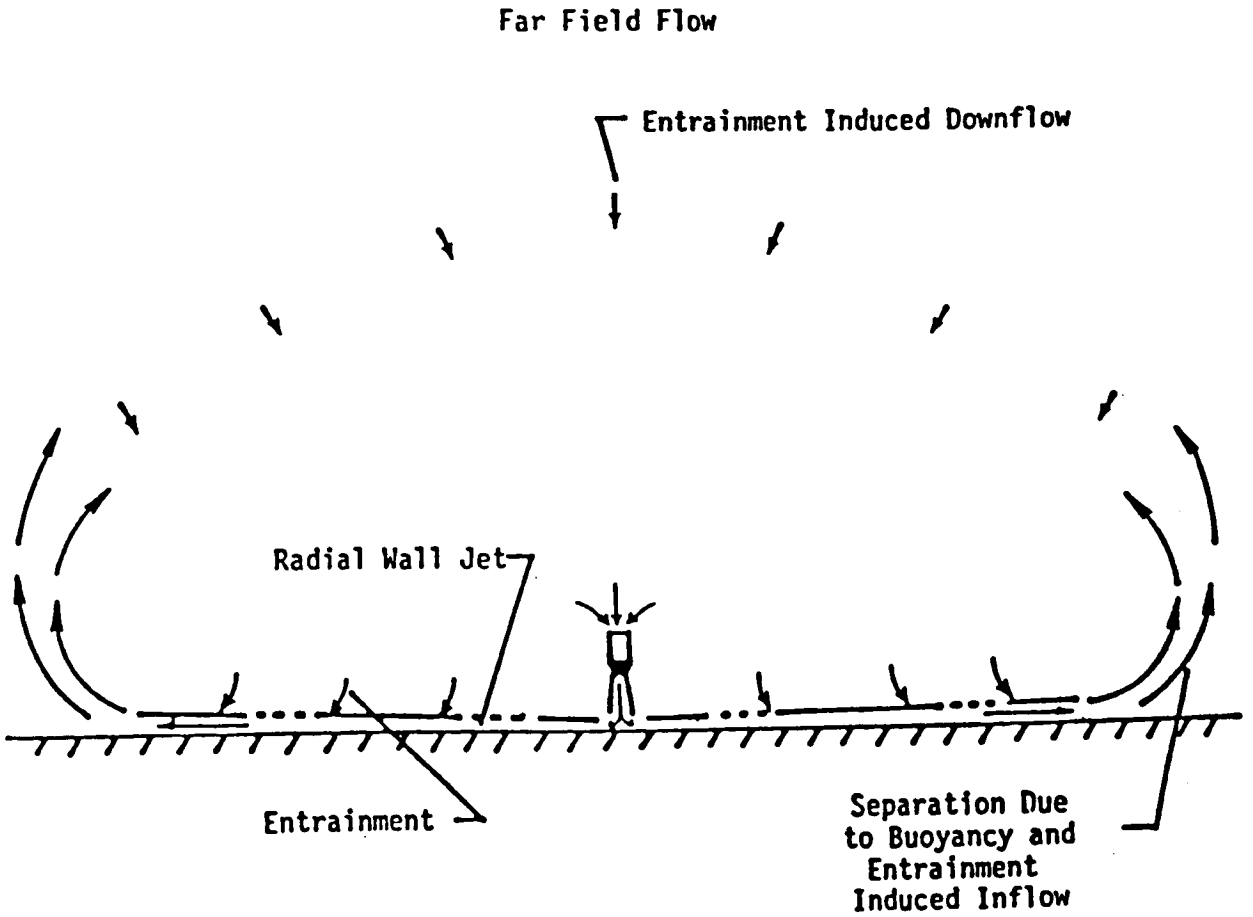

Figure 64.- Far field ingestion.

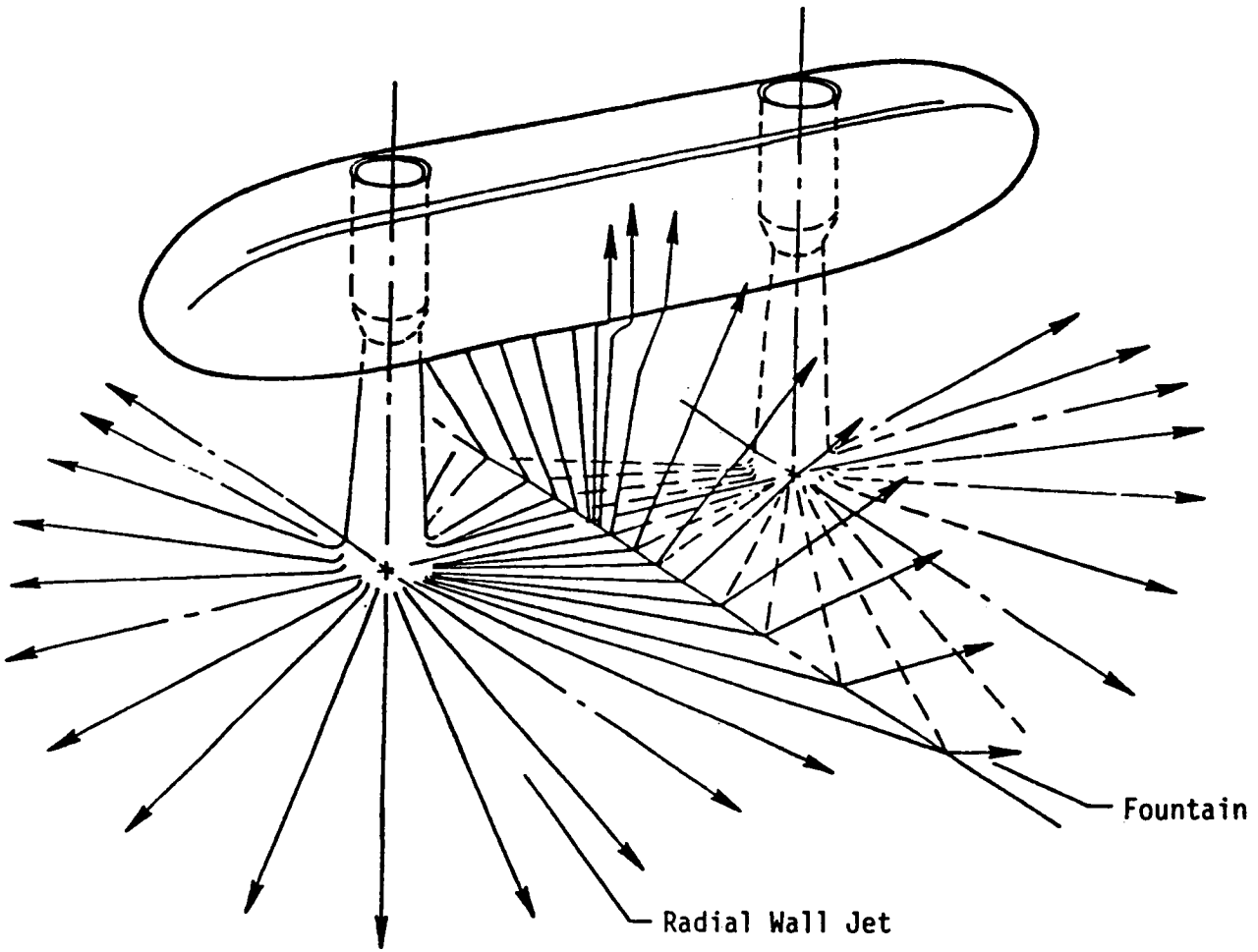

Figure 65. Fountain Flow Field

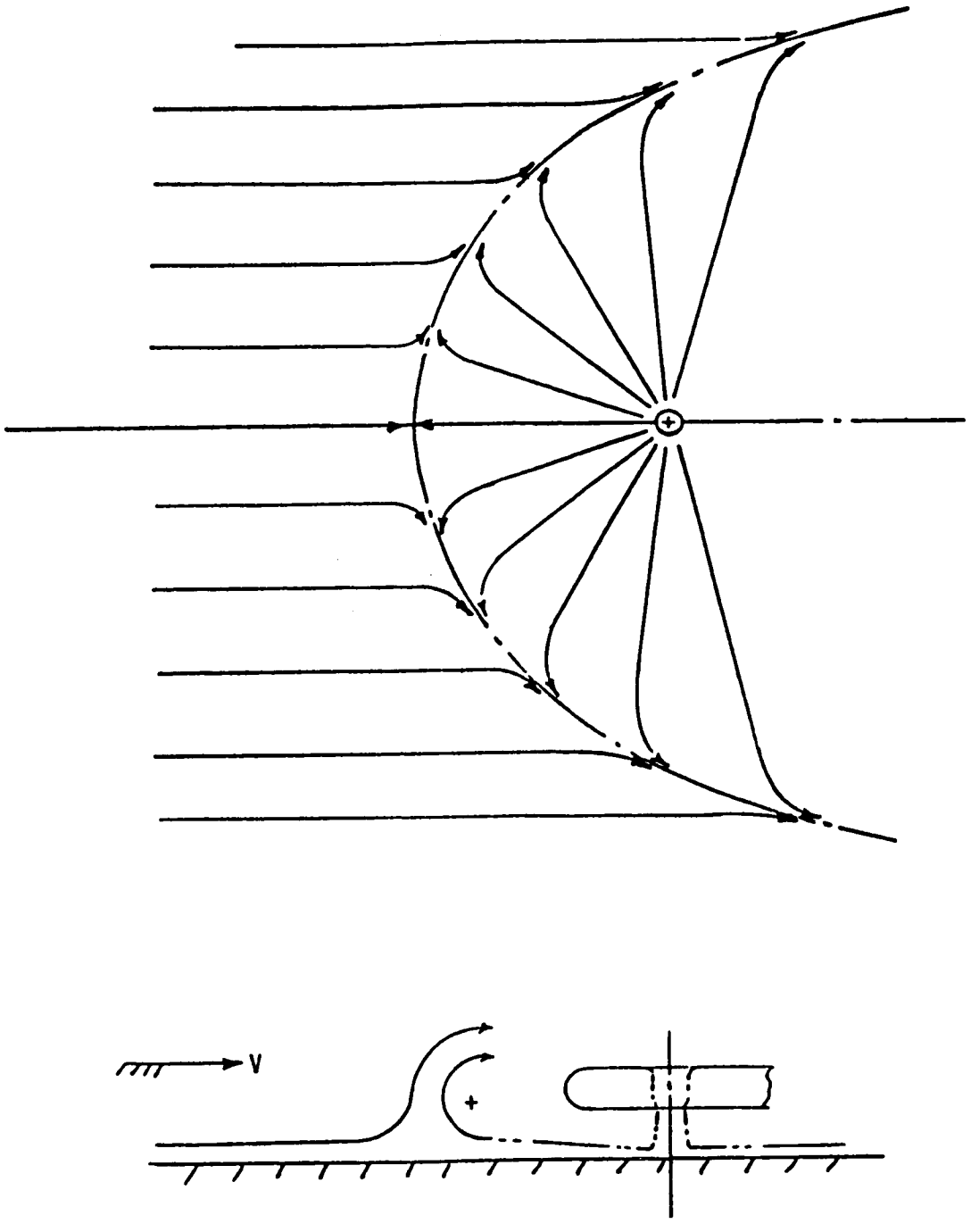

Figure 66.- Ground vortex flow field.

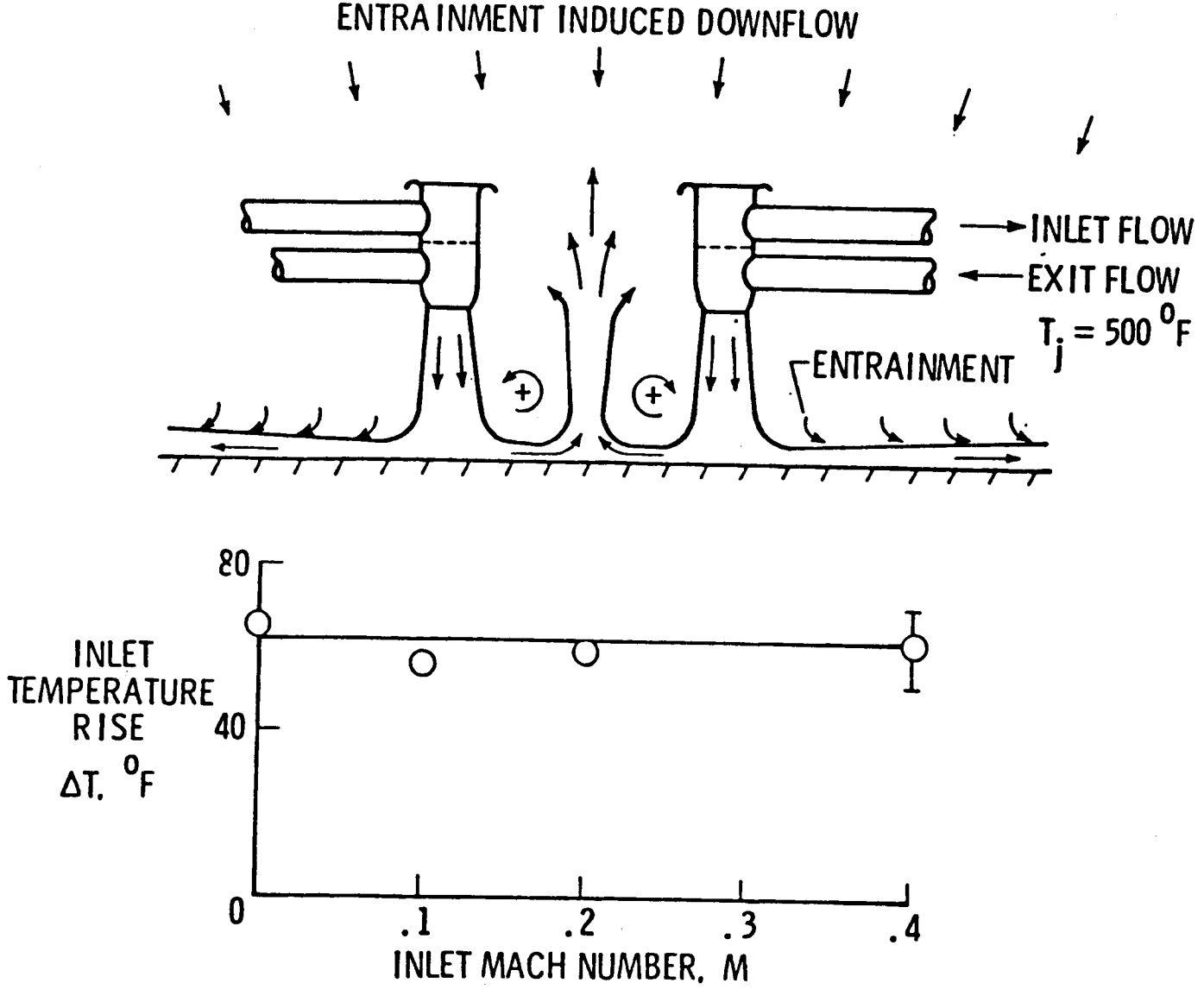

Figure 67.- Inlet temperature rise with two isolated jets. (Ref. 12)

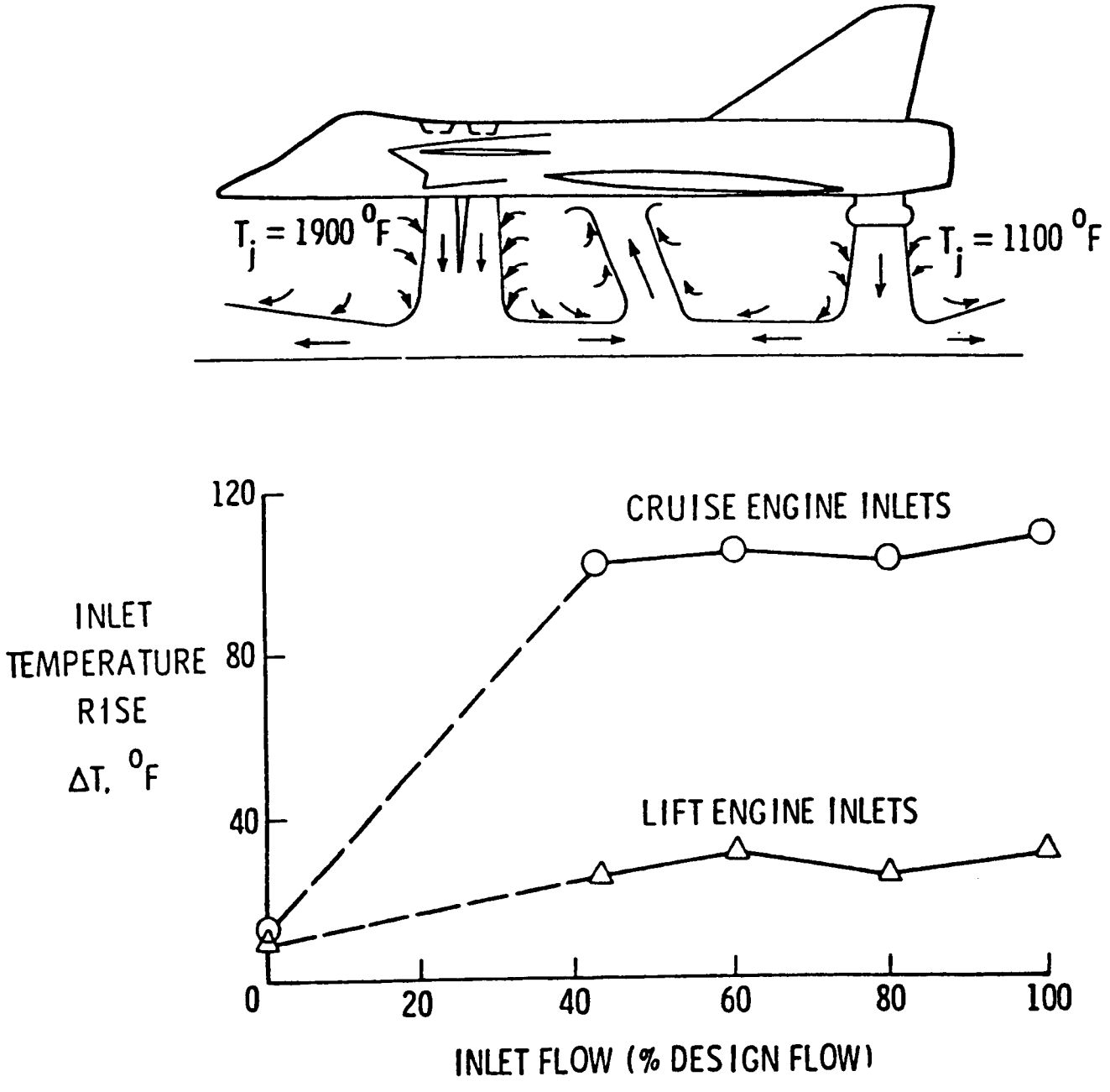

Figure 68.- Inlet temperature rise with fountain inpingement. (Ref. 23)

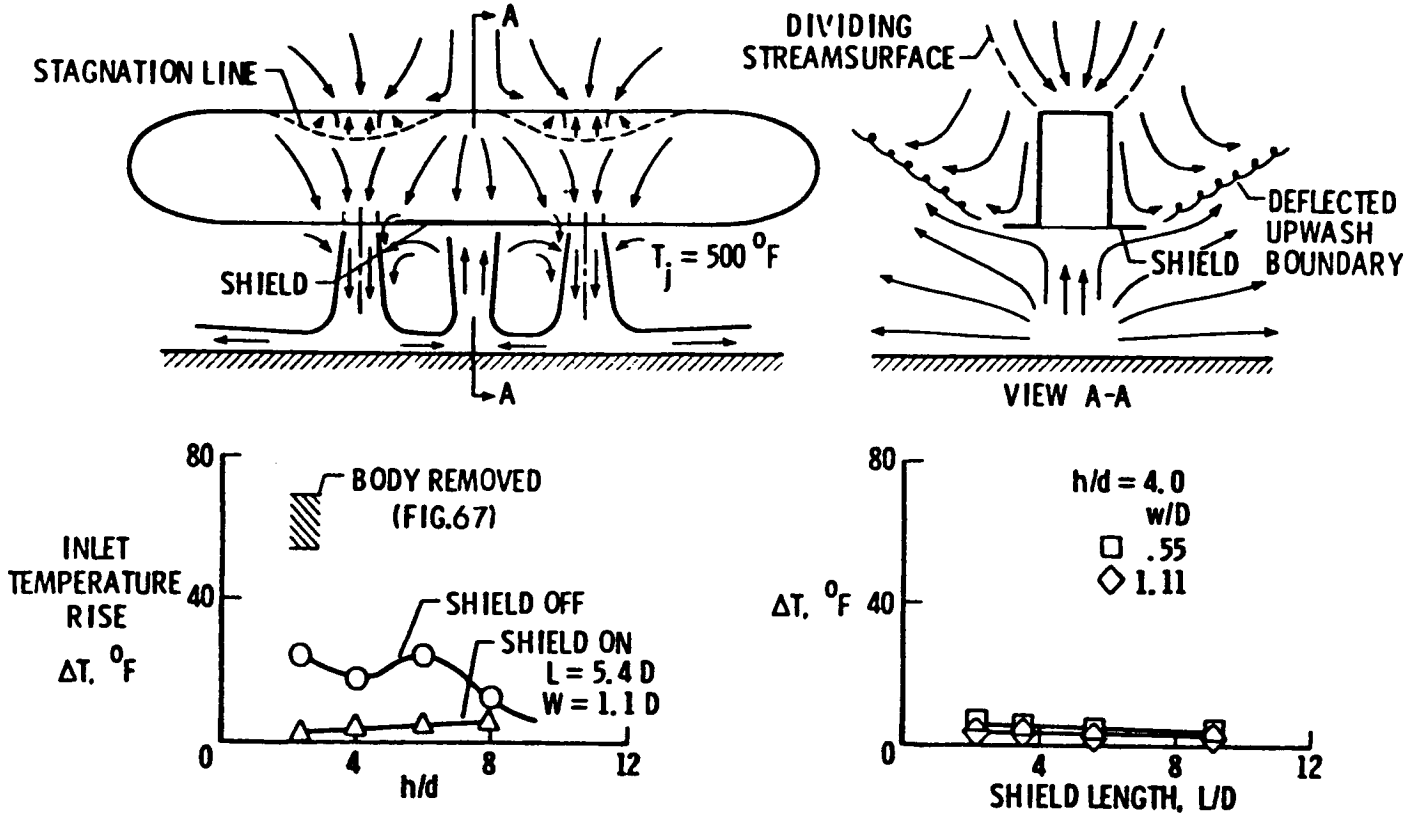

Figure 69.- Effect of exit plane shields. (Ref. 40)

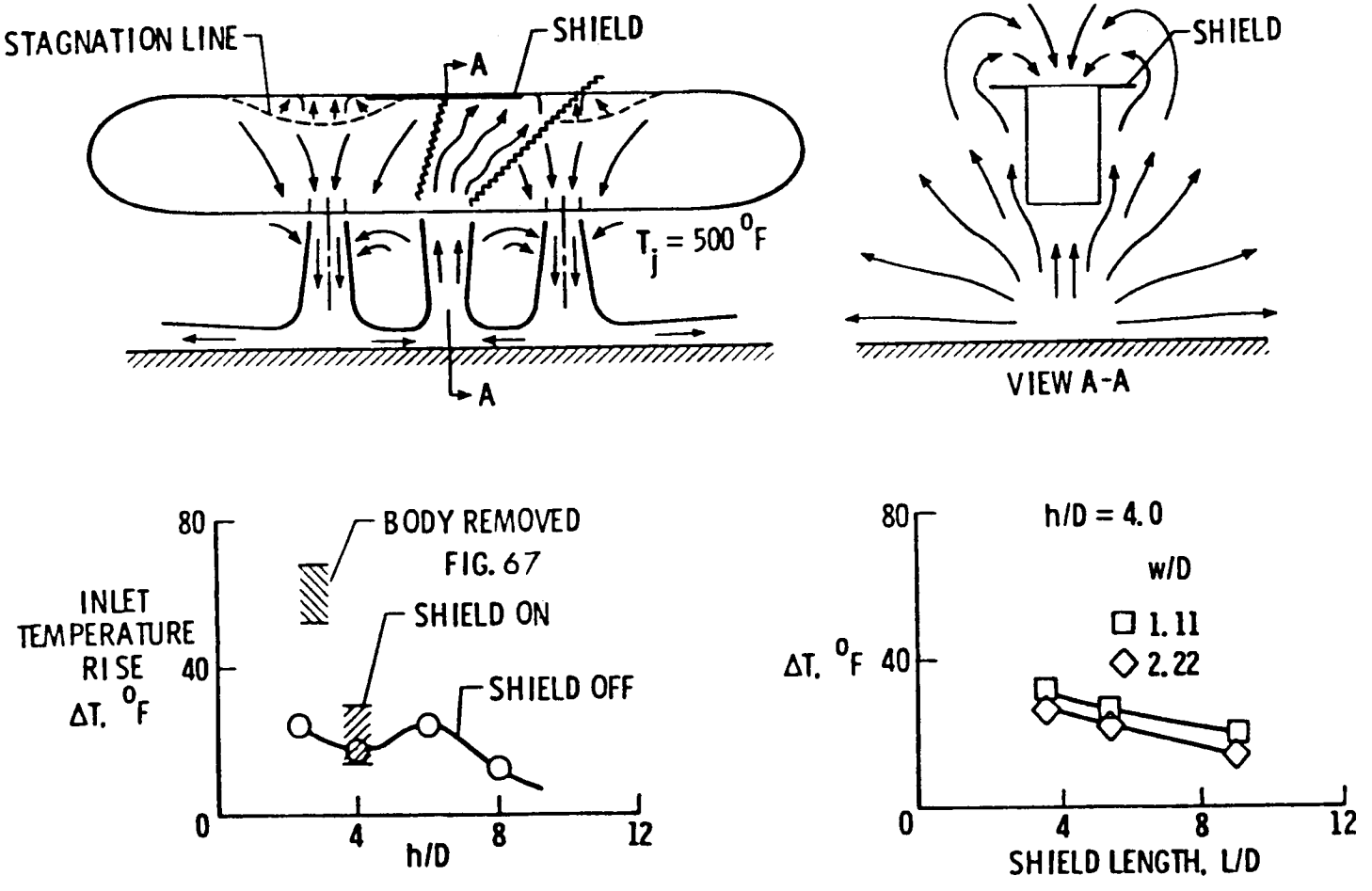

Figure 70.- Effect of inlet plane shields. (Ref. 40)

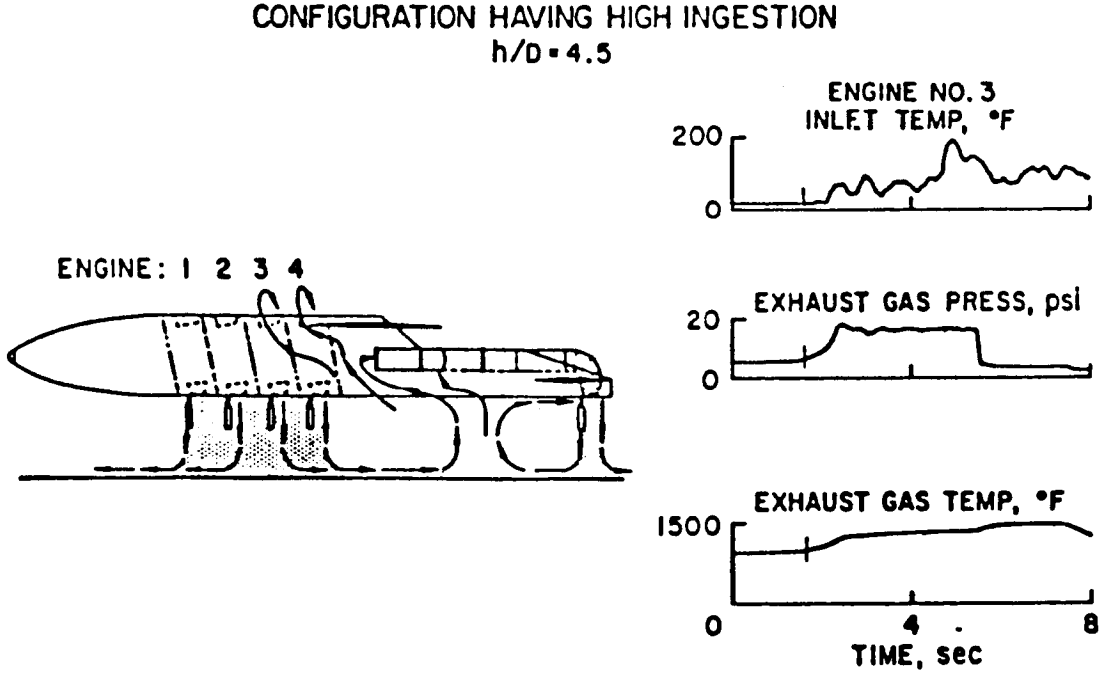

Figure 71.- Inlet temperature history for configuration having a high level of ingestion. (Ref. 41)

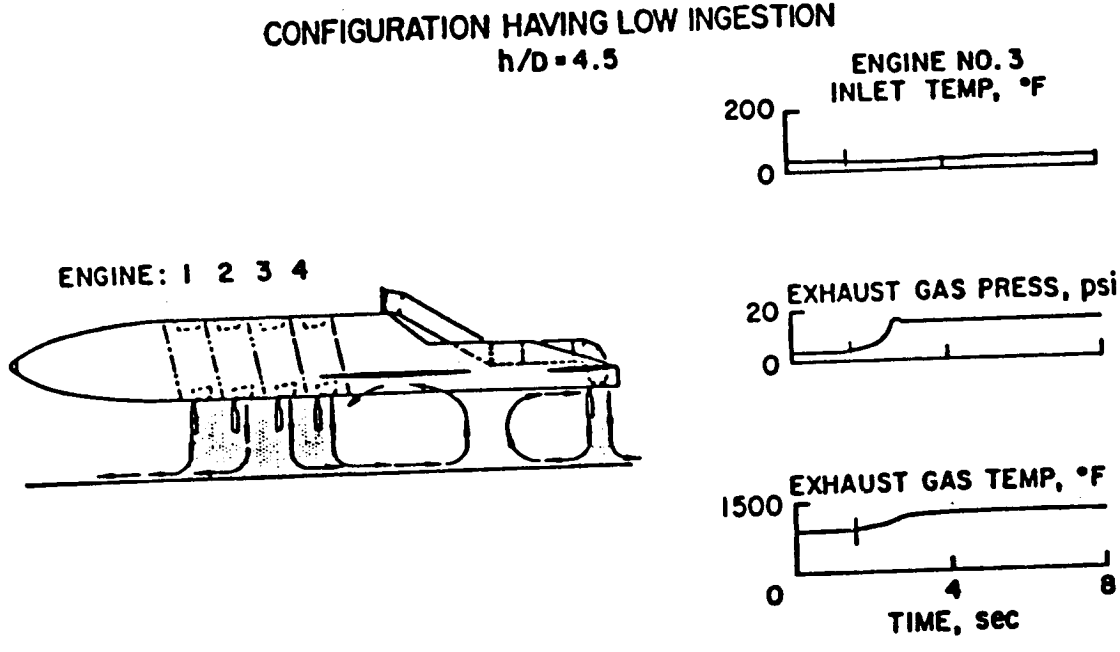

Figure 72.- Inlet time history for configuration having negligible ingestion. (Ref. 41)

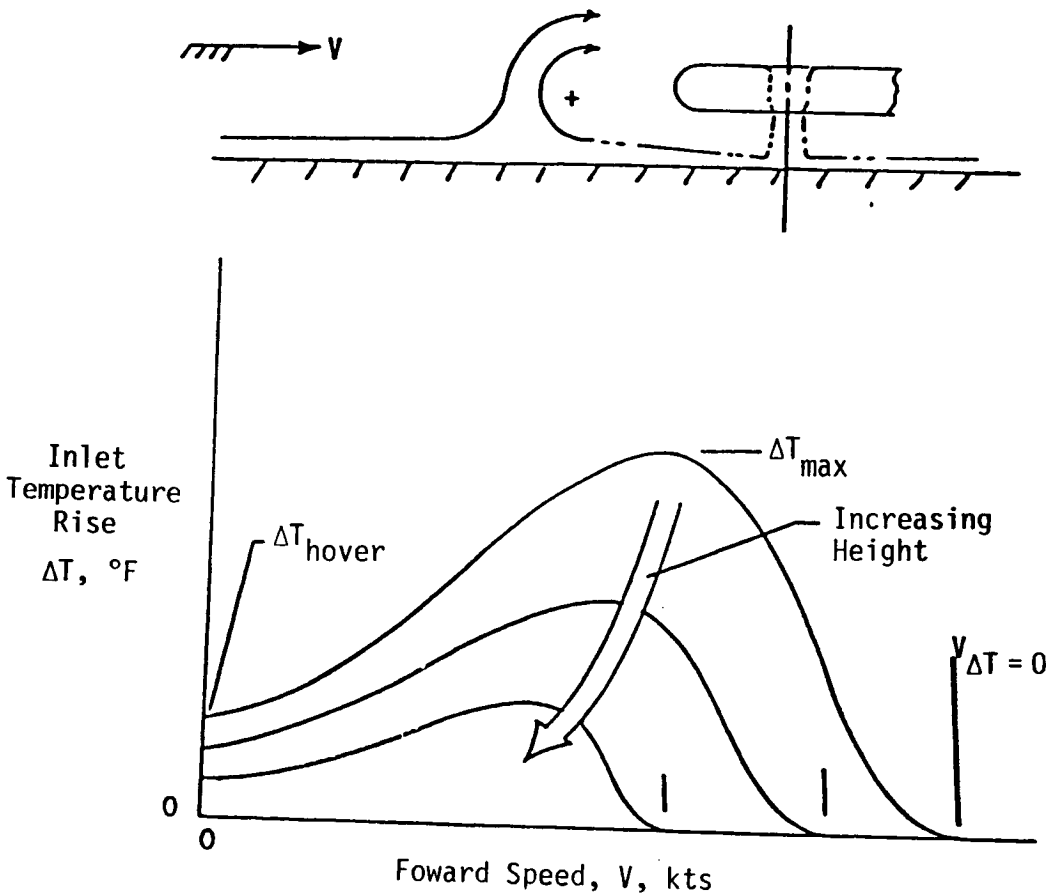

Figure 73.- Typical variation of inlet temperature rise with foward speed.

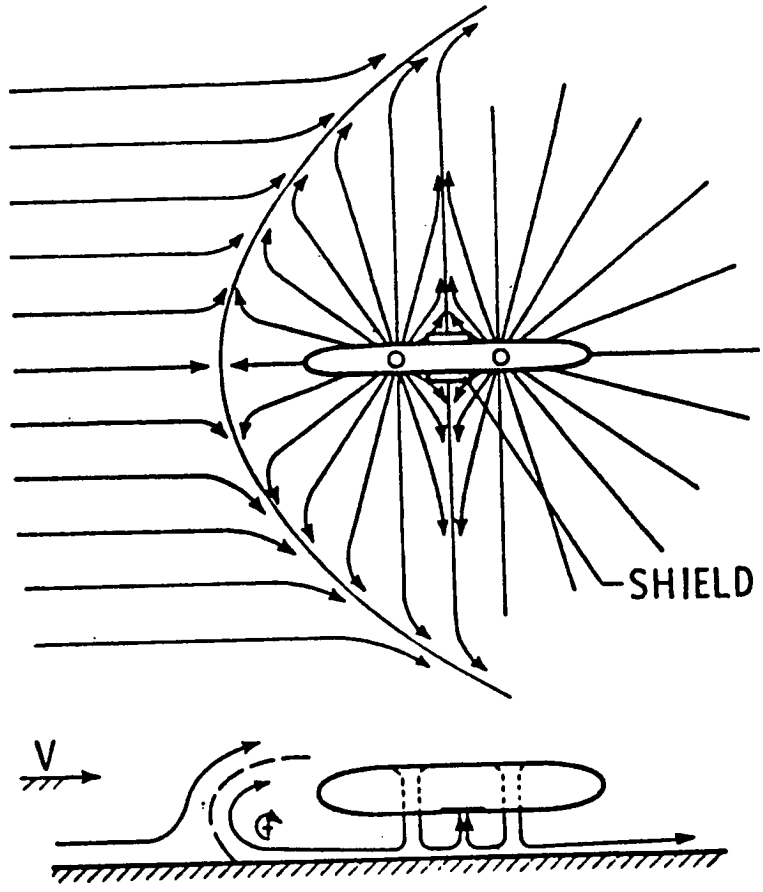

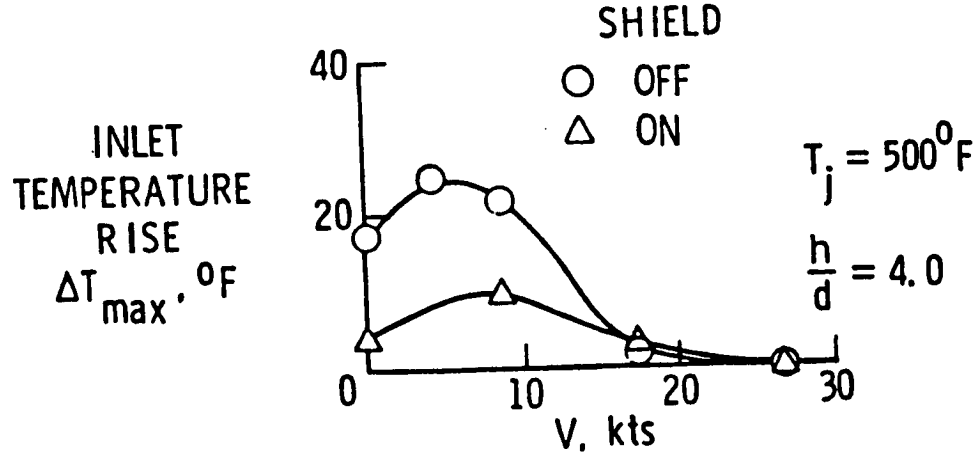

Figure 74.- Effect of free stream on configuration with two jets inline. (Ref. 40).

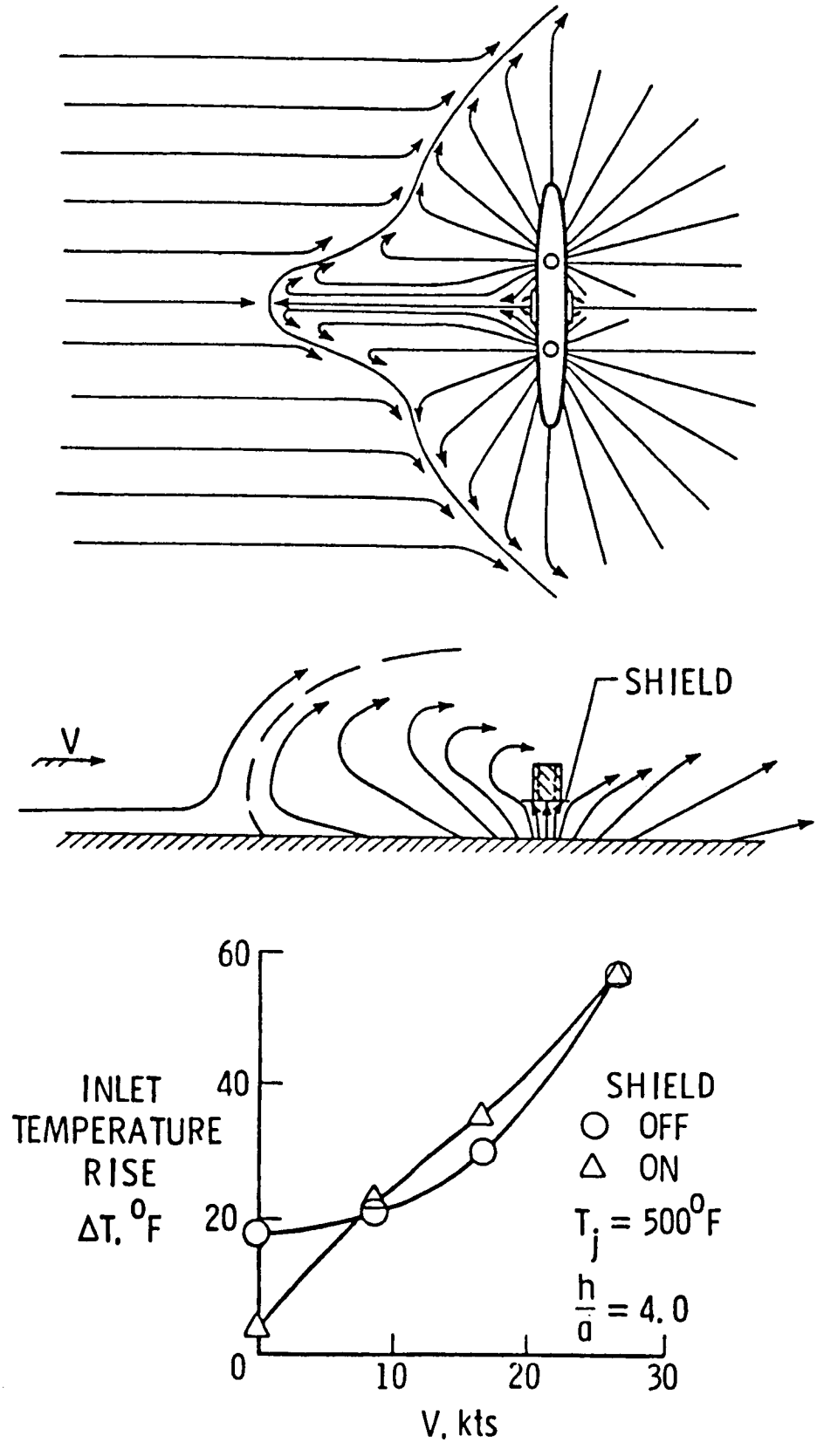

Figure 75.- Effect of free stream on side-by-side configuration. (Ref. 40)

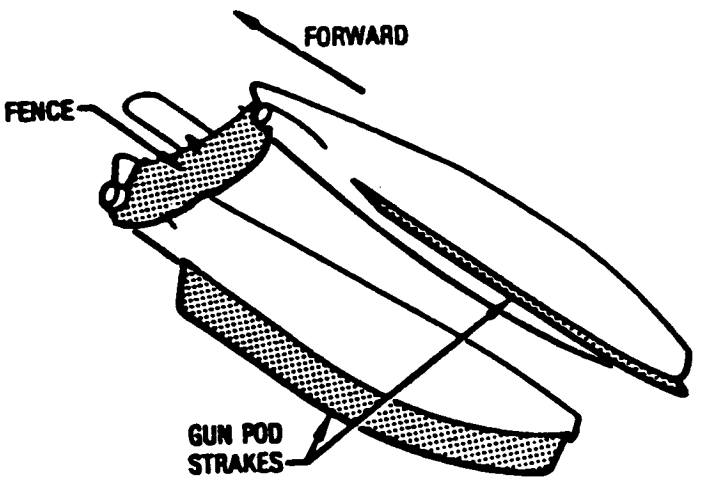

Figure 76.- Lift improvement devices on AV-8B. (Ref. 43)

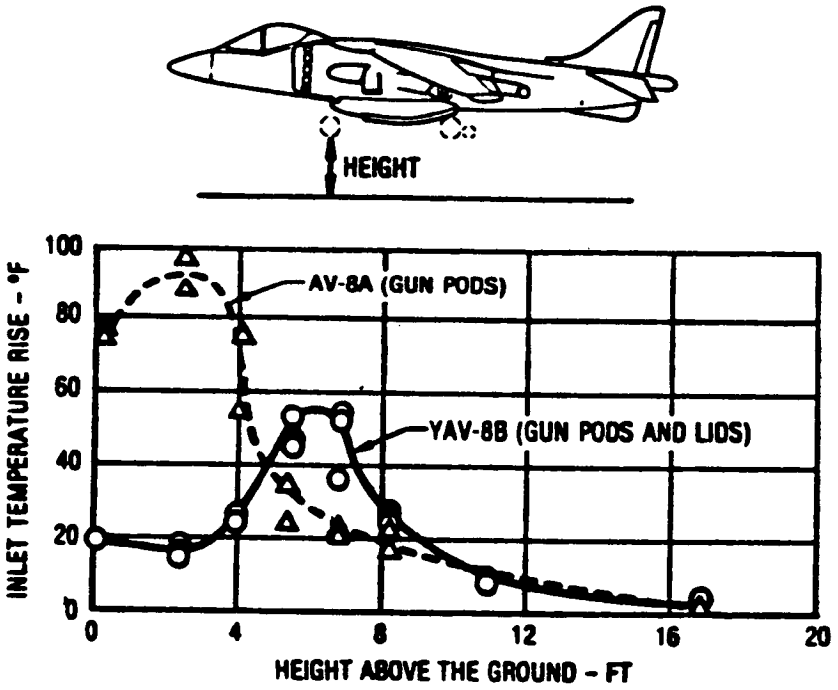

Figure 77.- Inlet temperature rise due to hot gas reingestion.
Static Scale Model Results Nozzles Vertical

(Ref. 43)

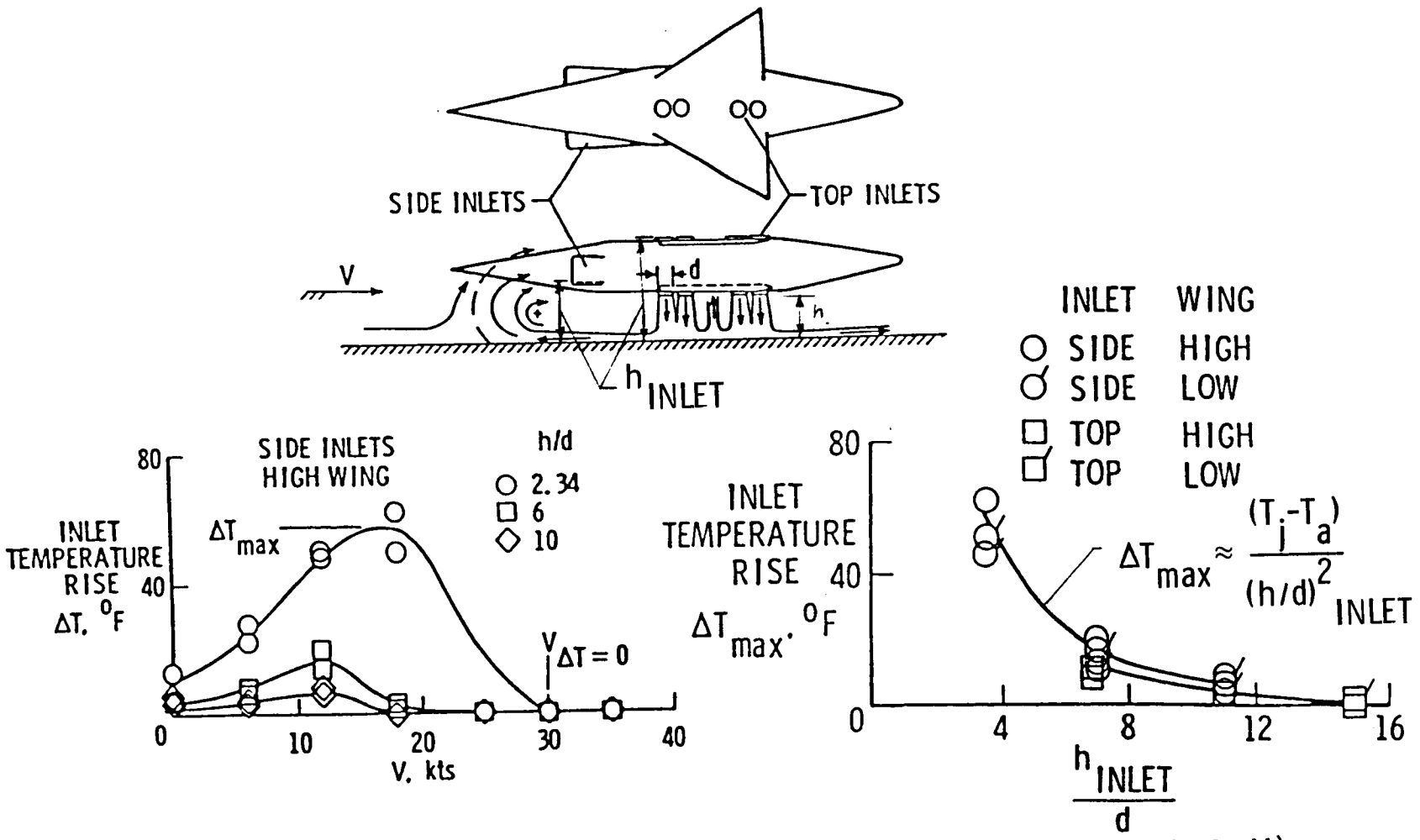

Figure 78.- Effect of height and velocity; four-jet in-line configuration. (Ref. 44)

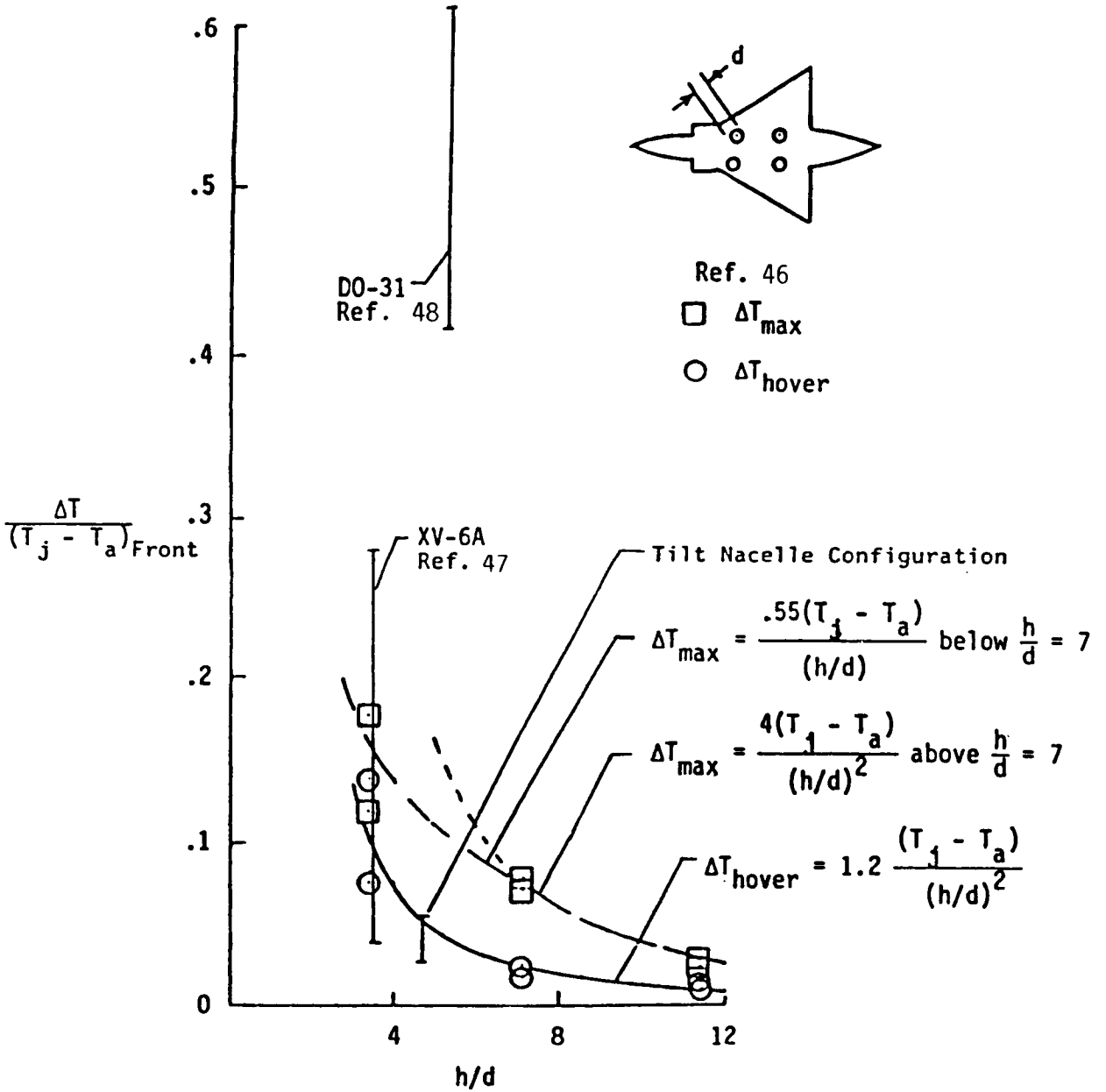

Figure 79.- Correlation of inlet temperature rise data, Ref. 45 configuration with side-by-side front jets.

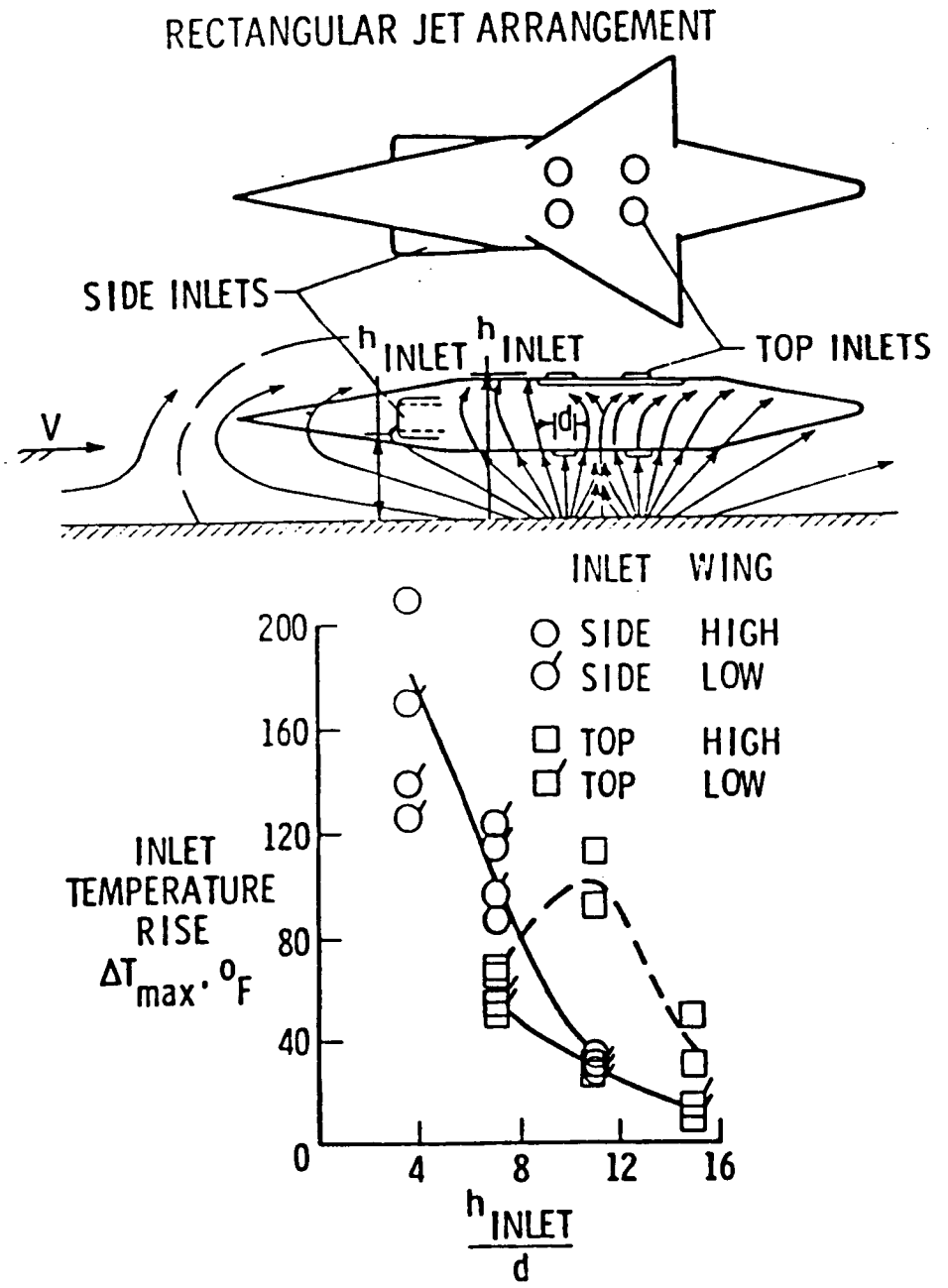

Figure 80.- Effect of inlet and wing location, Ref. 44; rectangular jet arrangement.

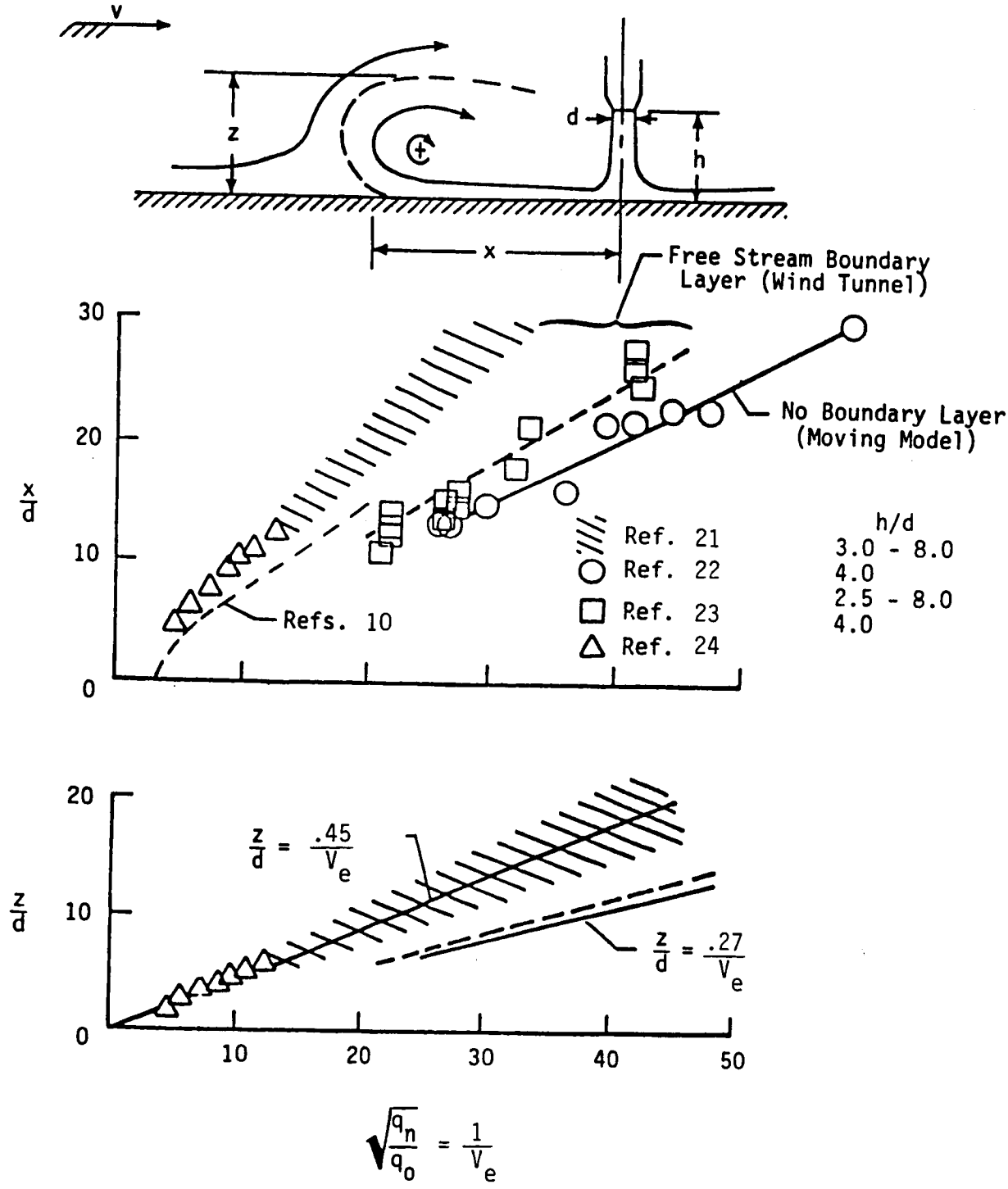

Figure 81- Size of Ground Vortex Recirculating Flow Region Generated by a Single Jet.

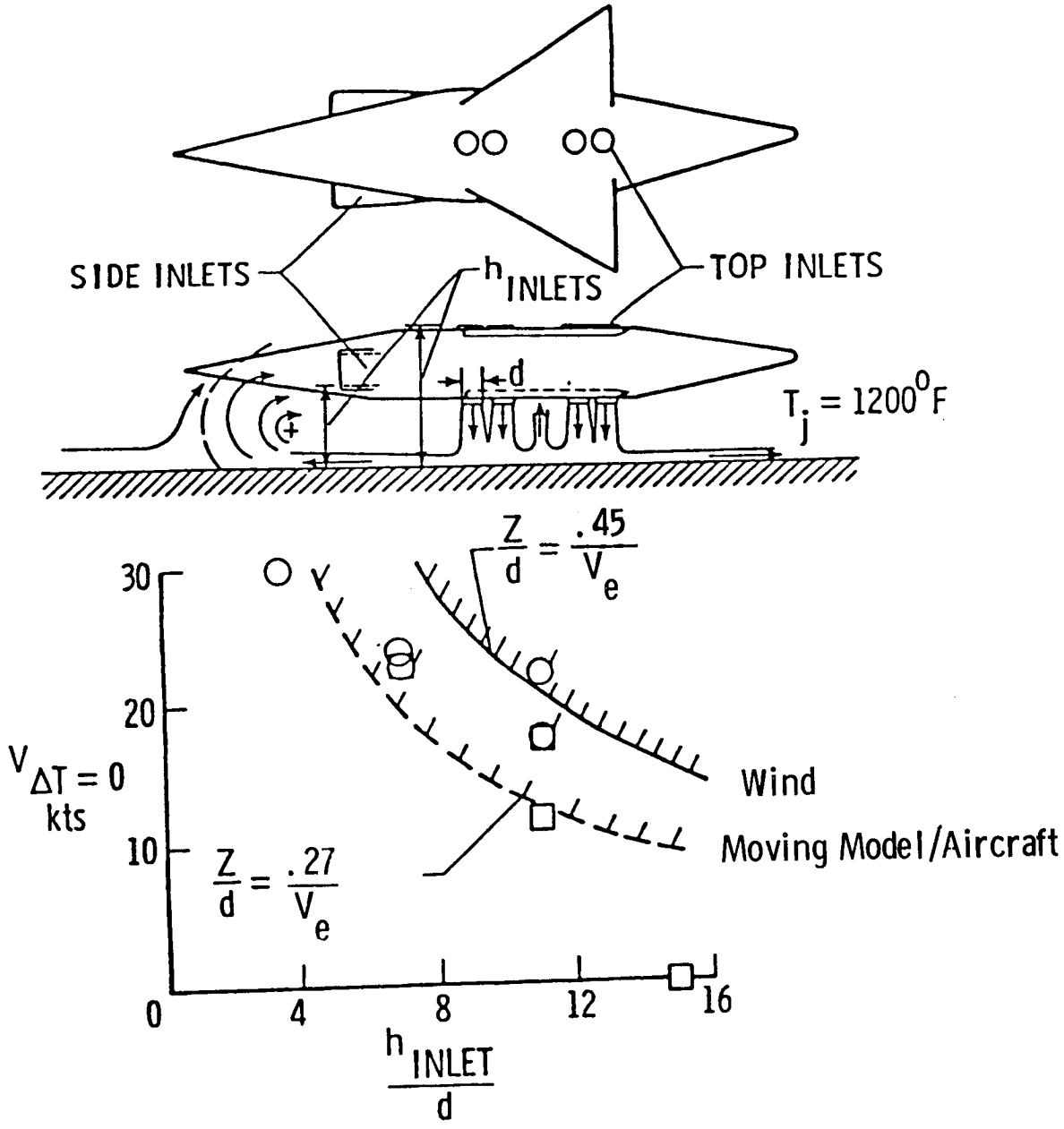

Figure 82.- Velocity required to avoid ingestion; in line jets. (Ref. 44)

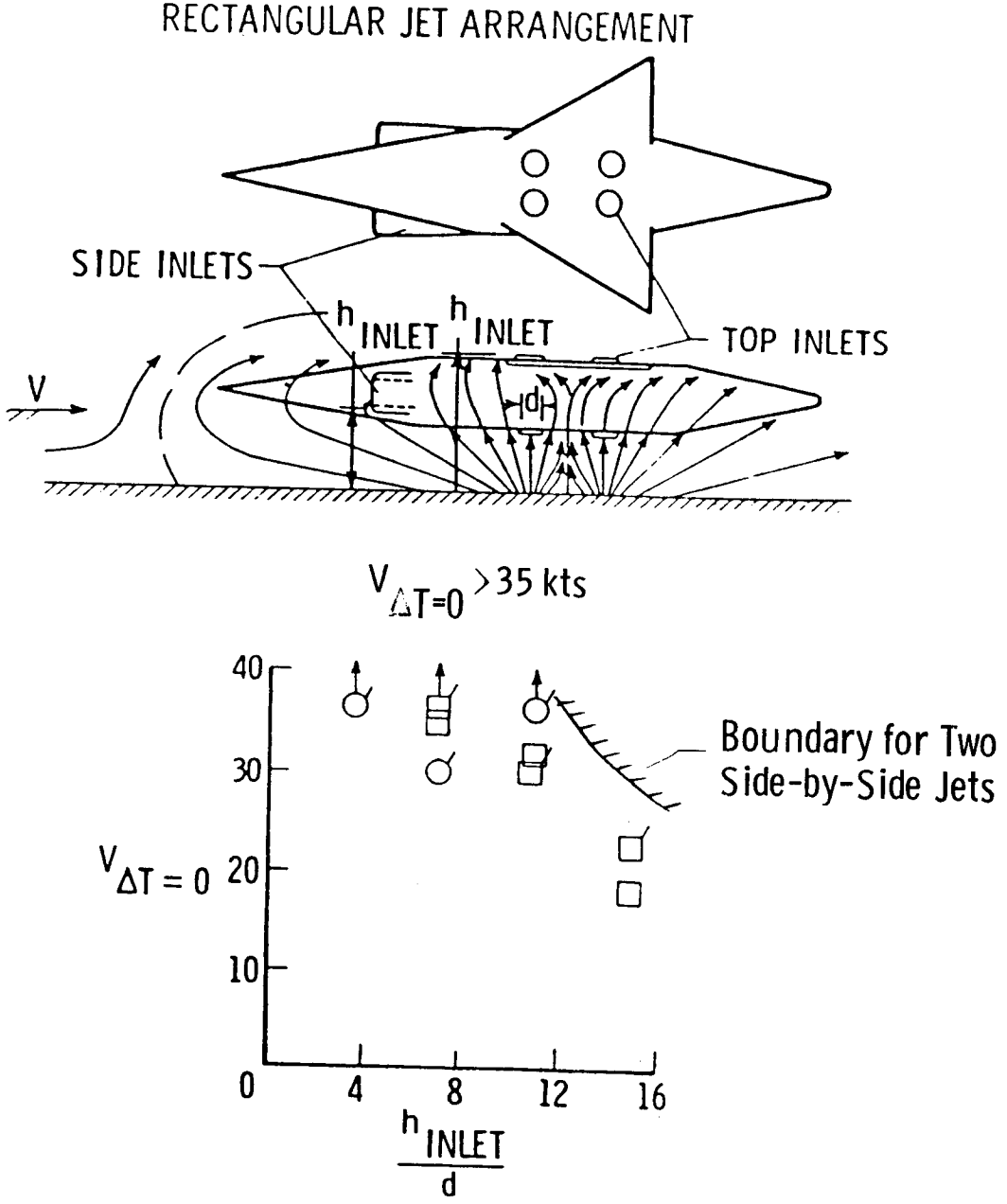

Figure 83.- Velocity required to avoid ingestion; configuration with foward fountain arm. (Ref. 44)

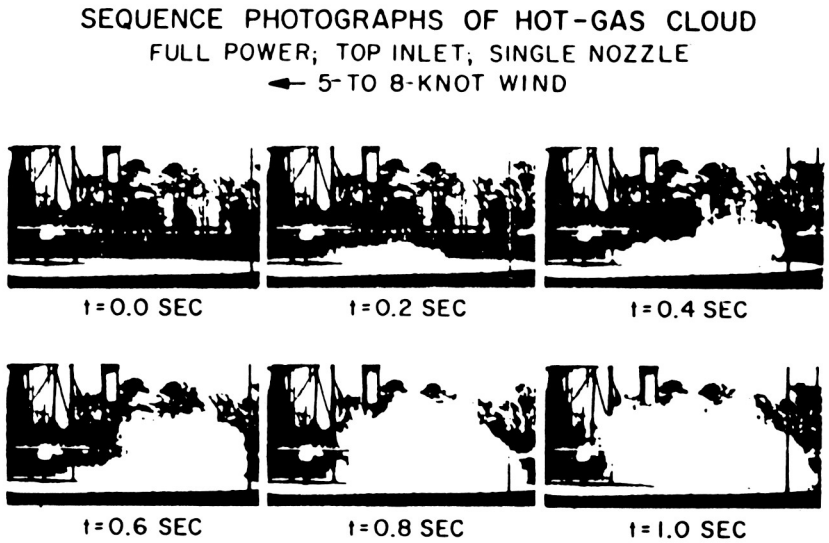

Figure 84.- Development of hot-gas cloud. (Ref. 50)

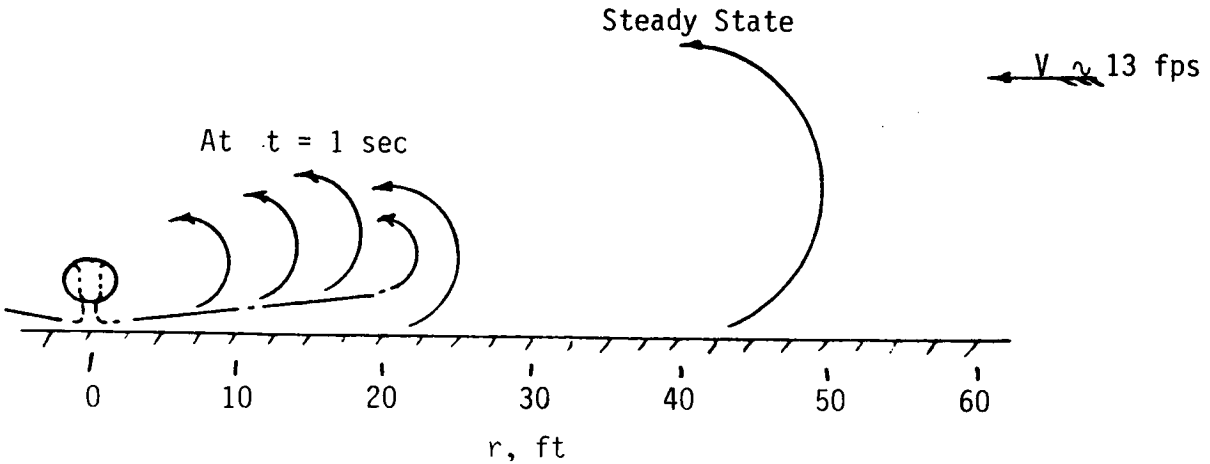

(a) Approximate flow field for configuration of Ref. 50.
$V_e \sim .015$, d = 12"

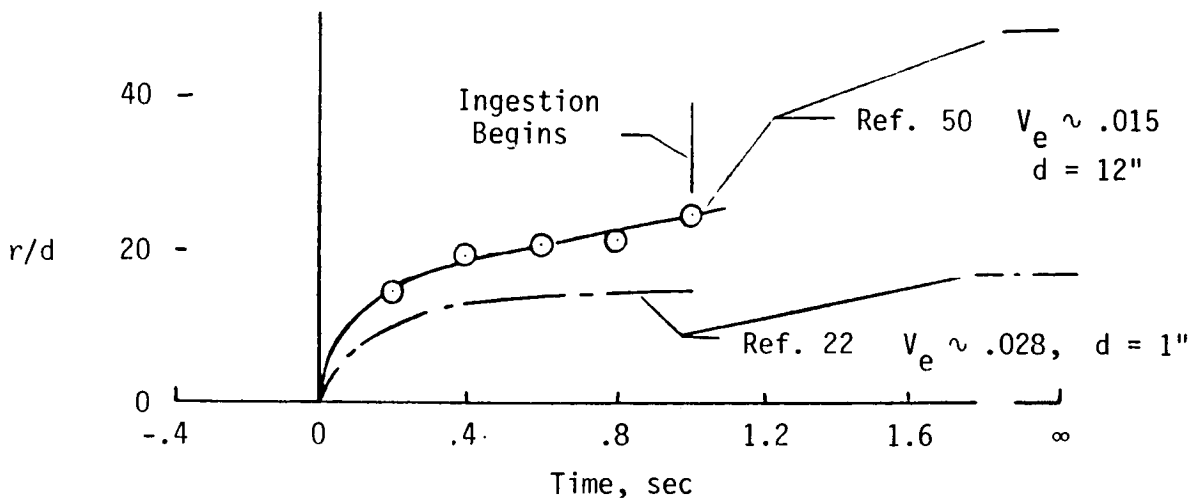

(b) Time history of size.

Figure 85.- Growth of hot-gas cloud.

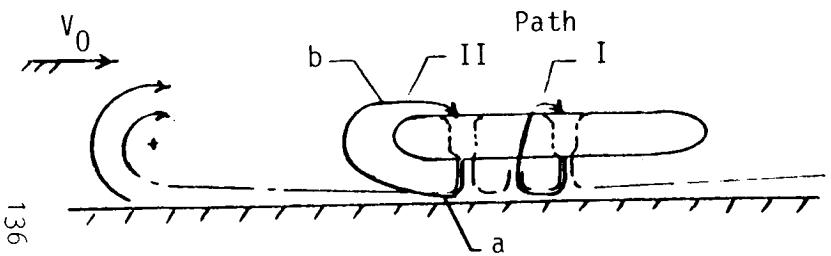

	Full Scale	1/10 Scale
Diameter	1'	.1'
Path I (Fountain)		
Distance	8' - 12'	.8' - 1.2'
Velocity $\rightarrow V_j$	Say 800 - 1200 fps	800 - 1200 fps
Time	.007 - .015 sec	.0007 - .0015 sec
Path II (Ground Vortex Flow)		
Distance	10 - 15'	1 - 1.5'
Velosity		
at a $\sim V_j$	1200 - 2000 fps	1200 - 2000 fps
at b $\sim V_0$	10 - 50 fps	10 - 50 fps
Time	.5 - 1.5 sec	.05 - .15 sec
Rate of Sink	$\sim$ 3 fps	$\sim$ 30 fps

Figure 86.- Time scaling considerations.

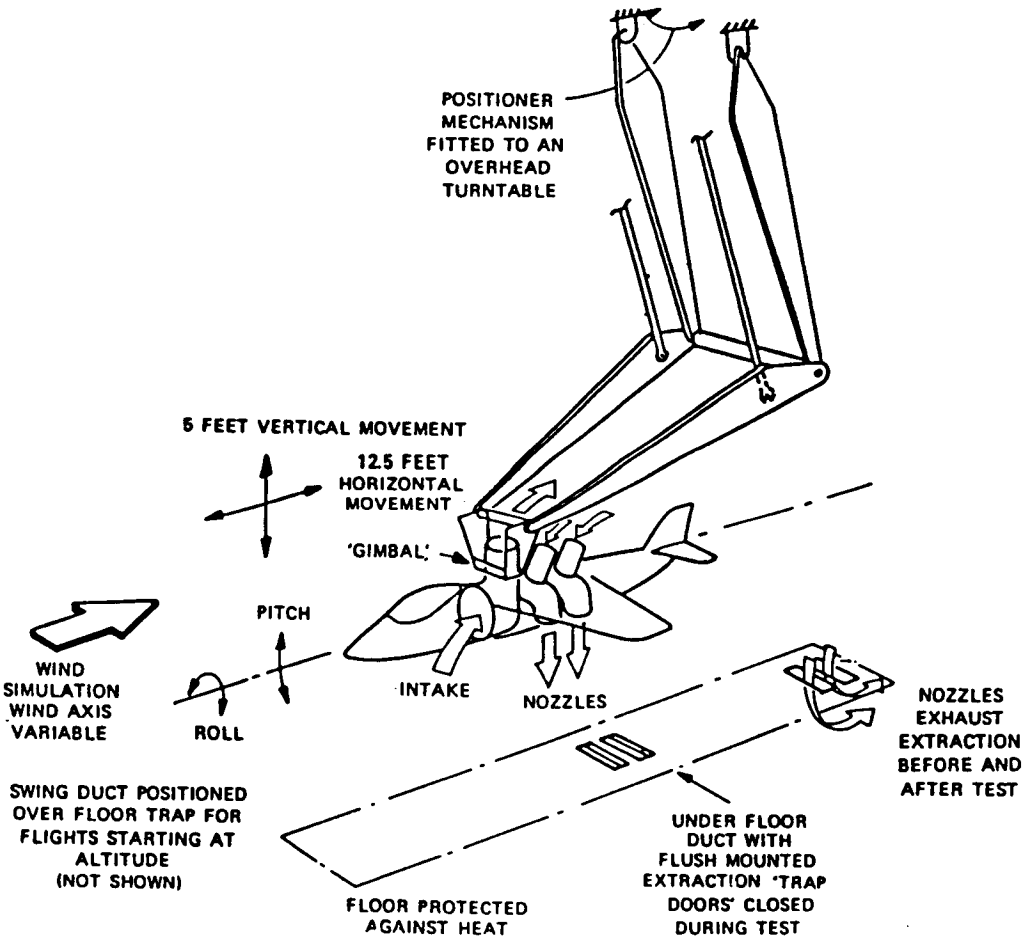

Figure 87.- British Aerospace Dynamic Hot-Gas Ingestion Test Rig, (Ref. 51).

$$\Delta T = k_1 (T_j - T_a) \quad \text{Abbott, Ref. 52}$$

$$\Delta T = k_2 (T_j - T_a)\left(\frac{T_j}{T_a}\right)^{-\frac{1}{2}} \quad \text{Milford, Ref. 53 and 54}$$

$$\Delta T = k_3 (T_j - T_a)\left(\frac{T_j}{T_a}\right)^{-n} \quad \text{Bore, Ref. 51}$$

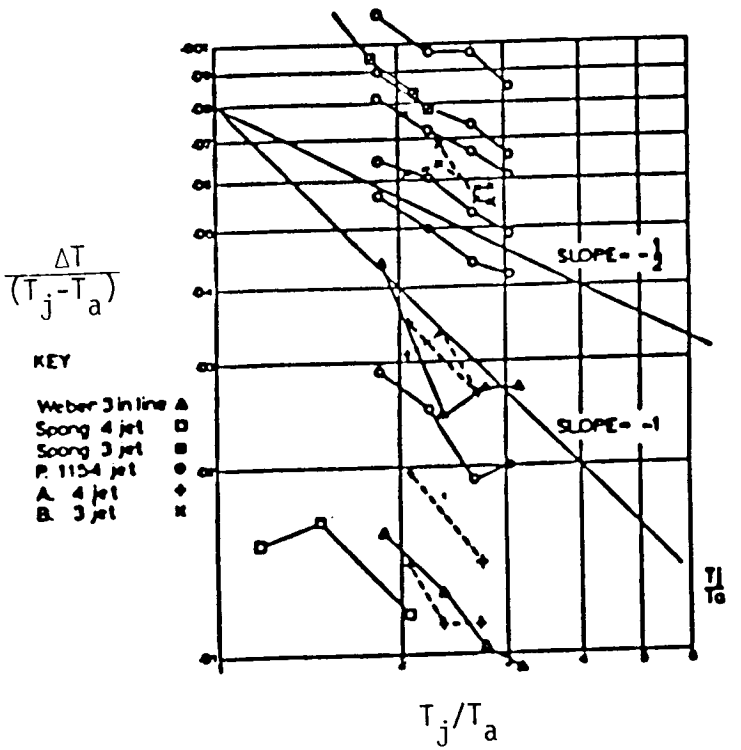

Figure 88.- Inlet temperature rise scaling.

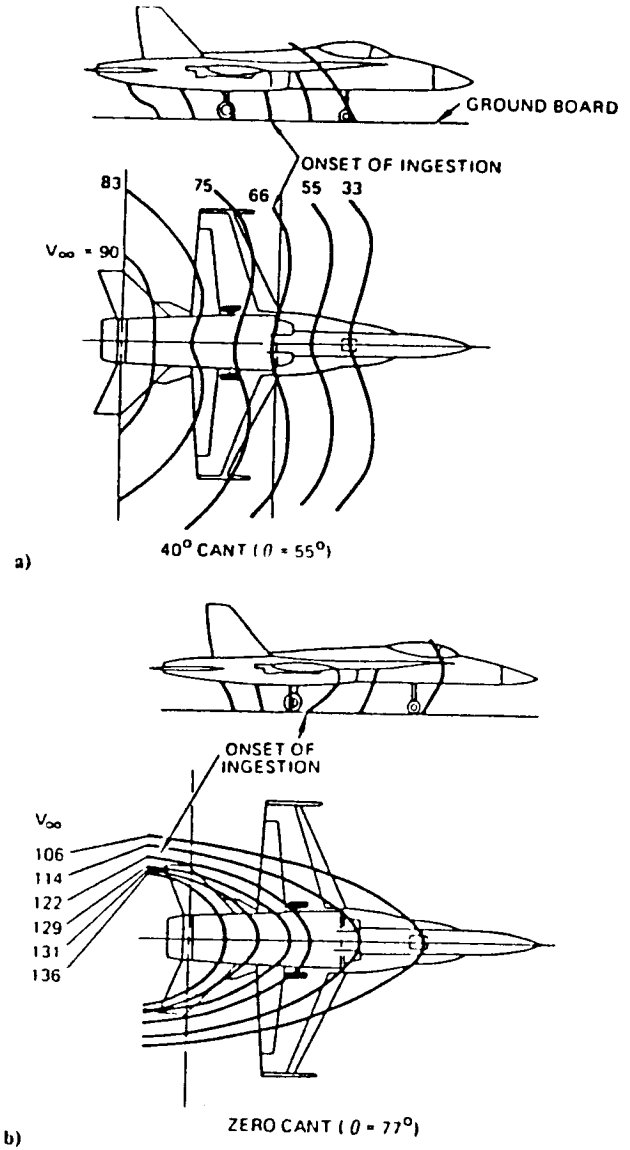

Figure 89.- Effect of lateral cant angle of thrust reverser flow on foward projection of hot gas flow. (Ref. 55)

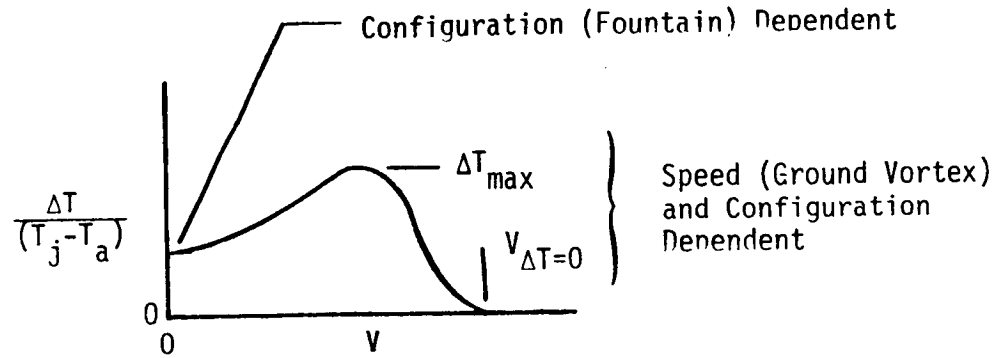

Vary
- Jet Configuration
  - Single Jet
  - Side-by-Side Jets
- Inlet Position
- Pressure Ratio
- Velocity Ratio
- Jet Deflection and Cant Angles

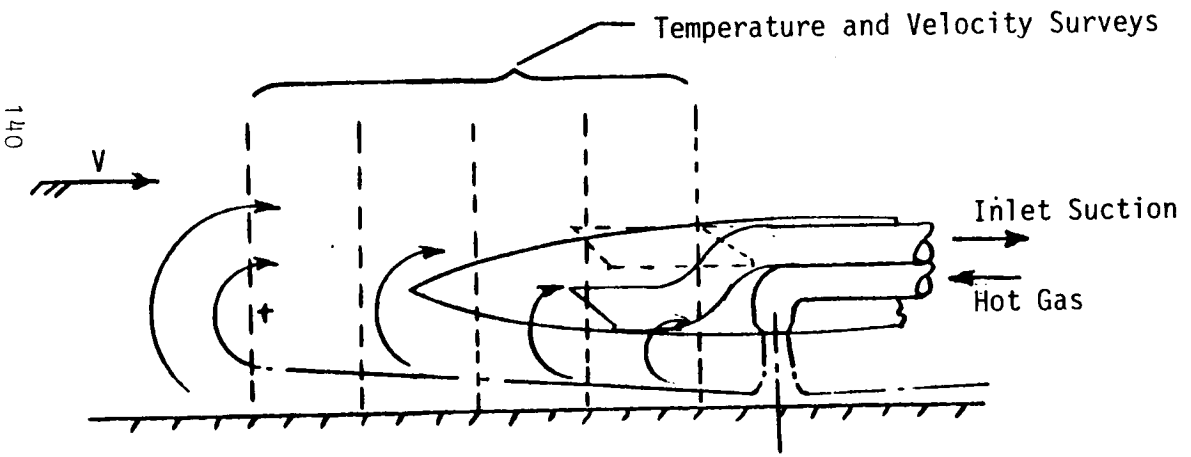

Figure 90.- Investigate rate of development and steady state flow field.

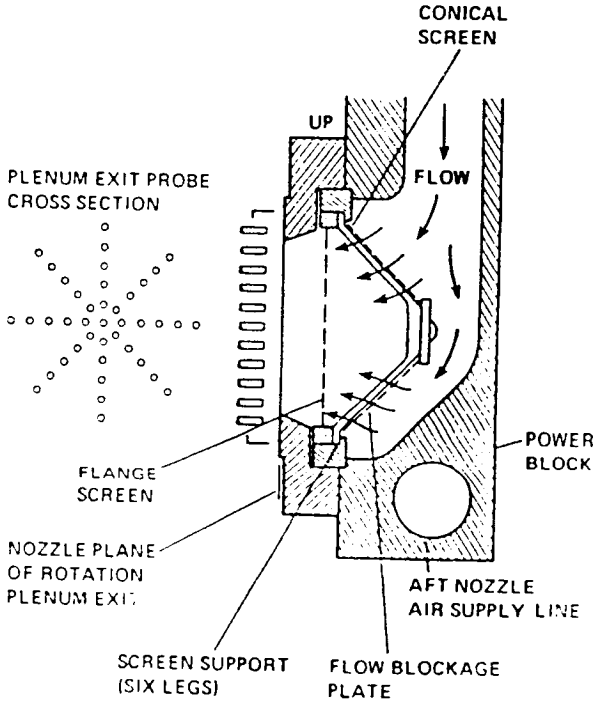

(a) Nozzle/Air-Feed design for limited space, (Ref. 19).

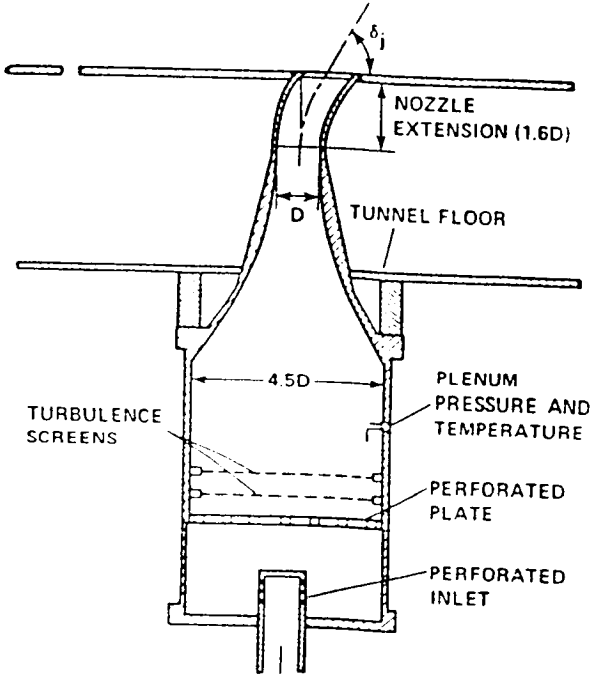

(b) Nozzle/Plenum-Chamber Design for good quality jet flow, (Ref. 57).

Figure 91.- Typical systems for using high pressure air for jet simulation. (Ref. 56)

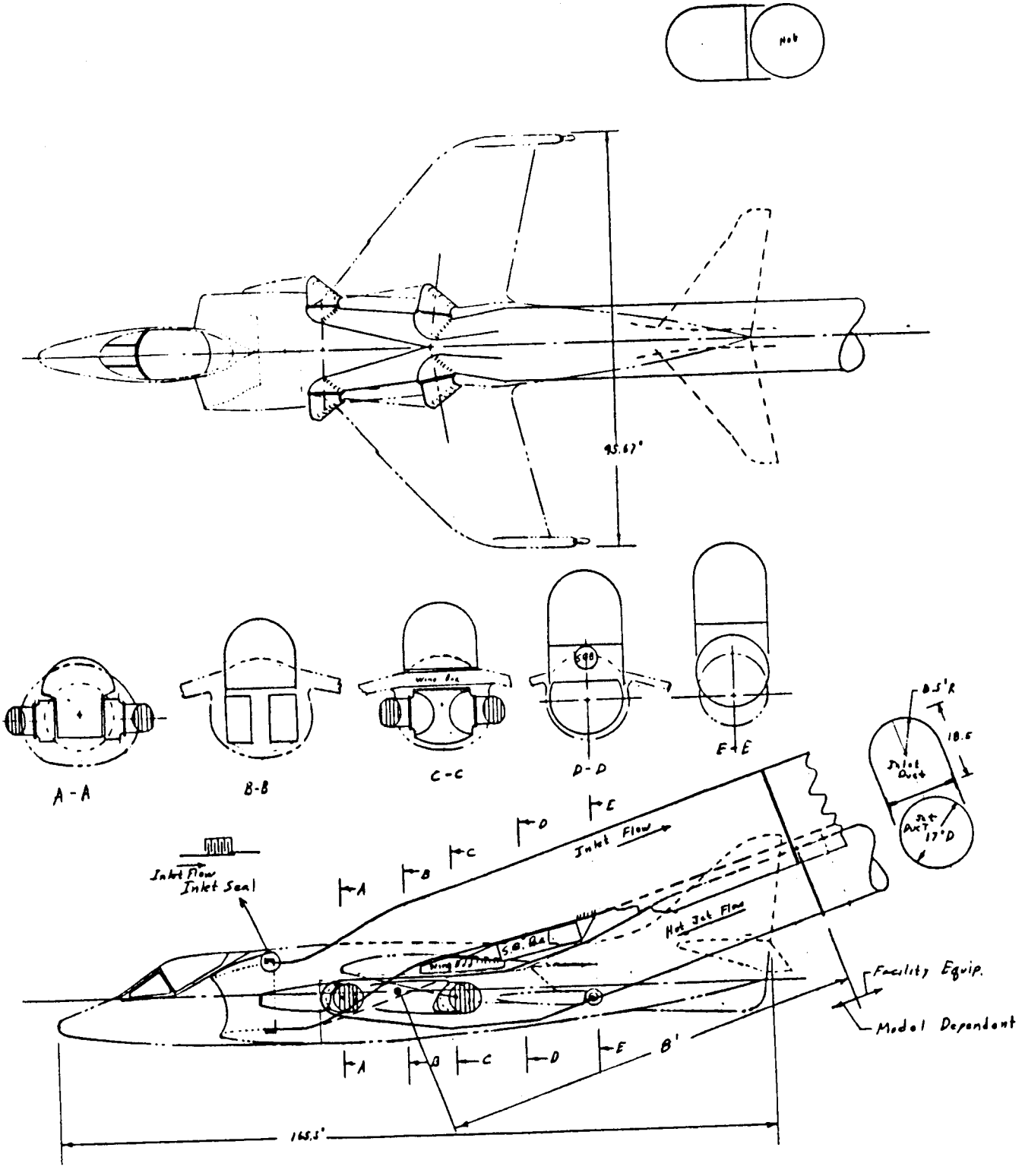

Figure 92.- Remotely powered Harrier type model.

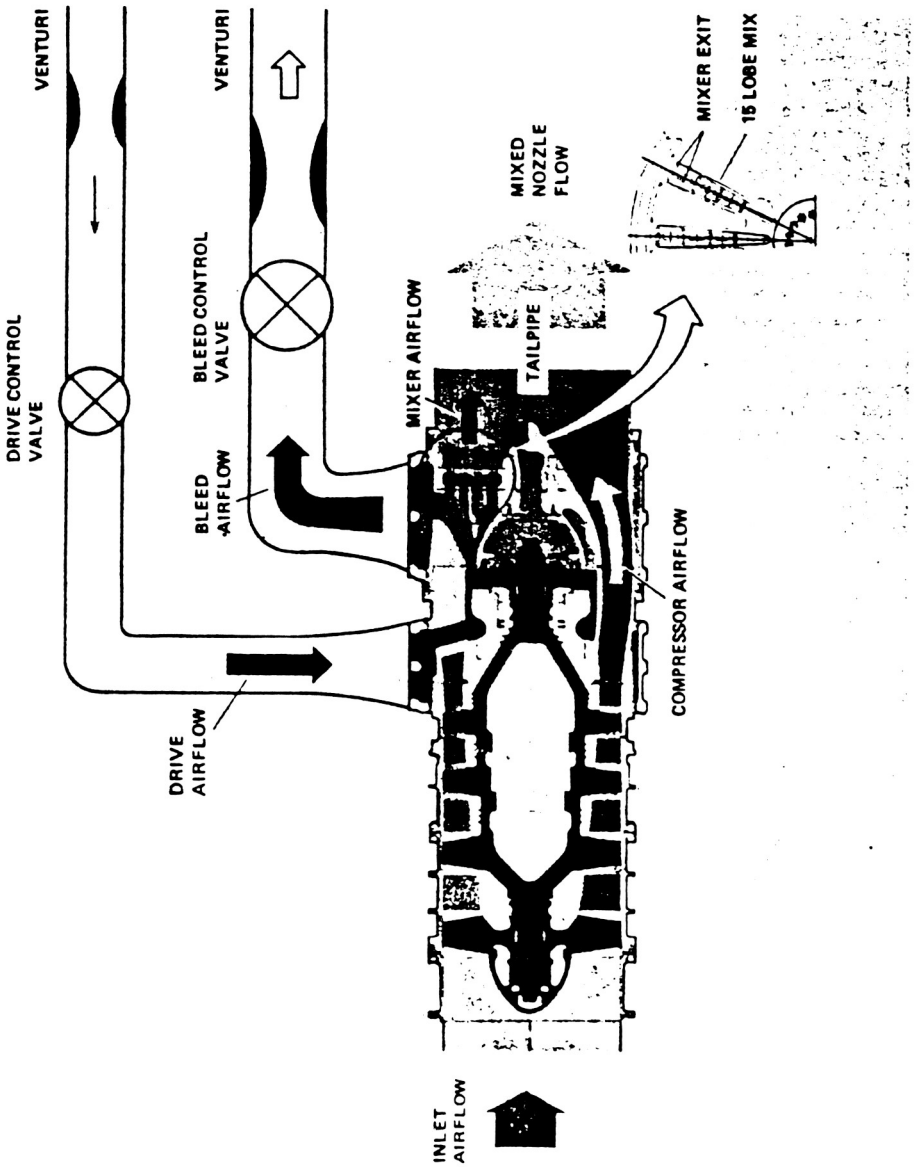

Figure 93.- Schematic of compact multimission aircraft propulsion simulator. (Ref. 56)

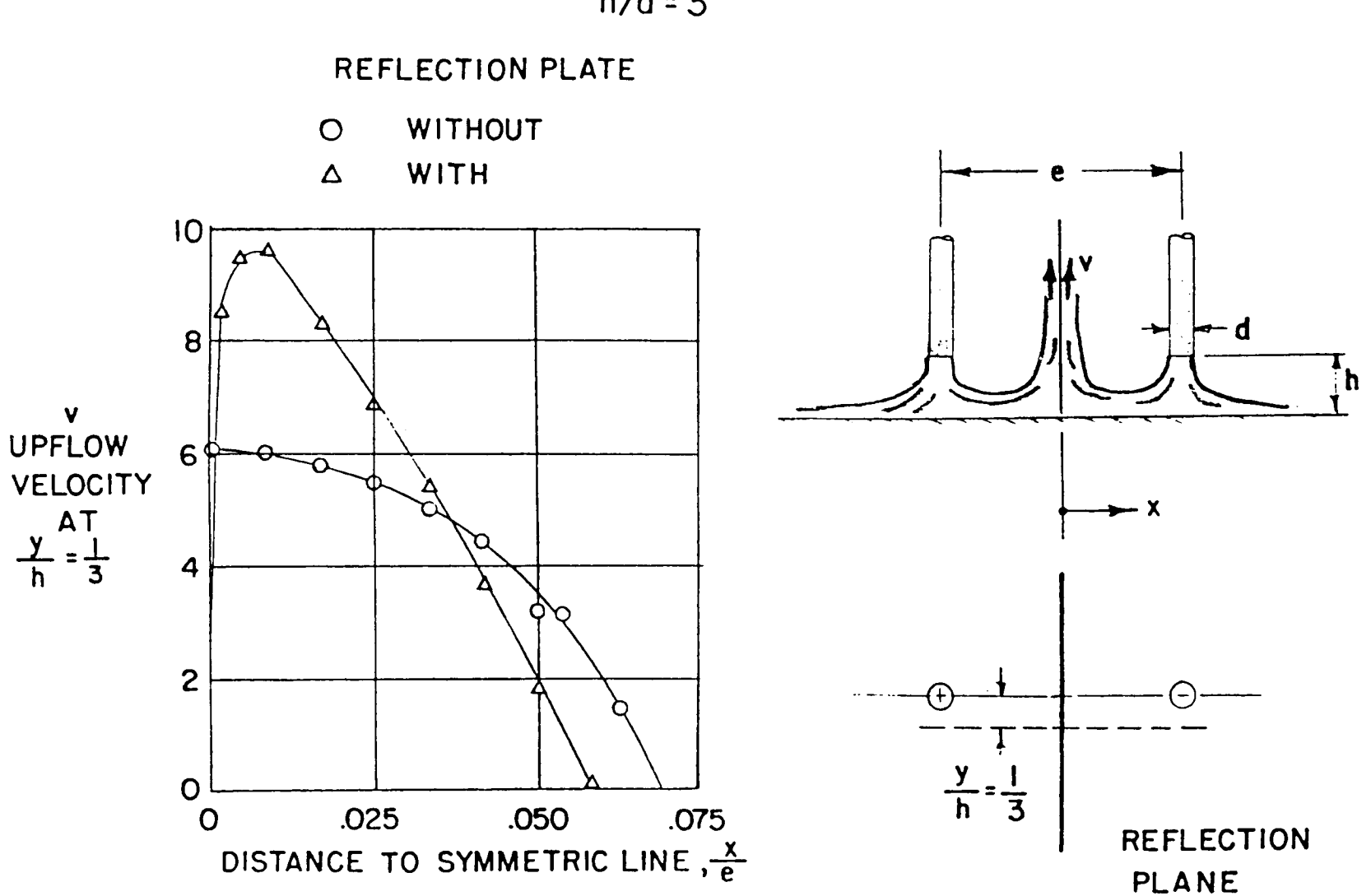

Figure 94.- Effect of a reflection plane on the measured upflow velosities in the fountain flow caused by two jets exiting vertically near the ground. (Ref. 58).

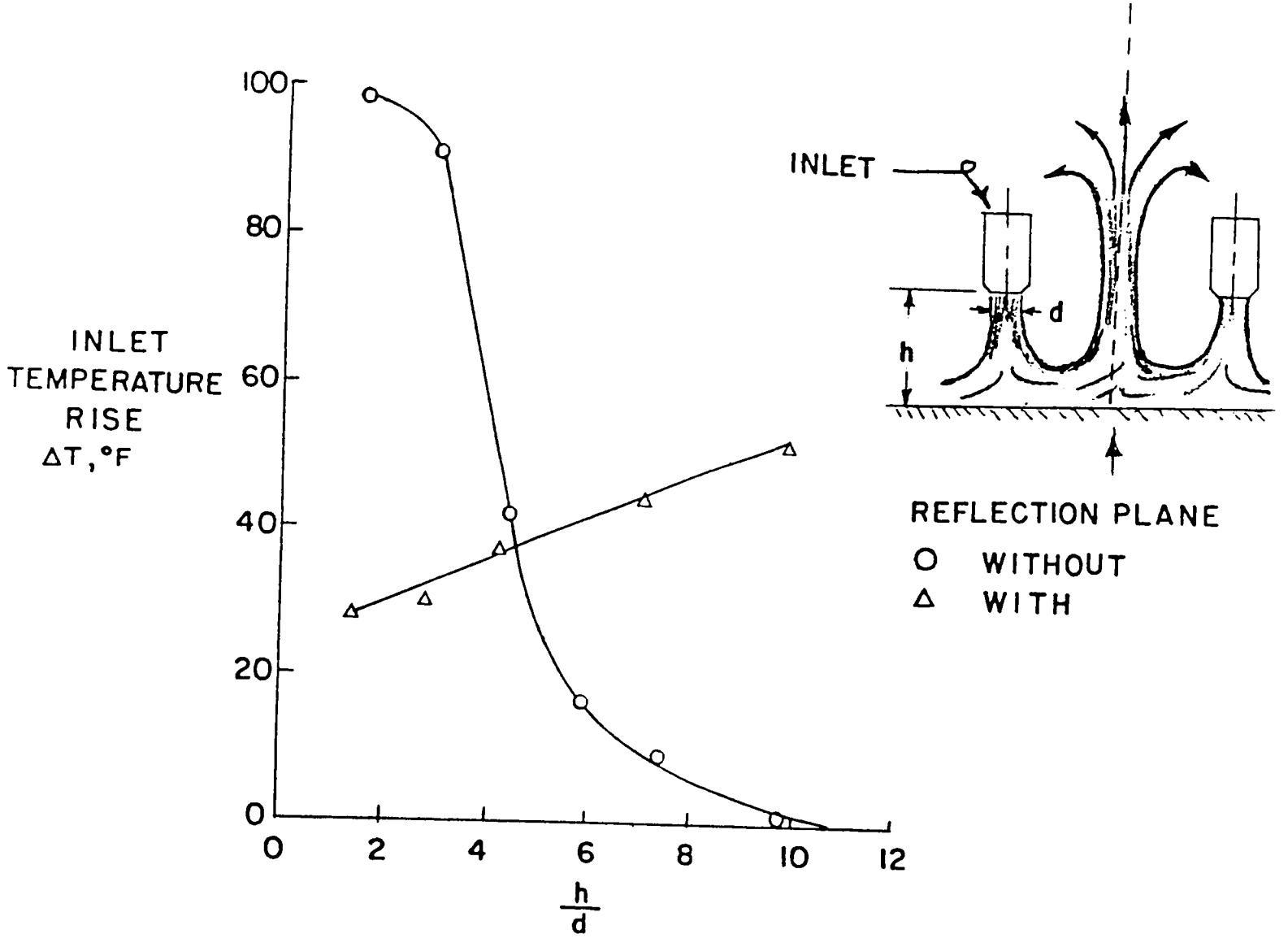

Figure 95.- Effect of a reflection plane on the measured inlet air temperature rise resulting from the fountain flow caused by two jets exiting vertically near the ground. (Ref. 59)

LASER DOPPLER VELOCIMETER MEASUREMENTS IN A 3-D IMPINGING TWIN-JET FOUNTAIN FLOW*

K. R. Saripalli**
McDonnell Douglas Research Laboratories
St. Louis, MO 63166

Abstract

Mean velocity and turbulence measurements were conducted on the three-dimensional fountain flowfield generated by the impingement of two axisymmetric jets on a ground plane with application to vertical-take-off and landing (VTOL) aircraft. The basic instantaneous velocity data were obtained using a two-component laser Doppler velocimeter in a plane connecting the nozzle centerlines at different heights above the ground emphasizing the jet impingement region and the fountain upwash region formed by the collision of the wall jets. The distributions of mean velocity components and turbulence quantities, including the turbulence intensity and the Reynolds shear stress, were derived from the basic velocity data. Detailed studies of the characteristics of the fountain revealed self-similarity in the mean velocity and turbulence profiles across the fountain. The spread and mean velocity decay characteristics of the fountain were established. Turbulence intensities of the order of 50% were observed in the fountain.

Nomenclature

D	Exit internal diameter of the nozzle or the exit jet diameter
H	Height of the nozzle exit above the ground plate
Re	Reynolds number based on the exit jet diameter and the exit jet velocity
S	Center distance between the jets
U	Mean velocity in the streamwise direction
V	Mean velocity in the cross-stream direction
u	Fluctuating component of the mean velocity in the streamwise direction
v	Fluctuating component of the mean velocity in the cross-stream direction
U_J	Jet centerline velocity at the exit
U_{max}	The local maximum streamwise velocity in the fountain
$X_{1/2}$	The fountain half width where $U = \frac{1}{2} U_{max}$
X	Distance parallel to the line connecting the nozzle centerlines
Y	Distance perpendicular to the line connecting the nozzle centerlines and parallel to the ground plane
Z	Perpendicular distance from the ground plane

Introduction

The impinging lift jets of a vertical take-off and landing (VTOL) aircraft hovering in ground proximity produce complicated three-dimensional flowfields. These 3-D flowfields shown schematically in Fig. 1 for the case of two-jets, involve strong interactions between the impinging lift-jet streams, the airframe surface and the ground. An important feature of this flowfield is the fountain upwash flow generated by the colliding wall jets. The fountain is fan-shaped (Fig. 1), spreading radially in all directions with increasing width away from the ground. The impingement of the fountain on the aircraft increases lift, elevates skin temperatures and causes possible reingestion into the inlets. Detailed studies of the structure and development of the fountain upwash flow are thus essential for the successful design of efficient VTOL aircraft. Toward this objective, a unique set of velocity and turbulence data on an axisymmetric twin-jet fountain flow are presented.

Background

References 1-4 report some of the earlier measurements of fountain upwash flow properties. Reference 1 reports mean velocity measurements in

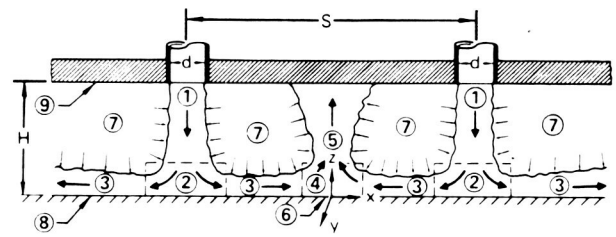

1. Lift jet flow
2. Jet impingement region
3. Wall jet flow
4. Fountain formation region
5. Fountain up-wash flow
6. Wall jet interaction stagnation line
7. Entrainment
8. Ground plane
9. Blocking surface

GP21-1126-3

Fig. 1 Schematic illustration of twin-jet impingement flow.

*This research was conducted under the McDonnell Douglas Independent Research and Development program.
**Scientist; Member AIAA.

the wall jet and the fountain for twin axisymmetric jet impingement using hot-wire techniques for S/D = 12 and H/D = 5. The fountain formation and development characteristics were obtained for a range of the important parameters that influence the flow. The flow angularity in the fountain in the plane connecting the nozzle centerlines was reported to vary randomly. Reference 2 presents pitot pressure profiles in the fountain for twin-axisymmetric jet impingement with S/D = 6 and $2 \leq H/D \leq 6$. Strong fluctuations were reported in the upwash flow properties, and the magnitude of these fluctuations increased with jet height above the ground. Also, highly fluctuating flow angularity, with frequent complete velocity reversals, was reported in the regions outside of the main upwash fan and the shear layers of the incident jets, and sometimes even in the central upwash region. Therefore, it was recommended that pitot probes be used in the measurement of mean flow properties in the fountain upwash.

Reference 3 reported measurements in a two-dimensional fountain upwash, indicating high turbulence levels and spreading rates in the fountain. The first set of careful measurements conducted in a two-dimensional fountain upwash using x-wire hot film anemometer were presented by Gilbert,[4] who reported detailed mean velocity and turbulence measurements, including decay and spread characteristics of the fountain. The observed levels of turbulent intensities in the fountain were similar to those in an ordinary two-dimensional free jet; however, high growth rates were observed in the fountain. The fountains in References 3 and 4 were generated by two isolated, two-dimensional opposing wall jets, thus eliminating the jet impingement region as part of the fountain formation process.

Reference 5 presents mean velocity and turbulence measurements using hot-wire techniques in a fountain generated by the impingement of two-axisymmetric jets, with no definite conclusions on the fountain turbulence structure. References 6 and 7 describe fountain behavior for close nozzle spacing and also indicate the effect of the blockage by the probe support. Measurements reported in Refs. 8-11 do not reveal any additional features of fountain flows.

Although several investigations of the fountain flow have been carried out, interpretations of the measurements vary widely, primarily because of the difficulty in measuring highly unsteady flows using hot-film and pitot-probe techniques. Computational codes require a better definition of the fountain flow and its turbulence structure to make reliable predictions. Therefore, a need existed for a reliable, detailed mean-velocity and turbulence data base in a realistic 3-D fountain generated by the impinging jets using a suitable measurement technique.

Measurement Technique and the Working Medium

The measurement technique for studying the fountain flow was required to meet the following specifications: a) be nonintrusive so that no flow disturbance is caused, especially in the case of closely spaced jets, b) be able to sense the direction of flow in the recirculating regions, c) have a linear response, essential for accurate measurements in areas where the turbulence intensities are high such as the fountain. A laser Doppler velocimeter (LDV) meets these specifications[12,13]; in addition, LDV responds to a specific velocity component in 3-D flows and measures velocity directly without the need to correct for temperature effects.

As a working medium, water offers specific advantages compared to air; the tracers suitable for flow visualization in water are more numerous with better light-reflecting characteristics, and aerodynamic phenomena can be observed at a relatively slow speed for the same Reynolds number and model scale because of the difference in kinematic viscosities of air and water. Moreover, for laser Doppler velocimetry, the seeding of the flow is normally unnecessary in water because the natural suspended particles act as light scatterers. If seeding is necessary, it can be accomplished easily in water than in air by adding neutral-density plastic particles of the proper size.

Experimental Apparatus

Figure 2 shows the jet-impingement facility used for conducting laser-Doppler-velocimeter (LDV) measurements with water as the working medium. The

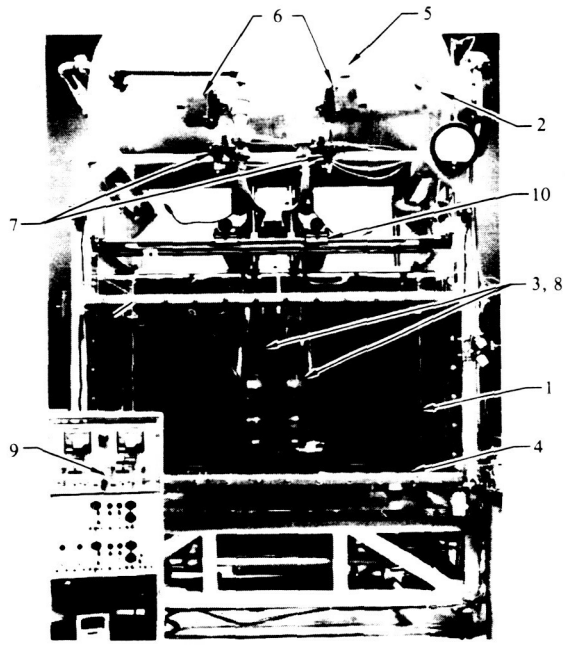

1 Main plexiglass tank
2 Header tank
3 Nozzle units
4 Ground plate
5 Turbine flow meter
6 Motor-operated flow control valves
7 Shut-off valves
8 Settling chamber of 3
9 Control panel
10 Traversing mechanism

GP41 1579 1 R

Fig. 2 Jet impingement facility.

primary components are (1) the main Plexiglas tank, (2) the header tank, (3) nozzle units, and (4) the ground plate. The large transparent main tank (1.88 x 1.52 x 1.37 m) has an approximate capacity of 3800 liters. The pressurized stainless steel cylindrical header tank, 91.4-cm diam., supplies water to the nozzle units and acts as a plenum to damp fluctuations produced by the pump.

The function of the Plexiglas nozzle units (Fig. 3) is to reduce turbulence and mean-velocity nonuniformities in the existing jet-flow to acceptable levels. Each nozzle unit consists of a flow distributor (diffuser) for decelerating the flow, a honeycomb and screens to establish a uniform flow with low turbulence, and a nozzle (2.54-cm exit diam., 16:1 contraction ratio) for accelerating the flow. The ground plate is held at a fixed height above the bottom of the main tank and acts as an impingement surface for the jets with sufficient edge clearance for passage of the flow. The position of the nozzle units is adjusted by a traversing unit that can accommodate as many as four nozzle units and mounted on the main tank.

The circulation system draws off water from under the ground plate and pumps it into the header tank, thus supplying water to the jets through a series of flow-control devices. With the available pumping capacity, jet Reynolds numbers up to 200 000 can be obtained in a typical twin-jet (2.54-cm-exit diam.) impingement configuration. The three-dimensional fountain flow is visualized through a series of two-dimensional images. Fluorescein-sodium, a fluorescent dye, is injected into the jet flow, which fluoresces bright yellowish-green when the desired cross-section is illuminated with a thin (1 mm) sheet of 488 nm wavelength light from an Argon-ion laser.

A two color (two-component) TSI laser Doppler velocimeter system (Fig. 4) is used in the dual-beam off-axis backward scattering mode with Bragg-cell frequency shifting. The probe volume is positioned at the required location using a remotely driven X-Y-Z traversing unit. The TSI counter-type signal processors were used to convert the Doppler signal into a form suitable for recording on a magnetic disk through a dedicated DEC MINC 11/23 Computer. Six groups of 256 samples each were taken at each data point. The recorded data on the disk were then processed on a DEC PDP 11/70 minicomputer and plotted on a Benson-Varian electrostatic plotter. The available city water did not have enough scattering particles to give good signal to-noise ratios in the backward scattering mode; seeding the test medium with 15.6 μm Dow Corning polystyrene particles resulted in signals of excellent quality. A TSI hot-film anemometer system with a TSI 1231 W conical hot-film probe was also used for diagnostic measurements of the jet flow at the nozzle exits. A detailed description of the experimental apparatus and the flow visualization and measurement techniques is given in Refs. 14-17.

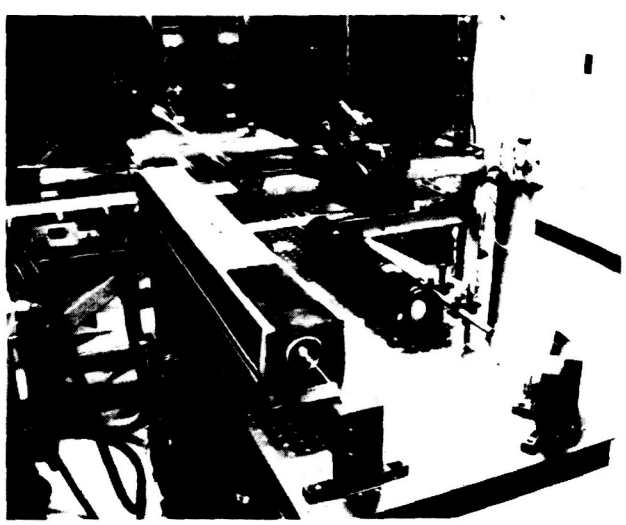

Fig. 3 Laser Doppler velocimeter.

Test Conditions

Extensive diagnostic flow visualization studies were conducted for equal strength jets and for varying heights of the nozzle exit above the ground and separation distances between the nozzles. The objective was to select a twin-jet impingement configuration which has a centrally located, strong isolated fountain rising from the ground plate without interference from the free jets. Based on these flow visualization studies, a normally impinging, equal-strength twin-jet configuration with S/D = 9.0 and H/D = 3.0 was selected for detailed LDV measurements. Figure 5 shows the corresponding flowfield visualized in a plane connecting the nozzle centerlines using the fluorescent dye/laser light sheet technique.

LDV measurements were taken for equal-strength jets at twelve heights (Z/D = 0.05 to 2.94) between the nozzle exits and the ground. The jet exit velocity (U_J) was 6.71 m/s, resulting in a Re = 1.70×10^4. All measurements were taken in the plane of symmetry connecting the nozzle centerlines. The time-dependent streamwise (U + u) and cross-stream (V + v) velocities in the X and Z directions, respectively, were measured directly by the LDV. The mean velocities (U, V) turbulence intensities ($\sqrt{\overline{u^2}}/U$, $\sqrt{\overline{v^2}}/U$), Reynolds shear stress ($-\overline{uv}/U^2$), and correlation coefficient ($-\overline{uv}/\sqrt{\overline{u^2}}\sqrt{\overline{v^2}}$) were derived from the basic velocity data.

Experimental Results

The experimental data are classified into three categories, (a) jet-exit flow; establishing the quality of the flow exiting the nozzles (b) jet impingement flow (c) fountain upwash flow.

Jet-Exit Flow Measurements were made in the free-jet flow exiting the nozzles to establish uniformity of the mean velocity profile and the core turbulence levels. Both the conical hot-film probe and the LDV were used to obtain a cross check of the data. Further, the hot-film measurements also facilitated spectral analysis of the velocity signals.

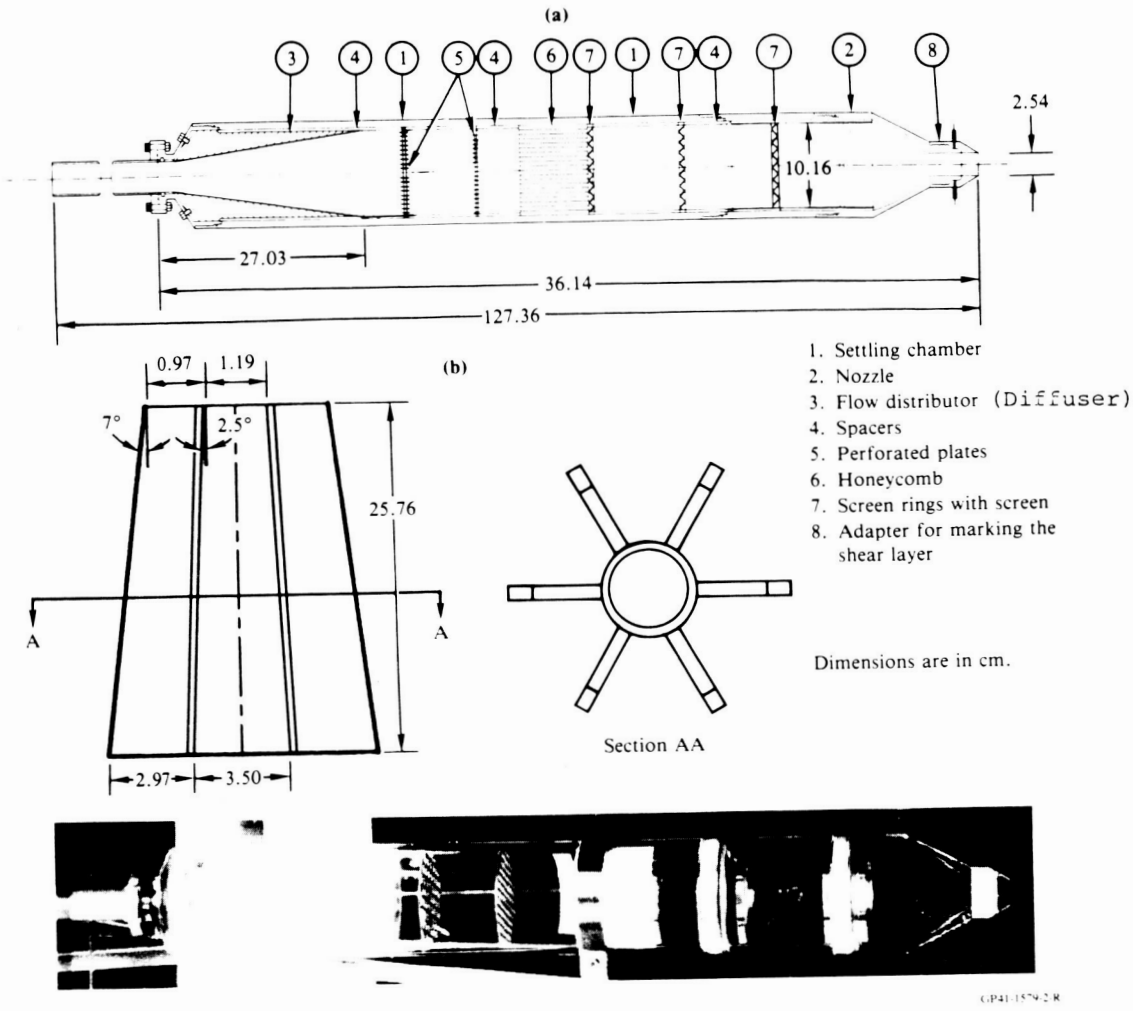

Fig. 4 (a) Schematic of the nozzle unit with the diffuser in place and (b) schematic of the diffuser splitter system.

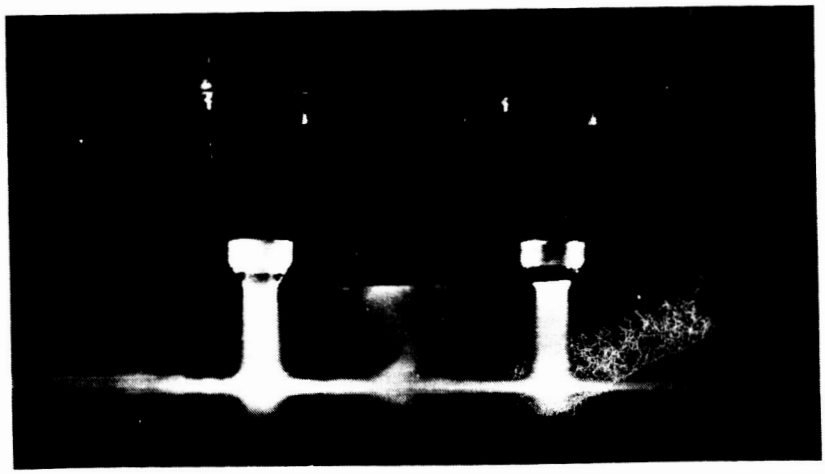

Fig. 5 Twin-jet impingement flow with fountain formation: S/D = 9.0, H/D = 3.0, Re = 1.70×10^5.

Figure 6 shows the mean-velocity and turbulence-intensity profiles across the jet operating at a Re = 1.70×10^5, taken 1.5 mm below the nozzle exit. Here U_J is the jet centerline velocity at the exit. The jet flow is uniform with a low level of turbulence in the core region; the shear layers are thin. The agreement between the LDV data and hot-film data is good. Because of the large velocity gradients across the probe volume, which was larger than the shear-layer thickness, the LDV gave higher turbulence levels in the shear layers. The frequency spectrum of the hot-film signal taken at the center of the jet showed no selective or specific peaks indicative of unwanted disturbances.

Jet Impingement Flow The mean-velocity and turbulence quantities in the jet were normalized with U_J. Figure 7 shows the streamwise (U/U_J) and cross-stream (V/U_J) components of the mean velocities across the impinging jet at several streamwise locations, with special emphasis on the stagnation region. The streamwise ($\sqrt{\overline{u^2}}/U_J$) and cross-stream ($\sqrt{\overline{v^2}}/U_J$) turbulence intensities are shown in Figure 8. The Reynolds shear stress ($-\overline{uv}/U_J^2$) profiles are shown in Figure 9.

The measurements, especially the V/U_J data near the ground plate, show a persistent symmetry in the flow about the centerline of the jet. The influence of the ground plate (jet impingement region, Fig. 1) extends to a height of Z/D = 0.75, where the jet still has a potential core in the streamwise mean velocity profile and the cross-stream component of the velocity is close to zero. Below Z/D = 0.75, the jet starts deflecting along the ground with a rapid decrease in U and increase in V. The dip in the U profiles at the center seems typical of jet-impingement flows, as also shown in the data of Donaldson and Snedeker (Ref. 18). Figure 8 shows that in the free jet, away from the ground, $\sqrt{\overline{u^2}} \approx 2\sqrt{\overline{v^2}}$; this trend reverses as the jet deflects near the ground. The Reynolds-shear-stress profiles (Fig. 9) near the ground show substantial regions of zero shear stress (Z/D = 0.2) despite the large velocity gradients, possibly because the turbulence exhibits a delayed response to the ground plate, as also evidenced by the profiles of $\sqrt{\overline{u^2}}$ and $\sqrt{\overline{v^2}}$ near the ground. Limited measurements on the second jet show similar initial profiles and jet development.

Fountain Upwash Flow Figure 10 illustrates the variations of the mean velocities (U and V) across the fountain. The distributions of V near the ground reveal that the fountain-formation region (Fig. 1) extends to Z/D = 0.5, where the variation in V across the fountain is comparable to that at stations farther downstream. However, it should be observed that even at Z/D = 0.2 and 0.3, the shape of the U profile resembles that typical for other downstream stations. The turbulence intensities $\sqrt{\overline{u^2}}$ and $\sqrt{\overline{v^2}}$ are of the same order of magnitude at a given station above the fountain-formation region Z/D > 0.5. In the fountain-formation region Z/D < 0.5, $\sqrt{\overline{u^2}}$ was observed to be relatively small because of the stagnating flow. The symmetry in the data distributions about the centerline of the fountain reflects the quality of the present measurements. The symmetry in the fountain data was a major problem in the majority of the earlier investigations.

Similarity of the Fountain Measurements Observation of the mean velocity (Fig. 10) and turbulence profiles in the fountain suggested self-similarity.

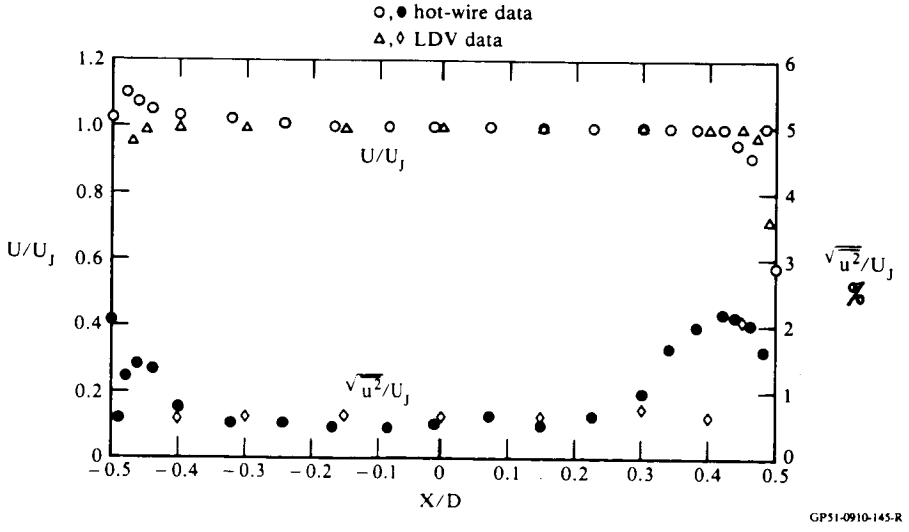

Fig. 6 Mean velocity (U/U_{max}) and turbulence-intensity ($\sqrt{\overline{u^2}}/U_J$) profiles at the jet exit.

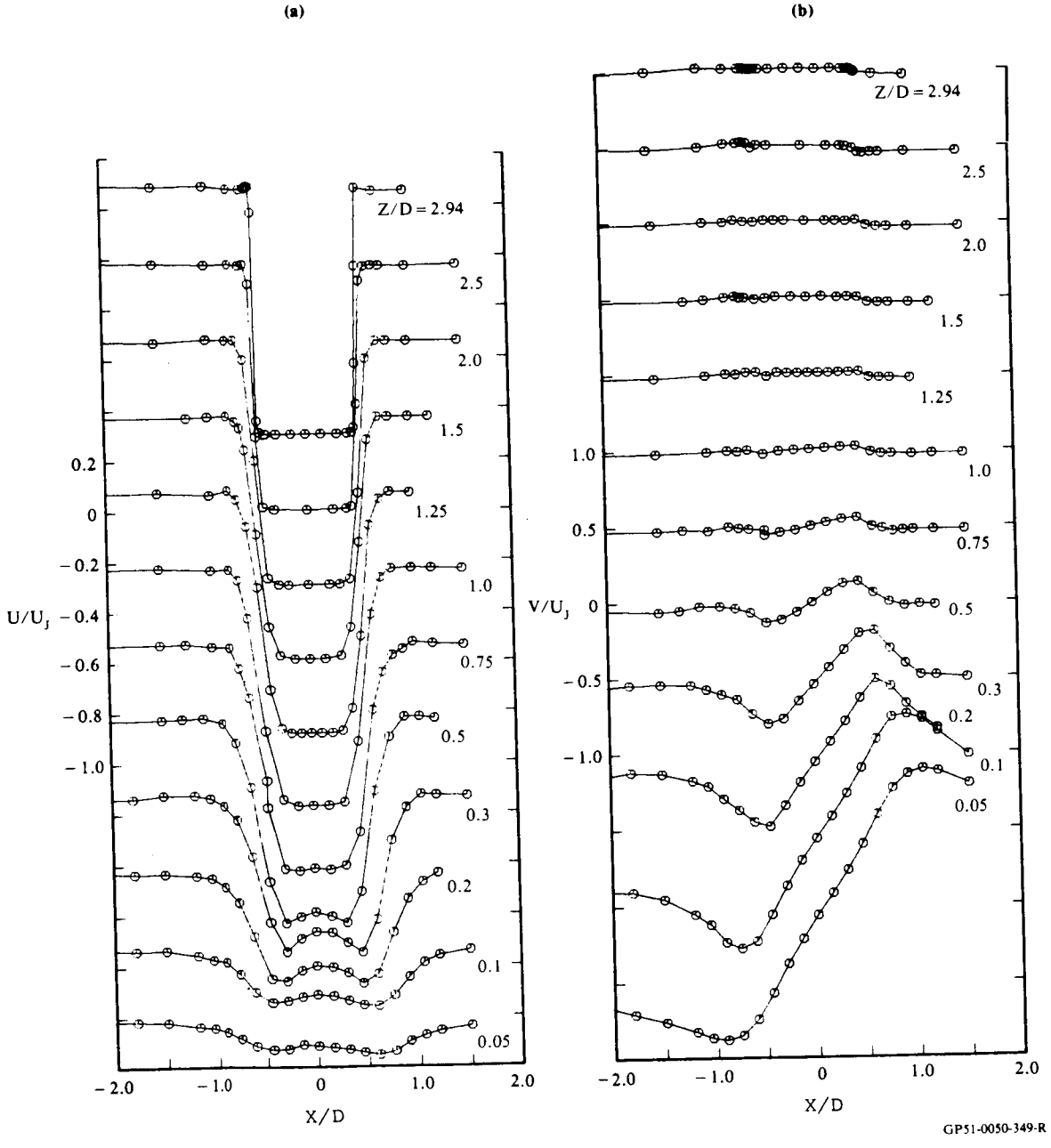

Fig. 7 Variation of (a) streamwise and (b) cross-stream mean velocities across the impinging jet.

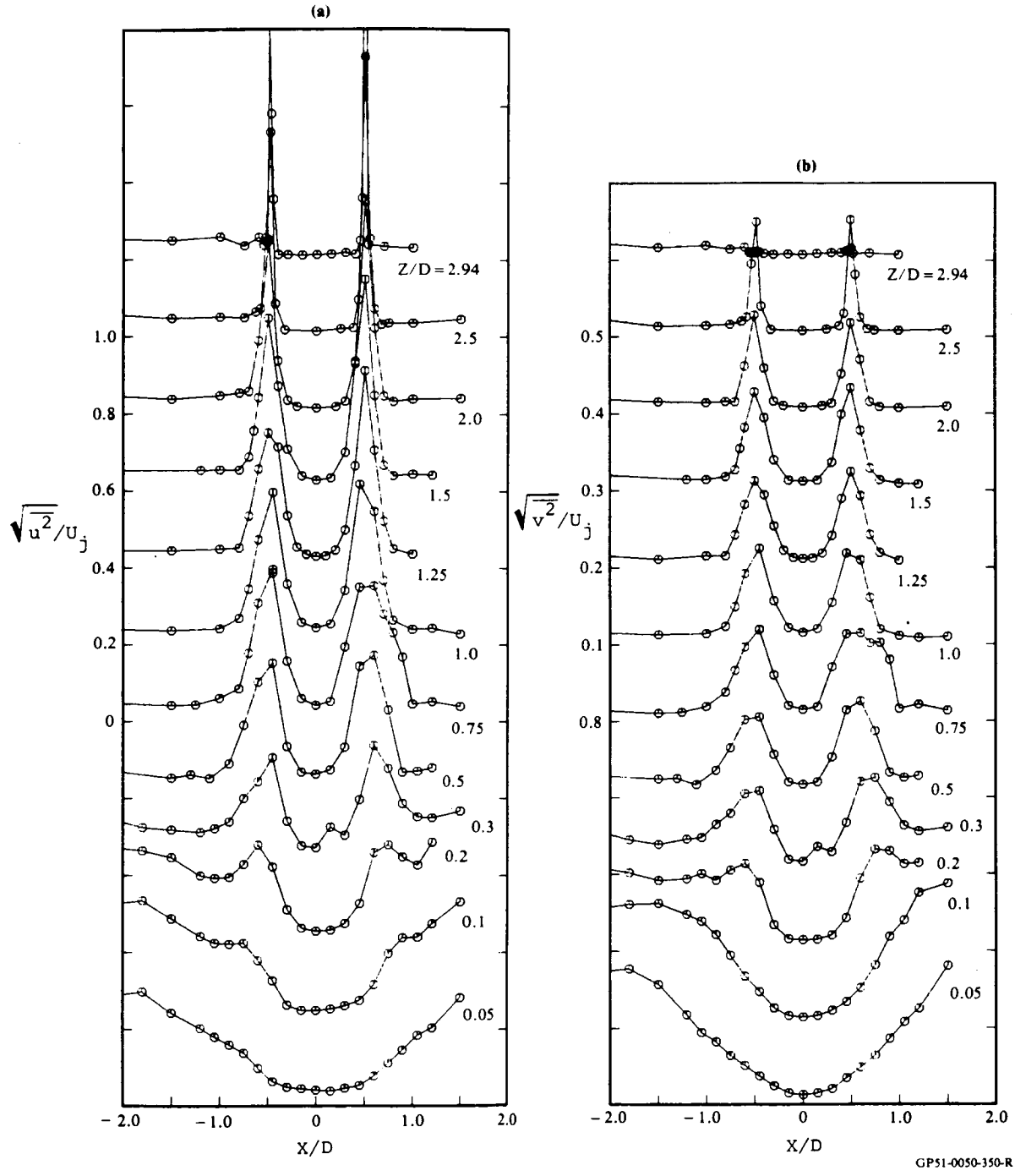

Fig. 8 Variation of (a) streamwise and (b) cross-stream turbulence intensities across the impinging jet.

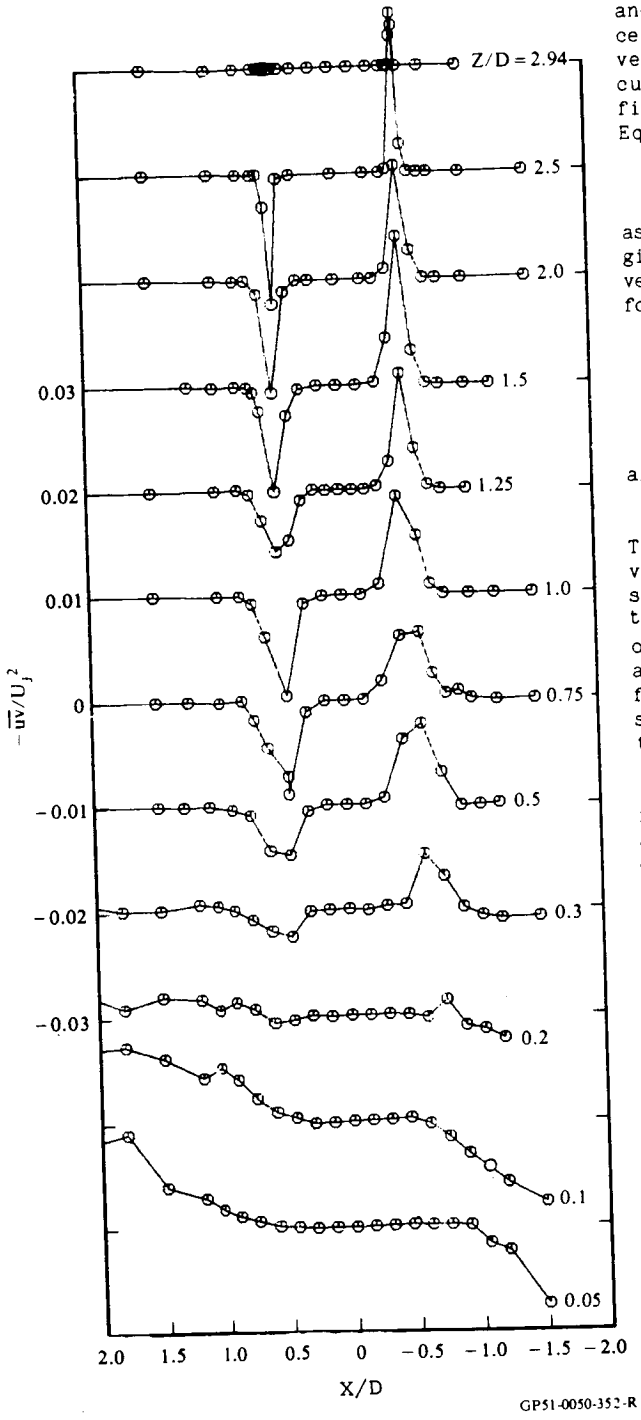

Fig. 9 Variation of the Reynolds shear stress across the impinging jet.

The fountain profiles were normalized with U_{max} and $X_{1/2}$ where U_{max} is the local maximum velocity and $X_{1/2}$, the half-width, is the distance from the center of the fountain to the point where the velocity is $U_{max}/2$. U_{max} and $X_{1/2}$ were obtained by curve-fitting the fountain mean velocity (U) profile with a least square curve of the form shown in Equation (1):

$$U = A + B \exp\left[-(X - X_o)^2/2\,S^2\right], \qquad (1)$$

as suggested by Gilbert (Ref. 4). This curve fit gives the symmetry coordinate X_o, the maximum velocity (A + B) and the parameter S related to the fountain half width $X_{1/2}$ by Equation (2).

$$X_{1/2} = \left[2\ \mathrm{LOG}\left(\frac{2B}{B - A}\right)\right]^{1/2} S \approx 1.177\ S \ (\text{for } B \gg A) \qquad (2)$$

also

$$U/U_{max} = \exp - 0.693\ (X/X_{1/2})^2 \ (\text{for } B \gg A).$$

The value of the X_o for Z/D ≥ 0.5 was found to be very small establishing once again, the inherent symmetricity in the present data. Figure 11 shows the linear growth of the fountain half-width ($X_{1/2}$) obtained by curve-fitting. The growth rate of about 0.16 is lower than that observed in Ref. (4) for two-dimensional fountain upwash. Figure 12 shows the decay of the maximum velocity (U_{max}) in the fountain again obtained by curve fitting.

Figure 13 shows the streamwise fountain velocity (U) profiles shifted to their symmetry point and normalized with respect to U_{max} and $X_{1/2}$, obtained by curve fitting. A striking similarity can be observed in the velocity profiles. Similar observations were made for two-dimensional fountain in Ref. (4). The profiles below Z/D = 0.5 were excluded because they fall into the fountain-formation region, although the profiles at Z/D = 0.3 and 0.2 do not differ much from the similarity form shown in Fig. 13. The profiles reach a similar form within a short distance (Z/D = 0.5) above the fountain-formation region, possibly because of greatly enhanced mixing at the base of the fountain.

The variation of the cross stream velocity V (Fig. 14) through the fountain was also found to be self-similar. These cross-stream mean velocity show an expected smooth variation from +ve on one side of the fountain to -ve on the other with zero crossing at the center of the fountain. The values of V at Z/D = 0.5 are slightly higher compared to the other downstream stations because of proximity to the fountain formation region.

Figures 15-18 show the various turbulence quantities across the fountain nondimensionalized with the similarity variables U_{max} and $X_{1/2}$ obtained by curve fitting. Once again similarity can be observed in the turbulence profiles at various downstream stations. The profiles of $\sqrt{\overline{u^2}}$ and $\sqrt{\overline{v^2}}$ (Figs. 15 and 16) show that they are generally of the same magnitude and shape. The maximum turbulence intensities are around 0.5, based on the

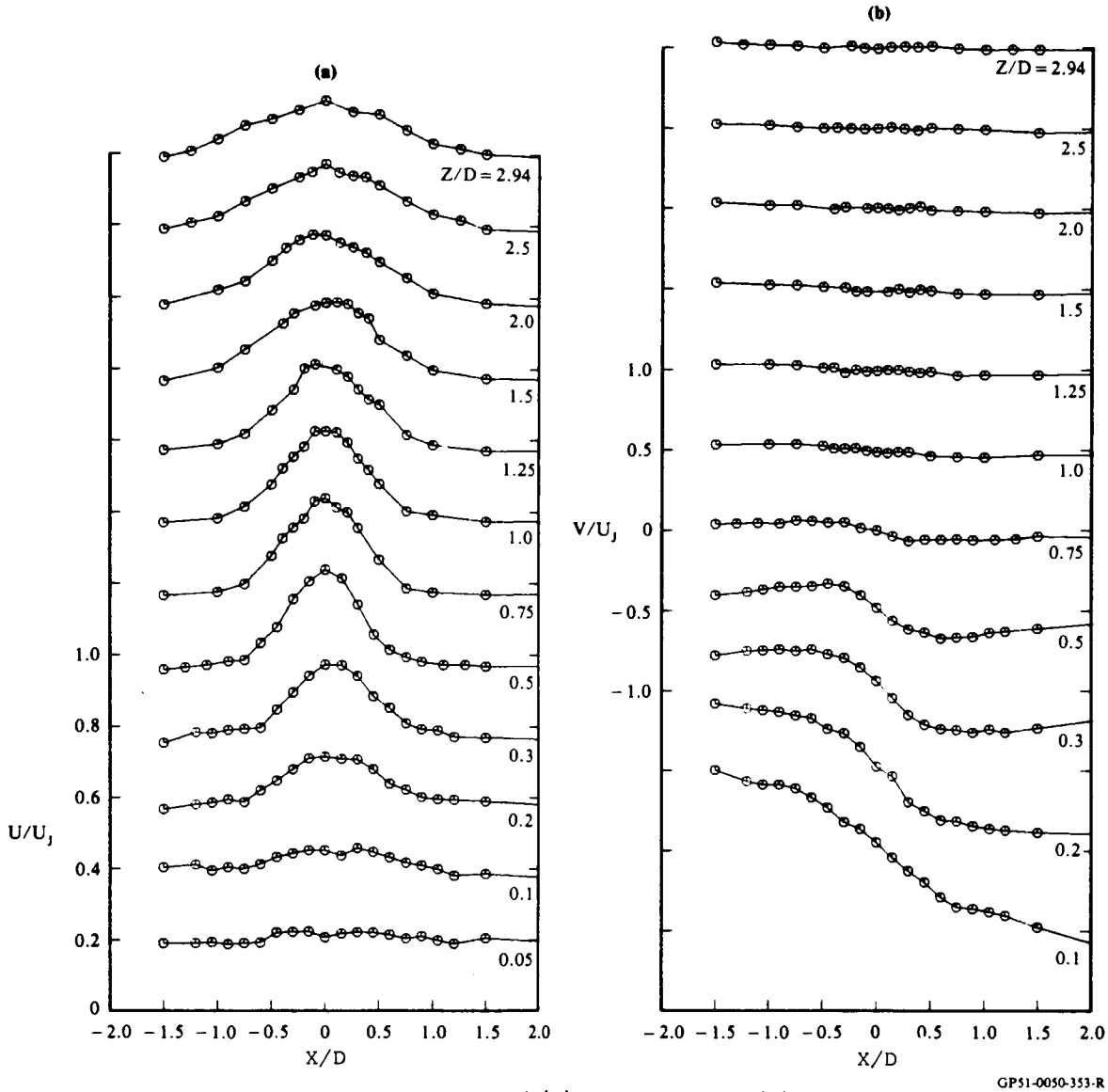

Fig. 10 Variation of (a) streamwise and (b) cross stream mean velocities across the fountain.

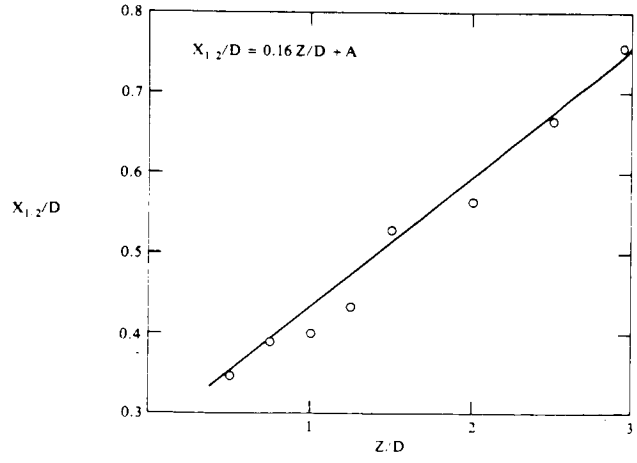

Fig. 11 Growth of the fountain half width ($X_{1/2}$).

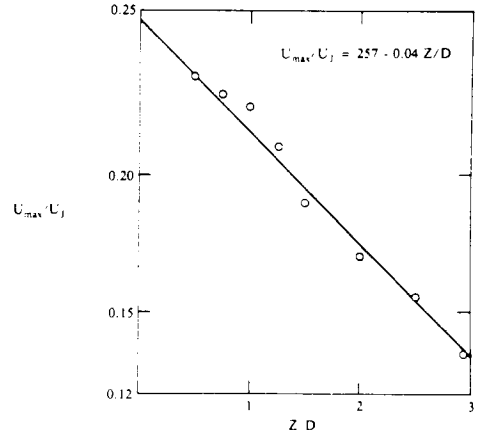

Fig. 12 Decay of the maximum velocity in the fountain ($U/_{max}$).

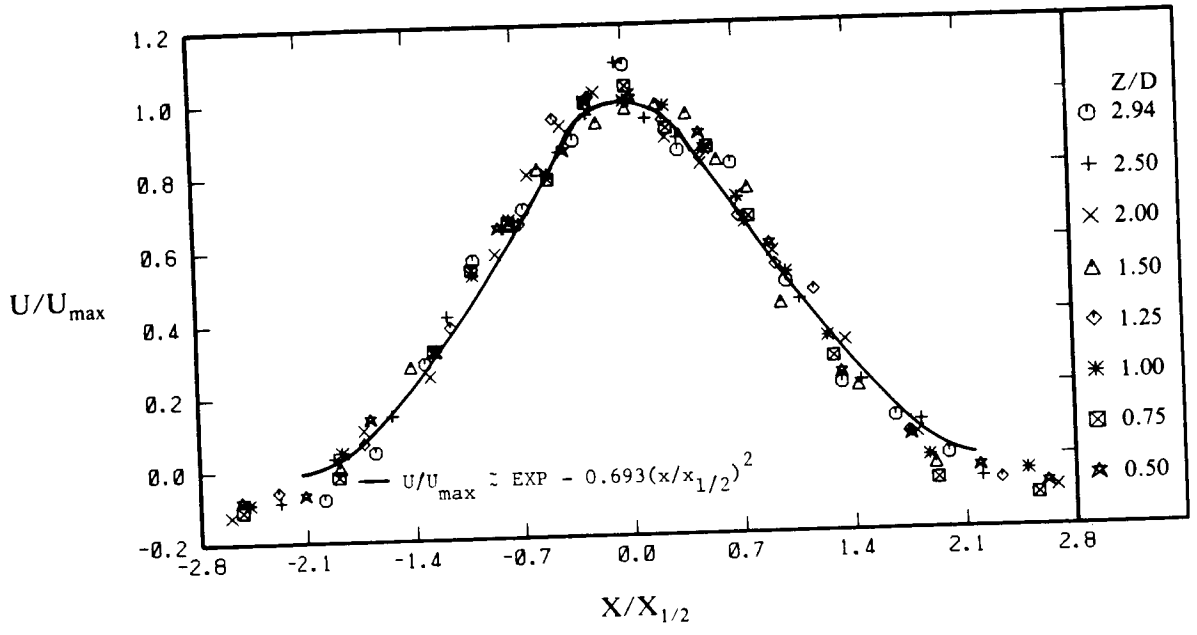

Fig. 13 Similar profiles of streamwise mean velocity (U/U_{max})

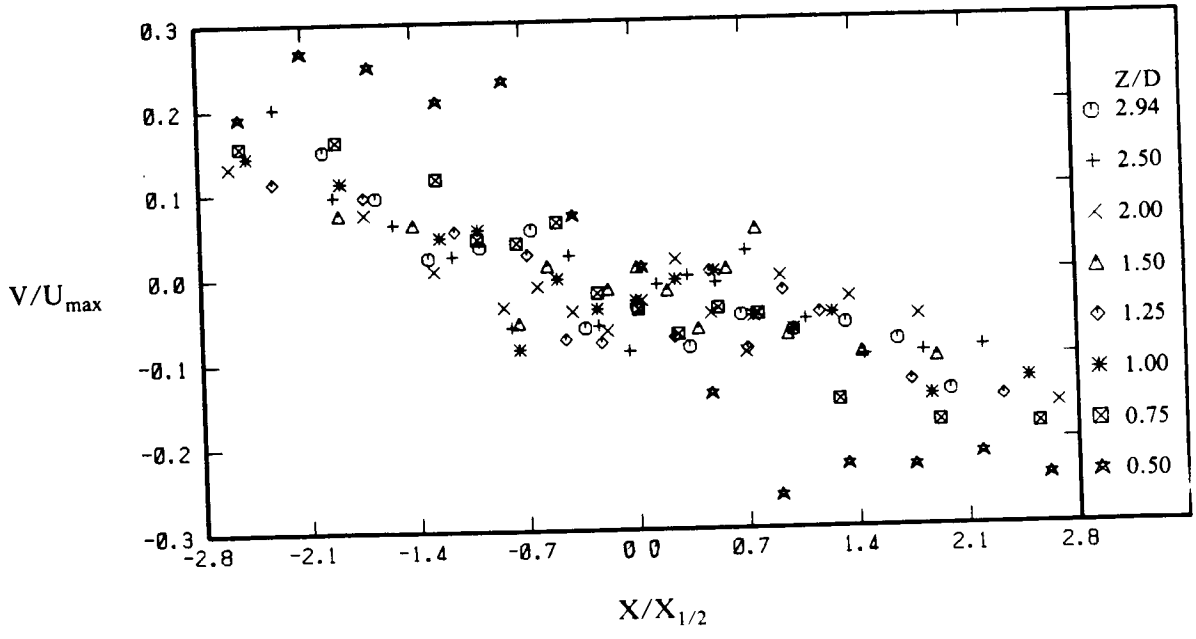

Fig. 14 Similar profiles of cross-stream mean velocity (V/U_{max}) across the fountain.

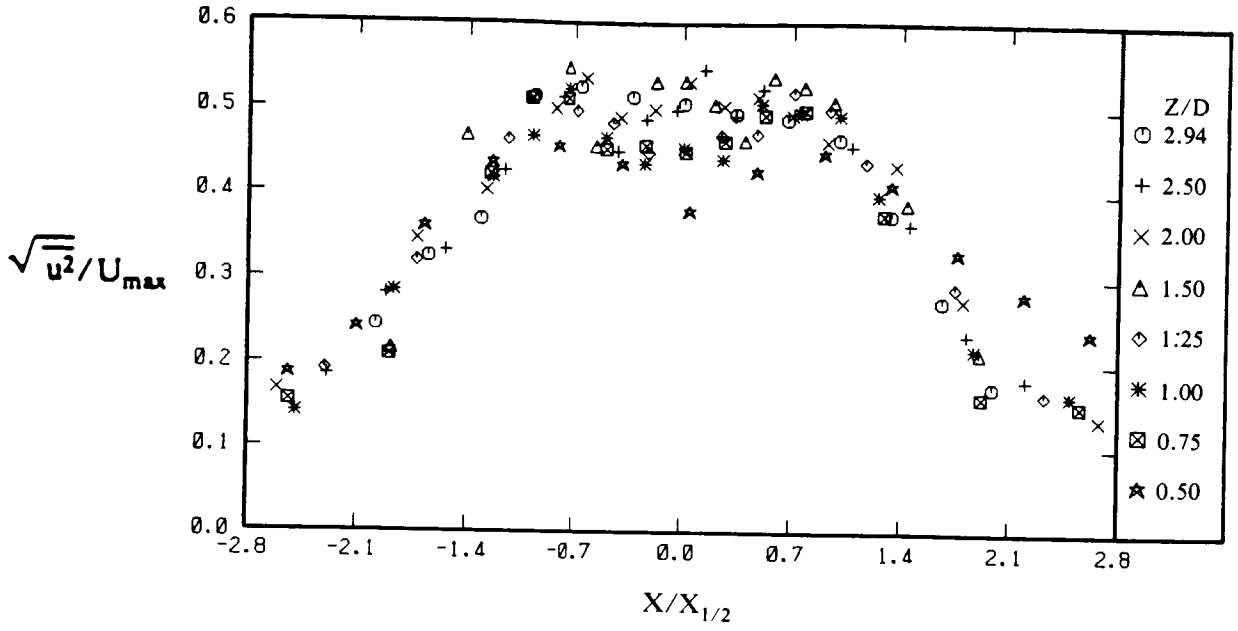

Fig. 15 Similar profiles of streamwise turbulence intensity ($\sqrt{\overline{u^2}}/U_{max}$) across the fountain.

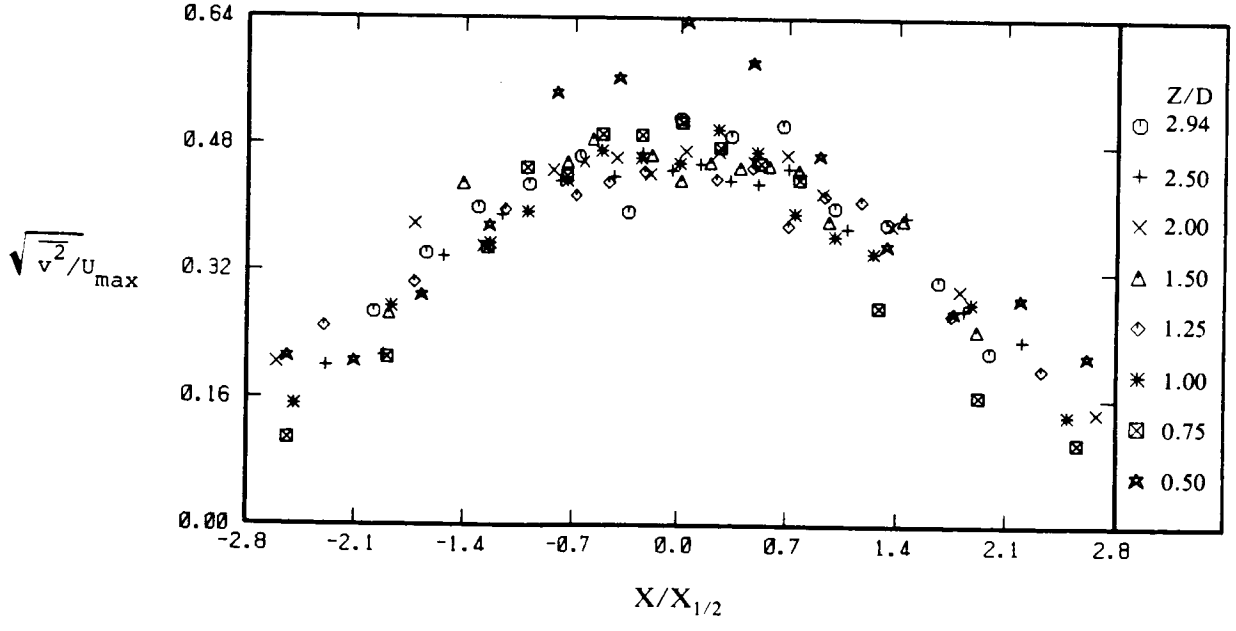

Fig. 16 Similar profiles of cross-stream turbulence intensity ($\sqrt{\overline{v^2}}/U_{max}$) across the fountain.

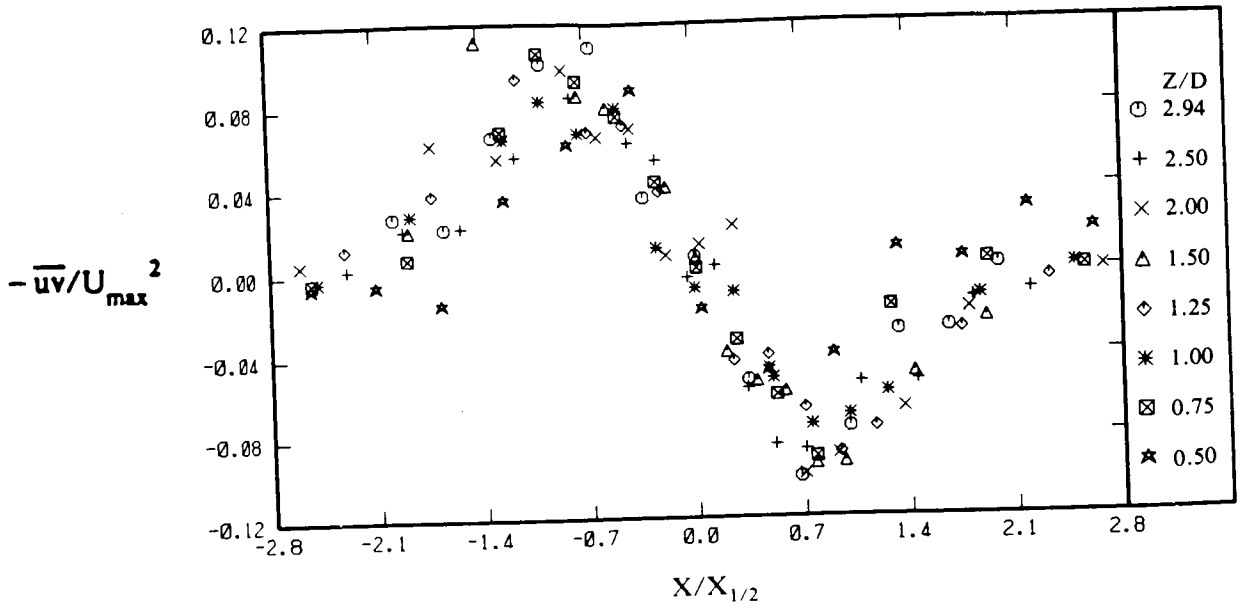

Fig. 17 Similar profiles of Reynolds shear stress ($-\overline{uv}/U_{max}^2$) across the fountain.

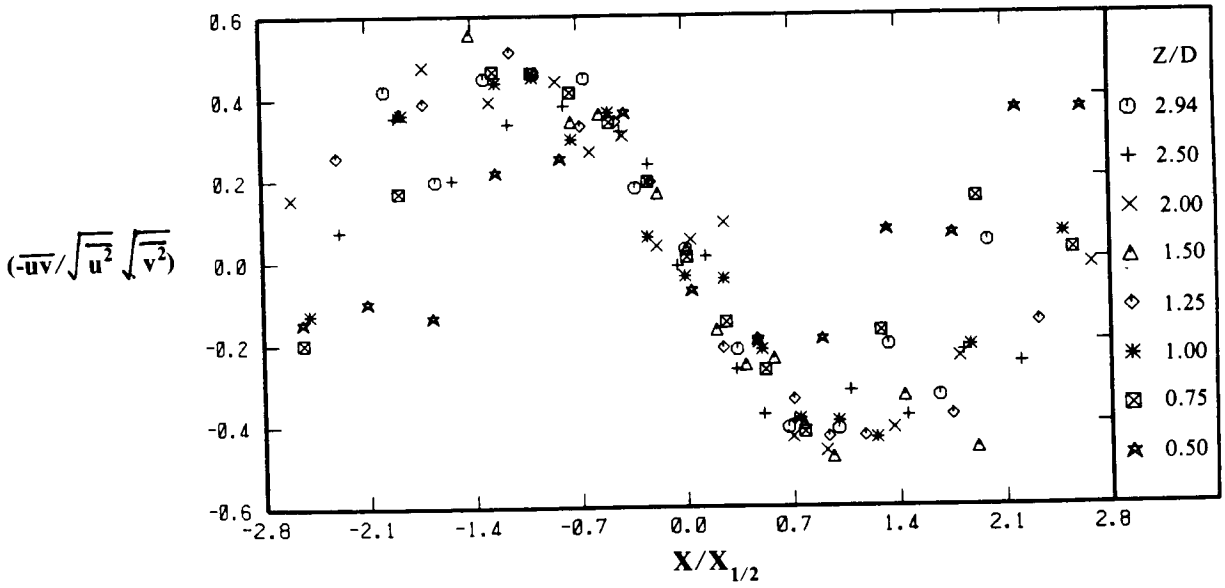

Fig. 18 Similar profiles of the correlation function ($-\overline{uv}/\sqrt{\overline{u^2}}\sqrt{\overline{v^2}}$) across the fountain.

local maximum velocity (U_{max}), suggesting the possibility for even instantaneous flow reversal; therefore the LDV is a more reliable instrument than the hot-film anemometer for measuring fountain flows. The similarity revealed by the Reynolds shear stress ($-\overline{uv}$) data (Fig. 17) is significant and indicative of the accuracy and precision of the experiment because the shear stress data in general are particularly sensitive to the measurement technique.

Figure 18 shows the similarity exhibited by the correlation function $-\overline{uv}/\sqrt{\overline{u^2}}\sqrt{\overline{v^2}}$. The scatter in the region beyond $X = X_{1/2}$ is primarily caused by the uncertainty in the measurement of small values of the respective turbulence quantities. The absolute maximum value of the correlation function is observed to be approximately 0.5.

In general, the turbulence profiles in the fountain were observed to take a longer distance to attain their self-similar shape than the corresponding mean velocity profiles.

Conclusions and Suggested Future Research

Mean velocity and turbulence profiles were obtained at 12 stations across the fountain upwash generated by the impingement of two axisymmetric jets using the laser Doppler velocimeter (LDV). Data were also reported on the impinging jet. The turbulence quantities included turbulence intensities, Reynolds shear stresses and correlation functions. The distributions of mean velocity and turbulence quantities across the fountain show self-similarity when nondimensionalized with proper parameters. The fountain flow was observed to be highly turbulent (≈ 50% turbulence intensity) requiring the use of an LDV. The growth of the fountain was observed to be linear at a growth rate of 0.16. The turbulence and the near ground mean velocity measurements in the three-dimensional fountain are believed to be the first data reported on such flows.

Additional measurements on the fountain flow away from the symmetry plane connecting the nozzle centerlines using a three component LDV are suggested to fully establish the fountain behavior. The effect of varying the nozzle separation and the height above the ground on the fountain behavior need to be established.

References

1. D. R. Kotansky and L. W. Glaze, The Effects of Ground Wall-Jet Characteristics on Fountain Upwash Flow Formation and Development, Report ONR-CR212-216-1F, 15 June 1980.
2. R. C. Jenkins and W. G. Hill, Jr., Investigation of VTOL Upwash Flows Formed by Two Impinging Jets, Grumman Research Department Report RE-548, November 1977.
3. R. J. Kind and K. Suthanthiran, The Interaction of Two Opposing Plane Turbulent Wall Jets, AIAA Paper 72-211, AIAA 10th Aerospace Sciences Meeting, San Diego, CA, Jan. 1972.
4. B. L. Gilbert, An Investigation of Turbulence Mechanisms in V/STOL Upwash Flow Fields, Grumman Aerospace Rept. Re-688, 1984.
5. W. H. Foley and D. B. Finley, Fountain Jet Turbulence, AIAA Paper No. 81-1293, AIAA Fluid and Plasma Dynamics Conf. Palo Alto, CA, June 1981.
6. M. J. Siclari, W. G. Hill, Jr., R. C. Jenkins, and D. Migdal, VTOL In-Ground Effect Flows for Closely Spaced Jets, AIAA Paper No. 80-1880, August 1980.
7. D. Migdal, W. G. Hill, Jr., R. C. Jenkins, and M. J. Siclari, VTOL In-Ground Effect Flows for Closely Spaced Jets, NASA CR-152321, December 1979.
8. G. R. Hall and K. H. Rogers, Recirculation Effects Produced by a Pair of Heated Jets Impinging on a Ground Plane, NASA CR 1307, May 1978.
9. A. Karemaa, C. W. Smith, H. A. Weber, and J. E. Garner, The Aerodynamic and Thermodynamic Characteristics of Fountains and Some Far-Field Temperature Distributions, Report ONR-CR 212-237-1F, July 1978.
10. J. R. Lummus, The Criticality of Engine Exhaust Simulations on VSTOL Model - Measured Ground Effects, Report ONR-CR212-255-1F, August 1979.
11. M. J. Siclari, W. G. Hill, Jr., and R. C. Jenkins, Investigation of Stagnation Line and Upwash Formation, AIAA Paper No. 77-615, AIAA/NASA, Ames V/STOL Conference, June 1977.
12. F. Durst, A. Melling, and J. H. Whitelaw, **Principles and Practice of Laser-Doppler Anemometry,** (Academic Press, NY, 1976).
13. T. S. Durrani and C. A. Greated, **Laser Systems in Flow Measurement,** (Plenum Press, NY, 1977).
14. K. R. Saripalli and J. C. Kroutil, A Novel Experimental Facility for Conducting Jet-Impingement Studies Related to VTOL Aircraft, AIAA Paper 85-0052, 1985.
15. K. R. Saripalli, Visualization of Multi-Jet Impingement Flow, AIAA Paper 81-1364, July 1981.
16. K. R. Saripalli, Visualization Studies of Jet Impingement Flows at McDonnell Douglas Research Laboratories, Third Intl. Symp. on Flow Visualization, Ann Arbor, Sept. 1983.
17. K. R. Saripalli, Visualization of Multi-Jet Impingement Flow, AIAA J. **21**, 483 (1983).
18. C. Donaldson and R. S. Snedeker, A Study of Free Jet Impingement. Part I. Mean Properties of Free and Impinging Jets, J. Fluid Mech. **45**, 281 (1971).

Numerical Investigation of V/STOL Jet Induced Interactions*

Magdi H. Rizk and Suresh Menon

Flow Industries, Inc.

Abstract

Direct numerical simulation using the full three-dimensional, time-dependent Navier-Stokes equations is used to investigate V/STOL jet induced interactions. The objective of this numerical simulation is to compute accurately the details of the flow field and to achieve a better understanding of the physics of the flow, including the role of initial turbulence in the jet, the influence of forward motion on hover aerodynamics, the collision zone and fountain characteristics. Preliminary results are presented.

*This work is supported by the Air Force Office of Scientific Research under Contract No. F49620-84-C-0027.

1. Introduction

The fluid dynamics of impinging jets of V/STOL aircraft is complex, to say the least. The complexity is compounded by compressibility, combustion and heat transfer, as well as complex interactions between airframe and ground, forward flight, oblique impingement, jet turbulence, jet exit profile shape, etc. Clearly, an accurate prediction of the aerodynamic forces and moments on the aircraft is not possible without understanding the associated flow physics.

V/STOL aircraft have different operating modes (hovering and transition in and out of ground effect). The flow fields associated with these modes of operation are substantially different. Many of the complex flow phenomena associated with these flow fields are poorly understood, thereby restricting our ability to optimize the aircraft design. Lifting jets entrain air, which leads to induced suction pressures on the aircraft lower surface. When the aircraft is hovering near the ground, further entrainment is caused by the wall jets (associated with the ground). This significantly increases the suckdown force on the aircraft. The problem becomes more complex in the case of multiple jets. Here the wall jets collide and form a fountain that impinges on the aircraft undersurface. While this impingement creates an upload, which partly offsets the suckdown force, the fountain flow causes further reduction in the pressure between the jets and the fountain. The complex flow fields associated with multiple jets in ground effect are also not well understood.

Presently, experimental work is the main avenue followed to gain an understanding of flows associated with V/STOL aircraft. However, such studies have addressed mostly global features and time-averaged measurements of impinging jets. Experiments in this configuration are extremely cumbersome, and measurements are crude and inaccurate owing to the flow being turbulent, globally unsteady and three-dimensional. Characterization of this flow will require measurements involving three-dimensional arrays of sensors. These sensors (hot-wires, for example) have the constraints that they cannot discriminate flow reversal from forward flow and are prone to probe interference. An array of LDAs would be prohibitively expensive.

Numerical simulation provides the opportunity of studying the detailed flow physics as a function of space and time. Although the complete flow field around a V/STOL aircraft will be difficult to solve today, because of the size limitation of present-day computers, some local flow domains, such as the impinging jet flow, can be studied. The simulation can be either a direct numerical simulation or a large-eddy simulation (LES) involving subgrid-scale modeling. In fact, numerical simulation provides a number of advantages: it provides the instantaneous distribution of all flow variables over the entire three-dimensional flow field considered; it allows "measurements" of flow properties not possible experimentally (for example, pressure within turbulent flows); it can provide simultaneous "flow visualization" and "measurements" in arbitrary planes.

Numerical experimentation is often more desirable than laboratory experimentation, because the former allows independent control of the flow parameters or any choice of arbitrary combinations of parameter values. Such independent control or arbitrary combination is difficult in any apparatus. Similarly,

variations of parameters like initial conditions, free-stream turbulence, excitation frequency, excitation amplitude, etc., can be typically more easily introduced in numerical experiments than in laboratory experiments.

The majority of the research work directed towards investigating V/STOL flows has been experimental. Only within the past few years have sufficient advances in computer capabilities made it feasible to attempt numerical simulation of the three-dimensional viscous equations for the V/STOL related flow fields. With present computer capabilities numerical simulations cannot replace experimental procedures. However, they can complement experimental efforts in gaining a deeper understanding of the complex flow phenomena associated with V/STOL flows. The design and analysis of traditional aircraft components have benefitted greatly from numerical computations. Computational methods are expected to have a similar impact on V/STOL problems.

The computational work initially was limited to solving two dimensional problems. Using an incompressible inviscid rotational flow model, Rubel (1978) investigated the normal impingement of axisymmetric jets and the oblique impingement of two-dimensional jets upon a flat surface. This model was then extended to allow three-dimensional computations (Rubel, 1981). Kotansky and Bower (1978) investigated planar turbulent jet impingement. They solved the time-averaged Navier-Stokes equations using a one-equation turbulence model. In this approach, it was necessary to specify the turbulence length-scale distribution. To avoid this disadvantage, Agarwal and Bower (1982) replaced the one-equation turbulence model by the two-equation ($k-\varepsilon$) turbulence model. The work of Kotansky and Bower (1978) was extended to solve the problem of three-dimensional lift jets in ground effect by Bower et al. (1979). This work was the first attempt to calculate interacting jets with fountain formation. Computer limitations restricted the calculations to a relatively coarse computational mesh and to low Reynolds number. More, recently Childs and Nixon (1985) solved the impingement problem for three-dimensional jets using the time-averaged Navier-Stokes equations in conjunction with the two-equation ($k-\varepsilon$) turbulence model.

Work is in progress at Flow Industries on the direct numerical simulation of complex V/STOL flows using the full three-dimensional, time-dependent Navier-Stokes equations. The objective of this numerical simulation is to compute accurately the details of the flow field and to achieve a better understanding of the physics of the flow, including the role of initial turbulence in the jet, the influence of forward motion on hover aerodynamics, the collision zone and fountain characteristics. The computational tools necessary have been partially developed. Preliminary calculations have been performed using a relatively coarse computational mesh for a low Reynolds number flow. The results presented here are not intended to be an accurate simulation of V/STOL flow configurations. Nevertheless, they do indicate the main features of these flows.

2. Approach

In turbulent flows, there is a wide range of spatial and temporal scales. The separation between the largest and the smallest scales of motion widens as the Reynolds number increases. For V/STOL flows, the numerical resolution of all relevant scales of motion is impossible. Modeling of some aspects of the flow is therefore necessary. In the classical approach, based on Reynold's ideas for solving turbulent flow problems, the Navier-Stokes equations are averaged. All fluctuations are modeled, and only mean flow variables are calculated. This approach has been used by various researchers but has met with only limited success. In the V/STOL problem, different flow regions exist in which the large-scale structures vary greatly from one to another. It is therefore difficult to model the large-scale structures. To avoid this difficulty, the large-eddy simulation (LES) approach is followed here. In this approach, the large scales, containing most of the turbulent energy and providing most of the important turbulent transport, are explicitly calculated. The small-scale turbulence structures, which are nearly isotropic and universal in character, are modeled in a simple, relatively crude manner. Furthermore, LES can be used to investigate the temporal development of the flowfield. This allows us to study a broader range of problems relevant to V/STOL flows, e.g., the unsteady separation in boundary layers produced by impinging jets (Didden and Ho, 1985), the evolution of large, spatially coherent structures in the jet (Crow and Champagne, 1971) and the different stability modes in the jet (Strange and Crighton, 1983).

The governing equations that are numerically solved are the full Navier-Stokes equation for incompressible flow. When the Reynolds number is too large to resolve numerically the entire range of energetic scales, filtering is used to eliminate the smaller (subgrid-scale) motions. Filtering introduces new terms, similar to Reynolds stress terms obtained in the Reynolds-averaged equations, that contain the effect of subgrid-scale motions on the numerically resolved motions. These subgrid Reynolds stresses can be modeled using an eddy viscosity (see Moin and Kim, 1982).

The finite difference approximations to the governing equations are written at the mesh points of a staggered grid (Harlow and Welch, 1965). The pressure is determined at each time step by solving the governing Poisson equation. Efficient methods for the direct solution of the discrete Poisson equation are used (Buzbee et al., 1970). The Adams-Bashforth scheme is used to advance the velocity in time.

The problem under investigation is that of an infinite row of jets impinging on the ground (see Figure 1). This problem, which contains the essential features of twin jets impinging on the ground (see Figure 2), simulates the hovering configuration. The jets may be inclined in the y direction, which leads to a configuration associated with an aircraft in pitch while hovering. By imposing a cross flow in the y direction, it is possible to study the effects of the aircraft's forward motion during takeoff and transition.

A computer code that solves the time-dependent Navier-Stokes equations has been developed with the purpose of numerically simulating the problem of an

infinite row of jets impinging on the ground. Subgrid-scale modeling, which would allow the solution of problems at higher Reynolds numbers is currently being introduced into the code. Although the code is not in its final form, it has been used to obtain solutions that indicate the main feature of V/STOL aerodynamics.

3. Numerical Results

The results presented here are preliminary examples that have been solved using the code in its present form. A relatively coarse numerical mesh was used, and the Reynolds number was assumed to be low enough so that filtering was not required. The results presented here are not intended to be an accurate simulation of V/STOL flow configurations. Nevertheless, the results of the steady-state examples presented here indicate the main features of the impinging jet flow. The unsteady behavior of the jet flow due to forcing at a specific frequency has also been investigated.

3.1 Steady-State Calculations

The following three examples indicate some of the main features of V/STOL flows. In these examples the plane $x=x_j$ (see Figure 1) is assumed to be a plane of symmetry and, unless otherwise stated, the computational domain is defined by

$$\begin{aligned} 0 = x_j \le x \le x_f &= 1 \\ -2 = y_B \le y \le y_b &= 2 \\ 0 = z_g \le z \le z_a &= 1 \end{aligned}$$

where all dimensions are normalized by the jet diameter. The jet velocity profile in the direction of the jet axis is assumed to be given by

$$Q_j(r) = 1 - \frac{r^2}{R_j^2} \qquad (1)$$

where R_j is the jet radius, r is the distance from the jet axis, and velocities are normalized by the maximum jet velocity. The Reynolds number in these examples is based on the jet diameter and the maximum jet velocity.

Example 1:

In this example, the jet axis is normal to the ground plane ($\alpha = 90°$) and there is no crossflow (V = 0). The jet at a Reynolds number (Re) of 300 is solved in a 18x72x18 (x,y,z) mesh.

Figures 3 through 9 show the main features of the flow generated by a row of vertical jets impinging on the ground. The velocity vectors in the planes $x = x_j$ and $x = x_f$ are shown in Figures 3 and 4, respectively. The fan-shaped fountain that results from the collision of the two wall jets is apparent in Figure 4. The jet, the wall jet, and the fountain can be seen in Figure 5. Figures 6

through 9 show the pressure contours that indicate high-pressure areas in the zones of jet-ground impingement, wall jet-wall jet collision, and fountain impingement on the upper boundary.

Example 2:

In this example the jet axis is inclined at an angle $\alpha = 60°$ to the ground. A crossflow of $V = 0.2$ is imposed on the flow field. The Reynolds number and mesh size is the same as in Example 1.

Figures 10 through 13 show the main features of the flow generated by a row of inclined jets impinging on the ground in a crossflow. In Figure 10 the ground vortex formed by the interaction of the crossflow and the wall jet is apparent. The effect of the crossflow on the fan-shaped fountain is shown in Figure 11, where it is no longer symmetric.

For the problem of a jet in a crossflow, two basic configurations are relevant to V/STOL aerodynamics. In the first configuration, the jet impinges on the ground. The main features of this flow are indicated in Example 2. A second configuration results as the distance between the aircraft and the ground becomes large and/or as the forward aircraft speed becomes large. In this case, the jet does not impinge on the ground. This configuration is shown in the following example.

Example 3:

In this example $\alpha = 90°$, $V = 0.7$, and $Re = 60$. A 7x28x14 mesh is used. The computational domain is defined by

$$\begin{aligned} 0 = x_j \leq x \leq x_f &= 1 \\ -2 = y_B \leq y \leq y_b &= 2 \\ 0 = z_g \leq z \leq z_a &= 2. \end{aligned}$$

Figures 14 through 18 show the main features of this flow. Figure 14 indicates that the jet changes its direction before it reaches the ground. As indicated in Figure 15, no fountain flow develops in this example since there are no wall jets. The double vortex generated by the jet-crossflow interaction is shown in Figure 16. As indicated by the pressure contours shown in Figure 17, a high-pressure region develops upstream of the jet, while a low-pressure region develops downstream of the jet in its wake. Figure 18 shows the vorticity distribution in the y-z plane.

To investigate the effect of different inflow jet velocity profile on the jet development, a series of steady-state calculations was carried out. Four different initial jet profiles were investigated: the r^n-profiles (where $n = 2,4,6$) and the tanh-profile. The computational domain and grid resolution were kept the same with the ground plane at $H/D = 8$, where H is the distance between the upper and lower walls while D is the jet exit diameter. This is in contrast to the steady-state calculations (Examples 1-3) where the ground plane was kept much closer to the jet exit. In this study, the ground plane was kept as far away as possible so that the jet development and stability

would not be directly affected by the resonance effect of the ground plane. The basic thrust of these steady-state calculations was to investigate numerically the experimental observation that the flatter profiles (e.g., tanh, top-hat) are inherently more unstable than the less flat profiles (e.g., parabolic). This experimentally observed instability has been attributed mainly to the initial shear layer instability, which is more pronounced for the broader profile (due to the thinness of the initial shear layer). However, to observe numerically the shear layer instability, a very high grid resolution is required near the jet lip, which at present is not possible due to computational limitations. Furthermore, to obtain accurate results with the available grid resolution, the Reynolds number and the computational domain had to be kept small, which is another limitation inherent in these calculations. However, we expected that there are other overall features of the jet development that will show the effect of varying the jet profile; the present steady-state calculations were directed towards determining these effects.

In the following, we present the steady-state solutions obtained for the different jet velocity profiles. We have assumed that the flow field is symmetric in the x-direction and, therefore, only the half-plane (with respect to the y-axis) is shown. The grid used in all these calculations is a 16x32x64 mesh, and the computational domain is defined as

$$\begin{aligned} 0 \leq x/D \leq 1 \\ -2 \leq y/D \leq 2 \\ 0 \leq z/D \leq 8 \end{aligned} \tag{2}$$

The ground plane is located eight jet diameters (H/D = 8) below the jet exit plane, and a uniform grid distribution is used in the whole computational domain. The jet velocity profiles are given by

$$\begin{aligned} &\text{Profile I:} && w_j = w_{jo}(1 - \eta^2) \\ &\text{Profile II:} && w_j = w_{jo}(1 - \eta^4) \\ &\text{Profile III:} && w_j = w_{jo}(1 - \eta^6) \\ &\text{Profile IV:} && w_j = \frac{w_{jo}}{2}\{1 + \tanh[b(\frac{1}{\eta} - \eta)]\} \end{aligned} \tag{3}$$

where $\eta = r/R$, R is the radius of the jet, and w_{jo} is the reference velocity, taken to be unity at the centerline of the jet. Here $b = 2R/\delta$, where δ is the momentum thickness. We took b = 25/16, from Strange and Crighton (1983) which is an empirical fit to Crow and Champagne's (1971) data two jet diameters below the exit plane.

In the following discussion, the velocity profiles given by Equation (3) will be identified as Profiles I through IV. Profile I is the parabolic profile, and Profiles II and III are the consecutive flattening of Profile I. Profile IV is based on the empirical fit obtained for Crow and Champagne's data and is the closest to what has been observed in experiments. Profile IV has a thinner initial shear layer that is naturally unstable. We therefore

expect Profile IV to be the most unstable among those studied, and the present calculations indicate that this is indeed so. It was found during our calculations that the flatter profiles (Profiles III, IV) became numerically unstable when the jet Reynolds number was increased. This is basically due to the lack of proper grid resolution, which is necessary for higher Reynolds number calculations. Therefore, to make proper comparisons and to keep the solutions time-accurate, the solutions presented here are all in the Reynolds number range from 200 to 300.

Figures 19a through 19d give the steady-state vorticity contours for the four velocity profiles (I through IV), respectively. [In all the following figures, unless otherwise stated, the y-z plane refers to the plane $x = x_j$, while the x-z plane refers to the plane $y = y_j$ (see Figure 1).] For direct comparison, the contour intervals are the same in all the figures. The Reynolds numbers are not the same for all the cases but are close enough to make comparison possible. Except for Profile IV, all solutions are at nearly the same elapsed time. Comparing the vorticity for different profiles shows that the vortex zone above the ground plane is much larger for Profile IV as compared to the other profiles. The vorticity levels also increase from Profile I to the much flatter profile (Profile IV). Near the ground plane there is an indication of a pinching effect on the vorticity line above the vortex zone in all the x-vorticity plots. This is perhaps because as the flow spreads on the ground plane, a part of the flow gets entrained into the jet region, thereby causing the vortex lines to get pushed towards the centerline.

In the wall boundary layer, a region of secondary vortical circulation opposite to the large primary vortex appears, as can be seen in the x-vorticity contours (Figure 19). Note here that solid lines indicate vorticity out of the plane and dashed lines indicate vorticity into the plane. This region of secondary vorticity also moves downstream along with the primary vortex. This formation of secondary vorticity in the wall boundary layer has been associated with boundary layer separation (Didden and Ho, 1985), and the present calculations seem to predict qualitatively their experimental observation. In Didden and Ho's experiments, they observed the secondary vorticity lifting off the plate and wrapping itself around the primary vortex. They also observed the breakup of the large primary ring vortex as the flow continues to spread on the ground and attributed this to possible azimuthal instability. This has not been observed in the present calculations, however, due to the proximity of the outflow boundary to the jet. With a larger computational domain and better resolution near the ground, it may be possible to study these experimental observations. The general picture is qualitatively the same for all the different profiles studied here and is consistent with general experimental observations. However, direct comparison is not possible due to the low-Reynolds-number simulations carried out here and also due to the possible effect of the type of boundary conditions employed. Higher resolution simulations on a large computational domain (in the x- and y-directions) and at higher Reynolds numbers are necessary for detailed comparisons with the available experimental data.

The appearance of the secondary vorticity of the opposite sign on the ground plane is observed for all the velocity profiles studied here. To get a better look at this secondary vorticity in the wall boundary layer, in

Figure 19e we show for comparison a higher resolution (24x48x24) calculation with the ground plane at H/D = 1 and at a Reynolds number of 600. For this calculation we assumed symmetry in both the x- and y-directions and, therefore, only the half-planes were calculated. The propagation of the primary vortex in the downstream direction is evident in this figure, and the formation of the secondary vorticity of the opposite sign is also very clear. Moreover, the initial attempt by the secondary vorticity to wrap itself around the primary vortex as they move downstream is also shown, consistent with the experimental observation (Didden and Ho, 1985). However, this process is affected by the outflow boundary location, and the wrapping process seems to be inhibited.

To determine details of the pressure variation, we show the variation of the pressure along the centerline in Figure 20a. The pressure values are normalized by the maximum value at the stagnation point, and the centerline location is also normalized by the distance between the jet exit and the ground plane. The variations for both Profiles I and III are quantitatively the same and, for comparison, some experimental data (Beltaos and Rajaratnam, 1973; Russell and Hatton, 1972) for the centerline pressure variation are also presented. We found that most of the experimental data available are for two-dimensional or axisymmetric high-Reynolds-number turbulent flows and, therefore, good agreement is not expected since the present calculations are for low-Reynolds-number, three-dimensional laminar flow. The variation of the calculated pressure is similar to that seen in experiments and indicates that the present calculations are predicting qualitatively the observed pressure distribution.

To determine the possible existence of an adverse pressure gradient, we plotted the variation of the wall pressure (normalized by the stagnation pressure) for both Profiles I and III, as a function of radial (x) direction, in Figure 20b. The pressure decreases from the maximum at the stagnation point until $x/H \simeq 0.085$ (for Profile III) and $x/H \simeq 0.1$ (for Profile I), at which point it starts to increase again indicating a change from a favorable to an adverse pressure gradient. We could conclude based on this figure that there is a possible occurrence of separation at $x/D = 0.80$ (for Profile I) and $x/D = 0.68$ (for Profile III). However, this separation effect is possibly due to the collision of the wall jets on each other and the formation of the fountain. Also shown in Figure 20b are the available experimental data for the high-Reynolds-number turbulent impinging jets, which indicate similar variation. The appearance of an adverse pressure gradient on the ground plane is interesting since it has been experimentally identified as the cause of unsteady separation of the wall shear layer. Additional data is required to confirm whether there is any separation occurring on the ground plane. For example, the pressure variation in the y-direction and the variation of the wall shear stress must be calculated to determine the location where it changes sign, which would then indicate the separation point. The grid resolution near the ground would also have to be improved to resolve the wall boundary layer. These factors will be considered in more detail in the future study.

Figure 20c gives the variation of the steady-state centerline velocity (normalized by the maximum velocity at the jet exit and the distance of the jet from the ground plane) as a function of distance to the ground plane for

Profiles I and III. Also shown are some characteristic experimental data for high-Reynolds-number turbulent impinging jets. Though direct comparison is not possible, the general trend in the present calculation is similar to that of the experimental data. The solution also indicates that the decay along the centerline is much slower for Profile III than for Profile I. This is probably due to the fact that Profile III, with its flatter profile shape, has a more distinct potential core as compared to Profile I, which is parabolic, with hardly any potential core. Since in potential core there is (by definition) no dissipation, the velocity decay occurs slower and hence closer to the ground plane for a Profile III-type jet as compared to a Profile I-type jet.

In general, the steady-state solutions presented above for impinging jets indicate qualitative agreement with experimental data. Four different initial jet profiles were studied, and the comparison indicates that the flatter profiles show more signs of instability. Furthermore, it was found that the flatter profiles showed numerical instability for higher-Reynolds-number simulations and, therefore, all the present calculations were carried out in the Reynolds number range from 200 to 300. This numerical instability is mainly due to the lack of adequate resolution in the computational domain and, due to the computer resource restrictions, the largest mesh used is (16x32x64). For quantitative comparison with experimental data and more detailed interpretation of the complex flow structures observed here, a higher resolution (and higher Re) simulation is envisioned in the future study.

The overall flow pattern indicates that the initial shear layer rollup is not observed due to lack of resolution near the jet exit. However, the formation of the large primary vortex ring is observed, and when this vortex ring impinges on the ground plane and spreads in the radial direction, the formation of secondary vorticity of the opposite sign in the wall boundary layer is also observed. This secondary vorticity in the wall layer may be due to separation, since the pressure data indicate the presence of an adverse pressure gradient near the outflow (in the x-direction). However, this is not exactly the same effect as observed by Didden and Ho (1980) due to the effect of the fountain in the present study. Comparison with experimental data for high-Reynolds-number turbulent impinging jets indicates qualitative agreement for the centerline and ground plane pressure variation and the centerline velocity variation.

3.2 Single-Frequency Forcing

3.2.1 Axisymmetric Forcing

The study of turbulent shear flows has undergone considerable change in the recent past, brought about by the discovery of large, spatially coherent structures in fully developed flows. Furthermore, it has been realized that the initial instability of the flow can have a strong influence on its subsequent evolution. For example, Crow and Champagne (1971) observed that growth and mixing of an axisymmetric jet were sensitive to harmonic forcing and found a "preferred" frequency for the development of the jet for a Strouhal number, $St(= fD/U)$, of 0.3. They also observed that, as the Reynolds number was increased from 10^2 to 10^3, the instability of the jet evolved from a sinusoidal to a helical mode and finally into a train of axisymmetric waves. It

has also been noted that the initial jet exit velocity profile plays an important part in determining the form of instability that is observed. A top-hat profile has been shown to be more unstable than a fully developed profile (Batchelor and Gill, 1962; Grant, 1974) due to the shear layer instability. In some experiments, the instability of the initial shear layer occurs through axisymmetric modes, whereas in other experiments a helical instability was observed first (Strange and Crighton, 1983; Hussain, 1983). Such differences are attributed, in part, to the initial conditions of the experimental setup. Therefore, to study the stability of jet flows, the initial instability mechanism must be understood. Moreover, since it has been shown that large eddies in jet flows can be controlled by harmonic forcing, the effect of controlled forcing on the instability mechanism is also important.

In the present numerical study of an impinging turbulent jet, the mesh resolution is limited by the available computer storage. It is, therefore, not possible to study the effect of a wide band turbulence, i.e., a wide range of disturbances in frequency and wave numbers. However, it is possible to look at the unsteady behavior of the jet flow due to forcing at a specific frequency of disturbance. We have done some preliminary forcing studies, whereby the initial jet exit velocity is perturbed at a given frequency of oscillation. An attempt has been made to determine the characteristic (or preferred) frequency for a given jet profile, and this frequency has been used to impose unsteadiness at the jet exit. We expect that, if the frequency of disturbance corresponds to the most unstable mode, some form of axisymmetric instability will be observed.

To further understand the effect of the initial instability, we have studied its effects on different velocity profiles, for example, Profiles I, II, and III. Moreover, since the helical mode of instability has also been experimentally observed, we have done some preliminary calculations by introducing at the jet exit an unsteady disturbance that has azimuthal variations. By imposing a disturbance in space (azimuthal) and time at the jet exit, we have attempted to force the shear layer similar to the experimental conditions. If the frequency of the disturbance corresponds to the most unstable mode, then the shear layer should roll up in a manner similar to the experiments. For both free and impinging jets (as in V/STOL flows), the most unstable frequency (due to shear layer instability) is probably the same since this type of instability is a function of the shear layer thickness at the jet exit, and the ground effect is negligible there. However, the jet preferred mode type of instability (based on jet diameter), which appears in the later stage of jet development, will probably be affected by the location of the ground plane due to possible pressure feedback and resonance effects. When the ground plane is far from the jet exit, this instability mechanism should correspond to that for a free jet. Some characteristic results are presented for the single-frequency forcing at St = 0.3 for the computational domain used in the steady-state calculations [(Equation (2)]. The forcing was begun after the flow field had reached steady state. Some studies were also carried out for the case when the forcing was initiated before the flow field reached steady state, or before the large primary vortex ring reached the ground plane, to determine the effect of initial transients on the instability mechanism and its effects on the primary vortex development.

For these single-frequency studies the jet exit velocity was perturbed such that

$$w_j = \bar{w}_j[1 + \varepsilon(t)] \tag{4}$$

where $\bar{w}_j$ is the original jet profile given by Equation (3) and $\varepsilon(t)$ is a sinusoidal pulse defined by a frequency, ω and an amplitude, A. At present, the frequency used in all the axisymmetric forcing studies corresponded to a Strouhal number, St = 0.3. The amplitude of the forcing was varied from 10 to 30 percent of the mean velocity. These forcing levels were relatively high as compared to experimental forcing studies (Crow and Champagne, 1971). However, numerical simulation with lower forcing levels would require more forcing cycles (partly due to the low Reynolds number) and hence more computer time, which was not available. Therefore, it was decided to study qualitatively rather than quantitatively the effect of forcing on the jet. It must be pointed out here that available literature indicates that numerical simulation of forced three-dimensional free or impinging jets has not been studied in detail and, therefore, these preliminary calculations are directed toward determining a possible future direction in the study of excited free and impinging jets. We intend to carry out more detailed and higher resolution forcing studies in the future that are tailored to make direct comparisons with experimental studies possible.

Figures 21a through 21e give the vorticity contours for a jet of Profile I at Re = 200 and forced at St = 0.3 with a 30-percent amplitude level plotted every $\pi/2$ intervals of a forcing cycle. The forcing was begun after the flow field had reached steady state, and the data shown are for the fourth cycle of forcing. All vorticity contour intervals are maintained the same to facilitate comparison. Periodic shedding of the large vortex ring is clearly evident in these figures. As the ring vortex approaches the ground, the vorticity spreads and the ring vortex loses its identity. The spreading of the vorticity also causes a bulge in the vortex lines as it approaches the ground. As the primary vortex moves down the jet, a new vortex ring appears there, which also subsequently is shed. Comparing Figures 21a and 21b, which show the vorticity contours at the beginning and the end of the fourth forcing cycle, we see that the solution essentially repeats itself. Hence, we can conclude that the period of vortex shedding is essentially the same as the period of forcing.

If we measure the distance between two successive primary vortex cores, we obtain a wavelength $\lambda/D \simeq 2.1$. This compares reasonably well with Didden and Ho's (1985) wavelength of $\lambda/D \simeq 1.7$. For St = 0.3, the frequency of the present forcing study is also 0.3 (since, here, D = U = 1). Then the convection velocity of the vortex ring is $U_c = \lambda f = 0.63$ U. The experimental data of Didden and Ho (1985) indicate $U_c = 0.61$ U, which indicates that the present simulation can predict reasonably the global behavior of forced impinging jets.

Comparing the y-vorticity component at different times, we see that the vortex has a tendency to elongate as it approaches the ground plane, where it finally merges into the originally steady ground vortex. The formation of secondary vorticity of the opposite sign in the wall layer is also observed in these figures. It is possible that, during these forcing studies, the wall boundary layer undergoes unsteady separation as was observed by Didden and Ho

(1985). In viscous flows, the wall acts as a vorticity source, and when the ring vortex impinges on the ground and starts to spread in the radial (x,y)-direction, it induces a shear layer on the wall where a secondary region of opposite vorticity appears. As shown by Didden and Ho (1985), this secondary vortex region can exist prior to separation and, therefore, separation is not the reason for the appearance of the secondary vorticity. However, due to the external forcing, the wall shear layer is also unsteady and may possibly separate, and secondary vorticity is always associated with separation. Lack of resolution near the wall made it difficult to determine the point of separation (if any) in these unsteady calculations. For comparison, we show in Figures 22a through 22d, the vorticity contours for the forced case of Profile III under the same conditions as for Profile I. In general, the vorticity pattern is similar though the levels are much higher and more details of the ring vortices are evident.

A similar forcing study was done with the flow at different stages of its initial development with a view to determining the effect of controlled forcing on the transient development of an impinging jet. This has some relevance to V/STOL-type flow fields, since in reality the steady-state situation is never achieved and instability waves are probably excited during the transient development. In general, the forcing study with initially unsteady flow indicates that the primary vortex ring is shed periodically as before, with the shedding repeating itself each period. This indicates that the unsteadiness in the flow field does not significantly affect the flow region close to the jet exit partly due to the fact that the effect of forcing is much stronger near the exit. However, there is a clear indication that the consequent development of the primary ring vortex and its interaction with the ground plane does not repeat itself. There is also some indication of vortex stretching and tearing near the ground. The region of secondary vorticity continues to increase as a function of time, and the initial ring vortex near the ground decreases in size and seems to stay fixed at its initial impact position.

To obtain an idea of how the vorticity field looks in three dimensions, we present a series of figures in Figure 23 in which we show the three-dimensional perspective view of the total absolute vorticity, $|\omega| = \sum_{i=1}^{3} |\omega_i|$, where i=1,3 indicates the three coordinates. The vertical axis is in the z-direction, and the x-y plane is shown at the bottom. Since we assumed symmetry in the x-direction, only the half-plane is shown. These perspective plots show the three-dimensional absolute vorticity surface at a given time. The level in the figure indicates the value of the $|\omega|$ surface shown, such that all values of $|\omega|$ greater than the given level are contained within the three-dimensional $|\omega|$ surface. These levels were chosen such that 12 percent of the volume of the computational domain is contained within the three-dimensional surface. If the level of vorticity is increased, the higher values of vorticity that would be shown would be contained in a smaller volume. The 12-percent value was chosen since it gave the best overall perspective of the vorticity surface in three dimensions. These plots do not show the vorticity direction, since only the absolute value of the vorticity is shown.

Figure 23a gives the three-dimensional vorticity surface for steady state of Profile I at Re = 200. The primary vortex structure above the ground can be clearly seen. Also observable is the secondary vorticity imprint on the

ground plane. The space between the two vortex tube-like structures in the jet does not imply that there is no vorticity present there. Instead, what it means is that the vorticity level there is lower than the level shown. Figure 23b gives the three-dimensional vorticity surface in 12-percent volume for the case of forcing at St = 0.3 of Profile I flow. This figure shows the characteristic bulges due to the primary vortex shedding and also indicates that the vorticity level shown does not remain similar to the steady-state case shown in Figure 23a. Figure 23c shows the steady-state vorticity surface (again in 12-percent volume) for Profile III at Re = 200. The vorticity levels are higher, indicating that in the same volume as in Figures 23a and 23b, more vorticity is present. The structure of the ground plane vortex is also quite different. Forcing this steady-state solution at St = 0.3 shows a more distinct pattern of vortex shedding as can be seen in Figure 23d, which is the forced vorticity surface for Profile III.

Three-dimensional perspective plots, such as those shown in Figure 23, can be used to get an idea of the complicated three-dimensionality of the flow field and the associated structures in the flow. It cannot, however, be used to obtain a detailed picture of the actual flow (as shown in the vorticity contours before) since the final details are usually smeared and hidden inside the vorticity surface such as that shown in Figure 23.

3.2.2 Axisymmetric Forcing with Crossflow

The numerical code developed so far is capable of investigating additional flow phenomena relevant for VTOL-type flow fields. Examples of such flows are impinging jets in a crossflow, which models the forward motion of a VTOL aircraft close to the ground, and inclined impinging jets, which models a VTOL aircraft in a climb mode. We have carried out some preliminary forcing studies for such complex phenomena. For these simulations we used an 18x72x18 mesh in a computational domain defined by

$$\begin{aligned} -1 \leq x/D \leq 1 \\ -2 \leq y/D \leq 2 \\ 0 \leq z/D \leq 1 \end{aligned} \tag{5}$$

such that the ground plane is very close to the jet exit. We therefore expect the presence of the ground to have an effect on the flow field generated.

In the following, we discuss the effect of unsteady forcing at the jet exit in the presence of crossflow. The grid mesh used in these calculations was 18x72x18 with symmetry in the x-direction. These simulations were carried out with forcing at St = 0.3 and a crossflow of 40 percent of the mean velocity. The amplitude of the forcing was also 40 percent of the mean value. Simulation with 20-percent forcing amplitude was also carried out, and the results were qualitatively the same, though the higher amplitude forcing case showed the features of the flow field more clearly and is presented here. The results presented in the following figures are at equal time intervals and therefore do not correspond to any one complete cycle of the forcing. However, they show some interesting flow phenomena that merits presentation.

Figure 24a gives the velocity distribution in the y-z plane as a function of time. The solution indicates the periodic formation of a clockwise vortex near the ground. This vortex is a direct consequence of unsteady separation of the wall shear layer. This is due to the adverse pressure gradient that periodically occurs on the ground plane. Examining the pressure gradient for the corresponding times (not shown here) indicated that there is high pressure ahead of the vortex zone and lower pressure behind the vortex zone, resulting in separation of the wall shear layer and lift off from the ground, which results in the vortex formation. The vortex disappears when the pressure gradient periodically changes from adverse to favorable. Though the solutions presented in these calculations are not for any complete forcing cycle, the results do indicate that the vortex forms due to the periodic variation in the jet velocity. This results in periodic formation of the adverse pressure gradient near the wall, causing the wall shear layer to undergo unsteady separation and form the vortex zone.

Figure 24b gives the corresponding velocity distribution in the x-z plane at $y = y_d$ (see Figure 1) for the same times. The flow field shows that the large primary vortex zone completely dominates the region above the ground plane. This is due to the proximity of the ground to the jet exit. The flow patterns also indicate the periodic formation of a "kidney"-shaped vortex region. Note that this kidney-shaped vortex zone is not the same as the one observed in jets with crossflow (Andreopoulos and Rodi, 1984).

Figures 25a and b gives the corresponding vorticity in the two center-planes. The shedding of the primary vortex is clearly evident. However, the vortex ring is no longer symmetric and is compressed on the side that faces the crossflow, as can be seen in the y-z plane. The vorticity pattern is much more complex, with the primary vortex ring distorted by the effect of cross-flow. The secondary vorticity region is clearly evident in both the y-z and the x-z planes. However, the region of secondary vorticity also periodically moves, indicating that the location of the separation point is also a function of the periodic formation of the vortex zone. The secondary vorticity zone also shows periodic attempts to wrap itself around the primary vortex core (x-z plane), but does not seem to complete itself, perhaps due to the proximity of the downstream boundary.

In conclusion, single-frequency axisymmetric forcing studies at St = 0.3 have been carried out for various initial jet profiles. The solutions indicate good qualitative agreement with experimental observations of impinging jets. The flatter profiles (Profiles III and IV) show more signs of instability as compared to Profile I. The primary vortex shedding frequency corresponds very closely to the forcing frequency. These forcing studies show that the axisymmetric instability mode can be excited, but additional forcing simulations need to be carried out to determine the most unstable frequency (for jet preferred instability), since a range of $0.2 < St < 0.5$ has been observed to be unstable experimentally. Also, it is not clear at present what the presence of the ground plane has on the instability mechanism in terms of modification of the unstable frequency. Due to lack of resolution, the most unstable frequency for the shear layer instability was not observed. This frequency would correspond to $St \simeq 0.017$ (based on the shear layer momentum thickness). But forcing studies at this frequency have not been carried out at present because of the lack of resolution to observe the shear layer rollup. However, the forcing at

the jet preferred mode (for St = 0.3) showed a periodic shedding of axisymmetric vortex rings. The calculations also indicate the formation of secondary vorticity in the wall shear layer of the opposite sign consistent with experimental observation (Didden and Ho, 1985). This region of secondary vorticity may be due to separation of the wall shear layer, and there are some indications that this is indeed so. The presence of the adverse pressure gradient on the ground plane is probably due to the collisions of the wall jets at the base of the fountain. There is some indication of unsteady separation on the ground plane. This unsteady separation phenomenon seems to be a consequence of external forcing and indicates that the forcing technique can be used to study the separation phenomena, which is of great interest and is a region not well understood. More detailed calculations with a higher resolution grid are necessary before any further conclusions can be made.

Our forcing study of the impinging jet in a crossflow indicates that there is an unsteady formation of a ground vortex, again probably due to the change in the pressure field (due to forcing), resulting in unsteady separation of the wall shear layer and the consequent rollup of the wall shear layer.

The effect of the ground plane on the forcing seems to be minimal when the ground plane is far from the jet exit. More research is necessary, however, to determine how the ground plane location would modify the instability mechanism. It is clear that the jet shear layer instability mode (not observed here) would not be affected by the ground plane, though the jet preferred mode would probably be affected by the wall due to possible feedback from the wall resulting in pressure resonance effects. The present calculations are for incompressible flows and, therefore, there is no acoustic field (noise) generation during the impingement process. There could, however, be effects of the variation of the hydrodynamic pressure in the region between the jet and the impinging wall, which could result in some modification of the impinging jet stability mechanism. This is due to the fact that for impinging jets there are three modes of instability: the jet shear layer instability (based on the shear layer thickness), the jet preferred mode (based on the jet diameter), and the resonance mode (based on the location of the ground plane). All three modes of instability can be excited and are very important in the study of impinging jets. At present, only the jet preferred mode has been studied in these simulations, and additional parametric studies are necessary to determine the interaction between the three modes of instability. This is an area of research that will be considered in more detail in the future study.

3.2.3 Single-Frequency Forcing with Azimuthal Variation

Forcing studies were also carried out to determine whether the helical mode of instability can also be excited. For this purpose the jet was forced at a given frequency with an azimuthal variation. The forcing function is assumed to be of the form

$$w_j(x, y, t) = \overline{w_j}(x, y)\,[1 + \varepsilon_H(x, y, t)] \qquad (6)$$

where the forcing function $\varepsilon_H(x, y, t)$ is defined as

$$\varepsilon_H(x, y, t) = A \sin(n\omega t + k\theta) \tag{7}$$

where ω is the forcing frequency and $n = 1, 2, \ldots$ gives the various modes. Also, A is the forcing amplitude and θ [$= \tan^{-1}(y/x)$] is the azimuthal variation with k as the wave number. The solutions presented here are for $n = k = 1$, which corresponds to the fundamental mode excitation with an azimuthal variation. Results for some preliminary calculations were recently presented (Rizk and Menon, 1985). These results indicate that the helical instability mode can be excited by forcing with azimuthal variation. The initial forcing simulations were carried out with a coarse (14x17x32) mesh at a low Reynolds number of 100. The ground plane was located at H/D = 5 and, therefore, the initial jet development is close to that for a free jet. The Strouhal number corresponding to the frequency of forcing was varied ($0.08 < St < 0.5$) to determine the effect of the frequency on the excitation of the instability. The results shows that the effect of forcing on the jet development is significant, even in these low-Reynolds-number and coarse-grid calculations. In these preliminary study, the excitation was begun before the jet reached the ground plane and, therefore, the instability was excited during the unsteady development of the jet. Characteristic vorticity contours for helical forcing at St = 0.165 is presented in Figure 26 which showed some sort of alternate vortex shedding. There seems to be an indication that a flapping mode of instability has been observed, but due to the fact that these studies were with a coarse mesh, the details of the instability are not clear.

To study the helical instability mechanism in even more detail, a series of forcing simulations for St = 0.3, 0.46, 0.67 was carried out using the higher resolution grid (16x32x64) and the computational domain given by Equation (2). The general pattern of instability was observed to be similar, and here we show the characteristic results for the forcing case with St = 0.3. In this calculation, the forcing amplitude was 30 percent of the mean, and the forcing was initiated after the flow field had nearly reached steady state. Due to computer resource limitations, it was decided not to take the solution out to complete steady state at present. Figure 27 gives the vorticity contours in the two planes for forcing at St = 0.3 plotted every $\pi/2$ of the seventh period of forcing. Note here again that no symmetry assumptions have been made and the whole computational domain given by Equation (2) has been calculated. The jet is therefore located in the center of the top surface. Since these figures represent a complete cycle of forcing, we can follow the development and the convective motion of the vortex rings. As can be clearly seen in these figures, the vorticity is shed alternately at the jet exit, and there is no sign of the axisymmetric mode of the instability. There is also an indication that the vortex core may be undergoing some sort of pairing. The period of vortex shedding is the same as the period of forcing, as can be seen by comparing the figures for the beginning and the end of the period. As pointed out by Hussain (1983), it is possible that what is observed may not be the helical instability but rather tilting of the axisymmetric ring vortex due to the azimuthal variation of the flow velocity. It is clear that the form of instability observed during forcing with azimuthal variation is quite different from that observed during the axisymmetric forcing studies.

In conclusion, detailed calculations with a relatively fine mesh have been carried out to study the effect of both axisymmetric and helical forcing of a low-Reynolds-number impinging jet. Only a single-frequency forcing study has been carried out in detail. The results indicate the characteristic shedding of the vortex rings as a function of forcing frequency during axisymmetric forcing, and the twisting and alternate shedding (or tilting) of vorticity is observed for helical forcing. Pressure variation along the ground plane shows the appearance of an adverse pressure gradient in the x-z plane, which is probably due to the fountain effect in the outflow boundary. A region of secondary vorticity is present in the ground plane, which is consistent with experimental observation (Didden and Ho, 1985). Due to lack of resolution and data (in the y-z plane) in the wall region, it was not possible to determine conclusively whether there was any unsteady separation in the wall layer during the forcing, which has been experimentally observed. The present calculations indicate that the numerical simulations carried out here for both steady-state and forcing cases showed qualitative agreement with experimental observations. However, there are many aspects of the study that warrant improvement and that will be considered in the future research. For example, the grid resolution and the Reynolds number will be increased for a more realistic simulation by using subgrid-scale modeling and grid refinement. Additional forcing studies to determine the effect of the ground plane on the instability development will also be carried out. More realistic turbulence simulations will be carried out by imposing a random turbulence field at the jet exit. Grid resolution near the jet exit will be refined to observe the shear layer rollup. Additional data in the ground plane will be sampled to determine whether there is any unsteady separation occurring in the wall shear layer during forcing.

References

Agarwal, R. K., and Bower, W. W. (1982) "Navier-Stokes Computations of Turbulent Compressible Two-Dimensional Impinging Jet Flowfields," AIAA J., Vol. 20, May, pp. 577-584.

Andreopoulos, J., and Rodi, W. (1984) "Experimental Investigation of Jets in a Crossflow," J. Fluid Mech., Vol. 138, pp. 93-127.

Batchelor, G. K., and Gill, A. E. (1962) "Analysis of the Stability of Axisymmetric Jets," J. Fluid Mech., Vol. 14, pp. 529-551.

Beltaos, S. and Rajaratnam, N. (1973), "Plane Turbulent Impinging Jets," J. Hydraul. Res., Vol. 11, No. 1, pp. 29-59.

Bower, W. W., Agarwal, R. K., Peters, G. R., and Kotansky, D. R. (1979) "Viscous Flowfields Induced by Two- and Three-Dimensional Lift Jets in Ground Effect," Report ONR-CR215-246-3F, March.

Buzbee, B. L., Golub, G. H. and Nielson, C. W. (1970) "On Direct Methods for Solving Poisson's Equations," SIAM J. Numer. Anal., Vol. 7, December, pp. 627-656.

Childs, R. E. and Nixon, D. (1985) "Simulation of Impinging Turbulent Jets," AIAA Paper 85-0047, January.

Crow, S. C. and Champagne, F. H. (1971) "Orderly Structure in Jet Turbulence," J. Fluid Mech., Vol. 48, August, pp. 547-591.

Didden, N. and Ho, C.-M. (1985) "Unsteady Separation in a Boundary Layer Produced by an Impinging Jet," To Appear in J. Fluid Mech.

Grant, A. J. (1974) "A Numerical Model of Instability in Axisymmetric Jets," J. Fluid Mech., Vol. 66, Part 4, pp. 707-724.

Harlow, F. H., and Welch, J. E. (1965) "Numerical Calculation of Time-Dependent Viscous Incompressible Flow of Fluid with Free Surface," Phys. Fluids, Vol. 8, pp. 2182-2189.

Hussain, A. K. M. F. (1983) "Coherent Structures - Reality and Myths," Phys. Fluids, 26, pp. 2816-2850.

Hussain, A. K. M. F. and Zaman, K. B. M. Q. (1981) "The 'Preferred Mode' of the Axisymmetric Jet," J. Fluid Mech., 110, pp. 39-71.

Kotansky, D. R. and Bower, W. W. (1978) "A Basic Study of the V/STOL Ground Effect Problem for Planar Flow," J. Aircraft, Vol. 15, April, pp. 214-221.

Moin, P. and Kim, J. (1982) "Numerical Investigation of Turbulent Channel Flow," J. Fluid Mech., Vol. 118, May, pp. 341-377.

Rizk, M. H., and Menon, S. (1985) "A Numerical Investigation of VTOL Aerodynamics," Communication No. 170, Research and Technology Division, Flow Industries.

Rubel, A. (1978) "Computations of Jet Impingement on a Flat Surface," AIAA Paper 78-207, January.

Rubel, A. (1981) "Computations of the Oblique Impingement of Round Jets Upon a Plane Wall," AIAA J. Vol. 19, July, pp. 863-871.

Russell, P. J., and Hatton, A. P. (1972) "Turbulent Flow Characteristics of an Impinging Jet," Proc. of Institute of Mech. Engineers, Vol. 186, pp. 635-644.

Strange, P. J. R. and Crighton, D. G. (1983) "Spinning Modes on Axisymmetric Jets, Part 1," J. Fluid Mech., Vol. 134, September, pp. 231-245.

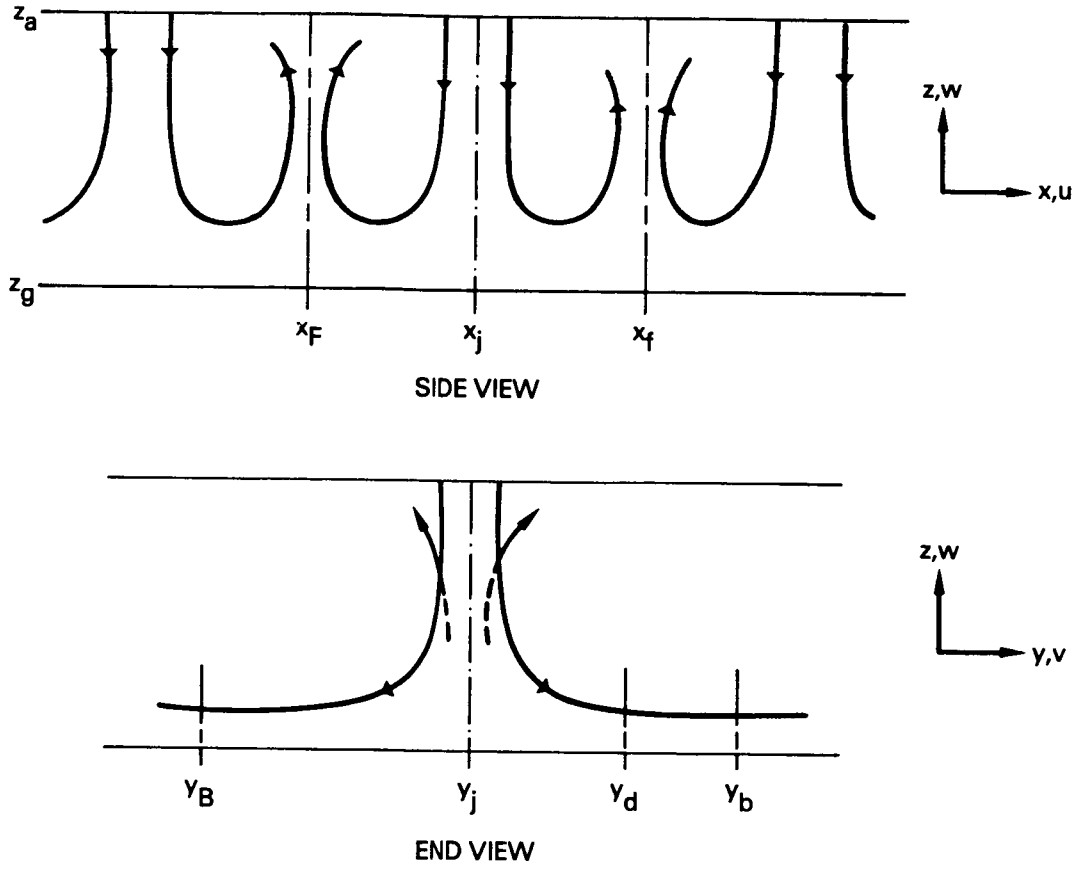

Figure 1. Model Problem for a Hovering VTOL Aircraft

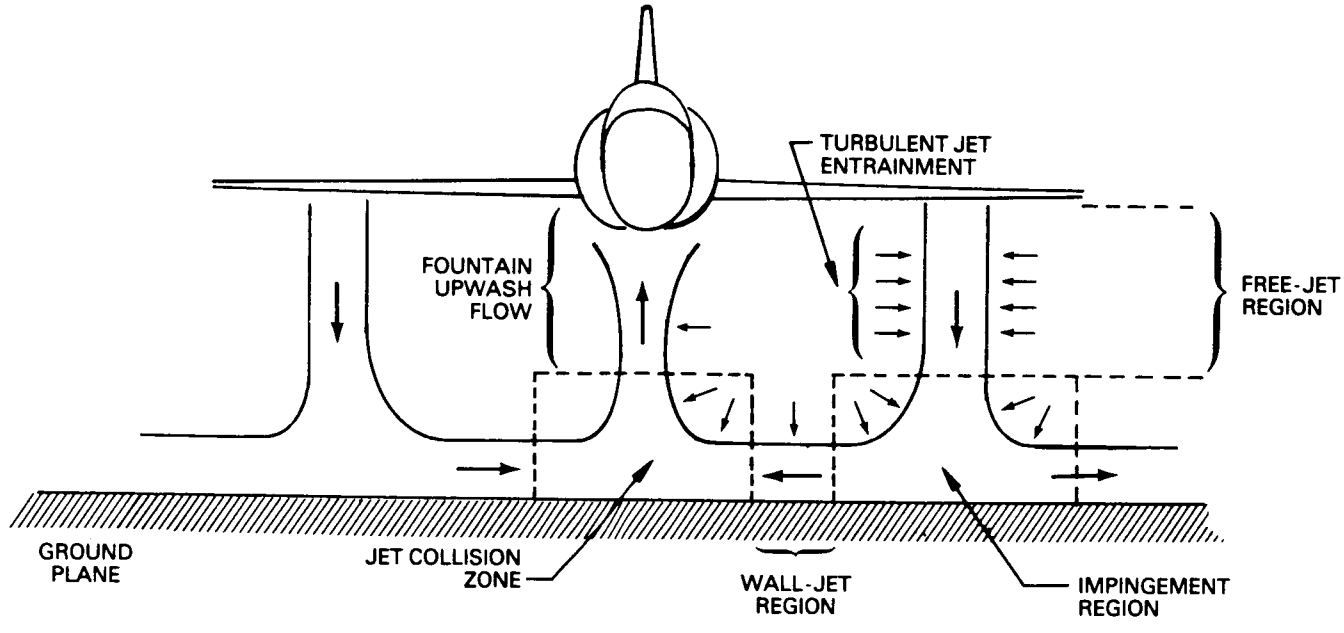

Figure 2. Schematic of Flow Field About a Hovering VTOL Aircraft

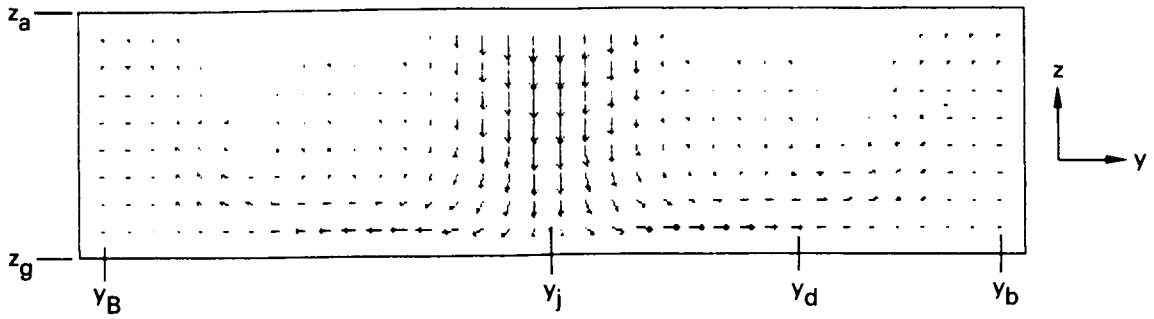

Figure 3. Example 1: Velocity Vectors in the Plane $x = x_j$

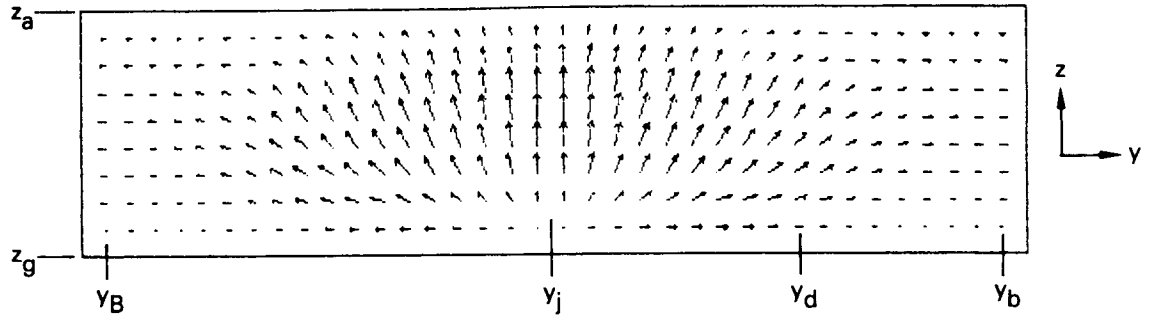

Figure 4. Example 1: Velocity Vectors in the Plane $x = x_f$

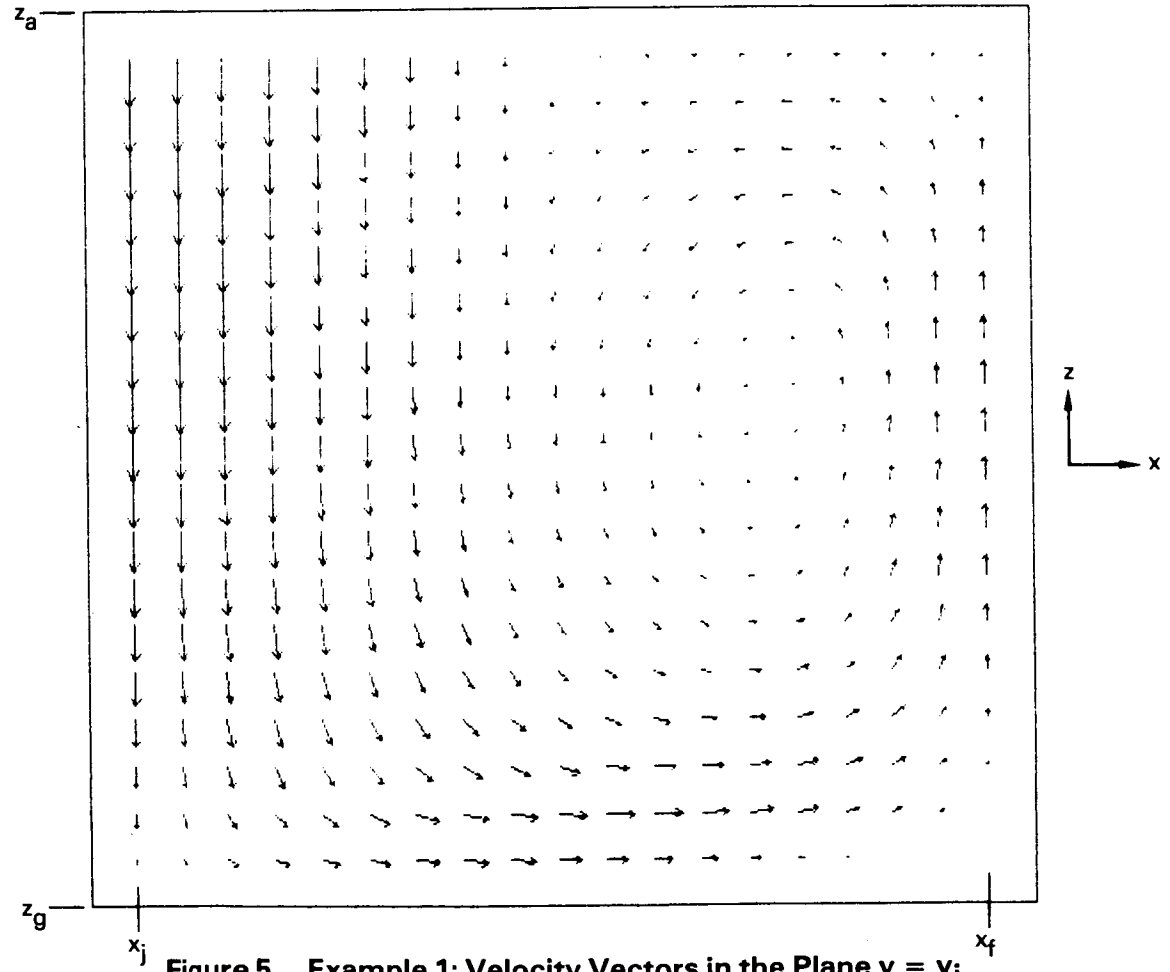

Figure 5. Example 1: Velocity Vectors in the Plane $y = y_j$

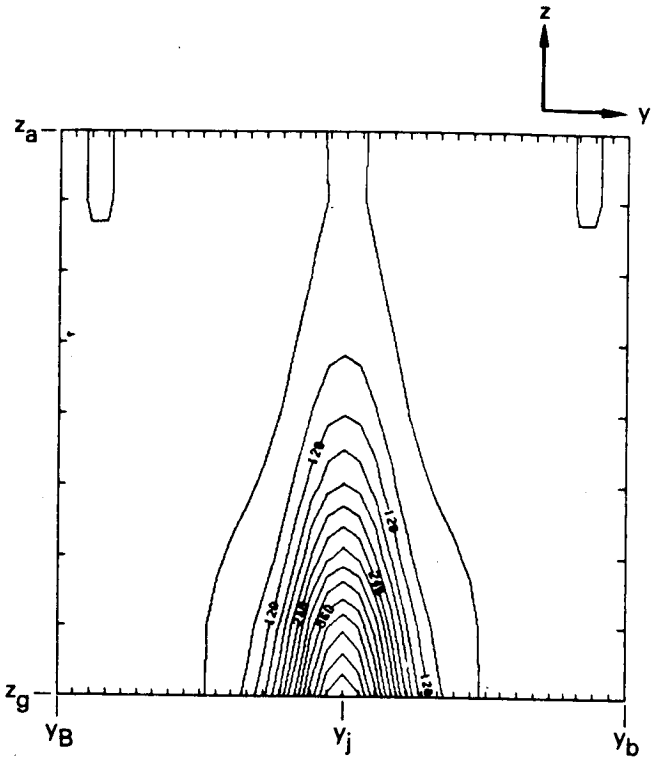

Figure 6. Example 1: Pressure Contours in the Plane $x = x_j$

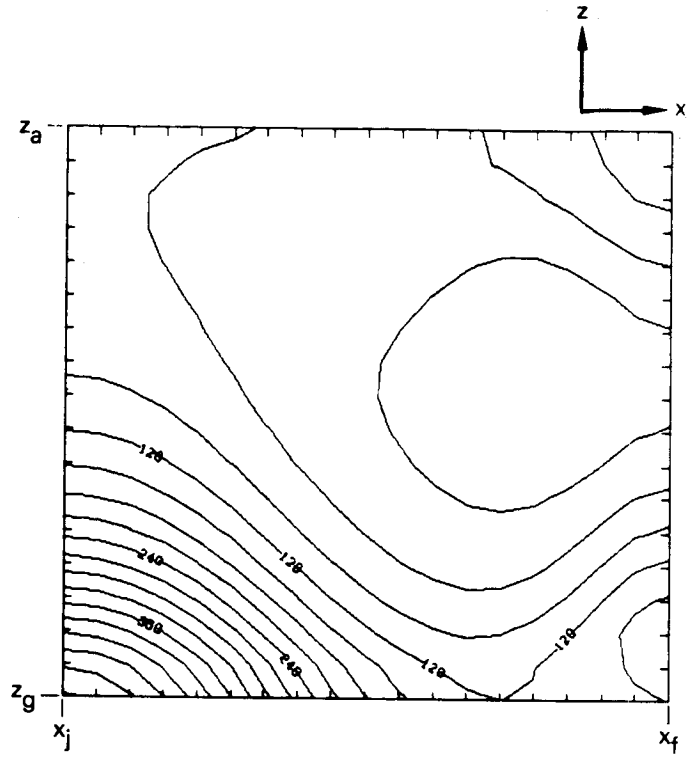

Figure 7. Example 1: Pressure Contours in the Plane $y = y_j$

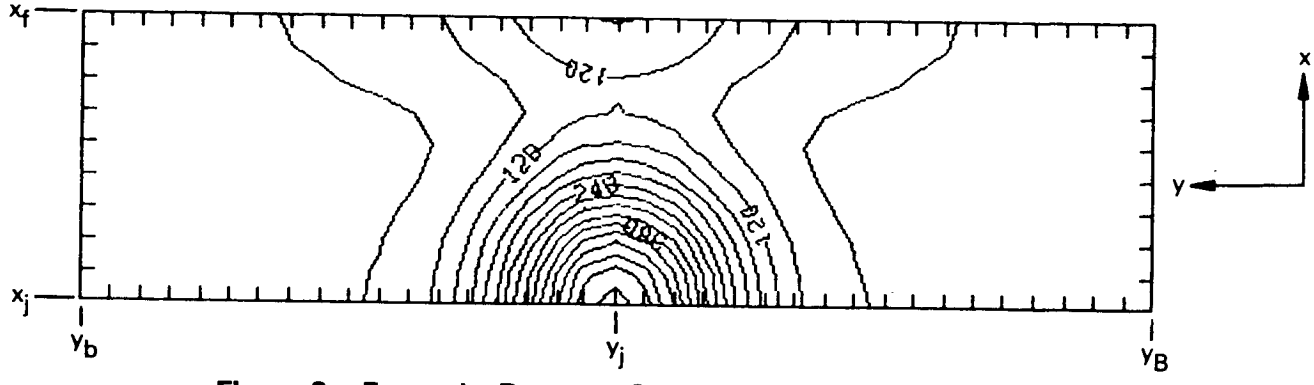

Figure 8. Example: Pressure Contours in the Plane $z = z_g$

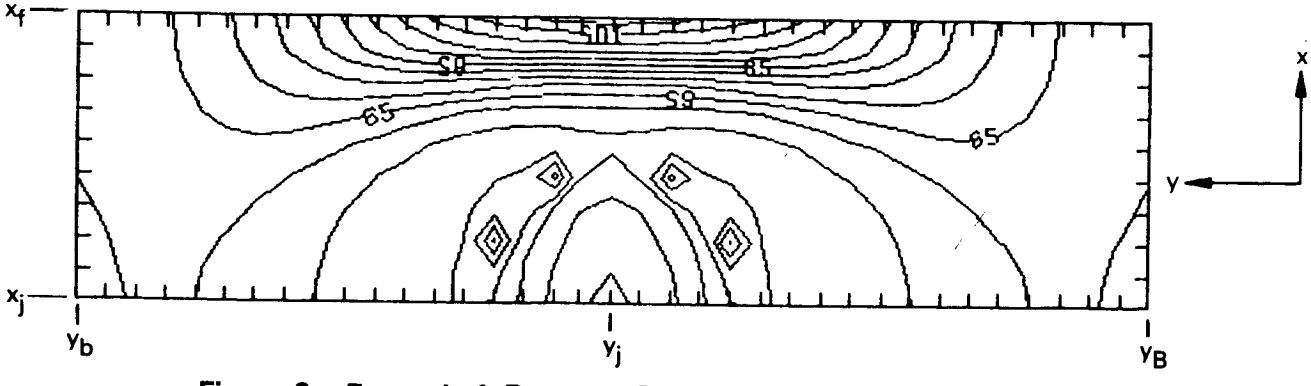

Figure 9. Example 1: Pressure Contours in the Plane $z = z_a$

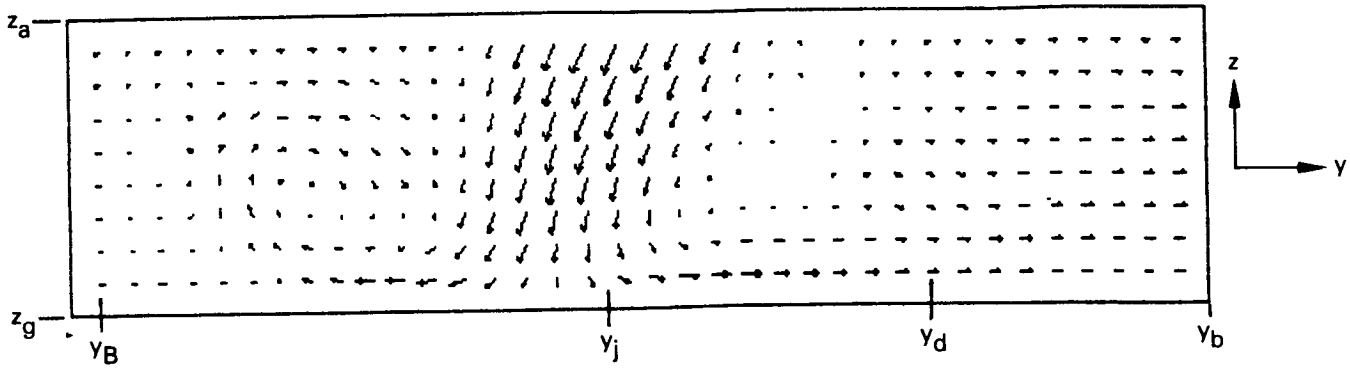

Figure 10. Example 2: Velocity Vectors in the Plane $x = x_j$

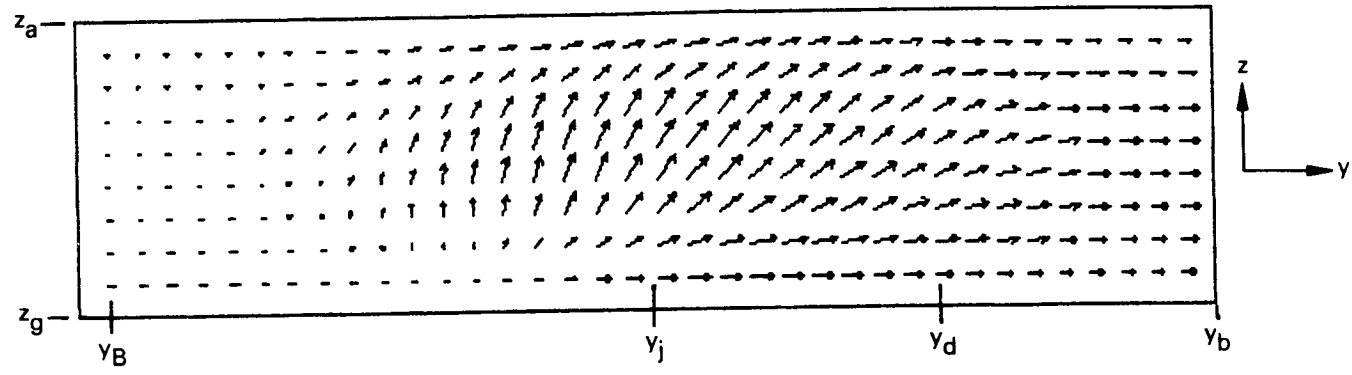

Figure 11. Example 2: Velocity Vectors in the Plane $x = x_f$

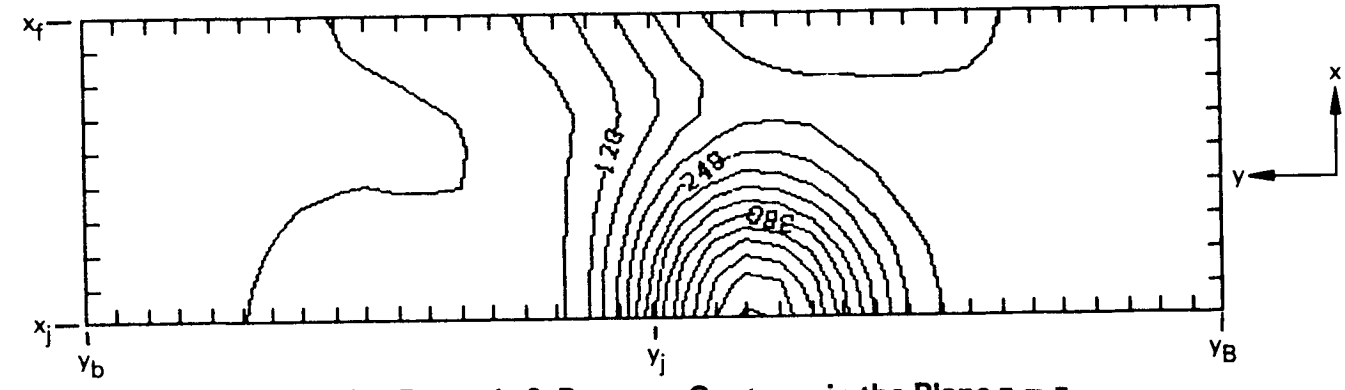

Figure 12. Example 2: Pressure Contours in the Plane $z = z_g$

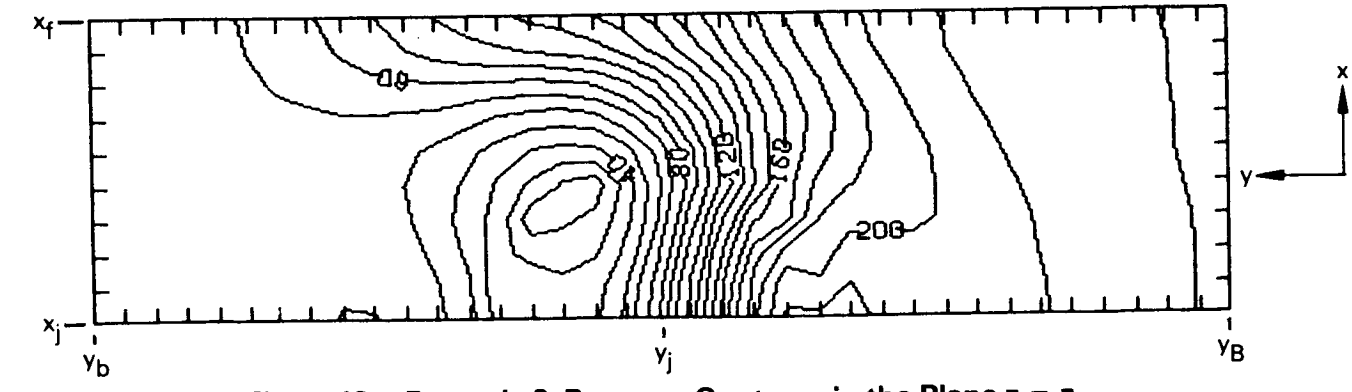

Figure 13. Example 2: Pressure Contours in the Plane $z = z_a$

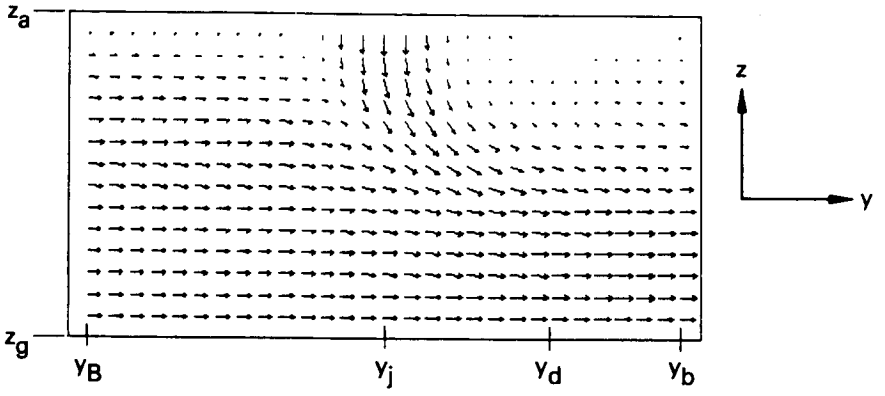

Figure 14. Example 3: Velocity Vectors in the Plane $x = x_j$

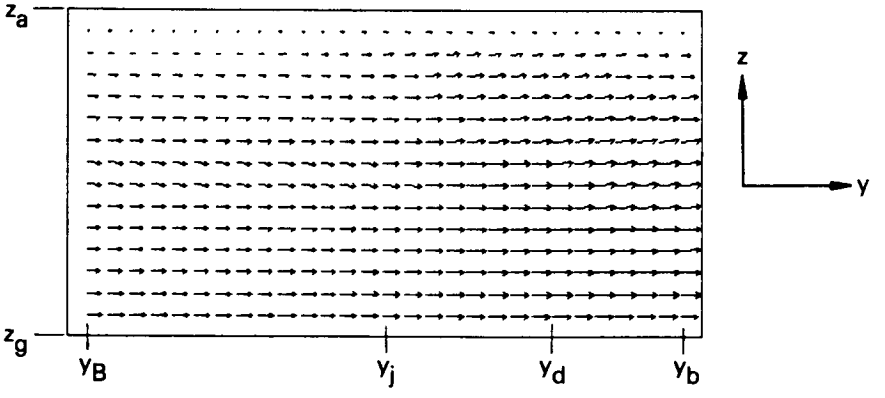

Figure 15. Example 3: Velocity Vectors in the Plane $x = x_f$

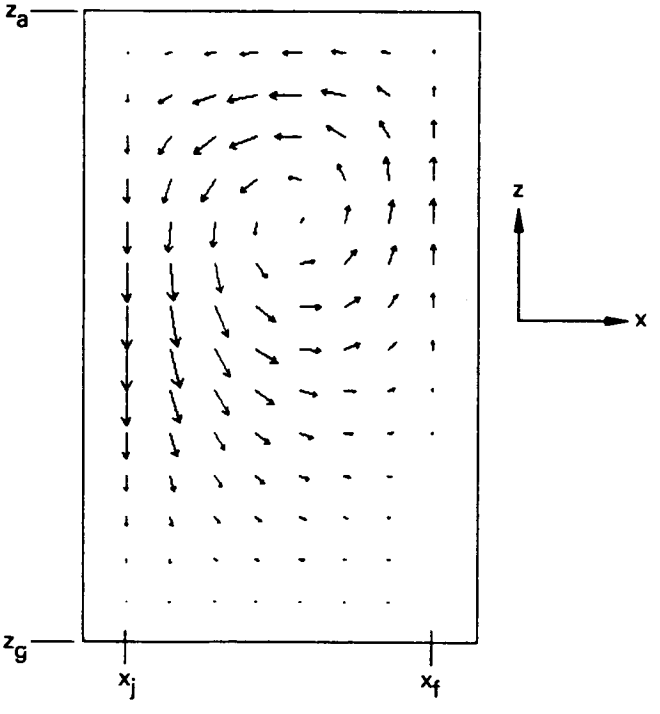

Figure 16. Example 3: Velocity Vectors in the Plane $y = y_d$

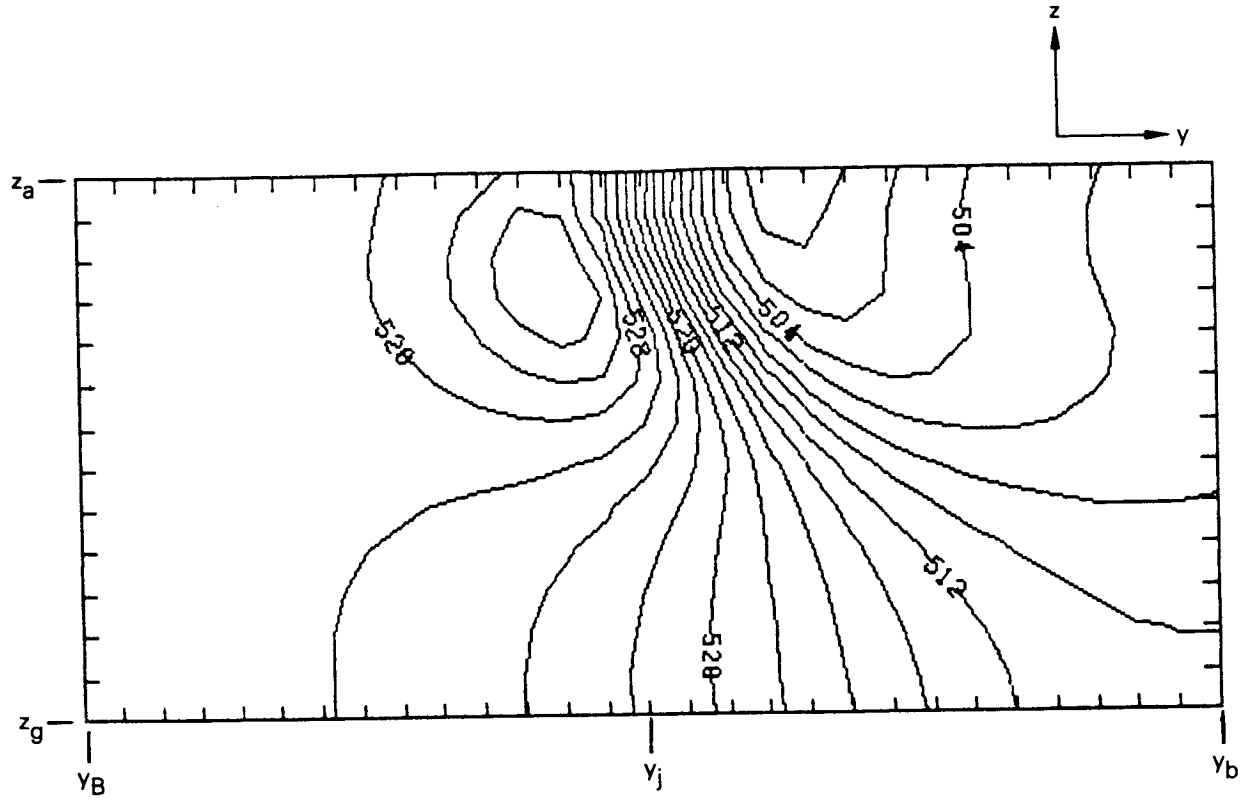

Figure 17. Example 3: Pressure Contours in the Plane $x = x_j$

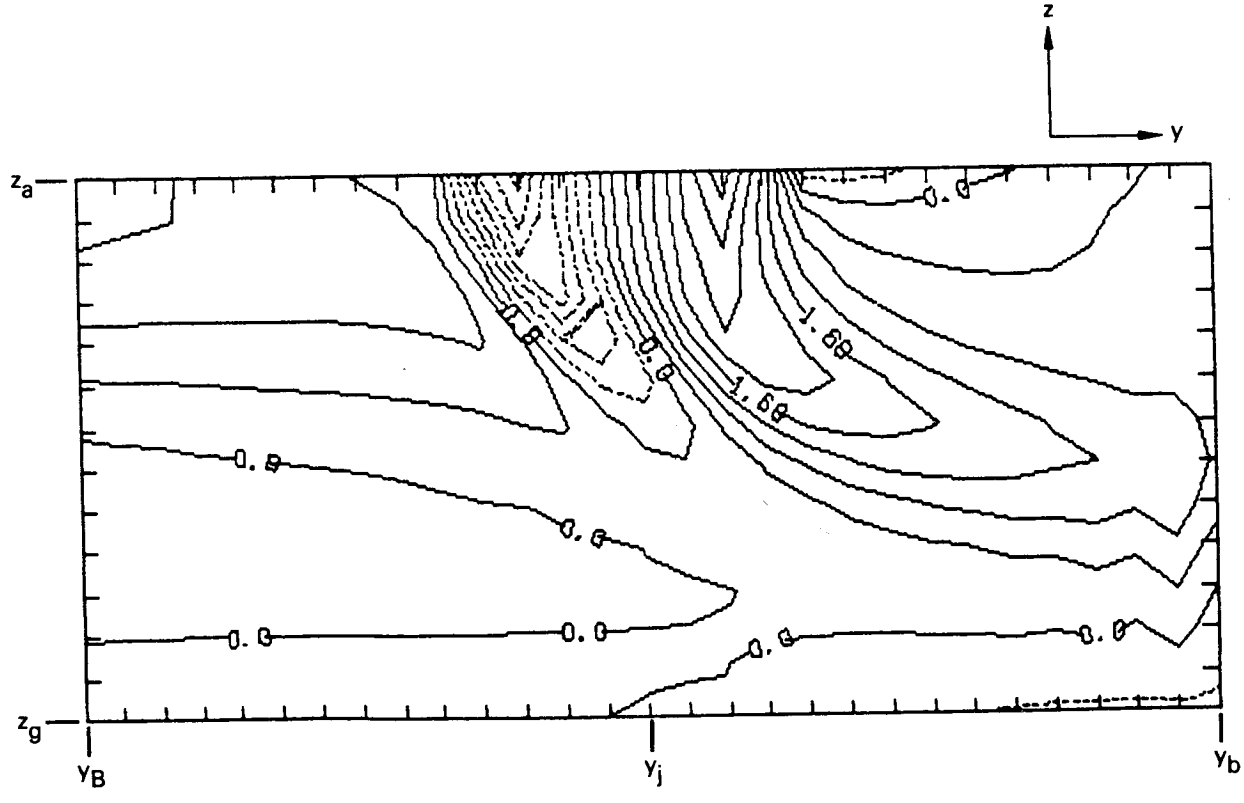

Figure 18. Example 3: x-Vorticity Component in the Plane $x = x_j$

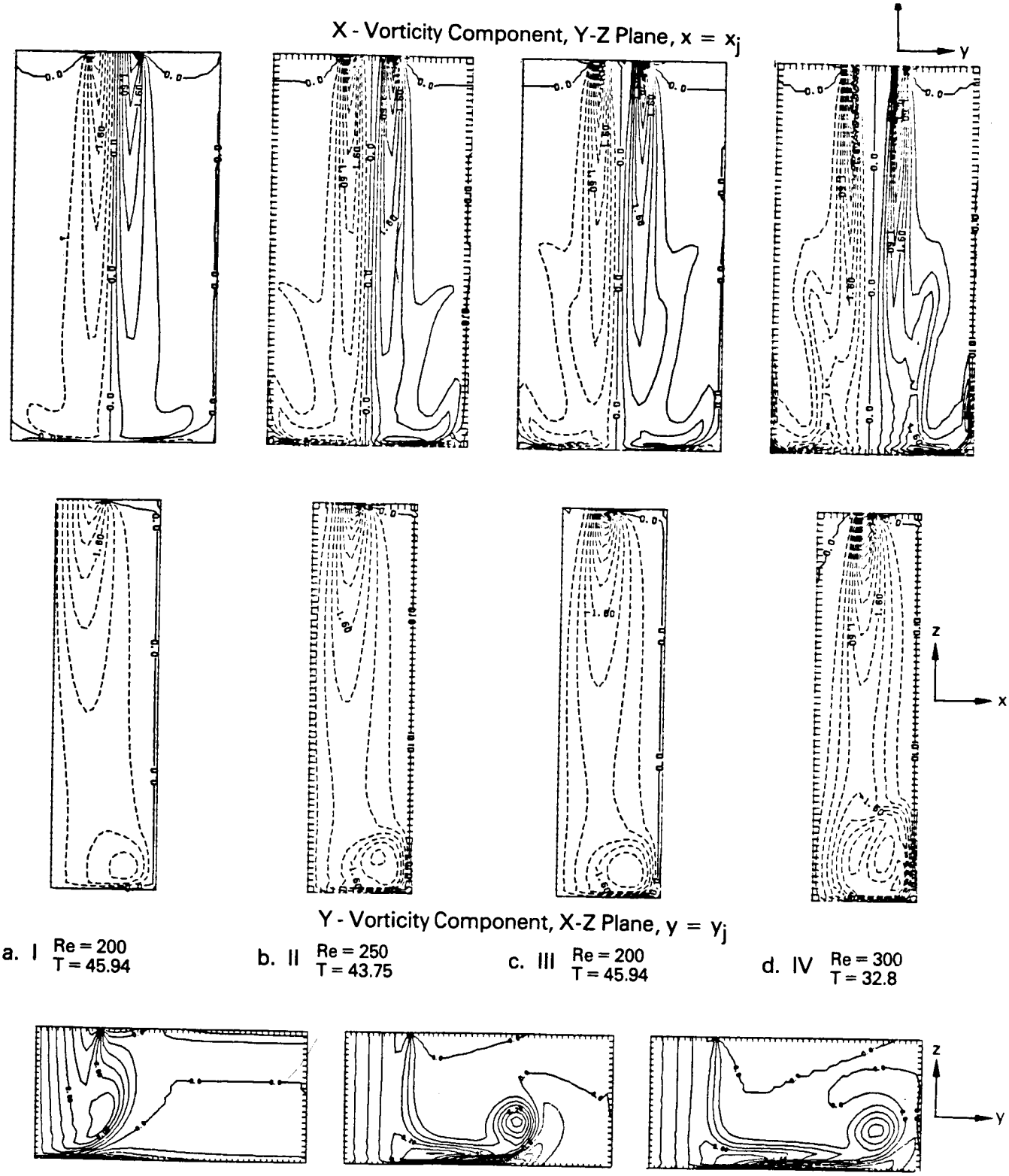

e. Primary Vortex Propagation on the Ground for Profile I, Re = 600, Mesh = 24 × 48 × 24

Figure 19. Steady State Vorticity Contours for Profiles I - IV

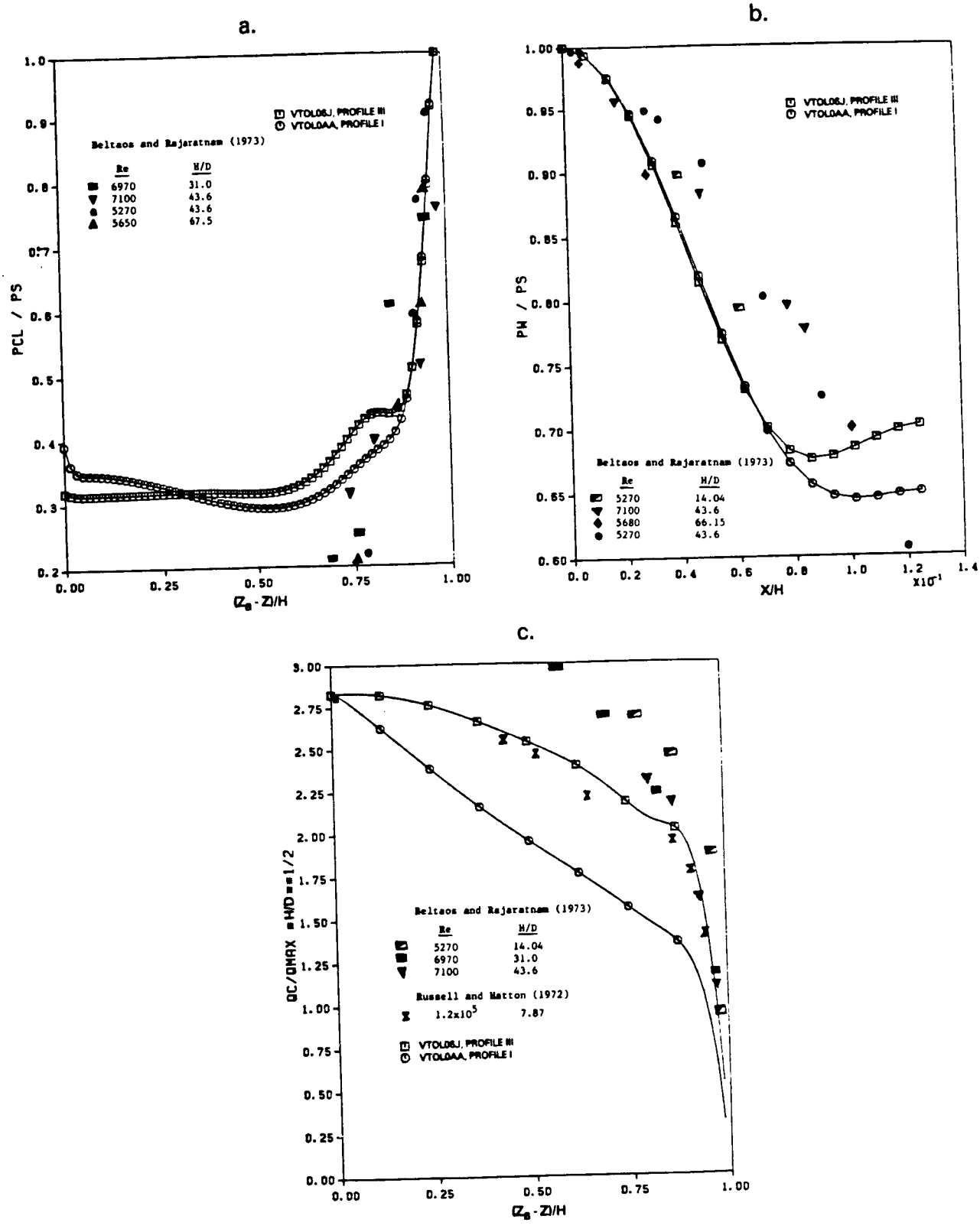

Figure 20. a. Steady State Pressure Variation Along Centerline. Re = 200, T = 45.94
b. Steady State Ground Plane Pressure Variation in X-Z Plane. Re = 200, T = 45.94
c. Steady State Centerline Velocity Variation. Re = 200, T = 45.94

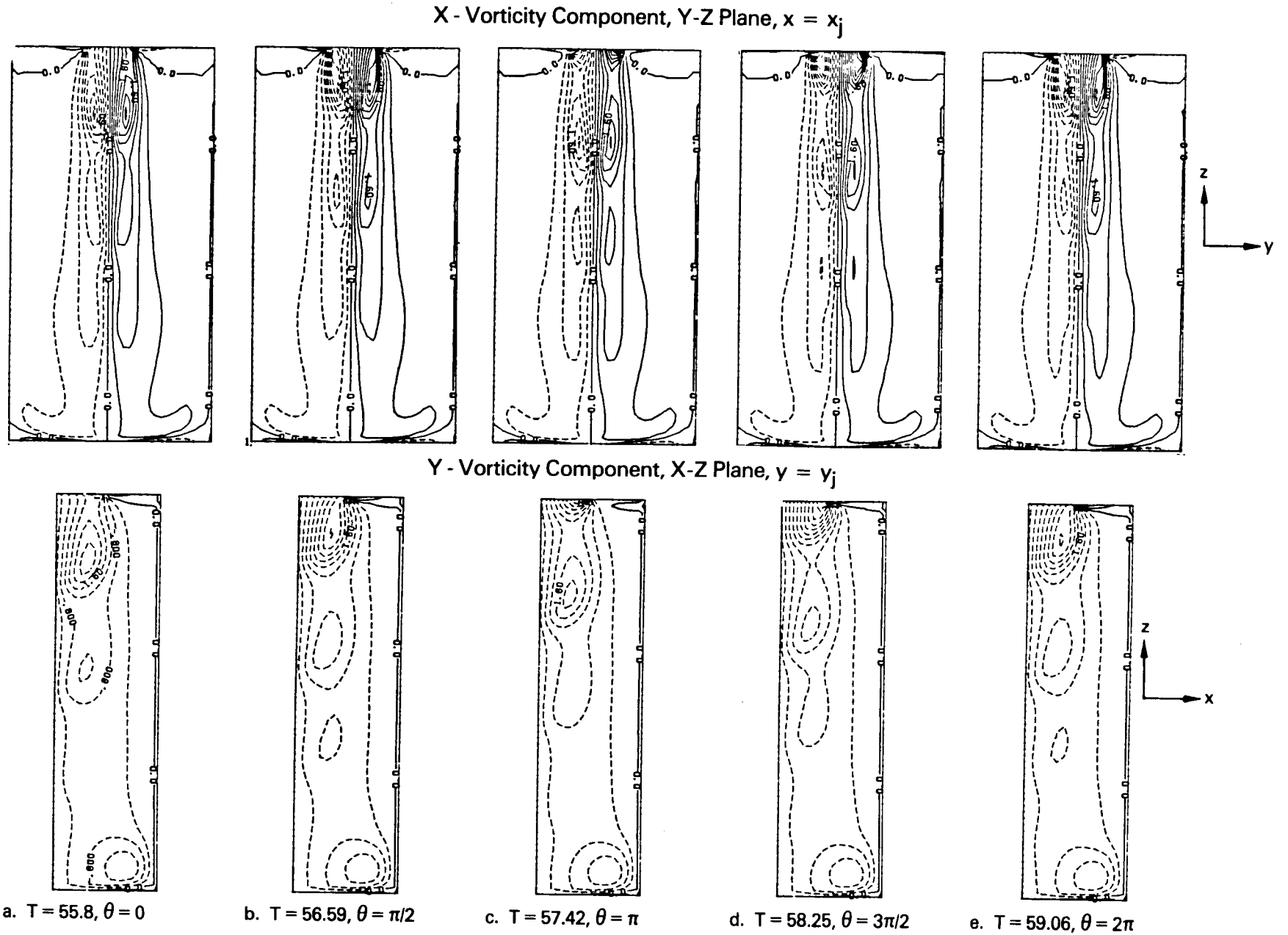

Figure 21. Vorticity Contours for Profile I at Re = 200 and Forced Axisymmetrically at St = 0.3. Plots are Every π/2 of the Fourth Period

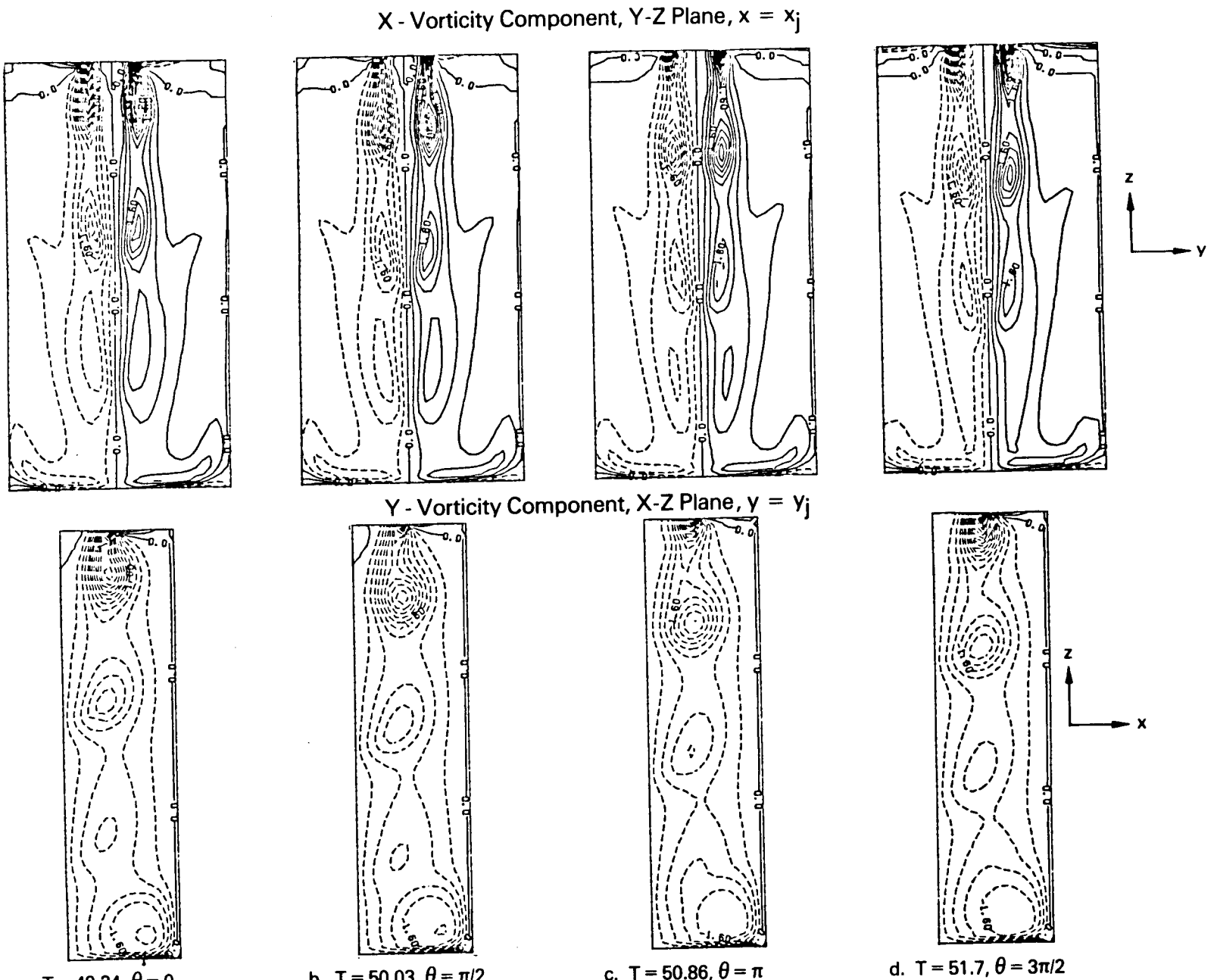

Figure 22. Vorticity Contours for Profile III at Re = 200 and Forced Axisymmetrically at St = 0.3. Plots are Every π/2 of the Fourth Period

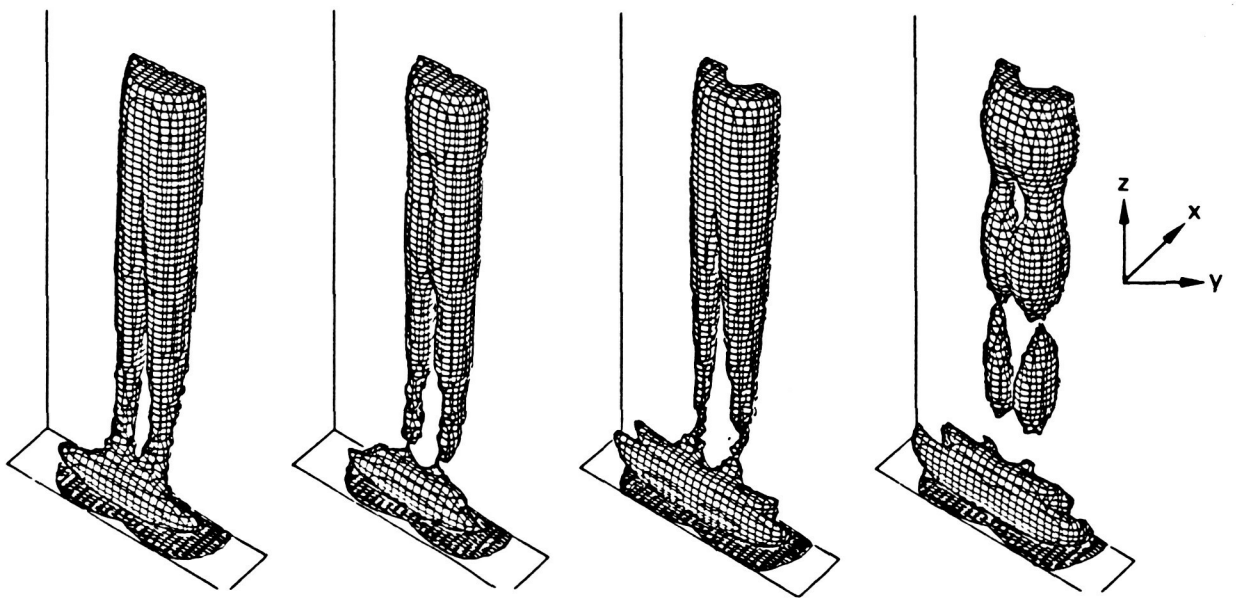

a. Profile I, Re = 200 Steady State
b. Profile I, Re = 200 Forced
c. Profile III, Re = 200 Steady State
d. Profile III, Re = 200 Forced

Figure 23. Perspective Plot of the Absolute Total Vorticity Surface in Three Dimensions

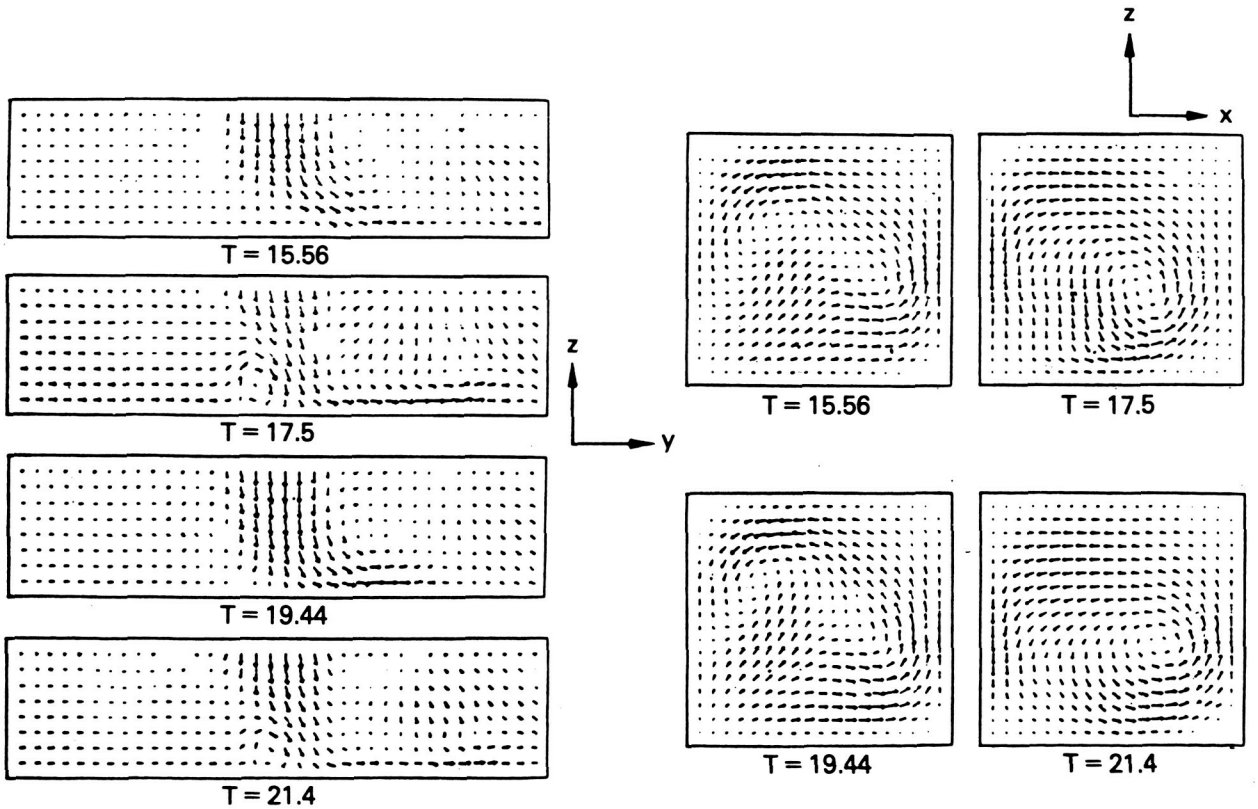

a. Y-Z Plane, $x = x_j$

b. X-Z Plane, $y = y_d$

Figure 24. Velocity Distribution for Profile I at Re = 300 with 40% Crossflow and Forced Axisymmetrically at St = 0.3

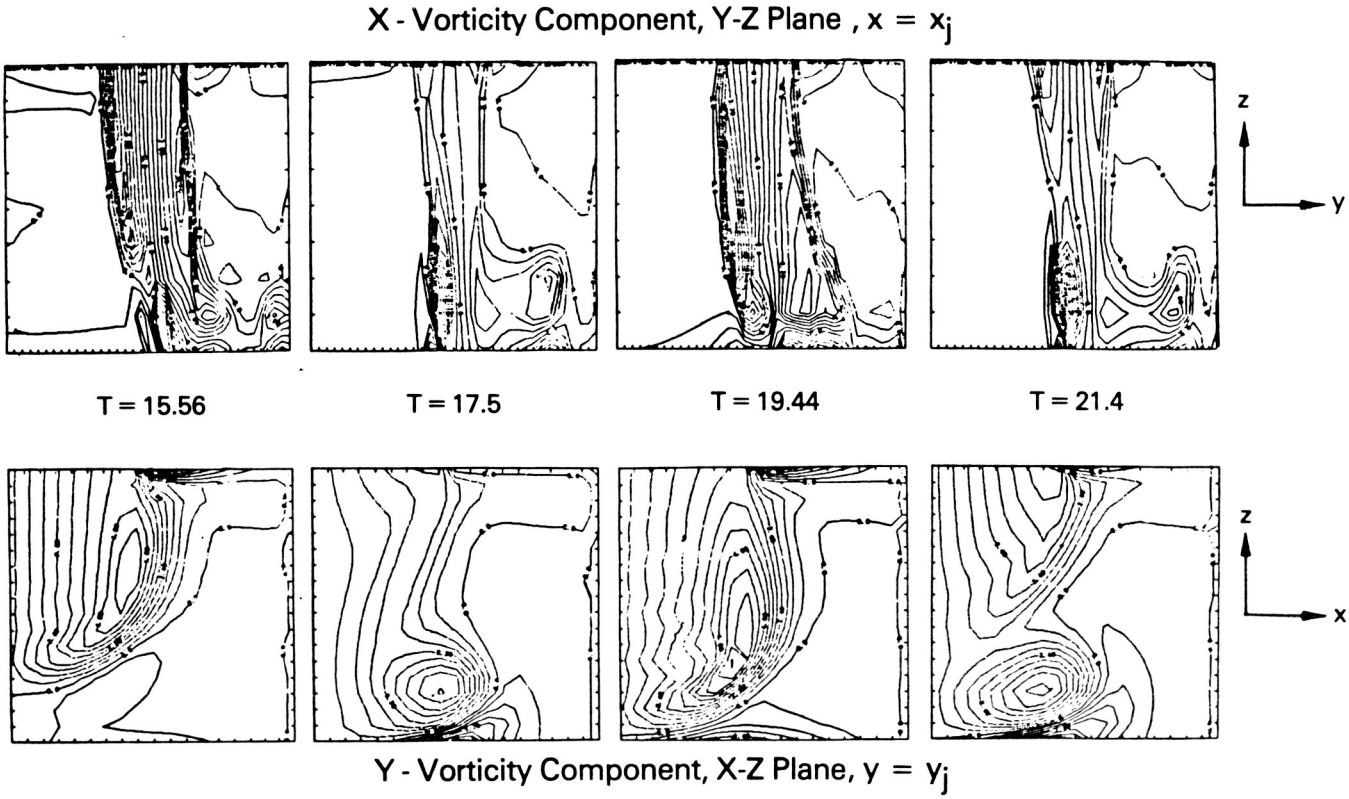

Figure 25. Vorticity Contours for Profile I at Re = 300 with 40% Crossflow and Forced Axisymmetrically at St = 0.3

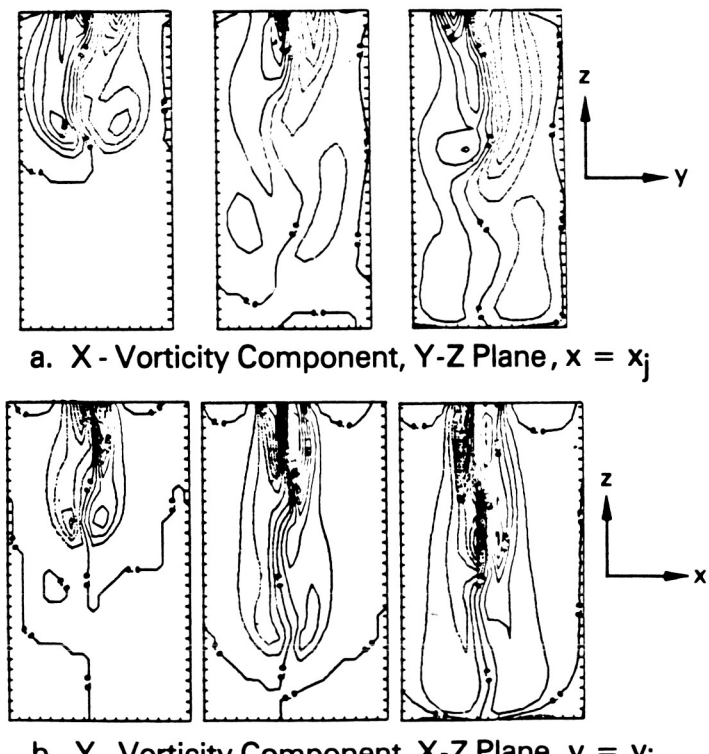

Figure 26. Vorticity Contours for Profile I at Re = 100 and Forced Helically (Azimuthal Variation) at St = 0.165

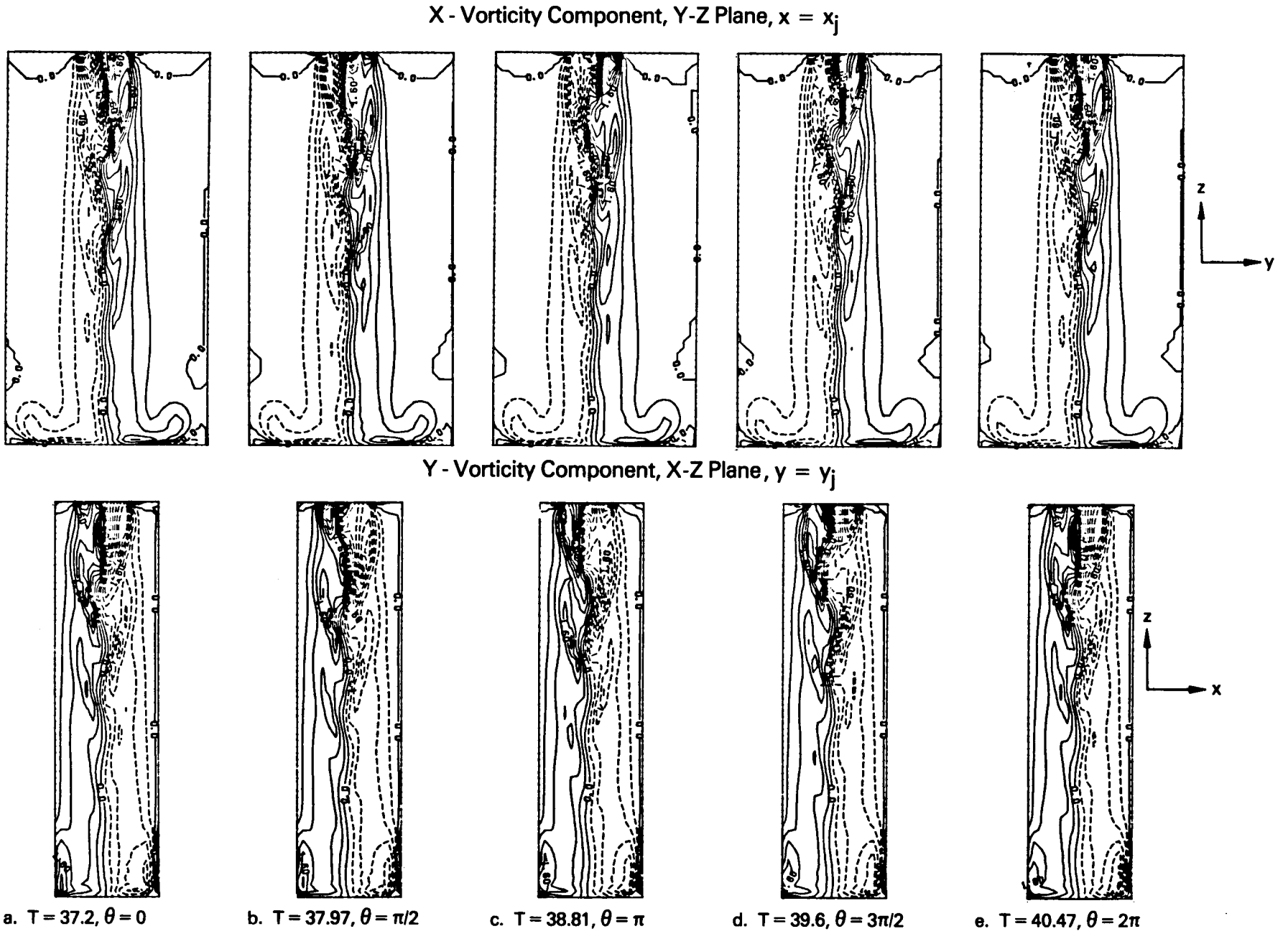

Figure 27. Vorticity Contours for Profile I at Re = 300 and Forced Helically (Azimuthal Variation) at St = 0.3. Plots Every π/2 of the Seventh Period

UNSTEADY THREE-DIMENSIONAL SIMULATIONS OF VTOL UPWASH FOUNTAIN TURBULENCE

Robert E. Childs and David Nixon
Nielsen Engineering & Research, Inc.
Mountain View, CA 94043

ABSTRACT

Numerical simulations of a planar turbulent wall jet and a planar VTOL upwash fountain have been performed. These are three-dimensional simulations and they resolve large scale unsteady motions in the flows. The wall jet simulation shows good agreement with experimental data and is presented to verify the simulation methodology. Simulation of the upwash fountain predicts elevated shear stress and a half-velocity width spreading rate of 33% which agrees well with experiment. Turbulence mechanisms which contribute to the enhanced spreading rate are examined.

1. INTRODUCTION

The desire to have a VTOL supersonic fighter has increased in recent years as there are many advantages in having an aircraft that can be based independent of conventional runways. VTOL capability is provided by some combination of downward thrusting jets. In ground effect these jets produce fluid dynamical problems that are not typically encountered in conventional aircraft. A complete list of ground effects problems would be rather large and would include, for example, the Reynolds number scaling of the "suck-down" effect, the enhanced spreading rate of the upwash fountain, hot gas reingestion of the fountain or ground vortex fluid, and aircraft stability problems due to interaction with the fountain or the ground vortex.

The key to an understanding and a predictive capability in many of the above problems is in the ability to understand the turbulent mixing. The suck-down effect and the fountain's spreading rate are almost purely turbulence problems; the ground vortex also depends on inviscid and bouyancy phenomena. These are complex turbulent flows, involving combinations of "turbulence modifiers" that are rarely encountered in other applications and, therefore, it will be difficult to develop adequate models for these flows.

This paper focuses on the turbulence in the upwash fountain, sketched in Figure 1, which is important for several practical reasons. The upwash is hot, it strikes the underside of the aircraft, it contributes to lift, and it may lead to exhaust gas reingestion. From a scientific standpoint the upwash spreading rate is an anomaly which begs to be explained. The combination of streamline curvature and velocity gradient can have a pronounced effect on turbulent mixing [Refs. 1, 2, 3]. Present understanding indicates that the combination of curvature and velocity gradient, like that in a boundary layer on a convex surface, should stabilize the turbulence in most of the turning region of the fountain. However, just the opposite occurs and the shear stresses and spreading rate are two to three times greater than in a conventional jet. There is a near-wall region which has shear of the opposite sign, and for which the curvature-velocity gradient combination effect should be destabilizing. This region is small in the wall jets and in the fountain, but in the collision zone it encompasses much of the reversed-flow zone under the fountain. However, it seems unlikely that this relatively small region of the flow could energize the turbulence in all of the fountain.

The high stresses and spreading rate are underpredicted by most classes of current turbulence models: the k-ε, the algebraic Reynolds stress, and the Reynolds stress transport models [Ref. 4 and Launder, private communication]. These models seem to be insensitive to the turbulence mechanisms in the fountain's turning region. For obvious reasons it is desirable to have a model that gives improved results for this flow. Additionally, it is clear that these potentially significant mechanisms are not represented in the modeling of other flows, where their absence, not being as critical, has escaped detection. The essential feature of the upwash fountain is colliding wall-bounded shear layers with strong curvature at the collision point. A two-dimensional boundary layer with a reversed flow region has similar features at the separation point.

Finally, it is worth noting that experimental studies of the fountain are difficult to perform. The flow is highly unsteady with frequent flow direction reversal in the critical region where the wall jets collide. Laser instrumentation would seem to be necessary for this work, but has only recently been employed [Ref. 6]. Furthermore, the large pressure gradients in a region of unsteadiness indicate that pressure fluctuations may be important and these cannot be measured at present. The pressure-strain term in the Reynolds stress transport equations has, therefore, not been directly measured although it is thought to be important in curved flows.

1.1 The Approach

In this work two flows are simulated, the planar wall jet, chosen because it is a well documented flow which can be used to validate the numerical method, and the planar upwash fountain. There are many advantages to studying the planar flow rather than the fountain resulting from radial wall jets, which more closely resembles the VTOL ground effect flow field. These include the ability to use periodic boundary conditions in one direction and shorter computing times for good statistics.

The simulations are done by specifying unsteady inflow conditions that approximate the turbulent wall jets. These flows then evolve in the streamwise direction before they are evaluated, in the case of the wall jet simulation, or collide with another wall jet, in the fountain simulation. Instantaneous and time-averaged data are obtained from the simulation. This makes the work similar to an experimental program except that the type and quantity of data available can be greater. To date single point correlations of velocities, velocity gradients, pressure and density have been obtained. These terms give us, from the Reynolds-averaged standpoint, the ability to determine most of the mechanisms critical to the turbulence in the fountain. This work is similar to the work in Large Eddy Simulation (LES) reviewed by Rogallo and Moin [Ref. 7], for example. Many differences distinguish LES from the present effort, which we call Very Large Eddy Simulation (VLES).

2. METHODS

2.1 Equation Set and Numerical Algorithm

The simulations have been performed using a conventional finite difference method that is often used for steady-state Reynolds-averaged calculations of aerodynamics problems. The viscous conservation equations for mass, energy, and momenta in three directions (commonly, the Navier-Stokes equations) are used for the simulations. They are written in a conservation law form common for high speed aerodynamics. The solution algorithm is the 1981 implicit-explicit MacCormack method [Ref. 8]. The implementation of the algorithm includes modifications to improve its efficiency for this application; these are discussed in Childs and Nixon [Ref. 5]. The two significant modifications are: 1) viscous diffusion terms are first order in time, as opposed to the second order accuracy of the original algorithm (not a significant disadvantage since the sub-grid-scale turbulence model, which dominates viscous diffusion, has no formal accuracy at all, and convective terms are still second order in space and time); and 2) the time step is chosen such that the algorithm is explicit in the two directions parallel to the wall. The implicit step is only used normal to the wall. Due to the grids which are used the algorithm is entirely explicit away from the grid clustering at the wall. This minimizes the dissipative effects of an implicit method, but does not overly restrict the time step.

The difficulty at solid boundaries with the 1981 MacCormack method [Ref. 9] has not been a problem in the present work since the time steps needed to resolve the turbulence are relatively small and give a maximum CFL number of 20, typically.

The simulations are performed on rather coarse grids because of computer limitations and only the largest scales of turbulence can be simulated. Therefore, the equations are Reynolds-averaged and a sub-grid-scale (SGS) model is used for the unresolvable scales of turbulence which, it is assumed, are more easily modeled and less critical to the turbulent processes than the large scales. We use an eddy viscosity which is proportional to the magnitude of vorticity

$$\nu_t = C\Delta^2 \sqrt{\omega_i \omega_i} \qquad (1)$$

The value of $C\Delta^2$ represents the square of the SGS mixing length. A constant characteristic grid spacing Δ is used, since the grid spacing in the x- and z-directions is nearly constant in the collision zone. The coefficient C takes the value of $C = 0.14$ which is close to the values used for LES in References 10 and 11, except near the wall. At the wall C approaches zero according to the Von Karman formula so that the log-law profile is reproduced.

2.2 Boundary Conditions

There are several types of boundary conditions which must be applied in these simulations. The straight-forward ones will be discussed first, then the more difficult inflow and outflow conditions will be given.

In the z-direction the flow is periodic. This condition is imposed by over-writing the boundary points with data from the first interior point at the opposite side of the grid. At the solid wall the no-slip condition is applied to velocities and a zero-gradient condition is applied to the density and energy. The wall falls between two grid points and these conditions imply a zero-gradient on temperature and pressure.

At the top of the domain there is outflow in the fountain and slow flow, either in or out, on either side of the fountain. This boundary is treated with a zero-gradient extrapolation condition on all variables. There is no effort to obtain meaningful data at this boundary. The primary concern is that there be no reflection of pressure waves. From analysis of outflow boundary conditions (c.f. Ref. 12) the imposition of pressure and extrapolation of density and velocities is correct for steady calculations. However, imposing a pressure at the top would produce pressure reflections.

The side boundaries above the wall jets must provide a small amount of inflow for entrainment into the jet. It would be incorrect to specify the inflow because that could amount to specifying the entrainment into the jet. A zero-gradient condition on the velocities permits the inflow to adjust as necessary to satisfy the entrainment. The density is set to ambient. At some point the pressure must be tied to ambient conditions and there is no other suitable place to do this since all other boundaries will experience significant pressure fluctuations. A "loosely tied pressure" condition is used, which provides a small "pull" towards ambient pressure, but permits the pressure to deviate if the interior flow so requires. The loosely tied pressure is computed as a weighted average of the local interior pressure and the fixed ambient pressure. Typically the weighting is about 30% on the ambient pressure and 70% on the interior pressure. A similar type of pressure

boundary condition was used by Boris [Ref. 13] in the simulation of turbulent outflow.

The inflow conditions are clearly the most difficult. They must approximate the mean and turbulent flow in a fully developed turbulent wall jet. There were two guiding principles used in determining the inflow. Firstly, it should give correct values for the mean flow and basic statistics, the normal and shear stresses. Secondly, the unsteady inflow should "look right" when compared to flow visualization pictures. A third condition, on the turbulent energy spectrum, may be examined in the future.

The unsteady inflow profiles are constructed from a combination of Chebyshev modes normal to the wall and Fourier modes in the z-direction and time. This is added to a mean inflow profile determined from experimental data [Ref. 14, p. 434]. The following expression gives the unsteady streamwise velocity perturbation

$$u'(y,z,t) = \overline{U}_{max} \sum_{\ell,m} \alpha_{\ell,m} T_m(y) \sin(\omega_\ell z \pm c_\ell t) \qquad (2)$$

The Chebyshev polynomials are represented by $T_m(y)$. The ω_ℓ are wavelengths, the c_ℓ are wave speeds and the $\alpha_{\ell,m}$ are weighting coefficients. The lateral and vertical components are specified as functions of the streamwise fluctuations.

$$\begin{aligned} v' &= u' [\pm \beta_1 + \beta_2 \sin(\omega_p z) \sin(t)] \\ w' &= u' [\quad \beta_3 \sin(\omega_p z) \sin(t)] \end{aligned} \qquad (3)$$

The many coefficients in Equations (2) and (3) must satisfy certain constraints. The velocity perturbation goes to zero at the wall and the edge of the jet, and the maximum values of the normal and shear stresses must agree with experiment. These conditions do not uniquely determine the coefficients and the condition on the "appearance" of the unsteady profile was employed to determine ratios between some coefficients. The inflow density was set to ambient and the pressure was extrapolated from the interior. Specification of the above boundary conditions completes the description of the method.

2.3 Grids, Statistics and Computation Times

Cartesian grids with stretching in the x- and y-directions are used. The grid is clustered at the wall and in the center of the domain (for upwash simulations) where the fountain is expected to form. Simulations have been run on two grids with different resolutions for both the wall jet and the fountain. The results showed grid dependence in magnitude but not in character; in particular, the spreading rate of the fountain was very similar in both cases. The finer grid results are shown. For the fountain the grid has 40 by 32 by 25 points in the x, y, and z directions; for the wall jet the grid has 32 by 32 by 32 points.

Analysis of the turbulence is done by accumulating single point statistics of velocities, velocity gradients, pressure, density and energy. These are then processed to provide the turbulent correlations. The flow is two-dimensional in the mean and statistical averaging is done over time and the z-direction, which is the mean-invariant direction. Turbulence evaluation is based on the assumption of constant density, which is sufficiently accurate for the present purposes.

The integration times are, so far, marginally adequate for some correlations, which are still changing slowly with time. Second order correlations, which give the Reynolds stresses and pressure-strain terms, appear to be stable to within 5% for the wall jet simulation but variations of 20% may be seen in the fountain results. Higher order statistics are not sufficiently converged for many purposes. Variations of 50% may be seen before they stabilize. The reason is that higher order statistics are formed from small differences between lower order statistics. Small variations in the lower order statistics can produce large changes in the higher order correlation. The higher order statistics are given to show orders of magnitude and trends, which are firmly established.

These calculations have been run on a CRAY X-MP. The upwash fountain was run for 90 minutes of CPU time and statistics were taken over the last 45 minutes. This provided 110 units of physical time nondimensionalized on the acoustic speed and initial wall jet half-velocity thickness, or approximately 1.7 "flow-through" time periods (time for the maximum-velocity fluid to transit the domain).

3. RESULTS

The results will be presented in two stages. The first step is to validate the simulation, which is done for the wall jet. The accuracy of the wall jet simulation will indicate what accuracy can be expected for the fountain simulation. The second stage is to examine the results for the fountain and investigate the turbulence mechanisms.

3.1 The Wall Jet

The simulation is of a two-dimensional wall jet on a plane surface with no streamwise pressure gradient. The calculation was run with a mean maximum inflow Mach number of 0.65, which is slow enough to minimize compressibility effects yet fast enough to maintain good computational efficiency. The wall and the "freestream" were given a velocity of 10% of the inflow maximum. This gives clearly defined inflow and outflow boundaries. Since the freestream and wall have the same velocity the flow has the conditions required for self-preservation. The added velocity is removed from all data analysis and the results. The Reynolds number based on maximum velocity, U_m, and half-velocity thickness, $y_{1/2}$, is 20000. The data to be used for comparison were compiled by Launder and Rodi for the 1980-81 Stanford-AFOSR

Conference [Ref. 14] from several experiments referenced therein.

For the comparison we use time-averaged results from the unsteady simulation. Figure 2 gives the velocity vectors at every fourth streamwise grid line. The dimensions in all two-dimensional figures are normalized on the half-velocity thickness at the inlet. The inlet velocity profile is specified to match experimental data. Between x=1 and x=9 the profile departs from experiment and shows a velocity profile which is too steep in the outer third of the jet. By x=10 the velocity profile is once more in agreement with experiment, as shown in Figure 3. There are small errors near the wall, but this is where the grid resolution in the x- and z-directions is the poorest relative to the need, and most of the shear stress is carried by the SGS model. The growth rate of the half-velocity thickness (at x=10) is 0.067, which is 9% below the experimental value of 0.073. Although the mean velocity profile has stabilized at this point, many of the turbulent statistics have not. The flow is not yet self-preserving.

In Figure 4 the resolvable components of the normal stresses are given. Clearly, the SGS contribution to the stresses should be positive (which eddy viscosity models don't guarantee) and, thus, the total stresses would be greater than the values shown. The resolvable stresses are all within 20% of the experiment and predict the trends that are important, including the slight rise in the u' and w' near the wall. The reduction in u' and w' very near the wall is physically correct behavior, although the region where this occurs is too thick in the simulation. This is likely caused by inadequate numerical resolution, but may also be due to the SGS model.

The resolvable and resolvable-plus-SGS shear stresses are shown in Figure 5. Consider first only the resolvable stress. The stress in the outer 75% of the wall jet is well predicted, although the location and magnitude of stress at its maximum are slightly high. In the near-wall region the stress is badly underpredicted. Considering the poor resolution here this problem was not unexpected. When the SGS stress is included, the near-wall results improve and give nearly the correct skin friction. However, the stress in the outer layer is now overpredicted by about 60%.

Figure 6 gives the triple velocity correlations of $\overline{u'u'u'}$, $\overline{u'v'v'}$ and $\overline{v'v'v'}$. These terms are responsible for the turbulent transport of the Reynolds stresses. They are important to understanding the turbulence, to multi-equation models, and to validating the present simulations. The results show that, in general, the trends and orders of magnitude are well predicted, with the exception that the near-wall region of $\overline{v'v'v'}$ is not. The overprediction of $\overline{u'u'u'}$ in the outer layer is consistent with the overprediction there of $\overline{u'u'}$. The prediction of $\overline{u'v'v'}$ (shear stress transport) is the best of the three and is only in significant error in the near-wall region. It should be noted that measurement errors of triple products are of the order of 15% to 30%, under the best conditions.

In summary for the wall jet the following are the major points. The resolvable normal stresses are predicted to within 20% of experiment, with the streamwise fluctuations being high and the vertical fluctuations being low. The shear stress in the outer layer is overpredicted by a significant amount. We do not believe this error will degrade the fountain simulation, for two reasons. In the fountain simulation the grid resolution of the wall jets is less and the turbulence levels are lower than in the pure wall jet simulation. Elevated turbulence in the fountain is, more than ever, due to mechanisms in the collision zone. Also, the turbulence levels in the fountain are many times greater than in the wall jet, so the turbulence production in the collision zone over-powers the wall jet turbulence. The third order correlations are adequate away from the wall, but are underpredicted in the near-wall region, which is due primarily to inadequate grid resolution in the x- and z-directions. In general, the turbulence in the wall jet is sufficiently close to experiment to permit useful study of the upwash turbulence.

3.2 The Upwash Fountain

The objective of this study is to examine the turbulence in the upwash fountain. The simulation was run by colliding two turbulent wall jets and permitting the upwash to develop naturally. The wall jets are run with the same inlet conditions as the pure wall jet.

For a point of comparison, the results from a steady state Reynolds-averaged calculation using a k-ε model are given in Figure 7. Although not shown, the turbulence levels and spreading rate are typical for the values seen in a "normal" free jet, and significantly underpredict the values seen in upwash fountains.

Figure 8 gives the mean velocity vectors and Mach number contours from the unsteady simulation, similar to Figure 7 from the steady calculation. Rapid spreading of the fountain is clearly seen. Initially a velocity deficit at the center of the fountain is seen but it quickly disappears above the collision zone. Streamlines, shown in Figure 8-c, reveal a two stage collision process. First the wall jets separate and flow over relatively large reversed flow regions. Then they collide above the separation zone and are redirected upward. The half velocity width of the fountain is plotted in Figure 9; it grows at a rate of 33% just above the collision zone. This compares well with experimental values in the range of 24% to 32% [Refs. 15, 16]. The data of Gilbert [Ref. 15] are included and show good agreement midway up the fountain, but poorer agreement at the bottom and top. It is likely that measurement errors (hot wire anemometry) are significant at the bottom and that simulation errors are significant at the top. The fountain must eventually relax to a conventional plane jet, although this may be occurring too rapidly in the simulation. Turbulence near the top boundary is damped by the dissipative outflow boundary conditions and coarser grid spacing, which decreases the spreading rate. Large scale motions are also constrained by the periodi-

city condition because the width of the fountain near the top boundary is greater than the z-dimension of the physical domain (see Fig. 16).

Figure 10 gives the mean velocity profiles in the fountain at several heights. The fountain is not perfectly symmetric although it should be. The factors which contribute to this are non-symmetric truncation errors in the MacCormack algorithm and insufficient integration time. It should be noted that most experimental results show some asymmetry and, thus, the fountain may easily be disturbed from symmetric.

The streamwise normal stress is given in Figure 11. Data from physical experiments of Gilbert [Ref. 15], Kind [Ref. 16] and Saripalli [Ref. 6] are included. The "normal" plane free jet has been studied by Bradbury [Ref. 17] and his results are quite close to those of Gilbert. The simulated results are below those from Kind but generally above those of Gilbert. Also, a sharp dip in the stress is seen at the centerline in the present results and the results of Kind, but not in those of Gilbert or Saripalli.

Contour plots of some turbulence quantities are given in what follows. In these, the normalizing velocity scale is $\sqrt{2\Delta p}$, where Δp is the maximum pressure rise in the collision zone. This is approximately the maximum mean velocity of the colliding wall jets. The normalizing length scale is half of the width of the high pressure region. The time scale derived from the length and velocity scales is approximately the minimum time for fluid to transit through the collision zone. Figure 12 gives contour plots of the normal stresses. The maximum for $\overline{u'u'}$ is 0.28 (note these are lateral fluctuations with respect to the fountain), and is seen near the centerline in the upper half of the collision zone. This is the point where the wall jets collide after having been forced up and over the separation zone at the base of the fountain. It is also the region of maximum streamline curvature. The regions of maximum $\overline{v'v'}$ in the fountain are on both sides of the upwash and are in much the same regions as we expect for the shear stress. The regions of highest $\overline{u'u'}$ and $\overline{v'v'}$ do not overlap which suggests that an important mechanism may be the inter-component transfer from $\overline{u'u'}$ to $\overline{v'v'}$. The regions of highest $\overline{w'w'}$ are very near the wall at the base of the fountain and in the upper part of the fountain. However, $\overline{w'w'}$ is relatively large in all regions of turbulent flow and does not show the strong spatial variations displayed by $\overline{u'u'}$ and $\overline{v'v'}$.

The turbulent shear stress normalized on the local centerline velocity, including the SGS contribution, is given in Figure 13 at a few stations in the fountain. The SGS contribution to the shear stress is large in the wall jet (about 50%), but small (less than 10%) in the fountain. The maximum stress is predicted to be about 0.075, which is in reasonable agreement with the data of Saripalli, but is considerably higher than the value of 0.024 reported by Gilbert. The stress is roughly three times greater than the maximum shear stress of 0.022 in a "normal" planar jet [Ref. 17] and, therefore, consistent with the spreading rate which is three times greater than in the "normal" jet. Figure 14 gives the shear stress as a contour plot which shows regions of high stress in the fountain and along the edge of the separation bubble at the base of the turning region.

3.3 Instantaneous Flow Field

Flow visualization of the turbulence can provide insights that can never be gleaned from statistical data. The computer code is not currently capable of saving all of the time dependent information we desire; however, we can examine an instantaneous three-dimensional flow field and learn some important points about the fountain.

Figure 15 gives particle tracers started in the opposing wall jets of the instantaneous flow field. The tracers show a small amount of mixing, indicated by crossing paths, in the wall jets. In the fountain considerably more mixing occurs, especially for $y > 6$ which is the region of maximum spreading rate. A mechanism that appears to be important is this: Blobs of fluid with higher u' can penetrate through the mean centerline of the fountain. Once through the centerline the blob meets less resistance to its motion since it is moving into a weaker flow and no adverse pressure gradient. This blob now travels on a path that is very different from the mean flow, which gives high mixing and shear stress. Another feature of this figure is that the fountain is slightly tilted. The tilt might indicate a "turbulence" mechanism consisting of the fountain flapping back and forth. The tilt does appear in the mean particle paths (Fig. 8-c) which may indicate this is a problem of asymmetry induced by the numerics. It is also possible that a low frequency flapping motion of the fountain exists, which has not been removed by the time averaging; this would be difficult to study because of the long integration times required and the dependence on low frequency fluctuations of the inflow conditions.

Figure 16-a gives velocity vectors projected in the x-z plane in the fountain at y=12. This shows a region of fluid, denoted A, with a large negative u' component penetrating into relatively quiescent fluid. Mach number contours in the same plane, Figure 16-b, show that this is a region of high speed flow, indicating the vertical velocity is large as well (positive v'). Thus, this blob will contribute to negative $\overline{u'v'}$. There is also a region (B) where the fountain fluid appears to be ingulfing a large area of ambient fluid. This may be the remnant of an earlier high speed blob which is now "mushrooming out" and forming vortices similar to the starting vortices from a free jet.

The fluid interactions we have examined in this single "snapshot in time" indicate that the fountain turbulence has a large scale structure caused by the penetration of blobs of high speed fluid through the mean fountain centerline. Data at other times also show these phenomena. The evidence for a flapping motion is relatively weak. The next step is to examine the results in terms that are amenable to Reynolds-averaged turbulence modeling.

3.4 Turbulence Mechanisms

Evaluation of the mechanisms that contribute to the high turbulent stresses will be done within the framework of the Reynolds stress transport equations, which are given here in cartesian tensor notation.

$$\frac{D}{Dt}\overline{u_i'u_j'} = \underbrace{[-\overline{u_i'u_k'}\frac{\partial U_j}{\partial x_k} - \overline{u_j'u_k'}\frac{\partial U_j}{\partial x_k}]}_{I} \underbrace{- 2\nu\overline{\frac{\partial u_j'}{\partial x_k}\frac{\partial u_i'}{\partial x_k}}}_{II}$$

$$\underbrace{+\overline{\frac{p'}{\rho}[\frac{\partial u_i'}{\partial x_j} + \frac{\partial u_j'}{\partial x_i}]}}_{III} \qquad (4)$$

$$+ \underbrace{\frac{\partial}{\partial x_k}[-\overline{u_i'u_j'u_k'} + \nu\frac{\partial\overline{u_i'u_j'}}{\partial x_k} - \overline{\frac{p'}{\rho}(\delta_{jk}u_i' + \delta_{ik}u_j')}]}_{IV \quad V \quad VI}$$

The left hand side of Equation 4 represents the rate of change of the components of Reynolds stress along streamlines. In order, the right hand side terms represent: production, viscous dissipation, pressure strain, turbulent diffusion, viscous diffusion and pressure diffusion. The terms which are thought to be major ones will be given as contour plots. Identical contour levels and normalization are used for all terms so that valid comparisons of the terms can be made from these figures. Only resolvable turbulence contributes to these results; the SGS shear stress is not included.

The production term is important because it extracts energy from the mean flow and converts it to turbulence. The pressure-strain term cannot produce turbulence energy; it merely transfers energy among the different components. Pressure-strain interactions can affect the shear stress by changing the correlation between u' and v'. The objective in this examination is to determine which are the principal terms in the generation of the high shear stresses.

The production term for $\overline{u'v'}$ is given in Figure 17-a. Regions of high production are seen at the separation bubble at the base of the fountain and in the fountain and are nearly coincident with the regions of high shear stress given in Figure 14. Figure 17-b gives the pressure-strain term for $\overline{u'v'}$ and shows levels comparable to the production term, but in different locations. The highest levels are where the wall jets first separate and there are moderate levels near to, but on either side of, the fountain centerline. The production and pressure-strain terms have, locally, the same sign in most of the flow and combine to increase the level of shear stress. It appears that the pressure-strain term is more important at the base of the fountain but the production term is more important in the fountain.

The gain or loss of $\overline{u'v'}$ due to turbulent diffusion, term IV, is given in Figure 17-c. Gradient diffusion models are typically used to model the velocity triple correlations, [Ref. 18], which for this flow means that regions with the largest stress would experience the greatest loss in much the way heat diffuses. Comparison of Figures 17-c and 14 suggests that the gradient diffusion concept is correct near the outer edges of the fountain, but not in the central region of the fountain, between the points of maximum shear stress magnitude. Term IV is only slightly less in magnitude than the production or pressure-strain, and therefore relatively important.

For the normal stresses a clear picture emerges regarding the roles of the different terms. Figures 18-a and 19-a show the production of $\overline{u'u'}$ and $\overline{v'v'}$. Production of $\overline{u'u'}$ occurs primarily at the collision point; this is where the mean flow is redirected upward, but the higher speed blobs penetrate through the mean centerline. The primary contributor to this term is $\overline{u'u'}$ dU/dx, which is large because dU/dx is so large. Production of $\overline{v'v'}$ occurs mainly in the fountain where $\overline{u'v'}$ dV/dx is large. There is a region of negative production of $\overline{v'v'}$ at the base of the fountain; negative production is impossible to obtain with a positive definite eddy viscosity model. The pressure strain terms for $\overline{u'u'}$ and $\overline{v'v'}$, given in Figures 18-b and 19-b, are of comparable magnitude, but opposite sign, in the collision zone; this indicates a transfer of energy from $\overline{u'u'}$ in the wall jet to $\overline{v'v'}$ in the fountain (note that v' is streamwise in the fountain).

4. SUMMARY

Numerical simulations with the three-dimensional Navier-Stokes equations were used to study turbulence mechanisms in a VTOL upwash fountain. The primary characteristic of this flow, the abnormally high spreading rate of the fountain, was predicted. Large values of the Reynolds stresses were also predicted and these are in moderately good agreement with the (widely scattered) experimental data. The pressure-strain and production terms in the Reynolds shear stress transport equation have been compared and are shown to be of comparable magnitude and of the same sign. The principal mechanism for generating the high shear stress is the penetration of blobs of high speed fluid through the mean fountain centerline. This is reflected in the large magnitudes of the production terms for the lateral fluctuations ($\overline{u'u'}$) and the shear stress ($\overline{u'v'}$).

This is a flow for which advanced turbulence models have failed to give good results. The success of very large eddy simulation for what could be described as an engineering application may point the way for the prediction of other difficult turbulent flows.

The authors gratefully acknowledge the support of the Air Force Office of Scientific Research, External Aerodynamics, through contract No. F49620-85-C-0055, and the NASA Ames Reseach Center for use of the CRAY computer.

REFERENCES

1. Gillis, J. C. and Johnston J. P., "Turbulent Boundary Layer Flow and Structure on a Convex Wall and its Redevelopment on a Flat Plate," J. Fluid Mech. 135, pp. 123-153, 1983.

2. Bradshaw, P. and Castro, I. P., "The Turbulence Structure of a Highly Curved Mixing Layer," J. Fluid Mech. 73, part 2, pp. 265-304, 1976.

3. Moser, R. D. and Moin, P., "Direct Numerical Simulation of Curved Turbulent Channel Flow," Stanford Univ. Mech. Engrg. Thermo. Div. Rept. TF-20, 1984.

4. Childs, R. E. and Nixon, D., "Simulation of Impinging Turbulent Jets," AIAA-85-0047.

6. Saripalli, K. R., "Laser-Doppler-Velocimeter Measurements in a Three-Dimensional Fountain Upwash," to be presented at the AIAA/AHS/ASEE Aircraft Design, Systems and Operations Meeting, Colorado Springs, CO, Oct. 1985.

7. Rogallo, R. S. and Moin, P., "Numerical Simulation of Turbulent Flows," Ann. Rev. Fluid Mech. 16, pp. 99-137, 1984.

8. MacCormack, R. W., "A Numerical Method for Solving the Equations of Compressible Viscous Flow," AIAA-81-0110.

9. MacCormack, R. W., "Current Status of Numerical Solutions of the Navier-Stokes Equations," AIAA-85-0032.

10. Reynolds, W. C., "Computation of Turbulent Flows," Stanford Univ. Mech. Engrg. Thermo. Div. Rept. TF-4, 1975.

11. Moin, P., Reynolds, W. C., Ferziger, J. H., "Large Eddy Simulation of Incompressible Turbulent Channel Flow," Stanford Univ. Mech. Engrg. Thermo. Div. Rept. TF-12, 1978.

12. Yee, H. C., "Numerical Approximations of Boundary Conditions with Application to Inviscid Equations of Gas Dynamics," NASA TM-81265, 1981.

13. Boris, J., Oran, E., Grinstein, F., Oswald, C., and Gardner, J., "Direct Simulations of Spatially Evolving Compressible Turbulence: Techniques and Results," presented at Ninth International Conference on Numerical Methods in Fluid Dynamics, CEN - Saclay, France, June 1984.

14. 1980-81 Stanford-AFOSR-HTTM Conference on Complex Turbulent Flows, S. J. Kline et al., Eds., Stanford, CA, 1981.

15. Gilbert, B. L., "An Investigation of Turbulence Mechanisms in V/STOL Upwash Flow Fields," Grumman Aerospace Corp. Rept. RE-688, 1984.

16. Kind, R. J. and Suthanthiran, K., "The Interaction of Two Opposing Plane Turbulent Wall Jets," AIAA-72-0211.

17. Bradbury, L. J. S., "The Structure of a Self-Preserving Turbulent Plane Jet," J. Fluid Mech. 23, part 1, pp. 31-64, 1965.

18. Launder, B. E., Reece, G. J, and Rodi, W., "Progress in the Development of a Reynolds-Stress Turbulence Closure," J. Fluid Mech. 68, part 3, pp. 537-566, 1975.

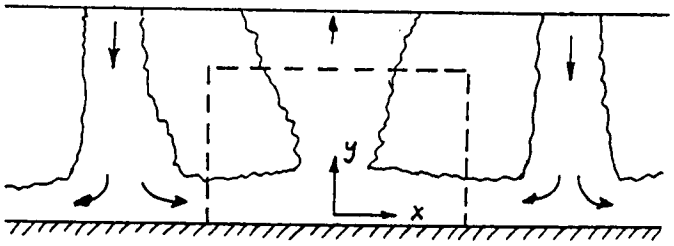

Figure 1. Sketch of impinging jets with upwash fountain, showing computational domain.

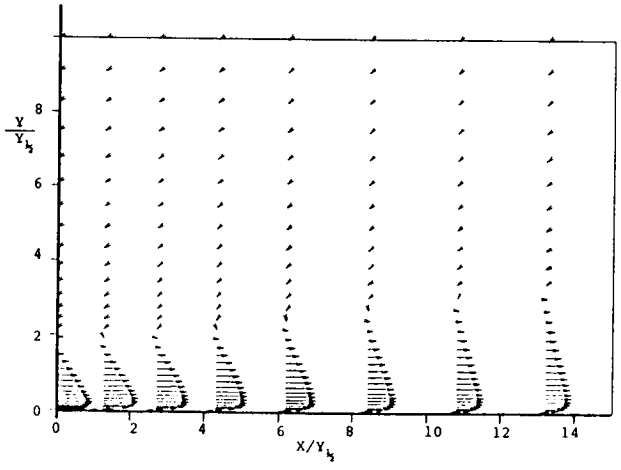

Figure 2. Time averaged velocity vectors in wall jet.

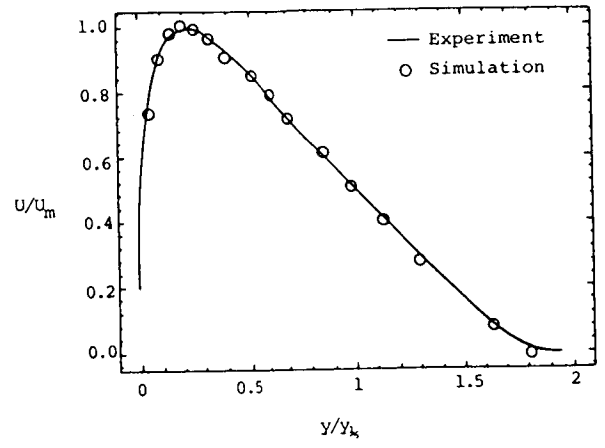

Figure 3. Comparison of velocity profile at x=10 with experimental data from Ref. 14.

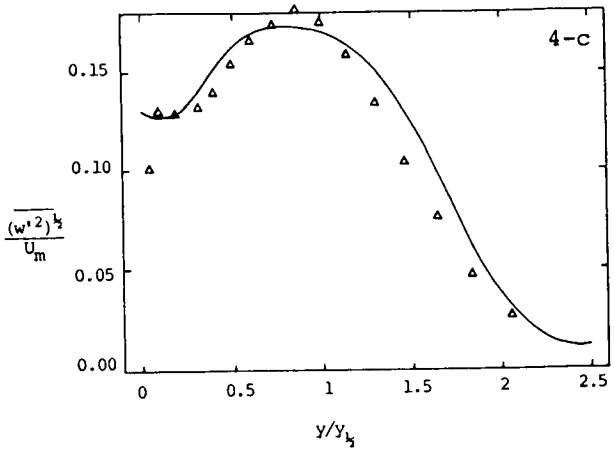

Figure 4. Normal stresses in the wall jet: a) gives u´; b) gives v´; c) gives w´.

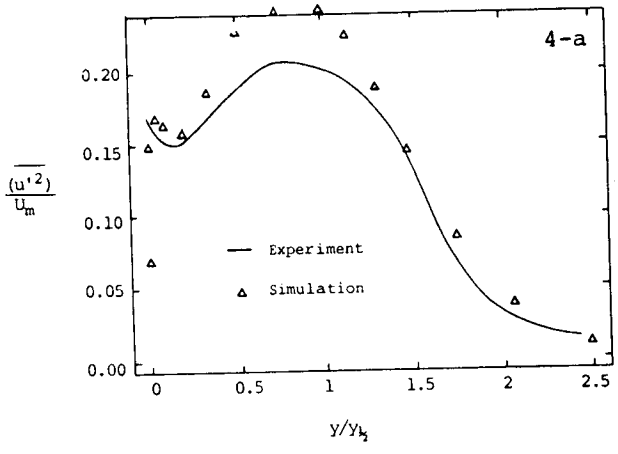

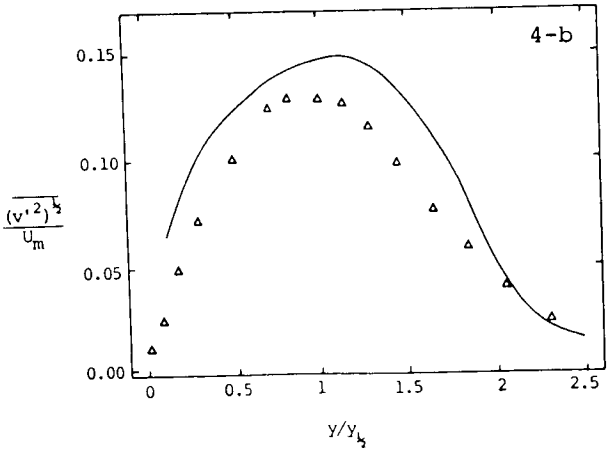

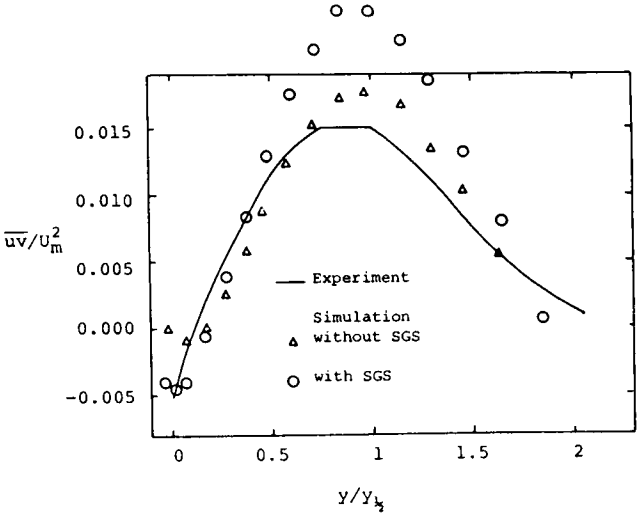

Figure 5. Shear stress in the wall jet, with and without sub-grid-scale contribution.

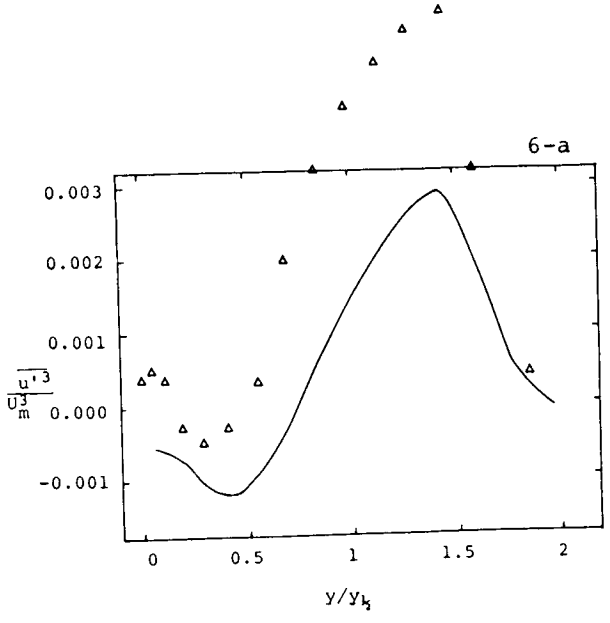

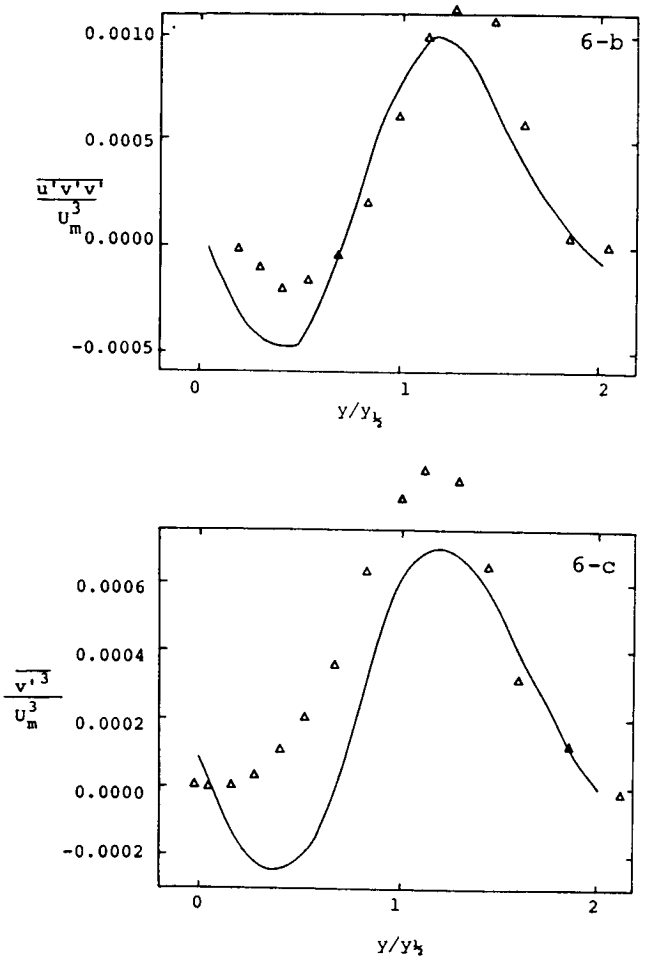

Figure 6. Triple velocity correlations in the wall jet: a) gives $u'u'u'$; b) gives $u'u'v'$, c) gives $v'v'v'$.

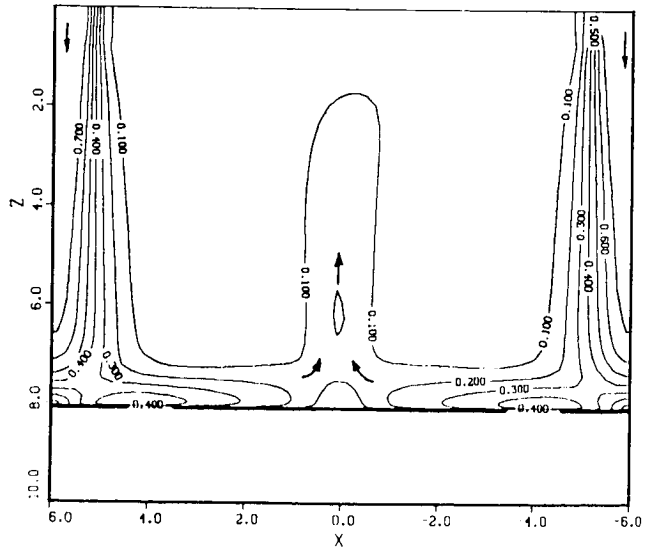

Figure 7. Mach number contours from a steady state k-ε calculation, which underpredicts the fountain spreading rate, from Ref. 5.

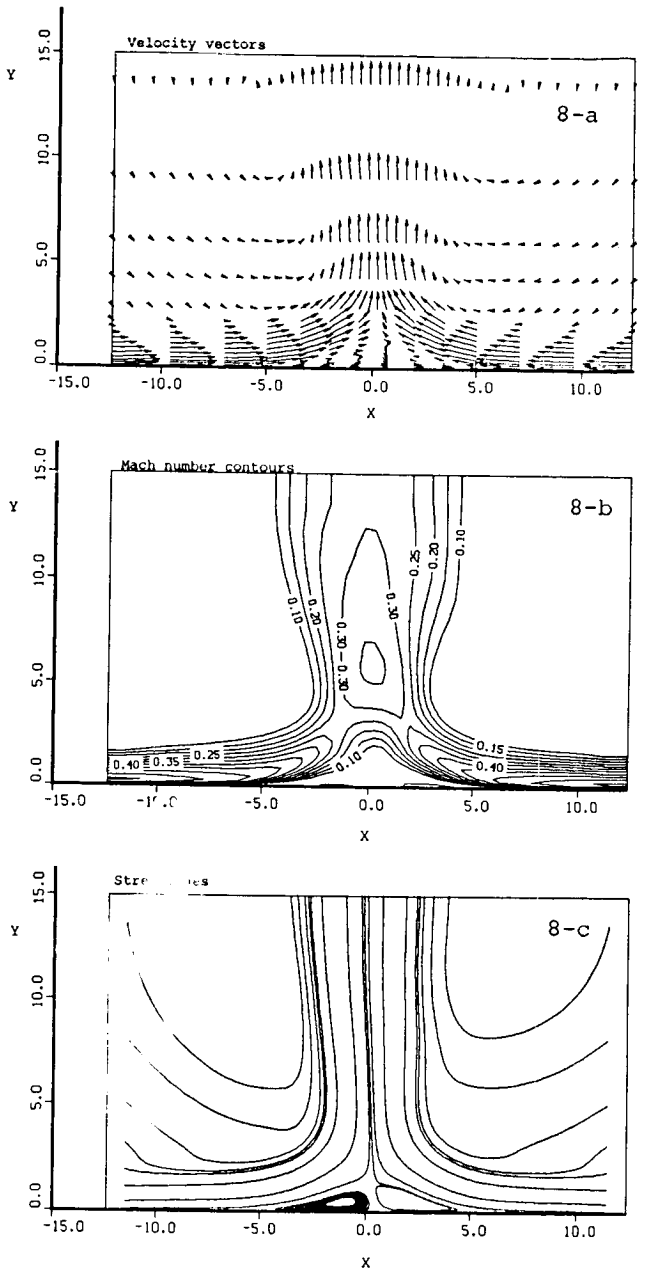

Figure 8. Mean results from unsteady fountain simulation: a) give velocity vectors; b) gives Mach number contours; c) gives streamline which show separation at base of fountain.

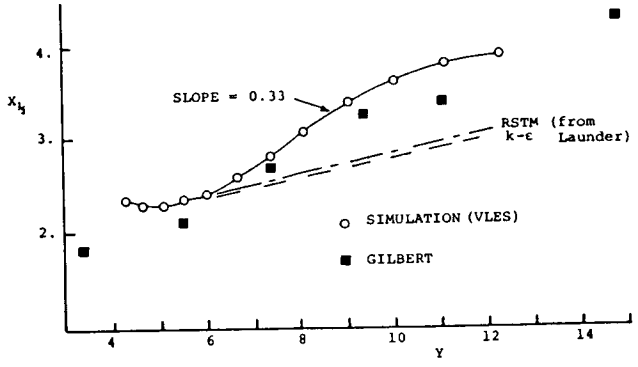

Figure 9. Half velocity width spreading rate in the fountain and comparison with data from Gilbert, Ref. 15.

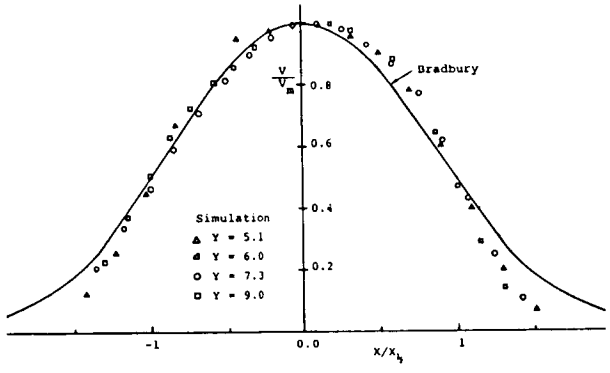

Figure 10. Mean velocity profiles in the fountain and comparison with "normal" plane jet, Ref. 17.

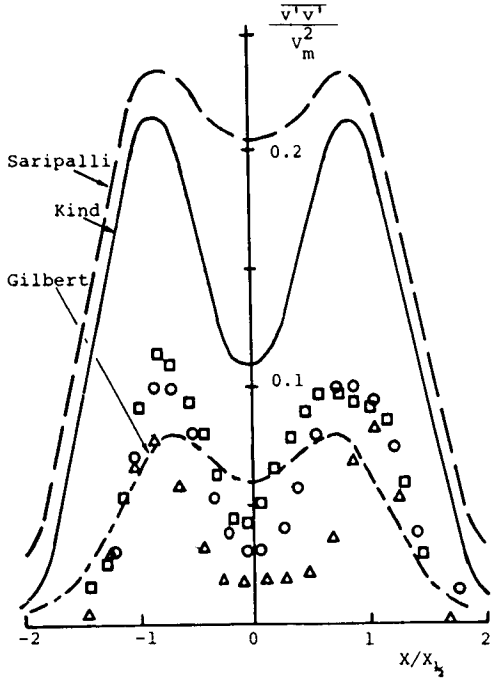

Figure 11. Streamwise normal stress, $\overline{v'v'}$, , in the fountain, comparison with Refs. 15 and 16; see Figure 10 for symbols.

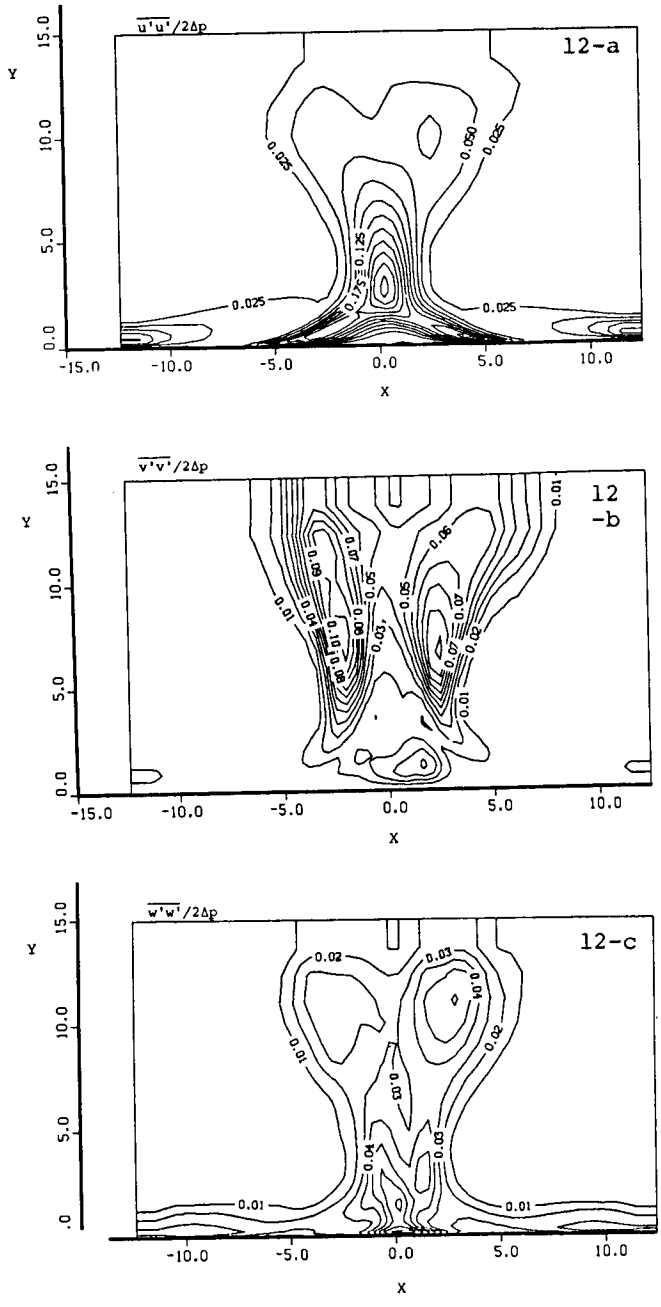

Figure 12. Contour plots of normal stresses: a) gives u´u´; b) gives v´v´; c) gives w´w´.

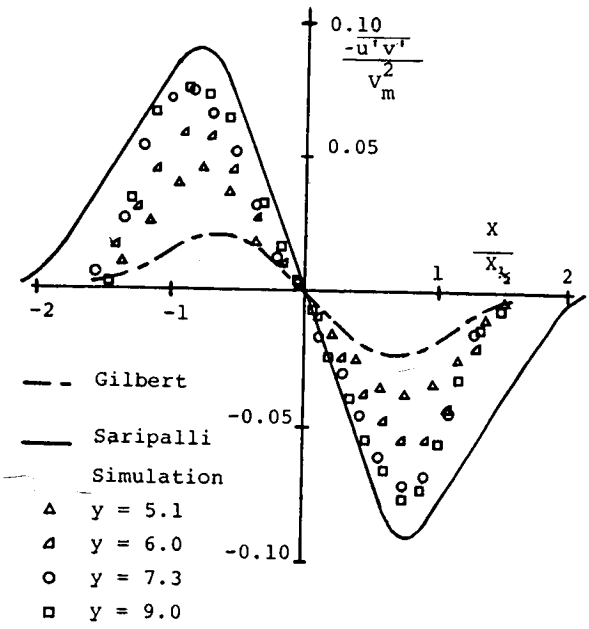

Figure 13. Shear stress in the fountain.

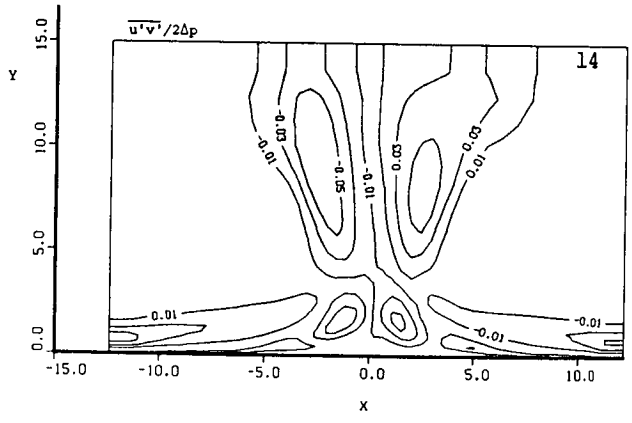

Figure 14. Contour plot of the shear stress, including SGS stress.

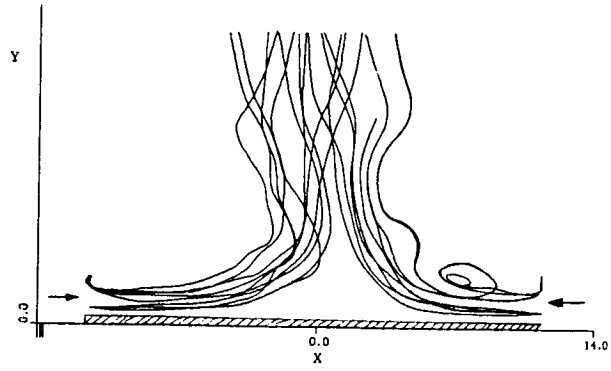

Figure 15. Tracer particles in an instantaneous flow field (see text).

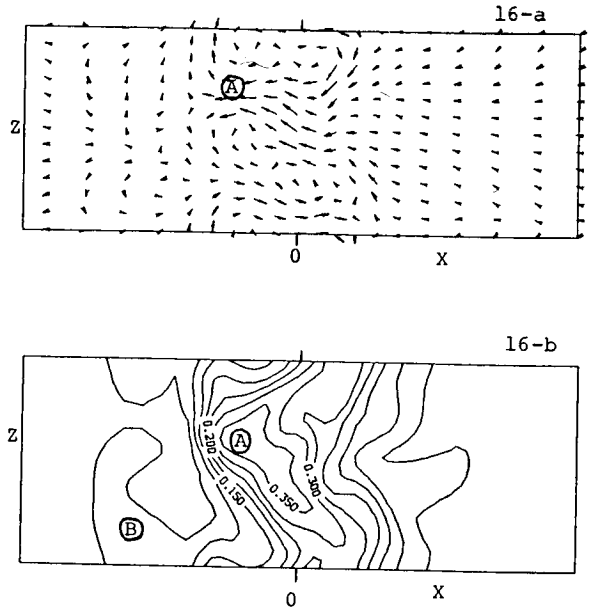

Figure 16. Instantaneous flow field in the fountain on a plane normal to the streamwise direction: a) gives velocity vectors; b) gives Mach number contours.

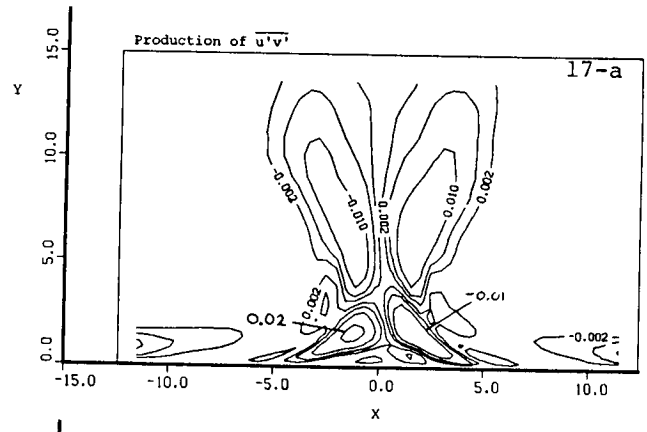

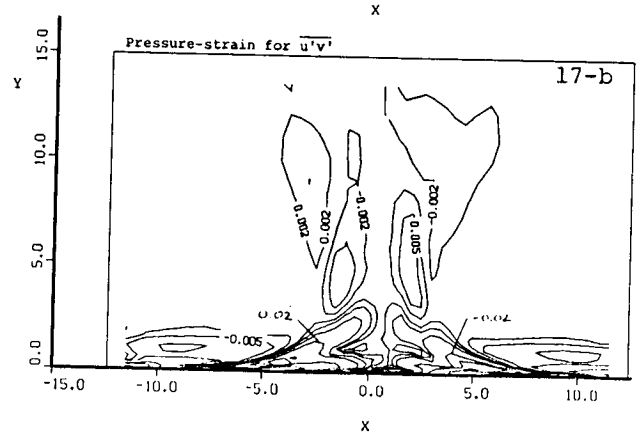

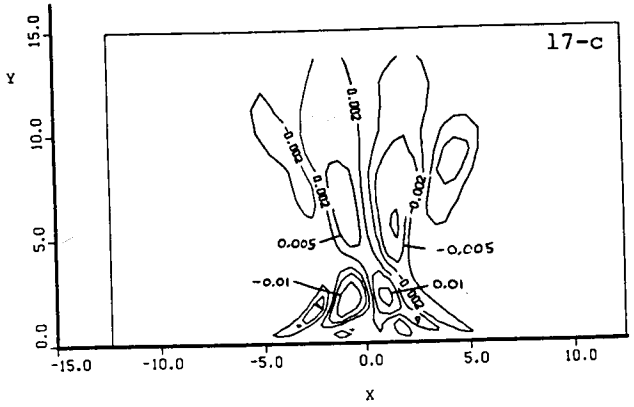

Figure 17. Terms in the Reynolds stress transport equation for $\overline{u'v'}$: ; a) production; b) pressure-strain; c) net gain or loss due to turbulent transport (term IV).

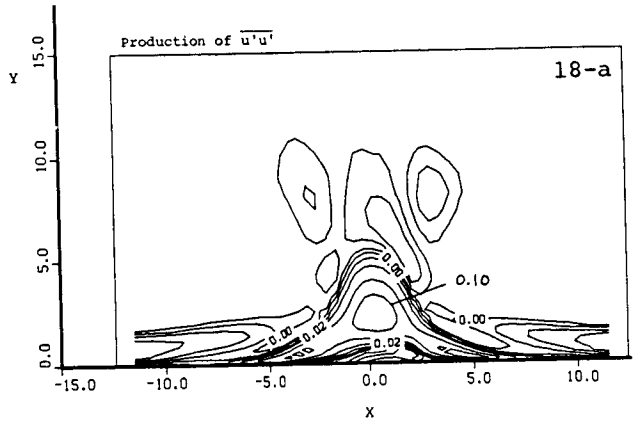

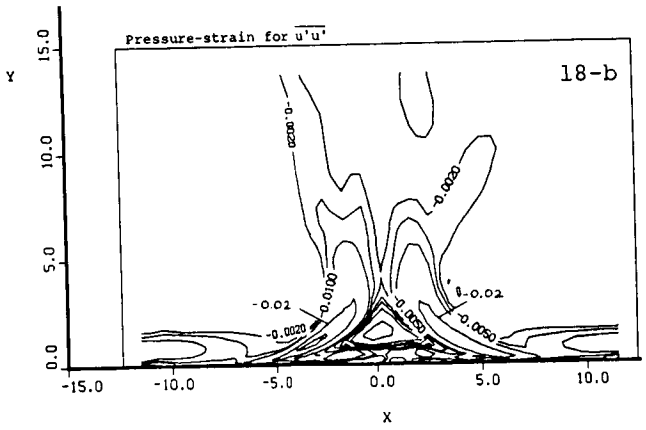

Figure 18. Terms in the Reynolds stress transport equation for $\overline{u'u'}$: a) production; b) pressure-strain.

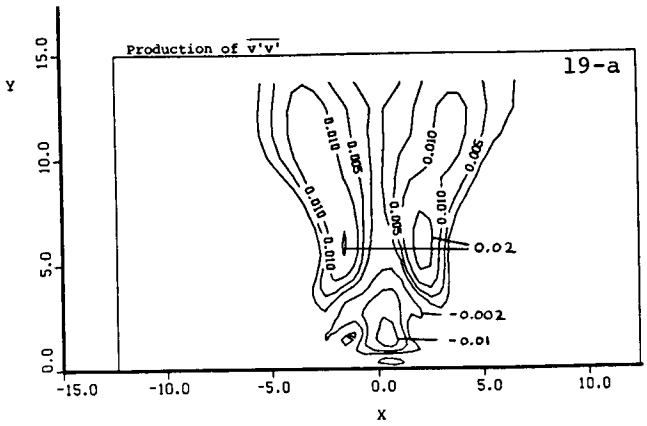

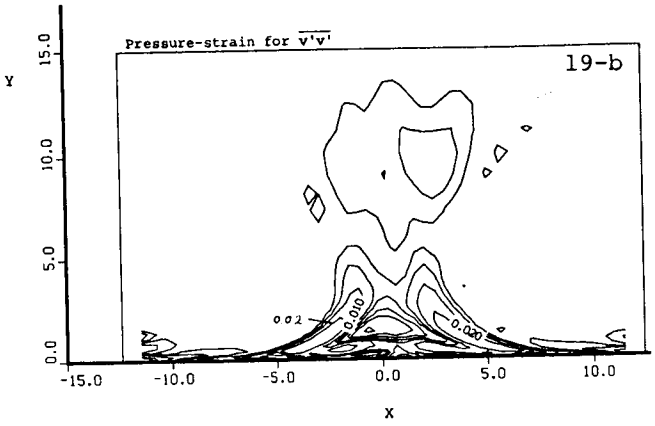

Figure 19. Terms in the Reynolds stress transport equation for $\overline{v'v'}$: a) production; b) pressure-strain.

SUMMARY OF STOL GROUND VORTEX INVESTIGATION*

Michael L. Billet

Applied Research Laboratory

The Pennsylvania State University

and

Marvin M. Walters

Naval Air Development Center

*This work was accomplished at the Applied Research Laboratory, The Pennsylvania State University under contract to the Naval Air Development Center.

List of Symbols

Symbol	
C_p	static pressure coefficient
D_j	inner diameter of jet
P_a	ambient pressure
P_o	maximum pressure in the impingement region
q_o	reference dynamic pressure, equal to $(P_o - P_a)$
V	velocity
V_j	velocity of jet at nozzle exit
V_o	reference velocity, equal to $\sqrt{\frac{2q_o}{\rho}}$
V	velocity at jet centerline
V_x	velocity in the x direction
V_z	velocity in the z direction
V_∞	wind tunnel velocity
Z_i	jet impingement point
Z_{le}	vortex maximum penetration point
Z_s	vortex separation point
λ^*	reference jet-to-crossflow velocity ratio = $\frac{V_o}{V_\infty}$

Introduction

The impingement of a concentrated circular jet exhaust flow on a ground plane results in the formation of a wall jet which flows radially from the point of impingement along the ground surface. Forward motion of the jet source or the introduction of a counter-flowing freestream interacts with the wall jet to create a stagnation line and tends to roll the wall jet back on itself forming a horseshow-shaped ground vortex, as illustrated in Figures 1 and 2. Generally taking the shape of an ellipse whose major axis is aligned with the freestream flow the location of this stagnation line is dependent on the relative velocity of the freestream and wall jet flows and the injection angle of the jet exhaust into the freestream flow. The location of the vortex is nearly coincident with the stagnation line but at a height above the ground which is also a function of the relative velocities of the jet and freestream flows. When flow conditions are appropriate for its formation, this vortex is a major source of the induced flow in the near field.

An experimental facility has been developed in the 1.23 m (48-inch) wind tunnel of the Applied Research Laboratory at The Pennsylvania State University to model this ground vortex. The purpose of this facility is to study the affect of various parameters on the location and characteristics of a ground vortex.

Previous studies concerning this type of flow are few and very limited in scope. Colin and Olivari [1] have experimentally determined the location and established the elliptical shape of the vortex line for one nozzle height. In addition a dimensionless relationship was proposed between the vortex separation point and the ratio of wall jet velocity at the impingement point

to the cross flow velocity. Parameters such as the presence or absence of a boundary layer on the ground plane have also been shown to influence the location of the ground vortex [2,3]. A recent survey on ground effects and testing techniques is given by Kuhn [4].

A recent effort by Stewart and Kuhn [5] to develop a prediction method for STOL ground effects indicated the need to not only establish the location of the ground vortex as it varies with parameters but also the strength of the resulting vortex. As a result, an experimental investigation was conducted in the 1.23 m (48-inch) wind tunnel into the formation, stability and strength of the ground vortex for several flow parameters. The intent of this paper is to summarize the design of the facility, special instrumentation and results.

Experimental Facility

All tests were conducted in the subsonic wind tunnel. This facility is a closed-circuit, closed-jet wind tunnel with an octagonal test section which is 1.2 m (4.0 ft) across and is 4.9 m (16.0 ft) long. The test section velocity can be varied continuously up to 36.6 m/s (120 ft/sec) and honeycombs and screens in the settling sections reduces the turbulence level in the test section to be less than 0.10 percent of the free stream velocity.

A 76.2 mm (3.00-inch) diameter open-jet was fabricated and inserted through one side of the test section as shown in Figure 3. The jet features a 16.0 to 1.0 contraction ratio and is equipped with two wire mesh screens and a honeycomb to reduce turbulence. The 45.7 m/s (150 ft/sec) jet was powered by a variable speed 3.7 kW (5-hp) blower which injested air from the wind tunnel at a port far downstream from the test camber.

The test facility was formed by two vertically mounted 2.4 m (8.0 ft) long wooden panels with circular arc leading edges. The jet tube extended

152.4 mm (6.0 inches) through the center of one of the panels. The movable ground board shown in Figure 4 was designed to facilitate conducting the various phases of the test program. The ground board was located between horizontal ceiling and floor inserts and could be positioned at 1, 2, 3, 4, or 6 jet diameters from the jet exit plane. At each position it could be moved and flared to control the static pressure gradient due to the wall boundary layer growth. In addition, a slot was included on the ground board for boundary layer control. The ground board was also equipped with interchangeable .6 m x .9 m (2 ft x 3 ft) window inserts. Three windows were available for various phases of the test program, i.e., a glass with fluorescent mini-tufts, a glass window for LDV surveys, and a plexiglass window instrumented with static pressure taps.

Instrumentation

The jet velocity was monitored via 3.17 mm (0.125-inch) diameter kiel probe in the plenum section and a static pressure tap in the wall of the jet tube. The wind tunnel velocity was measured by a 3.17 mm (0.125-inch) diameter pitot-static probe mounted on the floor insert midway between the sidewalls outside of all wall boundary layers. For the wall-to-wall flow surveys a miniature five-hole probe [8] fabricated at ARL/PSU was utilized. In addition, this five-hole probe was also used to determine the mean velocity jet characteristics and a single element hot wire anemometer was used to determine the turbulence characteristics. It is important to note that the jet characteristics were determined with the ground plane removed and the wind tunnel separated at points A and B as annotated in Figure 3.

Flow visualization tests to locate the separation line and the forward extent of the recirculation bubble on the ground plane were conducted with a

large matrix of fluorescent mini-tufts on the ground plane. This technique which was originally developed by Crowder [8] and was extended by Stinebring and Treaster [9] uses extremely fine fluorescent monofilament fibers [(0.178 mm 0.007-inch diameter)]. These fibers are attached to the window by a tiny drop of cyano-acrylate glue and illuminated by an ultraviolet light source to map the flow.

The static pressure distribution on the ground plane was measured via window insert having static pressure taps. In all, 56 static pressure taps having 0.787 mm (0.031-inch) diameter holes were used as shown in Figure 5.

All pressures in this test program were measured with individual transducers which could be sampled electronically. The temperature of the test environment was determined with a temperature probe and recorded as one of the input channels. All data were acquired on-line via the VAX 11-782 computer system which permitted on-site graphic terminal display of the primary and reduced test parameters and later hard copy output of the selected data.

Details of the ground vortex velocity field were determined by a five-beam, three-component laser Doppler velocimeter system. The system measured three velocity components at the crossing of three green beams and two blue beams by collecting the light scattered by the seeded particles in the flow. Thermal Systems, Inc., optics with a four-watt Lexal Argon-Ion laser was mounted on a three-axis traverse as shown in Figure 6. The digital output of the three counter processors were processed in a VAX 11-782 computer. The computer produces histograms of the measured velocities and computes the statistics of the flow including the mean velocity and turbulence intensity.

Summary of Experimental Results

Jet Characteristics

Velocity surveys to measure jet characteristics were conducted at x/D_j = 1.0, 2.0, 3.0, 4.0, and 6.0 with V_j = 45.7 m/s (150 ft/sec) across its potential core. The axisymmetric velocity profiles obtained with a 5-hole probe are shown in Figure 7 for the vertical plane. The surveys in the horizontal plane are virtually identical since the jet is axisymmetric. Shown in Figure 8 are turbulence measurements acquired by using hot-wire anemometry at x/D_j = 2.0. The turbulence intensity at the centerline and at x/D_j = 2.0 was experimentally measured to be less than 2%. The impingement point of the jet on the ground plane depends on the jet-to-crossflow velocity ratio (V_∞/V_j) and ground plane position (x/D_j). The variation of the jet impingement point with ground plane position for various jet-to-crossflow velocity ratios is shown in Figure 9.

Test Chamber Characteristics

The ground board location relative to the ground vortex location was varied longitudinally so that the LDV surveys could be centered at a position approximately 101.6 mm (4-inches) downstream of the window's leading edge. Thus, wall-to-wall surveys were conducted with no jet flow at the five x/D_j locations and crossflow velocities of 4.6, 9.1, 13.7, and 18.3 m/s (15, 30, 45, and 60 ft/sec). The data for 18.3 m/s (60 ft/sec) and x/D_j = 2.0 are shown in Figure 10 and is representative of the other velocity and location data. It is important to note that these survey data were obtained with the boards flared as to minimize the pressure gradient, and as the data of Figure 10 indicates, a uniform pressure from wall to wall was achieved.

Ground Vortex Position

The window instrumented with the fluorescent minitufts was used to obtain a first-order measurement of the ground vortex location. Photographs such as shown in Figure 11 were utilized to obtain the location of the separation line and the leading edge of the recirculating region (Z_{le}) on the ground board as shown in Figures 12-15. Z_s and Z_{le} were measured from the impingement point of the jet. The summary of the vortex position data are shown in Figures 16 and 17. In addition, data from tests conducted at Rockwell [10] are also included in Figure 17 and are shown to be in very good agreement. Several of the Z_{le} values at $V_\infty/V_j = 0.3$ and 0.4 were no longer on the viewing window as indicated in Table 1 which tabulates the various vortex parameters for each flow condition. Vortex oscillations were also noted and were most pronounced at $V_\infty/V_j = 0.1$ and 0.2.

Colin and Olivari [1] derived a dimensionless relationship between the vortex separation point and the ratio of wall jet velocity at the impingement point to the cross flow velocity. This relationship was derived by assuming that the energy in the wall jet equals the energy in the cross flow at the point of separation and is

$$\frac{Z_s}{D_j} = 1.03\ \lambda^{*0.9} \qquad (1)$$

where Z_s = vortex separation point and λ = reference jet-to-cross flow velocity ratio. Using the ground plane pressure data recorded earlier, the vortex separation point (Z_s) was calculated by Equation (1). These values are compared to theoretical values and flow visualization in Figure 18. Very good agreement was found although the boundary layer on the ground plane varied from 12.7 to 95.2 mm (0.5 to 3.75 inches) for the present study.

Laser Doppler Velocimeter Data

The 3-component LDV was utilized to measure the vortex velocity field on the ground plane. Initially, the shape of the vortex was visualized by micron particulate as they pass through a laser-light sheet. Photographs indicate that the vortex appears to be nonsymmetrical. In addition, flow visualizations indicated that very few of the cross-flow seeded particulate appeared in the core of the vortex structure where as most of the jet seeded particulate appeared in the core. Additional flow visualization tests are planned to document these particle trajectories.

Traverses through the center region of the vortex are shown in Figures 19-21 for the case of V_∞/V_j = 0.1, 0.2 and x/D_j = 3.0. Velocities in the wall jet region were measured to be approximately twice the velocities measured in the opposing cross-flow region. This result notes a nonuniform energy distribution as opposed to the classical free vortex shape.

Summary of Investigation

A test facility suitable for the study of the ground vortex resulting from a jet impinging on a ground board in the presence of a cross-flow has been developed. The aerodynamic characteristics of the test chamber and jet have been determined. Data on the ground plane static pressure distributions and flow patterns were obtained for many flow conditions. Experimental data have confirmed Colin and Olivaris model. LDV measurements of the ground vortex indicates a nonsymmetric velocity distribution. In addition, the velocity field appears to have oscillations.

The data reported in this paper represents only some of the test results. More detailed velocity data of the ground vortex are currently being obtained with the LDV system. In addition more tests are currently being planned to determine the influence of incoming ground board boundary layer on the vortex location and characterize the stability of the ground vortex.

References

[1] Abbott, W. A., "Studies of Flow Fields Created by Vertical and Inclined Jet When Stationary or Moving Over a Horizontal Surface," RAE CP No. 911, 1967.

[2] Colin, P. E. and Olivari, D., "The Impingement of a Circular Jet Normal to a Flat Surface With and Without a Crossflow," Von Karman Institute for Fluid Dynamics, Rhode-St. Genese Belgium, January 1969.

[3] Crowder, J. P., "Add Fluorescent Mini-Tufts to the Aerodynamicists Bag of Tricks," Astronautics and Aeronautics, Vol. 18, November 1980, pp. 54-56.

[4] Kuhn, R. E., "V/STOL and STOL Ground Effects and Test Techniques," NASA No. NAS2-11912, December 1984.

[5] Schwantes, E., "The Recirculation Flow Field of a VTOL Lifting Engine," NASA TT F-14912, June 1973.

[6] Stewart, V. E. adn Kuhn, R. E., "A Method for Estimating the Propulsion Induced Aerodynamic Characteristics of STOL Aircraft in Ground Effects," NADC-80226-60, April 1982.

[7] Steward, V. and Kuhn, R., "A Method for Estimating the Propulsion Induced Aerodynamic Characteristics of STOL Aircraft in Ground Effects," NADC Report No. 80226-60, Vol. 2, August 1983.

[8] Stinebring, D. R. and Treaster, A. L., "Water Tunnel Flow Visualization by the Use of Fluorescent Mini-Tufts, The Applied Research Laboratory, TM No. 83-24, March 1983.

[9] "Treaster, A. L. and Yocum, A. M., "The Calibration and Application of Five-Hole Probes," ISA Transactions, Vol. 18, No. 3, 1979, pp. 23-24.

TABLE 1. GROUND VORTEX DIMENSIONS

V_∞/V_j	Z_i/D_j	Z_s/D_j	Z_u/D_j
$X/D_j = 1.0$			
0.1	0.00	4.25	7.75
0.2	0.00	2.75	5.25
0.3	0.00	2.25	4.75
0.4	0.00	1.50	3.25
$X/D_j = 2.0$			
0.1	0.00	4.00	6.25
0.2	0.00	2.75	4.25
0.3	-0.25	1.50	2.75
0.4	-1.00	0.00	2.25
$X/D_j = 3.0$[(a)]			
0.1	0.00	5.50	7.75
0.2	-0.75	2.00	3.75
0.3	-1.00	0.25	2.25
0.4	*****	*****	1.00
$X/D_j = 4.0$[(a)]			
0.1	-0.50	5.75	8.25
0.2	-1.50	0.75	3.00
0.3	-2.75	*****	1.50
0.4	*****	*****	*****
$X/D_j = 6.0$[(a)]			
0.1	-0.5	4.50	7.50
0.2	-3.25	-2.25	1.75
0.3	*****	*****	*****
0.4	*****	*****	*****

(a) ***** indicates that the ground vortex was blown downstream off of the tuft window.

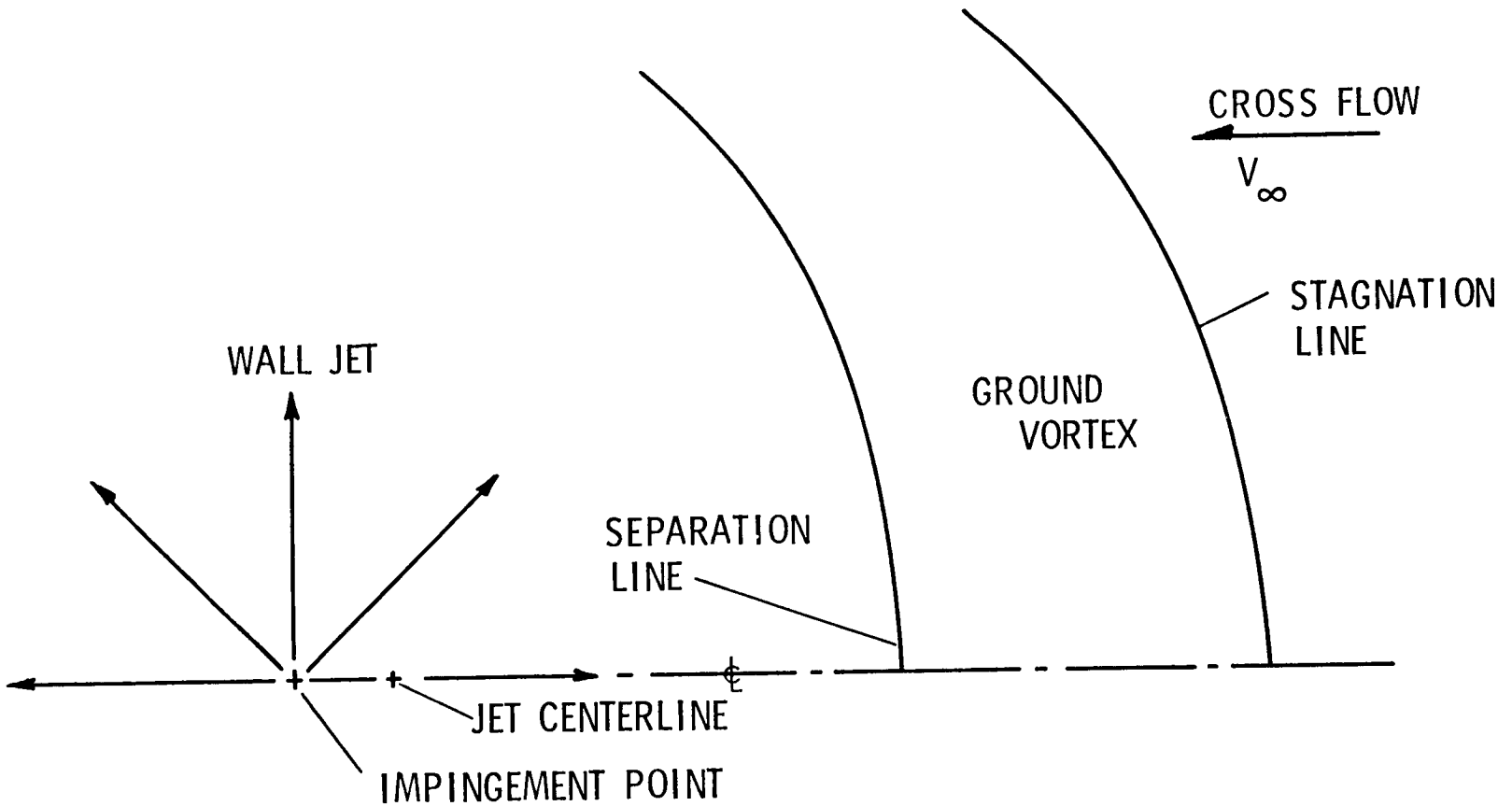

Figure 1. Top View of Ground Plane Flow Pattern

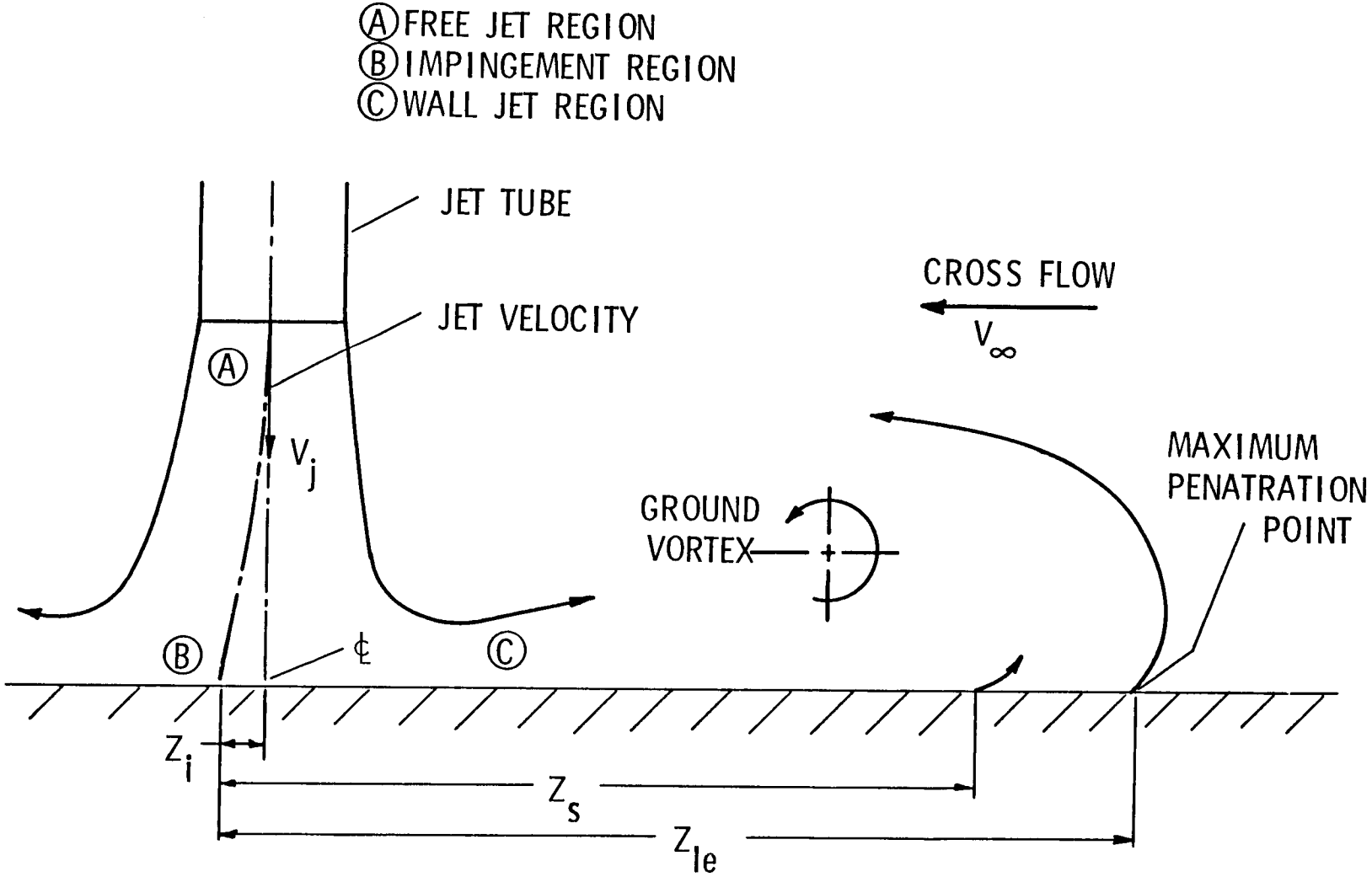

Figure 2. Vortex Formed by a Jet Impinging Normally on a Flat Plate in a Cross Flow

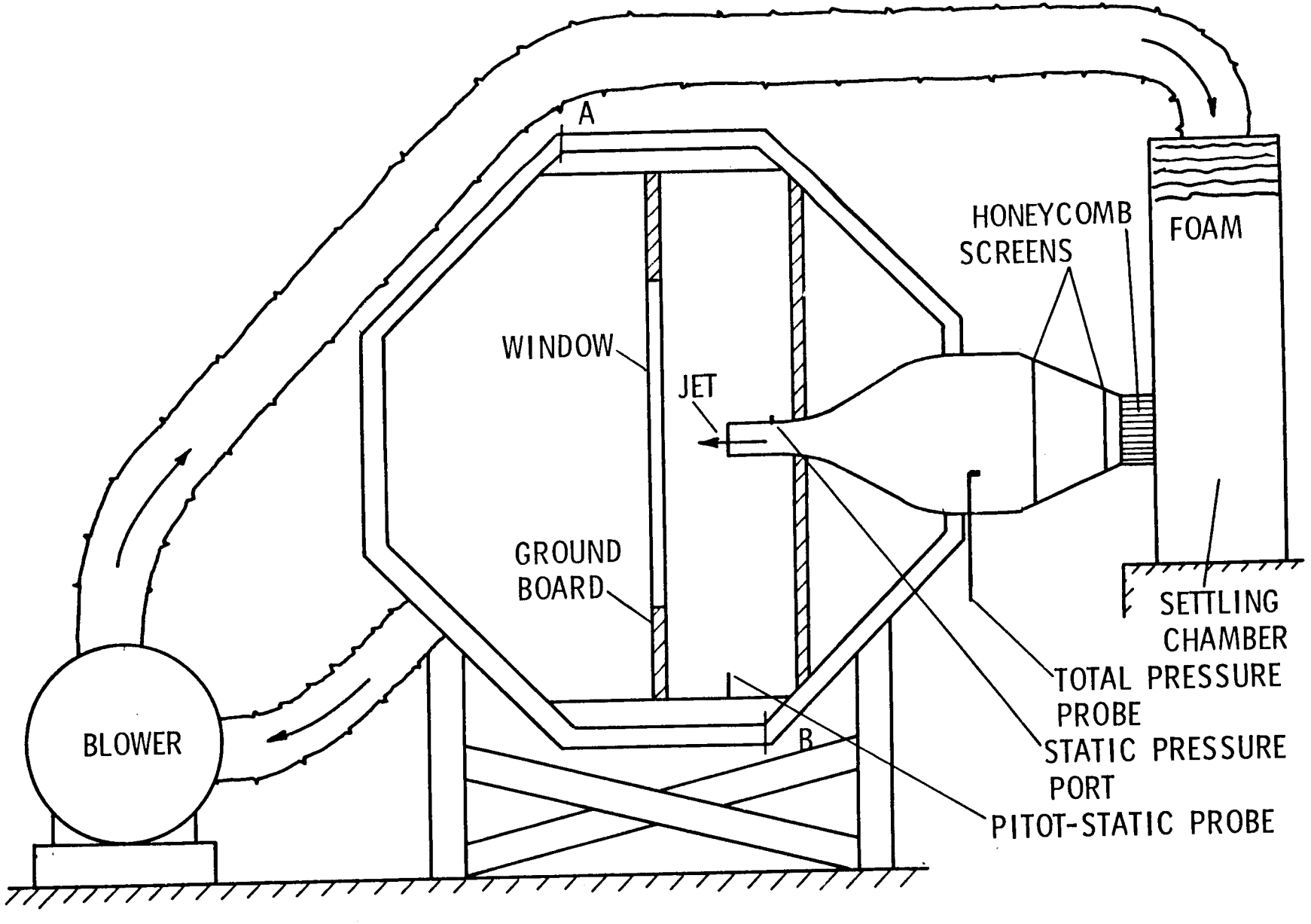

Figure 3. Jet Installation in Wind Tunnel

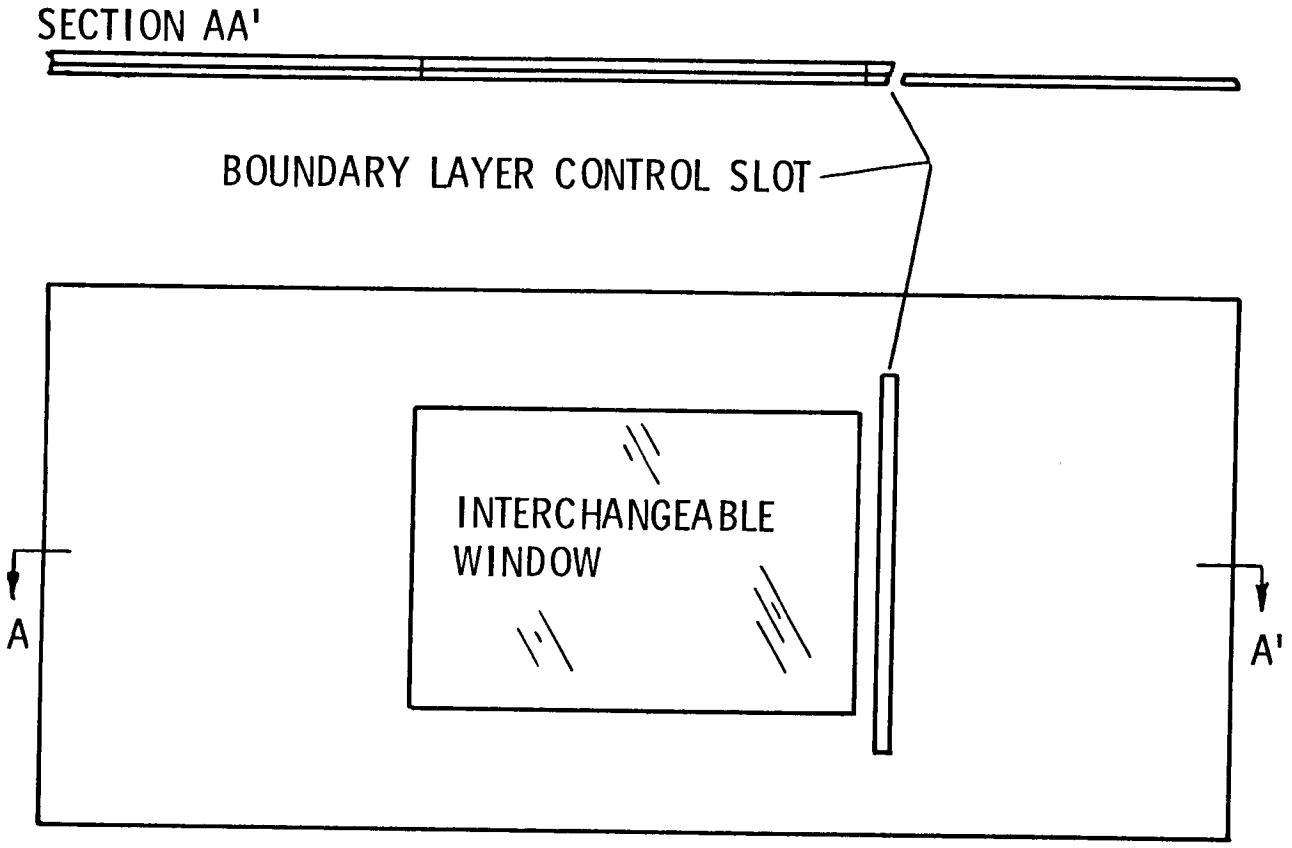

Figure 4. Ground Plane Configuration

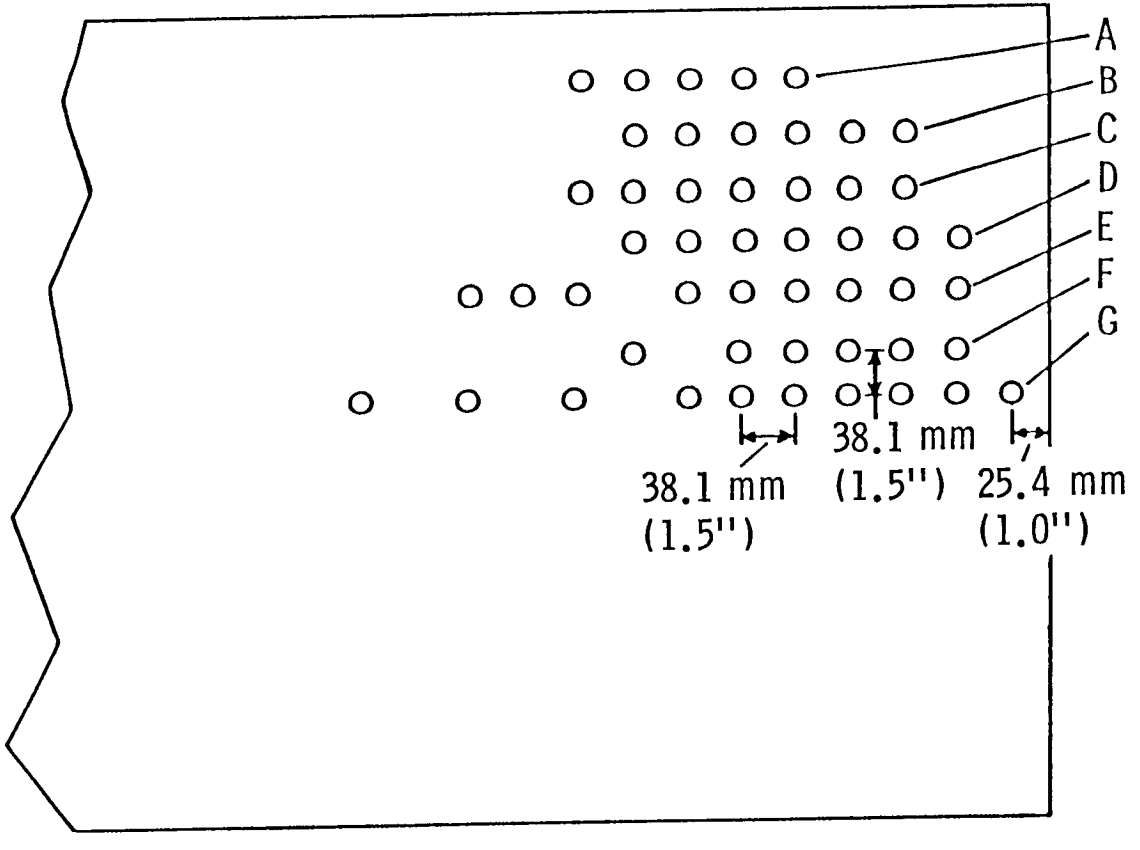

Figure 5. Pressure Window

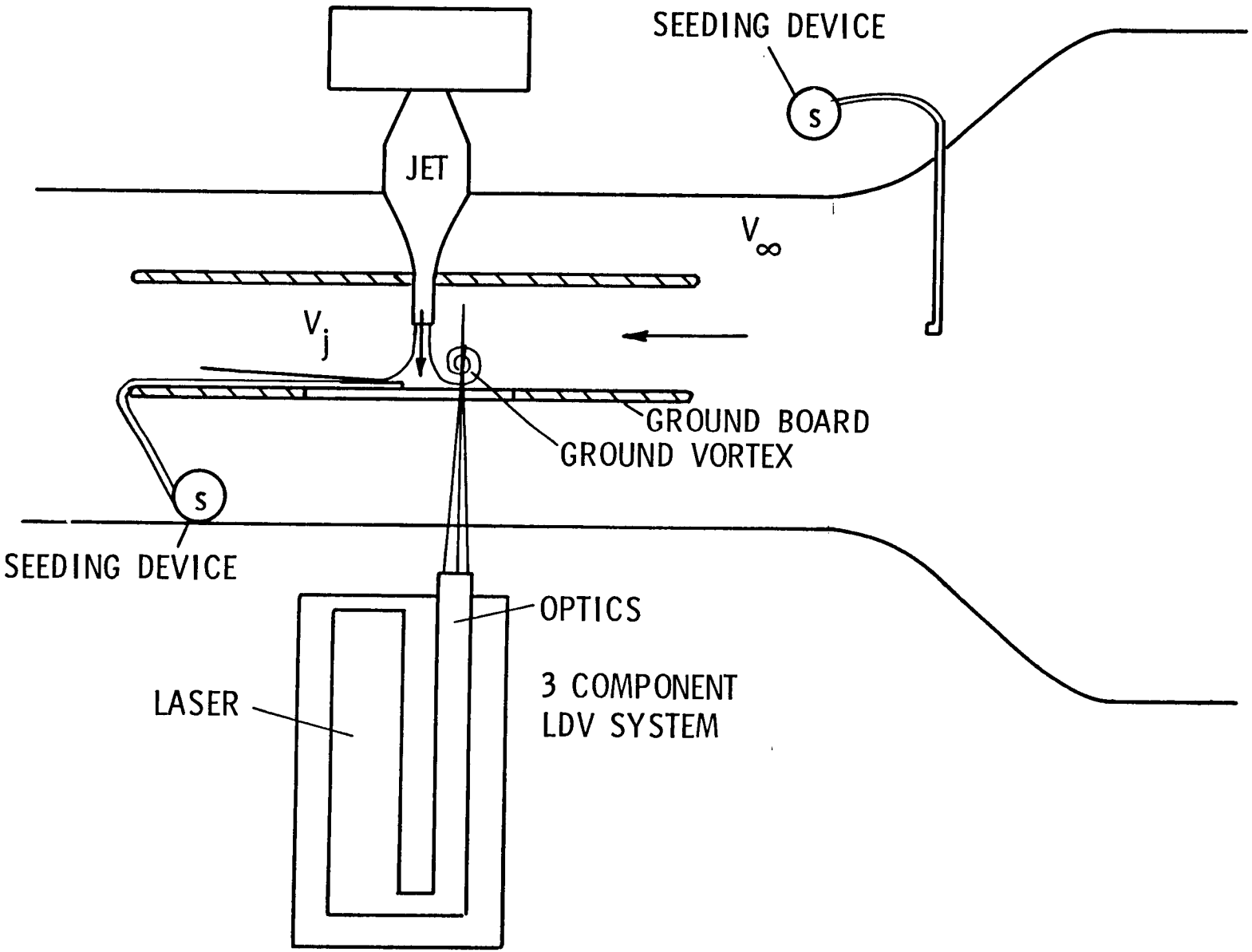

Figure 6. Laser Installation

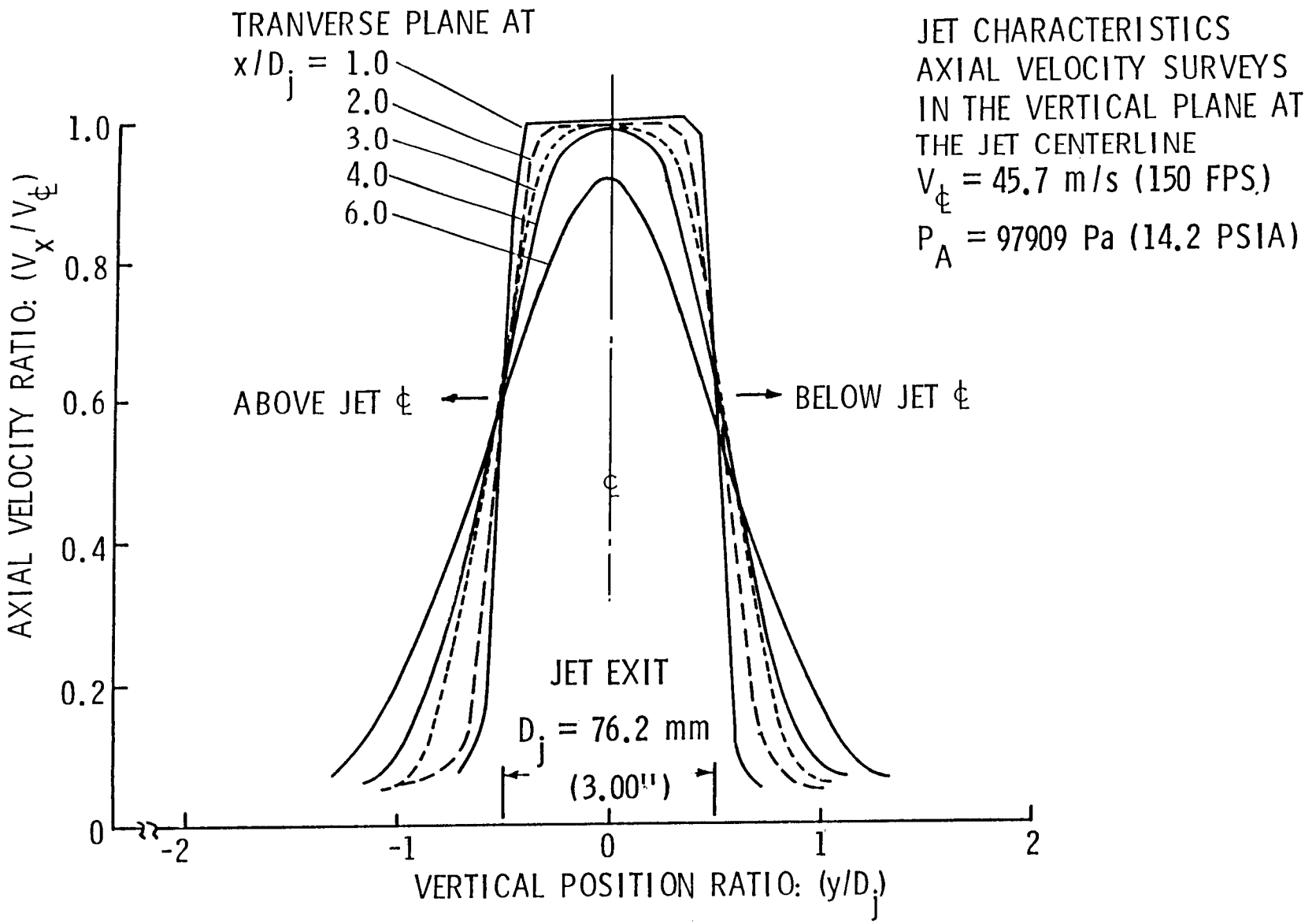

Figure 7. Jet Characteristics -- Velocity Surveys

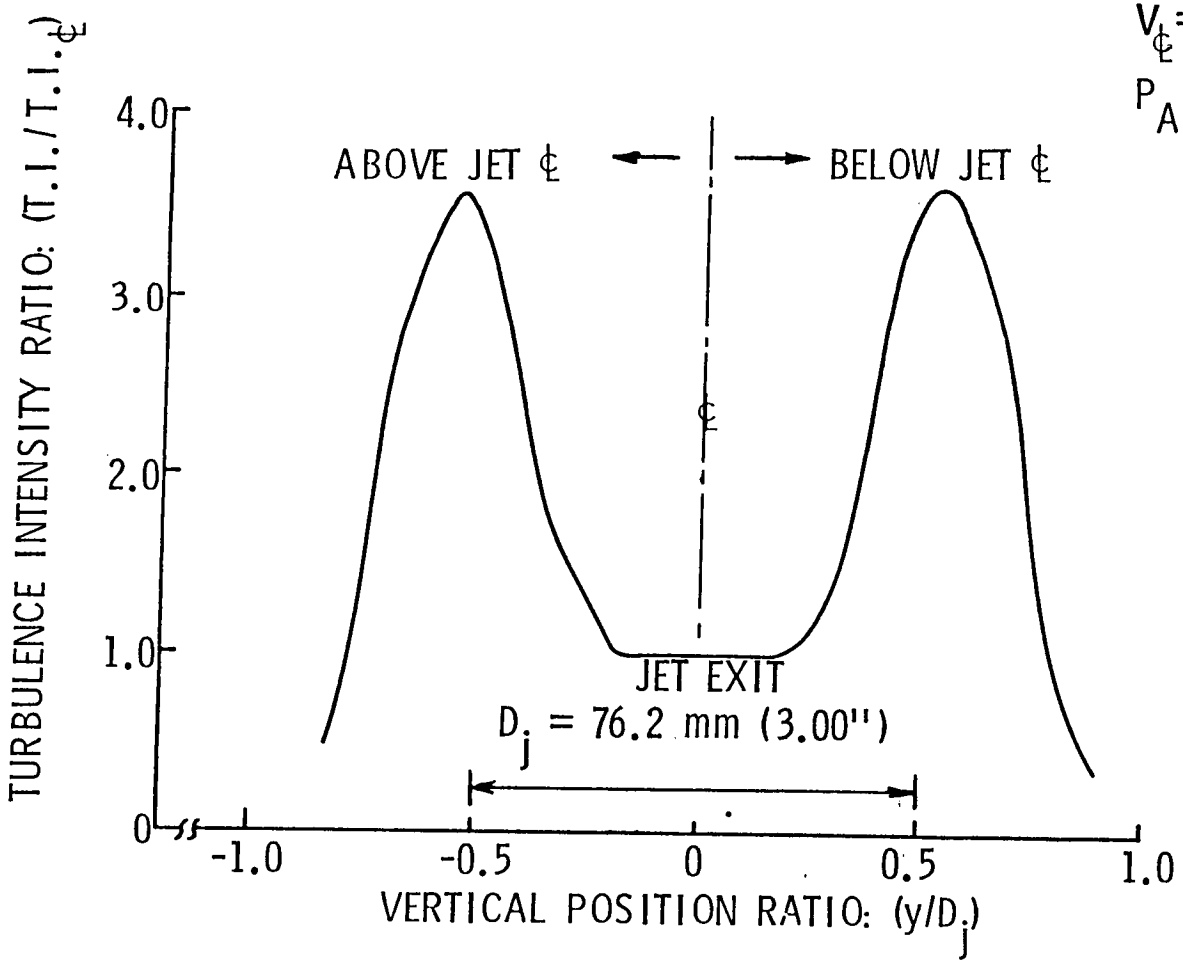

Figure 8. Jet Characteristics -- Turbulence Surveys

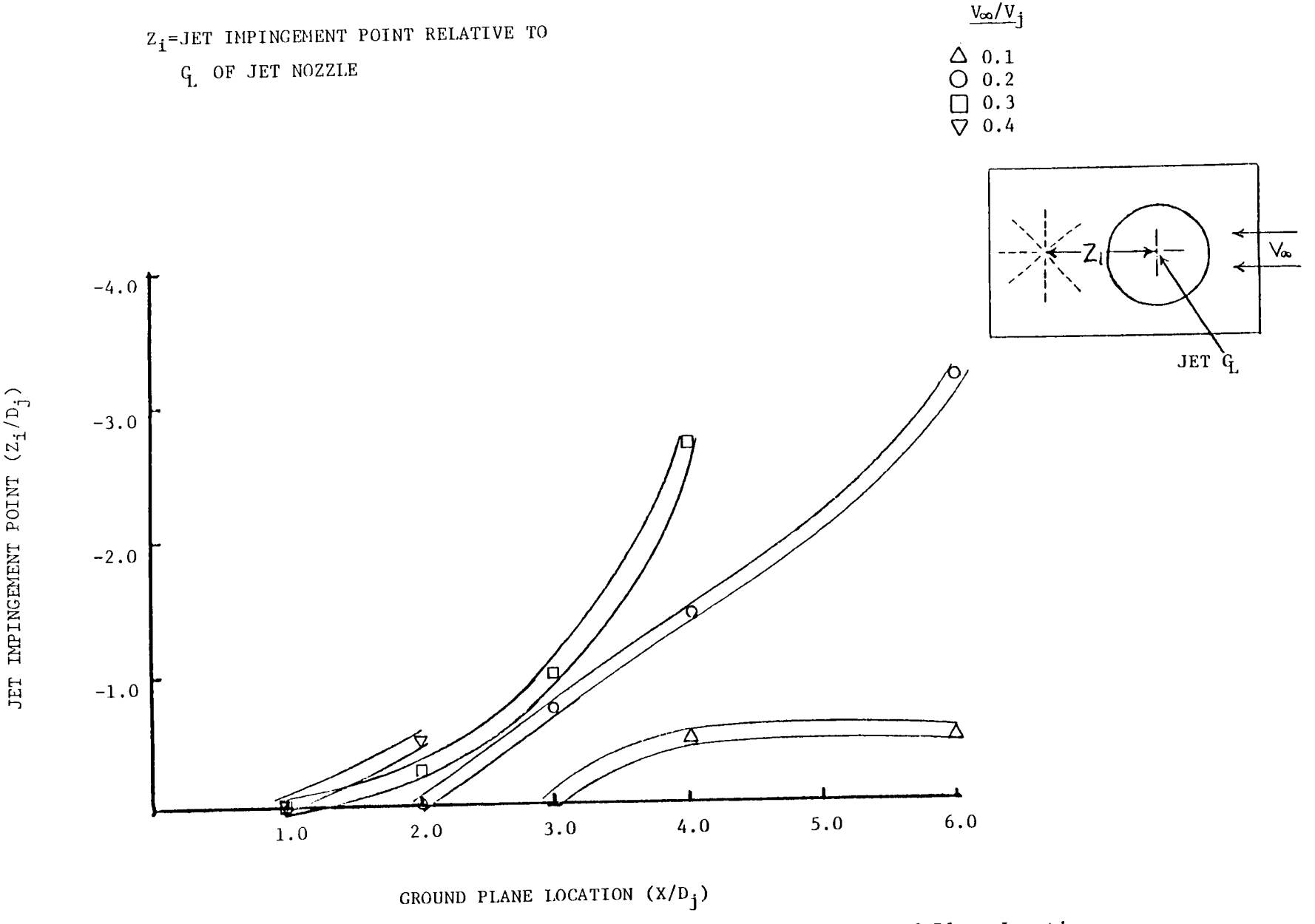

Figure 9. Variation of Jet Impingement Point With Ground Plane Location

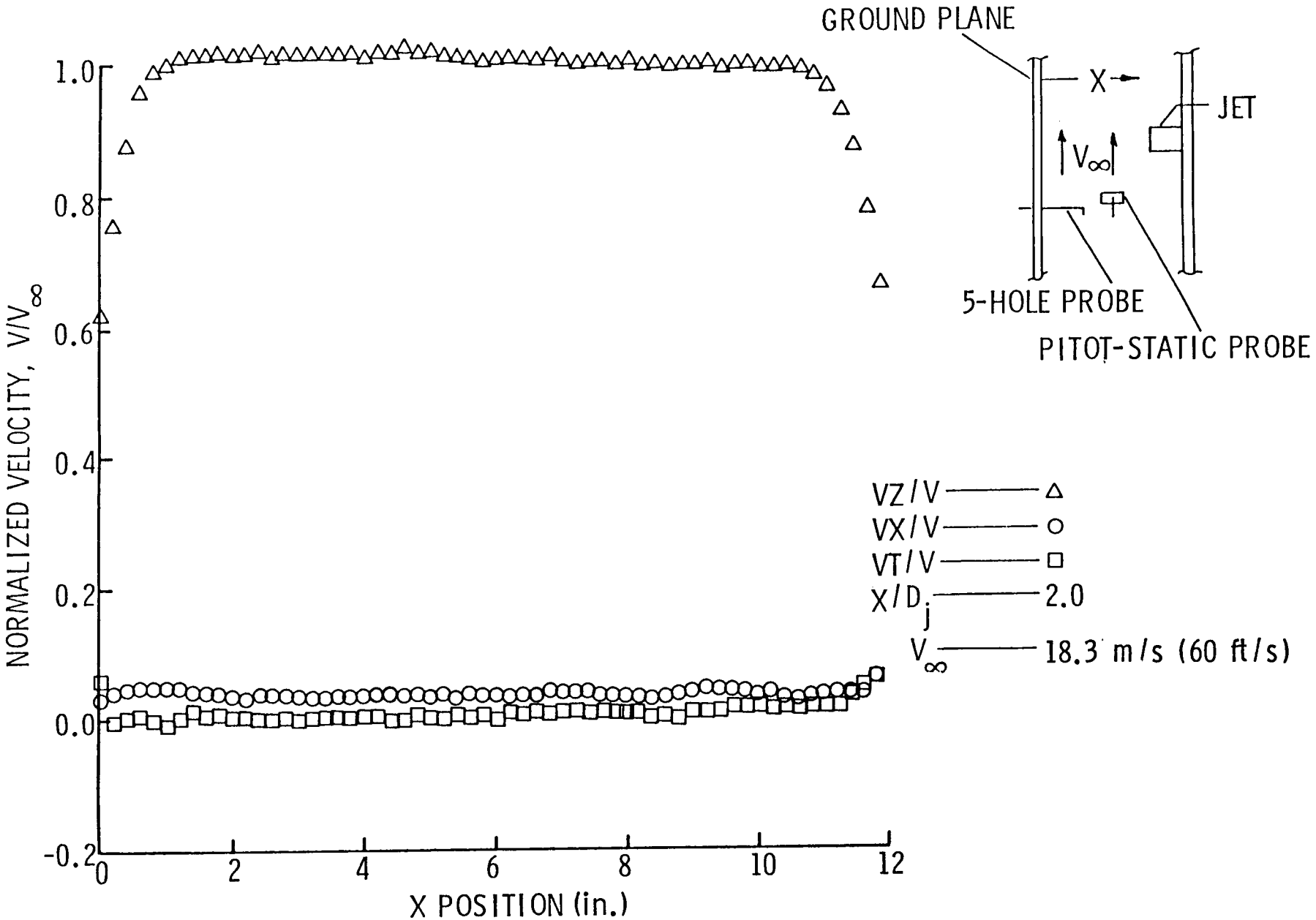

Figure 10. Test Section Velocity Surveys - $\frac{2C_{ps}}{2x} < .006$

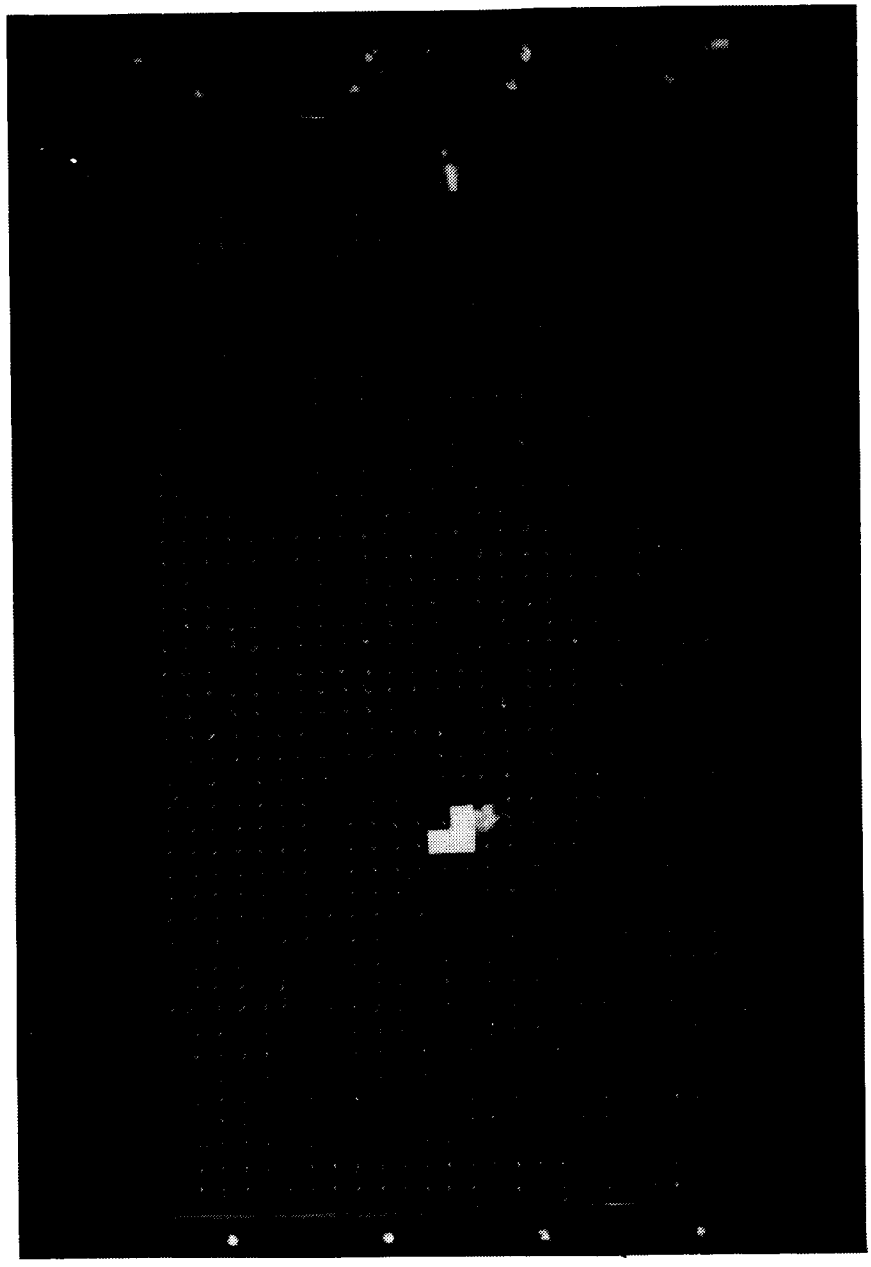

Figure 12. FLOW VISUALIZATION ($X/Dj = 3.0$; $V_\infty/V_j = 0.1$)

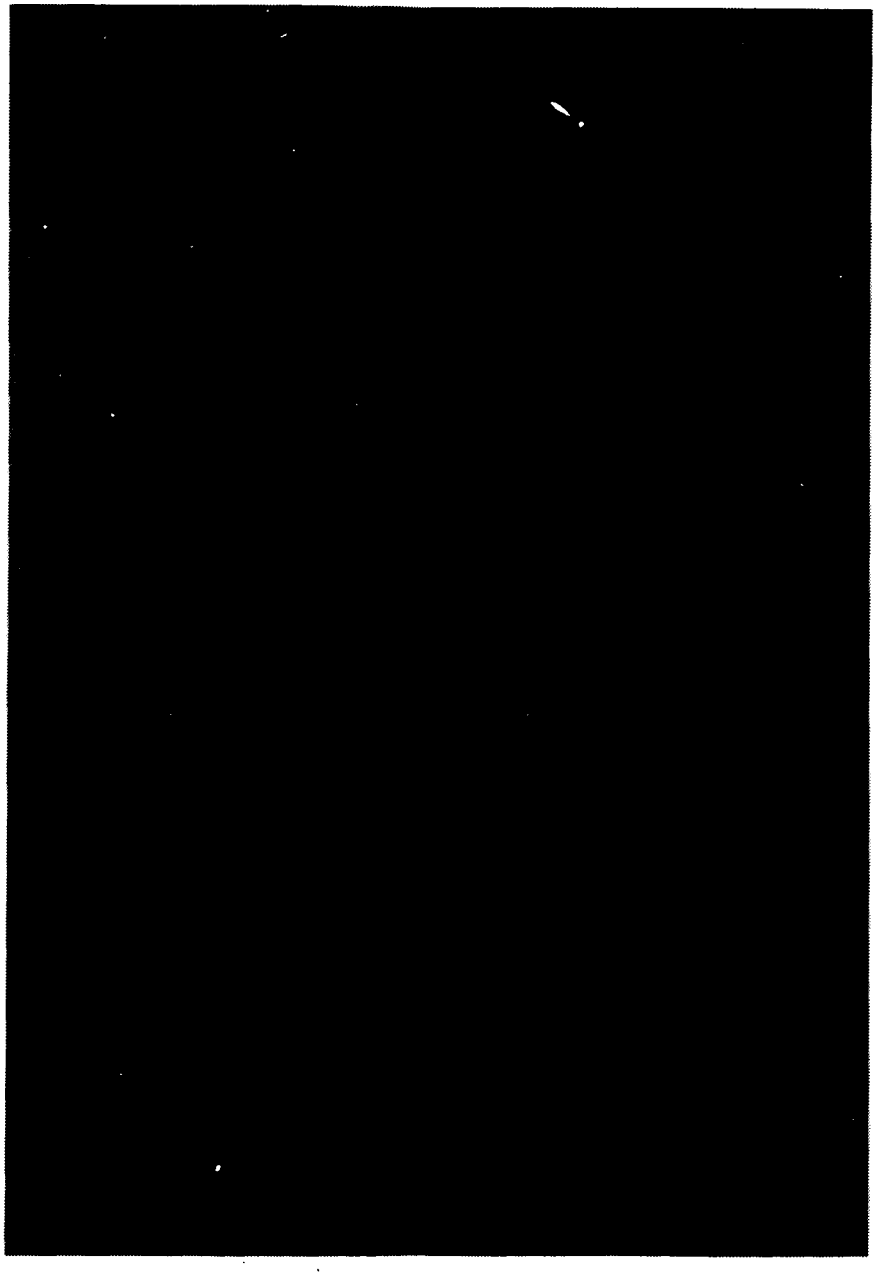

Figure 11. Flow Visualization - Mini Tufts (X/D_j = 2.0; V_∞/V_j = 0.3)

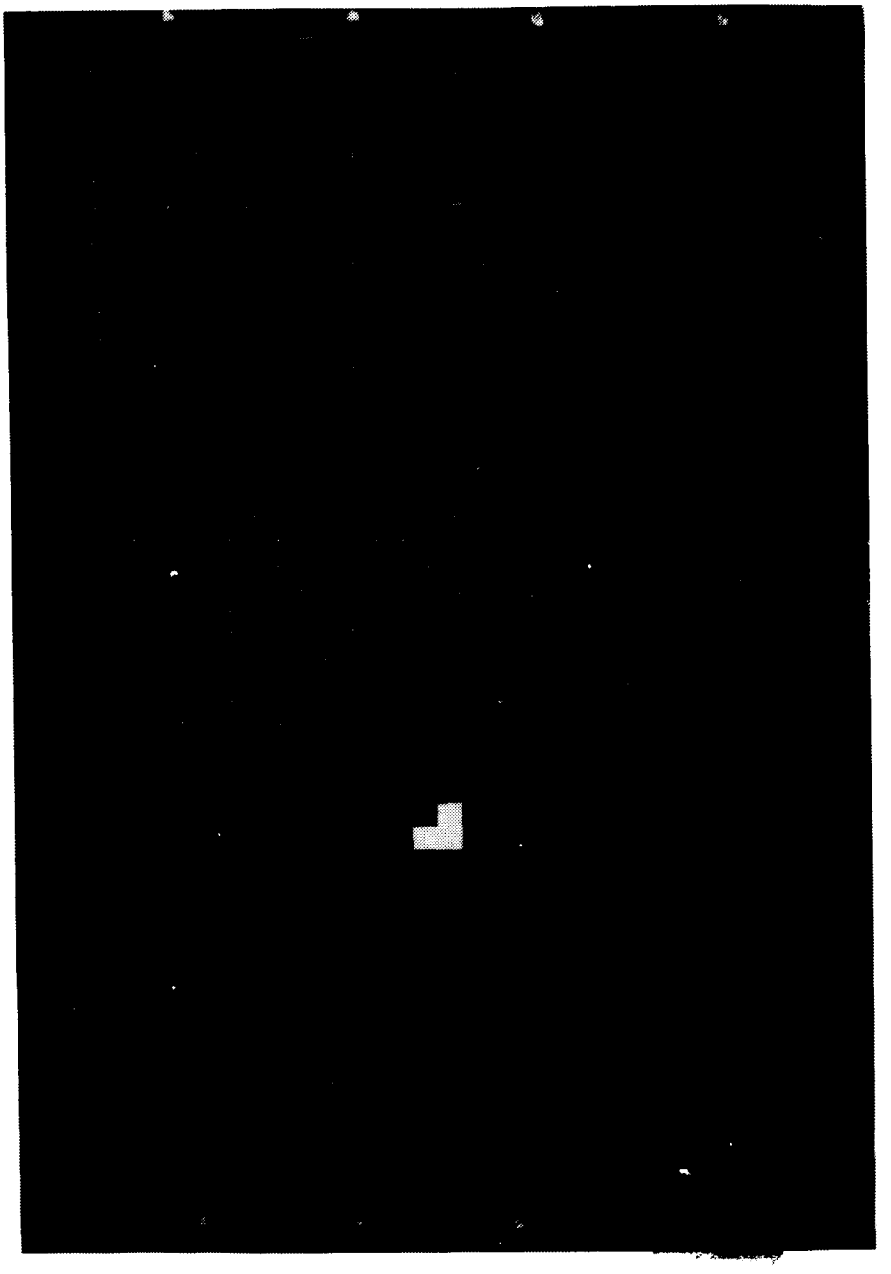

Figure 13. FLOW VISUALIZATION (X/D_j = 3.0; V_∞/V_j = 0.2)

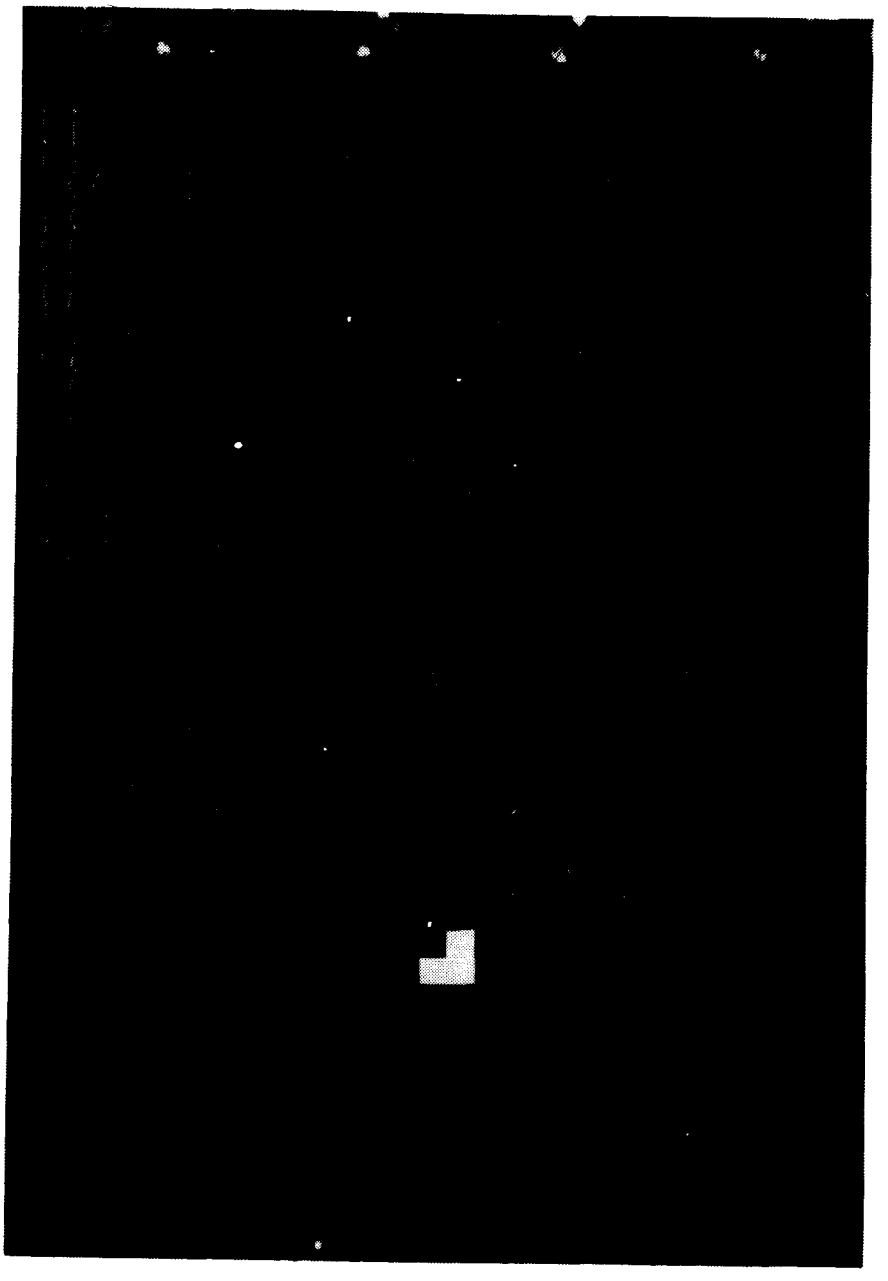

Figure 14. FLOW VISUALIZATION ($X/D_j = 3.0$; $V_\infty/V_j = 0.3$)

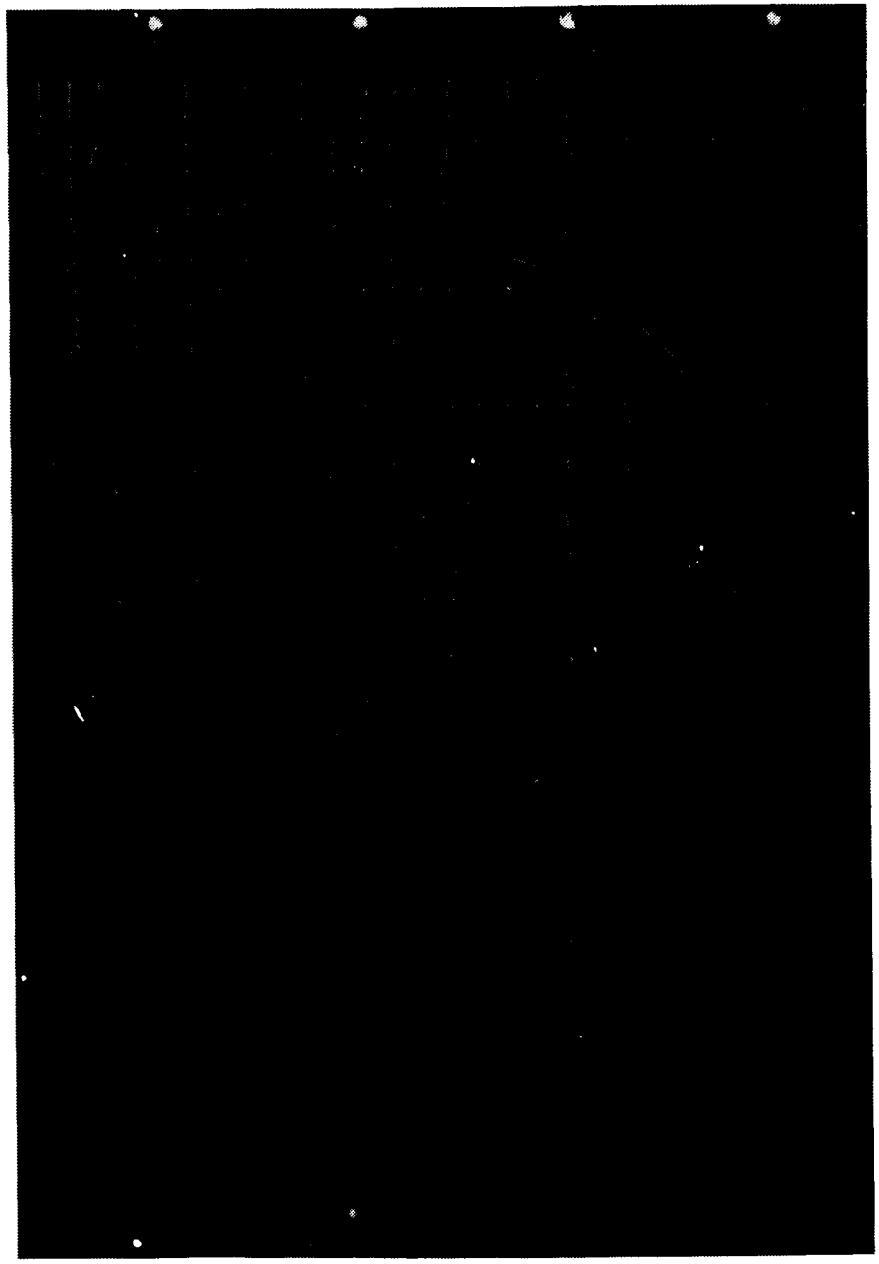

Figure 15. FLOW VISUALIZATION (X/D_j = 3.0; V_∞/V_j = 0.4)

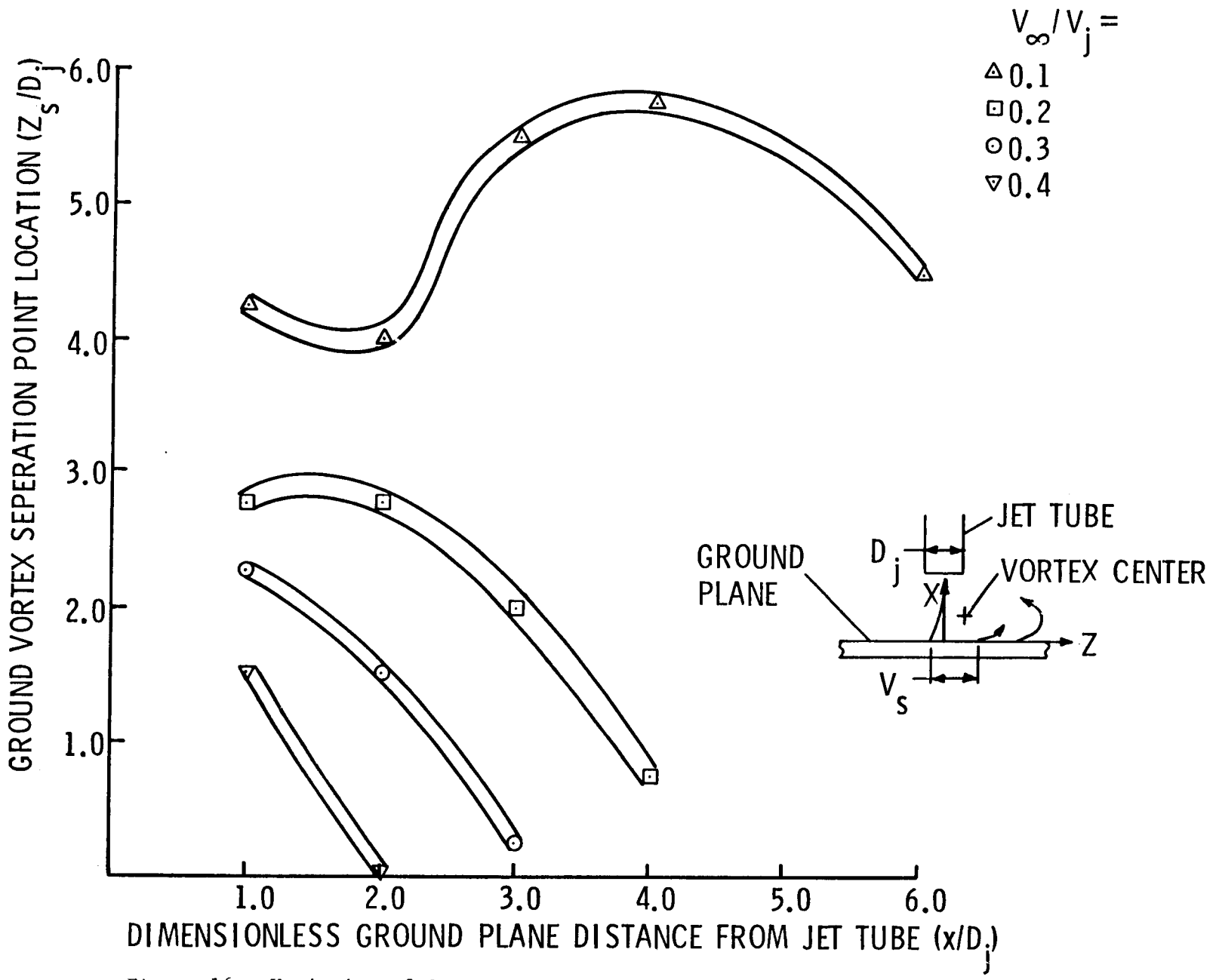

Figure 16. Variation of Ground Vortex Separation Point with Ground Plane-to-Jet Distance

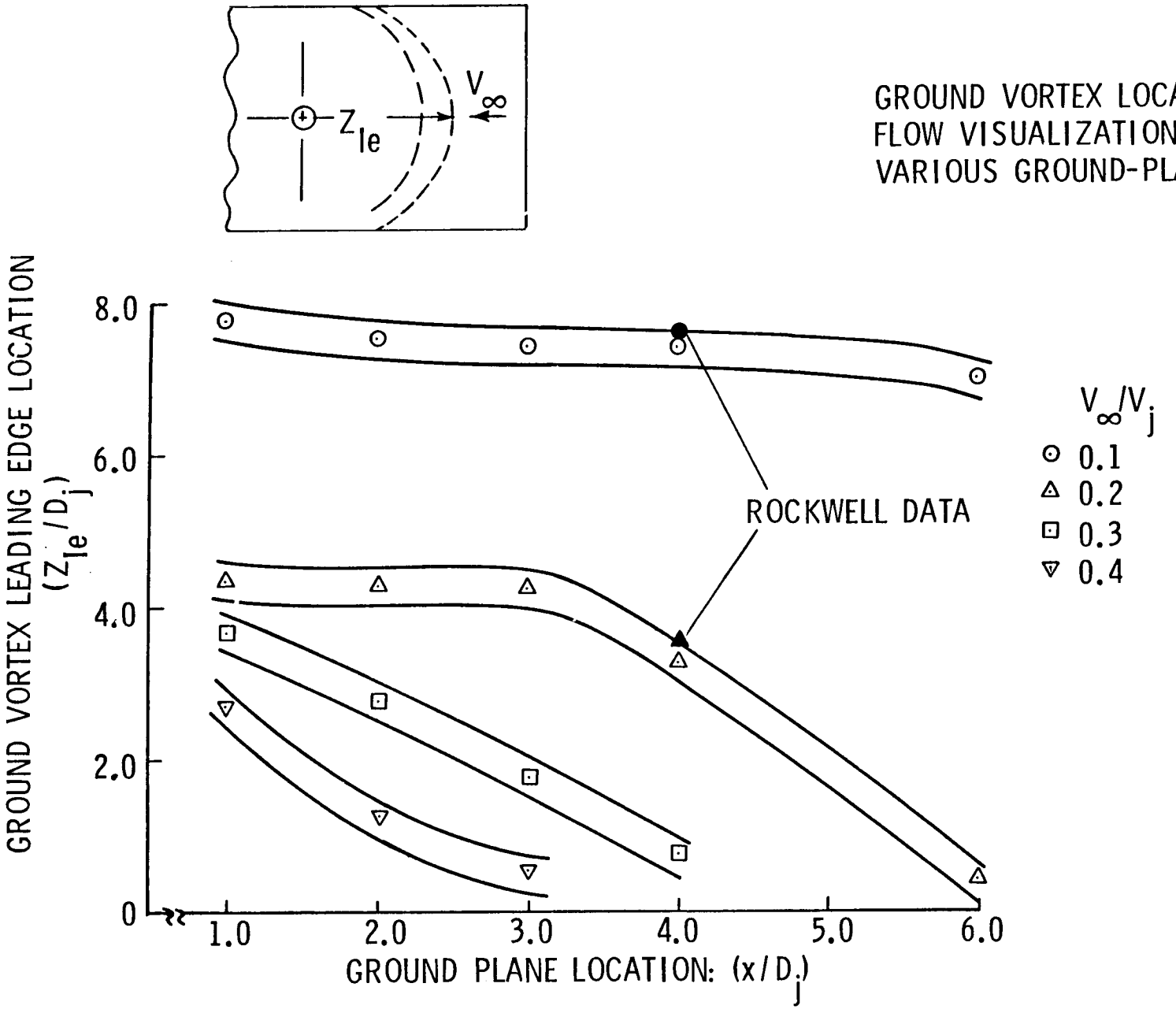

Figure 17. Ground Vortex Leading Edge Location from Flow Visualization

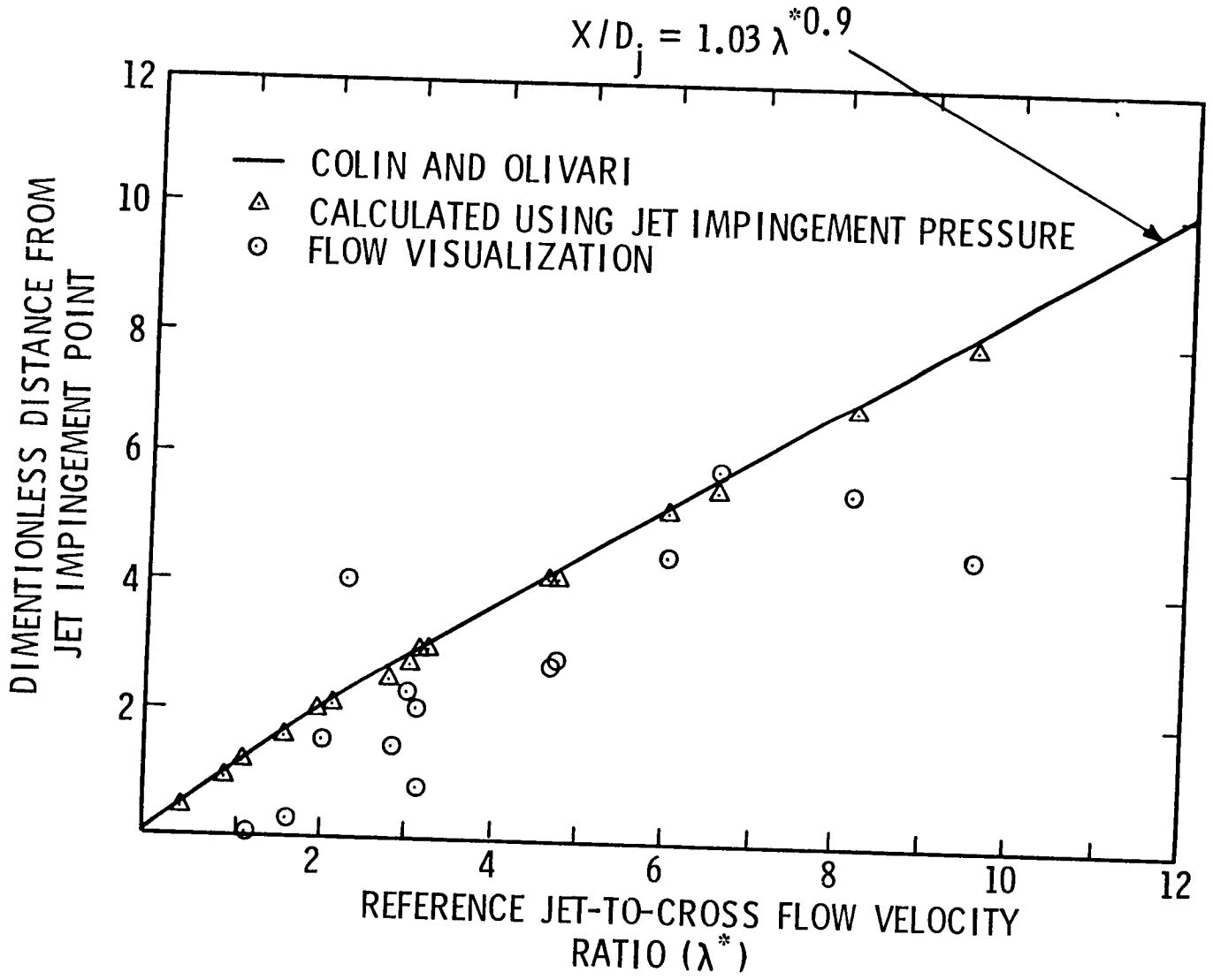

Figure 18. Variation of Ground Vortex Separation Point with Reference Jet-to-Cross Flow Velocity Ratio

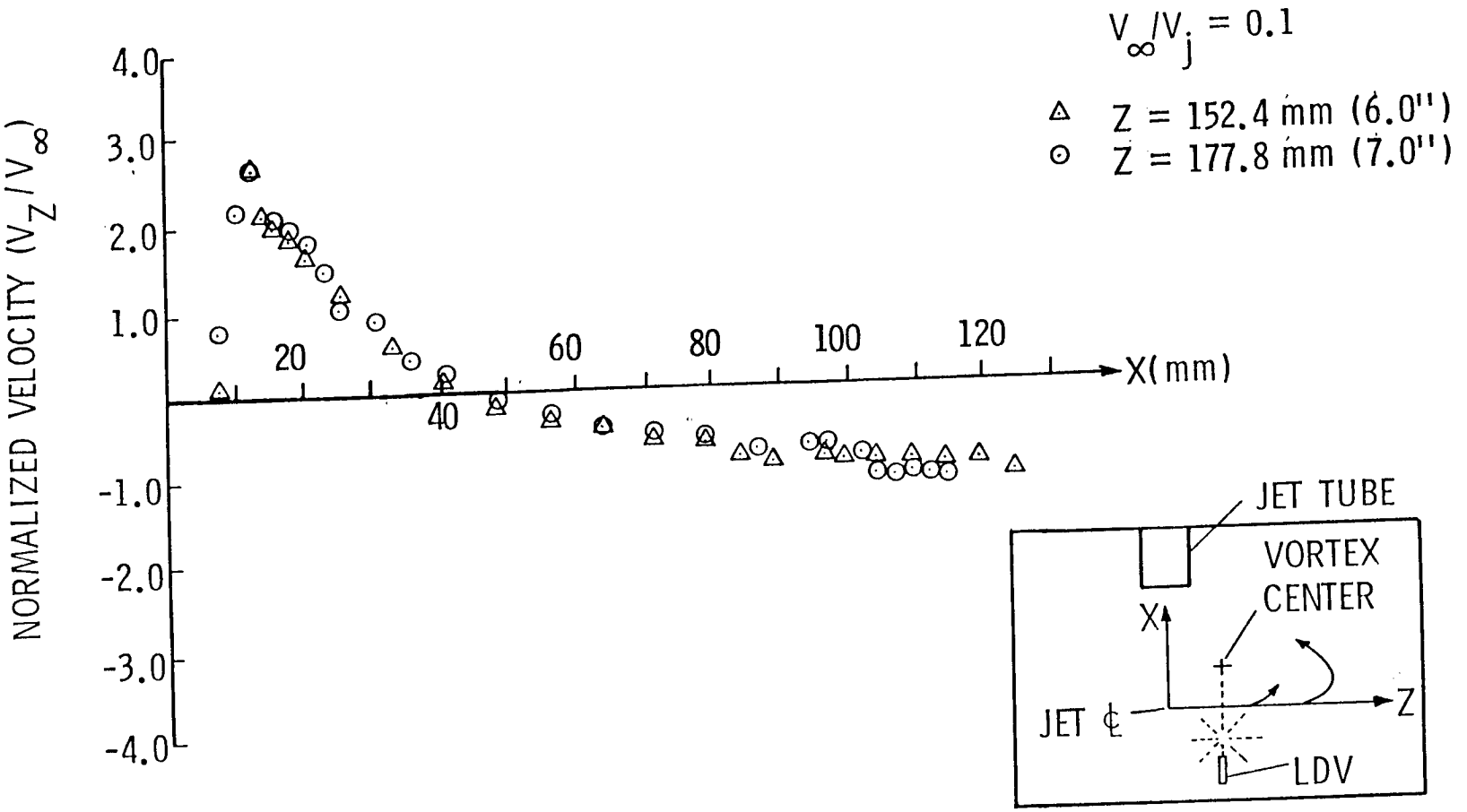

Figure 19. Velocity Distribution Through Vortex Centex

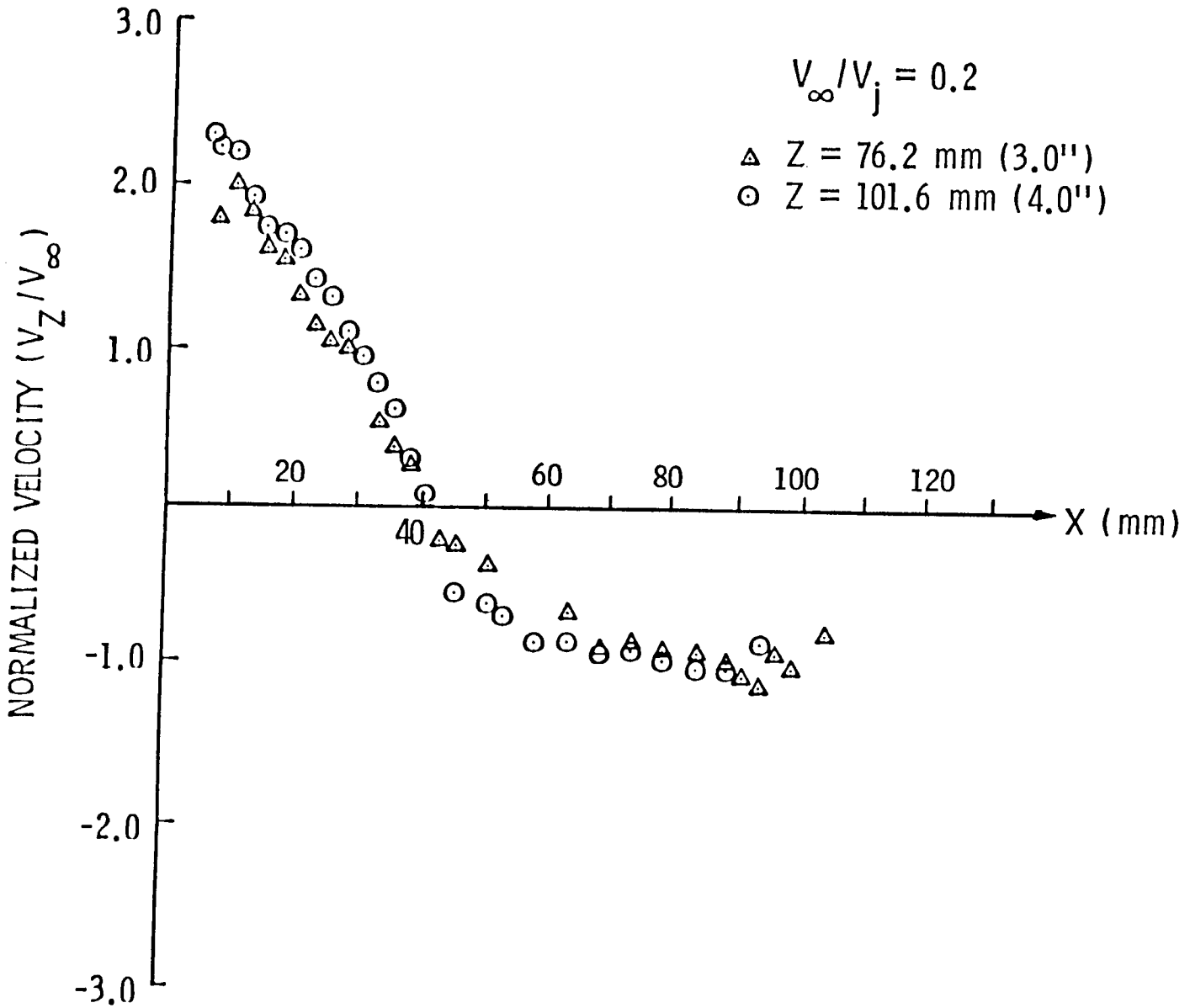

Figure 20. Velocity Distribution Through Vortex Centex

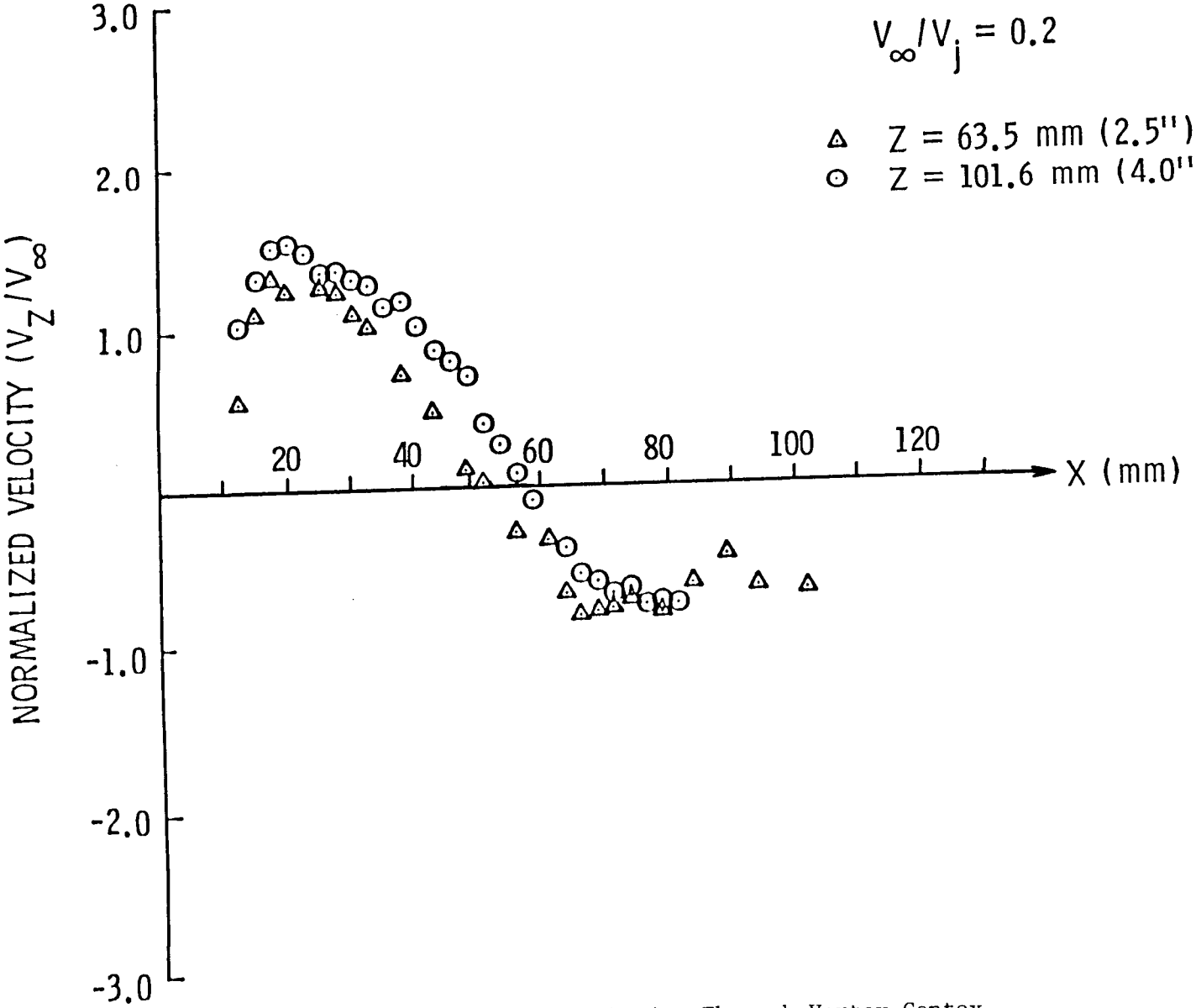

Figure 21. Velocity Distribution Through Vortex Centex

EFFECTS OF THRUST REVERSING IN GROUND PROXIMITY

BY

P. B. Joshi and R. V. Hughes
Northrop Corporation, Aircraft Division
Hawthorne, California

For Presentation at
NASA Ames Ground Effects Workshop
Moffett Field, California

August 20 - 21, 1985

EFFECTS OF THRUST REVERSING IN GROUND PROXIMITY

P. B. Joshi and R. V. Hughes

Northrop Corporation, Aircraft Division

Abstract

This paper describes the changes in stability and control characteristics encountered by a thrust-reversing aircraft during its final approach, landing, and ground roll. These changes include a strong pitch-up accompanied by the loss of horizontal tail and aileron control effectivenesses. The magnitudes of reverser-induced changes in ground effect are much larger than corresponding changes in free air. The paper also describes some unexpected unsteady motions exhibited in wind tunnel by an aircraft model with reversers operating in ground proximity. The cause of this oscillatory behavior was determined to be an unsteady interaction between the wall jets formed by impingement of reverser jets on the ground and the on-coming free stream. Time histories of rolling moments measured by the wind tunnel balance were analyzed. The effects of dynamics of the model balance/support system were removed and frequencies were scaled by Strouhal number to full scale. Corrected time series were used to simulate the motion of a fighter aircraft with thrust reversers in ground effect. The simulation predicted large roll angles and nose-down attitude at touchdown. Finally, the paper discusses some phenomena of jet attachment to solid surfaces and recommends areas for future research.

EFFECTS OF THRUST REVERSING IN GROUND PROXIMITY

P. B. Joshi and R. V. Hughes
Northrop Corporation, Aircraft Division

I. Introduction

The next generation of fighter aircraft will be required to have better STOL capabilities than the current generation. The emphasis on STOL results from the requirement that future fighters be able to operate from bomb-damaged runways. The emerging technology of in-flight thrust reversing enhances STOL capability by significantly reducing landing distances. Thrust reversing also has potential advantages under up-and-away conditions due to increased maneuverability of the aircraft.

Northrop Corporation, Aircraft Division, has recently completed an Air Force Program "Generic Thrust Reverser Technology for Near-term Application". The objective of this program was to develop design guidelines for integration of thrust reversers into an aircraft such that resulting stability and control impacts are minimal, both in and out of ground effect. As a part of this contract and concurrent Independent Research and Development Programs, a thrust-reversing aircraft model was tested in the Northrop 7 x 10 ft. low-speed wind tunnel. Testing was conducted both in and out of ground effect.

In this workshop, some results from the ground effect part of the test program will be presented. Additionally, limited data which are applicable to both free air and ground effect

will be presented. Basic flow mechanisms will be identified. Main consideration will be an unexpected unsteady flow phenomenon encountered during tests. Finally, some recommendations for future studies are given.

II. Test Model and Facility Description

Tests were conducted in the Northrop Aerosciences Laboratory 7 x 10 ft. low-speed wind tunnel. This is a single return, closed throat wind tunnel operating at atmospheric static pressure. The thrust-reversing aircraft model (Figure 1) was derived from a 0.08-scale model of the YF-17 aircraft by retaining the wing, forward and center fuselage sections. The afterbody/empennage assembly attached at an existing fuselage break near the wing trailing edge. This assembly represented a twin engine, twin vertical tail configuration based on 0.068-scale F/A-18A aircraft with reversing 2D-CD nozzles. A circular board in the test section simulated the ground plane.

The reverser jets emerged out of a non-metric plenum chamber mounted on the sting. The plenum was made non-metric to eliminate any contributions to true jet-induced loads from unbalanced reaction forces due to multiple reverser port arrangements. The plenum consisted of a rectangular steel box and an air pressure reduction and distribution system. Cold, high pressure air was supplied to the plenum by two lines connected to compressed air supply. Interchangeable, honeycomb inserts of rectangular shape, mounted flush with the plenum surface, were used to obtain reverser jets at various efflux

angles, port areas, and port aspect ratios. The axial position of the jets relative to the horizontal and vertical tails was varied by adding or removing spacers to and from the fuselage.

Aerodynamic loads induced on the metric part of the model by the reverser jets were measured on a 6-component balance. In addition, the vertical tails and the left and right panels of the horizontal tail were instrumented with individual 3-component balances for a direct measurement of induced loads in the near-field of the reverser jets. These balances yielded the normal forces, bending moments and torsional moments on the tails. To evaluate the contribution of the non-metric plenum box to the aircraft, a large number of static pressure measurements were obtained on both upper and lower surfaces of the plenum.

The model was tested at three different ground heights; free air, intermediate, and landing gear height. In "free air", the model was set midway between the circular groundboard and the tunnel ceiling. This corresponds to a ratio of height above ground to the wing span of approximately 1.2. The intermediate ground height represented Ø.36 wing span above the ground plane. At landing gear height the main gear was located Ø.75 inches off the ground board (height/span = Ø.18). This safety clearance was necessary to avoid grounding the metric airframe. Electrical contact "feelers" mounted below the main gear wheels alerted the tunnel operators of any contact between the ground board and the model.

The test approach was to vary each test parameter (reverser axial location, trailing edge flap deflection, for example) from its baseline and to obtain force, moment, and pressure measurements for a range of values of jet/free stream dynamic pressure ratio. The latter was varied by changing the tunnel speed at a fixed nozzle pressure ratio to simulate changing aircraft speed at constant power setting. Reverser parameters investigated were axial port location, jet efflux angle, cant or splay angle of lower reverser jets, port aspect ratio, and asymmetric thrust reversing. Several aircraft parameters were also varied. These included angle-of-attack, sideslip, horizontal tail deflection, wing trailing edge flap angle, and roll angle. Figure 2 shows schematically the various test parameters. Reference or baseline values of the parameters are shown in Table I.

III. Results and Discussion

Results on reverser-induced effects in ground proximity are grouped under the following three headings:

(i) Stability and Control Effects

(ii) Unsteady effects

(iii) Jet/Airframe Attachment Effects

Of these three effects, main emphasis will be on unsteady effects. Furthermore, the discussion on stability and control effects will be limited to the effects due to variation of aircraft height above the ground plane. A complete discussion of influence of aircraft/reverser parameters on induced effects

TABLE I

Definition of Versatile Model Baseline Configuration

Wing Flaps:	25 degree (leading)/20 degree (trailing)
Horizontal Tail Definition:	0 degree
Rudder Deflection:	0 degree
Landing Gear:	ON
Nozzle Pressure Ratio:	3.3 (Intermediate Power)
Nozzle Aspect Ratio:	2.0
Nozzle Port Area:	100 percent (No Aft Nozzle Flow)
Axial Port Location:	0.284 Wing Chords Aft of Vertical Tails
Nozzle Efflux/Cant Angles:	60 degree/0 degree

in ground proximity may be found in Reference 1.

(i) Stability and Control Effects

Figures 3 and 4 show the effects of varying ground height on jet-induced changes (i.e. jet-on minus jet-off values) in longitudinal stability and control for the baseline aircraft/reverser configuration. Corresponding changes in lateral-directional stability and control are shown in Figure 5. All data are presented with trailing edge flaps down (flap setting 25/20) and over a wide range of jet/free stream dynamic pressure ratios. The value of this ratio for typical approach speed of the F/A-18A aircraft is approximately 60.

Figures 3a and 3c contain increments in lift and pitching moment coefficients at the approach angle-of-attack of 8.5 degrees. It is seen that the configuration lift increases slightly at first (relative to its free air value) and then decreases rapidly as the aircraft comes in close ground proximity. This loss of lift increases significantly with increase in reverser jet/free stream dynamic pressure ratio. The incremental pitching moment curves in Figure 3c reveal that in free air and at intermediate ground height (h/b = 0.36), the reversers induce a relatively small pitch-up moment. However, in close ground proximity (h/b = 0.1 , the aircraft experiences a strong jet-induced pitch-up at approach dynamic pressure ratio of 60.

The changes in lift and pitching moment at zero degree angle-of-attack in ground effect, a condition which is representative of the aircraft attitude after touch down and rotation, are shown in Figures 3b and 3d. In contrast to the 8.5 degree angle-of-attack case, at landing gear height, the lift increases up to a dynamic pressure ratio of 70 and decreases thereafter. This increment in lift is accompanied by a strong pitch-up. Comparing the results for the two angles-of-attack, it is seen that at 8.5 degrees, the reverser-induced lift loss occurs aft of the moment reference center, in the vicinity of the trailing edge flap. On the other hand, at zero angle-of-attack, the initial reverser-induced lift gain occurs in the LEX/forebody region.

The reverser-induced pitch-up in ground proximity discussed above should be considered in conjunction with the induced changes in the horizontal tail control, which is used to trim out the incremental pitching moments. Figures 4c and 4d show the changes in horizontal tail effectiveness as a function of jet/free stream dynamic pressure ratio, with the ground height as a parameter. It is seen that in free air, there is a moderate increase in effectiveness at both zero and 8.5 degree angle-of-attack. In close ground proximity, however, there is a significant loss in effectiveness at 8.5 degree angle-of-attack. The situation is worse at zero degree angle-of-attack, where there is actually a reversal of the horizontal tail control. Thus, the loss of control effectiveness in ground effect can be a potentially serious problem.

Figures 4a and 4b show the reverser-induced changes in longitudinal stability, dC_m/dC_L, as a function of dynamic pressure ratio with the ground height as a parameter. Two horizontal tail settings, -10 and 0 degrees are shown. The values of dC_m/dC_L have been obtained from data at only two angles-of-attack, 0 and 8.5 degrees. Therefore, they should be interpreted only in qualitative terms. In free air, there is a small stabilizing change in dC_m/dC_L for both tail settings. As the aircraft approaches ground, the stability changes not only depend upon the ground height, but also upon the tail deflection. At the intermediate ground height (h/b = 0.36) and around approach dynamic pressure ratios, stability decreases significantly due to the reversers, for both tail settings. With the aircraft at landing gear height, the stability increases for δH = 0 degrees, Figure 4b, for all dynamic pressure ratios. However, a large decrease in stability occurs for δH = -10 degrees. The physical mechanisms behind this dependence of longitudinal stability on horizontal tail deflection are not fully understood. The mechanisms are complicated due to highly nonlinear wing and tail aerodynamics in ground effect. This is because a complex flowfield results when the reverser jets impinge on the ground and interact with the free stream. A substantial change in stability, accompanied by a large decrease in tail effectiveness, can be a cause of concern because the aircraft may not respond sufficiently quickly to tail deflection.

The effects of thrust reversing in ground effect on lateral-directional stability and control parameters are shown in Figure 5 for an angle-of-attack of 8.5 degrees. As seen in Figure 5a, over a wide range of jet/freestream dynamic pressure ratios, the directional stability increases significantly in free air as well as in ground effect. At the approach dynamic pressure ratio of 60, the increment in directional stability at landing gear height is larger than that in free air or intermediate height. The lateral stability also exhibits similar behavior (Figure 5b) in that it increases as the aircraft approaches ground at a given dynamic pressure ratio. The increase is the greatest in close ground proximity, small at intermediate height, and negligible in free air.

The effects of approaching ground with reversers deployed on rudder effectiveness and aileron effectiveness are shown in Figures 5c and 5d respectively. In free air the rudder effectiveness increases due to thrust reversing. As the ground height is reduced the rudder initially becomes less effective (relative to the jet-off value), and then becomes as effective as in free air. Figure 5d shows that reversers have negligible influence on aileron effectiveness in free air as well as at intermediate ground height. Aileron effectiveness data at landing gear height with the trailing edge flaps down are not available. However, data with trailing edge flaps up indicate a substantial loss in aileron effectiveness in close gruond proximity.

The flow mechanisms which result in the reverser-induced stability and control changes discussed above are extremely complex. However, some gross features of the jet-induced flowfield about the aircraft can in identified. The flowfield can be broadly divided into two portions, shown schematically in Figure 6. The top portion contains the two upper reverser jets in a cross flow determined by upstream aircraft components. The bottom portion consists of the two lower jets, their impingement on the ground plane and the resulting wall jets, a "fountain" region resulting from an interaction between the laterally-spreading wall jets, and an interface region resulting from streamwise separating wall jets as they meet the on-coming stream. It will be shown later that this interface exhibits markedly unsteady behavior which can lead to large unsteady forces and moments on the aircraft.

The upper reverser jets pass inbetween and close to the vertical tails and thus affect mainly the directional characteristics of the aircraft. Before discussing these effects, however it is helpful to understand the basic mechanisms associated with a jet in cross flow.

Figure 7 shows the schematic of a circular jet in a cross flow. There are two key mechanisms: blockage and entrainment. The blockage mechanism of jet/free stream interaction is related to the deflected jet acting as an equivalent solid body in the free stream. The presence of this body decelerates the flow upstream of it and accelerates the flow around it. Also, the flow separates behind the "bluff" body of the jet. These flow

changes cause regions of positive pressures immediately ahead of the jets and negative pressures around and behind the jets. The entrainment mechanism of jet/free stream interaction is related to the shearing of the jet fluid by the free stream and the resulting jet growth. The jet entrains or "sucks" free stream fluid from all around as it grows. Strongest entrainment, however, occurs in the region immediately behind the jet in the "wake" (Reference 1).

The mechanisms of blockage and entrainment operate simultaneously for a jet in cross flow. Each is dominant in different regions of the flow field around the jet. Furthermore, the extent of these regions varies with the dynamic pressure ratio.

Blockage is the dominant mechanism in the immediate vicinity upstream of and around the jet. The result is to induce positive pressures due to flow deceleration ahead of the port through which the jet issues. Negative pressures exist around the port due to flow acceleration. Entrainment causes the flow to accelerate into the jet. It therefore tends to counter the flow deceleration upstream of the jet and augments acceleration of the flow toward the wake region. Note that at distances sufficiently away from the jet (i.e., in the far-field), weak jet-induced entrainment persists all around the jet.

As the dynamic pressure ratio is increased, there is a general increase in relative strength of the entrainment

mechanism. The result is to reduce the extent of the blockage-dominated positive pressures upstream of the jets and to increase the extent of entrainment-dominated negative pressures around the jets. Increase in dynamic pressure ratio also dramatically increases the entrainment behind the jets.

In addition to blockage and entrainment, another effect called impingement or atttachment can occur if a jet directly impacts a solid surface or exhausts at a very shallow angle relative to a surface. Asymmetric attachment/impingement of reverser jets to an aircraft surface can lead to strong asymmetric forces and moments on the airframe. The mechanism of jet attachment is described briefly in a later section.

The reverser-induced increase in the directional stability of an aircraft with twin vertical tails (Figure 5c) can be interpreted in terms of the blockage and entrainment mechanisms. In positive sideslip, or with the nose of the aircraft to the left of the relative wind, the left-hand jet moves closer to the left vertical while the right-hand jet moves away from the right vertical (see inset in Figure 6). This increases blockage or positive pressure on the inner surface of the left vertical with simultaneous increase in entrainment (or reduction of blockage) on the right vertical. Then, the jet-induced incremental forces on the two verticals produce a yawing moment tending to point the aircraft into the wind. The result is increased directional stability in presence of the reverser jets. The reader may consult Reference 2 for a detailed description of flow mechanisms and stability and control effects.

The reverser-induced lift loss (Figures 3a and 3b) is partly understood in terms of the well-known suck-down effect observed for VTOL jets. This loss occurs primarily over the wing because the reverser jets propagate upstream after impingement on the ground. Smoke and water tunnel flow visualizations at Northrop have indicated that the jets eventually separate from the ground plane in a region under the wing. Upon separation, which was observed to be an intermittant process, the complete aircraft was immersed in a highly non-uniform, unsteady, vortical flow field. This flow field, in which the wings are likely to be immerged, can also contribute to the reverser-induced lift loss. The large degradation of horizontal tail effectiveness in ground effect can be attributed to this "spoiled" flow. The latter may also be responsible for the dependence of longitudinal stability on horizontal tail deflection.

The preceding paragraphs discussed the effects of ground height on jet-induced aerodynamic changes experienced by the airframe. It was seen that the induced changes in ground proximity differ characteristically from the induced changes in free air. For example, in free air, thrust reversers do not affect the lateral stability and control parameters, unlike in ground proximity. Also, for a given reverser configuration, the jet-induced pitch-up near ground is signifi-cantly greater than that in free air. The reasons for such differences can be understood by comparing the relative magnitudes of the contributions of various components of the air frame (horizontal tail, vertical tail, etc.) to the total induced change.

The contributions of horizontal and vertical tails can be readily obtained from the direct measurements of tail forces and afterbody pressures. The afterbody is the plenum box through which the jets emerge (Figure 2). The instrumentation for measuring the pressures and forces has been described under Test Model and Facility Description. The contribution of the wing-fuselage combination was determined by subtracting the contributions of the tails and afterbody from the main balance measurements. The latter represent reverser-induced effects on the complete aircraft.

Figure 8 contains the contributions of various aircraft components to the pitching moment, in free air and in ground effect. In free air, both the horizontal and the canted vertical tails contribute nose-up moments, Figures 8a and 8b. The afterbody and wing-forebody contribute nose-down moments, Figure 8c and 8d. Near the approach dynamic pressure ratio of 60, the moments due to the horizontal and vertical tails and the afterbody are comparable in magnitude. The wing-forebody moment is also of a similar magnitude, although slightly smaller. It is noted that the individual moment contribution due to each component is small. Moreover, their algebraic sum is even smaller. The largest contribution, due to the vertical tail, is equivalent to approximately 5 degrees of equivalent horizontal tail deflection. One further observation in free air is that there is negligible change in the configuration lift (Figure 3a). This suggests that most of the wing-fuselage effect occur on the portion of the body just forward of the plenum (Figure 2).

During transition from free air to landing gear height, around the approach dynamic pressure ratio, the horizontal tail contribution decreases from a nose-up moment to a nose-down moment (Figure 8a). The afterbody moment becomes more negative, i.e., there is a greater pitch-down than in free air (Figure 8c). The wing-fuselage contribution increases dramatically from a small pitch-down to a large pitch-up, equivalent to 30 degrees of horizontal tail deflection, jets-off. Furthermore, the magnitude of this contribution is several times greater than the contributions due to horizontal tail, vertical tail and afterbody. It may be recalled that the pitch-up at landing gear height is accompanied by large lift changes on the aircraft (Figures 3a and 3b). This suggests that in ground proximity the reverser jets primarily affect the aerodynamics of the wing, with only a small contribution from the fuselage.

At landing gear height, as the aircraft decelerates, or equivalently, as the dynamic pressure ratio increases, the reverser-induced pitching moment on the wing-fuselage decreases. However, this contribution is still much greater than that due to the horizontal and vertical tails and the afterbody.

In summary, in free air, the effects of reverser jets on the aerodynamics of the aircraft are generally small. These small effects are mostly felt on the tail-afterbody region of the aircraft. By contrast, in ground proximity, the reverser-induced effects are large and occur primarily on the wing, and are sensitive to the cant angle of the lower jets. The magnitude of these effects reduces as the jets are canted outboard.

(ii) Reverser-induced Unsteady Effects

During the ground plane test to evaluate reverser-induced stability and control effects, it was observed that the model experienced large (and totally unexpected) oscillations for certain reverser port arrangements. To the naked eye, the oscillations appeared to be primarily in roll. Upon recording the time-histories of outputs from the 6-component balance, it was found that oscillations occurred in yaw and pitch as well. The latter were much smaller in magnitude than roll oscillations, however. The oscillations were largest for uncanted lower reverser jets and diminished as the lower jets were canted outboard.

To better understand the flow field associated with reverser jets in ground proximity, smoke streaks were injected upstream of the model. It was observed that an unsteady boundary or interface existed between the reverser jets propagating upstream after impinging on the ground and the free stream. For uncanted lower reverser jets, the interface was located mainly underneath the wing, but it periodically engulfed the leading edge region of the wing. Large clumps of fluid were observed to break away from the oscillating boundary, sometimes passing over the wing and sometimes under.

The key question to be answered after the ground plane test was whether it was the model motion that was causing the unsteady jet/free stream interaction or whether there existed an unsteady jet/free stream interaction that was causing the model

to respond. The possibility that the jet itself may be unsteady, either due to a flapping motion or time-dependent mass flow, was ruled out by monitoring the weight flow through the reverser nozzles and by observing that a string attached at the nozzle exit remained steady. These diagnostic experiments were conducted during the ground plane testing. It was also made certain that the model did not exhibit any unsteadiness in close ground proximity when the free stream was off with only the reverser jets blowing and also when the jets were off with only the tunnel running.

To answer the question of the origin of the force, it was necessary to hold the model rigid during testing. A test was conducted in the Northrop water tunnel on rigid model/support system. Dye was injected in the reverser jets. It was observed that there existed a vortical interface between the separated reverser wall jets and the free stream. Moreover, this interface displayed oscillations in streamwise direction as well as periodic variations in its size. Figure 9 shows a still photograph from the water tunnel test and a schematic of the reverser jet/free stream interaction.

Upon determining that the existence of unsteady reverser jet/free stream interaction leads to the model motion observed in the wind tunnel, the next question to be answered is what are the consequences, if any, for a full scale aircraft. The nature of oscillating motions recorded in the wind tunnel depends on the dynamic characteristics of the model support system. To obtain the true "forcing function" resulting from the unsteady

jet/free stream interaction, the wind tunel time histories must be first corrected to filter out the support characteristics, and then their frequency content must be scaled properly. Such an analysis was performed in the frequency domain on the rolling moment output from the 6-component balance. As mentioned earlier, the model response in roll was the most significant. Furthermore, the high quality wind tunnel balance eliminated any significant interactions between motions in roll, pitch or yaw.

Figure 10a shows a typical time history of rolling moment response at approach dynamic pressure ratio for uncanted lower reverser jets. Also shown is the equivalent aileron deflection (assuming linear aileron effectiveness) to give the reader an appreciation for the large amplitudes of the oscillating rolling moments. A power spectrum of rolling moment showed a strong peak around 16.5 Hz which corresponded to the natural frequency of the balance/support system of the model in torsion. A simple single-degree-of-freedom analysis shown in Figure 10b was performed to filter out the balance/support characteristics. This led to Power Spectral Densities (PSDs) of the rolling moment forcing function due to jet/free stream interactions. Analysis was performed for a number of reverser geometries (jet efflux angles and lower jet cant angles) and jet/free stream dynamic pressure ratios. Results are shown in Figures 11 through 16.

Figure 11 shows the PSD of the rolling moment forcing function for an aircraft at zero angle of attack, landing gear height (h/b = 0.18) and jet/free stream dynamic pressure ratio

of 120. The latter corresponds to the aircraft in ground roll after touch down. Effects of jet/free stream dynamic pressure ratio on the forcing function are discussed later. The frequencies in Figure 11 have been converted to full scale aircraft using the Strouhal number. It is noted that the forcing function contains frequencies to which typical fighter aircraft are sensitive. The PSD is expressed in terms of (rolling moment coefficient)^2 per Hz. It is seen that the rolling moment forcing function due to 40-degree canted jets is at least an order of magnitude smaller than that for uncanted or slightly canted jets. This is expected since canted jets have a smaller dynamic pressure component which is directed upstream. For 40-degree canted jets, the effect of increasing the jet efflux angle (Figure 2) is to further reduce the forcing function magnitude.

Figure 12 shows the rolling moment forcing function expressed in terms of an equivalent aileron deflection (peak-to-peak) against the lower reverser cant angle, for various efflux angles. This plot was obtained from integrations of the curves similar to Figure 11 for 8-degrees angle of attack. To convert the rolling moment coefficients to aileron deflections, a representative aileron effectiveness for the F/A-18A aircraft was used. It is clear from Figure 12 that the aircraft is subjected to large rolling moment inputs for uncanted and insufficiently canted lower jets, in a frequency range to which the aircraft is sensitive. Even for practical values of lower jet cant angles, the rolling moment forcing is not reduced to

insignificant levels. Another practical aspect is that the magnitudes and frequencies (say 1-2 Hz, typically) of the input disturbance may require aileron deflections and actuation rates which are beyond the state-of-the-art.

Figure 13 shows the effect of jet/free stream dynamic pressure ratio on the rolling moment forcing function. These results are presented for reverser jets with lower cant angle of 40 degrees. This case is chosen because in practice the jets will be most likely canted outboard to avoid hot gas reingestion. Another reason for selecting canted jets is that the forcing function levels reduce with increase in outboard cant angle (Figure 11) and it is of interest to know if the reduced levels are still significant at dynamic pressure ratios typical of approach and touch down. Figure 13 shows that the forcing function has a maximum around dynamic pressure ratio of 90, which corresponds to a condition just after touch down and rotation for the F/A-18A aircraft. Near the approach dynamic pressure ratio of 60, the forcing function drops to approximately 30 degrees peak-to-peak equivalent aileron input. This level is not insignificant, and given the frequencies of 1-2 Hz, the aileron actuation rates required may be high.

The results presented above described the spectral characteristics of the disturbances due to unsteady interactions between the reverser jets impinging on (and then separating from) the ground plane and the free stream. How the full-scale aircraft responds to the disturbances is a matter of practical importance. Two types of analyses were performed to predict the

motion of an F/A-18A aircraft with thrust reversers operating in ground effect. First was a simplified analysis shown in the lower half of Figure 10b which led to the estimation of probabilities that the aircraft may exceed a given roll angle. This analysis assumes the aircraft response to be a narrow-band process. The second analysis was a simplified six-degree-of-freedom simulation of aircraft motion using the rolling moment time history obtained in the wind tunnel. The time history was corrected to full-scale by inverse of frequency determined from Strouhal number scaling. The details of both approaches are discussed in Reference 3 and only the final results are mentioned here.

Figure 14 shows a plot of the probability that the aircraft exceeds a given peak roll angle. The data are presented for reversers with 45 degrees efflux angle and 40 degrees outboard cant angle of the lower jets. Three different dynamic pressure ratios are shown. It is seen that even at the smallest dynamic pressure ratio of 60, which is typical of approach, the aircraft may exceed 20 degrees roll angle. For an aircraft such as the F/A-18A the wing tips will be very close to the ground for roll angles of this magnitude.

Figure 15 shows the results of a simulation of F/A-18A aircraft coming in to land with thrust reversers on. The efflux angle is 45 degrees and lower reverser jets are uncanted. The forcing function is in the form of a rolling moment time series. The aircraft response is plotted in terms of altitude, roll or bank angle, and pitch angle as a function of time. During the

simulation the control augmentation system was off, so that the response is purely a result of the aircraft's natural stability and control characteristics. It is seen that the aircraft lands in 'about 4 seconds with a 10 degree nose down altitude and 20 degree bank angle. The latter is significant and thus a cause of concern. The foregoing simulation results are somewhat simplified (for reasons to be discussed in next paragraph) and may exaggerate the response of an aircraft during a true landing transient. A novel study to obtain more accurate data for simulations has been planned and will be discussed later in this paper.

The analyses for predicting full-scale aircraft behavior using time series data obtained from the wind tunnel imply some obvious limitations/assumptions. The most important limitation is that the time histories were obtained for aircraft at fixed height above the ground, thus ignoring the build-up of ground effect as the aircraft descends to the ground. Another is that in the six-degree-of-freedom digital simulation, steady state, free air aerodynamic coefficient and control effectiveness data were used. An accurate simulation would require changing aerodynamic data due to the presence of the reverser jet/free stream/ground plane interaction as the aircraft approaches ground. It is necessary to simulate the aircraft's actual descent in an experiment. This is explained in Figure 16. As noted earlier (Figure 11), the characteristic frequency of the unsteady interactions between reverser jets and the free stream is of the order of 1Hz, full scale. Equivalently, the

characteristic period is of the order of 1 second. A STOL fighter will typically spend 1 to 2 seconds in ground effect prior to touch down, which is of the same order as the period of unsteadiness. It follows that an aircraft landing with thrust reversers will experience a continually changing flow field in ground effect. Moreover, the characteristics of this "transient" unsteadiness will probably be different from the "fully-developed" unsteadiness measured at a fixed ground height. Therefore, it is necessary to simulate the aircraft's descent during thrust reverser testing in ground effect.

The question naturally arises, "What is the rate of descent that must be simulated?" The answer is provided by the following similarity analysis. The dimensionless parameter to be matched between the model and full scale for unsteady flow problems is the Strouhal number, i.e.

$$S_{ms} = S_{fs} \qquad (1a)$$

where

$$S = \frac{fL}{U} \qquad (1b)$$

with f = frequency, L = characteristic length, and U = free stream velocity

'ms' denotes model scale and 'fs' denotes full scale

In addition, for dynamic similarity, the model must experience the same number of cycles of unsteadiness as the full scale, i.e.

$$N_{ms} = N_{fs} \qquad (2a)$$

where

$$N = fT \qquad (2b)$$

with T denoting the time spent in the unsteady transient.

Defining a vertical rate of descent,

$$V = \frac{L}{T} \qquad (3)$$

and combining the relations (1a), (1b), (2a), (2b), and (3), it may be verified that

$$\frac{V_{ms}}{U_{ms}} = \frac{V_{fs}}{U_{fs}} \qquad (4)$$

which shows that the rate of descent of the model in the wind tunnel must equal that for the full scale if the free stream velocity is maintained the same.

The rates of descent of modern fighter aircraft, which are of the order of 10 ft/sec, cannot be duplicated by conventional vertical traverse mechanisms of model support systems in wind tunnels. These mechanisms have vertical descent rates of a few inches per second. Then, the free stream speed will have to be reduced substantially to obtain the similarity in Equation (4). The reverser jet velocities will also have to be reduced to obtain a desired jet/free stream dynamic pressure ratio. At these very low jet and free stream speeds, the aerodynamic forces on the model are not of sufficient magnitiude for accurate measurement.

Northrop and NASA Langley Research Center with the support of the Air Force Flight Dynamics Laboratory have developed a novel test concept to simulate the required rates of descent (Figure 17). The proposed test facility is the Vortex Flow Research Facility at Langley. This facility was formerly a towing basin for measuring hydrodynamic forces on submerged and

semi-submerged bodies. Currently, the facility is not being used for hydrodynamic testing. The water has been drained completely, but the trolley from which the model support strut hangs is operational. It runs on rails, powered by an Oldsmobile engine, capable of speeds up to 70 mph. The model can be supported on a sting attached to a support strut. Forces and moments can be measured on a balance inside the model. Data are telemetered to a control room for processing in real time.

The test concept is to simulate the approach, touch down, and ground roll of a thrust reversing aircraft by traversing the model horizontally over a ramp followed by a straight section. Given a typical ramp angle of 5 degrees, rates of descent of up to 9 ft/sec can be simulated by traversing the trolley at different speeds. Transient time series data from six component balance outputs will be recorded on analog tapes for post-test analysis. In addition, strip chart recordings will also be obtained for visual examination. The duration of transient data samples is expected to be 4 to 5 seconds. A number of repeat runs are planned to obtain representative ensemble averages. Some flow visualizations using tufts on the model and on the ground plane are also planned. An important feature of the proposed test approach is that the boundary layer problems normally associated with ground plane testing are obviated.

Testing will be conducted on a NASA 0.07-scale YF-17 model with thrust reversing provided by the same plenum chamber/nozzle assemblies (Figure 2) as that used in Northrop's earlier tests. Test parameters will include different reverser geometries and

aircraft control surface deflections. The objectives of the test will be (i) to obtain transient aerodynamic data which can be used in a realistic simulation of motion of thrust-reversing aircraft in ground effect, (ii) to determine transient forcing function characteristics, and (iii) to identify critical aircraft/reverser parameters which affect jet/free stream interactions. The data analysis scheme for the proposed test is shown schematically in Figure 18.

The NASA/Northrop/USAF test will be conducted in the December 1985/January 1986 time frame.

(iii) Jet/Airframe Attachment Effects

During the calibration of reverser nozzles on a static rig prior to the wind tunnel test, an interesting jet flow attachment phenomenon was encountered. The rectangular reverser nozzles, shown schematically in Figure 19, were flush-mounted in pairs on a flat plate. Nozzle geometry variations included efflux angle (θ) and cant angle (Ψ). The actual efflux angles of the jet centerline were recorded as a function of nozzle pressure ratio under quiescent ambient conditions. A 4-inch length of thread was anchored at the centroid of the nozzle exit, and its position recorded by a video camera.

It was found that for certain combination of nozzle efflux and cant angles, the jets were "bent" down toward the flat plate, giving an error of 20 - 25 degrees between the actual and intended efflux angles. Surface flow visualization (Figure 20a) on the plate showed that under these conditions, jet flow was

contacting the plate. A strong cross flow existed in the scrubbed areas beneath the jet, suggesting perhaps an energetic vortex either surrounding the jet or between the jet and the plate. Under some conditions, the jets were observed to switch rapidly between the attached and detached conditions (Figure 19b).

For purposes of the Northrop wind tunnel test, the immediate objective was to "fix" the problem and restore the intended jet angles, and consequently, further investigation of the jet/surface reattachment phenomena was not undertaken. The fix was a low fence or spoiler (Figure 20a) mounted close to the exit on the side where attachment was observed, such that the upper edge of the spoiler just cleared the expected jet boundary. This was entirely successful in providing the required jet angles.

The jet reattachment phenomenon has been encountered on full-scale aircraft (Reference 4) and has serious implications in terms of asymmetric loads and thermal effects on the airframe. It is suggested that the presence of the ground might exacerbate the tendency of the lower jets to reattach during approach and landing. For example, the negative pressures underneath the airframe resulting from jet impingement and wall jet formation on the ground may be conducive to reattachment. Much work remains to be done in the area of jet attachment, and some recommendations are made in the following sections.

IV. Summary and Conclusions

In this paper three types of effects due to thrust reversing in ground proximity have been described: (i) Stability and Control Effects, (ii) Unsteady Effects Due to Jet/Free Stream Interaction, and (iii) Jet/ Airframe Attachment Effects.

The stability and control effects in ground proximity are characteristically different than those in free air. The effects are generally much larger in magnitude in ground proximity more so longitudinally than lateral-directionally. In ground proximity, the jet-induced flow field affects the entire aircraft, expecially the wing. This is in contrast to jet-induced effects in free air, which are confined to a region close to the jets in the vicinity of the empennage. The reverser-induced flow field in ground effect is significantly more complex than in free air. Some gross characteristics of this flow field were identified and used to explain the observed reverser-induced changes in stability and control parameters.

Large and totally unexpected rolling motions were observed on a thrust-reversing aircraft model in ground proximity. Time histories of rolling moment were analyzed to determine the spectral content of the forcing functions which drove the oscillations. The analysis revealed that the forcing function contained significant energies at frequencies to which typical fighter aircraft are sensitive (1 - 2 hz). The magnitude of the forcing function was found to be a strong function of the cant

or splay angle of the lower reverser jets. It was postulated that the unsteady behavior in ground effect was a result of an unsteady interaction between the reverser jets and the free stream. Water tunnel tests provided visual verification of this hypothesis and confirmed that the interface between the jet flow separating from the ground plane and the on-coming stream exhibits streamwise oscillations. The time histories from the wind tunnel test were used for a simplified digital simulation of aircraft motion in ground effect, after correcting for model support characteristics and proper frequency scaling. It was found that the aircraft experienced both large roll angles and a nose-down attitude at touch-down. A co-operative NASA/Northrop/ USAF test is planned to measure transient unsteady loads on a thrust-reversing aircraft during approach and landing.

A jet flow reattachment phenomenon was encountered during testing of rectangular reverser nozzles. Surface flow visualizations showed that for certain combinations of jet efflux and cant angles, the jets were attaching to the flat surface of the plenum through which they were exhausting. There were indications of strong vortical cross flow underneath the jets. Tendencies for intermittent separation and reattachment were also seen. The reattachment phenomena, which may be exacerbated in the presence of ground, have serious implications in terms of asymmetric and unsteady induced loads and thermal effects on the airframe.

V. Recommendations for Future Research

The following areas for further work in thrust reverser-induced effects have been identified from Northrop's experience in this field. Some areas apply to both free air and ground effect regimes.

(i) Ground effect test techniques:

A study is needed to establish accurate techniques for ground effect testing. The effects of moving ground plane boundary layer thickness need to be determined.

(ii) Effects of the main propulsive jet during partial reverser deployment:

The influence of the propulsive jet on the reverser-induced aerodynamics of the airframe needs to be determined through an afterbody test on a pressure-instrumented model.

(iii) Effects of jet temperature on entrainment:

Testing with hot jets to determine flow characteristics along adjacent control surfaces and changes in stability and control parameters is recommended.

(iv) Accurate measurements of transient, unsteady effects during approach and landing with thrust reversers:

The NASA/Northrop/USAF test should yield valuable data.

(v) Definition of reattachment effects:

Improved definition of angles at which jet attachment occurs, including effects of various nozzle shapes and

moldline contours. Also, determination of the influence of ground proximity on reattachment of lower jets is essential.

(vi) Determination of the importance of inlet flow interactions on jet-induced forces and moments:

Aeroforce testing with inlet and exhaust flow simulation will be necessary.

(vii) Criteria for the importance of induced forces in ground effect:

Reverser-induced changes in stability and control parameters in ground effect may appear large in terms of dimensionless coefficients. However, these changes occur at relatively low free stream dynamic pressures which are typical during approach and landing. It is necessary to interpret the reverser-induced changes in terms of aircraft weight-on-wheels and runway friction at touch-down and during ground roll, for example.

(viii) Better understanding of jet/free stream flow fields:

Effects of jet exit velocity profile, nozzle geometry and mutual interference for multiple jets should be studied experimentally. Detailed flow field measurements of jets-in-cross flow and jet/free stream interactions after impingement on ground plane are recommended.

VI. References

1. Joshi, P.B., et. al, "Generic Thrust Reverser Technology for Near-term Application", Volumes I - IV, AFWAL TR-84-3Ø94, Air Force Wright Aeronauticcal Laboratories, Wright-Patterson AFB, Ohio 45433, February 1985.

2. Glezer, A., et. al, "Thrust Reverser Effects on Tail Surface Aerodynamics of an F-18-type Configuration," AIAA-83-186Ø.

3. Joshi, P.B. and Compton, M., "Unsteady Thrust Reverser Effects in Ground Proximity," AIAA Paper No. 85-4Ø35, to be presented at AIAA/AHS/ASEE Aircraft Design, Systems and Operations Meeting, Colorado Springs, Colorado, October 1985.

4. Hellstrom, G., "Effects of Thrust Reversal on Aircraft Stability at Ground Roll for A/C 37," Paper No. FKMB-37-7Ø.74, USAF/RSAF Propulsion Conference, Wright-Patterson AFB, Ohio, December 197Ø.

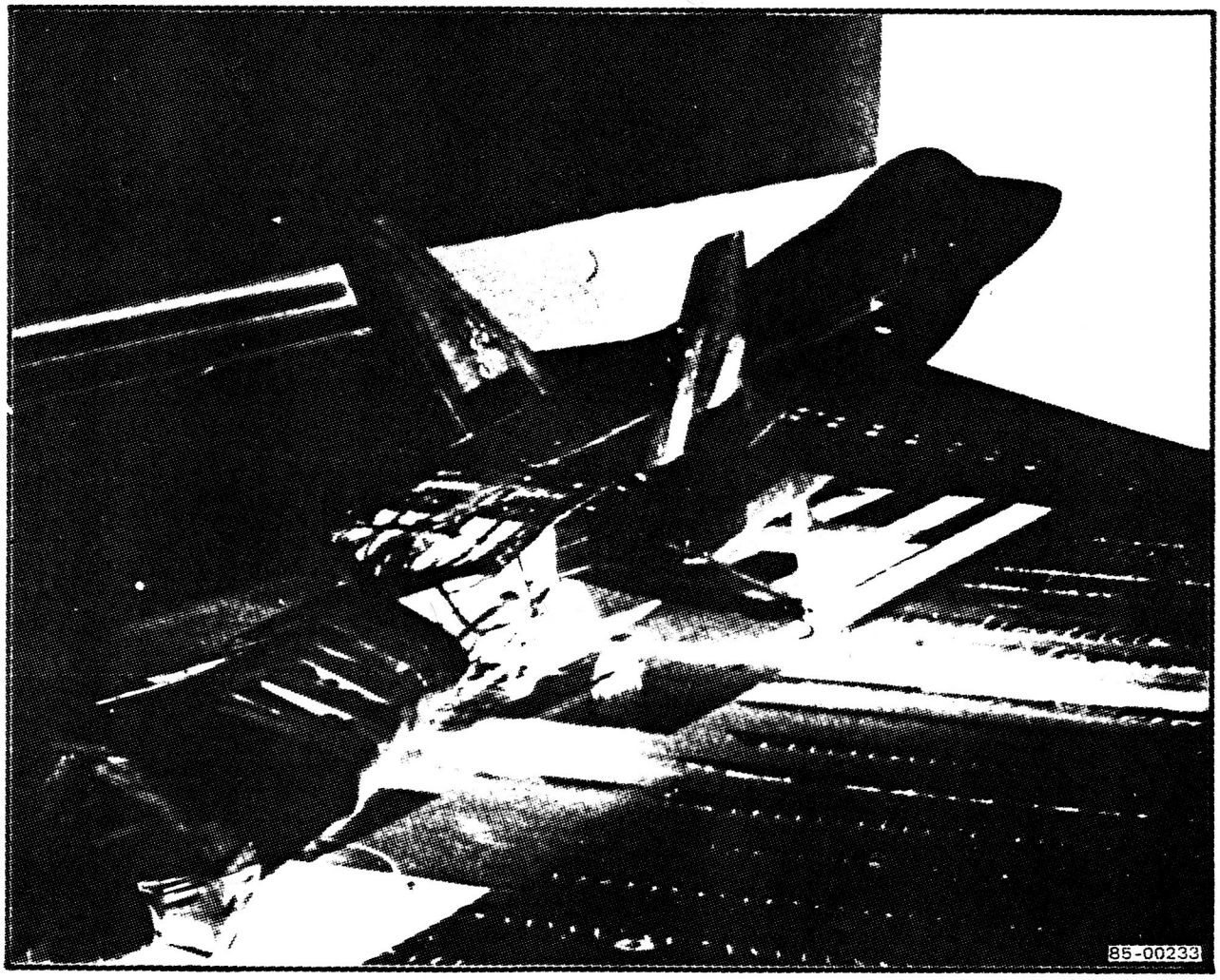

FIGURE 1. THRUST-REVERSING AIRCRAFT MODEL IN GROUND EFFECT TEST

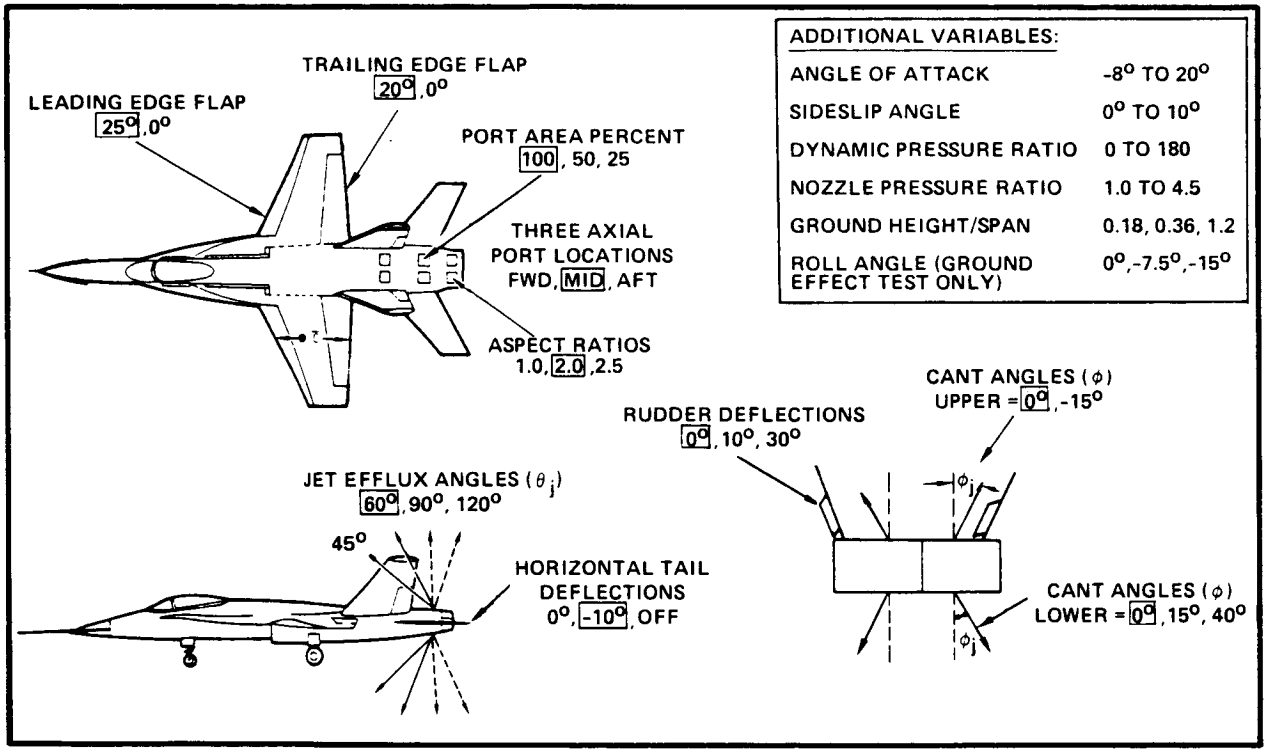

FIGURE 2. AIRCRAFT AND REVERSER TEST VARIABLES

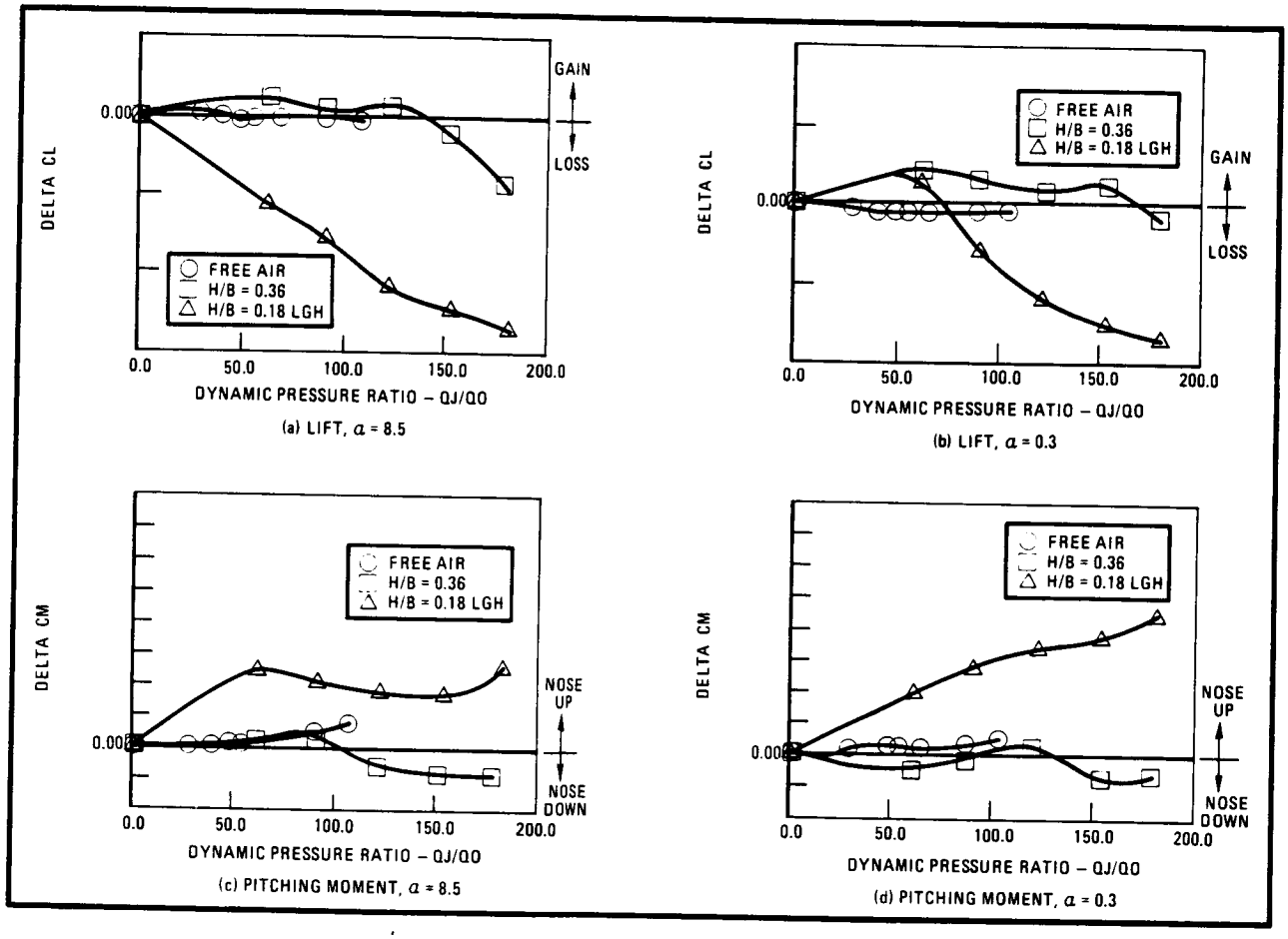

FIGURE 3. EFFECT OF GROUND HEIGHT VARIATION ON REVERSER-INDUCED LIFT AND PITCHING MOMENT, $\delta n/\delta f = 25/20$, $\delta H = -10$

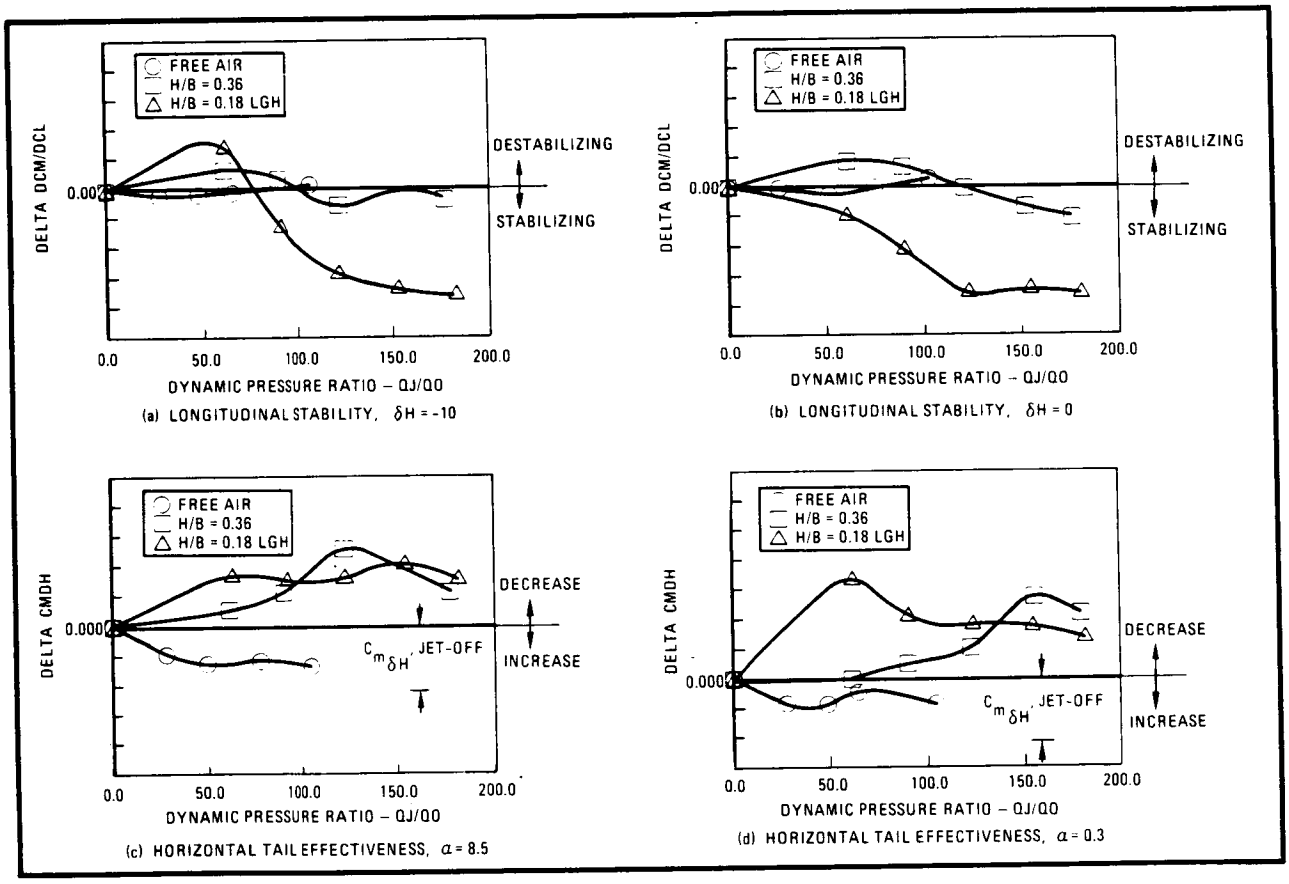

FIGURE 4. EFFECT OF GROUND HEIGHT VARIATION ON REVERSER-INDUCED CHANGES IN HORIZONTAL TAIL EFFECTIVENESS AND LONGITUDINAL STABILITY, δn/ δf = 25/20

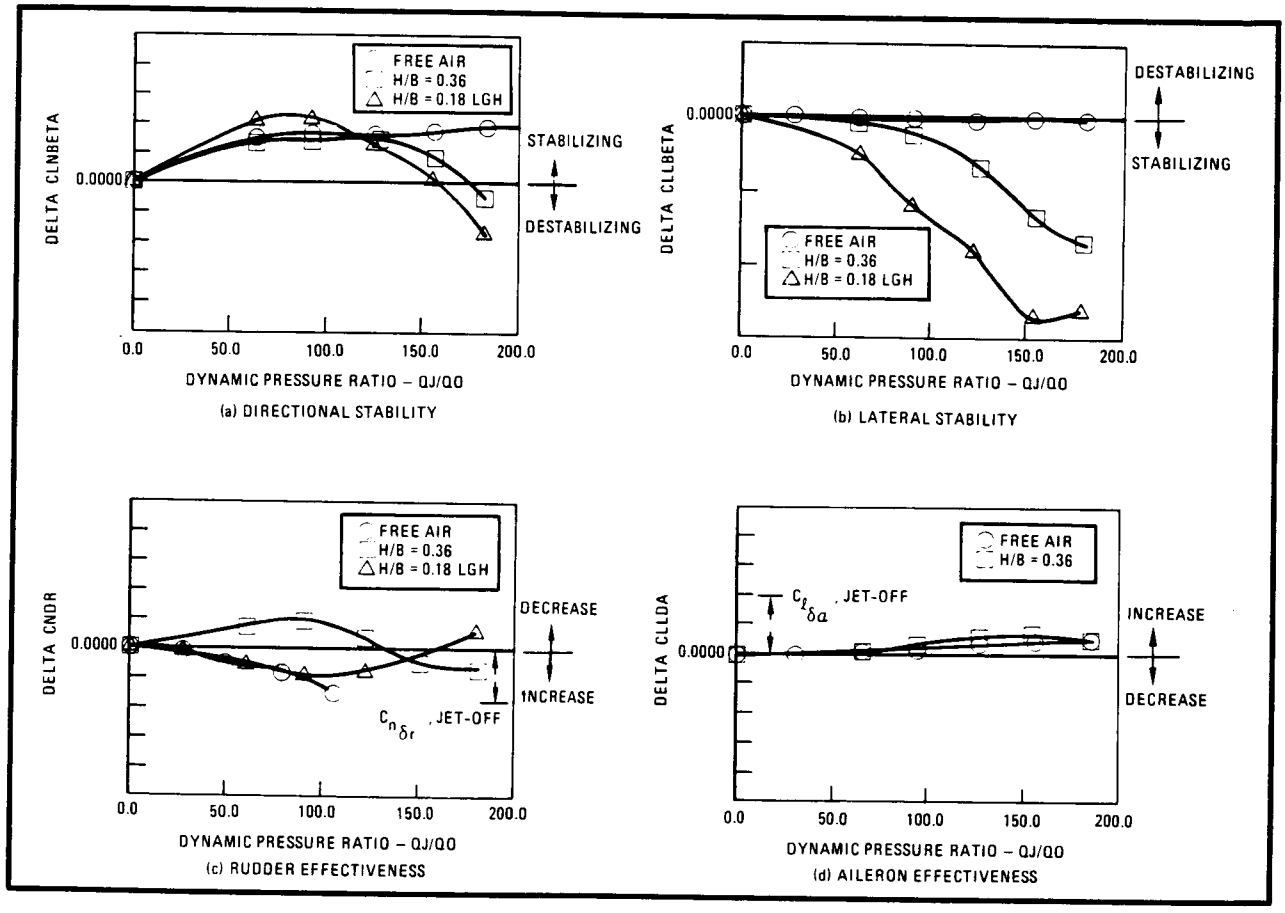

FIGURE 5. EFFECT OF GROUND HEIGHT VARIATION ON REVERSER-INDUCED CHANGES IN LATERAL-DIRECTIONAL STABILITY AND CONTROL, $\alpha = 8.5$, $\delta n/\delta f = 25/20$, $\delta M = 0$

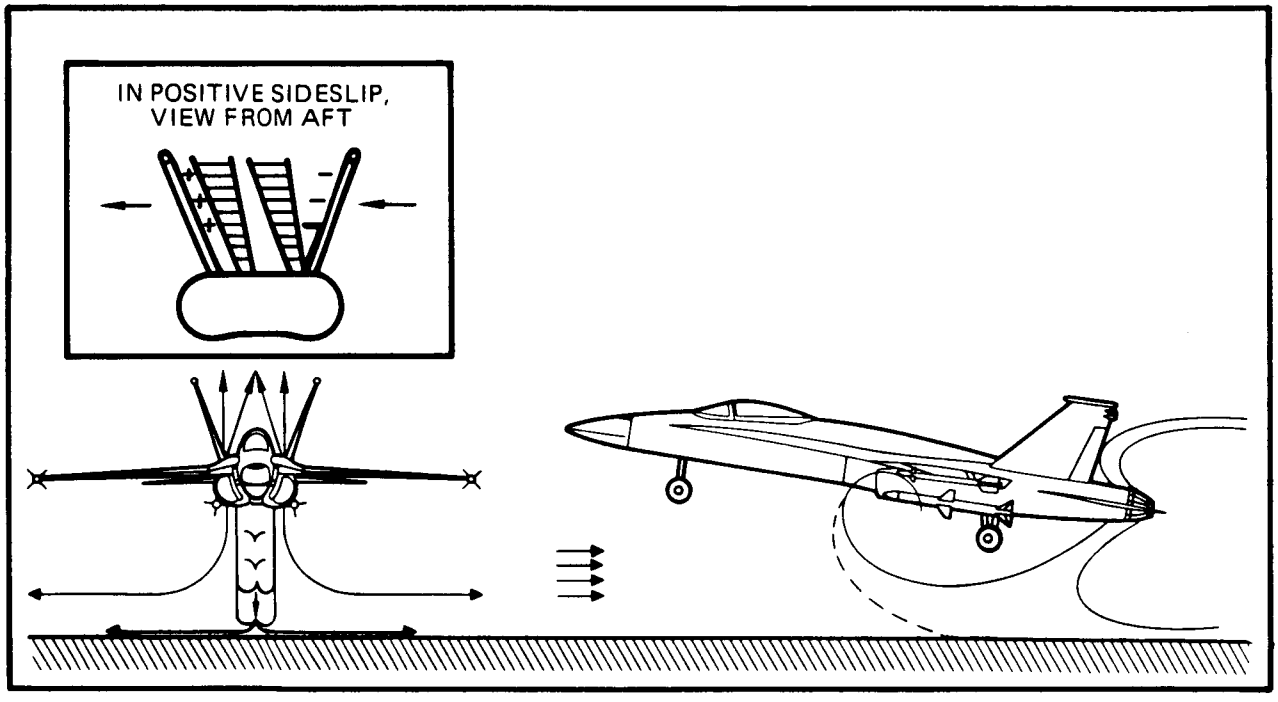

FIGURE 6. SCHEMATIC OF FLOW MECHANISMS IN GROUND EFFECT

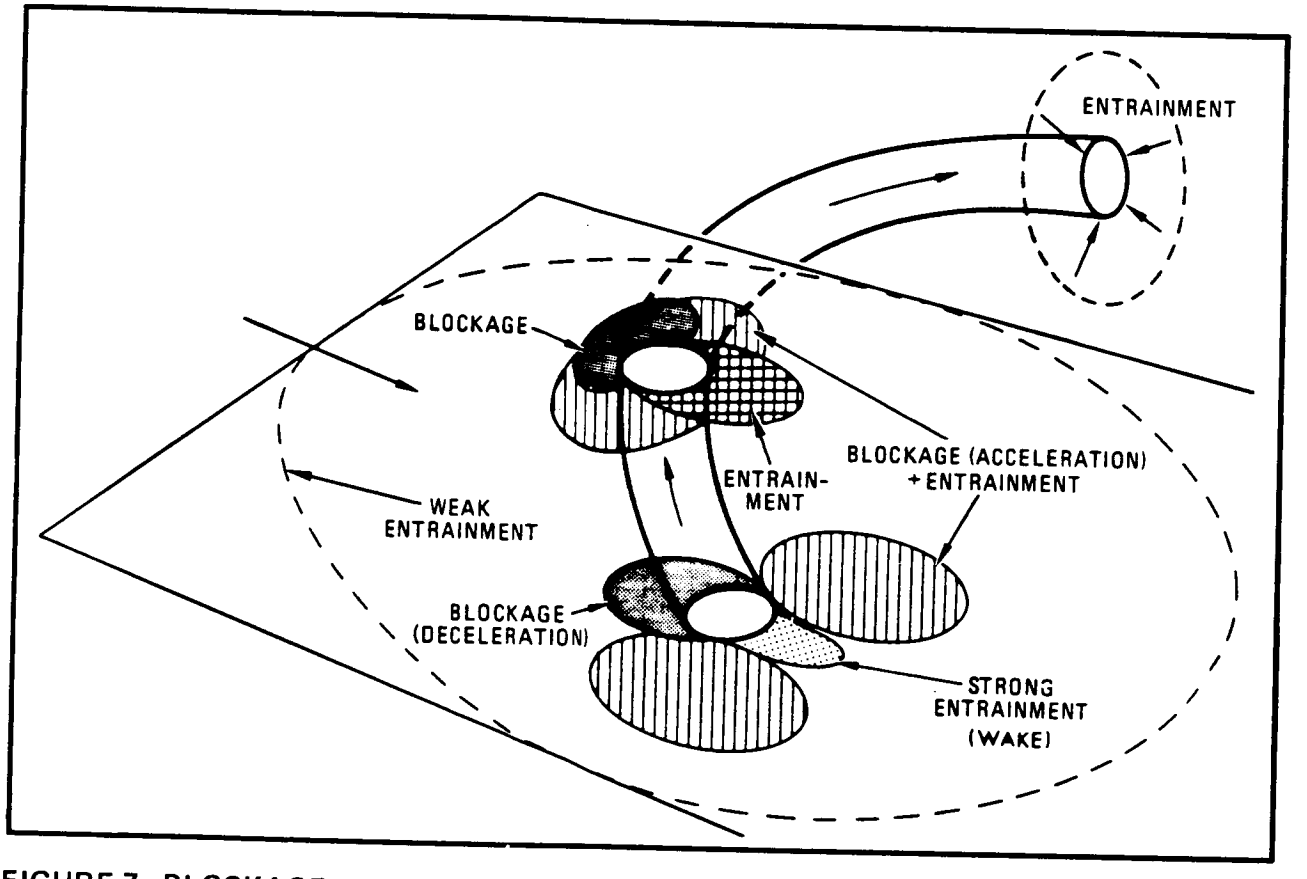

FIGURE 7. BLOCKAGE AND ENTRAINMENT DOMINATED REGIONS FOR A CIRCULAR JET IN CROSS FLOW

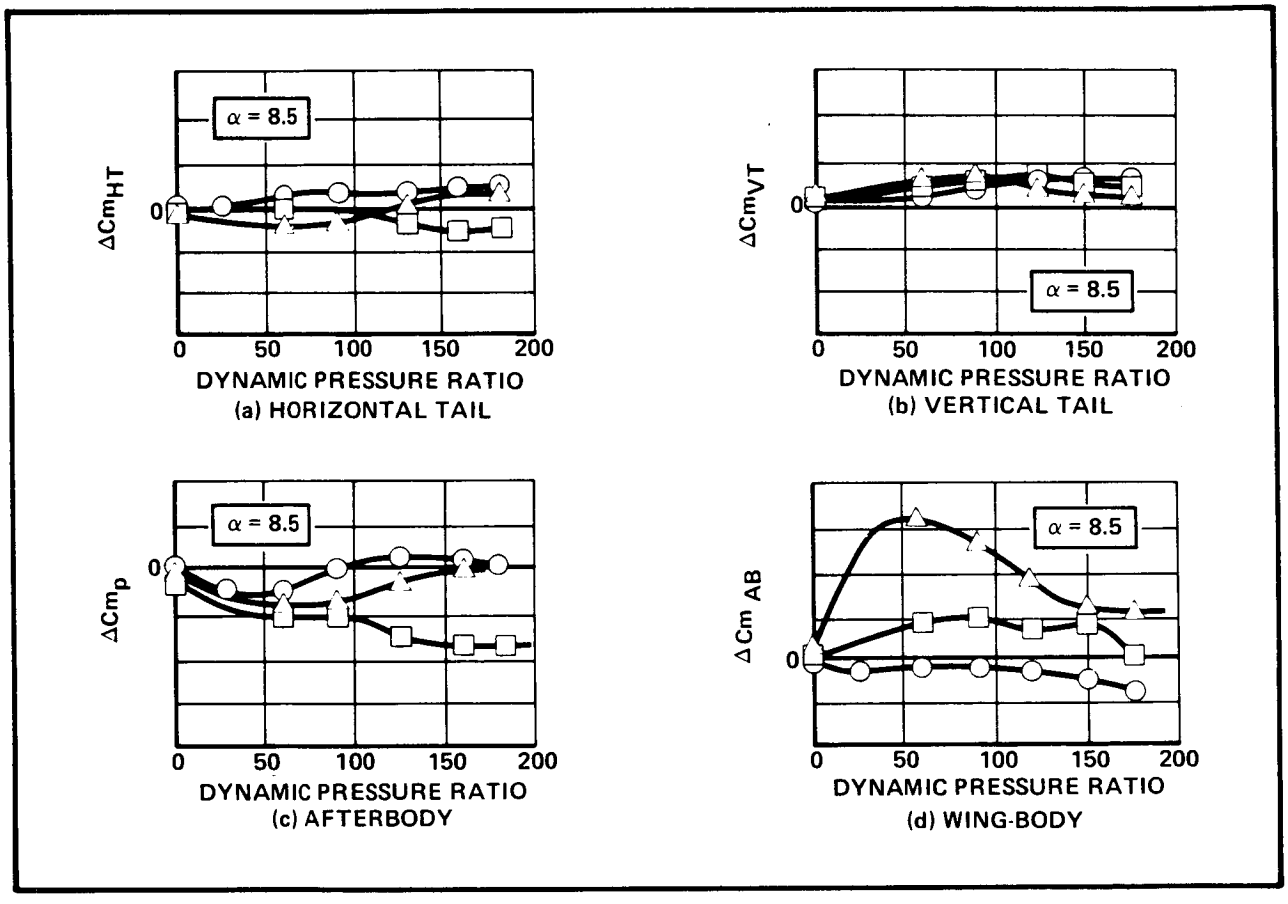

FIGURE 8. CONTRIBUTIONS OF AIRCRAFT COMPONENTS TO REVERSER-INDUCED PITCHING MOMENT AS A FUNCTION OF GROUND HEIGHT, α= 8.5, δH = -10, δn/ δf = 25/20

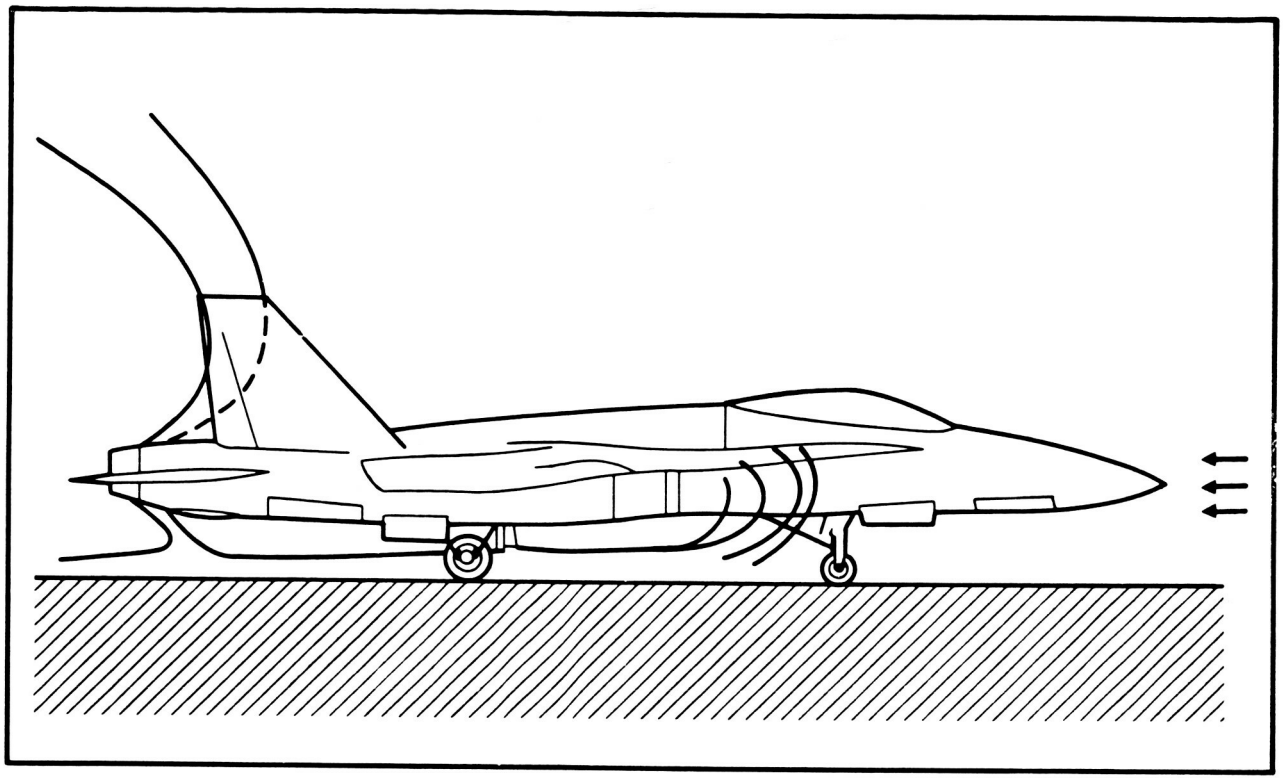

(a) SCHEMATIC OF INTERACTION

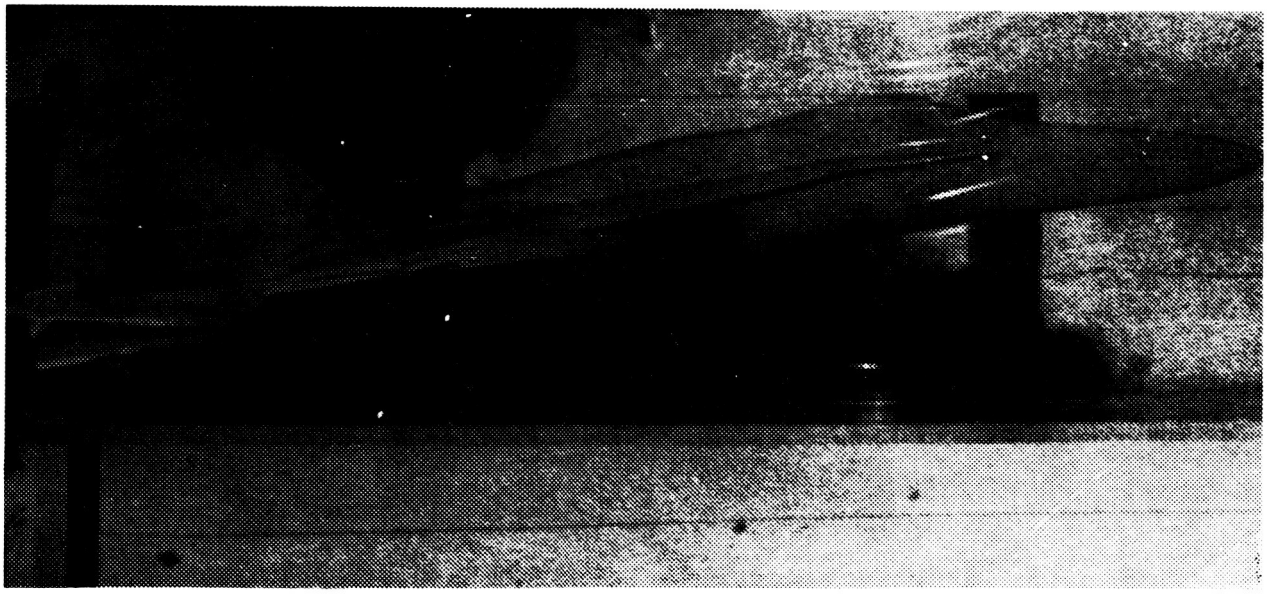

(b) WATER TUNNEL FLOW VISUALIZATION

FIGURE 9. UNSTEADY INTERACTION OF REVERSER JETS WITH FREE STREAM IN GROUND EFFECT

C-4

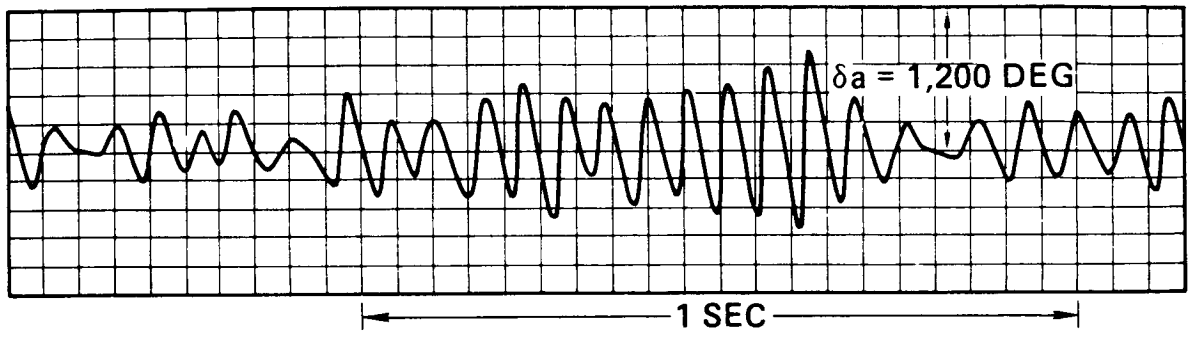

JET EFFLUX ANGLE = 45 DEG
SPLAY ANGLE = 0 DEG
DYNAMIC PRESSURE RATIO = 60 (APPROACH)
ANGLE OF ATTACK = 0 DEG

FIGURE 10a. TYPICAL ROLLING MOMENT TIME HISTORY

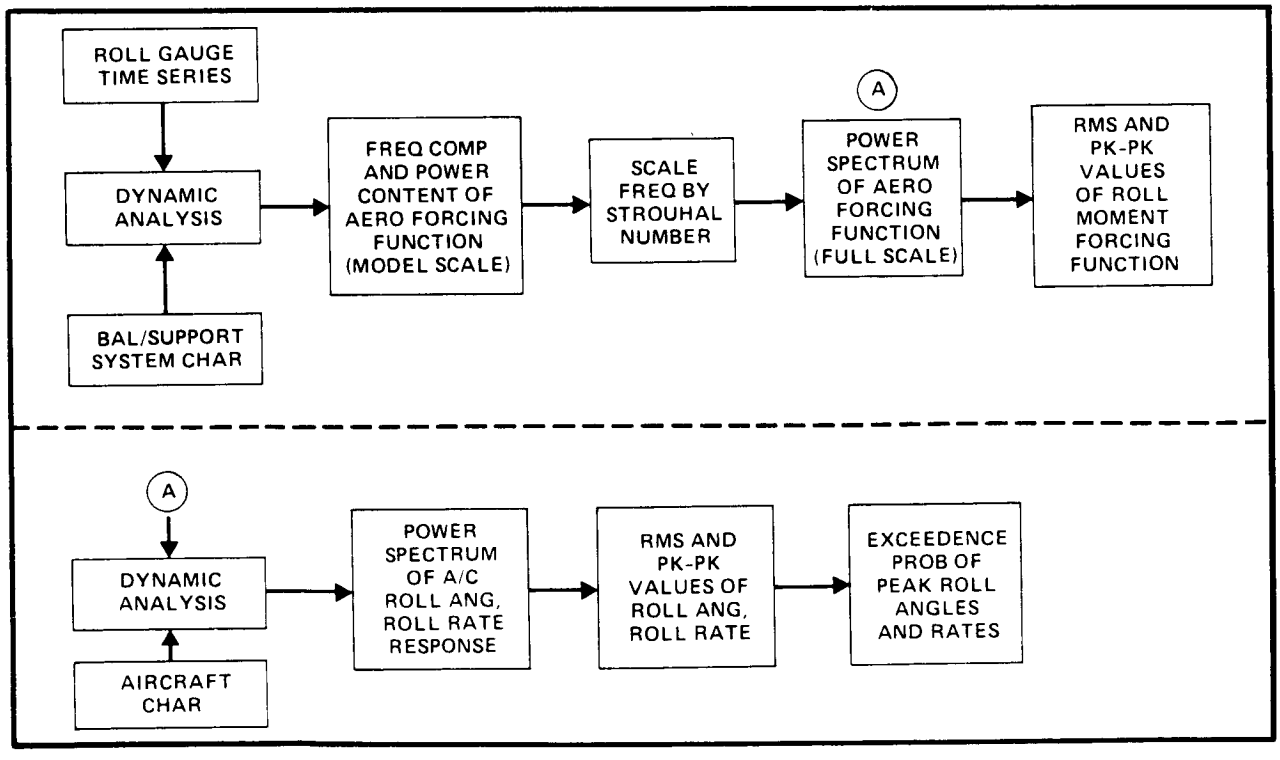

FIGURE 10b. SIMPLIFIED ANALYSIS OF ROLLING MOMENT TIME HISTORY

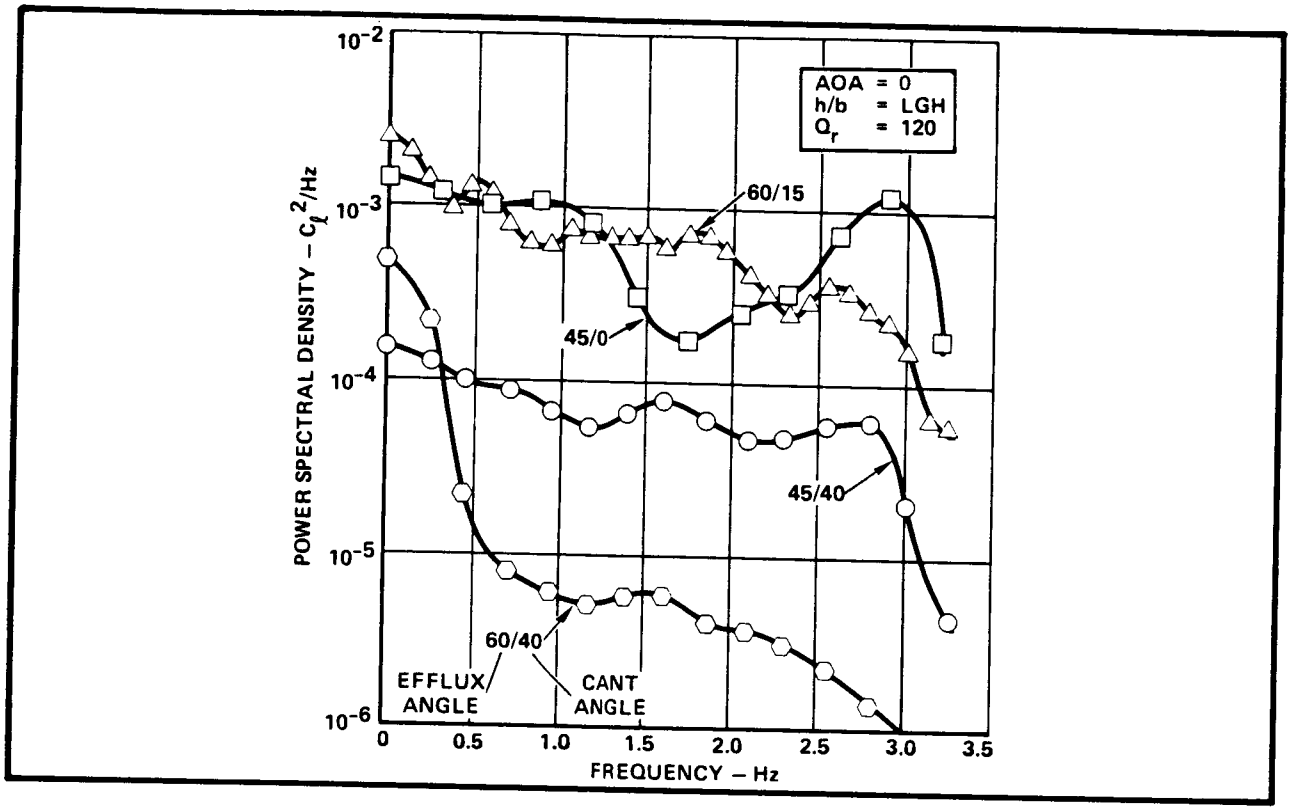

FIGURE 11. ROLLING MOMENT FORCING FUNCTION DUE TO REVERSER JET/FREE STREAM INTERACTION

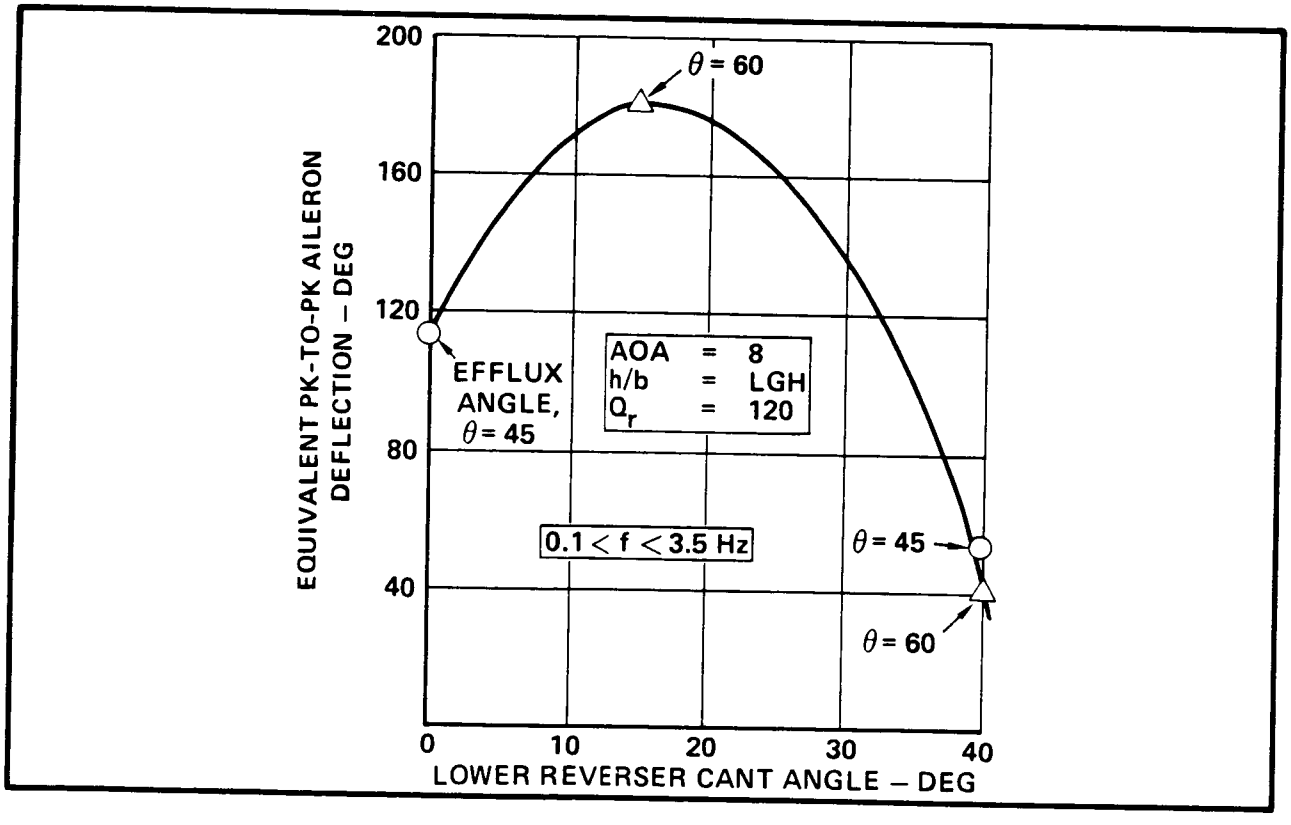

FIGURE 12. FORCING FUNCTION EXPRESSED AS EQUIVALENT AILERON INPUT

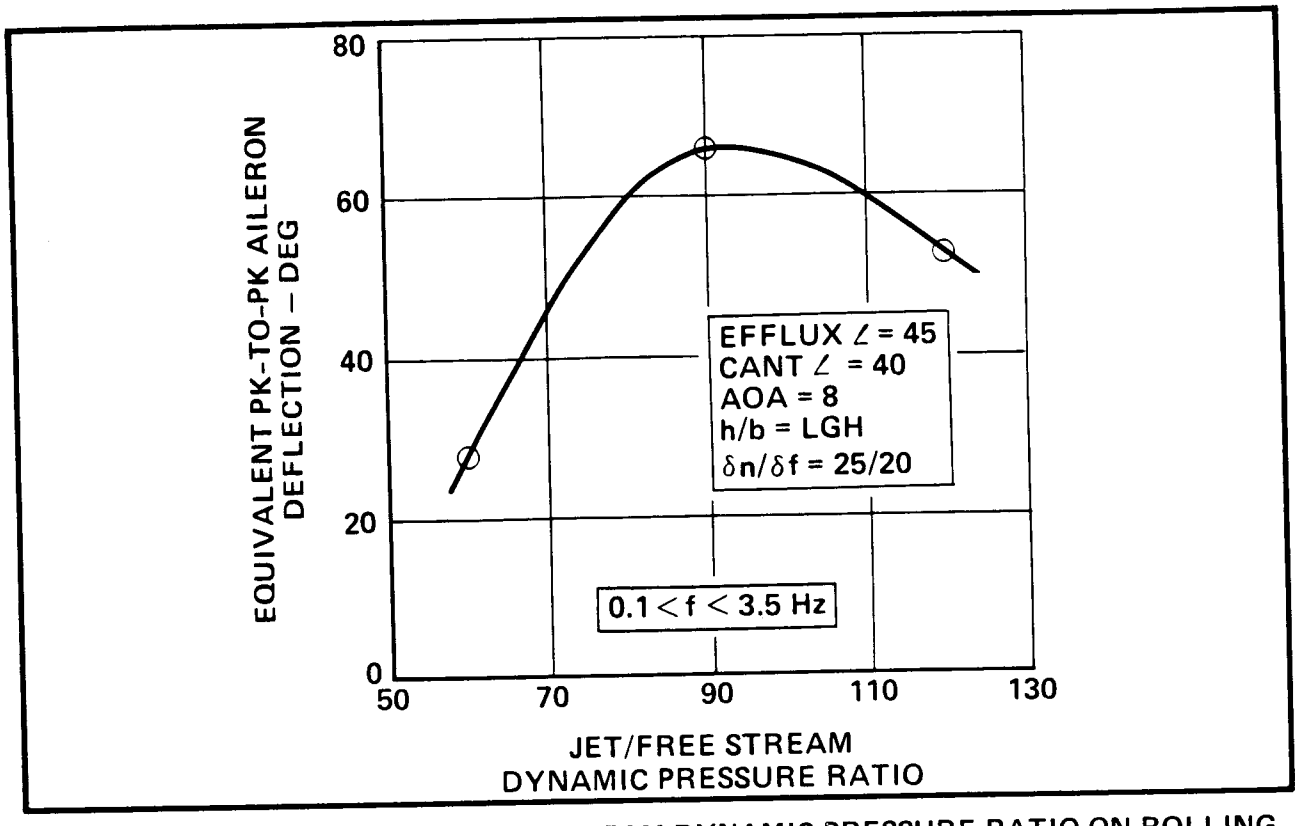

FIGURE 13. EFFECT OF JET/FREE STREAM DYNAMIC PRESSURE RATIO ON ROLLING MOMENT FORCING FUNCTION

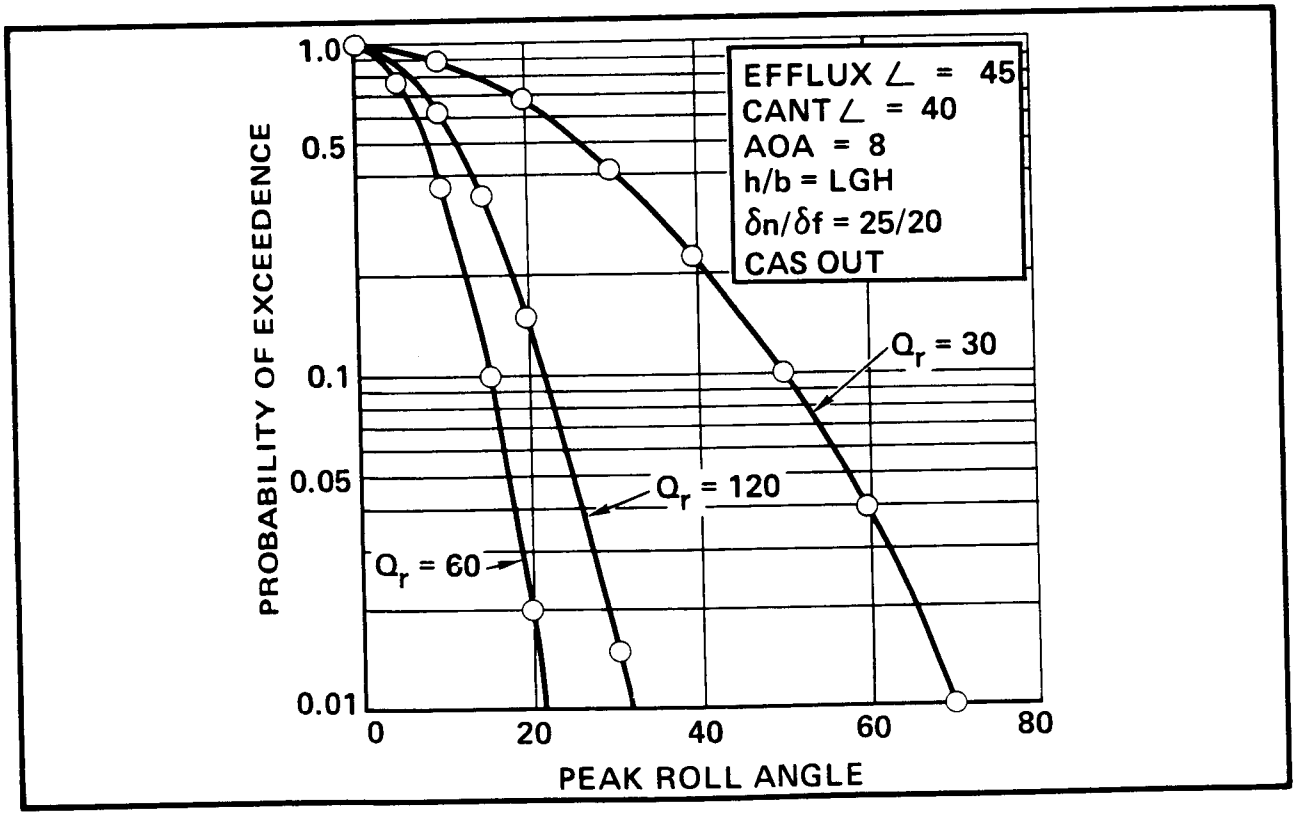

FIGURE 14. ROLL ANGLE EXCEEDENCE PROBABILITY

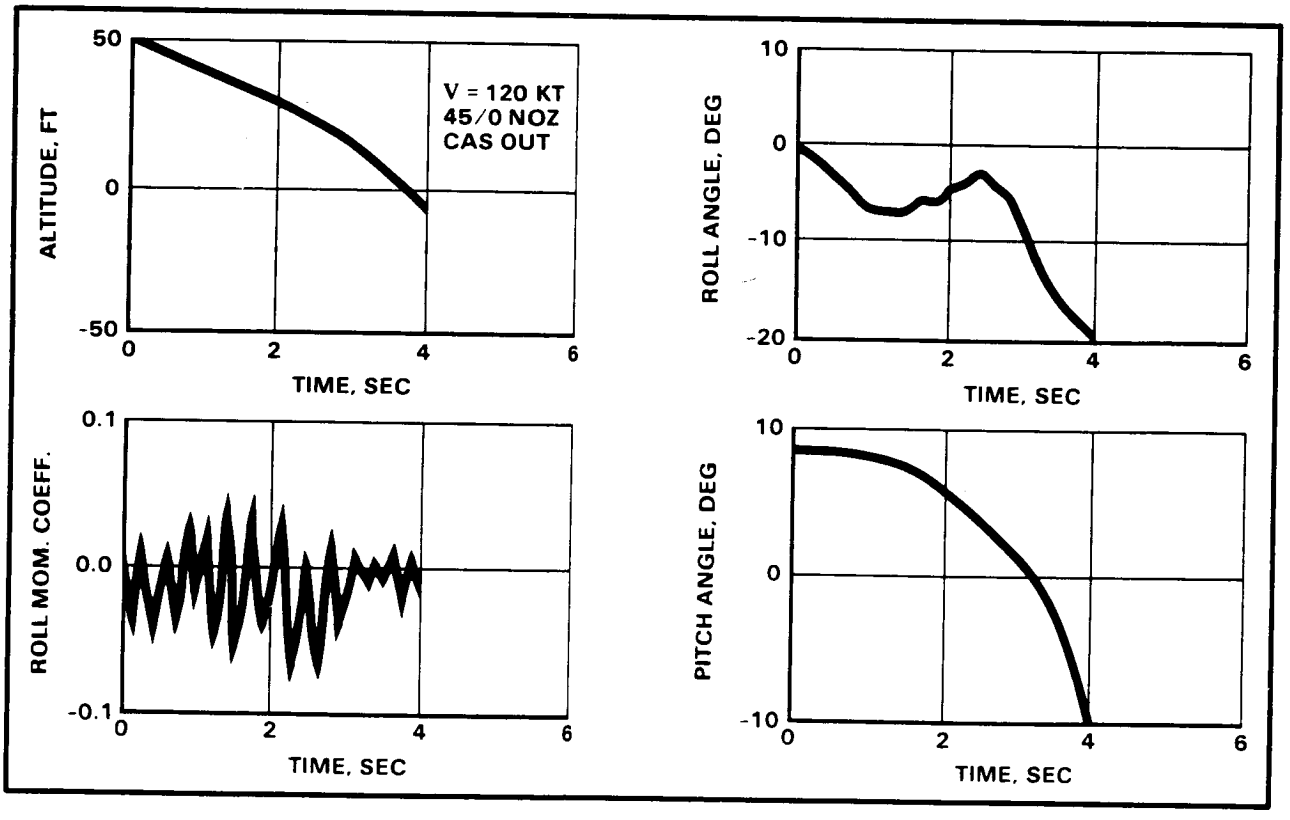

FIGURE 15. SIMULATION OF MOTION OF A THRUST-REVERSING AIRCRAFT IN GROUND EFFECT

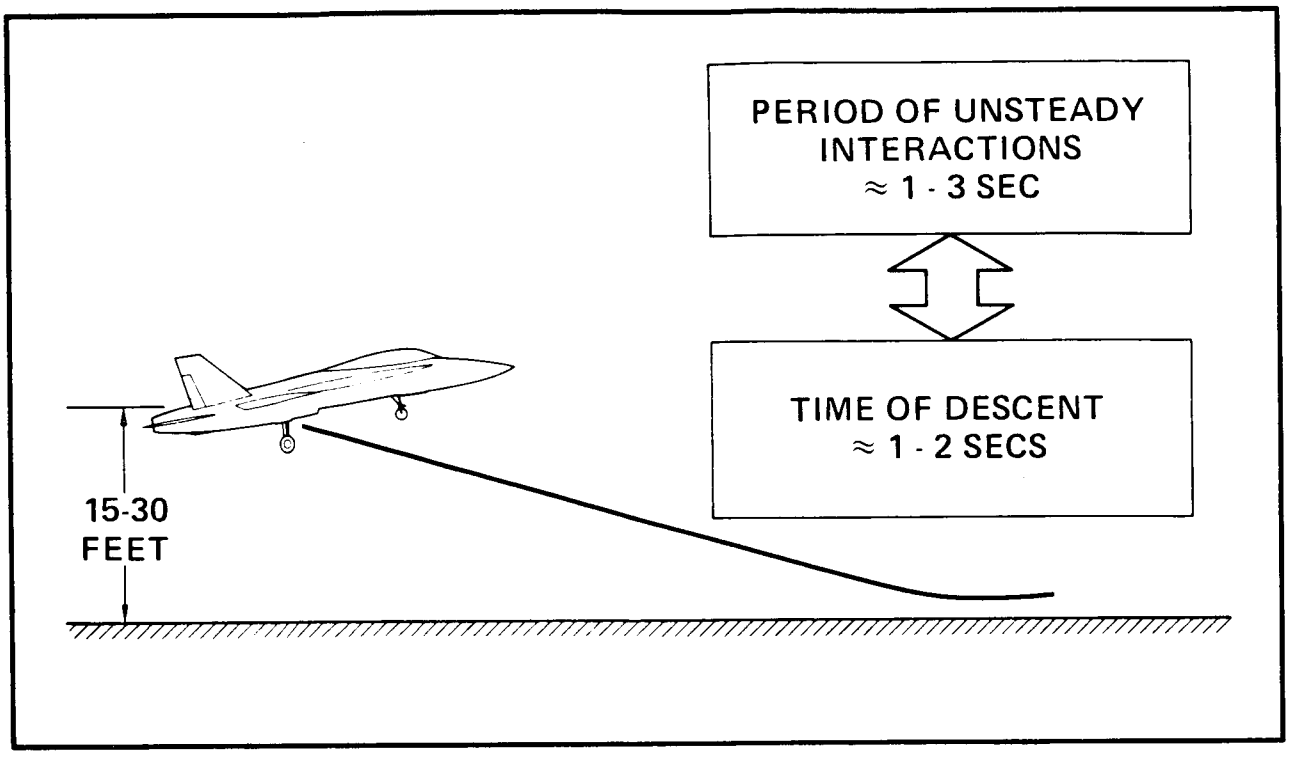

FIGURE 16. RATIONALE FOR SIMULATING RATES OF DESCENT IN GROUND EFFECT

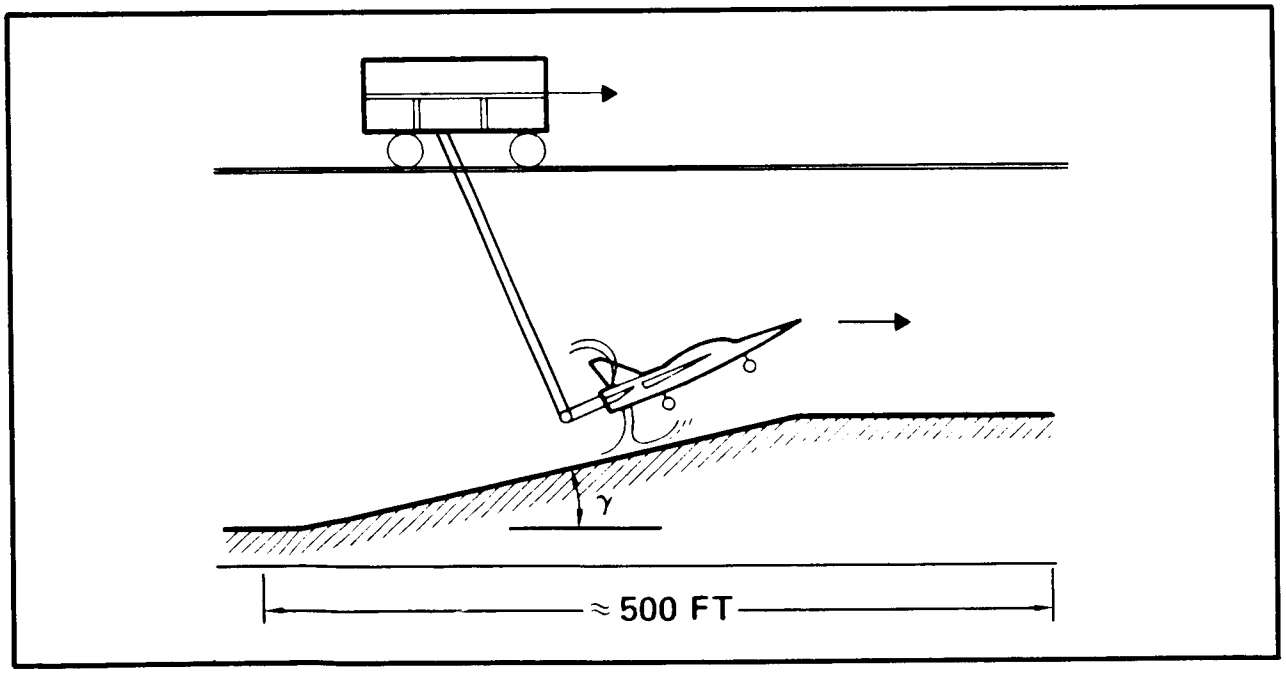

FIGURE 17. CONCEPT FOR NASA/NORTHROP/USAF TEST OF UNSTEADY THRUST REVERSER EFFECTS IN GROUND PROXIMITY

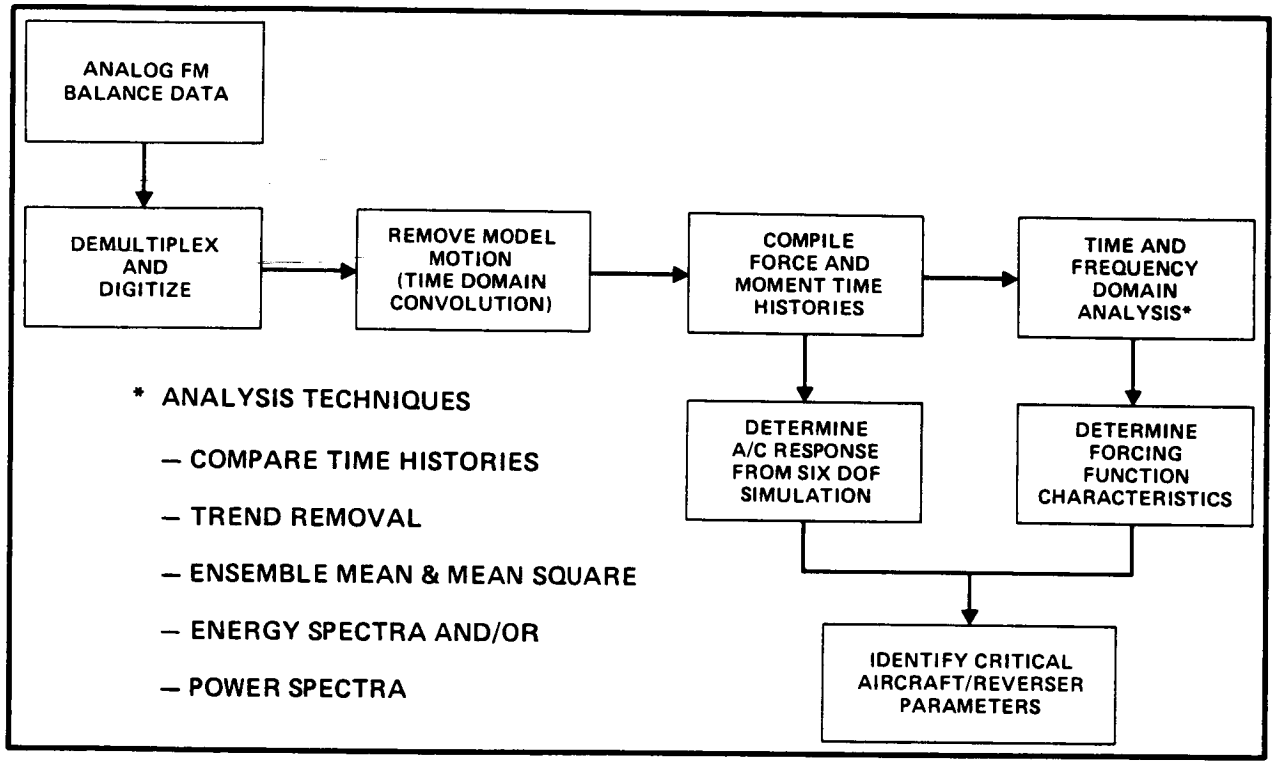

FIGURE 18. SCHEMATIC OF DATA ANALYSIS SCHEME FOR NORTHROP/NASA/USAF TRANSIENT GROUND EFFECTS TEST

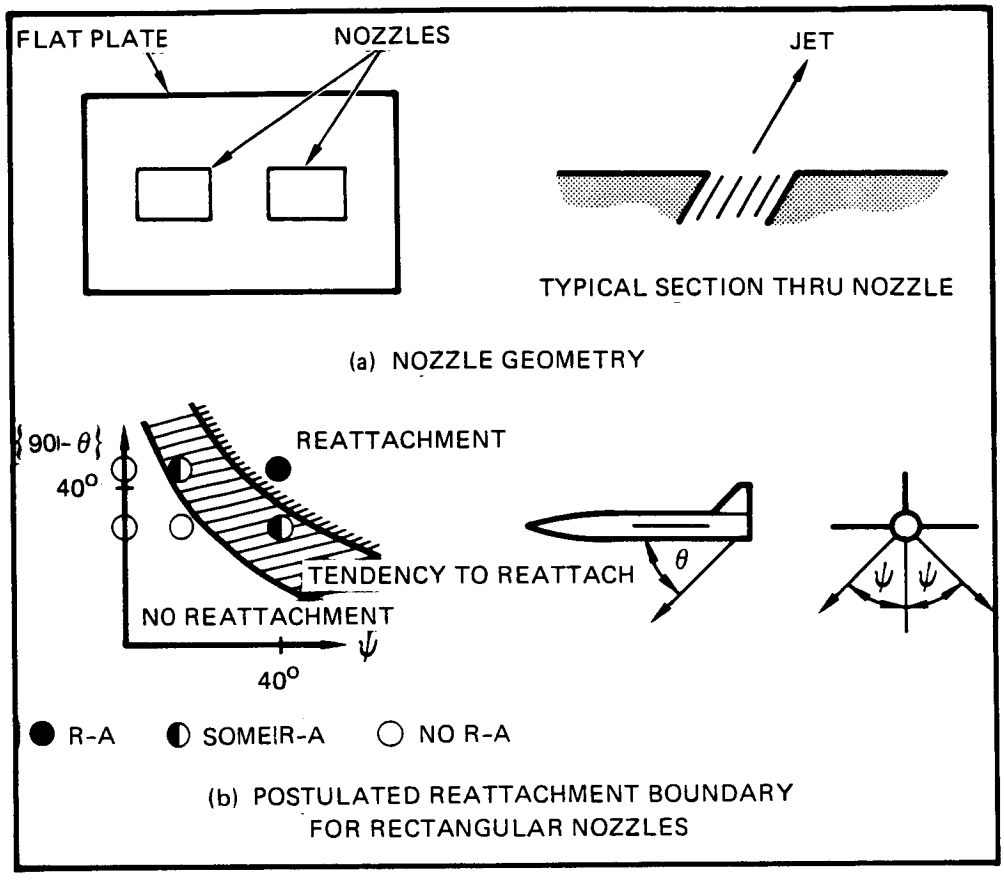

FIGURE 19. JET REATTACHMENT TO A FLAT SURFACE

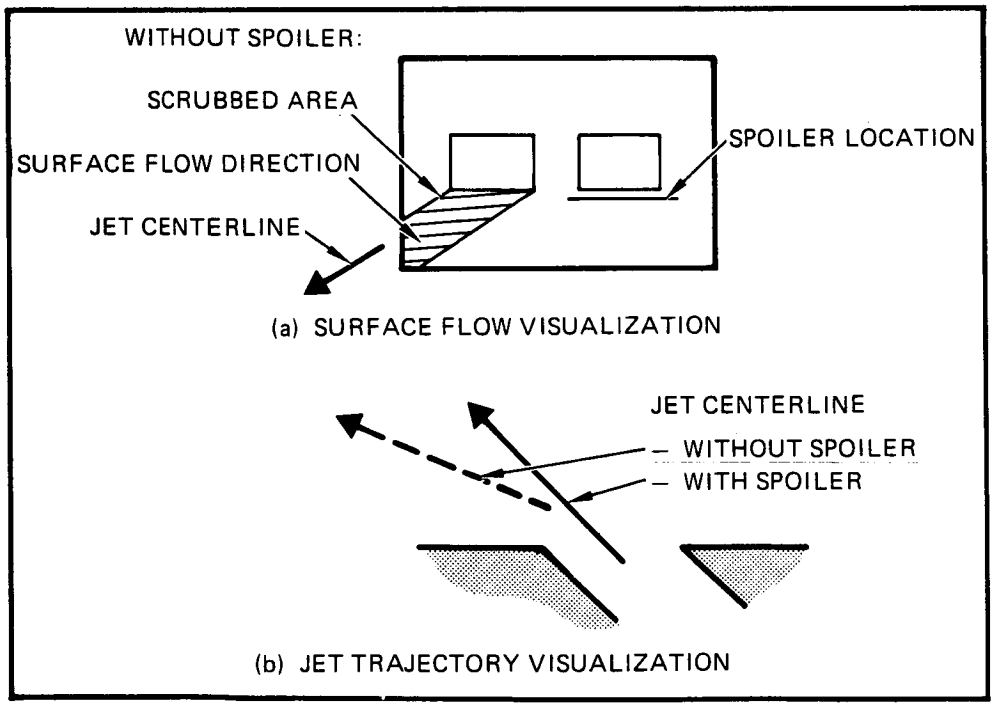

FIGURE 20. EFFECT OF SPOILER ON JET REATTACHMENT

FOR GROUND EFFECTS WORKSHOP
NASA AMES RESEARCH CENTER
20 AUGUST 1985

STOL LANDING THRUST - REVERSER JET FLOWFIELDS

D. R. KOTANSKY
L. W. GLAZE
MCDONNELL AIRCRAFT COMPANY
ST. LOUIS, MISSOURI

ABSTRACT

Analysis tools and modeling concepts for jet flowfields encountered upon use of thrust reversers for high performance military aircraft are described. A semi-empirical model of the reverser ground wall-jet interaction with the uniform cross-flow due to aircraft forward velocity is described. This ground interaction model is used to demonstrate exhaust gas ingestion conditions. The effects of control of exhaust jet vector angle, lateral splay, and moving versus fixed ground simulation are discussed. The Adler/Baron jet-in-crossflow model is used in conjunction with three dimensional panel methods to investigate the upper surface jet induced flowfield.

LIST OF SYMBOLS

A	Area
C^2	Freestream momentum correction factor
$C_{yV.T}$	Vertical tail side force coefficient
D	Diameter
f	Wall jet momentum azimuthal distribution function
h, H	Height above ground
M	Mach number
$\dot{m}$	Mass flow rate
NPR	Nozzle pressure ratio
NTR	Nozzle temperature ratio
q	Dynamic pressure
R	Radial distance
$R_{V/2}$	Radial distance in free jet from centerline to the point where the velocity is 1/2 of the centerline value
U_R	Wall jet radial velocity
V	Velocity
x, y, z	Cartesian coordinates
α	Angle of attack
γ	Momentum correction (see Reference 1)
δ_L	Thrust reverser lower vane deflection angle
δ_{je}	Jet injection angle
θ	Stagnation line slope
ρ	Density
ϕ'	Computational azimuth angle
ψ	Freestream-to-jet exit velocity ratio (V_c/V_{je})

Subscripts

c	Cross-flow, freestream
jc	jet centerline
je	jet exit
max	Maximum
min	Minimum
R	Radial
wj	Wall jet

EXHAUST GAS INGESTION

The impingement on the ground of VTOL aircraft lift jet flows in the presence of cross-winds or the impingement of STOL aircraft vectored jets (considering aircraft forward motion) creates a situation related to, but significantly different from the impingement of jets in a static environment. The significant difference is the presence of a mean flow (due to the cross-flow or aircraft motion) which is superimposed on the multiple jet impingement flowfield. The interaction of the mean flow with the existing wall jets and fountains produces a class of turbulent flow interactions which are more complex. Within this class of interactions, there is an additional difference, namely, the effect of forward motion of the aircraft produces a flow without a boundary layer, whereas the cross-flow includes a surface boundary layer. Empirical and analytical tools for the analysis and prediction of the interaction of a mean flow with a single impinging jet will be presented. Specifically, the interaction of a turbulent wall jet with a cross-flow with and without a boundary layer will be addressed. Analysis and prediction of these types of interaction is vital to the prediction of engine exhaust gas ingestion during the landing of a STOL aircraft with thrust reversers.

The ground flowfield associated with thrust reversal in STOL landing is depicted in Figure 1. V_c is the aircraft forward velocity, and δ_L is the thrust vector angle with respect to the aircraft longitudinal axis. In most applications, δ_L is 115° to 150° depending on the aircraft configuration. At high values of V_c, the ground stagnation line is located in the aft region of the aircraft flowfield, but as the aircraft decelerates, the stagnation line moves forward, increasing the potential for exhaust gas ingestion. Since the cross-flow deflects the fountain upwash in an aft direction, a conservative boundary for exhaust gas ingestion is the condition for which the ground stagnation line is located directly below the aft-most portion of the inlet.

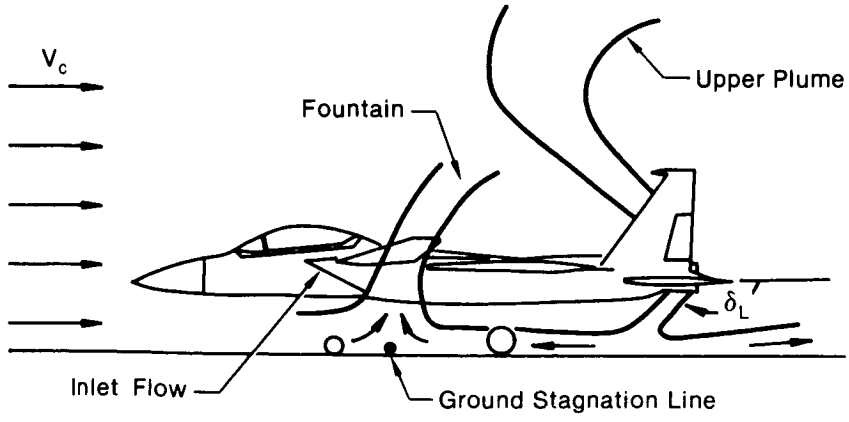

Figure 1. Ground Flowfield With Thrust Reversal

Using this criterion for the potential initiation of exhaust gas ingestion, the problem becomes that of predicting under what condition the ground wall jet stagnation line reaches this location. Additionally, once this condition is reached, for whatever imposed precautionary margin, the problem is to control the flowfield to preclude exhaust ingestion. Methods to achieve this control of jet effects will be discussed later.

The basic relationships for the interaction of a uniform cross-flow with a wall jet emanating from an impinging jet can be derived for an elemental control volume located on the stagnation line. The control volume for this case is shown in Figure 2. Employing a momentum balance normal to the stagnation line for this control volume:

$$\rho V_c^2 \sin\theta \; dy \; dz = \rho U_R^2 \sin(\phi' - \theta) \; R \; \partial\phi' \; dz \tag{1}$$

Integrating Equation (1) to the wall jet height, h, yields:

$$\rho V_c^2 \sin\theta \; h \; dy = \frac{\gamma f \dot{M}_j}{2\pi} \partial\phi' \sin(\phi' - \theta) \tag{2}$$

whereas for an impinging jet (Reference 1):

$$\rho R \; \partial\phi' \int_0^h U_R^2 \, dz = \frac{\gamma f \dot{M}_j}{2\pi} \partial\phi' \tag{3}$$

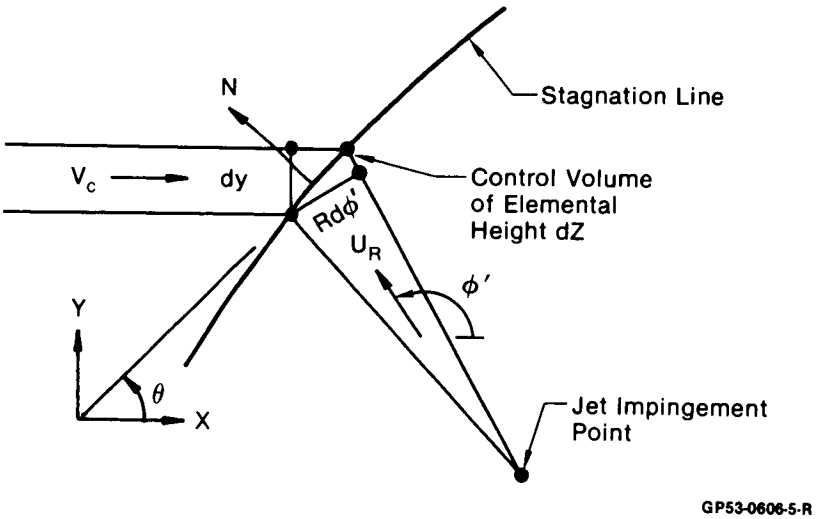

Figure 2. Control Volume for Cross-Flow/Wall-Jet Interaction

To implement the momentum flux density method (MFDM) for $\theta \cong \frac{\pi}{2}$ (see also Reference 2), the left and right hand sides of Equation (2) are divided by their respective momentum flux areas, h dy and h R $\partial\phi'$, yielding:

$$\rho V_c^2 \sin\theta = \frac{\gamma f \dot{M}_j}{2\pi R h} \sin(\phi' - \theta) \tag{4}$$

The above can be solved for the slope of the stagnation line in the ground plane, yielding:

$$\tan \theta = \frac{\beta \sin \phi'}{1 + \beta \cos \phi'} \tag{5}$$

where:

$$\beta = \frac{\gamma f \dot{M}_j}{2\pi R \, h \, \rho V_c^2} \tag{6}$$

For a jet impinging symmetrically with respect to the cross-flow direction, $\phi' = 180°$ and $\theta = 90°$, and the stagnation line distance is given by:

$$R = \frac{\gamma f \dot{M}_j}{2\pi \, h \, \rho V_c^2} \tag{7}$$

However, h is a function of R, and to solve Equation (7) this relationship must be considered. The relationship can be derived from existing wall jet data, and in general, h may be assumed to be a linear function of R. (A slightly more complicated expression for h(R) was derived in Reference 1 based on the data of Reference 3. Either expression yields a quadratic equation which can be solved for R.)

It is instructive to compare the results of the MFDM with those of the momentum flux method, MFM. The MFM result can be derived starting with the fundamental result expressed by Equation (2). Additionally from Figure 3, the following geometric relationships can be obtained:

$$d\ell = \frac{R \, \partial\phi'}{\sin (\phi' - \theta)} = \frac{dy}{\sin\theta} \tag{8}$$

or:

$$\partial\phi' = \frac{\sin (\phi' - \theta)}{R \sin \theta} \, dy$$

Substituting Equation (8) into Equation (2) yields:

$$h \, \rho V_c^2 \sin^2 \theta = \frac{\gamma f \dot{M}_j}{2\pi R} \sin^2 (\phi' - \theta) \tag{9}$$

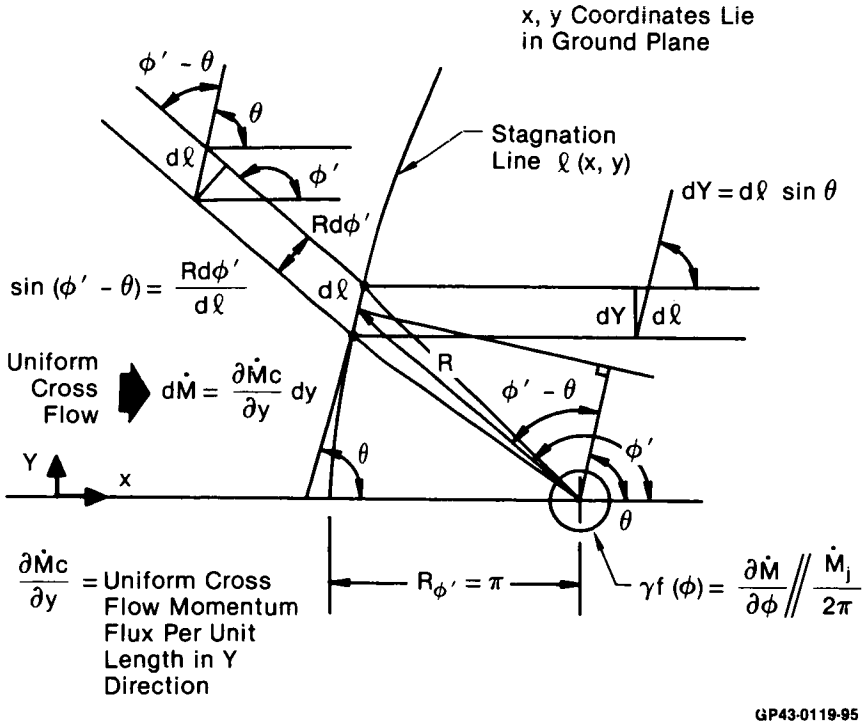

Figure 3. Interaction Geometry - Radial Wall-Jet and Uniform Cross-Flow

This result was first derived in Reference 1, in which the quantity $\frac{\partial \dot{M}_c}{\partial y}$, Figure 3, represented the momentum flux per unit length in the y direction. Equation (9) can be obtained from the results of Reference 1 by selecting:

$$\frac{\partial \dot{M}_c}{\partial y} = \rho V_c^2 h \tag{10}$$

Equations (10) and (2) are based on the assumption that the cross-flow momentum flux per unit length in the y direction need include only that amount contained in an area defined by dy and the height of the interacting wall jet, h. (There is no characteristic height in the uniform cross-flow.)

In the momentum flux method, the slope of the stagnation line in the ground plane can be obtained by solving Equation (9):

$$\tan\theta = \frac{\beta \sin\phi'}{1 + \beta\cos\phi'} \tag{11}$$

where:

$$\beta = \sqrt{\frac{\gamma f \dot{M}_j}{2\pi R \rho V_c^2 h}} \tag{12}$$

For a jet impinging symmetrically with respect to the cross-flow direction, $\phi' = 180°$ and $\theta = 90°$, and the stagnation line distance, from Equation (9), is:

$$R = \frac{\gamma\ f\ \dot{M}_j}{2\pi\ h\ \rho\ V_c^2} \tag{13}$$

which is identical to Equation (7). Therefore, based on the assumption of Equation (10), both the MFDM and the MFM yield the same result for the distance of penetration of the wall jet into the uniform cross-flow.

Comparisons of stagnation line computations based on the stagnation line slope equations, Equations (5) and (6) versus (11) and (12), show very little effect on stagnation line position or shape. Therefore, the MFDM has been incorporated into the MCAIR ground flowfield prediction methodology. The linear relation relating the wall jet height, h, to the radius, R, developed in Reference 1, is also used.

$$h = \sigma_1 + \sigma_2\ R \tag{14}$$

Comparisons of the above results with the experimental data of Reference 4 indicated that an additional empirical correction was required to obtain agreement with the experimental data for wall jet penetration into a uniform cross-flow. The empirical correction is applied to the cross-flow momentum flux per unit length, dy, as given by

$$\frac{\partial \dot{M}_c}{\partial y} = C^2\ \rho V^2\ h \tag{15}$$

Equations (5), (6), and (7) then become:

$$\tan\theta = \frac{\beta\ \sin\phi'}{1 + \beta\cos\ \phi'} \tag{16}$$

where

$$\beta = \frac{\gamma\ f\ \dot{M}_j}{2\pi\ R\ h\ C^2\ \rho V_c^2} \tag{17}$$

and

$$R = \frac{\gamma\ f\ \dot{M}_j}{2\ \pi h\ C^2\ \rho\ V_c^2} \tag{18}$$

The values of C^2 for wall jet penetration into uniform cross-flows and for cross-flows with boundary layers was determined from References 4 and 5 respectively.

In Reference 4, the penetration of a single impinging jet into a uniform cross-flow was studied for both hot and ambient temperature jets. The uniform cross-flow interaction was simulated by moving the impinging jet through ambient air, supporting it on a rotary support system. Except for minor centrifugal effects, this test technique correctly simulates the STOL jet impingement situation, including the retardation of the wall jet due to the relative motion of the nozzle along the fixed ground plane. The correct simulation can be obtained in a conventional wind tunnel only through the use of a moving ground plane. The correlation of penetration distance into the cross-flow is shown in Figure 4, taken from Reference 4. The geometry and nomenclature are defined in Figure 5.

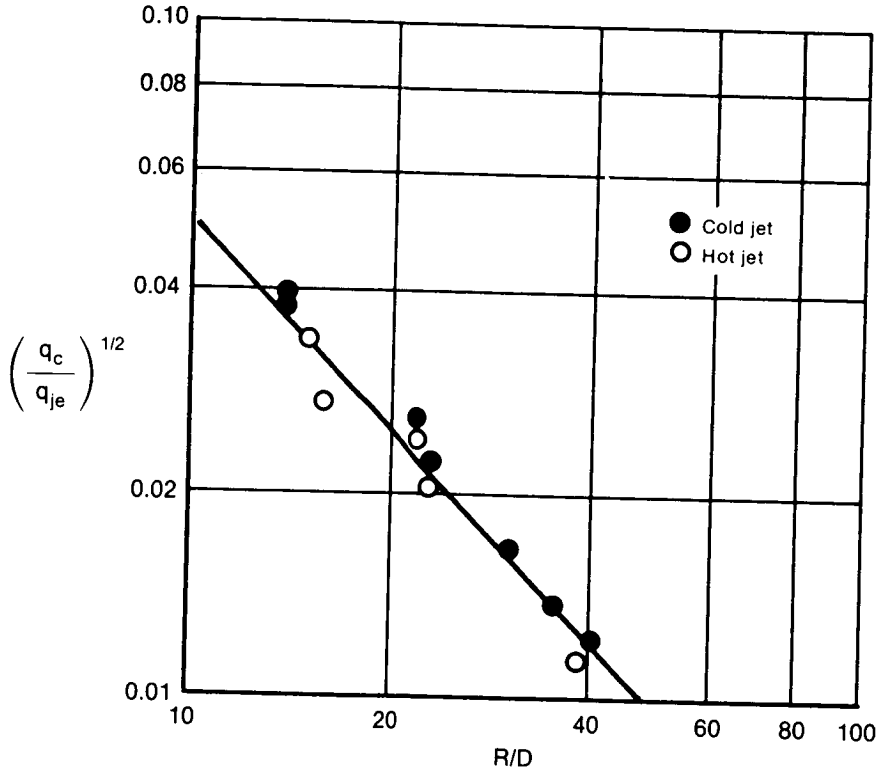

Figure 4. Jet Penetration Into Uniform Cross-Flow for Hot and Cold Jets

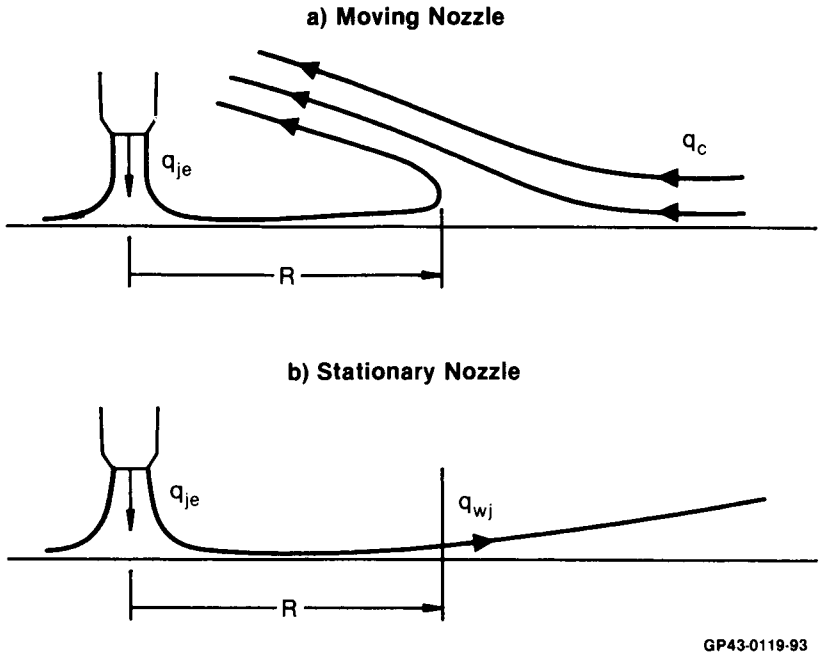

Figure 5. Jet Penetration Nomenclature

Another empirical correlation from Reference 4 shows that:

$$(q_c/q_{wj})^{1/2} \cong 0.5 \tag{19}$$

which indicates, from Figure 5, that the stagnation line in the cross-flow situation occurs at a distance corresponding to the static jet impingement situation where:

$$q_{wj} \cong 4\, q_c \tag{20}$$

In other words, the wall jet penetrates into the cross-flow much less than would be expected from an equivalence of local dynamic pressures. This can be accounted for in the analytical models by artificially increasing the cross-flow momentum as shown in Equation (15).

From Reference 4 it can be expected that $C^2 = 4$ for the uniform cross-flow case without a cross-flow boundary layer. Equations (16), (17), and (18) were used to determine the value of C^2 to fit the data correlation of Reference 4, shown in Figure 4. The empirically determined value of C^2 was found to be:

$$C^2_{\text{uniform cross-flow}} = 3.61 \tag{21}$$

This value of C^2 is used in the MCAIR ground flowfield methodology for the uniform cross-flow interaction with no cross-flow boundary layer and where the wall jet is retarded by the relative motion of the ground plane. The interaction with and without a moving ground plane is shown in Figure 6. With a fixed ground plane, the jet impinges statically, and the cross-flow includes a boundary layer. In the moving ground plane situation which simulates a STOL landing, the stagnation line shifts aft due to the lack of a boundary layer in the cross-flow and due to the retardation of the wall jet.

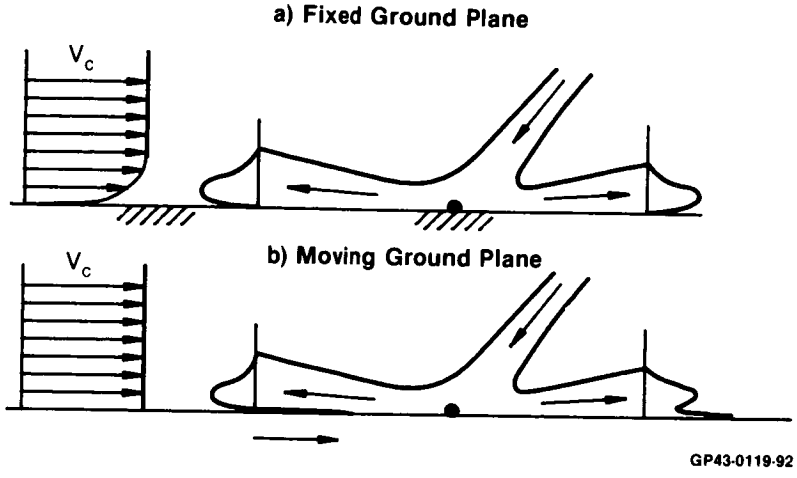

Figure 6. Fixed vs Moving Ground Plane Interactions

In the case of a fixed ground plane, Figure 6a, C^2 would be expected to be less than the value of 3.61 obtained for the moving ground plane case. The data of Reference 5 was used to determine C^2 for this situation. This data is correlated analytically as:

$$\frac{R}{D} = 0.61\left(\frac{q_{je}}{q_c}\right)^{1/2} \tag{22}$$

The data correlated by Equation (22) also included variations in nozzle exit flow temperature.

For this situation, the correlating value of C^2 for use in the MCAIR ground flowfield methodology was determined to be:

$$C^2_{\text{fixed ground plane}} = 2.40 \tag{23}$$

These correlations are summarized in Figure 7, where the variation of the wall jet stagnation line or separation distance is shown as a function of the dynamic pressure ratio between the nozzle exit and the cross-flow. The curve labeled "Uncorrected MFDM" corresponds to $C^2 = 1.0$, which usually overpredicts the penetration of the wall jet into the cross-flow. The correlations corresponding to the moving ground and fixed ground plane situations were obtained using the values of C^2 given in Equations (21) and (23), respectively, based on the data of References 4 and 5. Shown also in Figure 7 are data correlations for two values of H/D from wind tunnel and moving ground vehicle tests of ingestion boundaries for the Concorde aircraft configuration with $\delta_L = 115°$. These correlations contain both fixed and moving ground data (Reference 6).

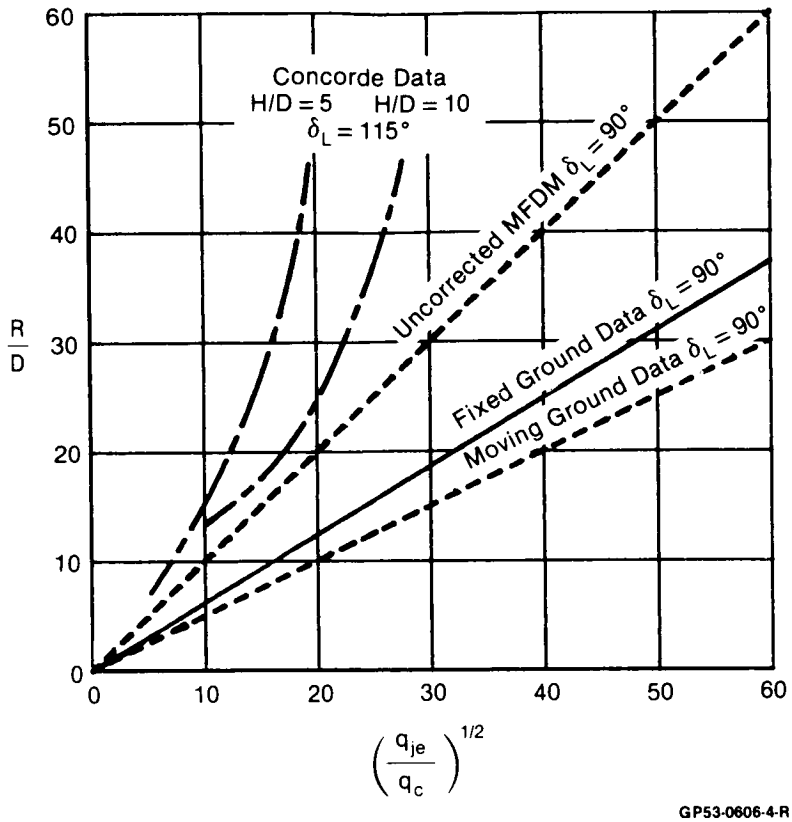

Figure 7. Correlation of Wall-Jet Penetration Results - Cross-Flow/Wall-Jet Interaction

To further validate the above computational model, MCAIR determined the value of C^2 that most closely matched a lower surface exhaust deflection schedule developed from two experimental data correlations and a MCAIR empirical technique. The data correlations used were developed for a high performance aircraft during STOL landing ground deceleration and were valid for fixed ground plane simulations. A value of C^2 of 2.50 was found to satisfactorily match the data correlations. This compares well with the previously determined value of 2.40 (Equation 23).

Additional useful information on the effects of fixed versus moving ground plane testing can be found, for example, in References 7 and 8. Reference 8 contains an extensive list of earlier work. Figure 8, taken from Reference 7, substantiates the results presented in Figure 7 in terms of the thrust reverser shown in the figure, which included forward vectoring for reverse thrust plus outboard splay of the reverser jets. It is seen from the figure that the rollout speed for ingestion with the moving ground plane simulation was approximately 15% less than for a fixed ground plane. The effect of NPR is also indicated for this reverser configuration, and in general indicates the expected trends with forward vectored reverser jet impingement for a wide range of configurations. The differences between moving and fixed ground plane simulations may not appear to be large; however, the desired landing rollout distance goals are quite short compared to CTOL high speed aircraft landing distances, and these differences may be critical.

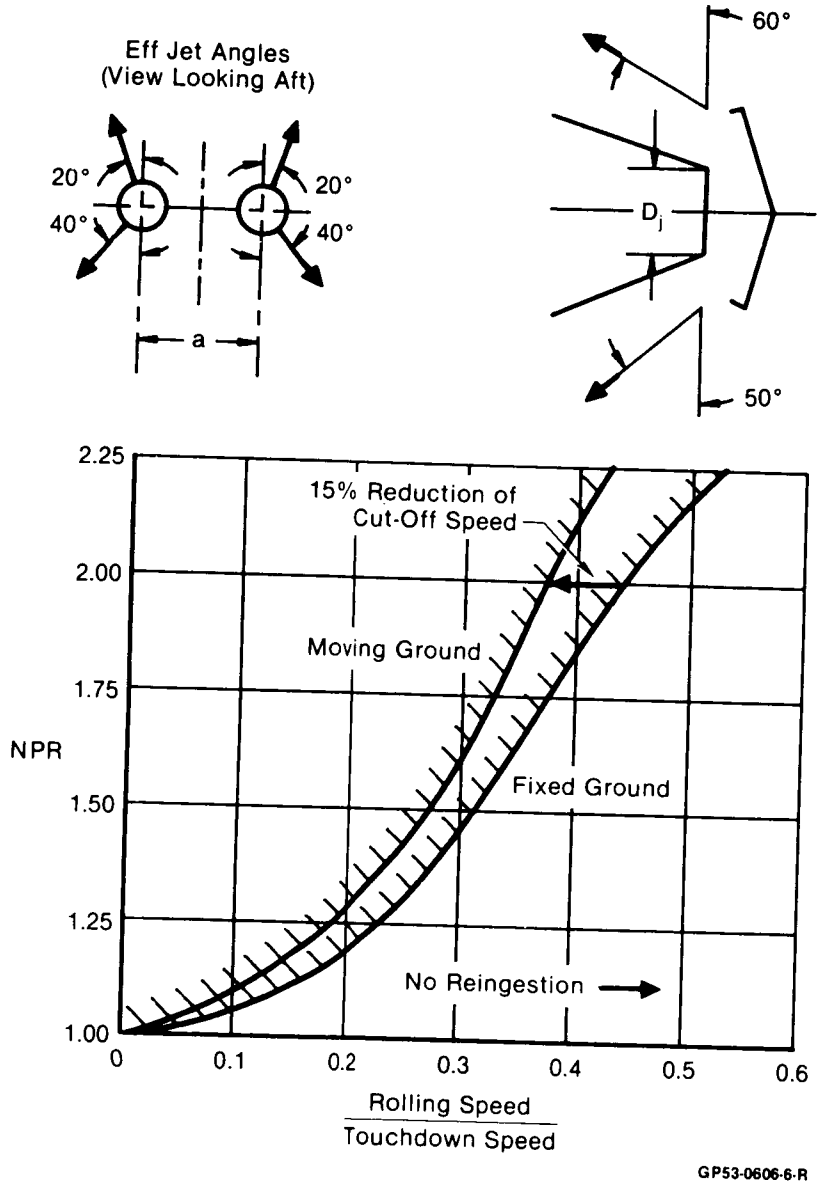

Figure 8. Thrust Reverser Operation Boundary Due to Ingestion for Fixed and Moving Ground Plane Simulations

An alternate empirical method is also used by MCAIR to predict the exhaust gas ingestion potential for STOL aircraft employing thrust reversers during landing rollout. This method is based on the balance of local dynamic pressure in the turbulent wall jet with the dynamic pressure of the cross-flow. A typical decay in the dynamic pressure of a wall jet with increased radius is shown in Figure 9. These data also include cases with elevated nozzle exit flow temperatures.

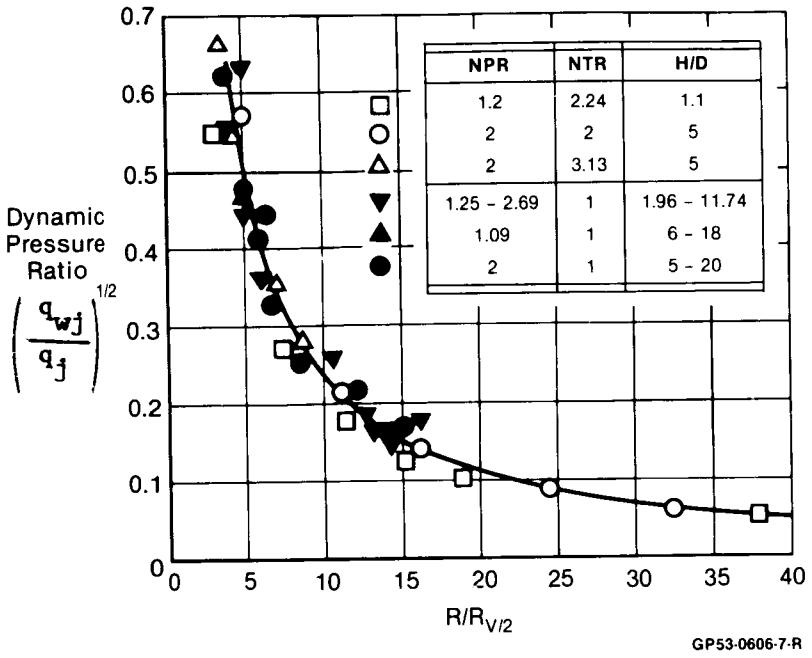

Figure 9. Dynamic Pressure vs Radial Position - Vertical Impingement

Here, q_j is the free jet dynamic pressure locally at the distance down the jet corresponding to the distance from the nozzle exit to the jet impingement point. $R_{V/2}$ is also determined from the free jet velocity profile at this point.

In the fixed ground plane situation, the location of the stagnation line is taken to be at the point where:

$$q_c = q_{wj} \Big|_{\text{average}} = 0.457\, q_{wj} \Big|_{\text{max}} \tag{24}$$

Equation (24) is also used in the moving ground plane situation, but, the cross-flow dynamic pressure is multiplied by a factor of four; i.e.,

$$q_c \Big|_{\text{moving ground}} = 4\, q_c \tag{25}$$

which relates to Equation (20) based on the data of Reference 4.

Figure 10 presents computations of the ground stagnation line for a typical high speed fighter employing thrust reversers. Stagnation line locations predicted by the MCAIR empirical method are shown as a function of aircraft ground roll speed (headwind velocity) for thrust reversal with and without lateral splay. The beneficial effect of splay is apparent; however, a component of reverse thrust can be lost if the splay is not obtained through a rotation of the reverser about the aircraft longitudinal axis.

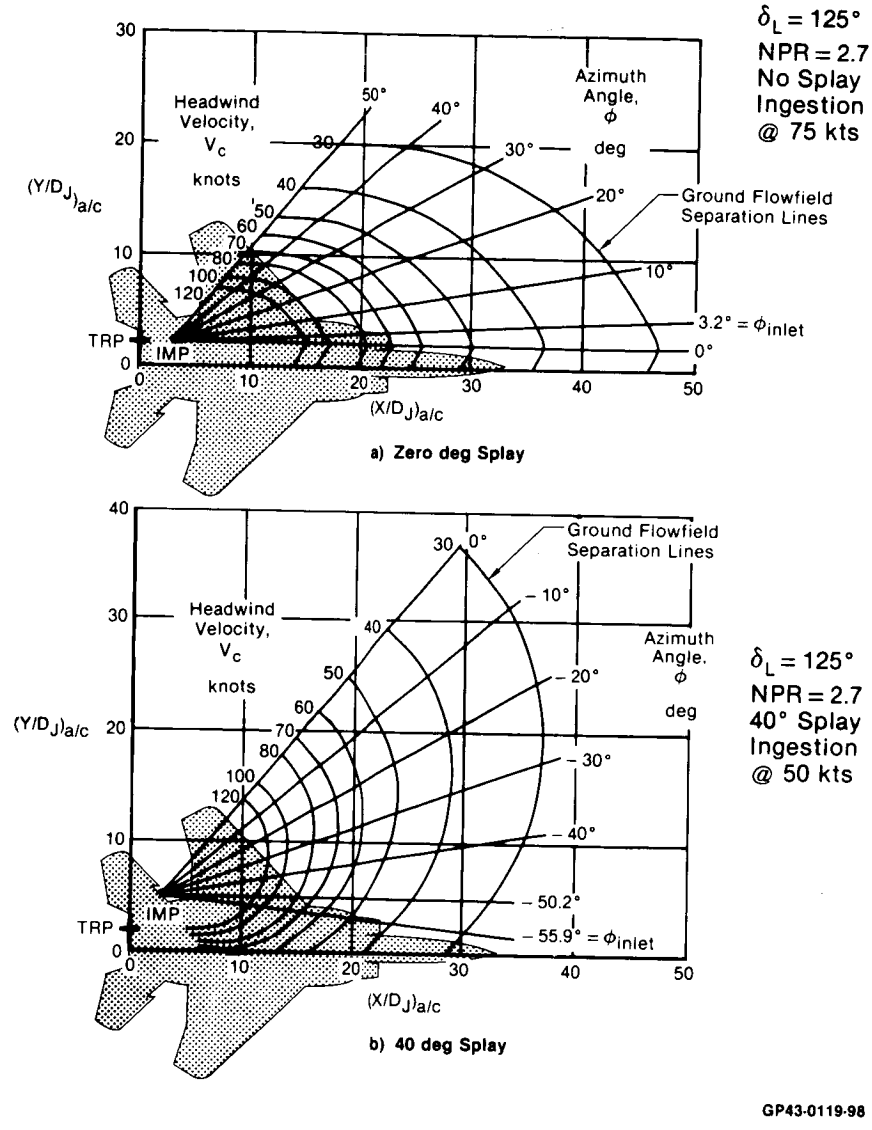

Figure 10. MCAIR Empirical Method Ground Separation Line Predictions

Exhaust gas ingestion can be reduced, and in fact eliminated, on ground rollout through thoughtful configuration design, and, additionally, through active control of the direction of jet efflux. Thrust reverser designs employing variable vectoring vanes can be used to direct the jet efflux to maintain the ground stagnation line aft of the aircraft inlet as the rollout velocity is reduced, while still providing significant reverse thrust. These systems, combined with conventional mechanical wheel braking, can provide excellent STOL landing performance.

UPPER SURFACE JET FLOWFIELD

The jet efflux from upper surface thrust reversers can considerably alter the aircraft upper surface flowfield. Elements of concern include:

- Effects on tail mechanical loads,
- Changes in stability and control characteristics in ground effect,
- Aircraft surface temperatures.

Some features of the upper surface flowfield can be predicted by panel methods such as PANAIR or MCAERO, used in conjunction with a suitable jet-in-cross-flow model. The following will describe the jet-in-cross-flow model used at MCAIR.

The MCAIR V/STOL Methodology currently derives information on jets emanating from circular (or nearly circular) nozzles from the Adler-Baron Jet-In-Cross-Flow program, JICP, (Reference 9). The basic method was developed for incompressible jets submerged in a uniform cross-flow. The jet injection angle, δ_{je}, and freestream-to-jet-exit velocity ratio, ψ, are variable over a useful range. (MCAIR has modified the basic Adler-Baron formulation to include some non-circular jet exit shapes, and also to permit forward jet injection angles, for analysis of thrust reverser flowfields).

A schematic of jet-in-cross-flow development is shown in Figure 11. The jet is deflected downstream by the momentum of the cross-flow. As the jet develops downstream, the vorticity generated by the basic jet injection, combined with the flow of the cross-flow around the jet, forms a pair of contrarotating vortices which tend to dominate the downstream development of the jet. Induced flowfield velocities result from:

(a) the basic blockage of the jet,
(b) the turbulent entrainment (similar to a free jet), and
(c) vortex induction.

In general, the centerlines of the vortices lie above the nominal jet centerline. Trajectories of both the jet centerline and the vortex centerlines are given in Reference 10 for round jets.

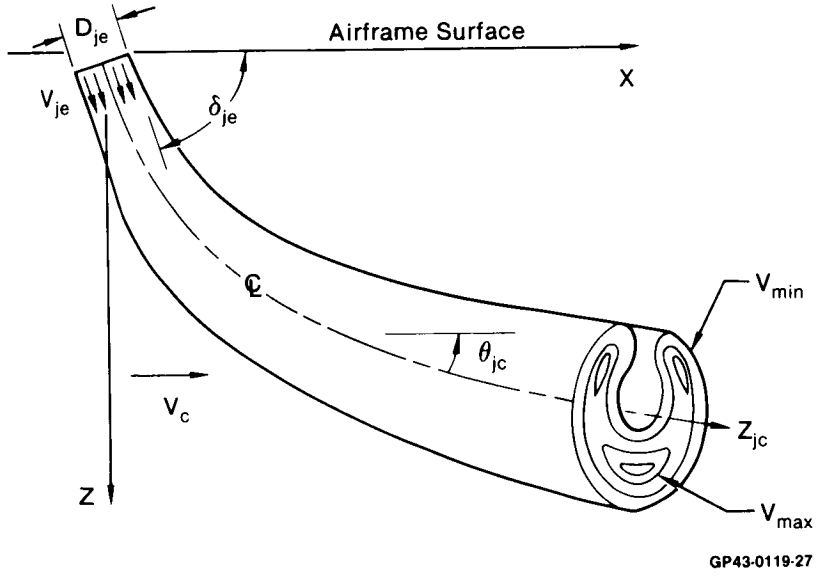

Figure 11. Jet-In-Crossflow at High Injection Angle

The basic Adler-Baron model (Reference 9) incorporates some simplifying assumptions, namely: 1) external flowfield is irrotational; 2) the mixing field is isothermal and of uniform composition (no heat transfer or diffusion); 3) the flow is turbulent; 4) the flow is incompressible and steady; 5) the jet centerline is defined as the locus of the momentum centers of cross sections; 6) velocities are parallel to the centerline; 7) cross-section boundary of the jet is the locus of points at which the velocity excess in the direction of the centerline vanishes (or is smaller than a prescribed small value); 8) pressure on cross sections is uniform and proportional to $V_c \cos\theta_{jc}$; 9) most of the entrainment takes place in the vortex pair tail.

A control volume in the jet is used to derive the governing two momentum equations of the integral model. These two integral momentum equations, together with four additional equations - i.e., the expansion rate equation, the shape equations, and the normalized velocity profile equation - describe the jet mixing field completely.

Two momentum equations are developed: one parallel to the jet centerline and one perpendicular to it. The momentum balance includes entrained momentum, surface forces on the jet (drag force) and centrifugal body forces. To complete the formulation, one must determine the rate of the jet growth, the shape of the cross sections, and the velocity profiles. t is assumed that the jet cross-section area growth is a linear superposition of two growing mechanisms: 1) growth of a straight turbulent jet in a quiescent environment; and 2) growth of a vortex pair (in accordance with Assumption 9). Although this model of jet growth seems to be an over-simplification, it yields acceptable results.

The cross-section shape calculation predicts approximately the development of the geometry (but not the areas) of these shapes from a circle into the developed horseshoe configuration. This shape development contains much of the nonsimilarity of the mixing process, so that its prediction is essential for a representative model. The cross-section distortion is determined by evenly seeding a finite number of vortices, N, on the instantaneous boundary of the jet and calculating their displacement over a small time period due to their induced velocity. The induced velocity components of each vortex are calculated, and the vortices are displaced accordingly, as the computation progresses down the jet.

The internal jet velocity profiles are obtained from a solution of Poisson's equation within the jet cross-section, combined with empirical parameters.

The Jet-In-Cross-Flow Program is restricted to one isolated jet issuing from a flat plate into the freestream. Due to the weak effect of the airframe on the jet, it is reasonable to calculate the jet properties in isolation. For multiple jets, the program is executed once for each jet. For tandem jets, as is the case for the YAV-8B, the upstream jet exerts a large influence on the downstream one, and the jets tend to coalesce. The method of Wooler (Reference 11) is used to determine the blockage effects of the upstream jet on the downstream jet. The merged single jet properties are determined to a first order approximation by simply combining the effects of the individual jets without coalescence.

The accuracy of the Adler-Baron JICP is shown in Figures 12-15, where the predicted jet centerline trajectory, cross-sectional area ratio, entrained mass flux, and jet velocity profiles are compared with experimental data, (Reference 12). For the cases examined, the agreement is good. MCAIR extensions of the Adler-Baron JICP for upstream jet injection are shown in Figure 16.

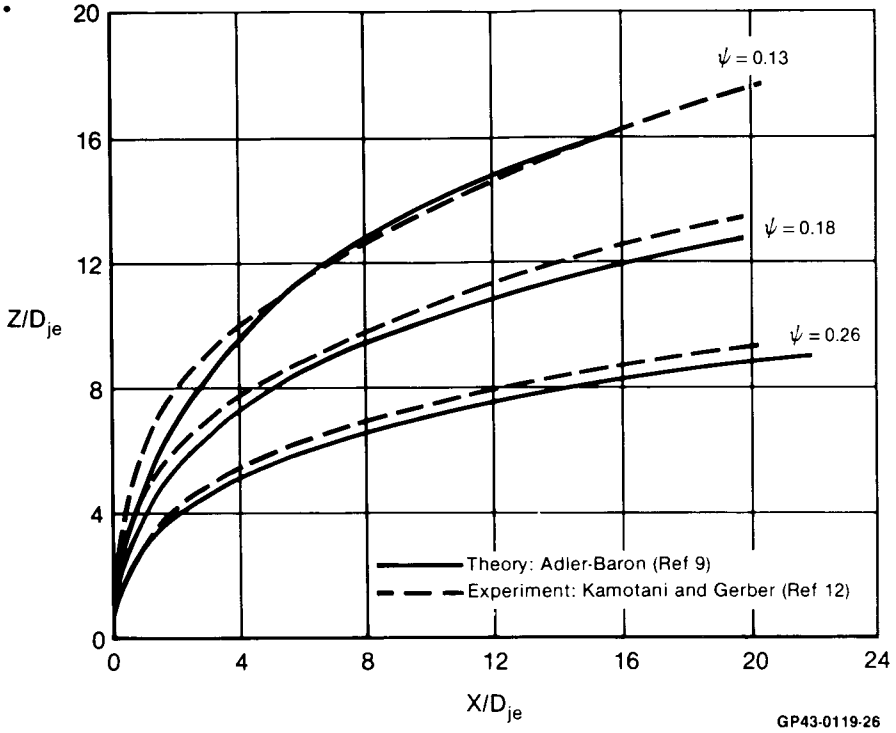

Figure 12. Locus of Peak Jet Velocity Centerline Trajectory
90° Injection Angle

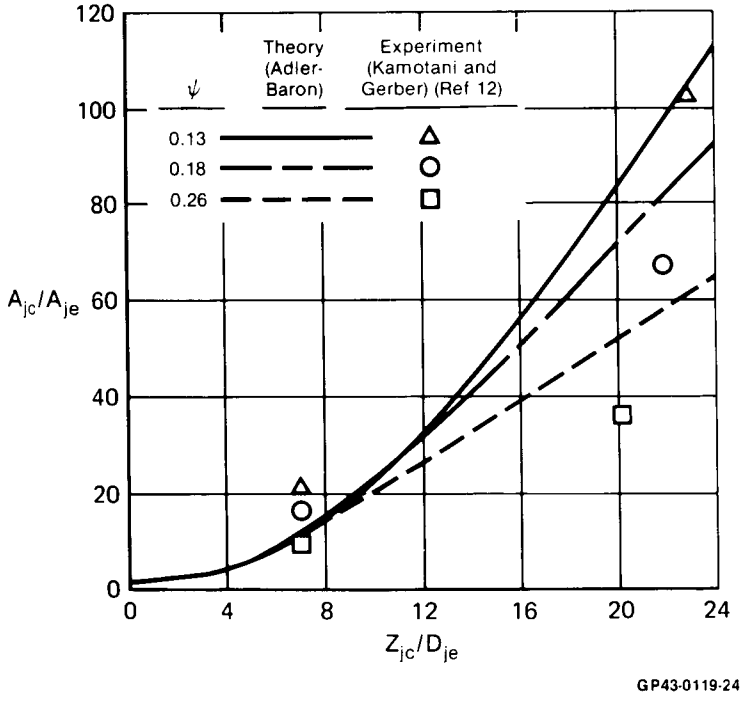

Figure 13. Jet Cross-Sectional Area Ratio Comparison
90° Injection Angle

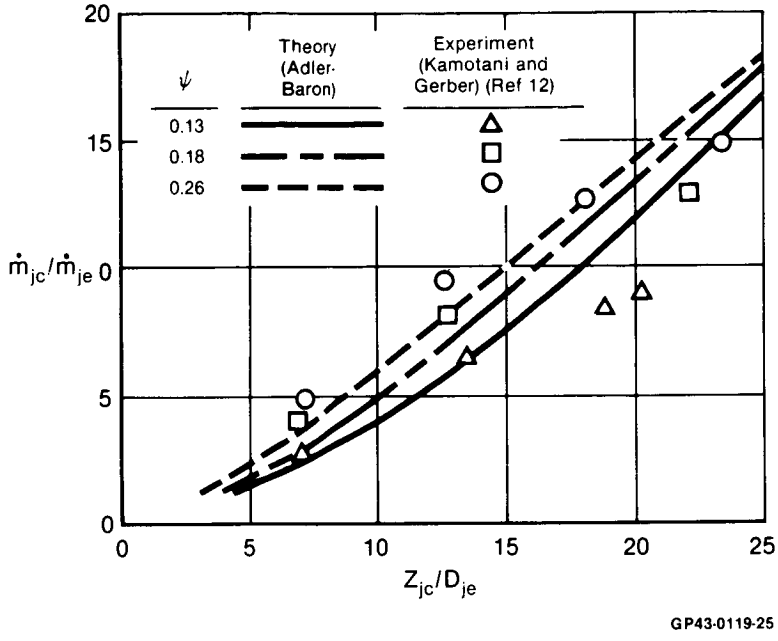

Figure 14. Entrained Mass Flux Comparison
90° Injection Angle

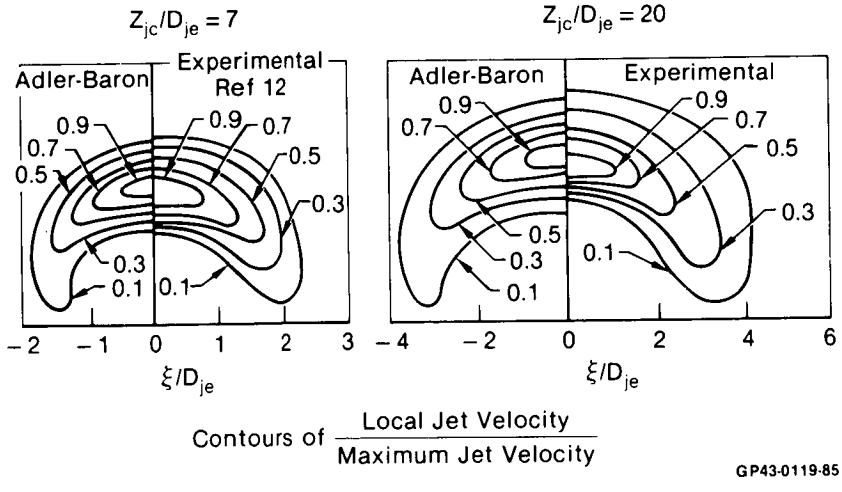

Figure 15. Jet Velocity Profile Comparison
90° Injection Angle $\psi = 0.26$

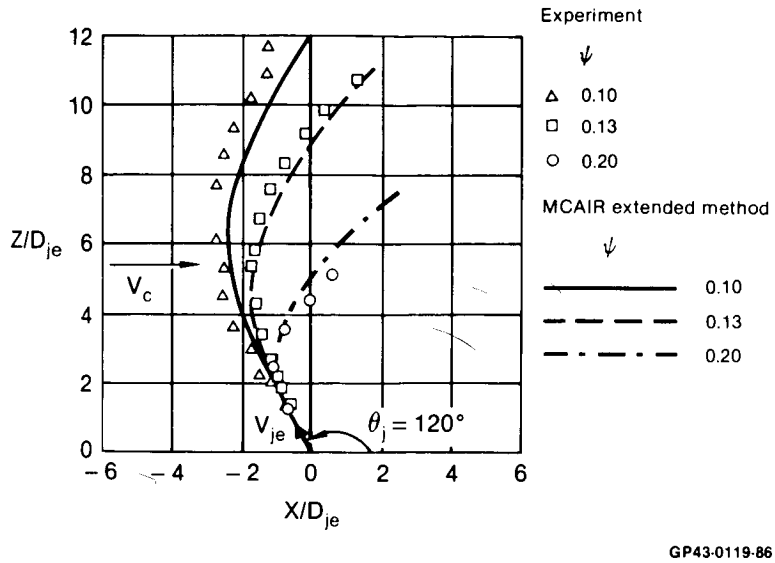

Figure 16. Peak Jet Velocity Centerline Trajectory for Jet Injection Against the Freestream

The MCAIR V/STOL methodology requires the jet-in-cross-flow characteristics obtained from the Adler-Baron JICP to be modelled in the MCAIR three-dimensional Subsonic Potential Flow Program. Figure 17 demonstrates the panelling model of the jet in cross-flow. The three-dimensional outer surface of the jet is obtained from the JICP. The "windward" side of the jet is panelled as a solid surface which models the blockage effect of the jet in cross-flow. The "leeward" side of the jet (shaded panels in Figure 17) is made up of panels with a prescribed distribution of normal velocities to simulate the entrainment and velocity distribution induced by the jet-in-cross-flow vortex structure.

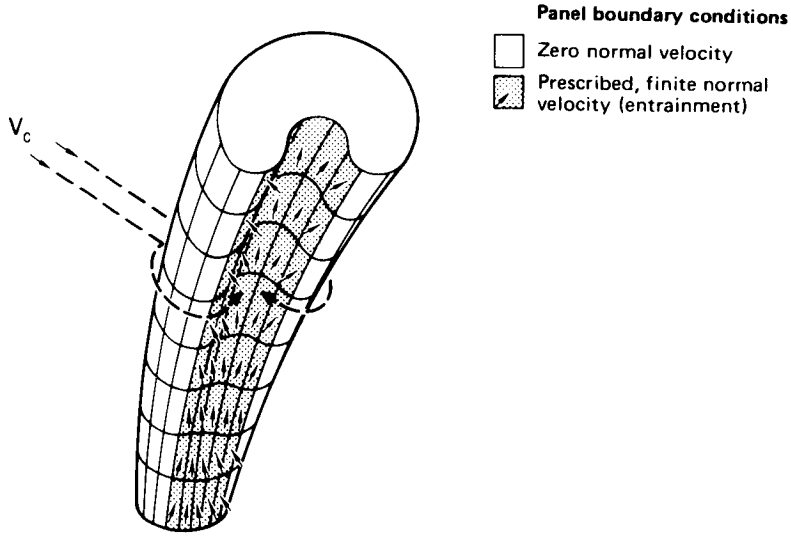

Figure 17. Paneled Representation of a Jet-In-Crossflow

To illustrate an application of the MCAIR jet-in-cross flow methodology to predict the effects of an upper surface jet flowfield, the blockage effects of a single thrust reverser jet on twin vertical tail loads were calculated. The analysis was performed for a thrust reverser jet injection angle (δ_{je}) of 135° and a freestream-to-jet velocity ratio (ψ) of .073. The thrust reverser jet trajectory and geometry were determined using the Adler-Baron Jet-in-Cross-Flow program, and the vertical tail loads and pressure distributions were calculated using MCAERO. Since only the local vertical tail flowfield was of interest, only the fuselage, vertical tails and jet were modeled. The jet exit was circular with an area equivalent to that of current twin reverser configurations.

The MCAERO analyses were performed both with and without the jet for $M = 0.2$ and $\alpha = 0°$. A vertical tail side force coefficient, $C_{y_{V.T.}}$, was calculated for each configuration (where $C_{y_{V.T.}}$ is based on the projected area of a single tail; positive outboard).

The analyses predicted a negative (inboard) side force on the vertical tails, both with and without the jet. However, with the jet, $C_{y_{V.T.}}$ was over 6 times greater than without the jet. The vertical tail chordwise pressure distributions calculated at the 35% span station illustrated increased suction on the inboard side of the tail. This indicated that the jet blockage produced a venturi effect, accelerating the flow over the inboard surface of the tails. The local angle of attack of the vertical tails was changed also, with the flow becoming more inboard with the jet on.

It should be re-emmphasized that this analysis represented the blockage effects of the jet only; no attempt was made to model the jet entrainment. However, specification of entrainment velocities on the paneled jet model would be expected to further reduce $C_{y_{V.T.}}$.

These results apply only to the case presented and may differ qualitatively as well as quantitatively with variations in jet injection angle or velocity ratio.

REFERENCES

1. Kotansky, D. R.; Durando, N. A.; Bristow, D. R.; and Saunders, P. W., "Multi Jet Induced Forces and Moments on VTOL Aircraft Hovering In and Out of Ground Effect," Final Technical Report, NADC Report 77-229-30, June 1977.

2. Kotansky, D. R., "Jet Flowfields," Paper No. 7, Special Course on V/STOL Aerodynamics, AGARD Report No. 710, April, 1984.

3. Donaldson, C. du P., and Snedeker, R. S., "A Study of Free Jet Impingement, Part I - Mean Properties of Free and Impinging Jets," Journal of Fluid Mechanics, Vol. 45, Part 2, pp 281-319, 1971.

4. Abbott, W. A., "Studies of Flow Fields Created by Vertical and Inclined Jets when Stationary or Moving Over a Horizontal Surface," Aeronautical Research Council Current Paper No. 911, Great Britain, October, 1964.

5. Weber, H. A., and Gay, A., "VTOL Reingestion Model Testing of Fountain Control and Wind Effects," AIAA Paper 75-1217, Anaheim, CA, September, 1975.

6. Willmer, A. C., and Scotland, P. L., "Reverse Thrust Experience on the Concorde," AGARD-CP-150, March, 1975.

7. Lotter, K., and Kurz, W., "Aerodynamic Aspects and Optimization of Thrust Reverser Systems," AGARD-CP-150, March, 1975.

8. Margason, R. J., "Jet V/STOL Wind Tunnel Simulation and Ground Plane Effects," AGARD-CP-308, January, 1982.

9. Adler, D., and Baron, A., "Prediction of a Three-Dimensional Circular Turbulent Jet-in-Cross-Flow," AIAA Journal, Vol. 17, No. 2, pp 168-174, February 1979.

10. Fearn, R., and Weston, R. P., "Vorticity Associated with a Jet in Cross-flow," AIAA Journal, Vol. 12, No. 12, December, 1974.

11. Wooler, P. J., "Development of an Analytical Model for the Flow of a Jet into a Subsonic Crosswind," NASA SP-218, September, 1969.

12. Kamotani, Y., and Greber, V., "Experiments on a Turbulent Jet-in-a-Cross-Flow," NASA CR-72893, June, 1971.

THE SCALING OF MODEL TEST RESULTS TO PREDICT INTAKE HOT GAS REINGESTION FOR STOVL AIRCRAFT WITH AUGMENTED VECTORED THRUST ENGINES

C J PENROSE

MANAGER, MILITARY INSTALLATIONS

ROLLS-ROYCE LTD
P O BOX 3 FILTON
BRISTOL, ENGLAND
BS12 7QE

AUGUST 1985

THE SCALING OF MODEL TEST RESULTS TO PREDICT INTAKE HOT GAS REINGESTION FOR STOVL AIRCRAFT WITH AUGMENTED VECTORED THRUST ENGINES

C J PENROSE
MANAGER, MILITARY INSTALLATIONS

ROLLS-ROYCE LTD
P O BOX 3
FILTON
BRISTOL
BS12 7QE

ABSTRACT

The difficulties of modelling the complex recirculating flow fields produced by multiple jet STOVL aircraft close to the ground have led to extensive use of experimental model tests to predict intake Hot Gas Reingestion (HGR). Model test results reliability is dependent on a satisfactory set of sealing rules which must be validated by fully comparable full-scale tests.

Scaling rules devised in the U.K. in the mid 60's gave good model/full scale agreement for the BAe P1127 aircraft. Until recently no opportunity has occurred to check the applicability of the rules to the high energy exhausts of current ASTOVL aircraft projects. Such an opportunity has arisen following tests on a Tethered Harrier powered by an early standard Pegasus engine with Plenum Chamber Burning.

Comparison of this full-scale data and results from tests on a model configuration approximating to the full-scale aircraft geometry has shown discrepancies between HGR levels. These discrepancies although probably due, in part, to geometry and other model/full scale differences indicate some re-examination of the scaling rules is needed.

This paper reviews the scaling practices adopted in the U.K. in the light of the recent results, describes further scaling studies planned and suggests potential areas for further work.

INTRODUCTION

STOVL aircraft supported by multiple jet lift in operation close to the ground are susceptible to ingestion by the engine of hot exhaust gases reflected, on impingement with the ground, into the engine intake. This can produce a thrust loss and may induce engine surge. The extreme complexity of the jet induced recirculating flow fields, which are highly aircraft configuration dependent, poses a severe challenge to the flow modeller and has led to extensive use of experimental model tests to predict the intake hot gas reingestion (HGR) characteristics of candidate STOVL aircraft.

For model test results to be reliable a satisfactory set of scaling rules is necessary which must be validated by fully comparable full-scale tests.

Simulation of the recirculating flow fields has been undertaken by many experimenters notably in the U.K., U.S. and West Germany. U.K. studies, to date, have been undertaken employing scaling rules formulated from fundamental theoretical and experimental considerations by Cox and Abbott at RAE Pyestock in the mid sixties (Refs 1 and 2). The studies, including simulated aircraft vertical motion, have adhered to a flow buoyancy relationship which requires model jets to be tested at pressure ratios significantly lower than full-scale. U.S. and West German researchers (Refs 3-5) have ignored the buoyancy rules and tested at full-scale pressure ratios but with no aircraft motion represented.

The validity of the 'Cox and Abbott' rules was investigated by comparison of model and full-scale results for the BAe P1127 aircraft (Ref. 6) where good agreement was obtained. The agreement, it should be noted, was obtained for cold front, hot rear jet configurations with no central hot gas fountain control.

continued/.....

It has for some time been realised that the rules adopted in the U.K. have not been checked for applicability to ASTOVL projects employing augmented vectored thrust engines with high pressure/high temperature front and rear jets, maybe with inwards splay, and with mechanical deflectors for HGR fountain control (CADS/LIDS), where flow mechanisms may be radically changed.

The first opportunity to compare model and full-scale results for an augmented vectored thrust aircraft has been provided by the Tethered Harrier test rig at Shoeburyness, England. The rig comprises a Harrier aircraft fitted with an early standard Pegasus engine with Plenum Chamber Burning (PCB) installed on a hydraulic ram to afford vertical motion.

Results from full-scale tests on this rig and on model tests approximating to the full-scale configuration have recently become available. These show discrepancies between HGR levels for model and full-scale although it should be noted that these may be partly due to geometry and other differences between the model and the full-scale aircraft rather than to fundamental scaling law shortfalls.

This note reviews the scaling laws in the light of the recent results, describes further scaling studies planned in the U.K. and suggests candidate items where support from U.S. and other agencies would be valuable.

2. SYMBOLS

D - Diameter

g - Gravitational Constant

$K'_{1,2,3,4,5}$ - Scaling Constants

L - Length

P - Total Pressure

continued/.....

p	-	Static Pressure
q	-	Dynamic Head
Re	-	Reynold's Number
R*	-	Radial Separation Distance of Ground Jet due to Buoyancy
Rs	-	Radial Separation Distance of Ground Jet due to Headwind
T	-	Total Temperature
$\theta = T - T_\alpha$	-	Temperature rise above ambient
t	-	time
u	-	ground jet velocity
V	-	velocity
W	-	Mass Flow
Cp	-	Specific Heat
ρ	-	Density
μ	-	Kinematic Viscosity
$\overline{T}_{360}$	-	Mean Intake Temperature at Engine Face
$\overline{T}_{120}$	-	Mean Temperature in the 120^o Segment at the engine face producing the highest mean temperature in any 120^o segment.
Tc_{120}	-	Intake Temperature Distortion Coefficient $= \frac{\overline{T}_{120} - \overline{T}_{360}}{\overline{T}_{360}}$

continued/.....

Subscripts

∞	-	ambient
o	-	free stream
I	-	intake
J	-	Jet
m	-	model
FS	-	full-scale
HGR		Hot Gas Reingestion
PCB		Plenum Chamber Burning
CAD/LID		Cushion Augmentation Device/Lift Improvement Device

3. RECIRCULATION FLOW PATHS

Extensive theoretical, model and full-scale experiments have identified three ways in which the jet exhaust flows might recirculate back to the engine inlets. These are shown on Fig. 1 and comprise:-

1) Near Field Reingestion

Near Field Reingestion is caused by the flows from separate lift jets meeting on the ground creating an upward or fountain flow which impinges on and is redirected by the aircraft undersurface. Some travels directly on a short time scale to the engine inlets with little opportunity for mixing thereby retaining a high percentage of jet exit temperature and potentially causing severe HGR. Some success has been achieved in redirecting this flow away from the inlets by mechanical deflectors (CAD's/LID's).

continued/.....

2) Intermediate Thrust Reverser or Mid Field Reingestion

This is caused when:-

a) Some of the recirculating flow in the ground jet and the forward moving part of the fountain is blown back by headwind into the intake after some opportunity for mixing with ambient air.

3) Far Field Reingestion

Far Field Reingestion is caused when the ground flows travel radially outwards mixing progressively with exhaust air to recirculate into the intake on a much longer time-scale driven by the effects of buoyancy and entrainment. The reingested air temperature is then relatively low so Far Field Reingestion is not usually a serious problem.

4. SIMILARITY AND SCALING

Scaling rules are required fundamentally for two main purposes:

1) To set up a consistent set of test conditions which will produce geometric and dynamic similarity between the model and full-scale test conditions.

2) To scale the results from model to full-scale conditions using, where necessary, interpolation or extrapolation of model data to relate to full-scale conditions outside the envelope of conditions examined at model scale.

4.1 Similarity

Geometric and Dynamic Head similarity, Fig. 2 are generally accepted, practice in the U.K. being to express dynamic head in the dynamic pressure (total-static) form, as recommended in Ref. 1 , rather than the kinetic pressure ($\frac{1}{2}\rho V^2$) form.

continued/.....

Simple excess temperature similarity Fig. 2, designated the 'old' rule, has also been widely used although recent studies at Rolls-Royce, Ref. 7 , pursued at BAe Kingston (Ref. 8), have identified an "alternative rule" based on hot gas transport. The justification and evidence supporting the old and alternative rules are discussed in more detail in Section 4.3.2.

4.2 Scaling

Fundamental considerations of factors to be considered when scaling model test conditions can identify many scaling options and a selection is shown on Fig. 3. The first five relationships were identified by Cox and Abbott and have been adhered to in all U.K. originated HGR model tests.

Test conditions can, in fact, be fully defined by three relationships:-

1) Geometry scaling, limited by rig size and capacity

2) Temperature scaling, limited by rig constraints

and

3) Either Buoyancy (generally used in the U.K.) or Full-Scale Nozzle Pressure Ratio (U.S. and WG practice) or Other parameters as shown on Fig. 3.

Time Ratio is fully defined by geometric and dynamic head scaling.

It is clear from Fig. 3 that not all relationships can be satisfied at the same time and some concessions have to be made. In fact, adoption of full-scale nozzle pressure satisfies, or closely approximates to, most other transport parameters. This ignores buoyancy and places severe demands on rig/model supplies and capabilities as discussed in Section 4.3.4.

continued/.....

Adherance to dynamic pressure and excess temperature scaling allows, for simple cases, satisfaction of the buoyancy criteria implying tests at nozzle pressure ratios much lower than full-scale conditions. However, where different jet conditions exist, as in the front and rear jets of an augmented vectored thrust engine, it is not possible to strictly satisfy buoyancy and excess temperature relationships for both jets. A compromise has to be made. In general, since it has been found that near and intermediate field recirculations tend to dominate the HGR problem it has been the practice to satisfy buoyancy for the front jets and to satisfy the excess temperature scaling and accept some departure from buoyancy scaling for the rear jets. This on the premise that buoyancy is dominant mainly in the far field, see Section 4.3.3.

4.3 Implications of Scaling

4.3.1 Geometry

Linear geometric scaling is generally accepted for model tests. Large models require large rigs with high flow and power requirements. Small models limit instrumentation density and, depending on scaling assumptions, generally imply higher time-scale factors requiring faster response instrumentation for transport measurements. Current practice is to employ models in the 1/10th to 1/15th scale regime.

4.3.2 Excess Temperature

Rig material constraints have generally limited jet exhaust temperatures to about 800K, which are fully representative for early P1127/Harrier aircraft conditions, but which impose increasingly severe scaling requirements for advanced STOVL aircraft projects operating at jet exhaust temperatures in the range 1000K-1800K.

continued/.....

It had been assumed until recently that the recirculation temperature rise (θ_I) was a constant fraction of the jet excess temperature (θ_J) where the front jet conditions were used for multiple jet arrangements. However, recent re-examination of hot transport criteria, initially at Rolls-Royce and subsequently at BAe have identified a possible alternative rule which introduces a density term ($\propto \sqrt{T_J}$) into the scaling relationship so that

$$\left\{\frac{\theta_I}{\theta_J}\frac{\sqrt{T_J}}{\sqrt{T_\alpha}}\right\}_{FS} = \left\{\frac{\theta_I}{\theta_J}\frac{\sqrt{T_J}}{\sqrt{T_\alpha}}\right\}_{M}$$

This has been expressed in the form of a 'corrected jet excess temperature' by Milford at BAe Kingston where

$\theta_J^* = \theta_J\sqrt{T_\alpha}/\sqrt{T_J}$ so that θ_I / θ_J^* is constant rather than θ_I / θ_J as assumed by Abbott and Cox.

The validity of the two rules has been investigated by reference to model HGR tests from previous experiments(Refs 8&9) covering jet excess temperatures in the range 130°C-600°C. The results are inconclusive as some data can be found to collapse better on the old rule, some better on the alternative, with the effect, if any, on some being obscured by general data scatter. Some examples are shown on Figs 4a and 4b. It may be that the two rules are each applicable in particular regimes where different modes of hot gas transport are dominant. In spite of the uncertainty as to which rule to use an examination of the relative effect on full scale intake excess temperature estimation of employing the alternative rule can be seen on Fig. 5. This curve shows that for jet temperatures in the region of the P1127 the change is insignificant. At high jet temperatures,circa 1400-1800K,the alternative rule would give a predicted full scale intake temperature rise $\simeq$ 30% less than the old rule. A similar factor applies to intake temperature distortion (TC_{120}) where Tc_{120} represents a coefficient employed at Rolls-Royce which can be related to the amount of engine available surge margin erosion caused by intake

continued/.....

temperature distortion. For current projected STOVL aircraft with a target landing jet temperature of approximately 1000K the alternative rule implies estimates of intake temperature rise of $\simeq$ 10% less than the old rule.

The need for all HGR sensitive aircraft must be to reduce intake HGR to a very low level in which case the correction factor is relatively unimportant.

4.3.3 Relevance of Buoyancy

It can be argued that buoyancy scaling may have been adopted primarily for reasons of test technique. Adherance to the buoyancy rule permits model HGR tests to be carried out in a low speed wind tunnel at low model jet pressures with slow model motion and with instrumentation with moderate time response. The rule does, however, imply model tests at nozzle pressure ratios much less than full-scale where questions must be asked whether low pressure jets can correctly simulate the conditions present in high pressure choked jets.

The significance of buoyancy was originally assessed by Cox and Abbott in terms of its influence on the radial separation of a ground jet compared to the separation due to a relative headwind. Separation distance, non-dimensionalised by jet diameter D_J was found to correlate in terms of buoyancy and headwind parameters for model and full-scale, (Ref.1&10). The relationships can be used to produce carpet plots in terms of nozzle temperature and pressure ratio for buoyancy separation (Fig. 6a) and in terms of nozzle pressure ratio and headwind for headwind separation (Fig.6b). For relevant buoyancy scaled test conditions the separation distance due to buoyancy is typically 100 or more nozzle diameters. This is remote from the impingement source and from the inlet and is in

continued/.....

the 'far field'. For relevant buoyancy scaled test conditions the separation distance due to headwind is typically of order 10 nozzle diameters. This is in the 'near' and intermediate reingestion fields. This suggests that buoyancy is probably not critical for near or intermediate field HGR but does not necessarily imply that buoyancy scaling is incorrect.

4.3.4 Full-Scale Nozzle Pressure Ratio NPR

While full-scale NPR satisfies or closely approximates to most transport parameters adoption of full NPR requires simulation at model scale of full-scale headwinds, pressures, motion and time response instrumentation K_1 times full-scale for a model geometry scale K_1. To the Authors knowledge tests at full NPR have yet to address the problem of model motion as all tests to date have been at fixed height. Evidence in the U.K., albeit at buoyancy scaled conditions, shows that failure to represent model motion will give incorrect levels of intake HGR during simulated aircraft landing and take-off operations for full-scale aircraft, see Fig. 7, since landing into the developing hot gas pattern is essentially a dynamic process.

5. MODEL/FULL-SCALE AGREEMENT

5.1 P1127 Results

It was realised very early on in the U.K. studies that postulated scaling rules needed to be validated by comparative full-scale information. To this end a series of full-scale aircraft tests was commissioned covering take-offs and landings for comparison with test results from a model closely simulating the full-scale aircraft geometry. (Ref. 6). Agreement, in terms of mean intake temperature rise, relative to front jet excess temperature,

continued/.....

between the model and full-scale results is shown on Fig. 8 to be very good. Ref. 6 also indicated that temperature distortion contours were very close with a strong bias for hot gas to be present in the bottom portion of the intake. On the above evidence it was decided to retain the postulated scaling rules including buoyancy for all future studies. The good agreement was,of course, obtained for low temperature front jets, hot rear jets with no central hot gas fountain control.

5.2 Pegasus 2A/Tethered Harrier

Concern has been expressed for some time that the scaling rules adopted in the U.K. have not been examined in the context of the conditions relevant to current ASTOVL aircraft projects employing augmented vectored thrust engines with high pressure/high temperature front and rear jets and probably incorporating HGR avoidance devices such as nozzle convergence and/or CAD's. The Tethered Harrier Aircraft mounted on a dynamic ram on a large gantry at Shoeburyness, England has recently afforded a first opportunity to examine the applicability of the scaling rules. The full-scale installation is shown on Fig. 9.

The aircraft was fitted with an early standard Pegasus engine with PCB configured with 'TV' shaped front nozzles arranged, in the vertical nozzle setting, as shown on Fig. 10. The engine was instrumented with an array of 48 fast response thermocouples at the engine face.

The results obtained from some of the simulated landings carried out at full-scale for a range of front jet temperature augmentation up to 1400K have been analysed in terms of peak mean intake temperature rise encountered during a landing relative to front jet excess temperature,

continued/.....

Figs 11 and 12 refer,and for temperature distortion, Fig. 13. Fig. 11 presents results for a 20^{o} converged front nozzle configuration with a CAD fitted with data for the same CAD but with 10^{o} converged front nozzles on Fig. 12. Fig. 13 presents temperature distortion data for the 10^{o} converged nozzle with CAD. All curves are plotted with front jet mean temperature as abscissa. The mean intake temperature rise data,Fig. 11,is seen to collapse reasonably well in terms of simple jet excess temperature supporting the 'old' temperature scaling rule. Plotting the data on a 'corrected' jet excess temperature produces a significant positive gradient with increasing excess temperature.

The full-scale results can be compared with model test results obtained from tests on a model closely simulating the aircraft configuration with 10^{o} coverged front nozzles but with circular front nozzles rather than the 'TV' shaped front nozzles on the full-scale engine. The model test conditions were set up using the scaling rules, including buoyancy, to represent maximum engine conditions at full-scale i.e. a front jet temperature of 1400K. Fig. 14 shows the scaled and full-scale conditions with, for comparison, conditions used for the P1127 tests. The necessary small departure from correct rear nozzle buoyancy scaling can be seen caused by the requirement to satisfy the excess temperature and dynamic head scaling ratios derived when applying the buoyancy rule to the front nozzles.

Model results for the 10^{o} convergent nozzle + CAD geometry are superimposed on Figs 12 and 13 at conditions relevant to the full-scale engine conditions. It can be seen that the full-scale results for mean intake temperature rise relative to front jet excess temperature exceed the model by approximately 100%.

continued/.....

Further considerations of the configurations, however, indicated that the 'TV' shaped front nozzles of the full-scale aircraft aligned with the nozzles vertical so that a major portion of the ground sheet flow travelled forwards. The magnitude of this effect in terms of intake HGR has been estimated from the work of Kotansky, Ref. 11 to be of the order of 40% increase in mean temperature rise at the intake (Fig. 15). This reduces the model/full-scale discrepancy but a large difference still remains.

Further examination of the full-scale results indicated a severe temperature profile at the front nozzle exits - the model tests being carried out with a near uniform temperature profile. The full-scale profile contains a hot central core displaced somewhat aft of the nozzle centreline and surrounded by an annular ring of air at less than the mean temperature. It is not known how far downstream this profile persisted or the effect it might have on the intake temperature rise. It can be postulated that some gas at the mean jet temperature might enter the intake with little mixing thereby raising the mean intake temperature (as the full-scale results suggest). On the other hand the cool outer annulus flow at $<$ the mean jet temperature might be expected to shield the hot core flow from the inlets.

The model results for intake temperature distortion, Tc_{120} for the 10^{o} converged nozzles + CAD geometry, see Fig. 13 also indicate a discrepancy between model and full-scale - full-scale again exceeding the model data but this time by only about 25%. Further studies aimed at investigating this difference were made to examine the temperature contours at the engine face for model and full-scale. A typical comparison is made on Fig. 16. where a full-scale test point, obtained at a front jet temperature of $\doteq$ 900K, is compared with a model result, at similar aircraft height, landing velocity and headwind conditions, scaled to the same

continued/.....

jet temperature. In spite of differences in absolute levels for both mean temperature rise and temperature distortion the patterns exhibit similar characteristics with high temperature generally dominant in the lower portion of the intake.

A possible further factor which may affect model/full-scale agreement is that of jet turbulence. There appears to be little data in the literature but a relevant reference by Lummus, Ref. 12, suggests that fountain force on an aircraft planform in ground effect can be modified by changing jet turbulence. It can be concluded from this evidence that differences in jet turbulence might also be expected to influence intake HGR levels.

6. CURRENT POSITION

The current state-of-the-art in the U.K. on predicting full-scale HGR characteristics for STOVL aircraft from model tests set up using scaling rules originally proposed twenty years ago can be summarised:

The rules give good model/full-scale agreement for both mean intake temperature rise and temperature distortion contours for STOVL aircraft, such as the P1127/Harrier, with cool front jets (circa 400K) and hot rear jets (950K) with no fountain control devices.

Within limitations of current model/full-scale geometric similarity the rules appear to underpredict levels of mean temperature rise and temperature distortion from a 'test bed' type STOVL aircraft fitted with an augmented vectored thrust engine with front nozzle jet temperatures up to 1400K.

continued/.....

Additional observations for the Tethered Harrier programme can be made:

The full-scale data produces a good collapse of mean intake temperature rise with simple front jet excess temperature supporting the 'old' rule.

A greater discrepancy exists between full-scale and model predicted intake mean temperature rise than for temperature distortion.

Intake temperature distortion contours at full-scale, although higher than model predictions, exhibit the same general shape.

Accordingly it is considered that the scaling rules must be open to question and a programme of work has been outlined in the U.K. to investigate various aspects of scaling. These are discussed in the following section.

7. SUPPORTING EXPERIMENTAL PROGRAMMES

Future work plans fall into three separate categories (Fig. 17)

- Model and full-scale tests related to the Tethered Harrier Aircraft.
- Fundamental scaling law studies to be carried out with simplified aircraft configurations.
- Fundamental studies of jet wakes including entrainment and fountain flow properties.

continued/.....

7.1 Tethered Harrier Related Studies

Model studies are planned to directly reproduce conditions encountered during the full-scale tests to investigate the effect on HGR of 'TV' shaped nozzles, to study temperature profile and possibly jet turbulence. These studies are aimed directly at providing answers to questions raised concerning differences identified between model and full-scale results obtained on the Pegasus 2A installation. The tests will include some studies with jet conditions approaching full-scale values thereby ignoring the buoyancy scaling relationship.

A further programme of work is planned on the Tethered Harrier using a Pegasus 11 engine offering increased nozzle pressure ratio to the Pegasus 2A (circa 2.0:1). This work will extend full-scale data towards the jet conditions expected for future ASTOVL aircraft. This full-scale programme will be supported by tests on a model closely simulating the aircraft configuration. Scaling rules to be used for this model will depend on results from fundamental jet studies and simple aircraft configuration studies identified to examine the scaling rules in a systematic way. The studies are briefly outlined below.

7.2 Simplified Aircraft Configuration

A comprehensive set of experiments is proposed to measure intake HGR on simple aircraft configurations using the full range of projected ASTOVL aircraft jet pressure ratios and temperatures for different assumptions concerning the chosen scaling laws.

continued/.....

The studies will cover a far flowfield investigation for a single jet with jet pressure ratios from buoyancy scaled to full-scale simulation with variations in jet temperature to study excess temperature scaling. Studies will also be made for near field reingestion of a twin jet assembly, again over a full range of nozzle temperatures and pressures, to examine alternative scaling assumptions.

7.3 Basic Jet Flowfield Studies

Existing rigs in the U.K. used for HGR studies have been designed to buoyancy-scaled test conditions and therefore do not, at present, have sufficient capacity to test at full-scale nozzle pressure ratios. The rigs are not equipped for detailed jet flowfield surveys. Such studies have therefore been proposed using simple jets alone. Two programmes of work have been identified.

1. A study of single jet entrainment with measurements in the free jet wake and in the ground sheet after jet/ground impingement to determine the effects of jet Mach number. The study is planned to include the effects of imposed turbulence patterns on jet decay characteristics.

2. A study with multiple jets to investigate the effects of varying nozzle pressure ratio on flow behaviour in the ground jet and in the fountain regions. This study is intended to be complementary to the above single jet study.

continued/.....

REFERENCES

1. Studies of the Flow Fields created by single vertical jets diverted downwards upon a horizontal surface.
NGTE Report M390. M Cox and W A Abbott. Oct. 1964.

2. Estimation of Intake Temperatures during V/STOL Operation from Model Tests.
NGTE Note No. NT600. W A Abbott. March 1966.

3. VTOL Reingestion Model Testing of Fountain Control and Wind Effects.
AIAA 75-1217. H A Weber and A Gay.

4. V/STOL Aircraft Configuration Effect on Exhaust Gas Ingestion.
AIAA 79-1284. E D Spong, J H Kamman, C L Hall, and E T Seiffertt.

5. Hot Exhaust Gas Reingestion Characteristics of a Small-Scale Harrier Type V/STOL Aircraft Model.
McDD Report MDC A4225. Hall and Kamman. August 1977.

6. Full-Scale and Model Studies of Exhaust Ingestion on the Hawker Siddeley P1127 with Special Reference to Scaling Laws.
NGTE Note No. NT658. A W R Allcock and W A Abbott. Oct. 1967.

7. Hot Gas Reingestion Temperature Scaling Laws.
RR Report GN.20346. L R Harper. March 1982.

8. Scaling Factors for Hot Gas Recirculation.
BAe Kingston Report BAe-KAD-N-GEN-2878. C M Milford. August 1981.

9. VTOL Transport Exhaust Gas Ingestion Model Tests.
Proceedings of 7th Annual National Conference on Environmental Effects on Aircraft and Propulsion Systems.
Princeton New Jersey. Sept. 1967. A E Harris, J A Marbert, J W Tatom.

10. Studies of Flow Fields Created by Vertical and Inclined Jets when Statiionary or Moving over a Horizontal Surface. Note. Report M391. W A Abbott. Oct. 1964.

11. Investigation of the Interaction of Lift Jets and a Ground Plane.
NASA CR152343. D R Kotansky, L W Glaze. April 1980.

12. Critically of Engine Exhaust Simulations on VSTOL Model - Measured Ground Effects.
AIAA 80-0230. J R Lummus.

ACKNOWLEDGEMENT

The author wishes to acknowledge with thanks the assistance of his colleagues at Rolls-Royce and to Rolls-Royce Ltd. for permission to publish this paper.

4-POSTER PEGASUS HOT GAS RECIRCULATION MECHANISMS

'NEAR-FIELD' OR 'FOUNTAIN' TYPE

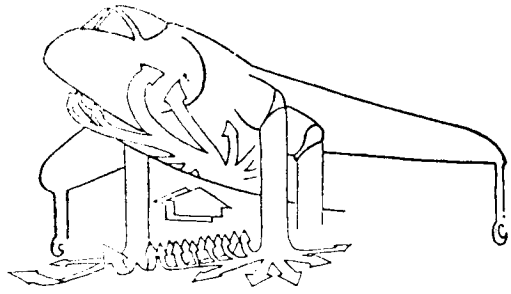

'INTERMEDIATE' OR 'THRUST REVERSER' TYPE

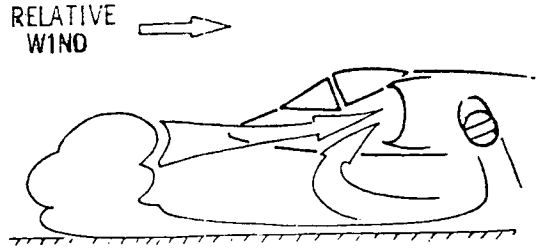

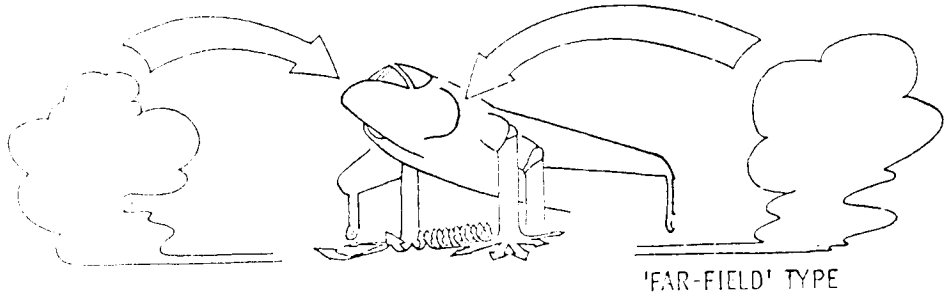

'FAR-FIELD' TYPE

FIG 1

SIMILARITY

- o GEOMETRY $\left(\frac{L1}{L2}\right)_{MODEL} = \left(\frac{L1}{L2}\right)_{FULL\ SCALE}$
- o DYNAMICS $\left(\frac{q1}{q2}\right)_{MODEL} = \left(\frac{q1}{q2}\right)_{FULL\ SCALE}$

[SIMILARLY $\frac{V_{MODEL\ ASCENT/DESCENT}}{V_{WIND\ TUNNEL}} = \frac{V_{AIRCRAFT\ ASCENT/DESCENT}}{V_{HEAD\ WIND}}$]

- o TEMPERATURE $\left(\frac{\theta_I}{\theta_J}\right)_{MODEL} = \left(\frac{\theta_I}{\theta_J}\right)_{FULL\ SCALE}$ (" OLD RULE ")
- o $\left(\frac{\theta_I}{\theta_J}\sqrt{\frac{T_J}{T_\infty}}\right)_{MODEL} = \left(\frac{\theta_I}{\theta_J}\sqrt{\frac{T_J}{T_\infty}}\right)_{FULL\ SCALE}$ ("ALTERNATIVE RULE")

FIG 2

SCALING RELATIONSHIPS

NGTE SCALING RULES

ITEM	RELATIONSHIP	COMMENT
GEOMETRY	$Dm / D_{fs} = K_1$	GEOMETRY SCALE
'DYNAMIC HEAD'	$(P-P_\infty)_m / (P-P_\infty)_{fs} = K_2^2$	$K_2^2 \ll 1$ FOR 'BUOYANCY SCALING $= 1$ FOR MACH NO OR NPR REPRESENTATION
TEMPERATURE	$(T-To)_m / (T-To)_{fs} = K_3$	K_3 AS CLOSE TO 1 AS FACILITY PERMITS
BUOYANCY	$\left[\frac{V_j^2 T_\infty}{\theta_j D_j}\left(\frac{T_\infty}{T_j}\right)^{1/2}\right]_{model} = K_4$	$K_4 = 1$ FOR BUOYANCY SCALING $K_4 \gg 1$ FOR NPR REPRESENTATION
TIME	$t_m / t_{fs} = K_1 / K_2'$	TIME SCALE
VELOCITY	$V_m / V_{fs} = K_2'$	$K_2' = K_2$ FOR CONSTANT DENSITY REGIMES
MOMENTUM FLUX	$\left(\frac{WV}{D^2}\right)_m / \left(\frac{WV}{D^2}\right)_{fs} = K_2'^2$	$K_2' \ll 1$ FOR BUOYANCY SCALING
MASS FLUX	$\left(\frac{W}{D^2}\right)_m / \left(\frac{W}{D^2}\right)_{fs} = K_2'$	$= 1$ FOR MACH NO OR NPR REPRESENTATION
HEAT FLUX	$\left[\frac{WC_p(T-T_\infty)}{D^2}\right]_m = K_2' K_3$	
REYNOLDS NO.	$\left(\frac{\rho VD}{\mu}\right)_m / \left(\frac{\rho VD}{\mu}\right)_{fs} = Re_m / Re_{fs} = K_5$	$K_5 < 1$ FOR NPR REPRESENTATION $K_5 \ll 1$ FOR BUOYANCY SCALING

FIG3

TEMPERATURE SCALING

(DATA SUPPORTS OLD RULE)

Ref: Harris et al Lockheed 1967

'OLD RULE'

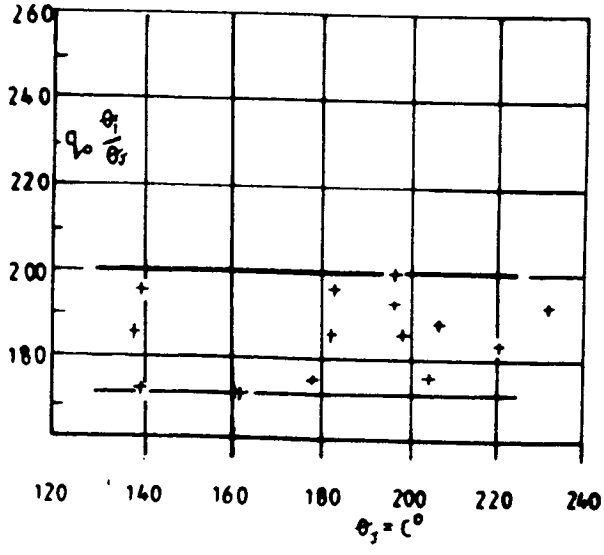

'ALTERNATIVE RULE'

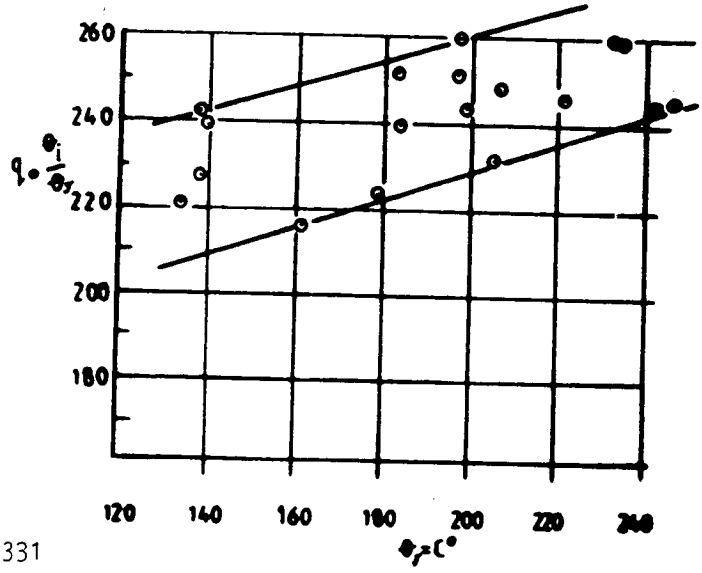

FIG 4a

TEMPERATURE SCALING

(DATA SUPPORTS ALTERNATIVE RULE)

OLD RULE

P1154 Model (1962)

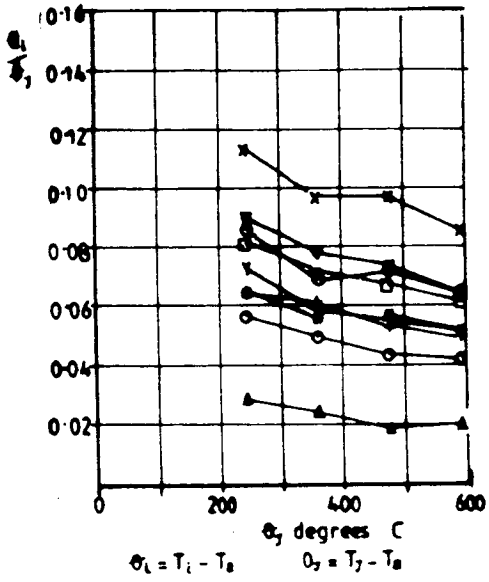

'ALTERNATIVE RULE'

P1154 Model (1962)

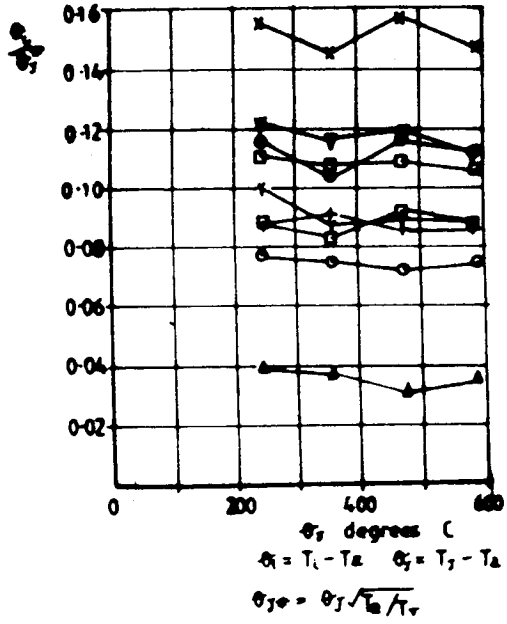

FIG 4b

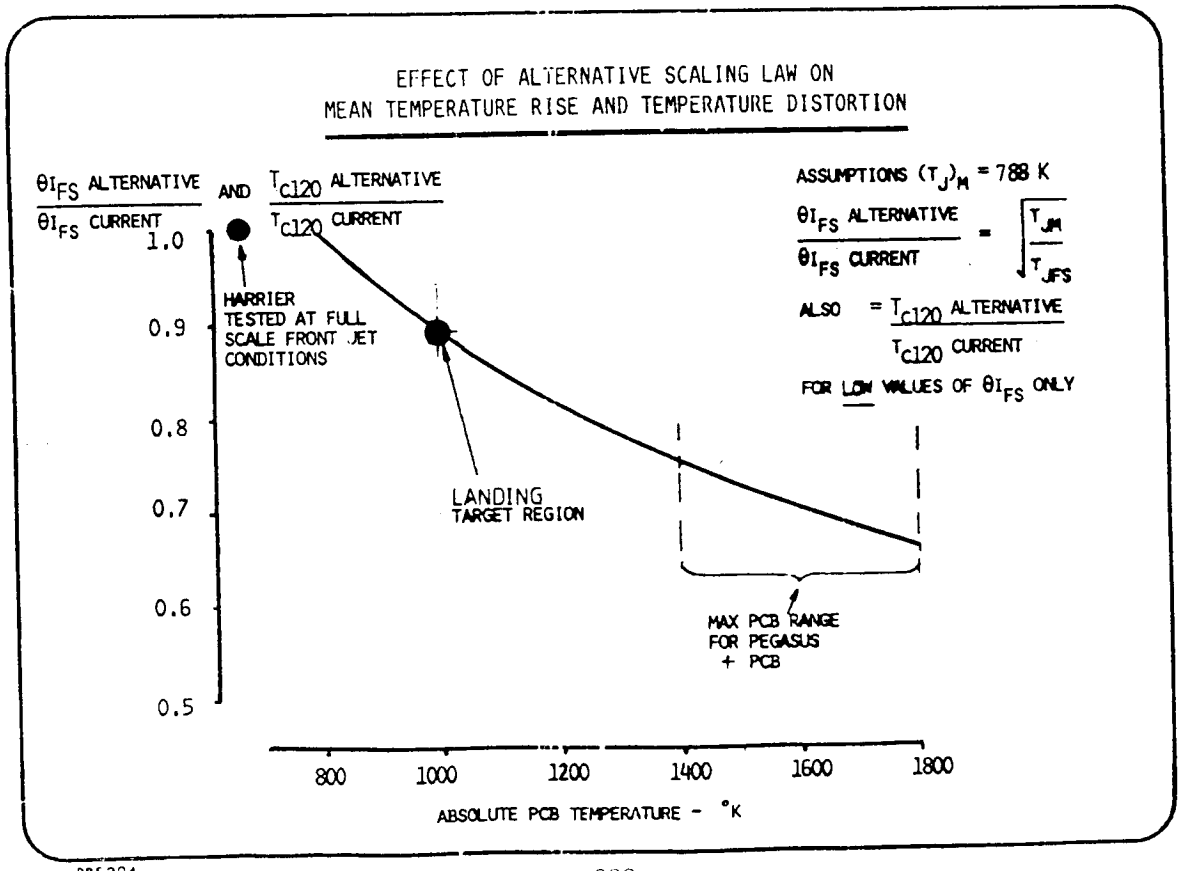

FIG 5

RADIAL SEPARATION OF GROUND JET DUE TO BUOYANCY

1/15th SCALE MODEL CONDITIONS. NOZZLE DIAMETER DJ = 1·6 INS.

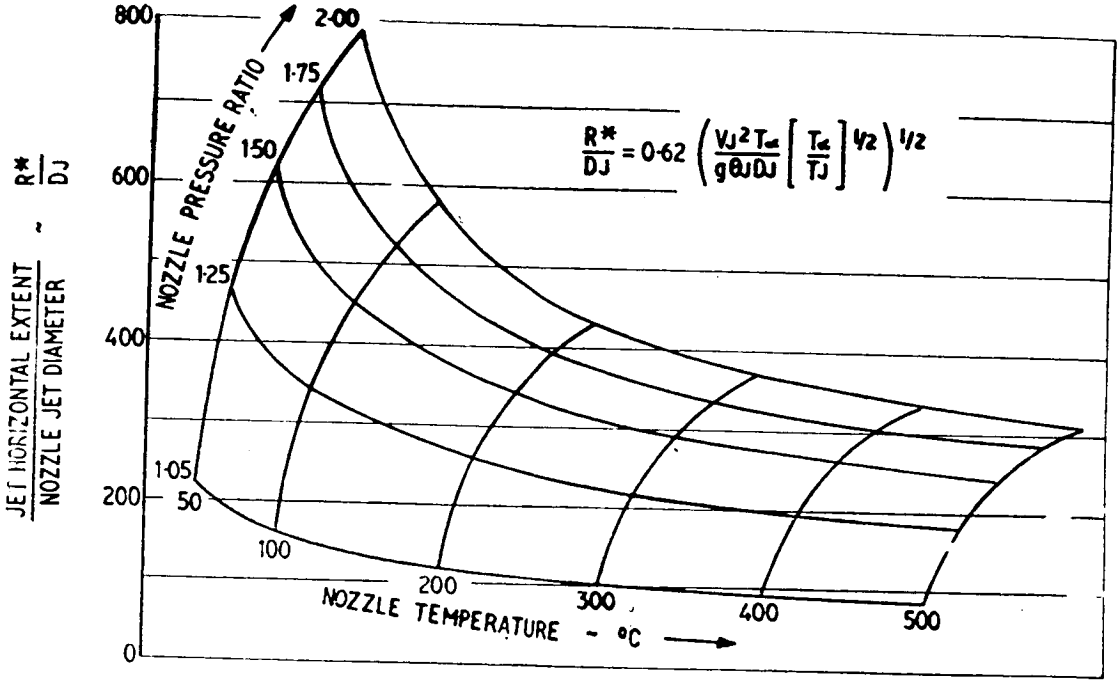

FIG 6a

VARIATION OF GROUND JET SEPARATION DISTANCE WITH HEADWIND

1/15th SCALE MODEL CONDITIONS. NOZZLE DIAMETER D_J = 1·0 TO 1·4 INS

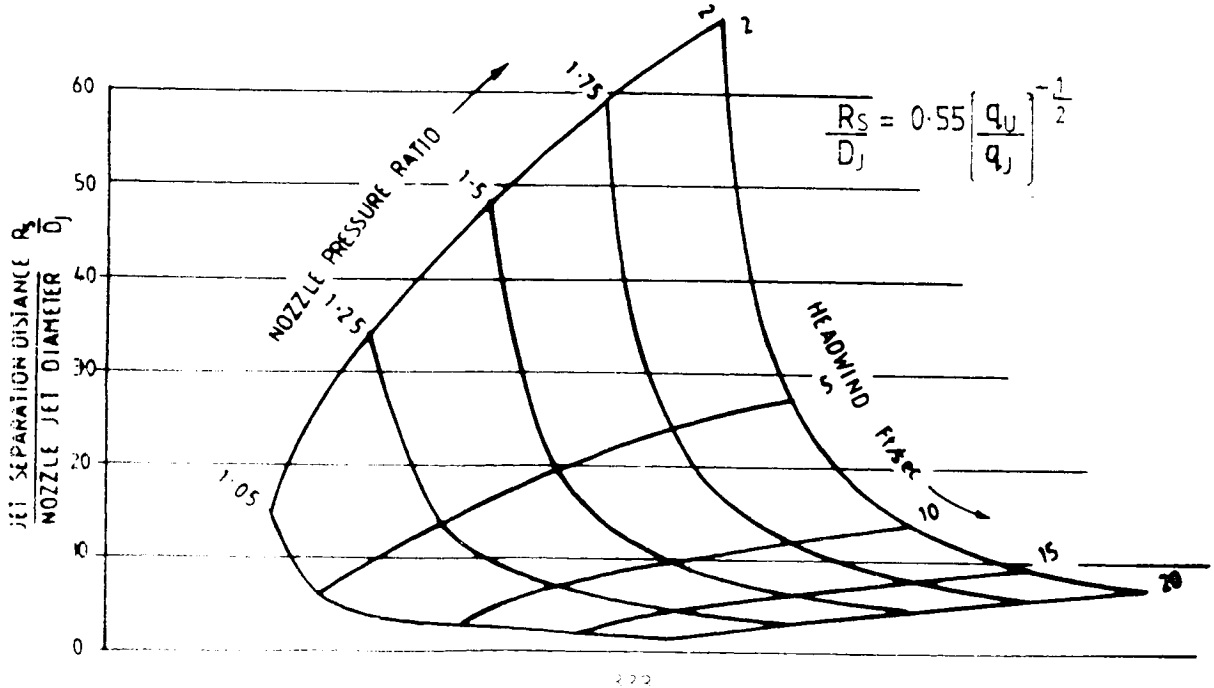

FIG 6b

COMPARISON BETWEEN PROLONGED HOVER AND MOVING MODEL TESTS

VARIATION OF PEAK MEAN INTAKE TEMPERATURE RISE WITH HEADWIND

10° CONVERGED NOZZLES CAD 'N'

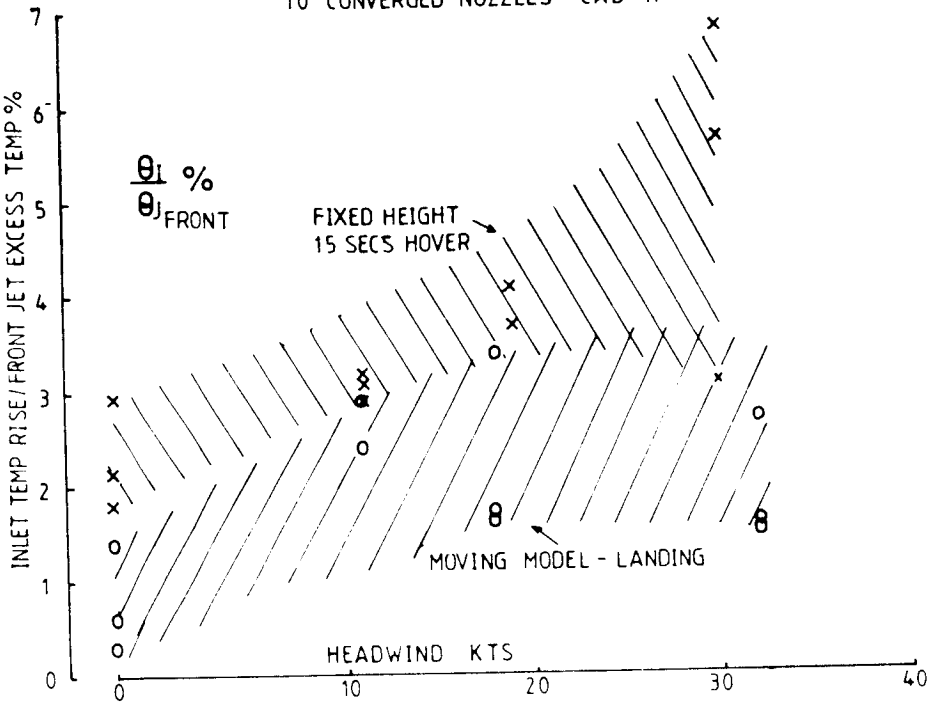

FIG 7

COMPARISON OF MODEL AND FULL SCALE RECIRCULATION TEST RESULTS (P1127 AIRCRAFT)

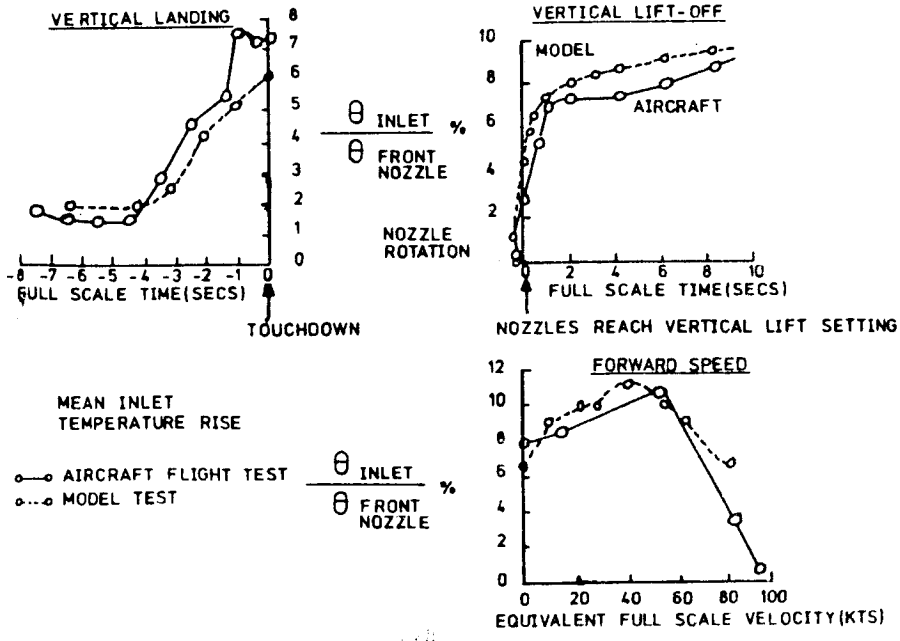

FIG 8

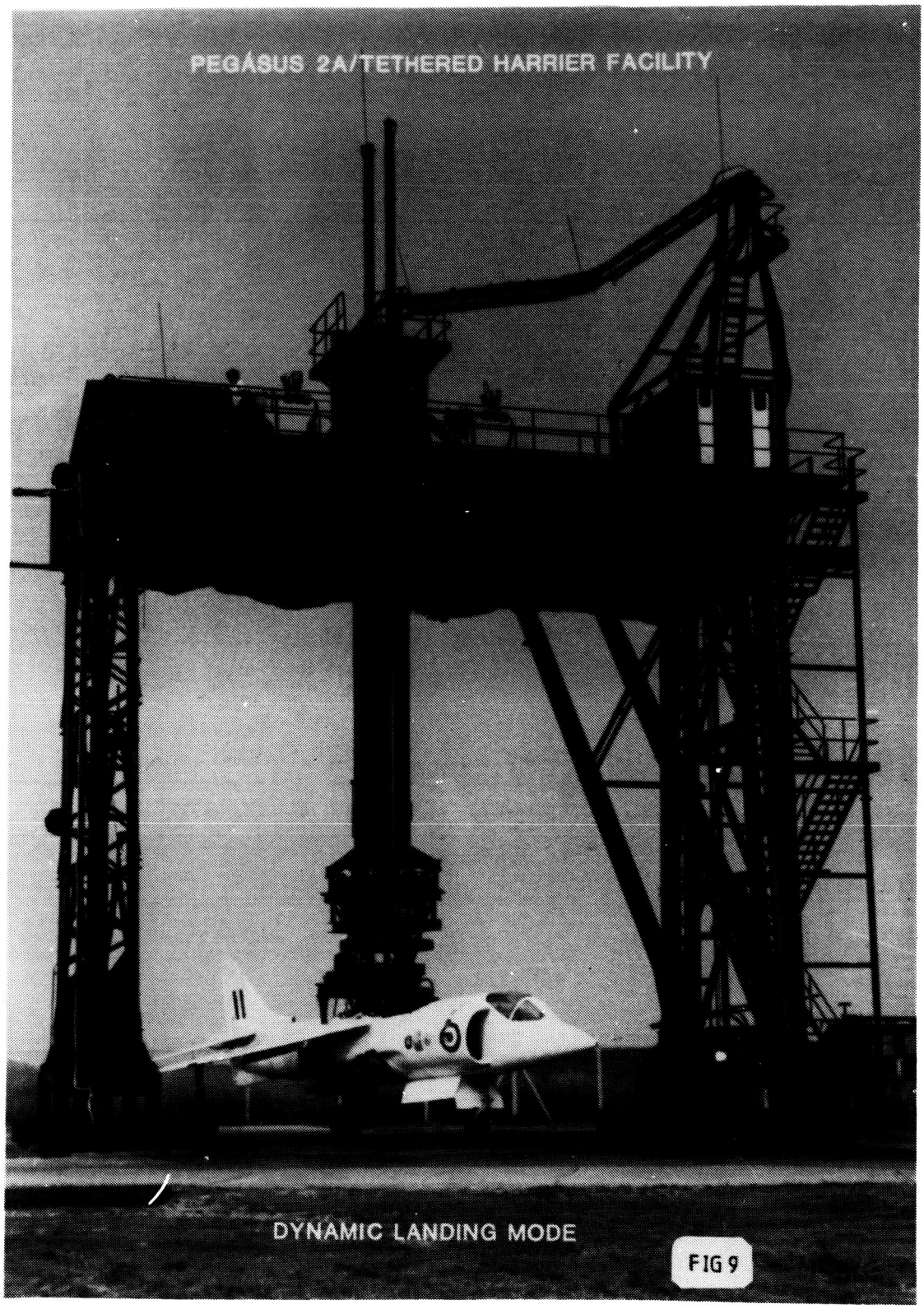

PEGASUS 2A / TETHERED HARRIER SIMULATED LANDING TESTS -DEC 1984

NOZZLE ORIENTATION

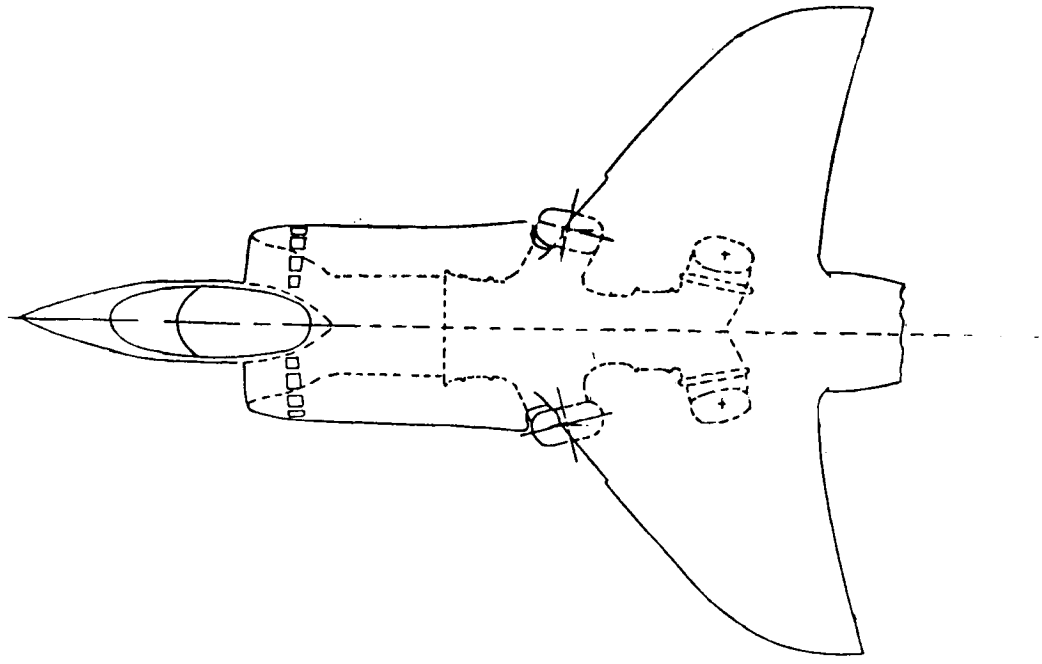

FIG 10

PEGASUS 2A / TETHERED HARRIER SIMULATED LANDING TESTS -DEC 1984

20 CONVERGED FRONT NOZZLES CAD AD+BA

MEAN INTAKE TEMPERATURE RISE / JET EXCESS TEMPERATURE

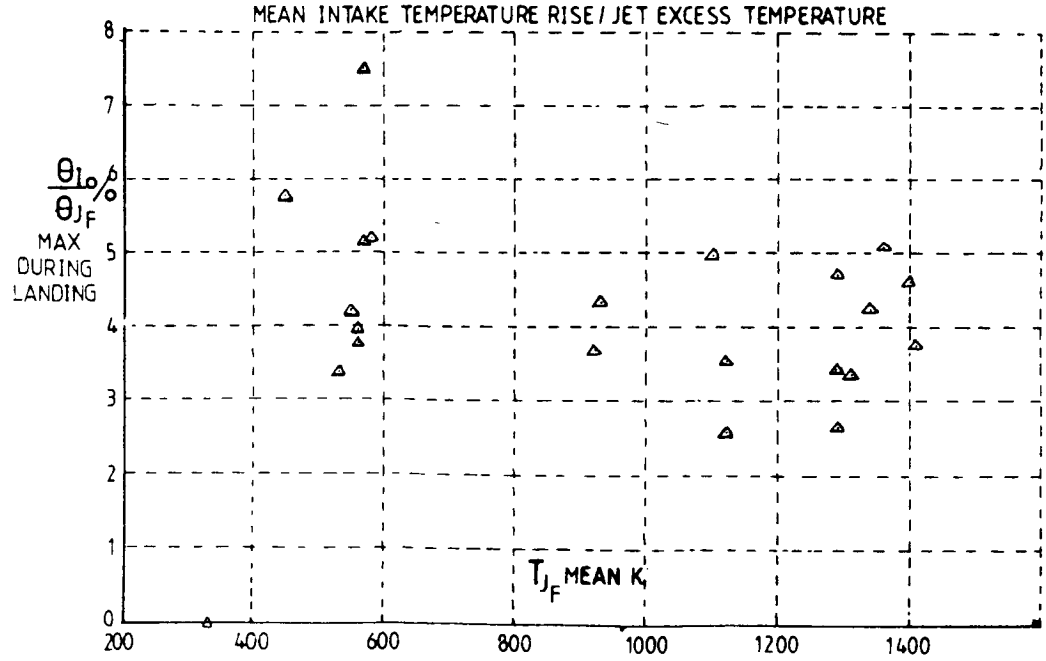

FIG 11

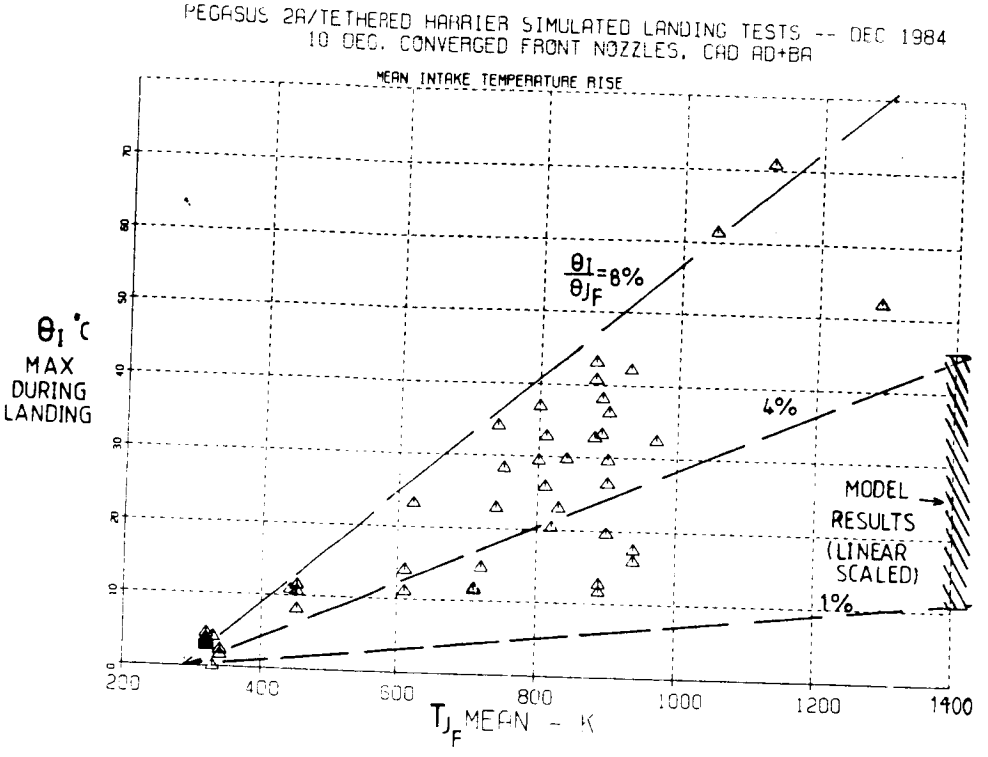

FIG 12

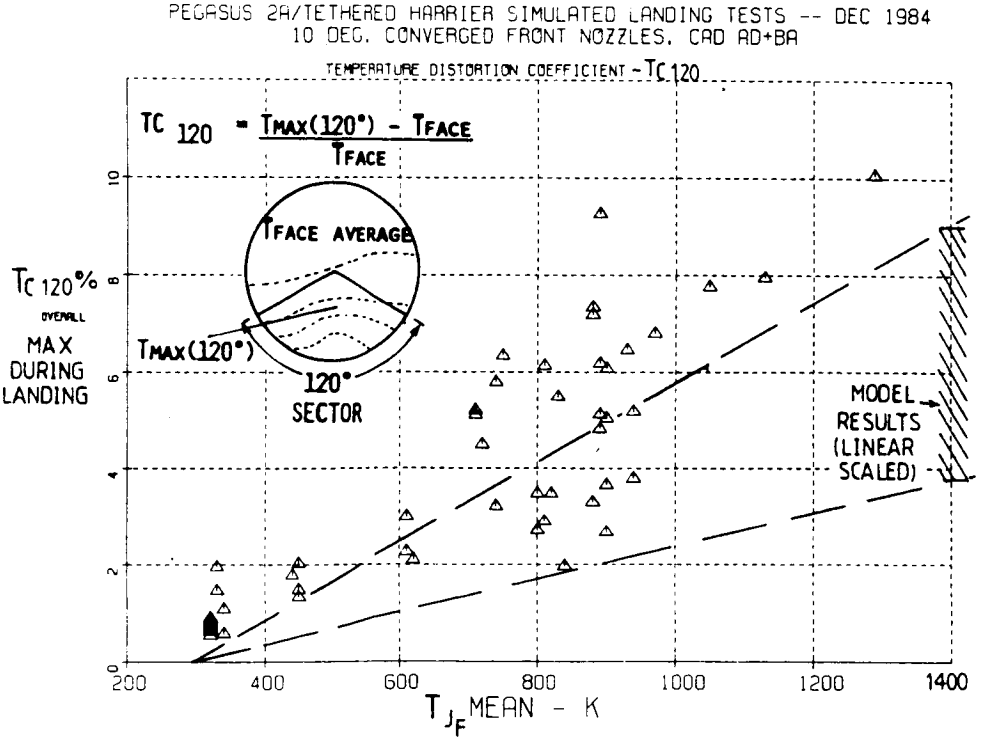

FIG 13

HGR MODEL SCALING PARAMETERS AND TEST CONDITIONS
BUOYANCY SCALED

	ITEM		PI127		PEGASUS 2A/TETHERED HARRIER	
			FULL-SCALE	MODEL	FULL-SCALE	MODEL
SCALING PARAMETERS	GEOMETRY FS/M		1·0	10	1·0	10
	DYNAMIC HEAD RATIO FS/M	FRONT	1·0	22·0	1·0	19·3
		REAR		22·0		19·3
	EXCESS TEMP RATIO FS/M	FRONT	1·0	2·33	1·0	2·78
		REAR		2·33		2·78
	BUOYANCY RATIO FS/M	FRONT	1·0	1·0	1·0	1·0
		REAR		1·18		0·91
	TIME RATIO FS/M		1·0	2·13	1·0	2·28
TEST CONDITIONS	FRONT NOZZLES	P_J/P_∞	1·83	1·038	1·5	1·026
		θ_J	70°c	30°c	1112°c	400°c
	REAR NOZZLES	P_J/P_∞	1·64	1·029	1·31	1·016
		θ_J	575°c	250°c	512°c	184°c

FIG 14

θ_I / θ_{J_F} RATIOS RELATIVE TO SHOEBURYNESS NOZZLES
FOR THREE NOZZLE HEIGHTS

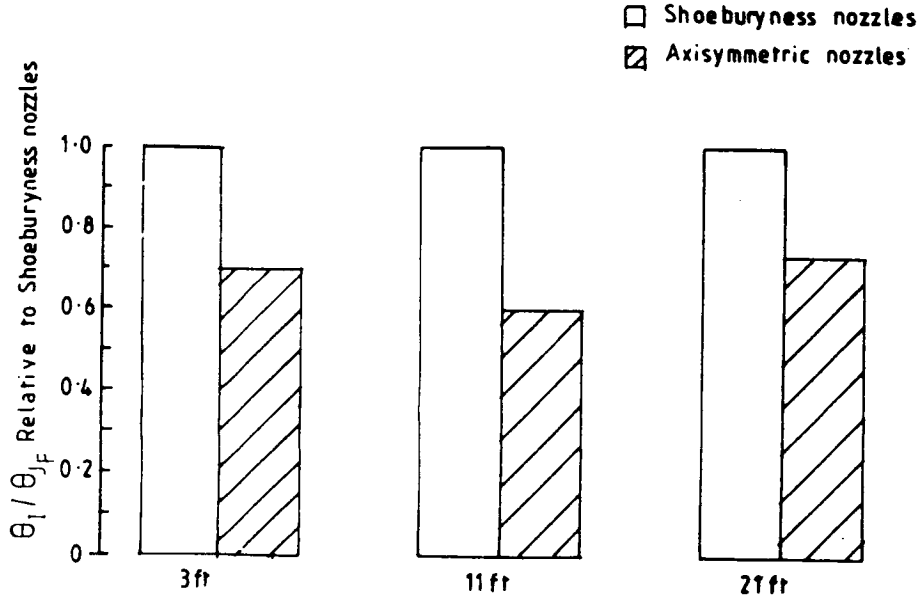

FIG 15

MODEL - FULL SCALE COMPARISON
PEGASUS 2A/TETHERED HARRIER RESULTS
INTAKE TEMPERATURE DISTORTION CONTOURS
MAXIMUM LEVELS DURING LANDING AT $T_{JF} \triangleq 900$ K
10 CONVERGED FRONT NOZZLES CAD AD + BA

FULL SCALE
LANDING VEL 1·5 M/S

HEADWIND ≙ 10 KTS
HEIGHT ≙ 1·1 M

MODEL
LANDING VEL 1·0 M/S

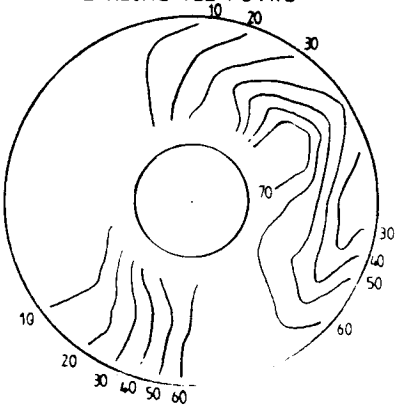

θ_I = 32·7 °C
$T_{C\,120}$ = 7·2 %

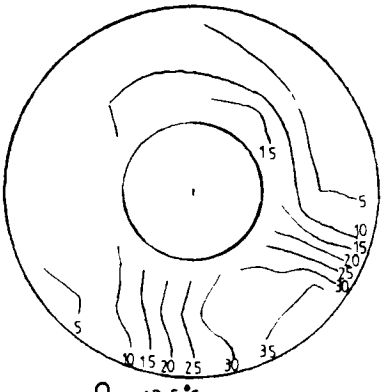

θ_I = 12·5 °C
$T_{C\,120}$ = 3·9 %

FIG 16

HGR SCALING - SUPPORTING EXPERIMENTAL PROGRAMMES

- o MODEL AND FULL-SCALE TESTS RELATED TO THE TETHERED HARRIER AIRCRAFT
  - NOZZLE GEOMETRY } MODEL TESTS BUOYANCY AND FULL
  - TEMPERATURE PROFILE } NPR SCALED
  - PEGASUS 11 FULL-SCALE AND MODEL
- o FUNDAMENTAL SCALING LAW STUDIES TO MEASURE INTAKE HGR FOR SIMPLIFIED AIRCRAFT CONFIGURATIONS.
  - FAR FLOWFIELD
  - NEAR FLOWFIELD
- o FUNDAMENTAL STUDIES OF JET WAKES INCLUDING ENTRAINMENT AND FOUNTAIN FLOW PROPERTIES.
  - EFFECT OF NPR
  - EFFECT OF JET TURBULENCE

FIG 17

NASA
Lewis Research Center

HOT GAS INGESTION:
FROM MODEL RESULTS
TO FULL SCALE ENGINE TESTING

BY

ALBERT L. JOHNS AND THOMAS J. BIESIADNY
NASA LEWIS RESEARCH CENTER

AND

L. L. PAGEL
McDONNELL AIRCRAFT COMPANY

GROUND EFFECTS WORKSHOP
NASA AMES RESEARCH CENTER

AUGUST 20-21, 1985

This presentation is an overview of a joint NASA Lewis-McDonnell Aircraft Company Hot Gas Ingestion (HGI) test program in NASA Lewis' 9'x15' Low Speed Wind Tunnel (LSWT). This initial program is scheduled for testing in late 1986.

Advanced short takeoff/vertical landing (ASTOVL) aircraft capable of operating from remote sites, damaged runways, figure 1, aircraft carriers (figure 2) and small air capable ships are being pursued for deployment around the turn of the century. To achieve this goal, it is important that technologies critical to this unique class of aircraft be developed, ref. 1. One of the ASTOVL concepts, the vectored thrust, has as its critical technology item, the potential of hot gas ingestion (which occurs during vertical flight operation while in ground effect) as a key development issue. Recognizing this need, NASA Lewis Powered Lift Section and McAir have defined a cooperative program for testing in the Lewis' 9'x15' LSWT.

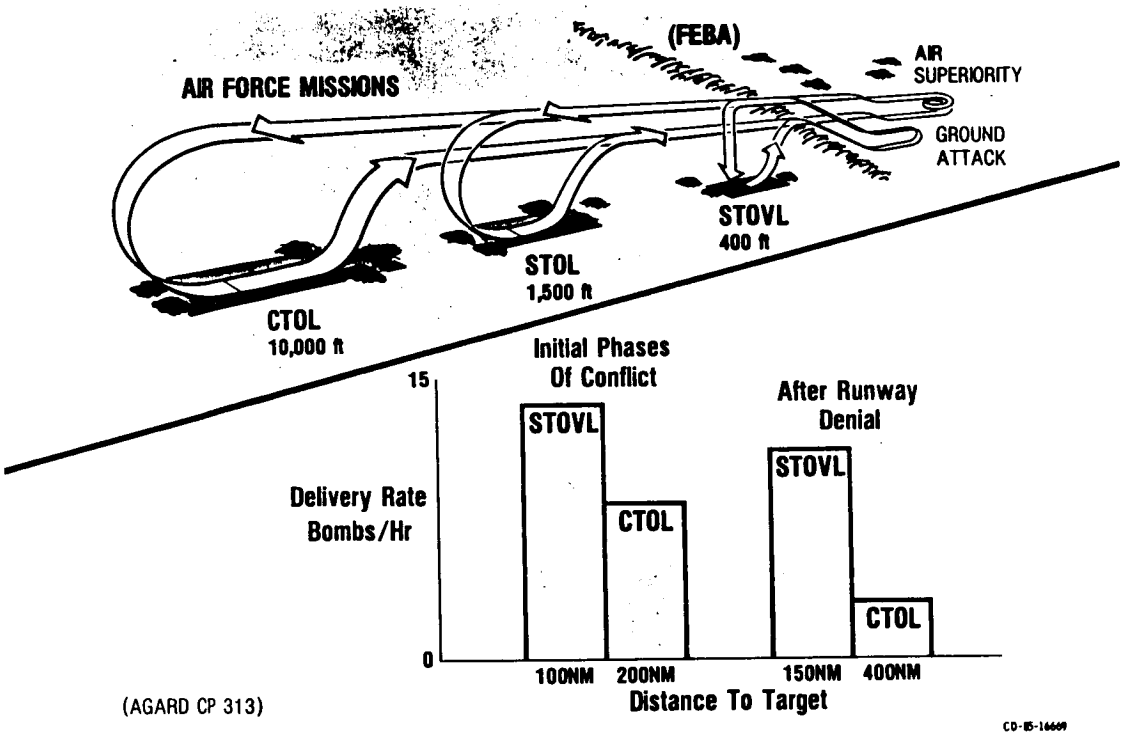

Figure 1.-STOVL improves Air Force operational effectiveness.

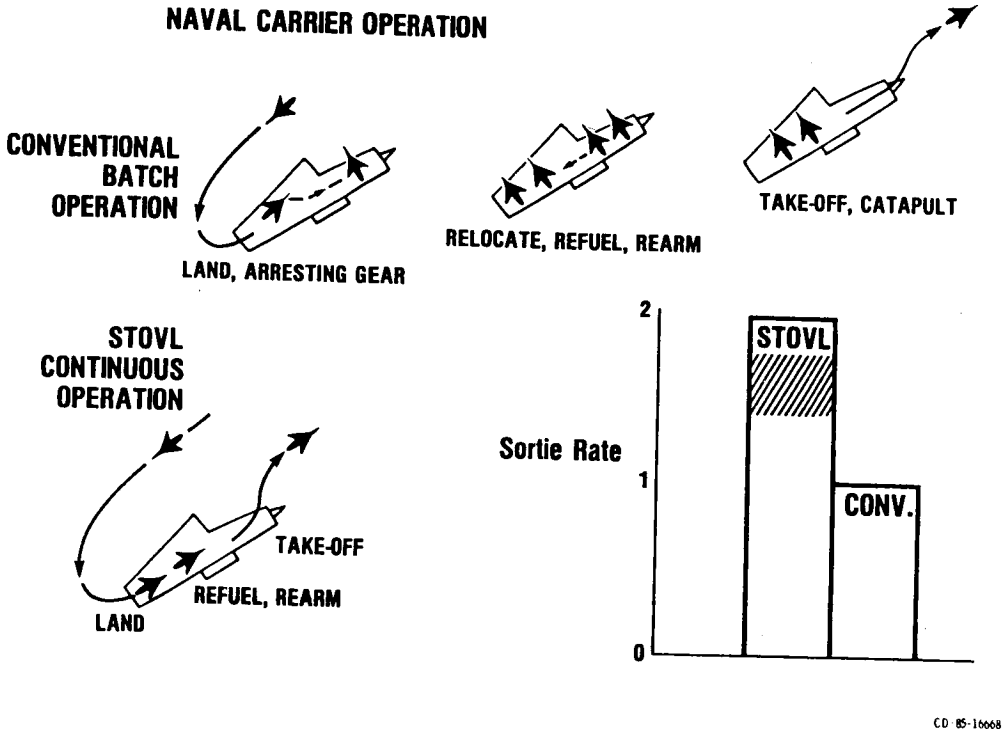

Figure 2. – STOVL improves Naval carrier operational effectiveness.

An artist's conceptual view of the vectored thrust concept (Model 279-3) is shown in figure 3. The aircraft concept consists of:

1. single engine;
2. bi-furicated inlet;
3. VTOGW 30,000 lbs;
4. M Max. = 2.0;
5. Four nozzles - two forward and two aft

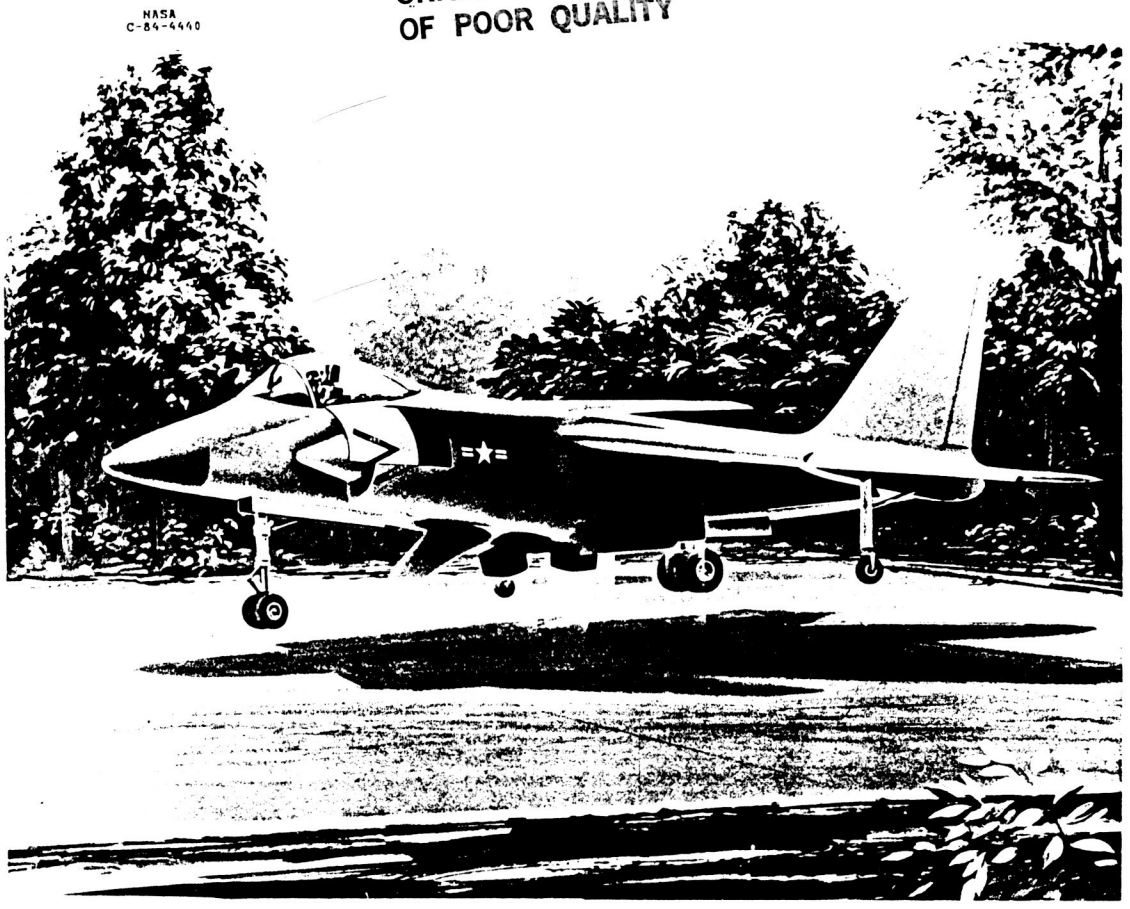

Figure 3. – Model 279–3 with improved LIDs and deflector.

The two front deflector nozzles will be required to accommodate burning of the fan airflow. The two aft deflector nozzles will control the core airflow. The concept may also have the following:

1. front flow deflector;
2. sidewall deflectors (streaks)

The testing of this vectored thrust concept requires a unique model support system and modification to the 9'x15' LSWT test section.

The next figure (4) shows a schematic of the 9.2% scaled Model 279-3 installed in the 9'x15' LSWT with the unique model support system. The model support system provides four degrees of freedom: Vertical movement, yaw, pitch, and roll capabilities. The vertical movement range is four feet above the ground plane; yaw angle range is + 180°; pitch angle range is + 30°, and the roll angle is + 20° range. Another feature shown in figure 4 is the: Ground plane which has a sliding trap door.

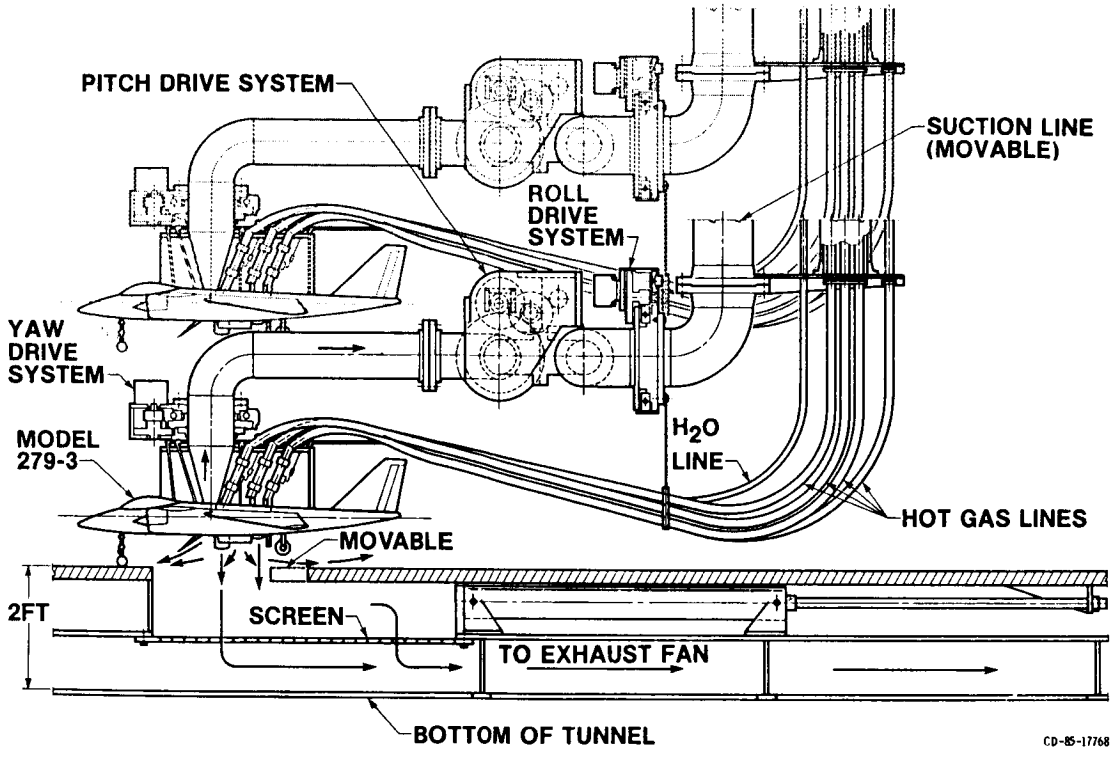

Figure 4.–Schematic of model 279–3 and support system installed in the 9'X15' LSWT.

We have built in flexibility in this program. The aircraft inlet airflow is controlled independently of the nozzle airflow. The inlet airflow is controlled by a vacuum system and the nozzle airflow is supplied by a high pressure-hot air system, with temperature ranging from ambient to 1000°F at the nozzles. The freestream velocity will vary from static to 65 kts.

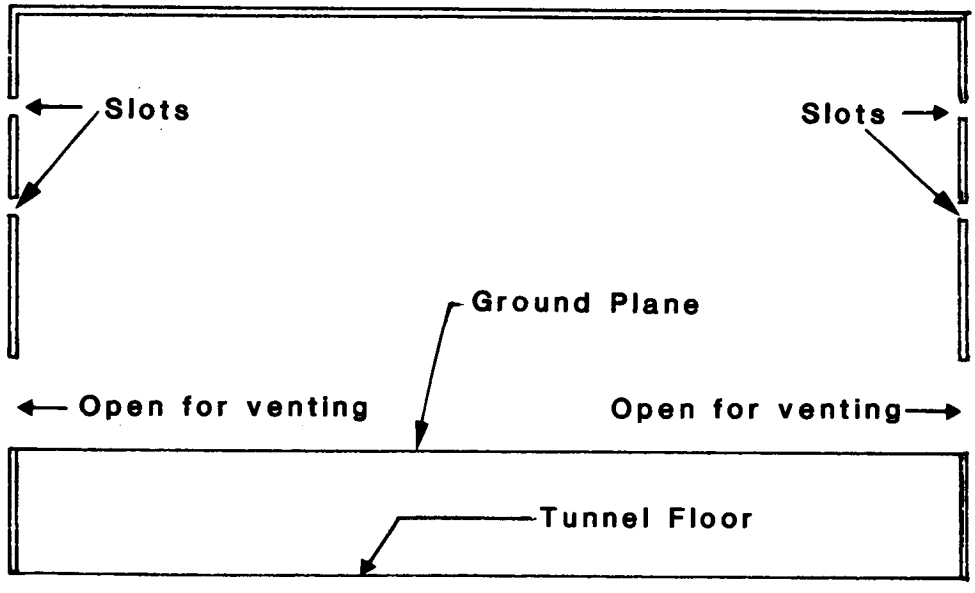

Figure 5. – Modified 9'X15' Low Speed Wind Tunnel.

A cross-section of the 9'x15' LSWT is shown in figure 5. The 9'x15' LSWT has slotted sidewalls test section. The tunnel sidewalls will have an opening near the ground plane to allow the laterally-flowing hot gas from the exhaust nozzles to exit the test section.

THE PRIMARY OBJECTIVES OF THIS COOPERATIVE PROGRAM ARE TO INVESTIGATE TECHNIQUES WHICH WILL:

- o MINIMIZE/ELIMINATE HOT GAS REINGESTION DURING VERTICAL FLIGHT OPERATIONS WHILE IN GROUND EFFECTS.
- o PERMIT PREDICTION OF OPERATING CHARACTERISTICS OF VECTORED THRUST CONCEPTS WITH FORWARD VELOCITY.

IN ADDITION, THE TEST PROGRAM WILL ESTABLISH A WIND TUNNEL HOT GAS INGESTION DATA BASE FOR:

- o BOTH NEAR/FAR FIELD INGESTION
- o FOUNTAIN FLOW EFFECTS, AND
- o GROUND VORTEX FLOW FIELD.

THE DATA BASE DEVELOPED SHALL BE APPLICABLE TO THE DEVELOPMENT OF UNIQUE ANALYTICAL CODES.

Figure 6.–Primary objectives.

The program objectives are shown in figure 6. In addition to the primary objectives, we shall establish a database in several needed areas, one of which is the ground-vortex-flow-field-jet interaction. The objective is to answer the question of what effect, if any, the boundary layer thickness has on the ground-vortex-flow-field-jet interaction.

The figures which follow are used to indicate the type of data parameters we will investigate. The trends shown on the figures are considered typical.

The results of the boundary-layer study, figure 7, will indicate the forward extent of the ground vortex flow field-jet interaction due to the boundary-layer thickness.

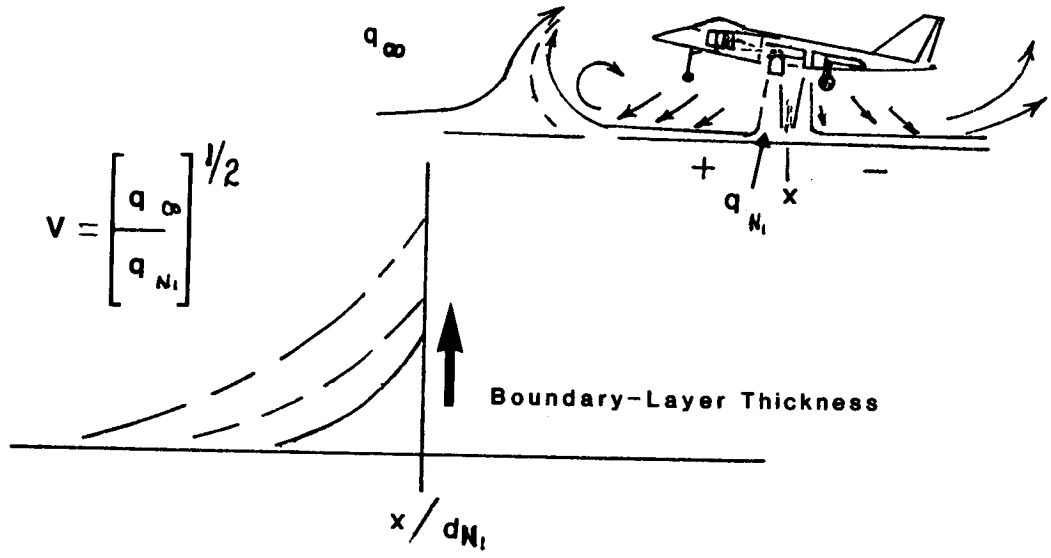

Figure 7.–Boundary-Layer thickness effect on the ground vortex flow.

Shown in figure 8 is a means of thickening the boundary-layer. Shown is a boundary-layer thickness configuration which consists of 1/4" dia. rods in four rows. The rods would extend the width of the ground plane. Several configurations could be utilized; for example, 3" height rods or 6" height rods, to obtain several different boundary-layer heights.

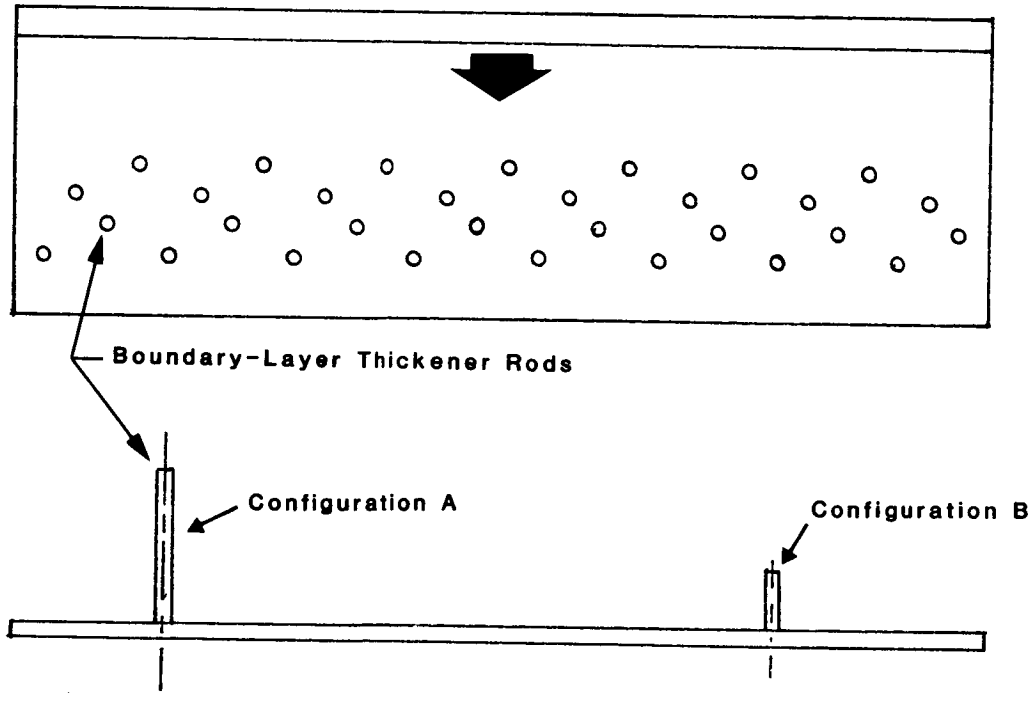

Figure 8.–Boundary-Layer Thickeners.

In addition to controlled thickening the boundary-layer, we also need to minimize the boundary-layer height due to axial distance. Figure 9 showns two methods of reducing the boundary-layer height. We have considered three techniques; a rotating belt was considered but was eliminated due to complexity and the temperature environment involved (1000°F). As shown, another concept involves using a suction pump(s), which is located outside of the test section. The suction pump(s) would remove part or all of the boundary-layer. The least concept involves lowering the front section of the ground plane. This technique would relocate the initial boundary-layer growth point. Prior to the use of either of these concepts, we shall have established the extent of the ground vortex flow field on the ground plane.

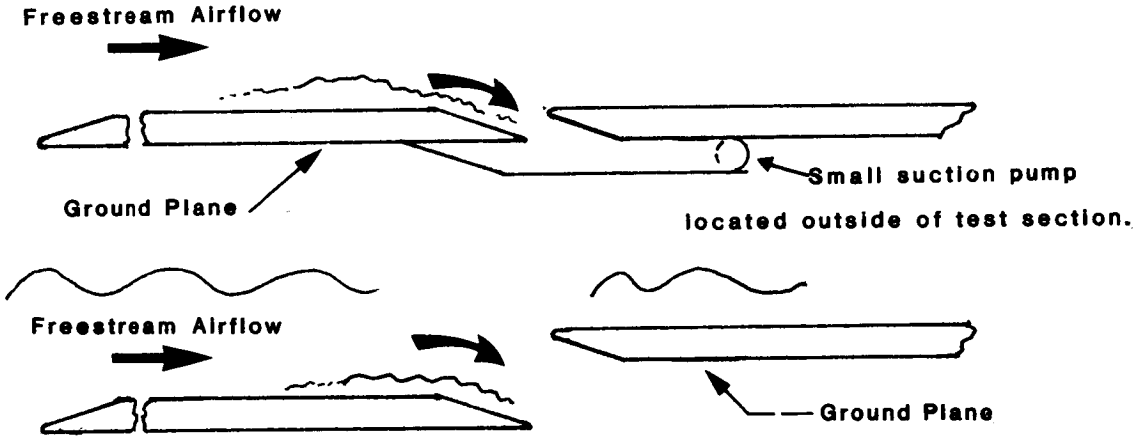

Figure 9.-Boundary-layer removal configurations.

One mechanism for near field ingestion is the jet fountain. If the velocity of the fountain or turbulence intensity is reduced, the effects of the near field ingestion will also be reduced. A means of reducing the fountain velocity and turbulence is to vary the front nozzles splay (laterally movement of the front nozzle) angle. It is anticipated that results will show a reduction in both fountain jet velocity and turbulence intensity with increasing splay angle, as shown in figure 10.

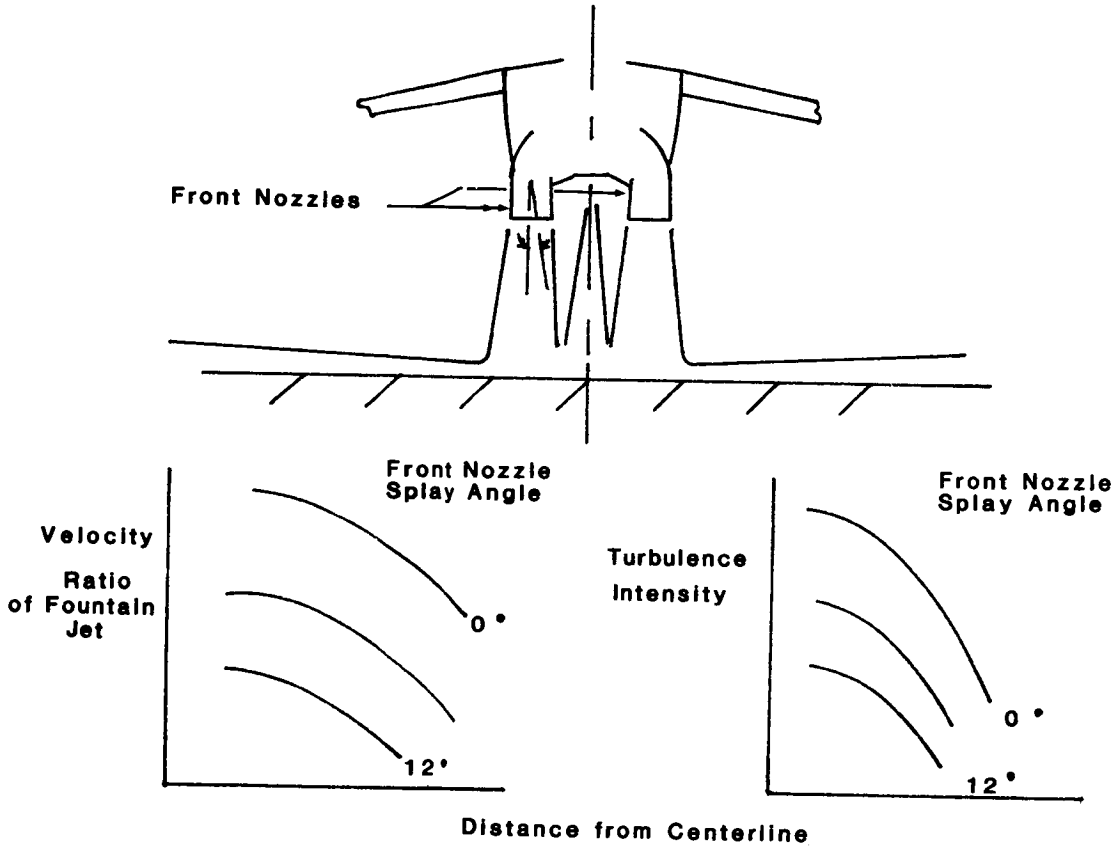

Figure 10.–Fountain turbulence and velocity.

Figure 11 illustrates the various configurations we will test to obtain the fountain flow characteristics. Shown is a schematic of four nozzle arrangements and the auxiliary inlets. The first configuration is Model 279-3 concept with both sets of nozzles flowing. The second configuration consists of only the front nozzles flowing. The third configuration consists of only the aft nozzles flowing. And the fourth configuration simulates a twin engine aircraft with one engine out. The jet temperature range is interchangable between the front and aft nozzles. These configurations will produce considerable information on the ground-vortex-boundary-layer-interaction.

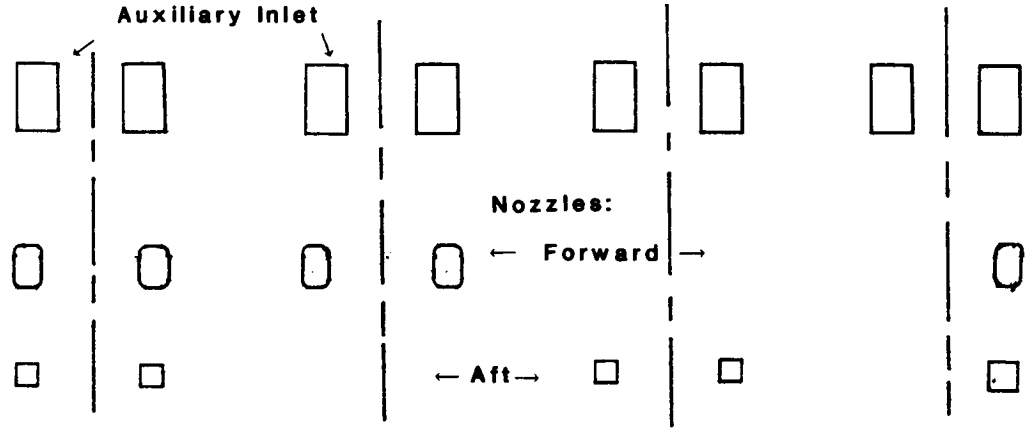

Figure 11.–Model deflected jet configurations.

Addressing the primary objectives of this joint NASA Lewis-McAir program, the major concern is hot gas ingestion in both the near and far field. In determining the effectiveness of the ingestion avoidance devices (IADs) for near field ingestion, the inlet temperature rise v.s. nozzle exhaust temperature will be plotted as shown in figure 12. Results from the configuration without IADs will be compared to a configuration with IADs. In general, a reduction should occur with ingestion avoidance devices.

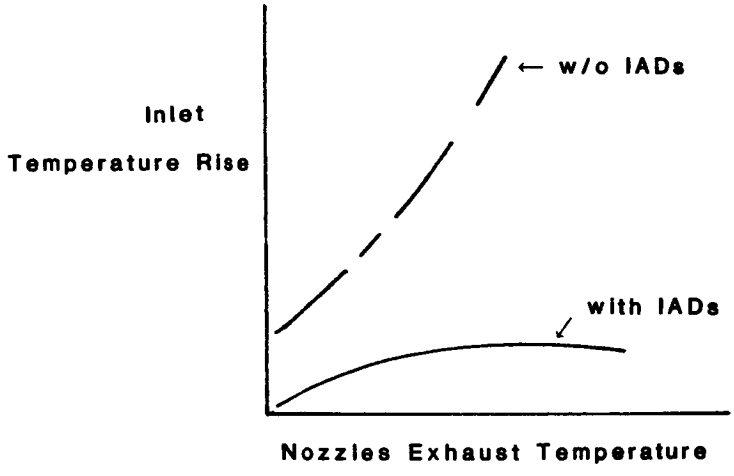

Figure 12.–Effectiveness of ingestion avoidance devices in reducing inlet hot gas ingestion.

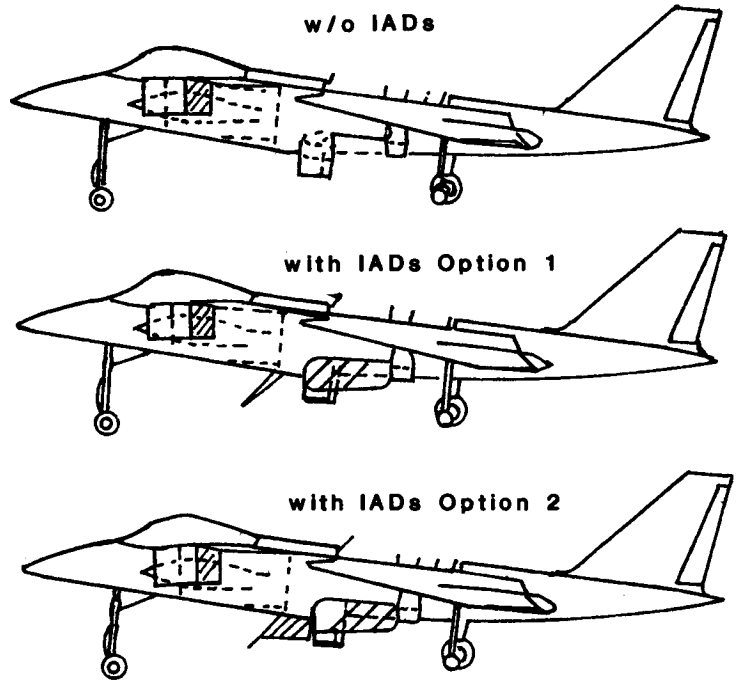

Figure 13. – Near field ingestion avoidance devices (IADs).

Figure 13 shows the three primary configurations:

1. without IADs,
2. with IADs, option 1: flow deflector and congitudinal streaks (2) installed,
3. with IADs, option 2: flow deflector and congitudinal streaks (2), aft fence and flow deflection sidewall (2) installed.

These configurations will be tested with the auxiliary inlets in the open and closed positions.

In addition to the near field, data applicable for determining the far field ingestion effect will also be obtained.

Pressure/temperature rakes are located on the ground plane (forward and aft of the model), figure 14. Also tufts will be located on the ground plane to give an indication of the far field airflow movement. The ground plane will contain static pressure and temperature taps. A thermo-vision system will be utilized to detect the most forward point of the hot gas at the various freestream speeds.

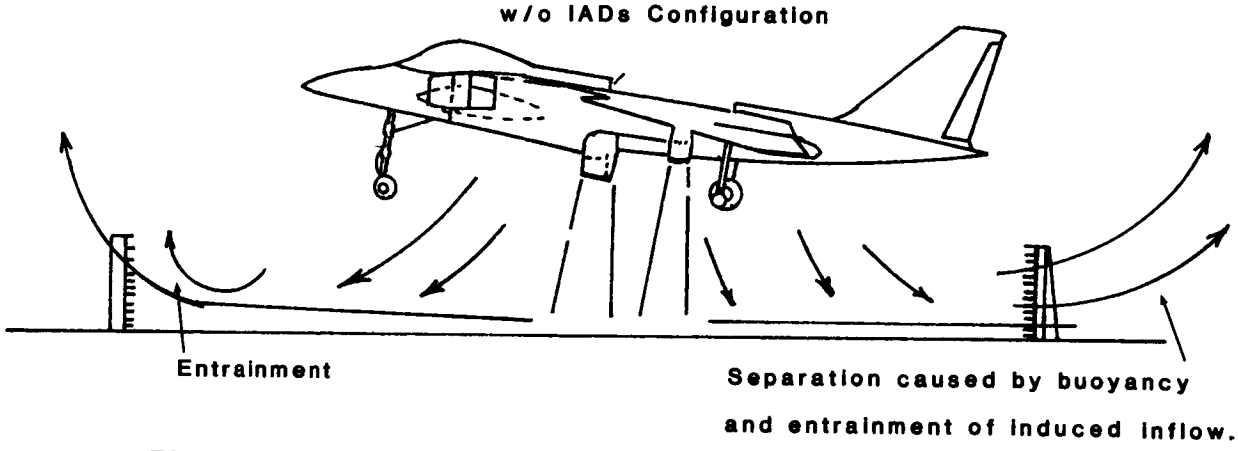

Figure 14. – Far field ingestion.

In the next several figures we shall briefly review some of the instrumentation to be utilized during the test.

Figure 15 illustrates several of the rakes installed on the model. They are as follows:

1. Nose boom rake which is used to measure the local freestream conditions.
2. Inlet plane undersurface rake which is used to measure the quality of air entering the inlet region.
3. Fountain upwash rake will measure the upwash flow characteristics.

The rakes contain both total pressure and temperature measurements.

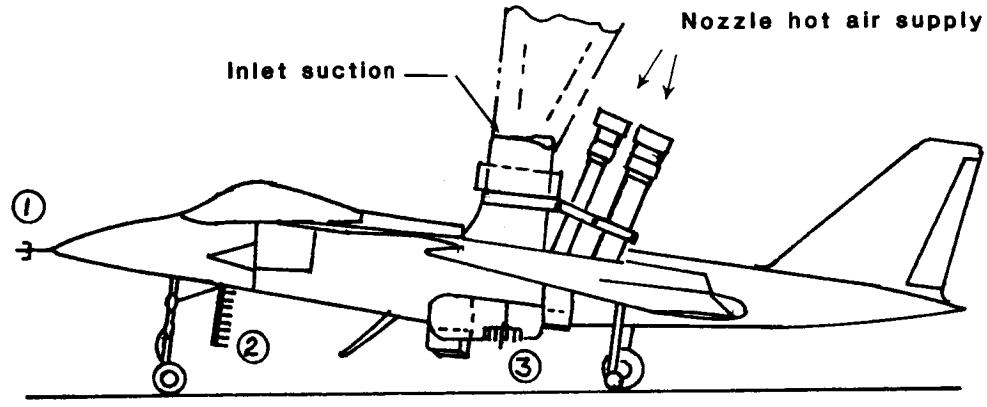

Figure 15. - Model 279-3 external instrumentation rakes.

In addition to rake instrumentation, static pressure taps and high response thermocouples are located along the bottom and sides of the fuselage, as can be seen in figure 16. Using the fuselage instrumentations, we should have a good indication of the thermo-profiles along the fuselage.

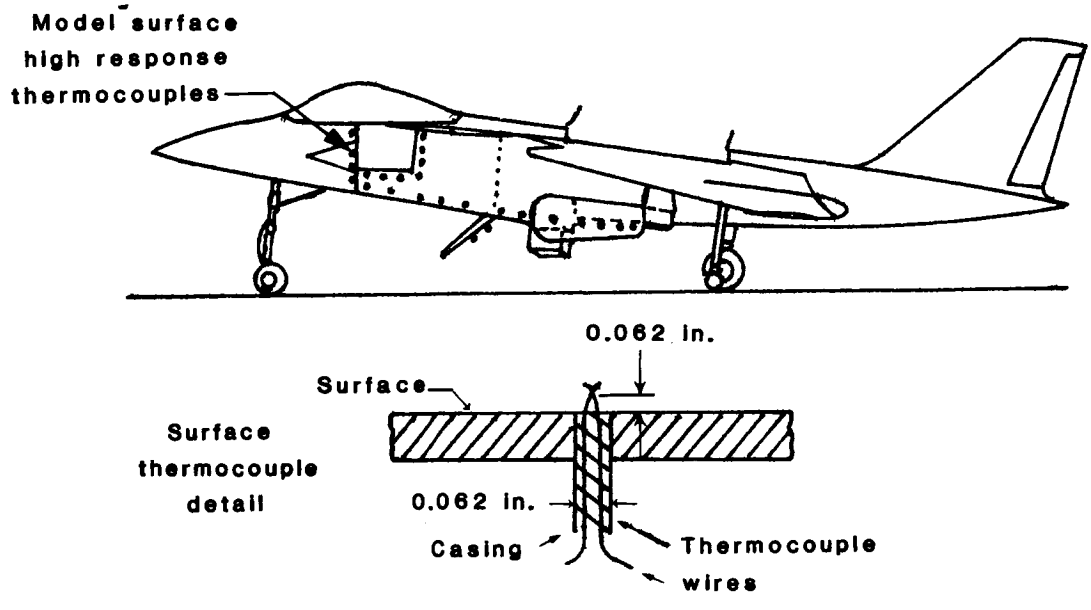

Figure 16. - Typical fuselage instrumentation.

Another major region of concern is the inlet. We need to know what effects inlet temperature rise has on the fan face Mach number rise. Figure 17 shows what might be a typical plot of inlet temperature rise vs inlet fan face Mach number. That is, the inlet temperature rise reaches a plateau at some fan face Mach number. This particular curve is a function of the model height above the ground plane.

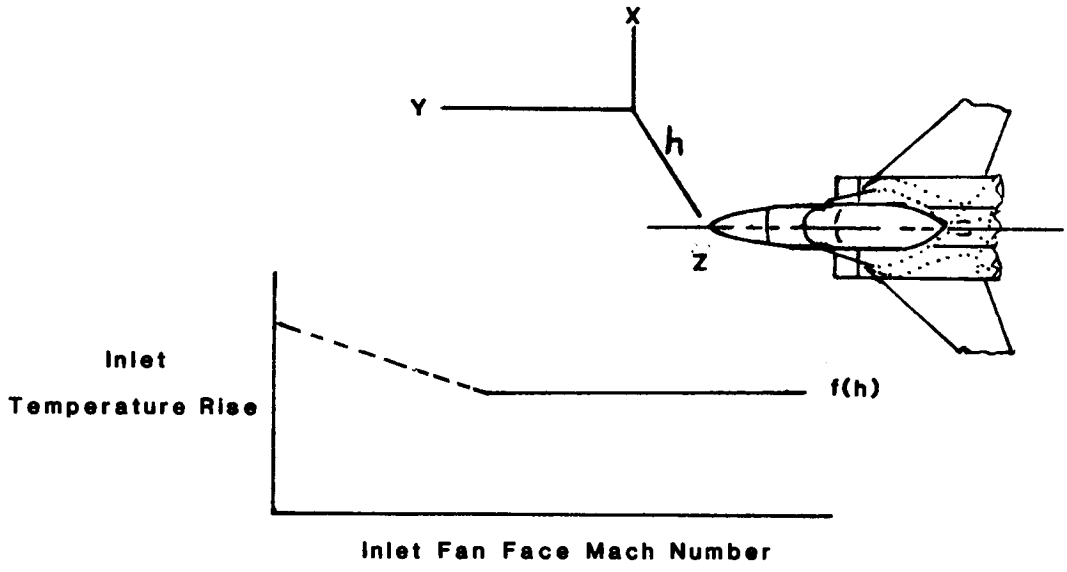

Figure 17. – Inlet fan face temperature rise.

Typical model inlet and nozzle instrumentations are shown in figure 18. The nozzles contain total pressure and temperatures probes. The engine fan face rake will also contain 32 total pressures and temperature measurements. To determine the severity of the hot gas ingestion, the inlet temperature rise and contour maps will be obtained utilizing the fan face rake. A typical contour map of a fan inlet instantaneous temperature profile is shown in figure 19.

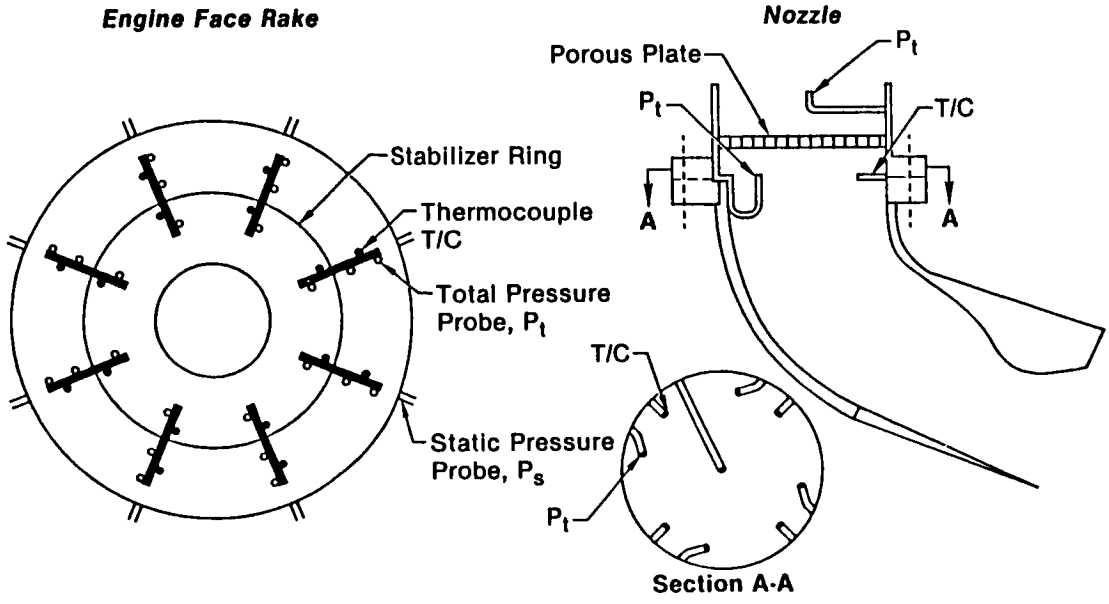

Figure 18. – Typical model inlet and nozzle instrumentations.

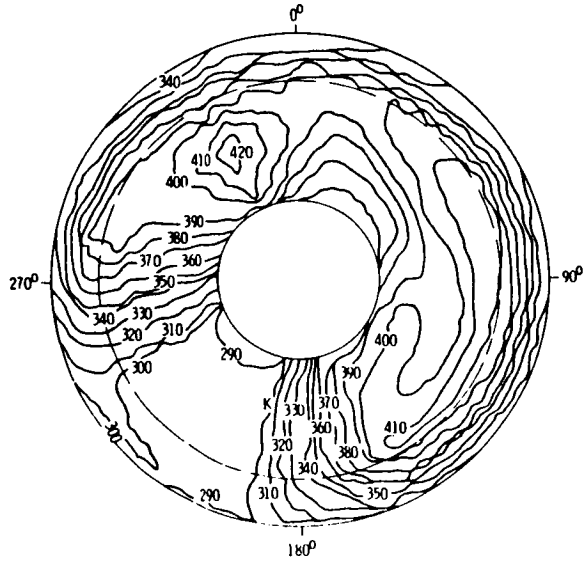

Figure 19. – Contour map of the fan inlet temperature profiles.

At the conclusion of the 9'x15' LSWT test, we will have pressure/temperature contour maps at the fan face for various freestream velocities and model attitudes. But what we would like to ascertain as an end item is the effect the hot gas ingestion has on the actual engine.

We anticipate, as a follow-on program, using both the pressure and temperature distortion profiles from the 9'x15' LSWT program and implement these into a full scale engine program. This full scale testing would establish the characteristics of the engine sentitivity due to the temperature, pressure and a combination of temperature-pressure distortion. At NASA Lewis Research Center, we have an altitude test chamber (PSL) in which we do full size engine testing. Figure 20 shows a view of the Altitude Test Chamber with a TF-34 engine installed. This facility's altitude simulation range from sea level to 100K feet.

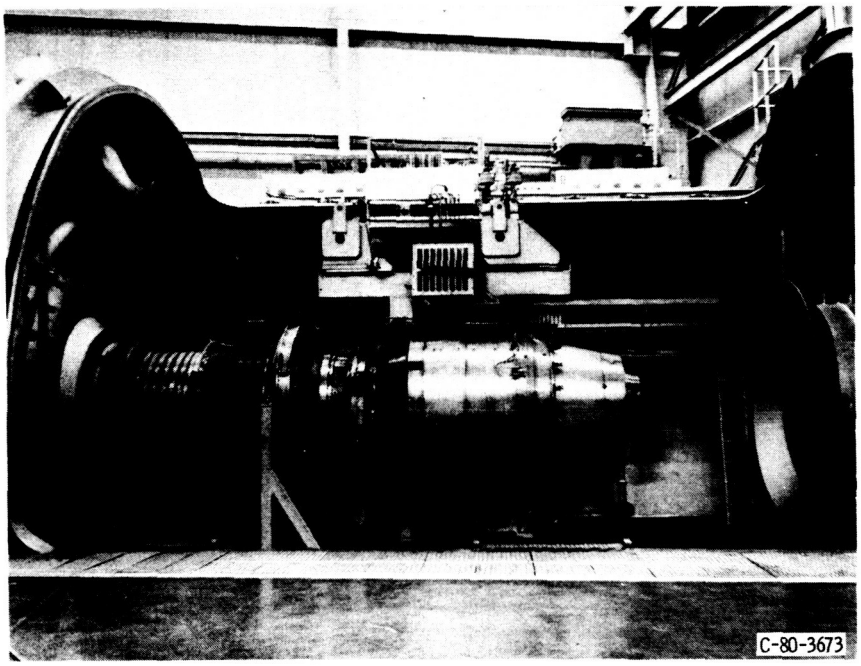

Figure 20. - TF-34 engine installed in the Altitude Test Chamber.

Figure 21 illustrates the extent of typical engine instrumentation. The instrumentation consisted of steady-state and dynamic total pressures, static pressures, and total temperature measurements. Transient total temperature and high-response pressure data are also recorded.

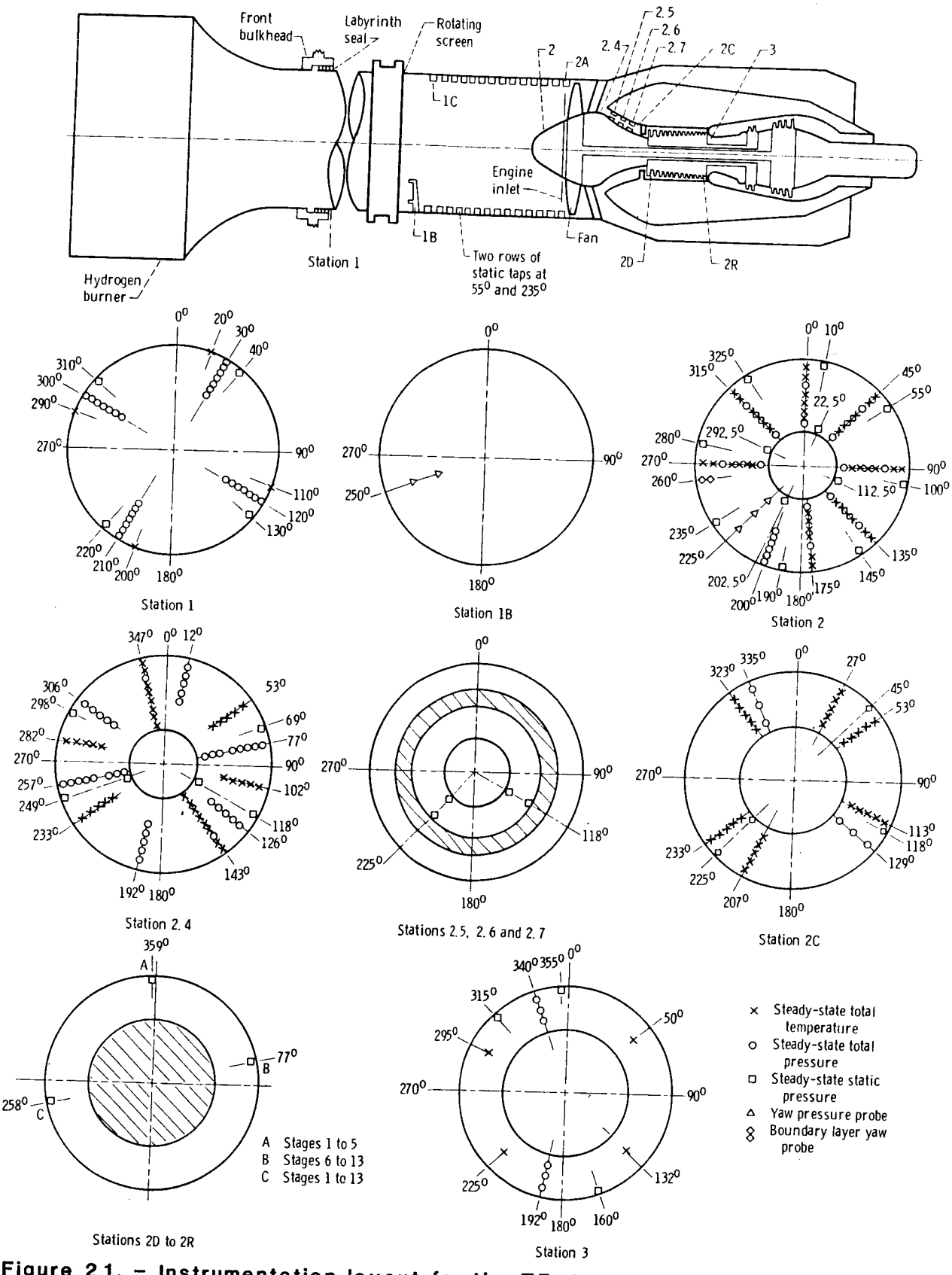

Figure 21. – Instrumentation layout for the TF-34 turbofan engine. (Stations viewed looking upstream. See symbols for description of station locations.)

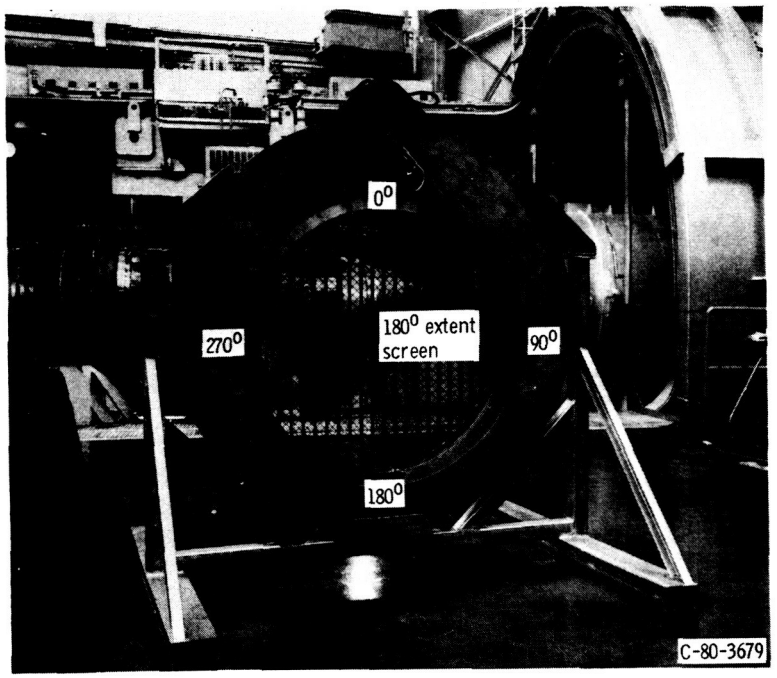

Figure 22. – Pressure distortion generator with rotatable screen assembly.

Pressure and temperature distortions can be imposed on the full size engine by using pressure and temperature distortion generators. Inlet pressure distortion (pressure lower than average) is generated using one of three screen configurations, figure 22. The pressure distortion circumferential extent of a 180° can be varied by a rotatable screen assembly which is mounted upstream of the engine inlet.

The gaseous-hydrogen-fueled burner device, figure 23, is used to produce the time-dependent temperature distortion and is installed upstream of the engine inlet bellmouth. The burner has the capability of being rotated + 30° from the center position and is divided into four individually controlled quadrants. Air passing through the burner is heated in selected 90° sectors. Each sector has the following:

1. 6 swirl-can pilot burners, ignition source for hydrogen.
2. 6 annular gutters supported by 1 radial gutter.
3. 6 circular-tube manifolds (1 inside each annular gutter) with small holes for hydrogen injection.

High-response valves could be energized in any desired combination to produce the temperature distortion.

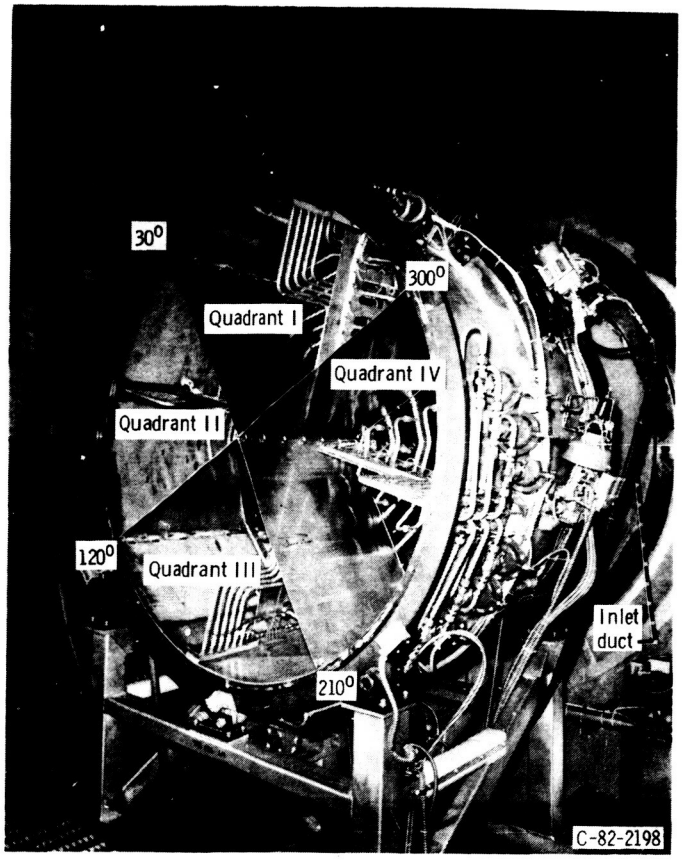

Figure 23. - Total temperature distortion generator with a gaseous-hydrogen-fueled burner.

By using the above distortion devices, we can arrive at the distortion sensitivity parameters for the engine inlet as shown in figure 24. The engine stall line is temperature and/or pressure distortion sensitive. This is ultimately the type of information you need to know about the model-inlet-engine characteristics.

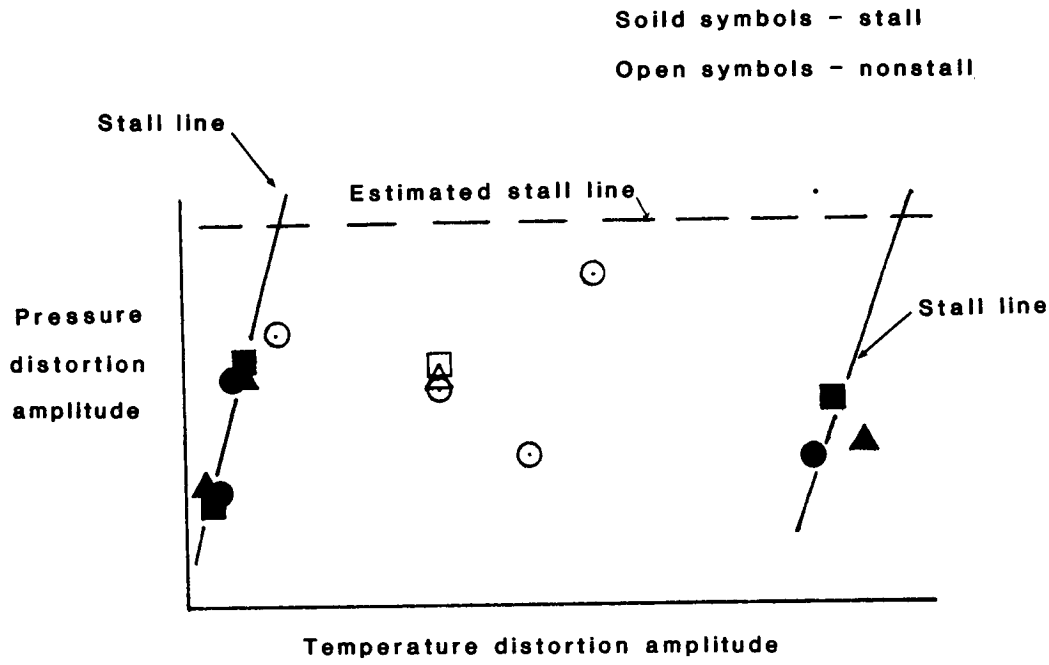

Figure 24. - Distortion sensitivity at the engine inlet.

In conclusion:

1. We shall obtain data which will permit prediction of operating characteristics of vectored thrust concepts with forward velocity.

2. We shall minimize/eliminate hot gas ingestion during vertical flight operations while in ground effects.

3. We shall establish a data base for near and far field ingestion, fountain flow effects, and ground vortex flow field - jet interaction.

4. We shall also obtain distortion results which can be utilized for full size engine testing in the altitude test chamber facility.

5. We shall obtain the extent of ground effects on the vectored thrust ASTOVL concept.

6. It is important to develop analytical codes which will predict the overall effects of hot gas ingestion.

REFERENCE

1. Kuhn, R. E. and Eshleman, J., "Ground Effects on V/STOL and STOL Aircraft - A Survey," NASA TM 86825, Nov. 1985.

INVESTIGATION OF DYNAMIC GROUND EFFECT

Ray Chung Chang
Aeronautical Research Laboratory, Taichung, Taiwan

Vincent U. Muirhead
University of Kansas, Lawrence, Kansas

SUMMARY

An experimental investigation of dynamic ground effect has been conducted in the University of Kansas wind tunnel using delta wings of 60°, 70°, 75° sweep; the XB-70 wing; and the F-104A wing. Both static and dynamic tests were made. Test data have been compared to other test data, including dynamic flight test data of the XB-70 and F-104A. Limited flow visualization tests have been conducted. A significant dynamic effect was found for highly swept delta wings.

INTRODUCTION

Beginning with Fredrick W. Lanchester in 1907, the circulation theory of wing lift and the effect of wing vortices have been under study and development. The effect on the lift of a finite wing in close proximity to the ground was first studied by Weiselsberger (1922) and Tani (1937). Choliasmenos (1962) investigated the ground effect on the lift of a wing with and without boundary layer control. Abercrombie (1967) also investigated the ground effect on wings with high circulation. Both Abercrombie and Choliasmenos used rectangular wings of medium aspect ratio in their studies. Both studies concluded that the interference of the ground on wing lift was a function of the circulation of the wing when it was out of ground effect. For lift coefficients under about 2, the ground effect was favorable and above 2, unfavorable. Although Abercrombie's theory accounts for high angles of attack, it, also, is not applicable to low-aspect-ratio and highly swept wings with sharp leading edges. Fox's (1969) theory provided a good prediction of lift and drag of sharp edged planar wings near the ground in comparison with static wind tunnel data. The work of Kemp (1966), Katz (1984) and Rolls (1966) show that the current theoretical methods, static wind tunnel tests and fly-by flight tests are in reasonable agreement.

Although for high-swept low-aspect ratio wings, theoretical predictions, static wind tunnel data and fly-by flight test data are in reasonable agreement, these data do not agree with flight test landing data. Schweikhard (1967) and Baker (1970) obtained landing data with the aircraft making an approach at constant angle of attack and constant power setting. Five aircraft were tested: F5D-1, F5D-1 with a modified ogee wing, XB-70-1, XB-70-2 and F-104A. As the landing approaches were made, significant changes were found in lift, drag and pitching moment. The magnitude of these changes did not agree with theoretical and wind tunnel predictions, indicating a dynamic effect not included in the previous methods.

This paper reports on the development of a method to simulate the dynamic landing condition in the wind tunnel. It compares the dynamic wind tunnel data with

static wind tunnel data in ground effect and the flight test data of Baker (1970). Limited flow visualization tests were conducted to provide preliminary study of the phenomena involved in dynamic ground effect.

SYMBOLS

AR	wing model aspect ratio, b^2/S
b	wing model span, centimeters (inches)
$\bar{b}$	width of sting cross section, centimeters (inches)
$C_D = \frac{D}{qS}$	coefficient of drag in ground effect
C_{D_∞}	coefficient of drag out of ground effect
$\%C_D$	percent increase in drag coefficient, $\frac{C_D - C_{D_\infty}}{C_{D_\infty}} \times 100$
$C_L = \frac{L}{qS}$	coefficient of lift in ground effect
C_{L_O}	coefficient of lift at zero angle of attack
C_{L_∞}	coefficient of lift out of ground effect
$\%C_L$	percent increase in lift coefficient, $\frac{C_L - C_{L_\infty}}{C_{L_\infty}} \times 100$
C_M	coefficient of pitching moment about reference point in ground effect
$C_{M_\infty} = \frac{P}{qS\bar{c}}$	coefficient of pitching moment about reference point out of ground effect
C_O	wing model root chord, centimeters (inches)
$\bar{c}$	wing model mean geometric chord, centimeters, (inches)
D	drag, Newton's (lbs)
H	ground height, the height of the quarter chord point of the mean aerodynamic chord above the ground, centimeters (inches)
$\bar{h}$	height of sting cross section, centimeters (inches)

$\dot{h}$	sink rate, meters/sec (ft/sec)
L	lift, Newton's (lbs)
ℓ_i	distance of the sting locations, i = 1, 2, ..., 5; centimeters (inches)
P	pitching moment, meter Newton's (ft lbs)
q	dynamic pressure, Newton's/m^2 (lb/ft^2)
R_N	Reynolds number based on mean aerodynamic chord
S	wing area, $centimeters^2$ ($inches^2$)
y	horizontal distance from centerline of wing model, centimeters (inches)
α	angle of attack, degrees
Λ_{LE}	leading edge sweep angle, degrees

MODELS, APPARATUS AND PROCEDURE

Five model wings were tested: 60, 70 and 75 degree delta wings, Figure 1; F-104A wing, Figure 2; and XB-70 wing, Figure 3 (Chang, 1985). The models were mounted to a sting support, Figure 4, through a bracket which determined the angle of attack for the test. The sting support strut was mounted vertically in the wind tunnel in two linear bearings, Figure 5. The sting was free to move vertically between limiting stops. The sting and wing were statically counterbalanced by an external mass. By moving the mass downward, the wing moved upward in the tunnel toward a ground board. The wing was allowed to pass through a spring loaded door in the ground board at a steady sinking rate. The final travel of the sting was cushioned as the wing began to open the spring-loaded door.

Both static and dynamic tests were conducted on the five model wings. A test Reynold's number of 7×10^5 was maintained by adjusting wind tunnel speed. Static tests were conducted at angles of attack of 4, 8, 10, 15, 20, 24, 28, 30, 32, and 34 degrees at heights above the ground plane of 38.1, 15.2, 10.2, 7.6, 5.1, 3.8, 2.5 and 1.9 centimeters (15, 6, 4, 3, 2, 1.5, 1 and .75 inches). The 38.1 centimeter (15 inch) position was approximately out of ground effect.

Dynamic tests were made at angles of attack of 10, 15, 20, 24 and 28 degrees at three sink speeds: .609, 1.219, 1.828 m/sec (2, 4, and 6 ft/sec). The F-104A and XB-70 wings were also tested at 4 and 8 degrees in order to compare with available flight data.

During the dynamic tests the data from the sting (three strain gaged bridge circuits for lift, drag, and pitch, and a linear potentiometer for height) were recorded on a visicorder. An analog-digital acquisition system with a Hewlett Packard 9826 microcomputer was used to record all other data. The visicorder data were

digitized for making calculations of lift, drag, pitching moment and height. Flow visualization tests were made with neutrally buoyant helium bubbles and tufted wire grid, Figures 6 and 7.

RESULTS

The three delta wings (60, 70 and 75 degrees) had been previously tested by Wentz (1968). Figure 8 is a comparison of the lift coefficient data for the two tests of 70 degree delta wing. It will be noted that there is a marked difference in the angle of attack of stall. Figure 9 from Erickson (1982) shows that the vortex breakdown angle of attack of the Wentz tests was the largest of those reported. The current test value falls almost in the middle of the data. This illustrates the influence of small changes initial conditions: (1) the apex of the model as used in the current tests was slightly blunted and (2) the mounting was different. The test model as used by Wentz (1968) was mounted in the tunnel using a single pivot support just forward of the trailing edge and a pitch rod near the apex of the model. The supports were underneath the model wing and retarded the center portion of the flow from underneath the wing. This appears to have had some stabilizing effect on the small vortex system. The slightly blunted apex and the presence of the sting mount appears to have provided less of a stabilizing influence.

Figures 10, 11 and 12 present the percentage change in lift, drag and pitching moment with height above the ground board for the 70 degree delta wing at an angle of attack of 22.1 degrees. As the minimum ground height was approached, the static tests yielded almost 100% increase in lift, 55% increase in drag and 100% increase in pitching moment (negative) over the dynamic test values.

Lift data for the F-104A are given in Figures 13 and 14. In Figure 13 the static wind tunnel data, dynamic wind tunnel data and flight test data show the same trend with change in angle of attack at a given height. The data are nearly of the same magnitude. The increase in lift in ground effect over lift out of ground effect decreases rapidly with increasing angle of attack. A comparison of the F-104A data at a constant angle of attack and changing ground height shows close agreement between the three sets of test data and Lan's (1985) Quasi-Vortex-Lattice Method.

Lift data for the XB-70 are presented in Figures 15, 16 and 17. The dynamic wind tunnel data, Figure 15, shows close agreement with the flight test data at an angle of attack of 9.3 degrees. Below a height of one half wing span above the ground the static wind tunnel data shows a rapid increase in lift over the dynamic data. At an H/b of .2 and .4 and flight test data and the dynamic wind tunnel data show much better agreement than either do with the static wind tunnel test data.

Figure 18 summarizes the ground effect data for the five wings tested at an angle of attack of 12.1 degrees and on H/b of .3 and .4. It can readily be seen that the dynamic effects play an increasing role on lift as sweepback is increased and aspect ratio is decreased. The F-104A data displays only a small variation due to the dynamic conditions. The XB-70 wing, 70 degree delta and the 75 degree delta wings show a large difference between the static and dynamic data.

A tufted wire grid, Figures 7 and 17, behind the 70 degree delta wing was observed during static and dynamic tests by use of a video camera. The locations of the vortex core centers during the tests were determined and plotted as shown in Figures 20 and 21. The dynamic tests were made at a fixed wing angle of attack of 20 degrees. Two sink rates were used to provide induced delta angles of attack of 2 and 4 degrees. The resulting angles of attack of 22 and 24 degrees were then compared with the corresponding static tests. Both comparisons show that the vortices have moved inboard during the dynamic testing relative to the static test positions. The change in vertical position could not be accurately determined.

DISCUSSION

As shown by the results, vortex behavior affects the lift, drag and pitching moment of the wing. The limited tufted wire grid tests demonstrated that vortex lag occurred during the dynamic tests. During these limited visual tests, vortex breakdown did not occur in the proximity of the wing.

Vortex behavior in free air is influenced by a number of items. Wentz (1968) demonstrated the effect of roughness on breakdown and in Schlieren photographs, Figure 22, showed the characteristics of the vortices at breakdown. A free air vortex was sustained by a strong axial core pressure differential by Muirhead (1971, 1977). Also demonstrated were the unsteady nature of the free vortex and it's susceptibility to small external pressure differentials perpendicular to the vortex axis. Erickson (1982), Figure 23, illustrated the effect of flaps on vortex behavior. The current reported tests demonstrated that (1) there is a lag in the movement of the wing vortices as the wing moves in ground effect, (2) the forces on the wing during the landing are not those of a wing operating at that angle of attack in steady flight at that height and (3) a change in wind tunnel mounting methods influence vortex behavior. Thus, any change in nearby geometry will cause a change in the behavior of wing vortices. Highly swept low aspect ratio wings appear to be most susceptible to these factors.

A computational simulation model for landing conditions must account for the following (assuming that vortex breakdown may also occur in the vicinity of the trailing edge under unsteady high angle of attack conditions):

1) axial core pressure gradient and pressure,
2) circulation,
3) axial external pressure gradient and pressure,
4) pressure gradients transverse to the axis of the vortex.

Further experimental investigations are needed to determine the strength and position of the vortices under various conditions.

A comparison of the limited flight test data on the XB-70, static wind tunnel data and dynamic wind tunnel data indicates that the method of dynamic testing developed provides more realistic data in the landing phase than the static wind tunnel data in ground effect. However, the effect of flaps, fuselage and canard were not accounted for in these tests.

CONCLUSIONS

The dynamic wind tunnel simulation which was developed provided a method to simulate the landing condition more realistically than by either static wind tunnel testing in ground effect or constant altitude fly-by testing. The wind-tunnel wing mounting had a distinct effect on the development of vortex breakdown at high angles of attack for the highly swept delta wings.

A significant dynamic effect was found for highly swept delta wings. The wing vortices exhibited a lag during the dynamic tests.

REFERENCES

1. Abercrombie, J. M.; "The Lift of High Circulation Wings in Ground Effect", Saint Louis, Missouri University, Thesis, 1967.

2. Baker, P.; Schweikhard, W.; Young, W.; "Flight Evaluation of Ground Effect on Several Low-Aspect-Ratio Airplanes", NASA TN-D-6053, October 1970.

3. Chang, Ray Chung, "An Experimental Investigation of Dynamic Ground Effect", University of Kansas, Dissertation 1985.

4. Choliasmenos, C. J.; "An Experimental Investigation and Theoretical Analysis of the Ground Effect on the Lift of a Wing With and Without Boundary Layer Control", University of Kansas Thesis, 1962.

5. Erickson, Gary E.; "Vortex Flow Correlation", ICAS Paper No. 82-6.6.1; 22-27 August, 1982, Seattle, Washington.

6. Fox, C. H.; "An Analytical Method for Predicting the Lift and Drag for Slender Sharp-Edge Delta Wings in Ground Proximity", M. S. Thesis, Virginia Polytechnic Institute, 1969.

7. Fox, C. H.; "Prediction of Lift and Drag for Slender Sharp-Edge Delta Wings in Ground Proximity", NASA TN-D-4891, 1969.

8. Katz, J; Levin, D.; "Measurements of Ground Effect for Delta Wings", Journal of Aircraft, Vol. 21, No. 6, June 1984.

9. Kemp, W. B.; Lockwood, V. E.; Phillips, W. P.; "Ground Effects Related to Landing of Airplanes With Low-Aspect-Ratio Wings", NASA TN D-3583, October 1966.

10. Lan, C. E.; "VORSTAB - A Computer Program for Calculating Lateral-Directional Stability Derivatives With Vortex Flow Effect", NASA CR-172501, January 1985.

11. Muirhead, V. U.; Eagleman, J. R.; "Laboratory Compressible Flow Tornado Model", Preprints Seventh Conference on Severe Local Storms, AMS, Kansas City, Missouri 1971.

12. Muirhead, V. U.; "Investigation of Compressible Vortex Flow Characteristics", NASA CR-145261, 1977.

13. Rolls, L. S.; Koenig, D. G.; "Flight Measured Ground Effect on a Low-Aspect-Ratio Ogee Wing Including a Comparison With Wind-Tunnel Results", NASA TN D-3431, 1966.

14. Schweikhard, W.; "A Method for In-Flight Measurement of Ground Effect on Fixed-Wing Aircraft", Journal of Aircraft, Vol. 4, No. 2, March-April, pp. 101-104.

15. Tani, I.; Taima, M.; Simidu, S.; "The Effects of Ground on the Aerodynamic Characteristics of a Monoplane Wing", Tokyo Imperical University, Aero Research Inst. Rept. 156, September 1937.

16. Weiselsberger, C.; "Wing Resistance Near the Ground", NACA TM77, April 1922.

17. Wentz, W. H.; "Wind-Tunnel Investigations of Vortex Breakdown on Slender Sharp-Edge Wing", Ph. D. Dissertation, University of Kansas, 1968.

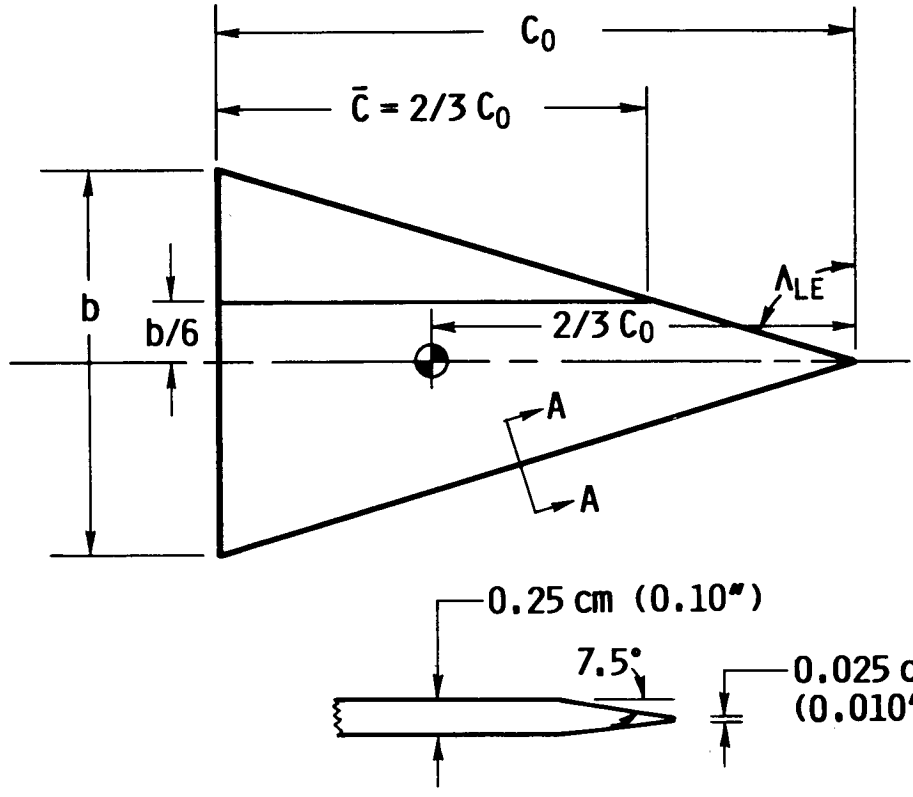

Wing Model	60° Delta	70° Delta	75° Delta
Root Chord, C_0 cm (in)	22.00 (8.66)	34.90 (13.74)	45.72 (18.00)
Span, b cm (in)	25.40 (10.00)	25.40 (10.00)	24.49 (9.64)

Figure 1. Model Geometry, Delta Wings

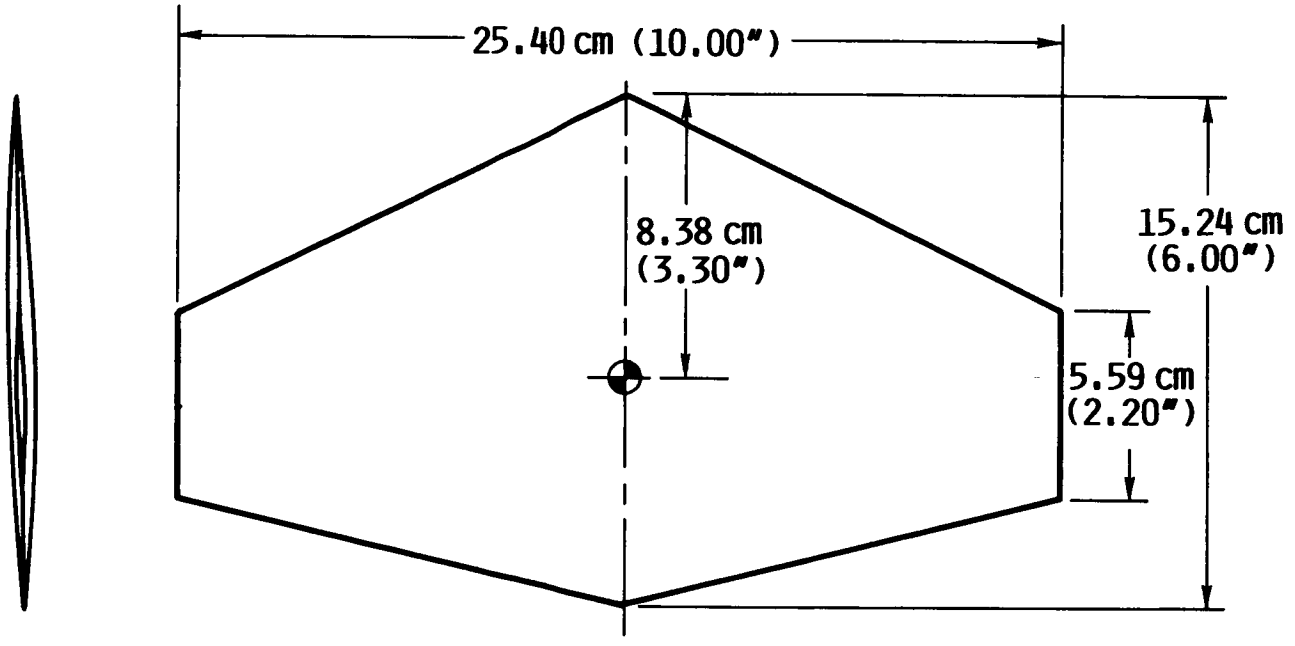

Figure 2. Model Geometry, F-104A Wing

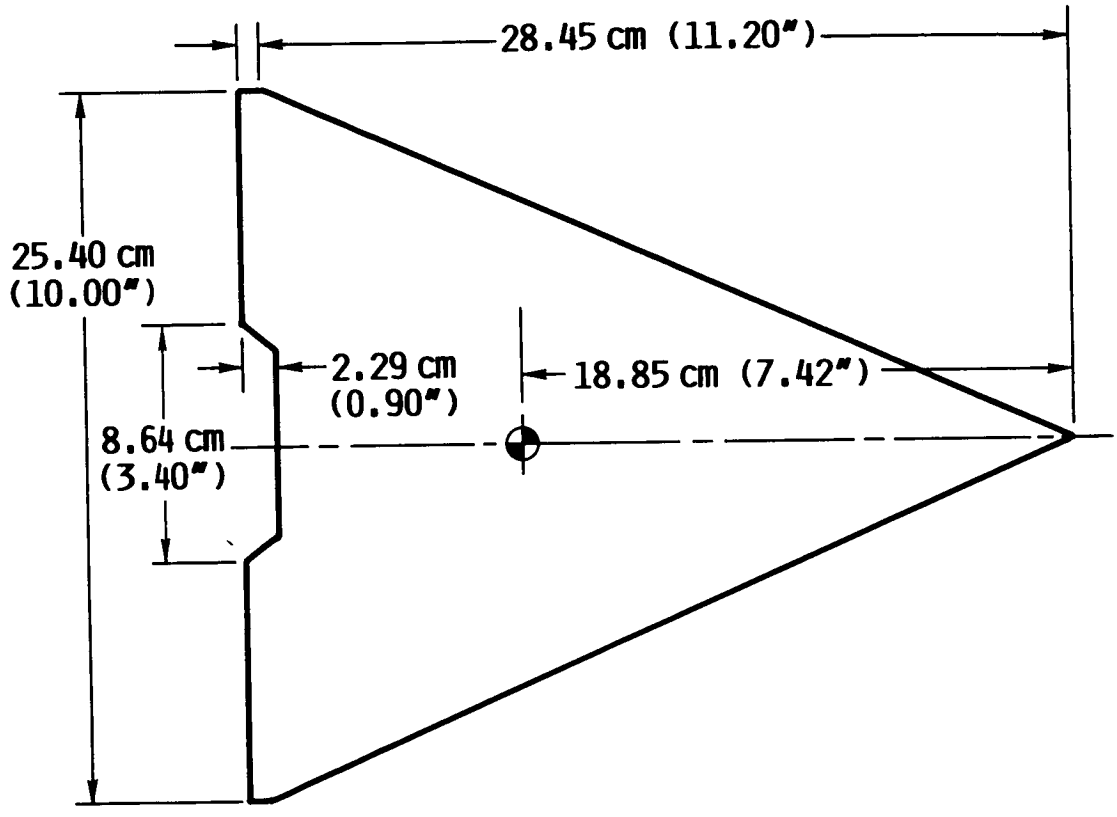

Figure 3. Model Geometry, XB-70 Wing

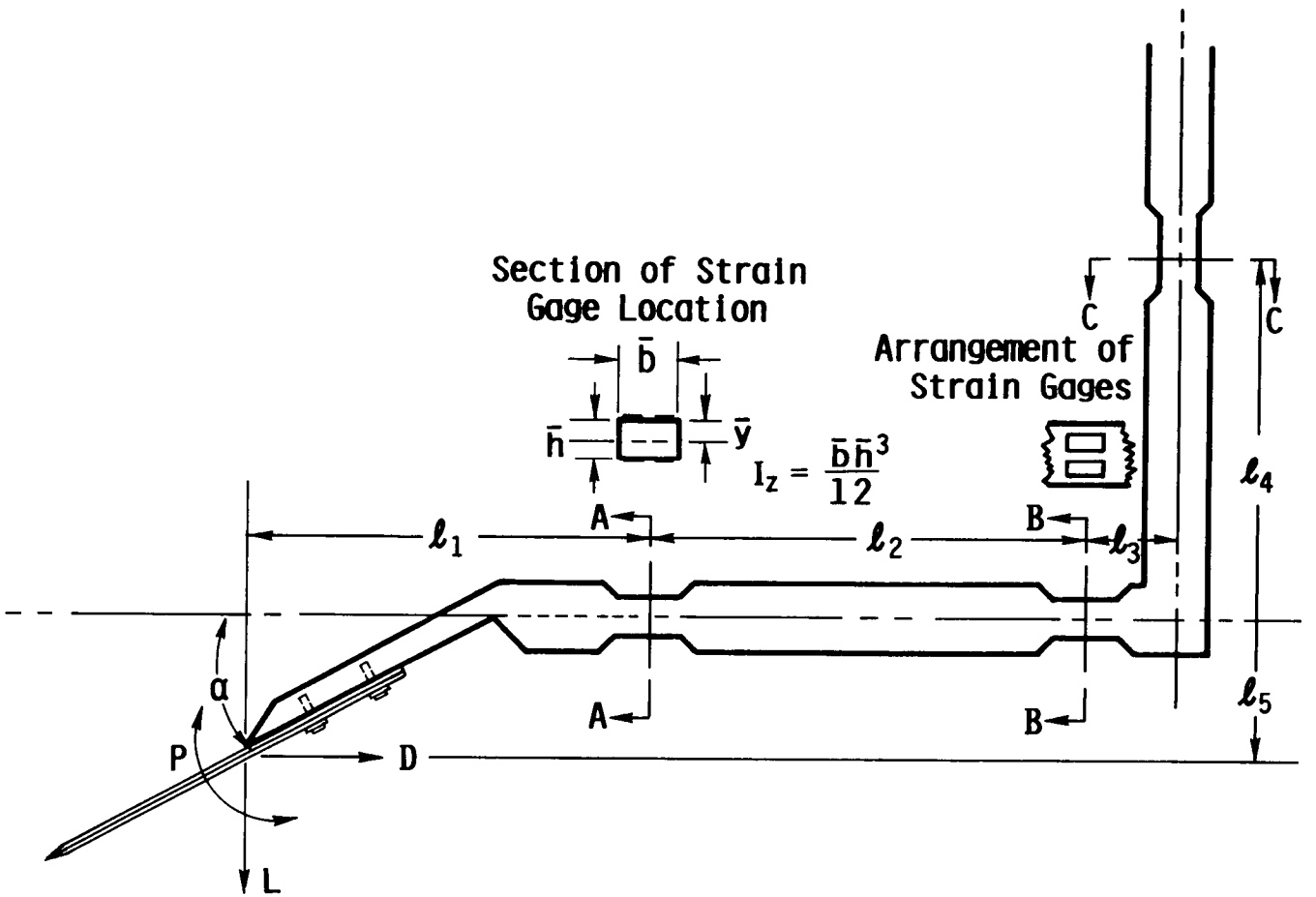

Figure 4. Sting Support and Strain Gage Arrangement

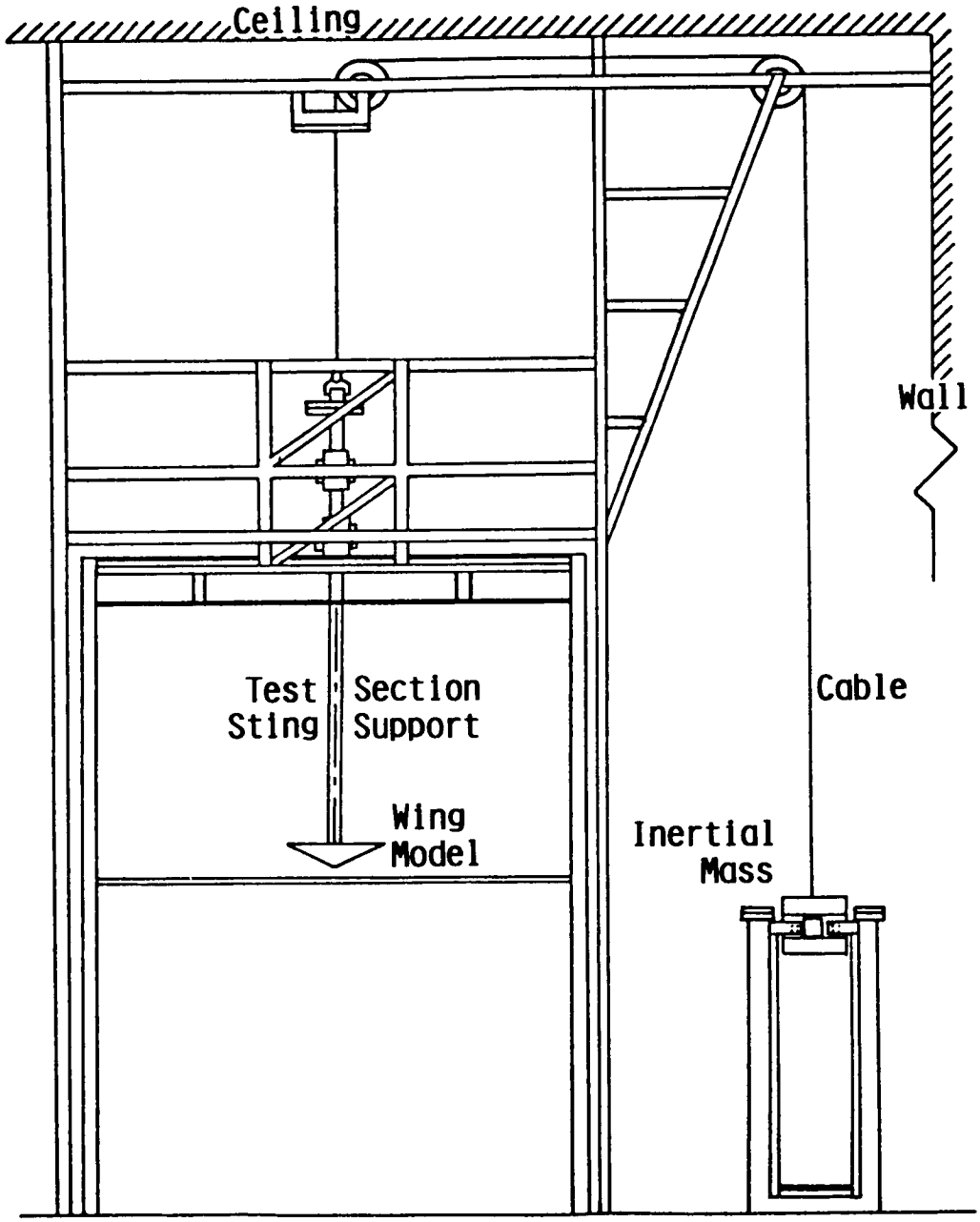

Figure 5. Airstream View of Test Stand

Figure 6. Flow Visulization Using Helium Bubbles

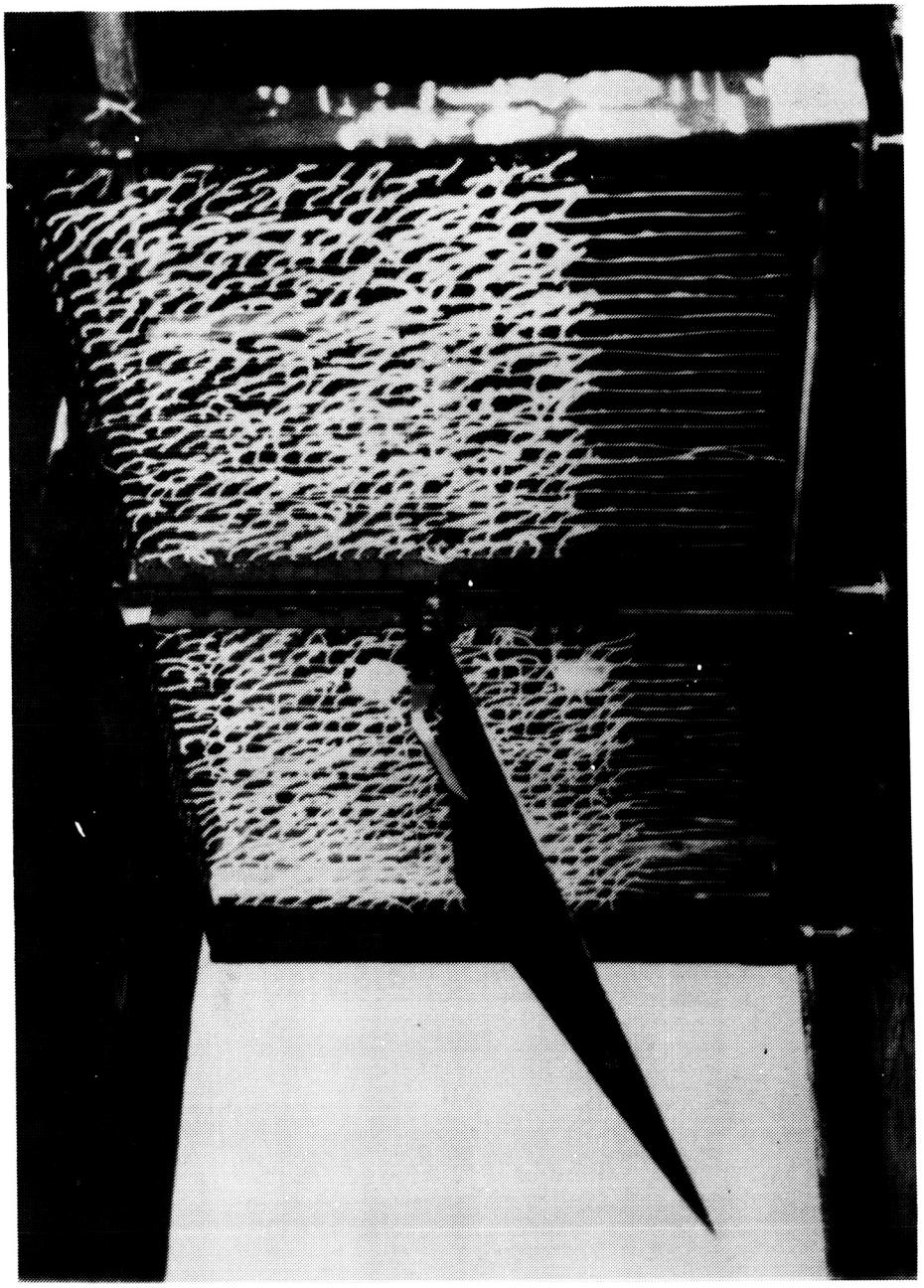

Figure 7. A Photograph of Tufted Wire Grid

C-5

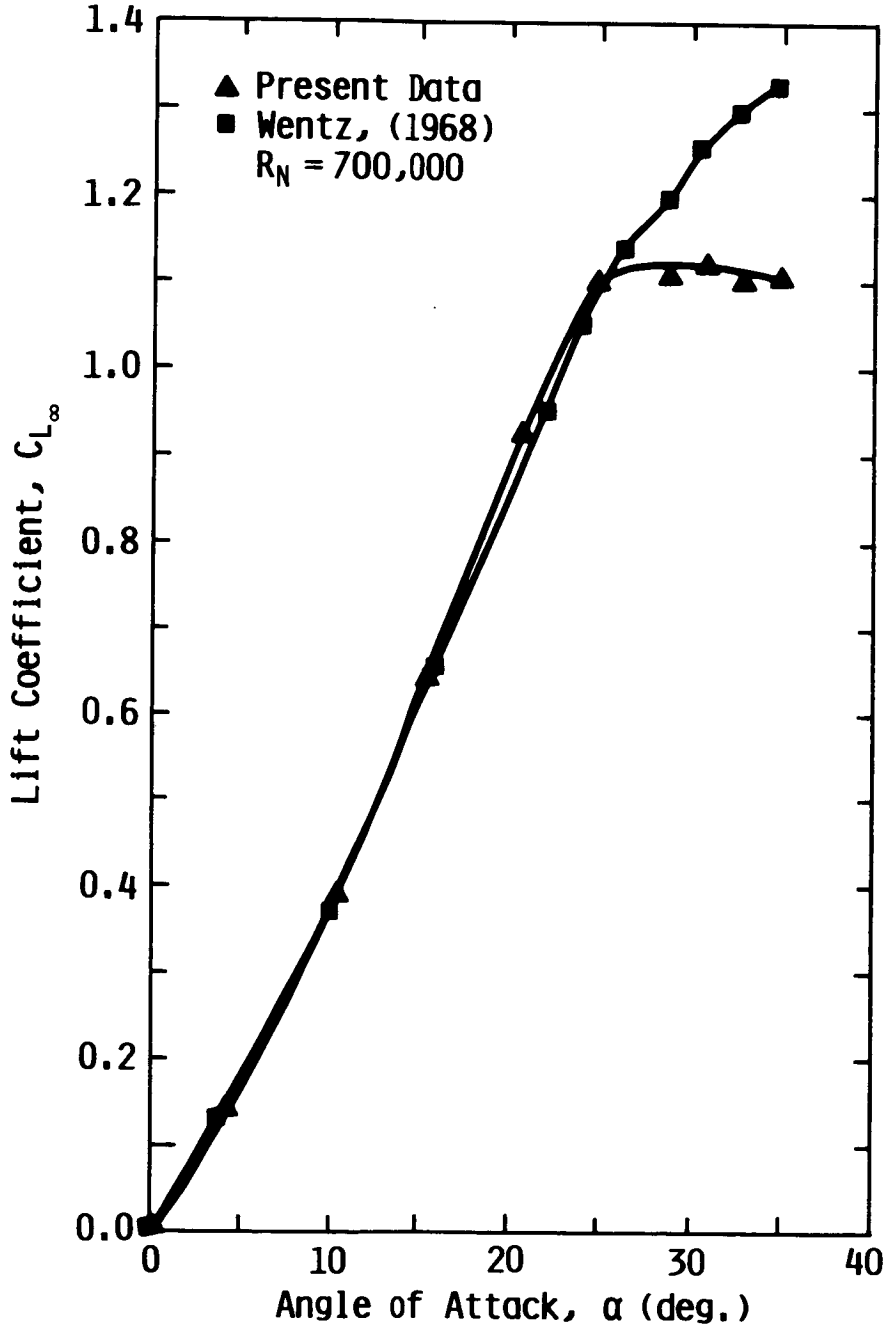

Figure 8. Comparison of Present Out-of-Ground-Effect Lift Coefficient Data for 70 Degree Delta Wing with Wentz's Data (1968)

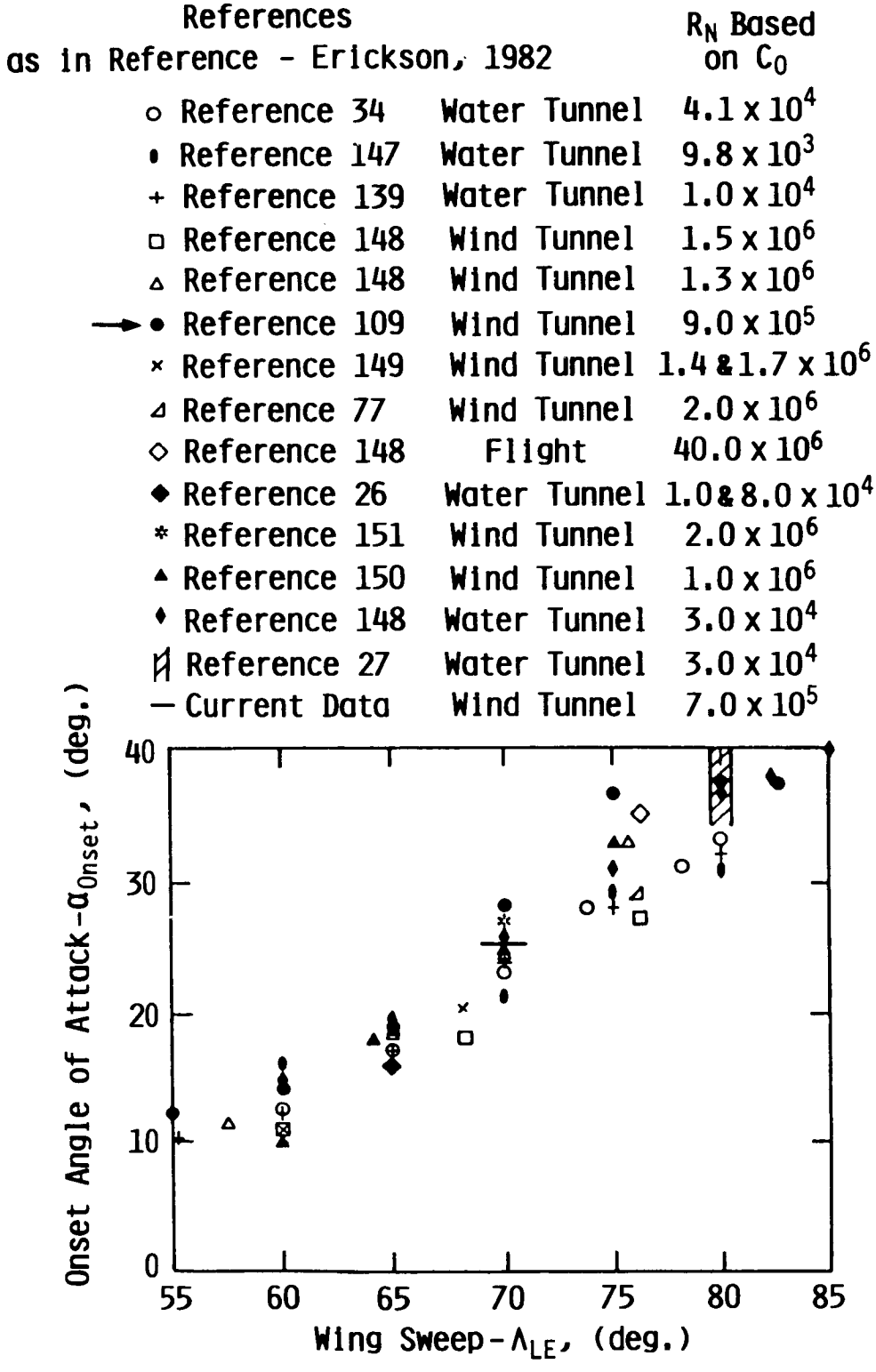

Figure 9. Effects of Wing Sweep and Reynolds Number on Delta Wing Vortex Breakdown at the Trailing Edge (Erickson, 1982) & (Wentz, 1968) (→ Wentz, 1968)

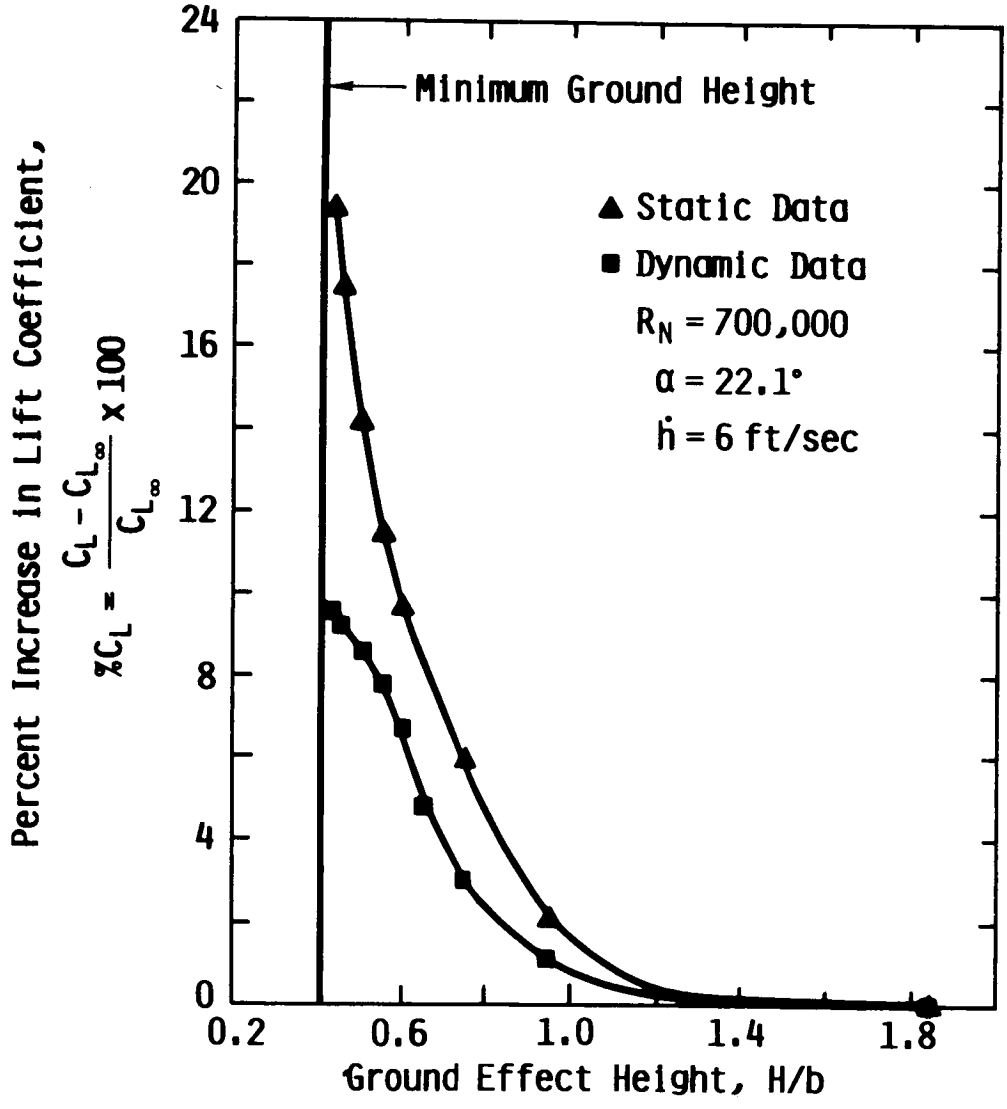

Figure 10. Comparison of Lift Increments for Static and Dynamic KU Wind Tunnel Ground Effect Data for 70 Degree Delta Wing at 22.1 Degree Angle of Attack

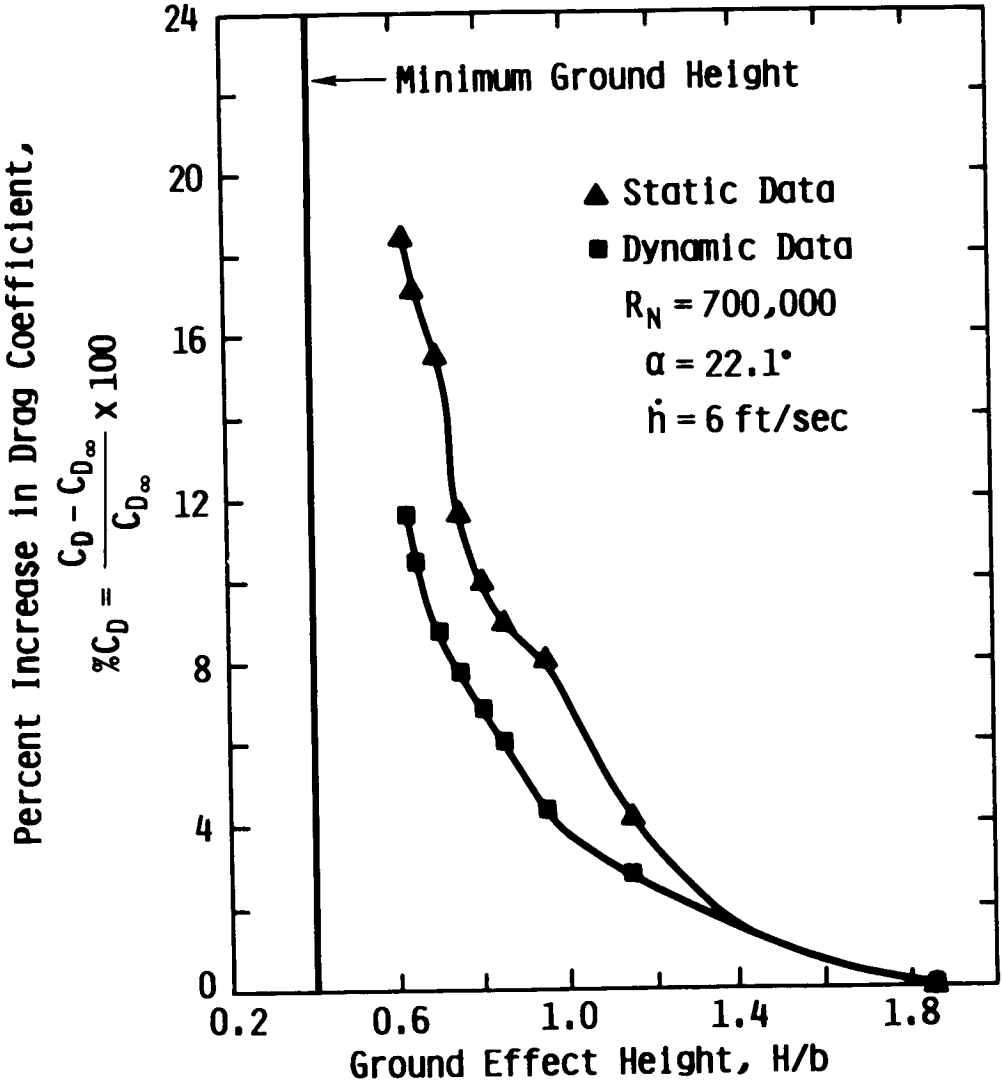

Figure 11. Comparison of Drag Increments for Static and Dynamic KU Wind Tunnel Ground Effect Data for 70 Degree Delta Wing at 22.1 Degree Angle of Attack

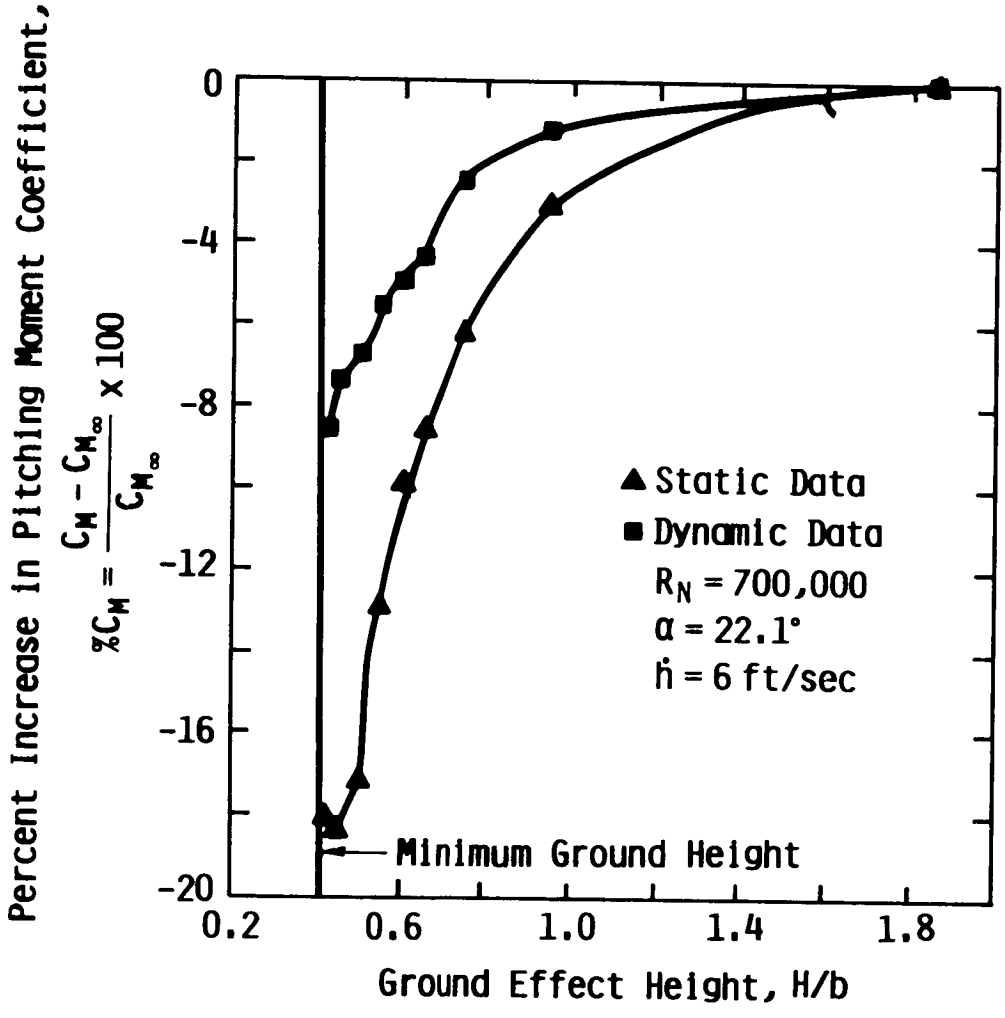

Figure 12. Comparison of Pitching Moment Increments for Static and Dynamic KU Wind Tunnel Ground Effect Data for 70 Degree Delta Wing at 22.1 Degree Angle of Attack

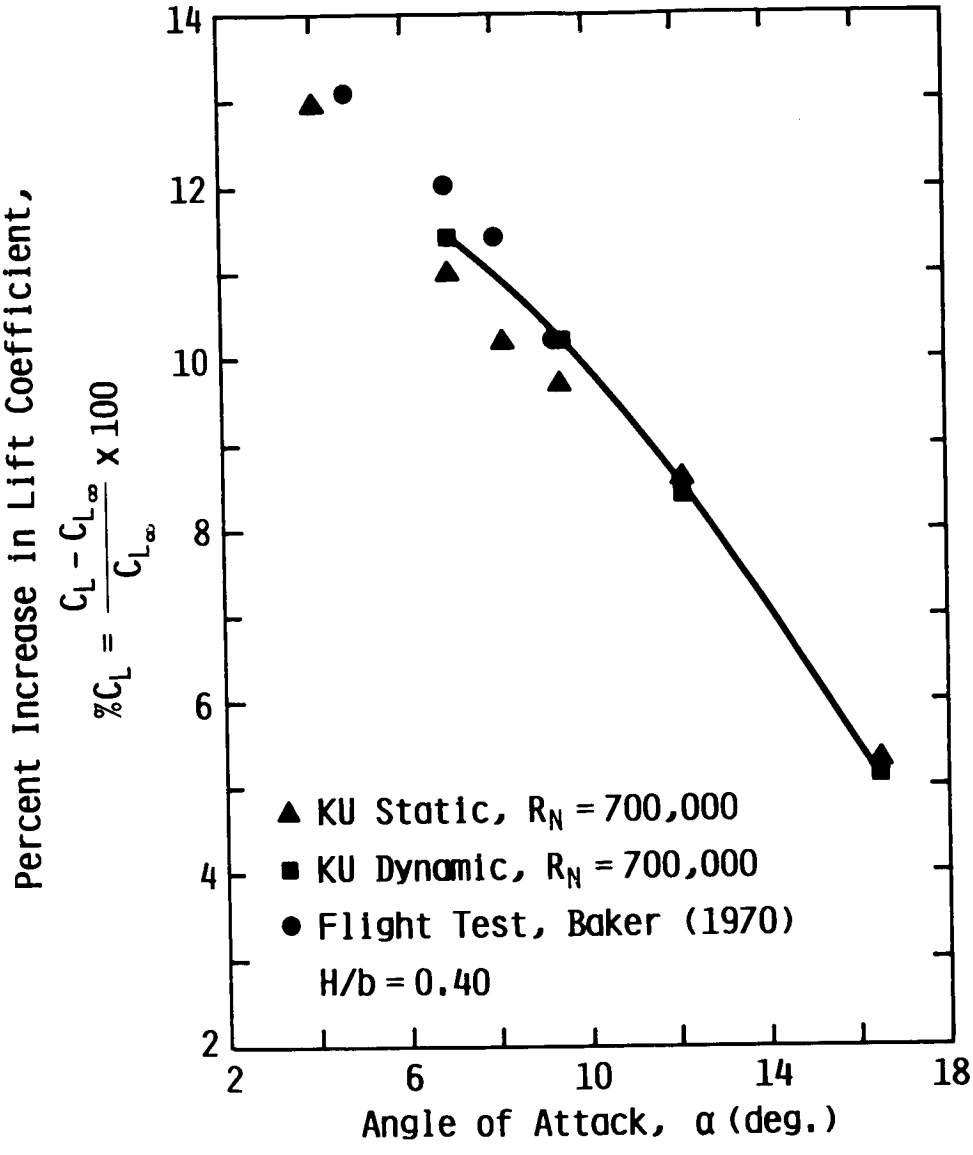

Figure 13. Comparison of Lift Increments for Static and Dynamic Wind Tunnel (Wing Model) Data with Flight Test Data for F-104A, H/b - 0.40

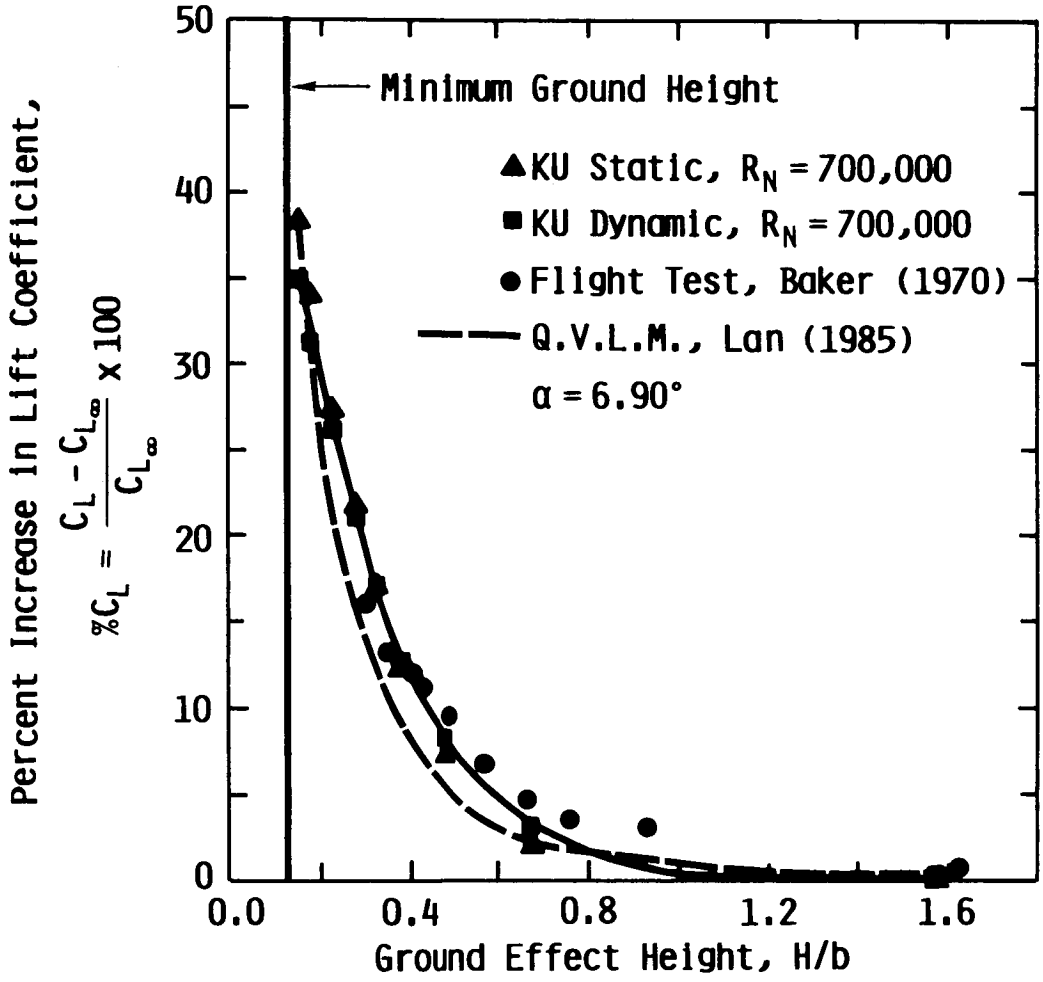

Figure 14. Comparison of Lift Increments for Static and Dynamic Wind Tunnel Data (Wing Model) with Flight Test (Airplane) and Q.V.L.M. (Wing Model) Data for F-104A, at 6.9 Degree Angle of Attack

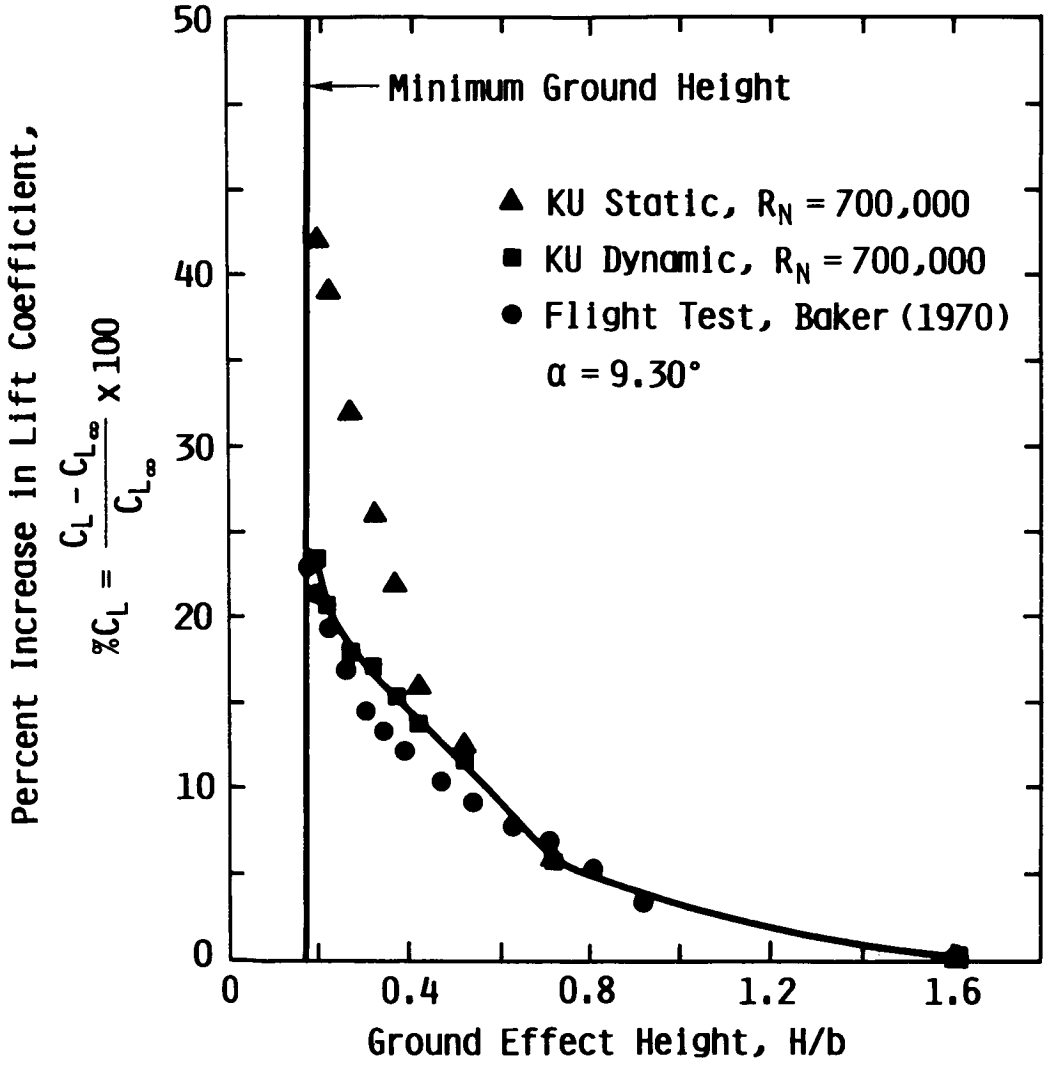

Figure 15. Comparison of Lift Increments for Static and Dynamic Wind Tunnel (Wing Model) Data with Flight Test Data for XB-70 at 9.3 Degree Angle of Attack

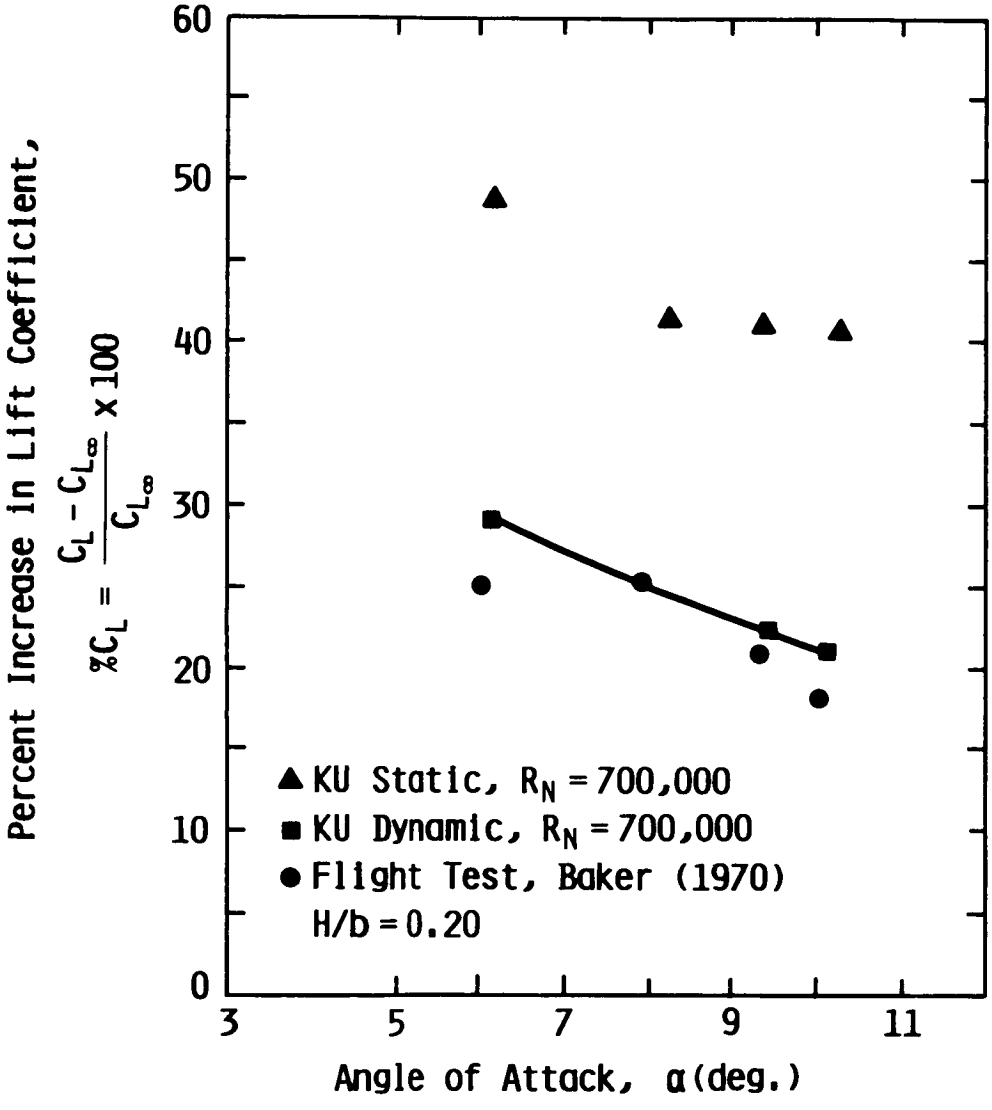

Figure 16. Comparison of Lift Increments for Static and Dynamic Wind Tunnel (Wing Model) Data with Flight Test Data for XB-70, H/b = 0.20

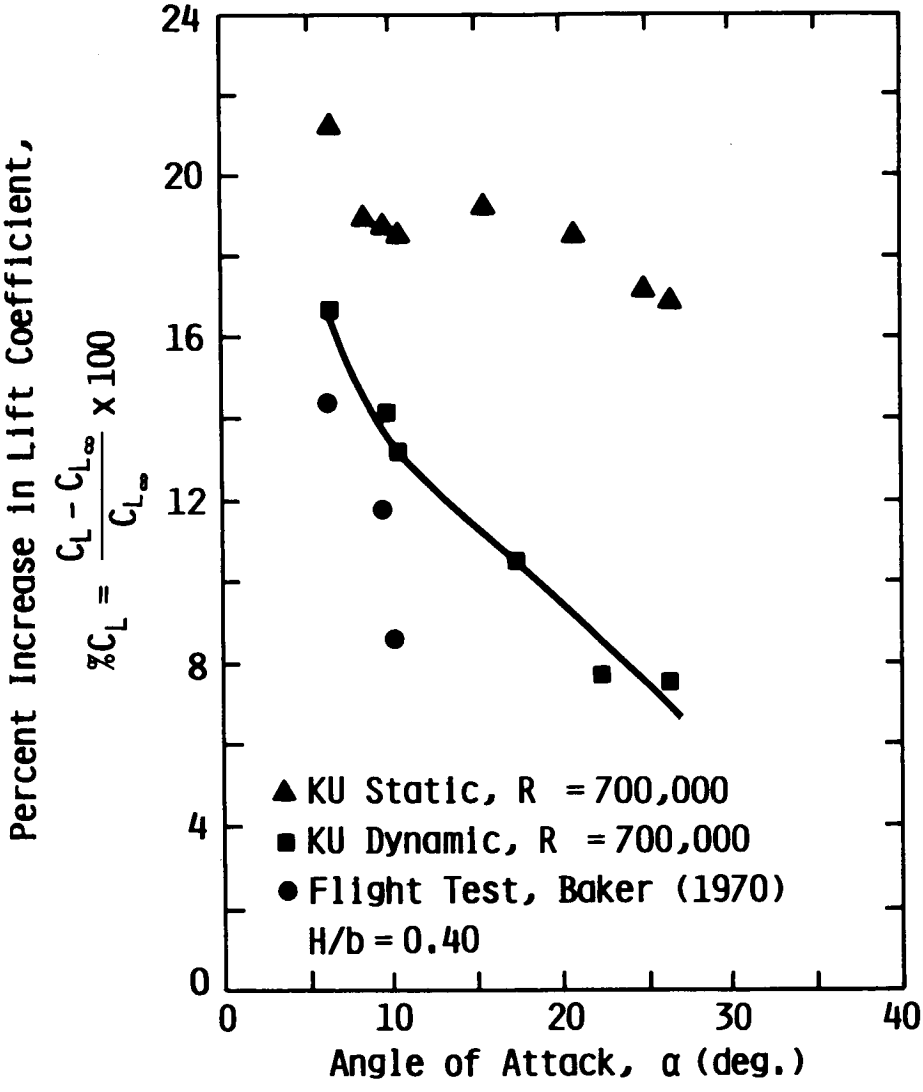

Figure 17. Comparison of Lift Increments for Static and Dynamic Wind Tunnel (Wing Model) Data with Flight Test Data for XB-70, H/b = 0.40

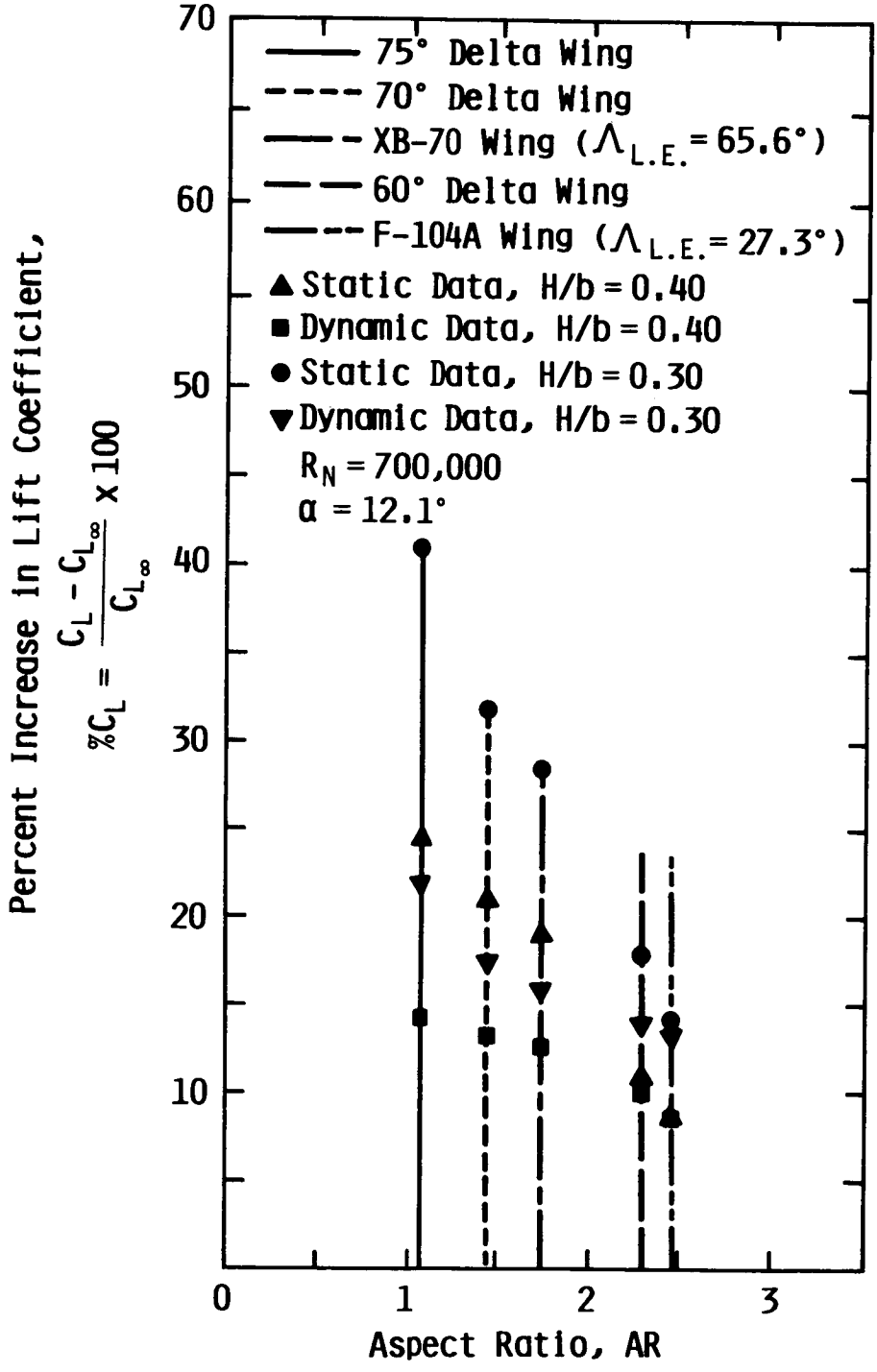

Figure 18. Variation of Incremental Lift Coefficient with Aspect Ratio for Static and Dynamic KU Ground Effect Data at 12.1 Degree Angle of Attack

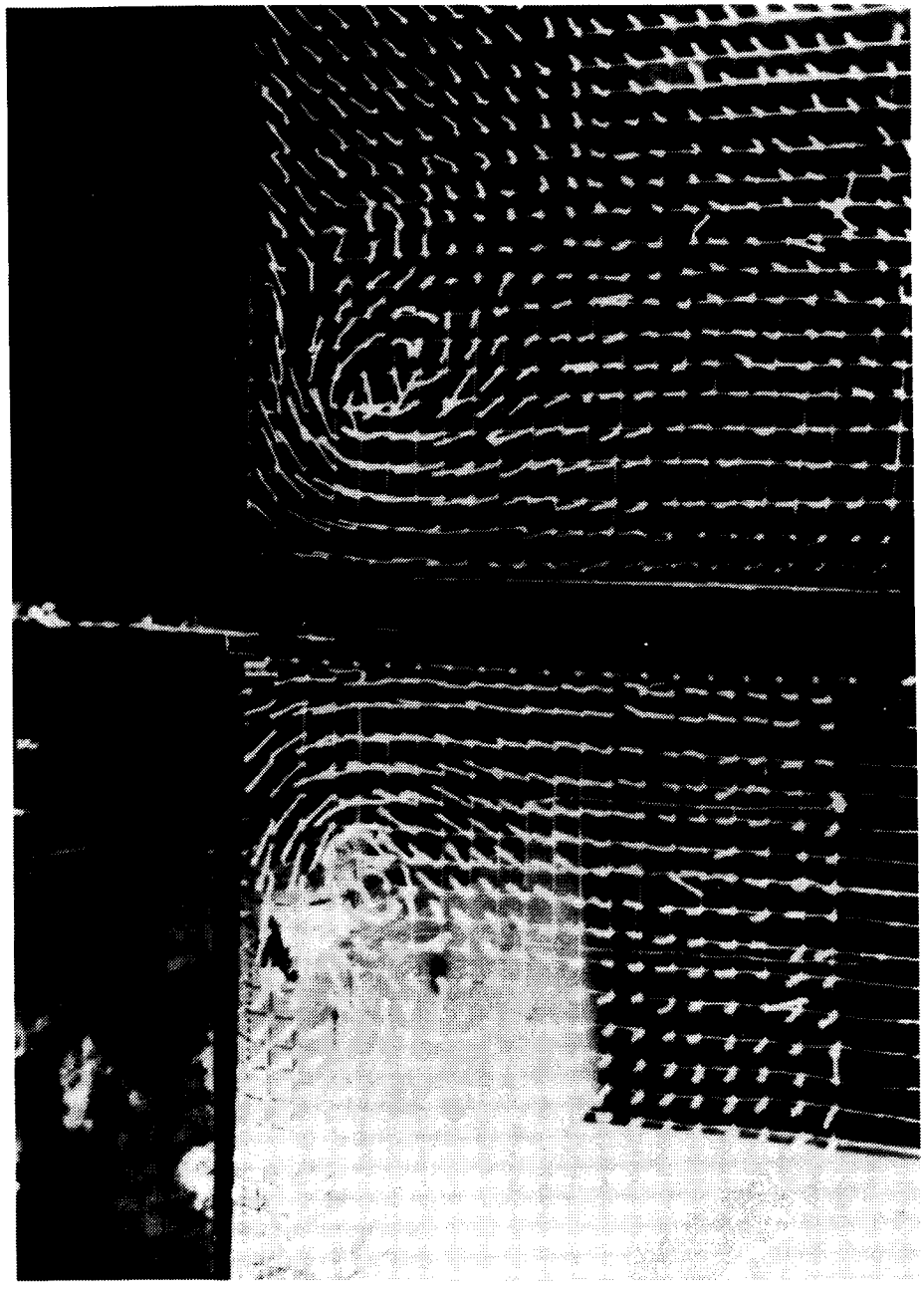

Figure 19. A Photograph of Tufted Vortex Visualization

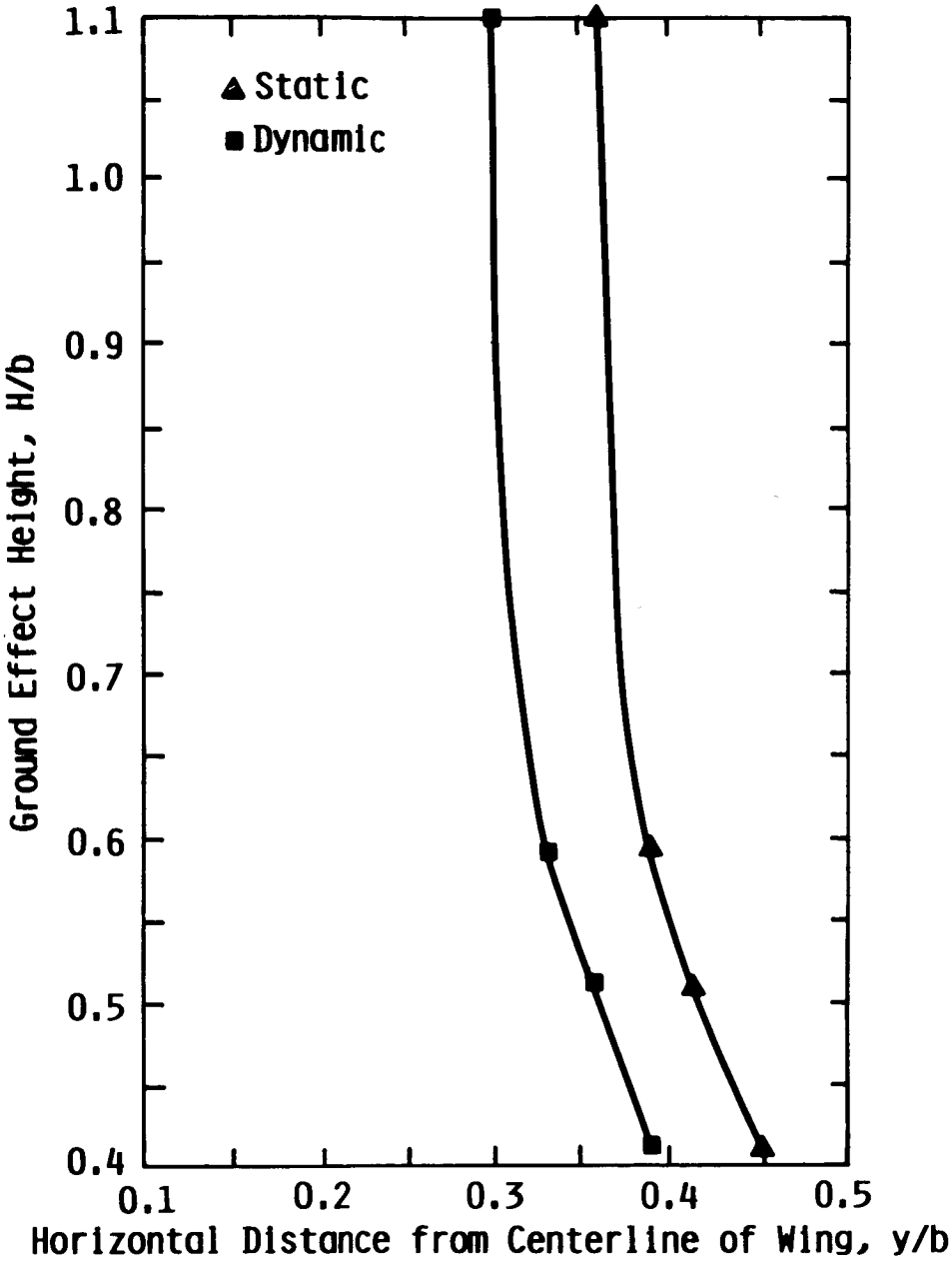

Figure 20. Comparison of Location of the Vortex Core Center for Static and Dynamic Ground Effect, for 70 Degree Delta Wing at 22 Degree Angle of Attack

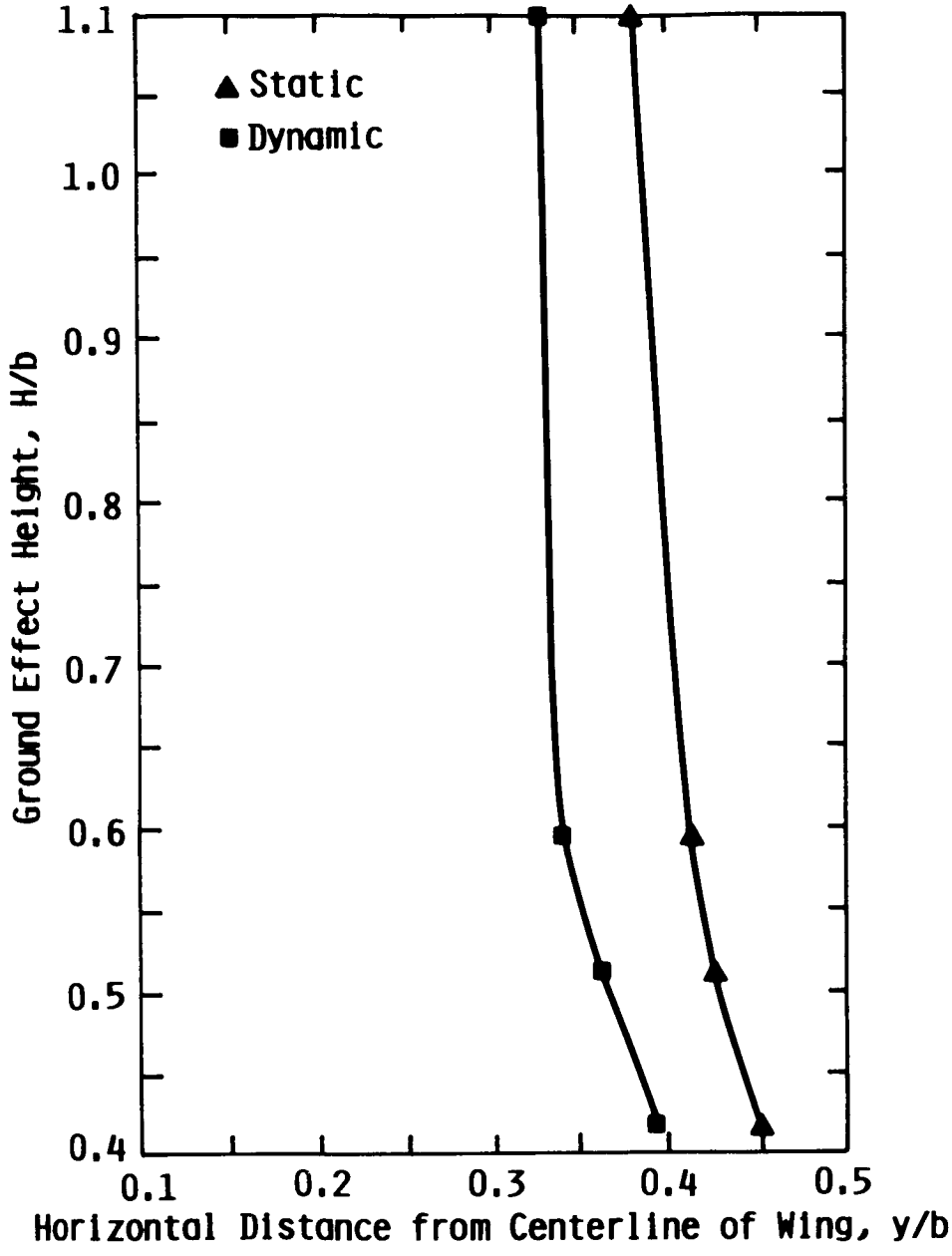

Figure 21. Comparison of Location of the Vortex Core Center for Static and Dynamic Ground Effect, for 70 Degree Delta Wing at 24 Degree Angle of Attack

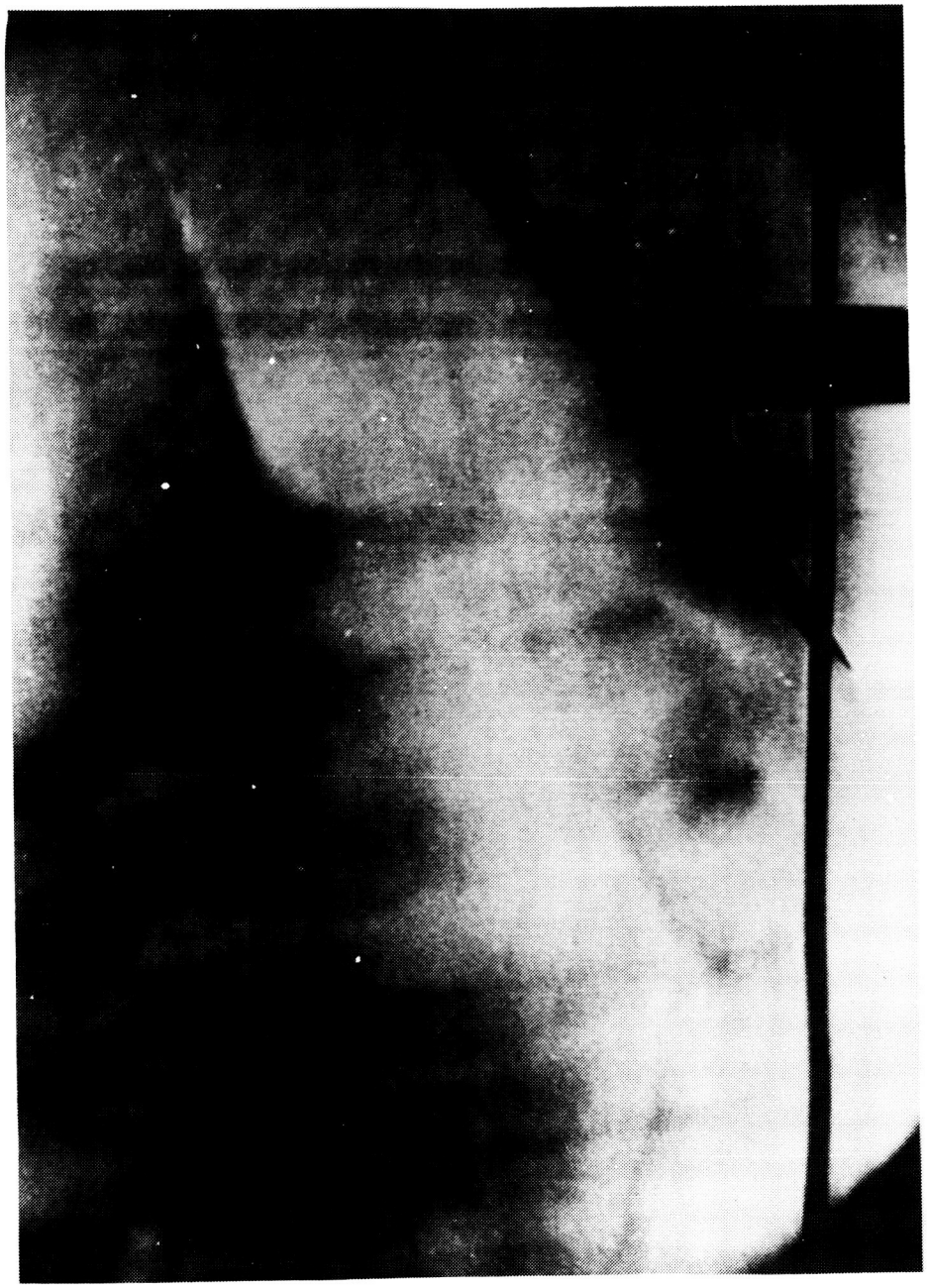

$\alpha = 27.5°$ No Breakdown

Figure 22a. Effect of Roughness on Breakdown Characteristics (72.5° Delta Wing) (Wentz, 1968)

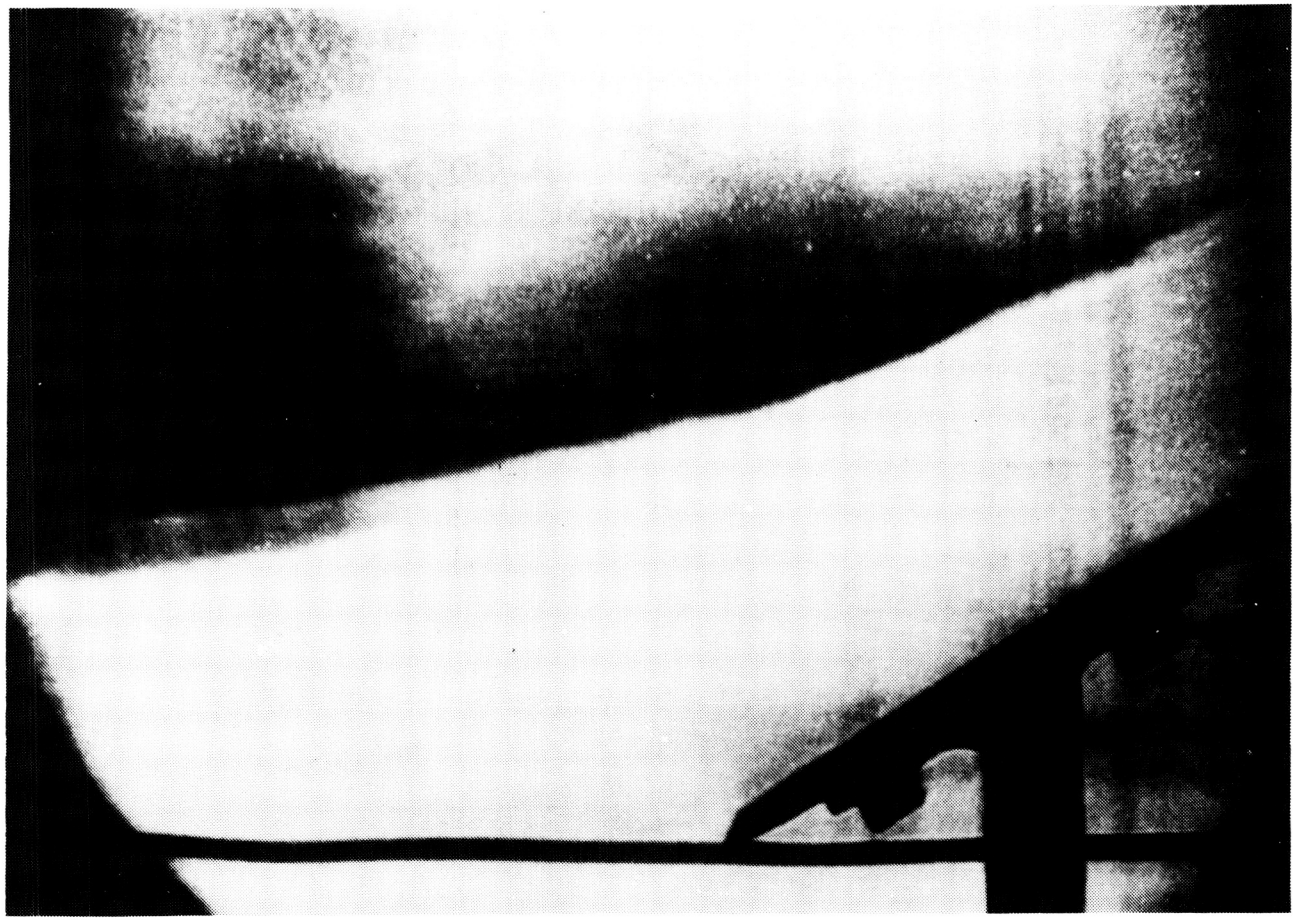

$\alpha = 32.5°$ Breakdown

Figure 22b. Effect of Roughness on Breakdown Characteristics (72.5° Delta Wing) (Wentz, 1968)

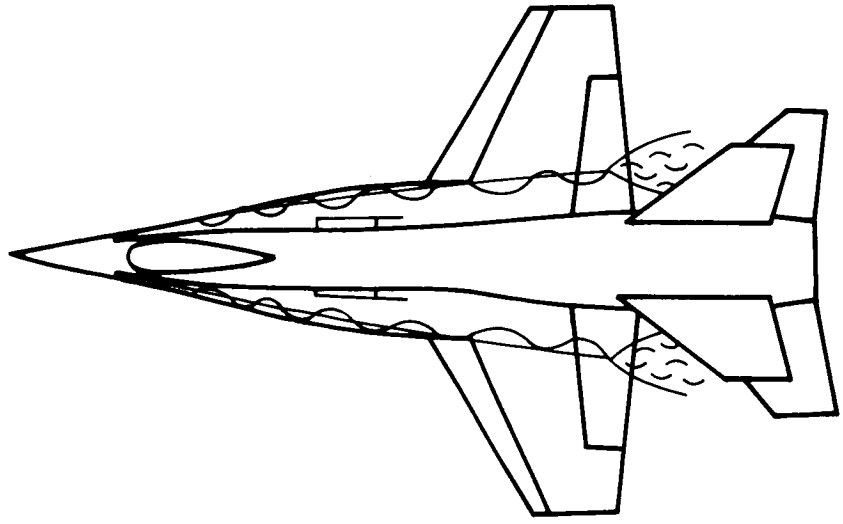

(a) Sketch of Northrop P-530 Wind Tunnel Model

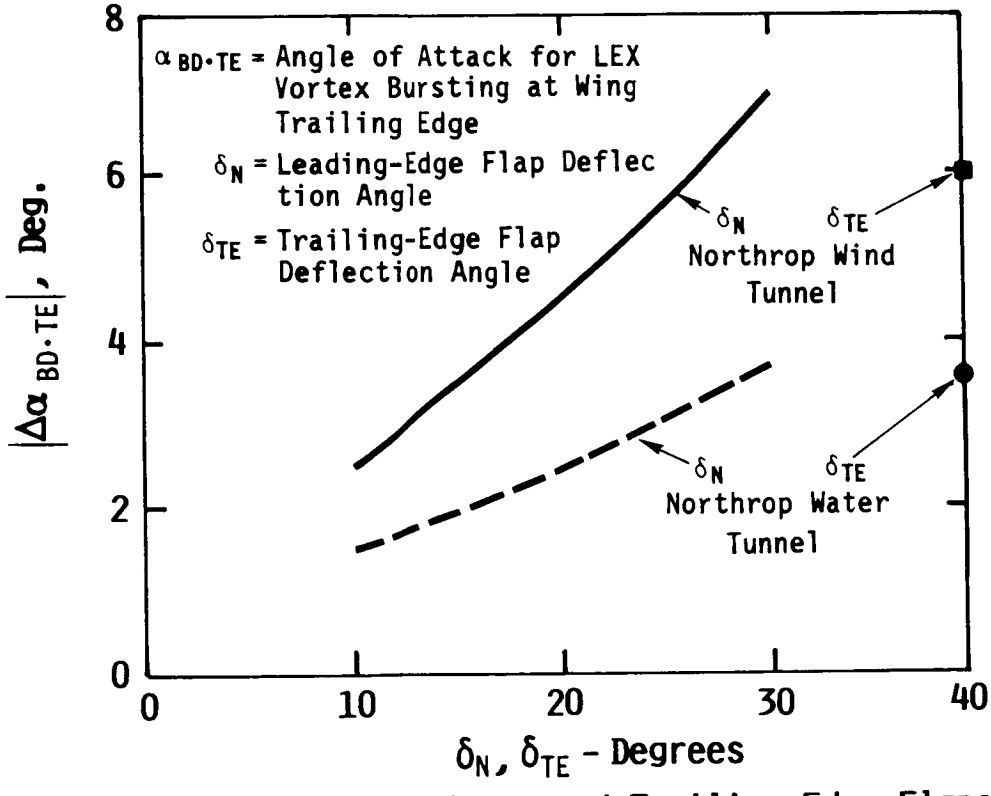

(b) Effects of Leading- and Trailing-Edge Flaps on Lex Vortex Stability

Figure 23. Deflected-Flap Effects on Vortex Behavior (Erickson, 1982)

THE GROUND EFFECTS OF A POWERED-LIFT STOL AIRCRAFT DURING LANDING APPROACH

Victor C. Stevens

Ames Research Center

SUMMARY

This paper presents the effects of ground proximity on a powered-lift STOL aircraft. The data presented in this paper are from NASA's Quiet Short Haul Research Aircraft (QSRA) flown at landing approach airspeeds of less than 60 knots with an 80 lb/ft^2 wing loading (C_L > 7). These results show that the ground effect change in lift is positive and does significantly reduce the touchdown sink rate. These results are compared to those of the YC-14 and YC-15. The change in drag and pitching moment caused by ground effects is also presented.

NOMENCLATURE

AGL	above ground level, ft
A_x	body-axis acceleration, fwd and aft (+ fwd), g's
A_z	body-axis acceleration vertical (+ up), g's
b	aircraft wing span, ft (b = 73 ft for QSRA)
C_D	measured-drag coefficient
C_{D_∞}	free-air drag coefficient (out of ground effect)
C_L	measured lift coefficient
C_{L_∞}	free-air lift coefficient (out of ground effect)
C_T	thrust coefficient
g	acceleration caused by gravity, 32.2 ft/sec^2
GE	ground effect
h	height above the ground, ft
h/b	wing height above the ground in terms of wing span

q	dynamic pressure, lb/ft^2
S	aircraft wing area, ft^2 ($S = 600\ ft^2$ QSRA)
TEU	trailing edge up
V	aircraft velocity, ft/sec
α	angle of attack, deg
δ_e	elevator position, deg
ΔV_I	induced velocity caused by image bound vortex, ft/sec
θ	pitch attitude, deg
$\dot{\theta}$	pitch rate, deg/sec
$\ddot{\theta}$	pitch acceleration, deg/sec^2

INTRODUCTION

Ground effects have a strong influence on an aircraft's landing performance. For STOL aircraft designed to use as little runway as possible, this influence of ground effects is even more significant. In the past, there has been a lack of agreement between ground effect data obtained from wind tunnel tests and that of aircraft flight testing, especially at high lift coefficients (refs. 1 and 2). This has created a need for more flight test data to accurately define the actual ground effects of powered-lift STOL aircraft for future designs and flight simulation math models. Other reports have previously presented the ground effects of the YC-15 powered lift STOL aircraft, which landed at lift coefficients slightly over 3 (refs. 3 and 4). This paper presents a technique to derive the ground effects from powered-lift aircraft flight data and then gives the results of using this technique for NASA's Quiet Short Haul Research Aircraft (QSRA) (fig. 1) landing at lift coefficients greater than 7. Comparisons are made between the YC-14, the YC-15, and the QSRA flight data.

TECHNIQUE

Ground effect data are analyzed in terms of aircraft wing height above the ground (h) divided by the wingspan (b). This normalized aircraft height, referred to as "h/b," allows comparison of ground effects among various aircraft configurations. At h/b = 1, for the QSRA the wing height above the ground is 73 ft. At

touchdown, the QSRA's wing height is 13.9 ft or h/b = 0.19. The normal assumption is that at h/b greater than 1, the ground effects have no appreciable influence on the aircraft. The primary problem in determining the magnitude ground effects is to separate the ground effects from the influence of pilot control inputs and atmospheric effects on aircraft dynamics during a landing approach. The flight maneuver used to obtain good ground effect data is a landing approach that minimizes pilot control inputs with the aircraft flown in calm wind conditions (less than 3 knots). The pilot's flight card read as follows:

> "Perform landing approaches to touch down with the following procedures to obtain ground effect data. Stabilize the aircraft 200 feet above ground level (AGL) during landing approach. Below 200 feet AGL do not change flaps or Engine Fan RPM, maintaining a constant airspeed with a minimum of control inputs. As the aircraft nears the ground (less than 40' AGL), use elevator control inputs to hold pitch attitude constant to touchdown (No Flare)."

The goal of these instructions is to force any dominant change in aircraft dynamics during the landing approach to be caused by the ground effects. The pilot must stabilize the aircraft out of ground effects (when h/b > 1) for sufficient time to obtain good average values of C_L, α, C_T, C_D, δ_e for each landing approach. These values can then be used as reference values in the small perturbation model equation (eqs. 2, 5, and 6).

Figure 2 is a plot of lift coefficient (C_L) versus normalized height (h/b) for a QSRA landing approach. The aircraft C_L (top curve) is calculated at each data point by:

$$C_L = Wt/qS\ (A_x \sin \alpha + A_z \cos \alpha) \qquad (1)$$

where $+A_x$ is fwd (body axis)
$+A_z$ is up

A plot of C_L versus h/b by itself cannot indicate the magnitude of the ground effects, since other quantities such as angle of attack, airspeed, and thrust coefficient may vary during the landing approach and thus change the value of C_L. To determine the magnitude of ground effects on lift coefficient, the measured lift coefficient (C_L) is compared to a small perturbation model for lift coefficient (C_{L_∞}). This small perturbation model of lift coefficient represents what the lift coefficient is for the same flight conditions in free air (out of ground effects) and takes into account changes in C_L due to small variations of angle of attack and thrust coefficient.

$$C_{L_\infty} = C_{L_{ref}} + \frac{\Delta C_L}{\Delta \alpha}(\alpha - \alpha_{ref}) + \frac{\Delta C_L}{\Delta C_T}(C_T - C_{T_{ref}})$$

(Small perturbation model of C_L) (2)

The values of $C_{L_{ref}}$, α_{ref}, and $C_{T_{ref}}$ are the averages of these quantities during each landing approach while the aircraft is stabilized at an altitude above which there is no significant ground effect influence on the aircraft. The change in lift caused by ground effects, ΔC_{LGE}, as shown in figure 2, is the difference between the measured lift coefficient C_L and the calculated equivalent free air lift coefficient C_{L_∞}. The validity of this procedure can be verified by the degree with which measured C_{L_∞} and modeled C_{L_∞} match out of ground effect (h/b > 1) (see fig. 2). The lift coefficient used in this paper is the total aircraft lift which includes the direct lift caused by the engine exhaust flow turning (ref. 5).

Figure 3 is a time history of a typical QSRA landing approach used to obtain ground effects data. Note the relatively constant pitch attitude (θ) during the approach, the constant engine fan % rpm (constant thrust) and the change in the elevator (δ_e) required to maintain the relatively constant pitch attitude to touch down. The reference values used in this landing approach ($C_{L_{ref}}$, α_{ref}, $C_{T_{ref}}$, etc.) were the average of these quantities from 22 seconds to 31 seconds as shown in figure 3. The α used in equation (2) is true alpha derived from θ and γ, not the noseboom vane alpha, α_V, which is shown in the time history of the landing approach. The flightpath angle, γ, is determined from the true airspeed and the barometric altitude rate of change.

AIRSPEED MEASUREMENT

Valid ground effect measurements require accurate airspeed measurements. Airspeed measurement for ground effects analysis is complicated since the ground effect itself causes errors in the aircraft's pitot-static system. One technique that can be used to evaluate the ground effect influence on the pitot-static system is to measure the difference between the barometric altitude above ground level and the radar altitude as the aircraft approaches the ground. Figure 4 shows this pressure altitude error for the Boeing YC-14 which has its static pressure source located just below the pilot's side cockpit window. Figure 5 shows the same error in pressure altitude due to ground effects for the QSRA with a noseboom static source. Since the QSRA's static source on the noseboom is 0.6 of a wingspan in front of the wing, the influence of ground effect is much less. Since the ground effect data are determined by taking a small difference between two relatively large values, this small correction to the noseboom airspeed must be made. At 60 knots airspeed, a 3 ft pressure altitude error is equal to a 1.6 knot airspeed error, which results in a 5% error in determining C_L. The equation to correct airspeed using the measured pressure altitude error is given by:

$$\Delta V_I = \frac{g\ \Delta h}{V} \tag{3}$$

where

g = 32.2 ft/sec (acceleration of gravity)
Δh = pressure altitude error, ft ($=h_{baro_{AGL}} - h_{radar}$)

This airspeed error that is induced at the noseboom results from the image of the bound vortex as shown in figure 6. As the aircraft descends to touchdown, the angle ψ between the induced velocity ΔV_I vector and the aircraft velocity vector increases. Thus, the ΔV_I component on the aircraft velocity is needed to correct airspeed error caused by ground effects. These airspeed corrections have been applied to the QSRA ground effects data of this study (and to the YC-14 data) to derive the correct values of lift coefficient.

Lift

Figure 7 shows the percent increase of lift, due to ground effect as a function of h/b for five QSRA landing approaches. This clearly illustrates that the influence of ground effect is increasing lift even while landing at high lift coefficients. The QSRA's percent change in lift due to ground effect is very similar in shape and magnitude to the plots of YC-15 flight data in figure 8 and to the YC-14 flight data in figure 9 landing at lower lift coefficients.

Drag

The change in drag caused by ground effects was determined by the same method as that used for lift. The change in drag due to ground effect was determined from the difference between the measured drag coefficient (C_D) and the expected modeled free air drag coefficient (C_{D_∞}).

$$C_D = Wt/qS\ (-A_X \cos\alpha + A_Z \sin\alpha) \qquad \text{(measured)} \tag{4}$$

where $+A_X$ is fwd (body axis)
$+A_Z$ is up

$$C_{D_\infty} = C_{D_{ref}} + \frac{\Delta C_D}{\Delta C_T}(C_T - C_{T_{ref}}) + \frac{\Delta C_D}{\Delta C_L}(C_{L_\infty} - C_{L_{ref}}) \qquad \text{(Free Air)} \tag{5}$$

The change in drag coefficient caused by ground effects is shown in figure 10. The data for the five QSRA landing approaches show a large variation in the change in drag coefficient caused by ground effect at $h/b \approx 0.2$. Also, this reduction in drag coefficient for the QSRA is much larger than that obtained by Dr. Parks for the YC-15 (ref. 4) as shown by the solid symbols in figure 10. If the $\Delta C_{D_{GE}}$ data are

divided by the square of the lift coefficients to normalize the curves, this data coalesce as shown in figure 11. This normalization by C_L^2 is logical since the ground effect is expected to cause a reduction in the induced drag which is proportional to C_L^2. This normalization not only causes the coalescence of the QSRA data, but brings the YC-15 data into much closer agreement with the QSRA data.

Pitching Moments

The change in aircraft pitching moment resulting from ground proximity can be evaluated by the amount of elevator required to maintain constant aircraft pitch attitude (θ) near the ground. Again, the measured elevator position (δ_e) is compared to the elevator (δ_{e_∞}) position of the model expected for the same flight conditions in free air (eq. 7).

$$\delta_{e_\infty} = \delta_{e_{ref}} + \frac{\Delta\delta_e}{\Delta C_T}(C_T - C_{T_{ref}}) + \frac{\Delta\delta_e}{\Delta C_L}(C_{L_\infty} - C_{L_{ref}}) + \frac{\Delta\delta_e}{\Delta\dot{\theta}}(\dot{\theta}) + \frac{\Delta\delta_e}{\Delta\ddot{\theta}}(\ddot{\theta}) \qquad (6)$$

$$\delta_{e_{GE}} = \delta_e - \delta_{e_\infty} \qquad (7)$$

Figure 12 shows the change in elevator position required to maintain constant aircraft pitch attitude for nine landing approaches. There is considerable scatter in the data at $h/b = 0.2$ (just before touchdown). Figure 13 shows the elevator position at $h/b = 0.2$ as a function of landing approach airspeed. This figure clearly shows the strong influence that airspeed has on the amount of elevator required to maintain constant pitch attitude. Since the ground effects are so dominant for the amount of elevator required, the simpler equation $\delta_{e_{GE}} = \delta_e - \delta_{e_{ref}}$ for relatively constant pitch attitude landing approaches will give a good first order indication of the elevator inputs required to compensate for ground effects.

DISCUSSION AND SIGNIFICANCE OF THE RESULTS

The most significant result of the increase in lift caused by ground effects is the reduction in touchdown sink rate which is a minimum of 2 ft/sec for the QSRA. This sink rate reduction data in figure 14 is the comparison of steady state sink rate and aircraft pitch attitude at $h/b = 1$ to the sink rate at touchdown.

The positive ground effects influenced the technique used in the QSRA carrier landing program (ref. 6). A sink rate was chosen for the carrier landings that would allow the QSRA to "punch" through the ground effect, but not exceed the landing gear sink rate limits. If a landing approach was made too shallow, at a glideslope angle less than 3°, the QSRA would float as shown in the time history in figure 15. This float increases the touchdown dispersion significantly. Note in this time history the airspeed increase caused by the reduction in drag in ground

effect. Note that the aircraft did not land until the engine thrust (engine fan rpm) was reduced.

The elevator position change required when $h/b < 1$ to counter the pitching moment change is very significant, especially considering the QSRA has a T tail. The elevator authority required to maintain constant pitch attitude with ground effects would increase significantly for a conventional, low-mounted tail. Figure 13 shows the strong influence of landing approach speed on the elevator authority requirement. Pilots are not generally aware of the large amount of elevator required to compensate for ground effects since most STOL approaches are flown with stability augmentation systems that input the delta elevator required to maintain constant pitch attitude.

Following the QSRA carrier landings, pilots reported that one of the few differences between the land-based carrier landing practice and the actual carrier landings was some "suck down" experienced just before touchdown on the carrier. The carrier landings were not preceded by steady state type approaches needed to get good ground effect data. The average change in flight data as the QSRA flew over the carrier ramp to touchdown in 46 landing approaches indicates the nature of the ground effects:

QSRA Carrier Landings Data
(Average Data for 46 Landing Approaches)

	At the Ramp	At Touch-down	Change	
Sink rate, ft/sec	8.36	6.9	-1.46	(reduction in sink rate)
Engine fan, % rpm	77.4	75.0	-2.4	(reduction in thrust)
Elevator, deg	-0.01	-8.12	-8.11	elev.(-TEU)
Pitch attitude, deg	2.18	1.38	-0.80	(nose-down pitch)

It appears that the 2-sec time period that it took the QSRA to fly from the aft ramp to touch down was enough time for the ground effect from the carrier deck to cause a nose-down aircraft pitch change which the pilots bring forward of the c.g. interpreted as suck down. Note also that for the carrier landings the sink rate is reduced (opposite of suck down). The pilot probably did not notice this during land based operations since the influence of ground effects was gradual, not abrupt as when he flew over the ramp of the carrier. This phenomenon is not unique to QSRA carrier landings. A similar experience occurred with the XV-15 Tilt Rotor simulator. After the XV-15 Tilt Rotor simulation math model was modified to include ground effects, the pilot stated, "Great, you've got the slight suck down we've

experienced just before touch down." The only modification made to the simulation model was the addition of the nose down pitching moment from ground effect, which again, the pilot being forward of the C.G. had interpreted a nose-down pitch change as suck down.

This tendency for powered-lift STOL aircraft to have a nose-down pitching moment at reduced landing approach speeds strongly suggests that future powered-lift STOL Aircraft be designed so they can tolerate nose-gear first touchdowns.

CONCLUSIONS

For the QSRA landing at C_L greater than 7, the change in lift due to ground effect is still positive. The percent increase in lift for the QSRA landing at high C_L is similar to that of other aircraft landing at much lower C_L. The ground effects reduced the sink rate for the QSRA by 2 ft/sec for no flare landings.

The reduction in drag due to ground effects for the QSRA is comparable to the drag reduction for the YC-15 when the change in drag coefficient is normalized with division by C_L^2. This reduction in drag along with the increase in lift caused by ground effects will tend to make the QSRA "float" for shallow glide slope (<3°) landing approaches.

A significant amount of elevator input is required to maintain constant aircraft pitch attitude upon entry into ground effect. The magnitude of elevator required to maintain a constant pitch attitude increases as the landing approach airspeed is reduced.

REFERENCES

1. Haak, D. E.; and Finch, R. D.: USAF Stability and Control DATCOM-AFFDL Wright-Patterson AFB, 1960 (revised 1975).

2. Gratzer, L. B.; and Mahal, A. S.: Ground Effects in STOL Operations. J. Aircraft, Vol. 9, No. 33, March 1972.

3. Stevens, V. C.; and Wingrove, R. C.: STOL Ground Effects determined from Flight Data. AIAA Paper 77-576, June 1977.

4. Parks, E. K.; and Wingrove, R. C.: Flight Test Measurements of Ground Effects - STOL Airplanes. 8th Annual Symposium of Society of Flight Test Engineers, August 1977.

5. Stevens, V. C.: A Technique for Determining Powered-Lift STOL Aircraft Performance at Sea Level from Flight Data Taken at Altitude. 13th Annual Symposium, Society of Flight Test Engineers, 1983.

6. Stevens, V. C.; Riddle, D. W.; Martin, J. L.; and Innis, R. C.: Powered-Lift STOL Aircraft Shipboard Operations; A Comparison of Simulation, Land-Based and Sea Trial Results for the QSRA. AIAA Paper 81-2480, 1981.

7. Vincent, J. H.; and Mowley, A. C.: Quiet Short Haul Research Aircraft Phase I: Flight Simulation Investigations, Vol. II. NASA CR 151965, March 1977.

Figure 1.- NASA Quiet Short Haul Research Aircraft.

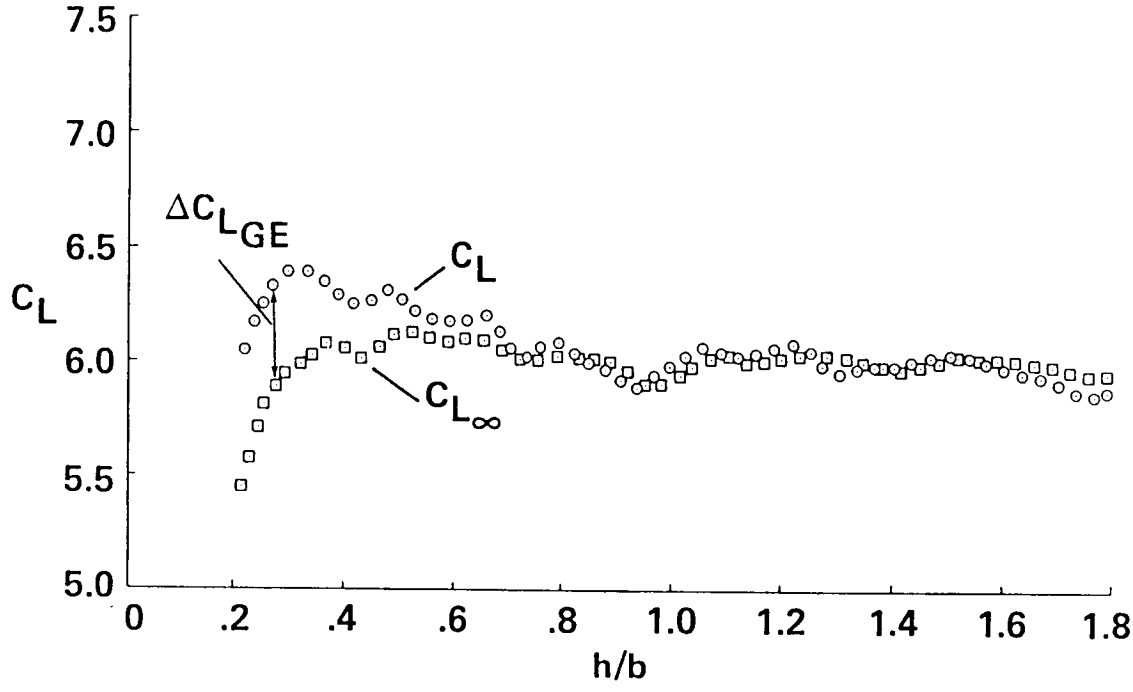

Figure 2.- Lift coefficient during a landing approach, for QSRA flight data.

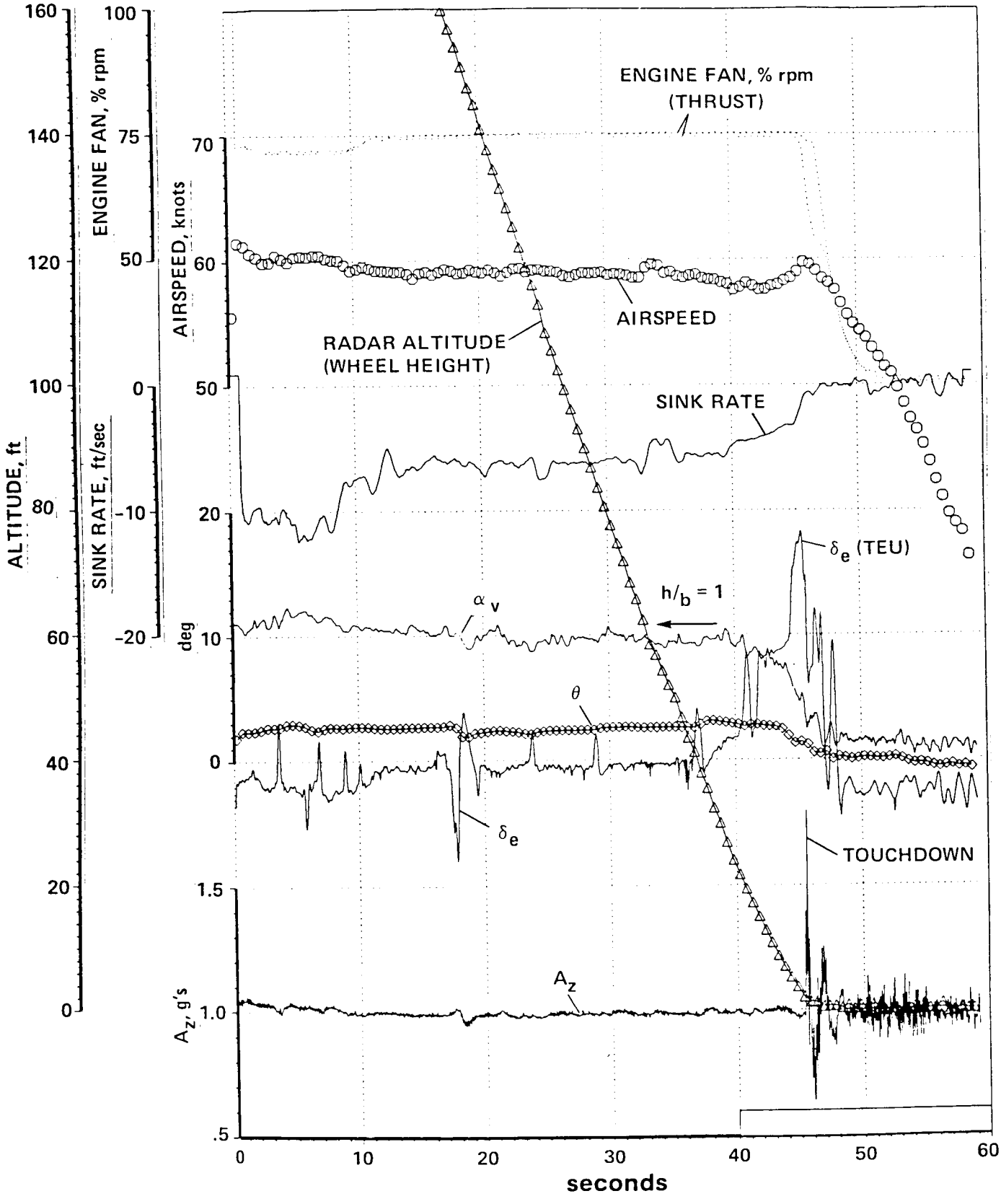

Figure 3.- Time history for a QSRA landing approach.

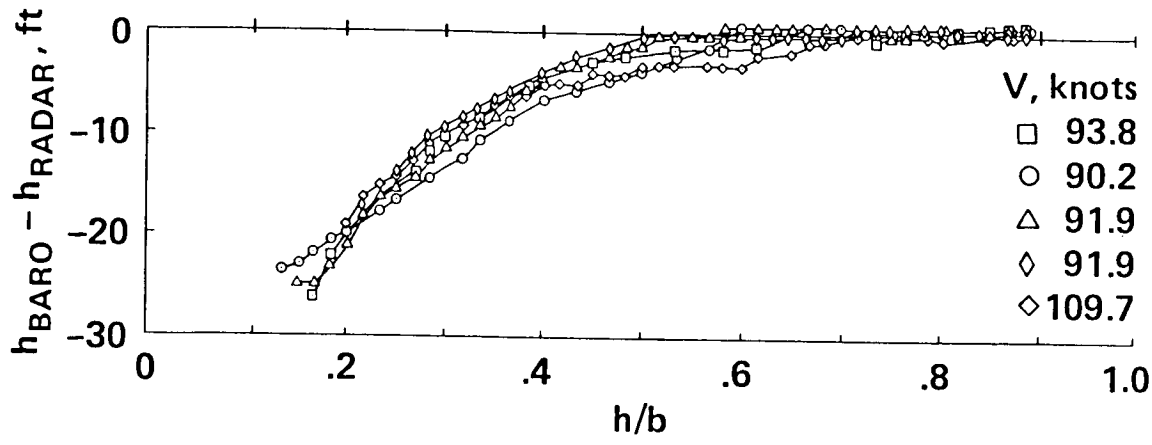

Figure 4.- Difference between barometric altimeter and radar altimeter for YC-14 data.

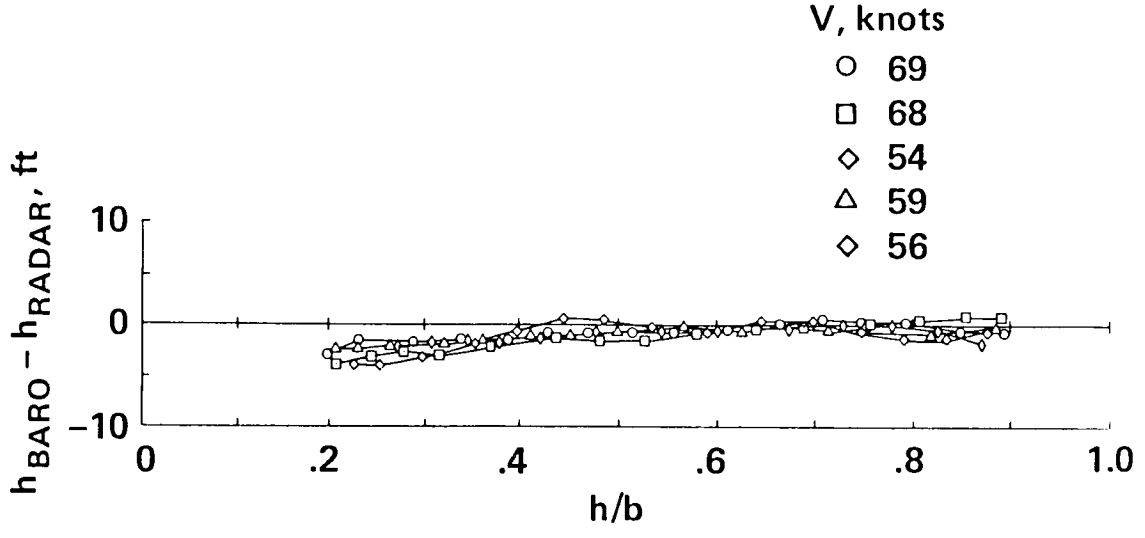

Figure 5.- Difference between barometric altimeter and radar altitude due to ground proximity; nose boom, QSRA flight data.

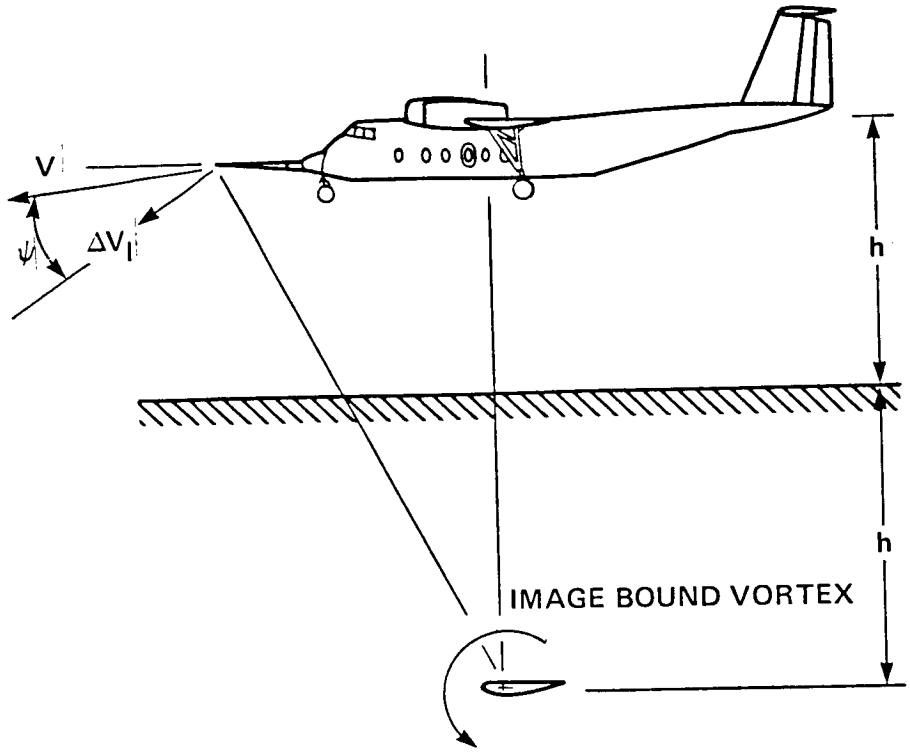

Figure 6.- Image-bound vortex influence on the nose-boom airspeed sensor.

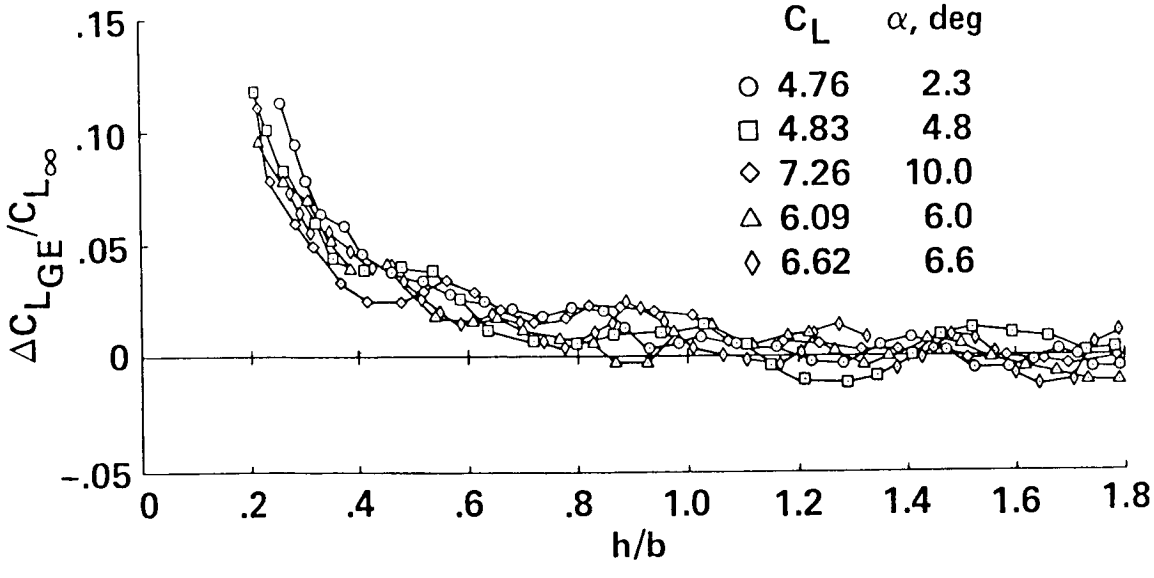

Figure 7.- Change in lift due to ground proximity, QSRA flight data.

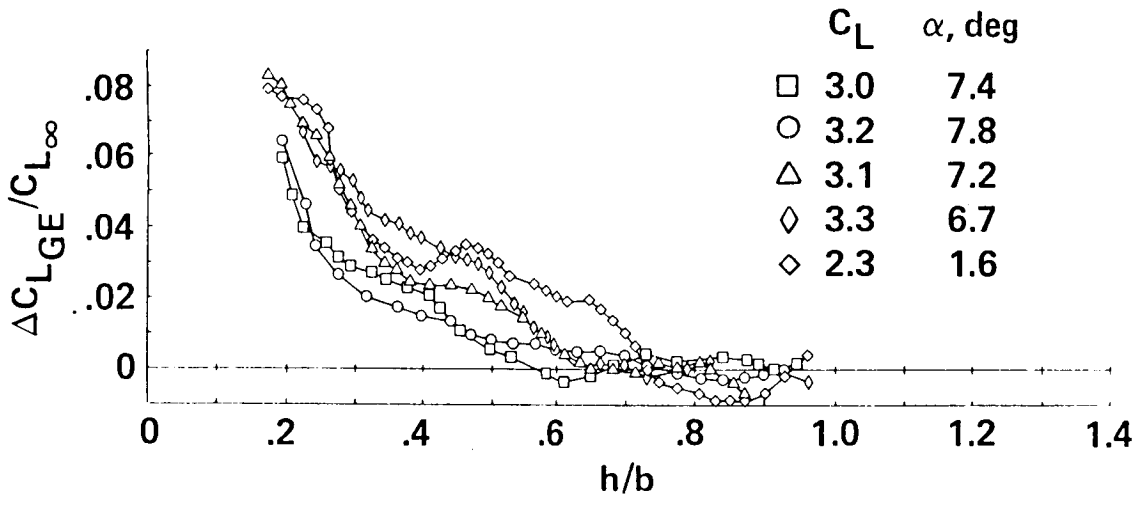

Figure 8.- Change in lift due to ground proximity, YC-15 flight data.

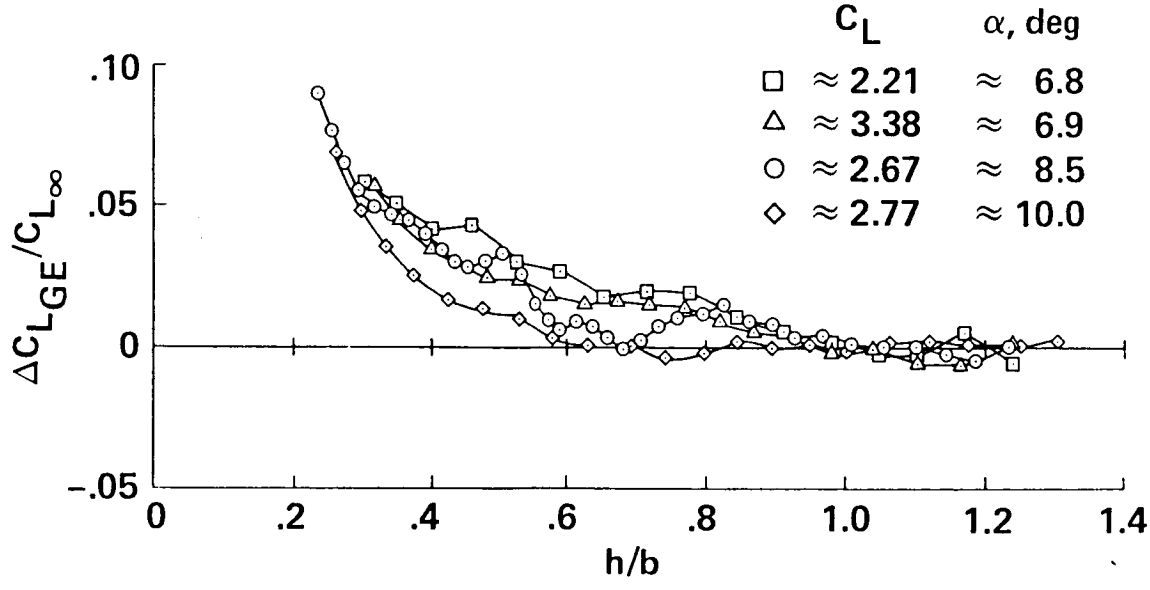

Figure 9.- Change in lift due to ground proximity, YC-14 flight data.

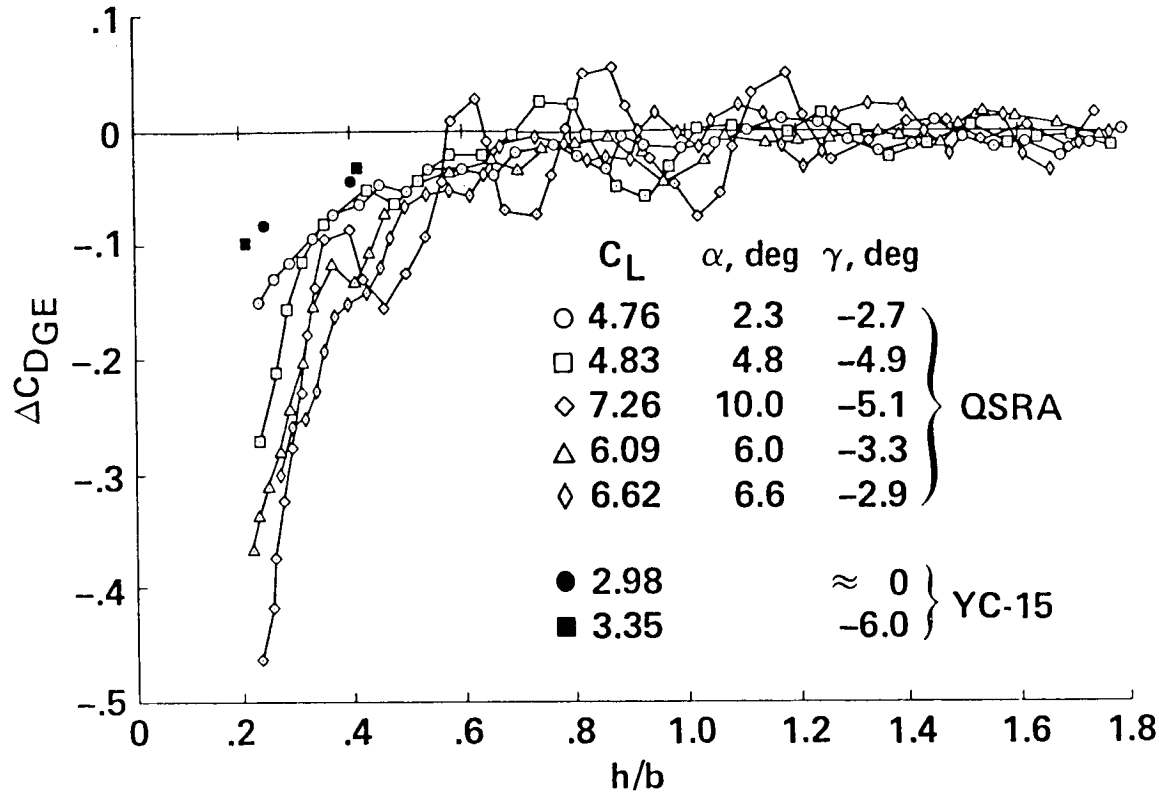

Figure 10.- Change in drag due to ground proximity for QSRA and YC-15 flight data.

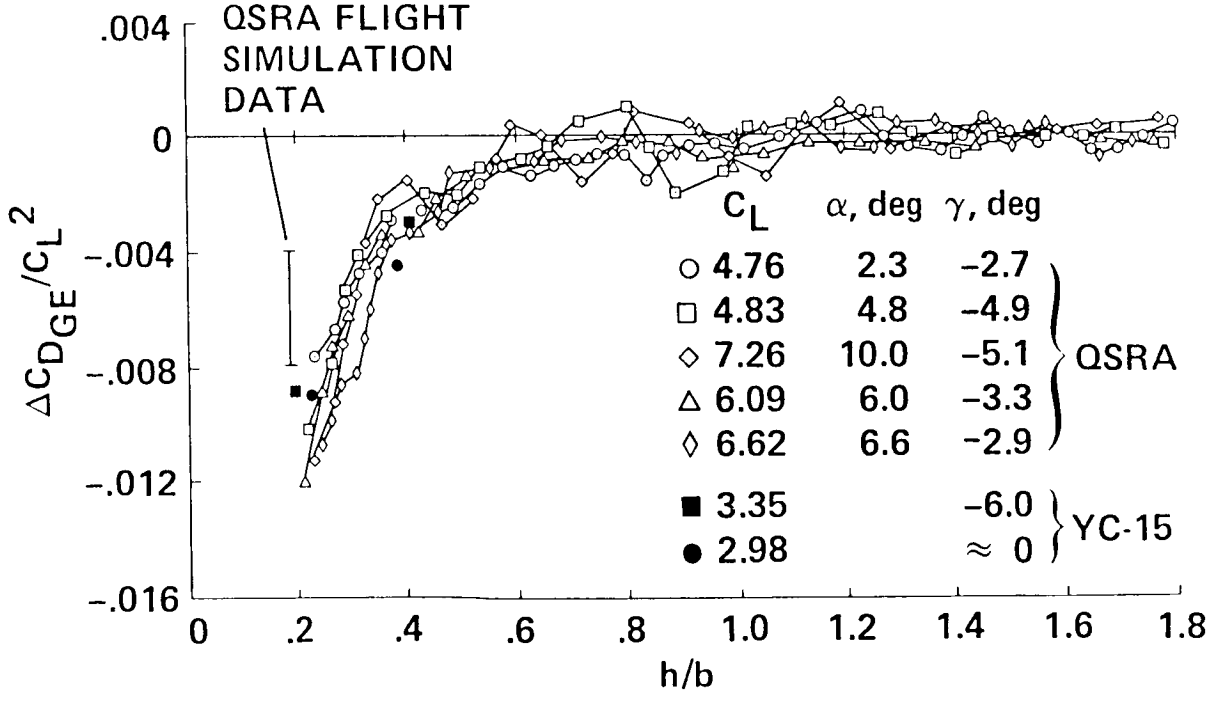

Figure 11.- Change in drag due to ground proximity for QSRA and YC-15 flight data.

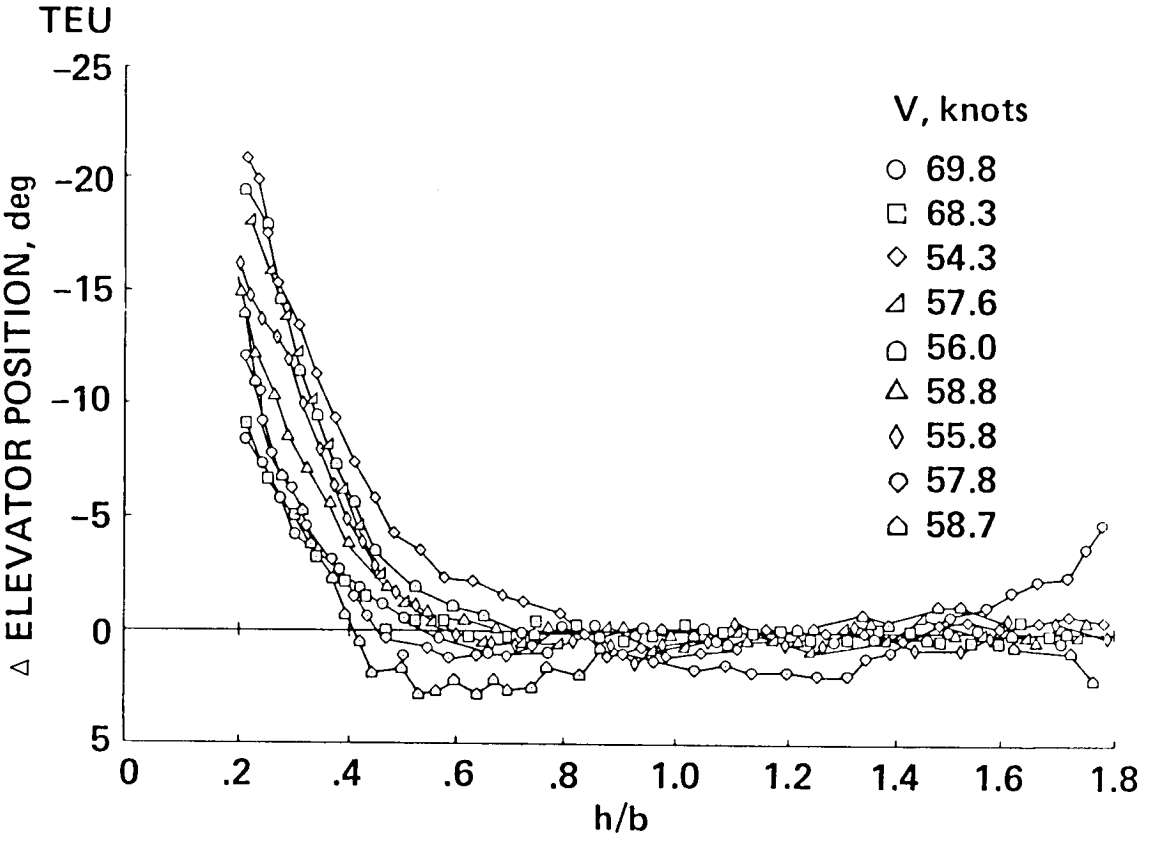

Figure 12.- Change in elevator position due to ground proximity, QSRA flight data.

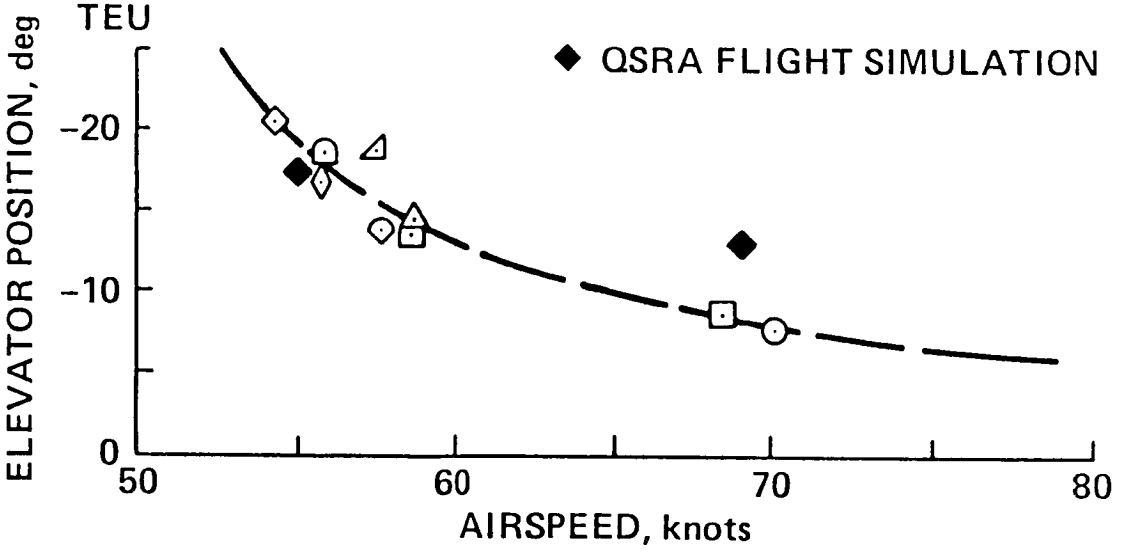

Figure 13.- Elevator position at touchdown required to maintain constant pitch attitude.

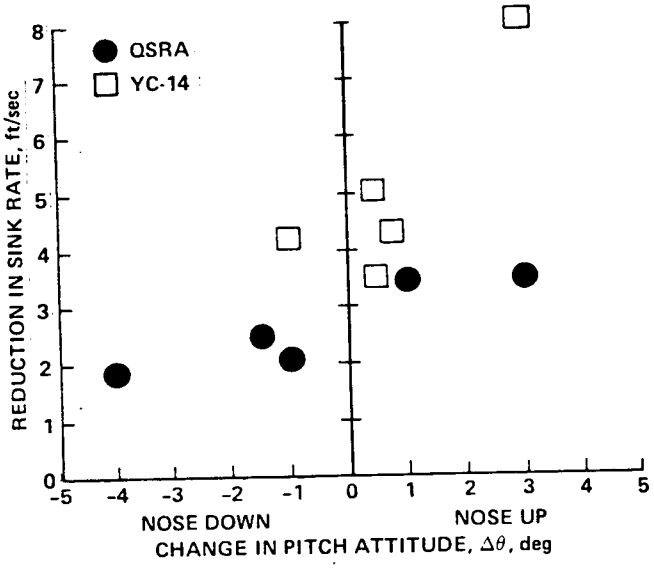

Figure 14.- Reduction of landing sink rate due to ground proximity.

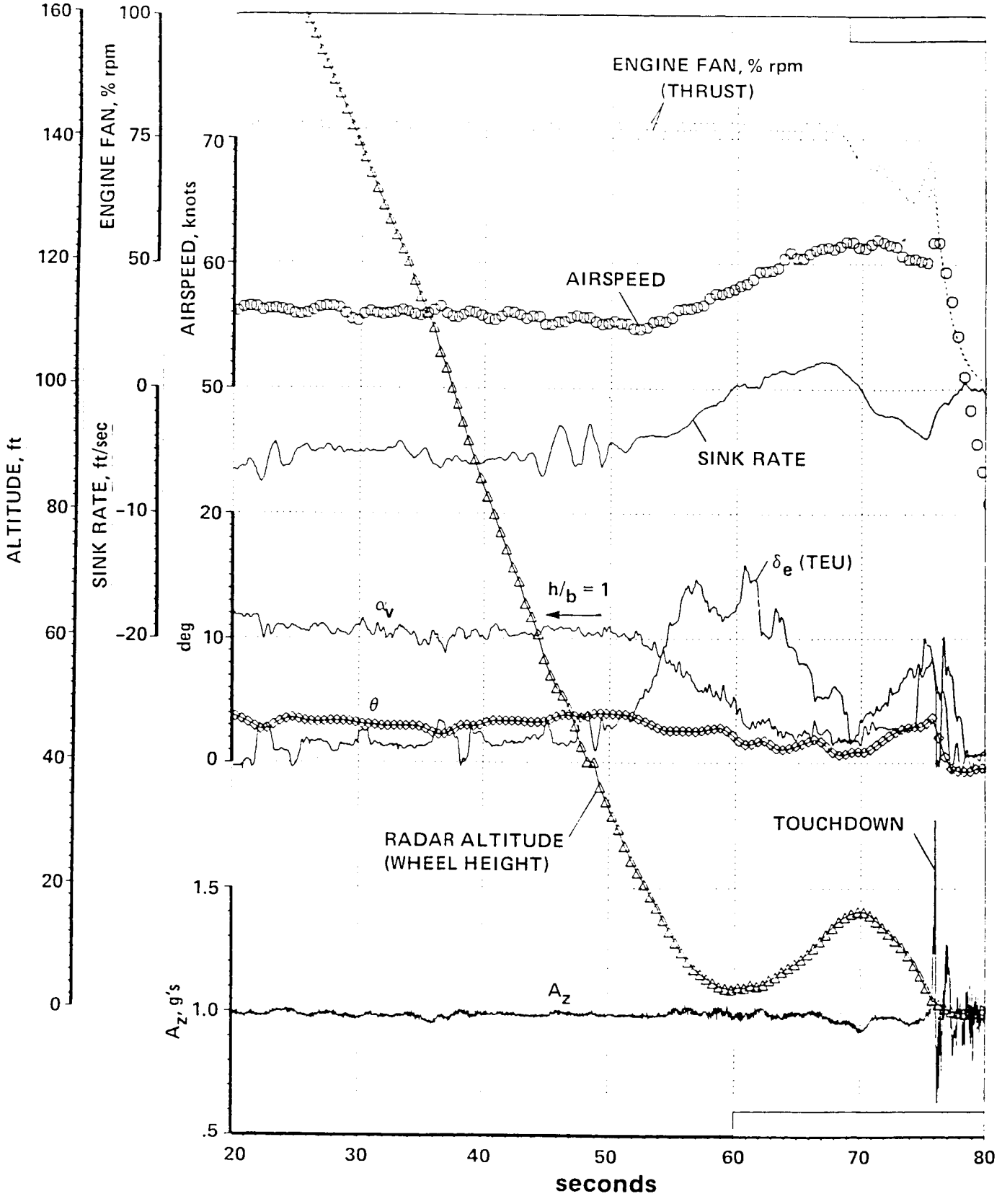

Figure 15.- Time history for a QSRA landing approach.

EFFECTS OF GROUND PROXIMITY ON A LOW ASPECT RATIO PROPULSIVE WING/CANARD CONFIGURATION

V. R. Stewart
Rockwell International Corp.
Columbus, Ohio

G. T. Kemmerly
NASA Langley Research Center
Hampton, Virginia 23665

ABSTRACT

The effects of near proximity to the ground are investigated on a low aspect ratio propulsive wing/canard concept at STOL conditions. Data have been obtained on a wing/body and wing/body/canard configuration at various heights above the ground, ranging from free air to approximately 1/4 of the mean aerodynamic chord (MAC) above the ground. The data presented and discussed include, force and moment coefficients, surface pressure distributions, and downwash angles measured one MAC behind the wing. The test technique, model requirements, and special considerations required for testing these configurations are also discussed. Special model requirements included evenly distributed exit nozzle pressures along four separate nozzles of lengths of one and two feet with only one air supply to the model. Test techniques must recognize and deal with the ground boundary layer as well as the air supply pressure measurement and management.

SYMBOLS

BP	Butt Plane
c	chord
$\bar{c}$	Mean Aerodynamic Chord
C_{LA}	Aerodynamic Lift Coefficient
C_L	Lift Coefficient
C_P	Pressure Coefficient
C_μ	Blowing Coefficient
h or H	Height Above Ground
δ_N	Nozzle Angle
δ_F	Flap Angle
θ	Thrust Angle
α	Angle of Attack

Subscripts

c	Canard
w	Wing

P	Pressure
V	Velocity
X	Longitudinal Distance
Y	Lateral Distance

INTRODUCTION

The testing of any powered configuration requires that several special considerations must be made if the results are to be satisfactory. These begin with the concept of the model and continue until the final data reduction. This paper first describes some of the more critical concerns which have been encountered in the tests of a distributed jet or jet flap configuration and in the second part describes some of the results obtained during testing in the presence of a fixed ground board. The testing in the presence of the ground imposes other constraints on the model and on the test facility. The model design and fabrication restraints to provide a slot nozzle with the required even flow distribution are discussed and the tunnel requirements to most nearly simulate the airplane are pointed out. Data recording and reduction requirements are also described. In the second part of the paper the test results are analyzed and discussed briefly.

MODEL CONSIDERATIONS

The powered model requirements are not specifically altered for testing in the presence of the ground. Equal care is required for either free air or ground effects testing. The first major consideration of the model is the method of delivery of the air to the nozzle. Care must be exercised in the design of blown models to isolate the air supply from the parameters of importance that are to be recorded during the testing. The purpose of the tests determines the type of installation required. For certain types of tests it may be possible to completely isolate the air supply, piping, and the nozzles from the force carrying portions of the model. In other cases, most likely in the majority of the cases, it becomes necessary to bring the air supply across the balance without imposing large forces on the balance. Models representing each of these approaches have recently been tested under contract to the Navy (NADC) and to NASA Langley, see References 1 and 2.

The first model concept, that which isolates the air supply from the metric (force measured) portions of the model, is shown mounted in the Rockwell V/STOL tunnel in Figure 1. Figure 2 shows the drawing of the air supply and model. The high pressure air is delivered to the model through the mounting strut and to the nozzles without crossing the balance. The balance is between the air supply and the model shell and records only the forces induced on the shell by the free stream or by the air jets. This

model was utilized for both concentrated jets and for distributed jets near the wing trailing edge as seen in Figure 1, although it was less than satisfactory for the distributed jet case due to the external ducting of the distributed jet air. This air supply approach is generally used when only the induced loads are desired, a pressure instrumented model is being used, or for other special test cases such as a ground flow study.

An example of the second model is shown installed in the NASA Langley low speed 4- by 7- Meter Tunnel in Figure 3, and discussed in Reference 2. In this installation the high pressure air is delivered through the sting by a single pipe. The air is directed inside the model into each of the individual wings and canards where it is internally ducted to a full span nozzle in the aft portion of the surfaces. This model has also been tested as a semi-span model utilizing the same air delivery principle, see Figure 4. The internal ducting provides a means of distributing the air from one inlet pipe to four linear nozzles with equal pressure ratio for each and relatively constant pressure distribution across the entire nozzle span. This is accomplished by maintaining a high pressure ratio in the internal ducts to the plenum just upstream of the nozzle. Figure 5 shows the internal ducting used in this particular model. The high pressure air from the tunnel source enters a common fuselage plenum From there it is divided into the four flow paths. Adjustable valves are utilized to maintain pressure balance to each surface. The air then exits into a high pressure plenum in each surface and from there into the nozzle plenum through a series of spanwise ducts which may be closed to control the spanwise distribution. These techniques resulted in spanwise pressure distributions as shown in Figure 6. Obtaining a satisfactory and a repeatable spanwise pressure distribution is essential to the test program, not only for repeatable data but also for test efficiency. The nozzle pressure ratio can be changed by control of the supply pressure. When the pressure drop from the supply to the nozzles and constant spanwise distributions for all nozzles have been established,the relationship between nozzles will not change as the pressure ratio changes. A pressure drop from approximately 150 psig at the supply to 15 psig at the nozzle is typical for this model or for any model of this type.

TEST AND TUNNEL REQUIREMENTS

Those items discussed above relating to the models do not pertain exclusively to testing of those models in near proximity to the ground, but rather, refer to all of the testing of powered models in any case. The data recorded and the special data reduction, likewise, are not limited to ground effects. However, some discussion of these also is in order. The flow parameters necessary to calculate the nozzle characteristics and thrust must be included. The forces of the propulsive wing concept and other propulsive lift systems are composed of two major forces. An

induced or aerodynamic force and a direct thrust force make up the total force on the model. Analysis of the configuration is simplified if these forces can be separated during the data reduction cycle. The thrust removed (aerodynamic) force and moment coefficients are calculated by subtracting the direct thrust component from the total force, ie,

$$C_{LA} = C_L - C_\mu \sin(\theta+\alpha)$$

The method used by the low speed tunnel to compute thrust removed coefficients required a wind-off run each time the thrust configuration was changed. The forces on the balance from this tare run were then used to obtain the thrust removed coefficients. This method is prefered as the actual thrust component is used in the data reduction. Also the wind off data is very valuable in understanding the thrust characteristics and should be obtained even though it was not to be used in the data reduction. This wind off data was used extensively in trouble shooting during and after the test. The wind off data was used to determine the thrust angles during the test and for this particular setup was used to discover and eliminate a model/sting foul.

The results of the test of the model described with the non-metric thrust system were used to determine the shape of the ground vortex with the distributed jet. The objective of the overall test and model was to investigate the induced forces on the model in the presence of the ground. The primary thrust devices to be tested were deflected thrust nozzles and for these nozzles the induced forces would be small relative to the thrust forces. An isolated thrust system appeared to offer the best setup to accomplish this goal. The isolated balance was used and it was then determined that the distributed jet tests would be limited in the data gathered. Model force data was recorded but the accuracy was rather limited. This result had been expected, however; the main desire of the test was to investigate the concentrated jets and the distributed jet case was an add on to get as much data as possible without a major system change. The thrust supply pipe which supplied the nozzle was external to the wing and reduced the area available to provide lift. This model, however, did provide a great deal of insight into the particular requirements of testing powered models and especially distributed jet models in ground effect. The ground board pressures and flow interference measurements were used to develop the model and test procedures for later testing of the propulsive wing/canard model.

A wall jet is formed when a concentrated jet strikes the ground and radiates out from the point of contact. The wall jet has been shown to roll up and form a ground vortex when it interacts with the oncoming airstream, see Figure 7. A similar condition exists for the distributed jet. The effects of the ground boundary layer on the vortex formed by the concentrated jet has not been adequately determined but the boundary effect on the distributed jet is expected to be more pronounced and should be eliminated when testing in the near proximity to the ground.

The ground vortex is one factor which determines the requirement to eliminate the ground boundary layer. Turner (Reference 3) investigated essentially the same effect by observing where a significant lift loss occured and recommended a test area in which a moving ground board would be required, see figure 10. Data obtained on the model tests of Reference 1 indicate that the critical ground conditions may exist at lower lift coefficients than those described by Turner. The presence of a ground vortex is shown by significant negative pressures on the ground. Reference 1 presents a discussion of the ground vortex and its formation. The ground pressure measurements under the wing of the distributed jet indicate that a ground vortex has formed at quite low lift coefficients. Figure 8 indicates that at ninety degrees deflection of the distributed jet a ground vortex has formed under the wing at a height of two chord lengths above the ground. Figure 9 shows the location of the ground vortex at a jet deflection of 45 degrees and 3/4 of a chord length above the ground (approximate wheel height for this configuration). The location of the vortex greatly influences the lift in the presence of the ground. In the first case, figure 8, the vortex is under the wing and a large lift loss is experienced; whereas, in the second case, figure 9, with the vortex behind the wing, an increase in lift greater than would be expected was seen. Both of the results are questionable and care must be taken to eliminate the boundary layer in the test procedure. The formation lift coefficients of the ground vortex are compared to the requirements of Turner in Figure 10. The lift coefficients for the ground vortex formation may be somewhat low due to the fabrication difficulty discussed earlier, but indicate the importance of removing the ground boundary layer. It appears that if a distributed jet configuration is to be tested with jet deflections at which ground impingement can likely be expected that the ground boundary layer should be removed.

Removal of the boundary layer can be accomplished by any of several techniques. The landing approach of an aircraft, of course, does not have the same boundary conditions as those developed in the wind tunnels unless a moving model technique is used. This more nearly duplicates the true ground effects to be experienced by the approach and landing. The real task with the moving model is the instrumentation and data retrieval task, and if these are solved, the technique is quite valuable. Two methods of boundary layer removal are suction to remove the boundary layer ahead of the model and blowing to speed up the boundary layer to match the free stream flow. The use of a moving belt in conjunction with the suction provides the best means of boundary layer control in the wind tunnel. The use of a moving belt does limit the instrumentation capability of the test setup. The use of the ground pressure as a measurement of the extent of the ground vortex is lost, at least in the case of a belt which extends the full width of the test section. Table 1 shows the effect of each of these simulations as related to an airplane during landing. Note that only the moving model is the same as the airplane and then only if there are no ambient winds which could be a fair percentage of the approach speed of a STOL

configuration. In order to simulate the ambient wind, a moving model in a large tunnel would be required.

TABLE 1

V_∞ - A/P RELATIVE TO AIR
V_H - A/P RELATIVE TO GROUND
V_a - AIR RELATIVE TO GROUND
V_j - JET VELOCITY
V_W - WALL JET VELOCITY
V_B - BELT VELOCITY

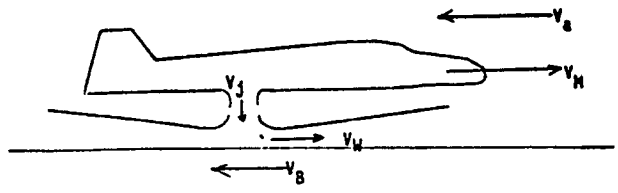

CONFIGURATION	V_H	V_a	V_W	V_B	RETARDING FORCE		PUSH BACK FORCE		GROUND BOUNDARY LAYER	
					AIR	GROUND FRICTION	AIR	GROUND	OUTSIDE JET	IN JET
A/P	V_∞	0	$V_j + V_\infty$	0	$V_j + V_\infty$	$V_j + V_\infty$	0	0	0	YES
MOVING MODEL	V_∞	0	$V_j + V_\infty$	0	$V_j + V_\infty$	$V_j + V_\infty$	0	0	0	YES (SAME)
FIXED MODEL - FIXED G.B.	0	V_∞	V_j	0	$V_j + V_\infty$	V_j	V_∞	0	YES	NOT SAME
FIXED MODEL - MOVING BELT	0	V_∞	V_j	V_∞	$V_j + V_\infty$	$V_j + V_\infty$	V_∞	V_∞	0	?
STATIC	0	0	V_j	0	V_j	V_j	0	0	0	YES

The propulsive wing/canard model shown in Figure 3 was tested in the presence of the ground during the tests of the effects of the relative wing/canard placement. Suction was used to remove the boundary layer ahead of the model during the tests. Measurements of the ground vortex or the ground boundary were not made. However, previous testing in the presence of the vortex has shown that either of two conditions can exist when the vortex is present. If the vortex is located under the wing, a negative pressure will be seen on the lower surface of the wing; and, when the vortex is located just aft of the wing these pressures will be positive and excessive lift increases will be indicated. The propulsive wing/canard model has extensive surface pressure instrumentation. Figure 11 presents wing pressure instrumentation locations. These static pressure measurements may be used to determine if a ground vortex is between the wing and the ground. Figure 12 presents the wing pressure distributions at a mid span location, BP 12. Pressures on the flap upper surface are not shown in order to remain on scale. A significant ground effect is seen in the surface pressures indicating that even though the suction was used to remove the boundary layer, the vortex is still present under the wing. The negative pressures at $C_\infty = 2.0$ indicate the vortex to be trapped under the wing. These results are not indicative of unsatisfactory test results. The vortex may be trapped under the

airplane wing in actual flight at these conditions. Additional testing is required to define the effect of the test procedures on the vortex and related aerodynamic increments.

EFFECTS OF THE GROUND ON THE AERODYNAMIC CHARACTERISTICS

The remainder of this paper will deal with the general aerodynamic phenomena that can be expected with a jet flap in ground effects. Force and pressure data taken specifically from the propulsive wing/canard investigation will be used to illustrate these flow characteristics.

With most wings in ground effects, upwash at the leading edge occures as ground height is reduced. This effect is magnified in the case of the jet flap because the jet acts as a flap extension and, thus, more of an obstruction below the wing than a mechanical flap. At even lower heights the jet can impinge on the floor (Ref. 4) and run foreward to form a vortex against the freestream, obstructing flow under the wing even further. This vortex formation will be discussed later. Figure 13 shows the development of this leading edge pressure spike at three different ground heights, and illustrates how sensitive it is to thrust coefficient. In this case there is no canard in front of the wing. A canard will provide a downwash field for the wing, thus, reducing this spike, and, as in the case of the example in Figure 14, can actually reverse the pressures very near the leading edge.

A jet flap on a wing increases circulation around the wing. This results in increased upwash at the leading edge, and, at high thrust coefficients, can separate the leading edge (Ref. 5). The combined effects of ground proximity and a jet flap can lead to leading edge separation at even moderate thrust coefficients. The data from the propulsive wing seem to indicate separation as can be seen by returning to Figure 13. A separation bubble apparently forms at $x/c=0.1$ and due to the strong boundary layer control properties of jet flaps, the flow appears to reattach near the line $x/c=0.55$. These flat pressure distributions may be the result of the supercritical airfoil section used rather than a separation bubble. There is insufficient data available to determine conclusivly. The effect can be seen to spread spanwise to the outboard portion of the wing as shown in Figure 15. Here, if separation has occured, it has occured behind only a mild, leading edge pressure rise. By comparing Figure 13 to Figure 14, the downwash of the canard is seen to improve the pressure gradient on the wing upper surface enough to aviod separation.

Another flow problem associated with jet flaps in ground effects is the separation of the jet from the upper surface of the flap. This can generally be avoided by careful flap design, but, indeed can occur. During the propulsive wing/canard investigation, because of proper design and the moderate blowing rates tested, this flow problem was not encountered, however, it

should still be addressed. At very high thrust coefficients the back pressure caused by close proximity to a ground plane can be sufficient to keep the jet from following the contour of the flap and, thus force it to separate from the flap. This will be noticed several places in the data obtained Downwash data will show a significant decrease in downwash angle and pressure data on the upper surface of the flap will indicate separation. Force data will also be a good indicator; drag and lift will both drop dramatically and pitching moment will, in general, either increase (for a low wing) or decrease (high wing) quickly.

The flow phenomenon most effected by a boundary layer on the floor of a wind tunnel is the vortex flow that can occur under a jet flapped wing in ground effects. Out of ground effects, the high speed flow issuing from the trailing edge of these wings entrains flow along the lower surface of the flap. The result is the reduced lower surface flap pressures seen in Figure 16. As the wing is moved closer to the ground the jet impinges on the ground and spreads both foreward and aft from a stagnation line. The foreward moving flow rolls up into a vortex very near the flap. Reduced ground height or increased blowing coefficient delivers higher energy jet flow to the ground. This more powerful flow drives the vortex front farther upstream, but the trailing edge of the vortex remains at the interface between the jet sheet and the low energy flow under the wing. An example of this type of vortex can be seen in Figure 17. If ground height is further reduced or if blowing coefficient is increased, the wall jet will travel even further upstream before being turned up into a vortex front by the freestream. The pressures indicate that the trapped vortex may then break into two disinct vorticies - one driven by the wall jet and rolled up by the oncoming flow; the other driven by the strong shear layer at the wing trailing edge. An example of this type of trapped pair can be seen in Figure 18. Again, the available data is not conclusive in this determination. The lower surface pressure distribution may be indicative only of a single oval vortex. Flow visualization of this area is required to finally isolate the shape of the vortex.

Figure 19 depicts a vortex system located under a wing with no canard in front of it. The location and strength of this system is heavily dependent on thrust coefficient. Consequently, the ground effects on pitching moment can be unpredictable and severe - especially at high thrust coefficients. Positioning a canard (also with a blown flap) in front of the wing moves the system farther back under the wing as the canard jet interacts with the wing's foreward moving wall jet. The new flow field is quite complex. Where the two jets meet on the inboard portion of the wing they create the fountain that can be seen in the pressure data in Figure 20. Moving outboard the fountain quickly looses its strength and two vorticies are seen to develop and continue outboard. One is the weak vortex formed in front of the fountain and the other is the stronger vortex formed behind it. From the available pressure data the location of this fountain/vortex system appears to remain relativly constant with increasing thrust coefficient. This would be expected as long as

the flow split between the wing and canard remains constant. Also, the total strength of this fountain/vortex system is only slightly dependent on thrust coefficient because increased blowing both increases the fountain's high pressure and decreases the low pressure of the vorticies.

CONCLUSIONS

The presence of a ground boundary layer will greatly effect the actions of these under-wing vorticies. Low energy flow near the floor will, initially alter the ground height and blowing coefficient necessary for the jet to establish a stagnation line on the floor. Also, a low energy boundary layer will allow the wall jet to travel much farther upstream before rolling up into a ground vortex. There is a need for either a moving model or a flight test data base of powered ground effects that can be directly correlated to wind tunnel data. This data base would perhaps provide a way to correct wind tunnel ground effects data or at least quantify the limits to which they could be measured accurately in wind tunnels.

Testing of STOL configurations in the near proximity to the ground requires that special considerations be given to the model, the tunnel, the instrumentation, and to the data reduction. The reaction of the jet with the ground is the most significant and the most difficult interference problem to solve.

The reaction of the jet and the ground form a wall jet which in turn is reacted on by the oncoming air stream to form a vortex. Careful planning must be accomplished to assure that this vortex and its effect on the model duplicate the effects which the airplane will encounter during the approach to the ground.

A test plan utilizing all ground board techniques and a generic model should be undertaken to answer questions regarding the use of each technique. Such a test should involve both deflected thrust as well as distributed jets (jet flaps) as the results will be considerably different.

REFERENCES

1. Stewart, V. R., and Kuhn, R. E.: "A Method for Estimating the Propulsion-Induced Aerodynamic Characteristics of STOL Aircraft in Ground Effect," NADC 80226-60, Aug. 1983

2. Stewart, V. R. and Paulson, J. W. Jr.: "The Aerodynamic Characteristics of a Propulsive Wing/Canard in STOL," AIAA Paper 84-2396,Oct. 1984

3. Turner, T. R. : " Endless Belt Technique for Ground Simulation," NASA SP-116, April 1965, pp. 435-446

4. Lowery, J. G., Riebe, J. M. and Campbell J. P.: "The Jet-Augmented Flap," IAS Paper 715, Jan. 1957

5. von der Decken, J.: "Aerodynamics of Pneumatic High-Lift Devices", Agard 1970

Figure 1. Distributed Jet Model in Wind Tunnel.

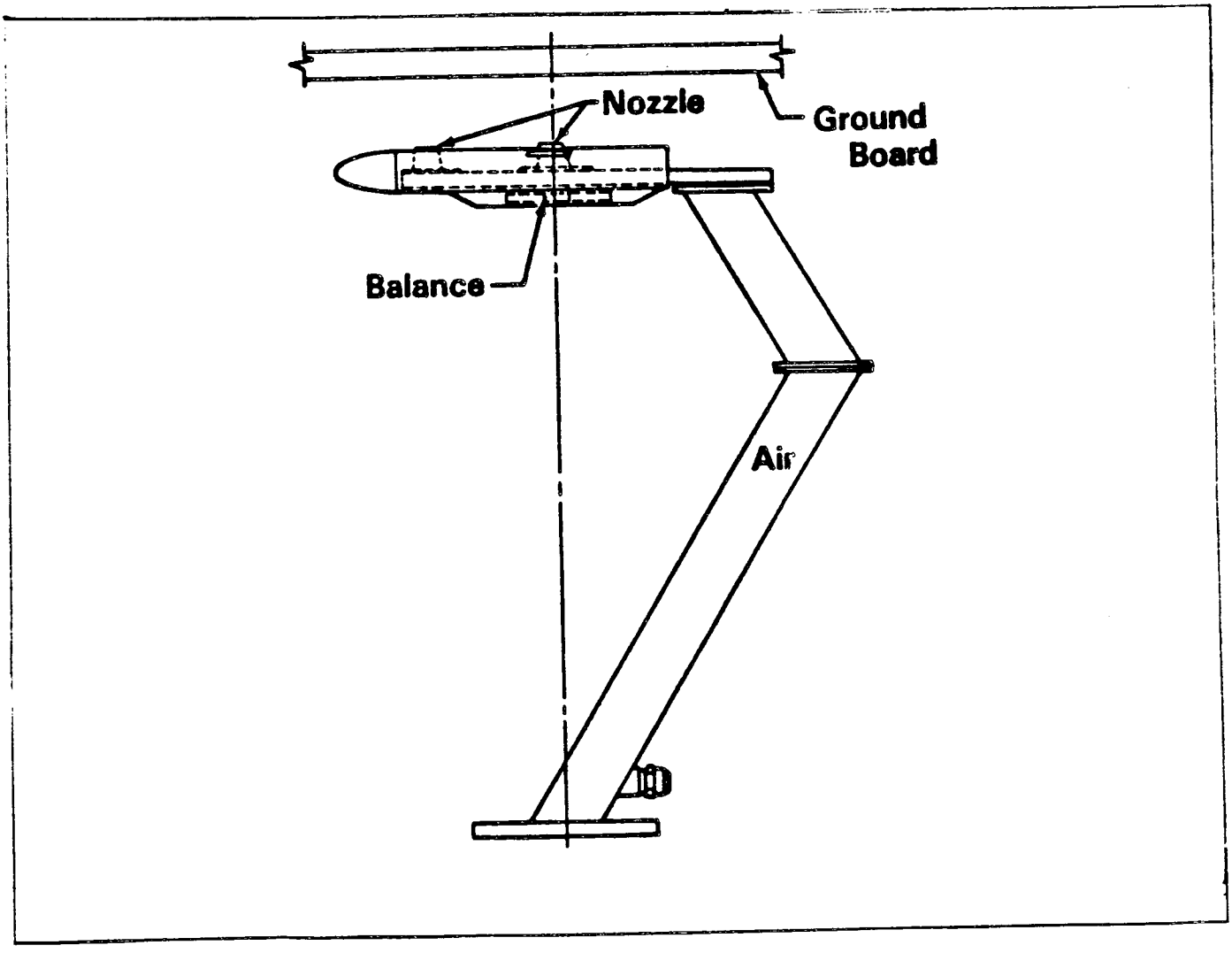

Figure 2. Model Installation

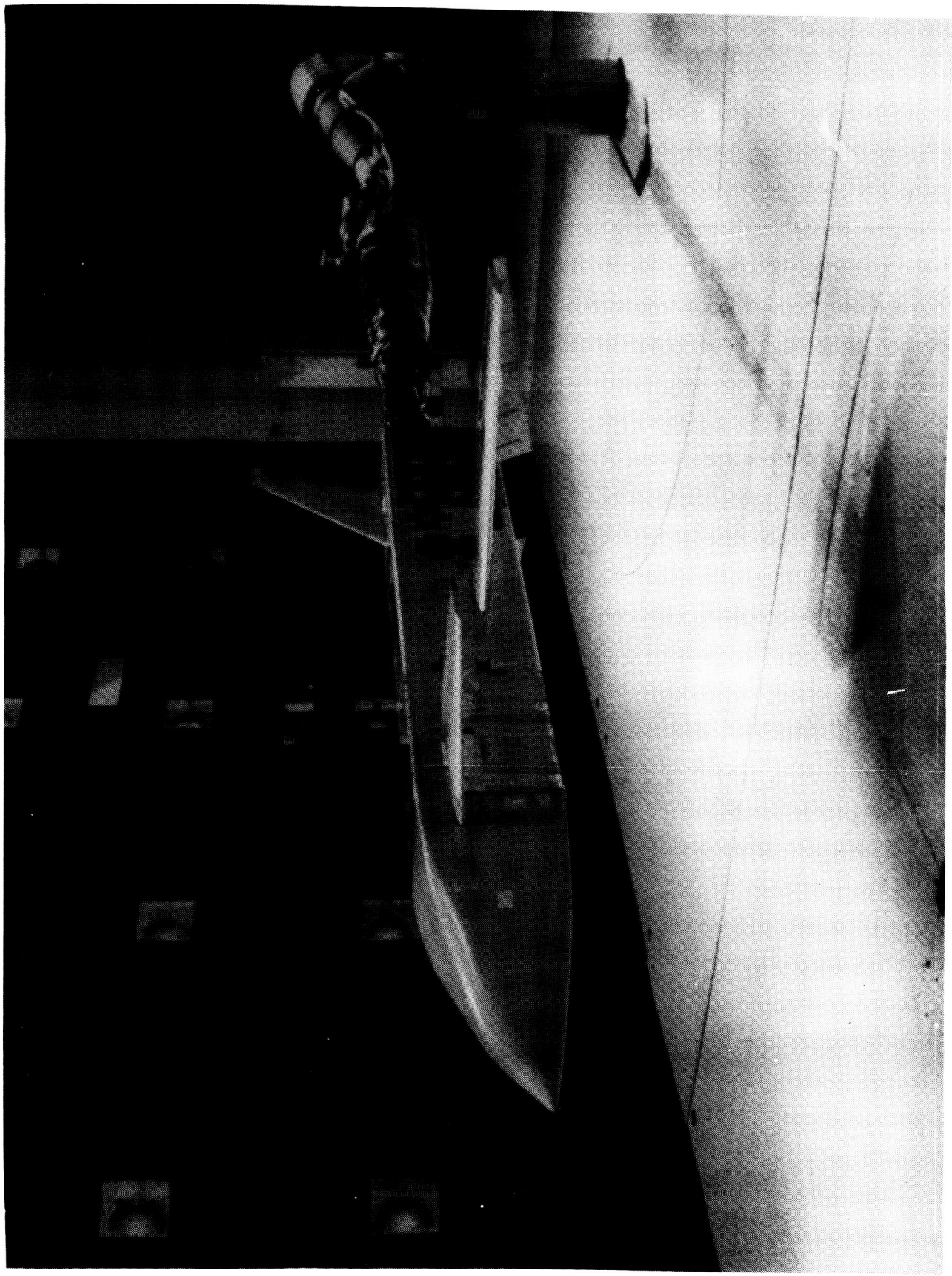

Figure 3. Propulsive Wing/Canard Full Span Model

Figure 4. Propulsive Wing/Carnard Semi-Span Model

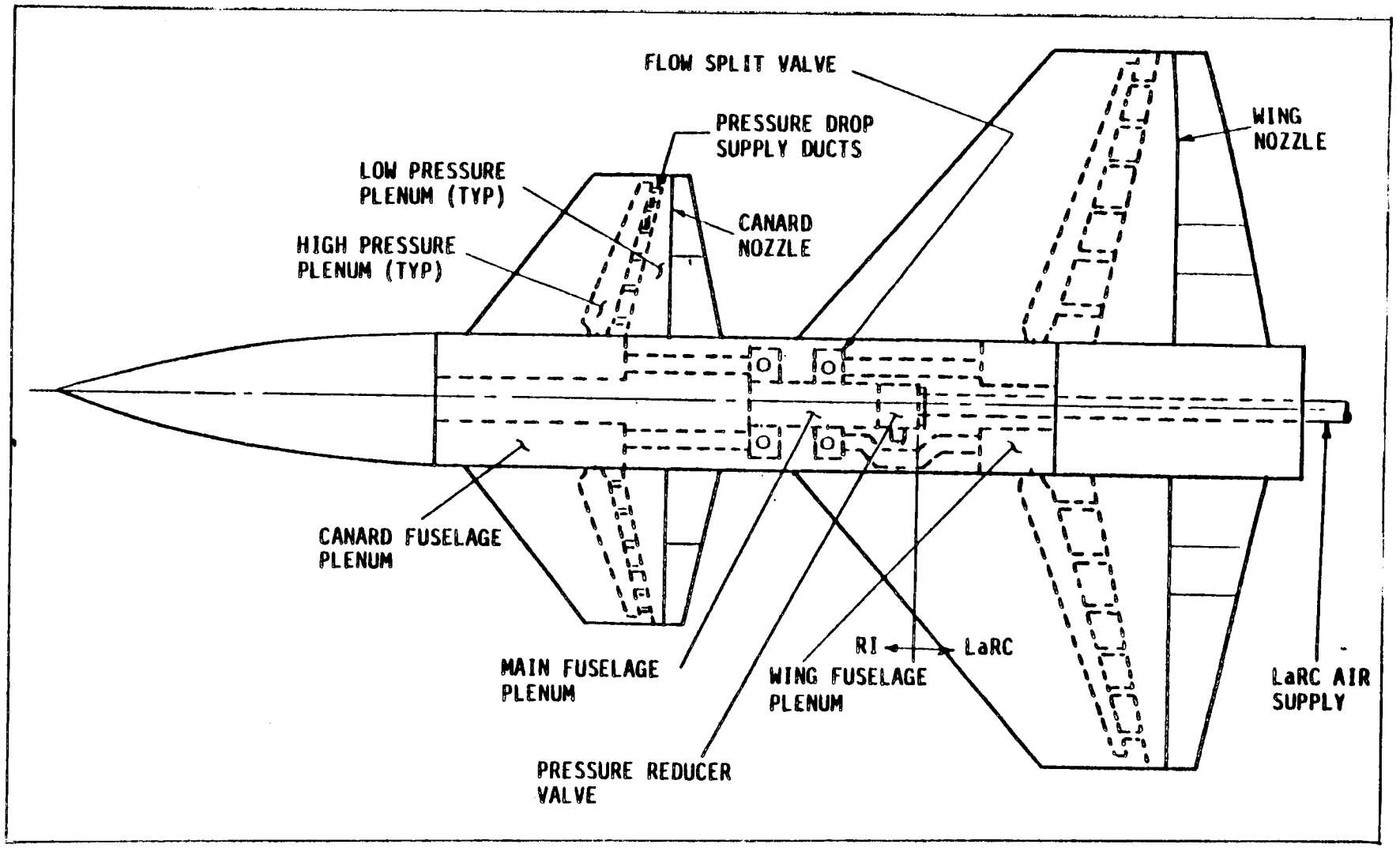

Figure 5. Air Supply System

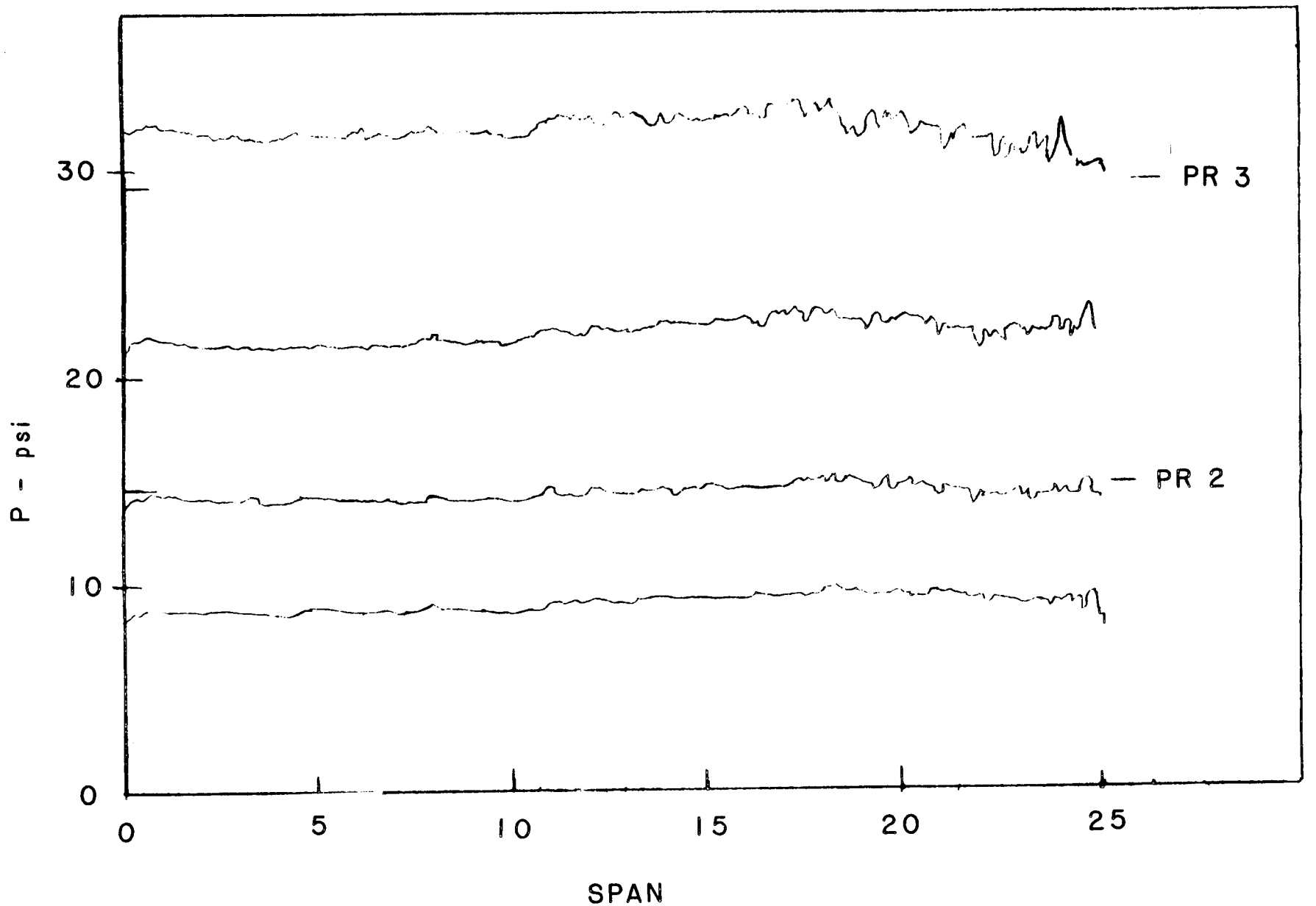

Figure 6. Nozzle Calibration, Left Hand Wing

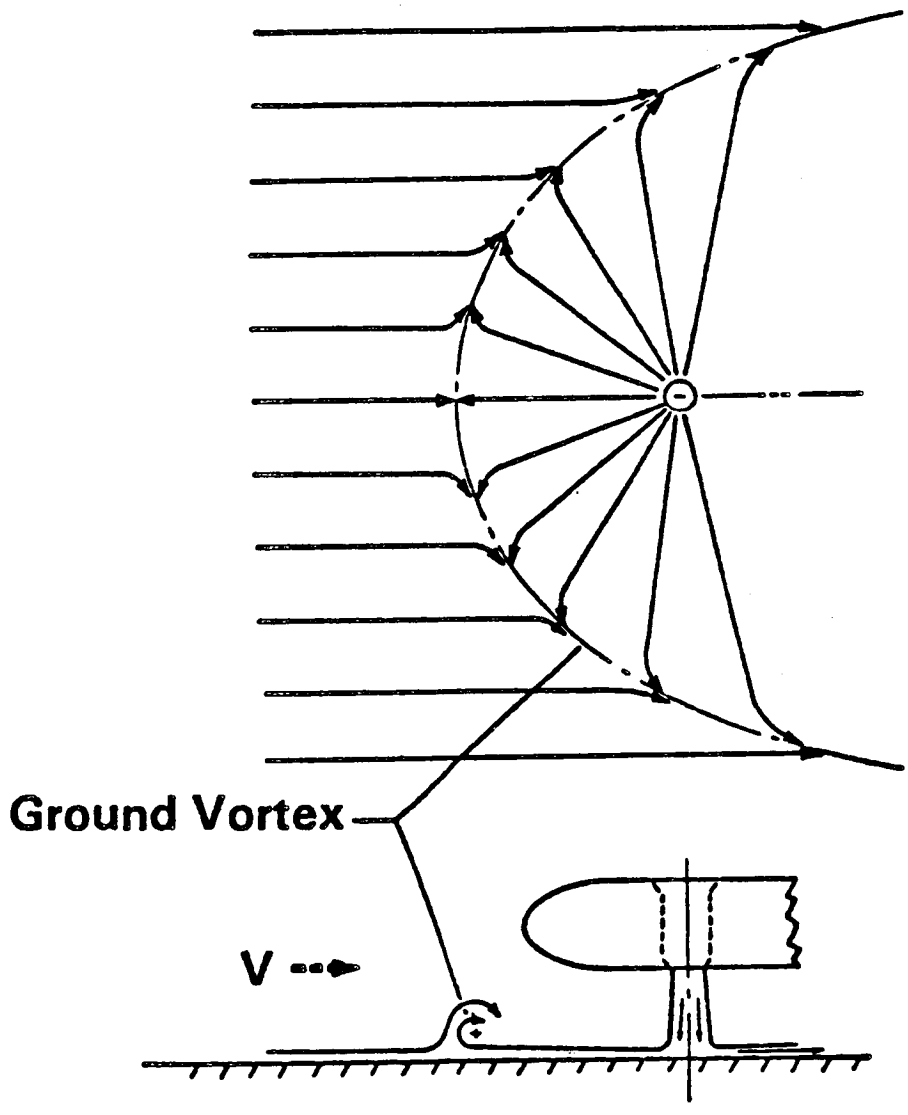

Figure 7. Ground Vortex Formation

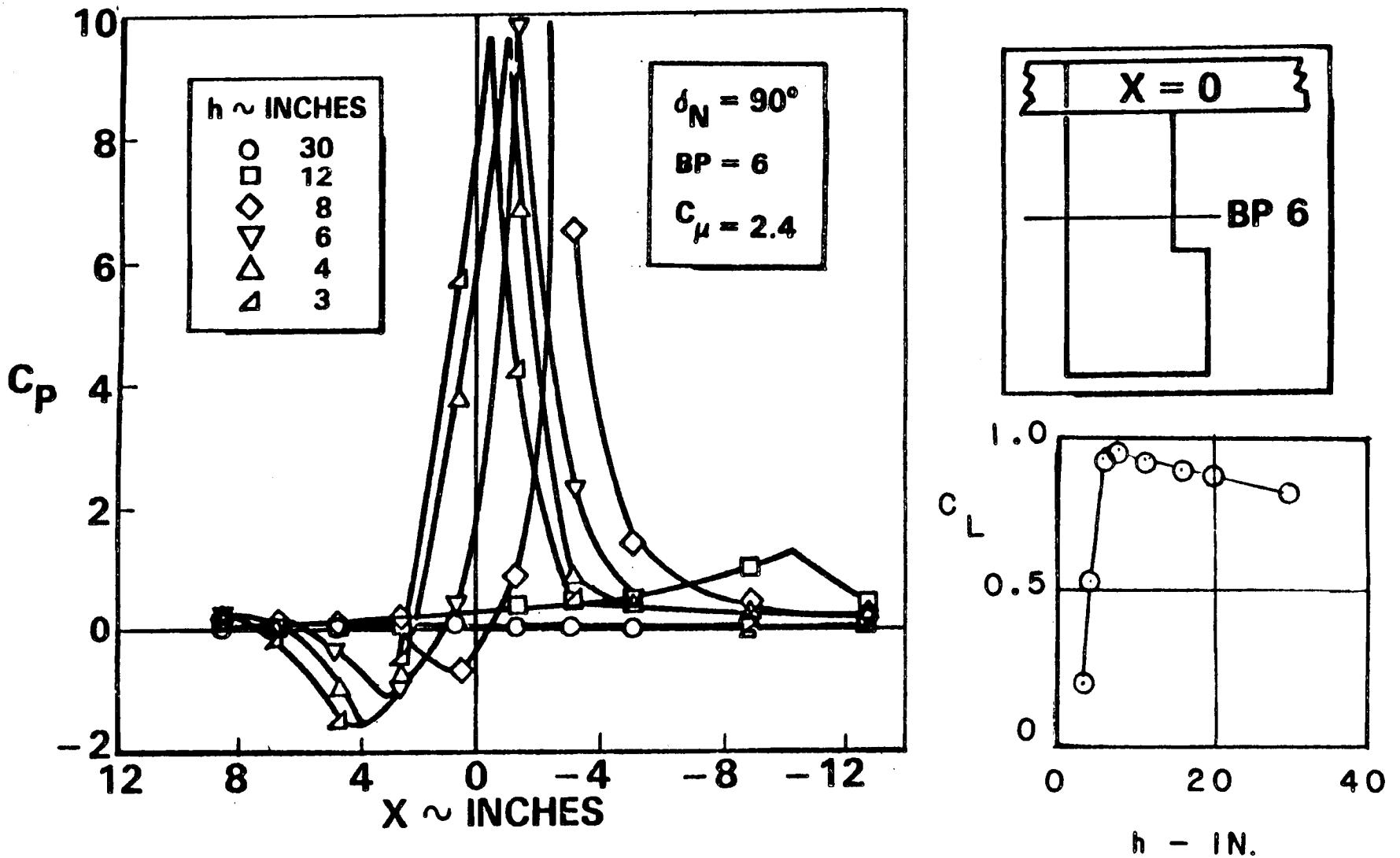

Figure 8. Ground Board Pressure Distribution

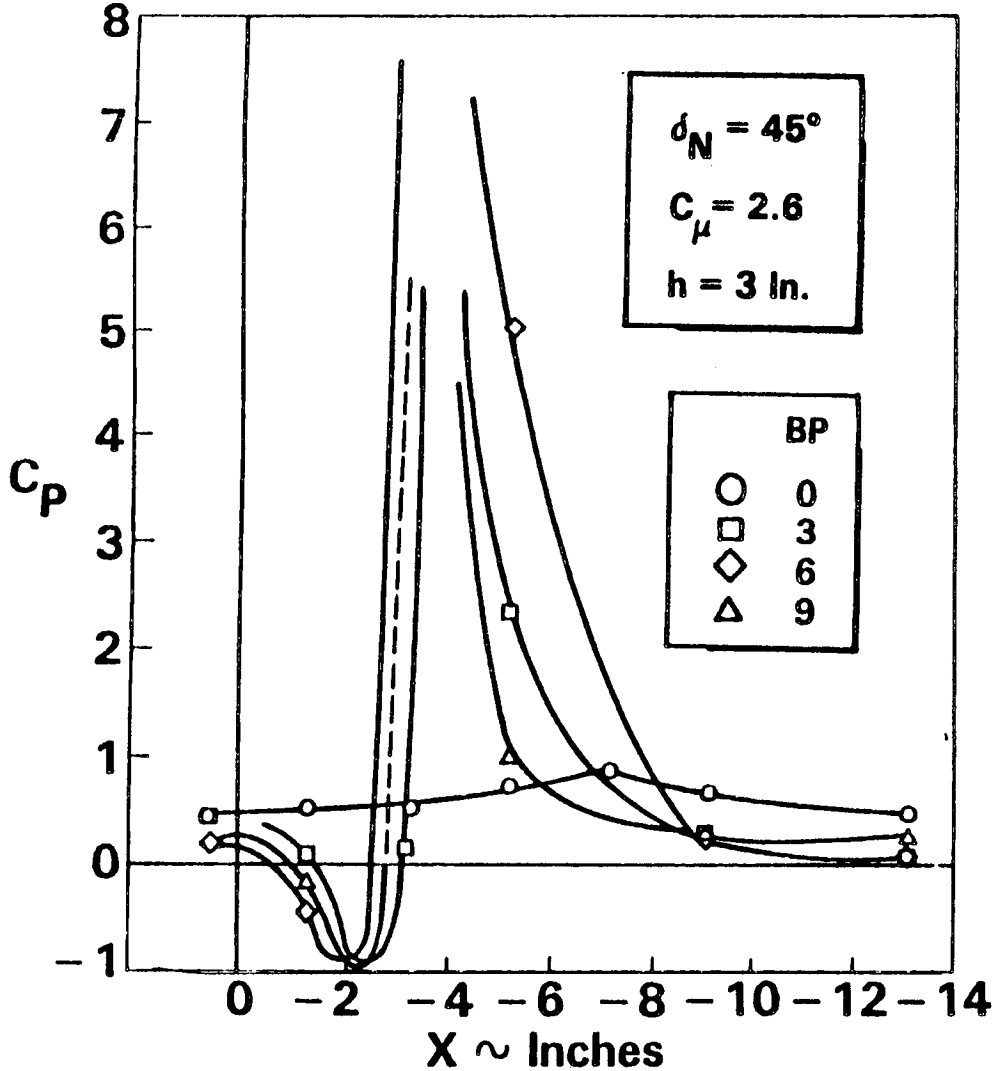

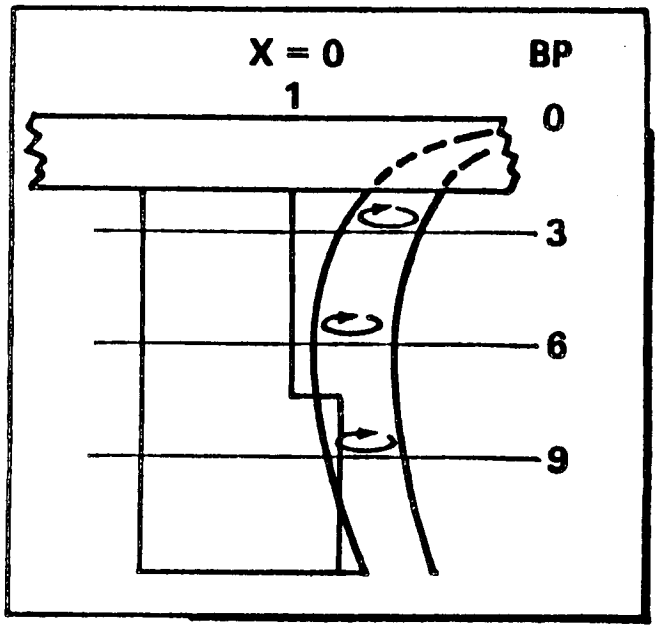

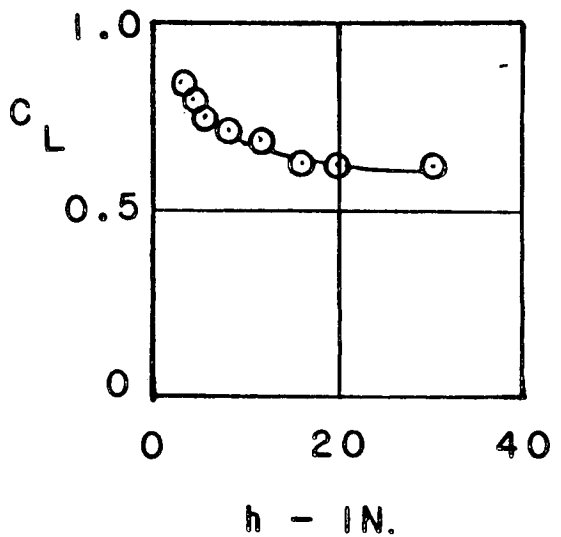

Figure 9. Ground Vortex Location

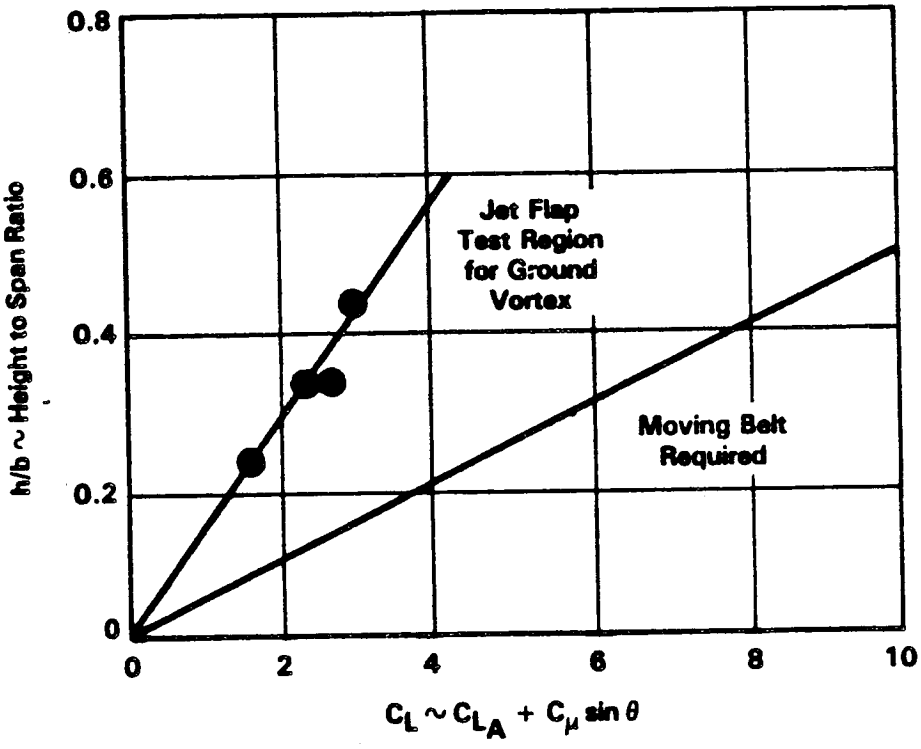

Figure 10. Moving Ground Board Requirement

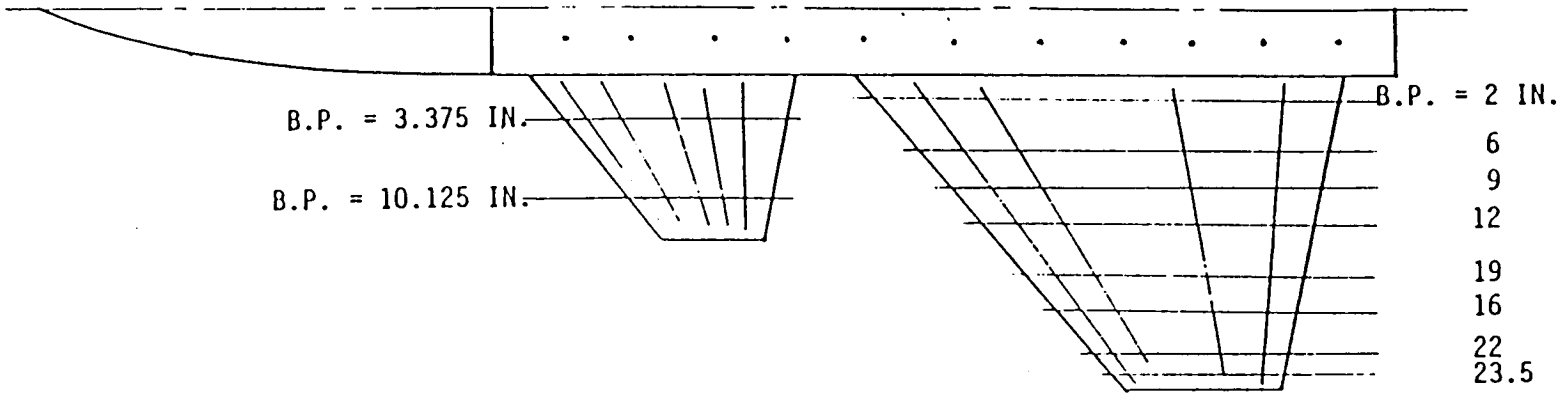

CANARD STATIC PRESS. TAP LOCATION				
	Yc (Dist. to Root Chord)			
	3.375		10.125	
% Chord	Up	Lwr	Up	Lwr
0	L.E.		L.E.	
2.5	X	X	X	X
5	X	X	X	X
10	X	X	X	X
15	X		X	
25	X	X	X	X
35	X	X	X	X
50	X	X		X
56	X		X	
65	X		X	
73		X		X
78	X		X	
79	X		X	
80.5	X		X	
81	X		X	
82	X		X	
84	X	X		X
87	X			
89	X		X	
93	X			
96	X	X	X	X
100	T.E.		T.E.	

WING STATIC PRESSURE TAP LOCATIONS																
	Yw (Distance to Root Chord)															
	2		6		9		12		16		19		22		23.5	
% Chord	Up	Lwr	Up	Lwr	Up	Lwr	Up	Lwr	Up	Lwr	Up	Lwr	Up	Lwr	Up	Lwr
0	L.E.		L.E.				L.E.		L.E.				L.E.			
2.5	X	X	X	X			X	X	X	X			X	X		
5	X	X	X	X			X	X	X	X			X	X		
10	X	X	X	X			X	X	X	X			X	X		
15	X		X				X		X				X			
24	X	X	X	X			X	X	X	X			X	X		
33	X	X	X	X	X	X	X	X	X	X	X	X	X	X	X	X
54	X	X	X	X			X	X	X	X			X	X		
65	X		X				X		X				X			
73.6		X		X				X		X				X		
78.5	X		X				X		X				X			
79.6	X		X				X		X				X			
80.5	X		X				X		X				X			
81.25	X		X				X		X				X			
82	X		X				X		X				X			
84	X	X	X	X			X	X	X	X			X	X		
87	X		X				X		X				X			
89	X		X				X		X				X			
93	X						X		X				X			
96	X	X		X			X	X	X	X			X	X		
100	T.E.		T.E.				T.E.		T.E.				T.E.			

Figure 11. Model Pressure Instrumentation

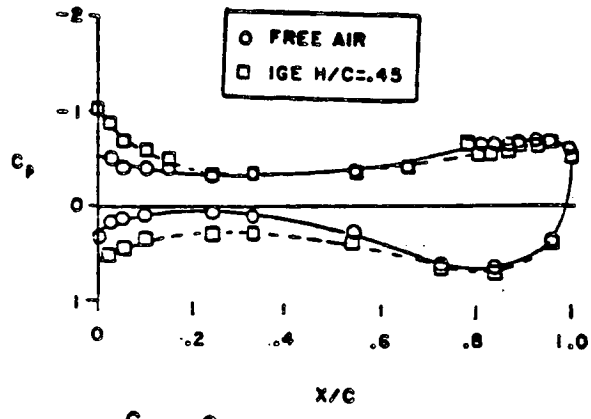

a. $C_\mu = 0$

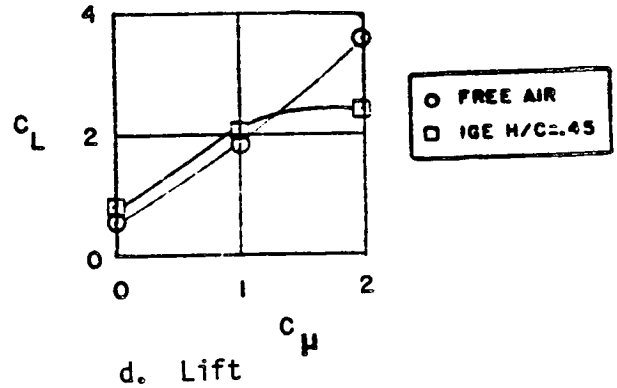

d. Lift

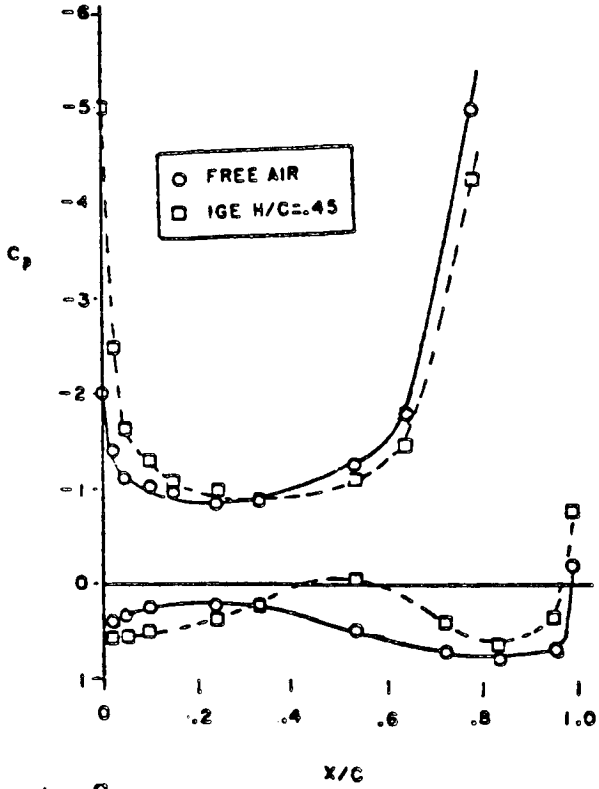

b. $C_\mu = 1$

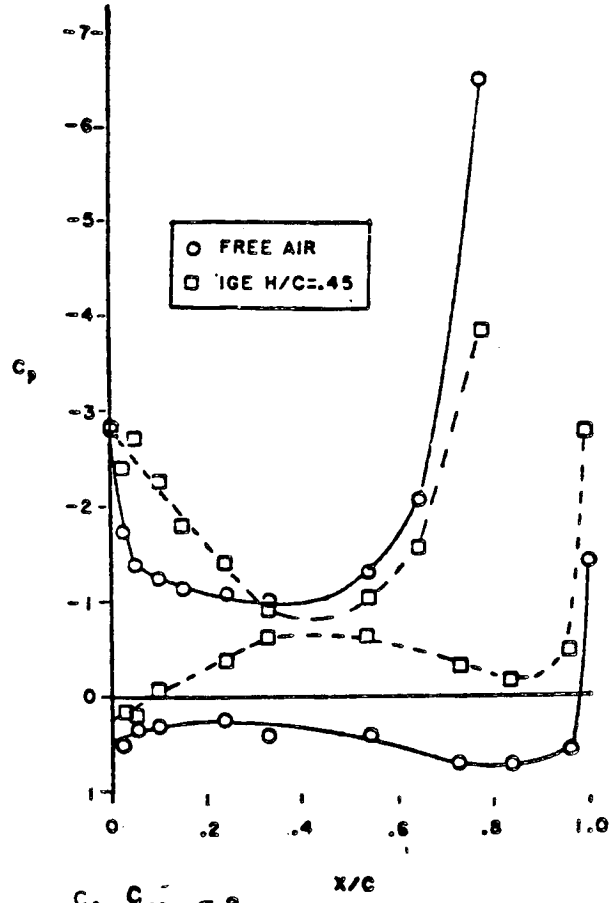

c. $C_\mu = 2$

Figure 12. Effect of Ground Proximity on the Wing Pressures

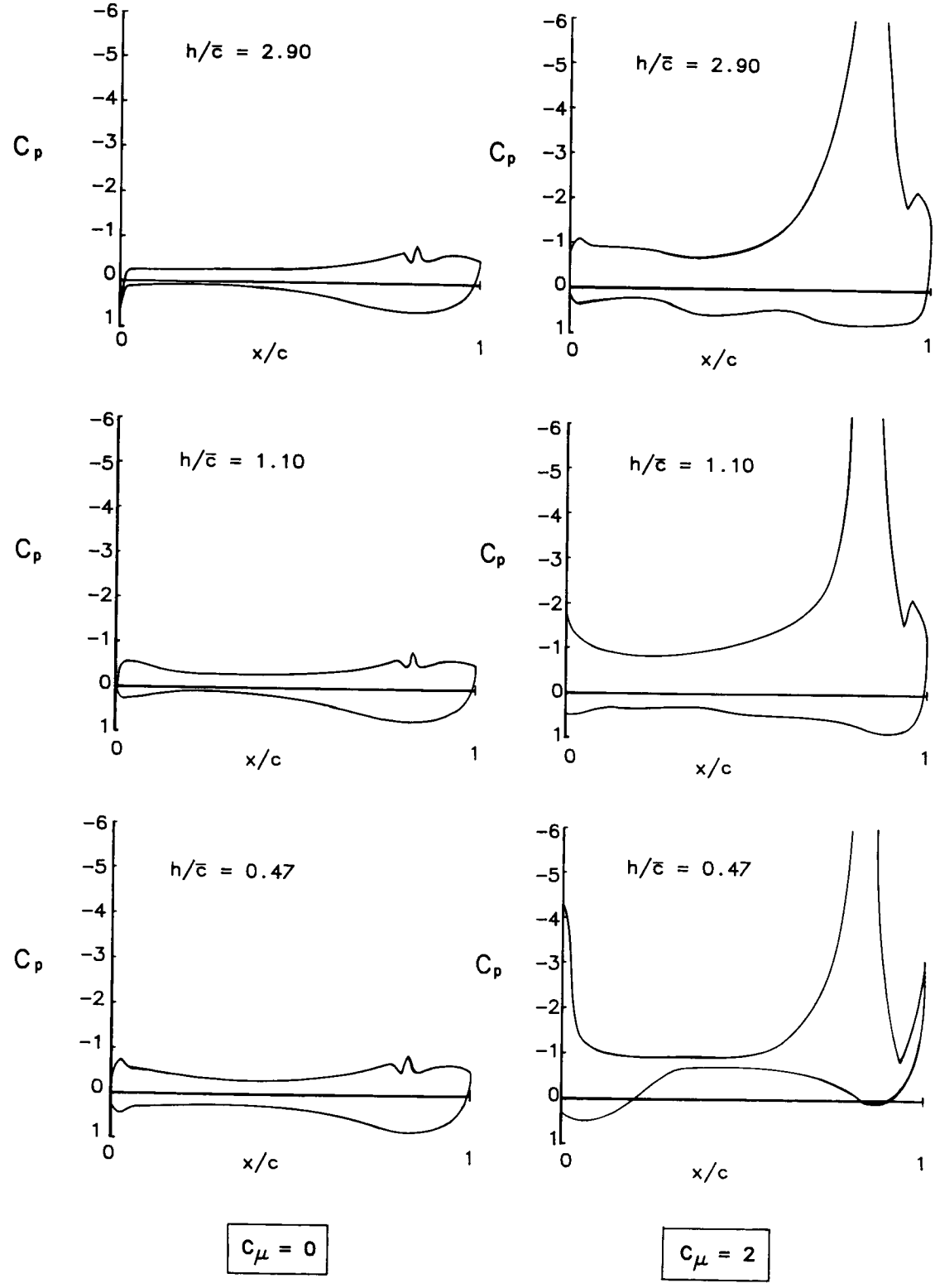

Figure 13. Ground effect on leading edge pressures.
$\alpha = 0^\circ$, $\delta_f = 45^\circ$, No canard

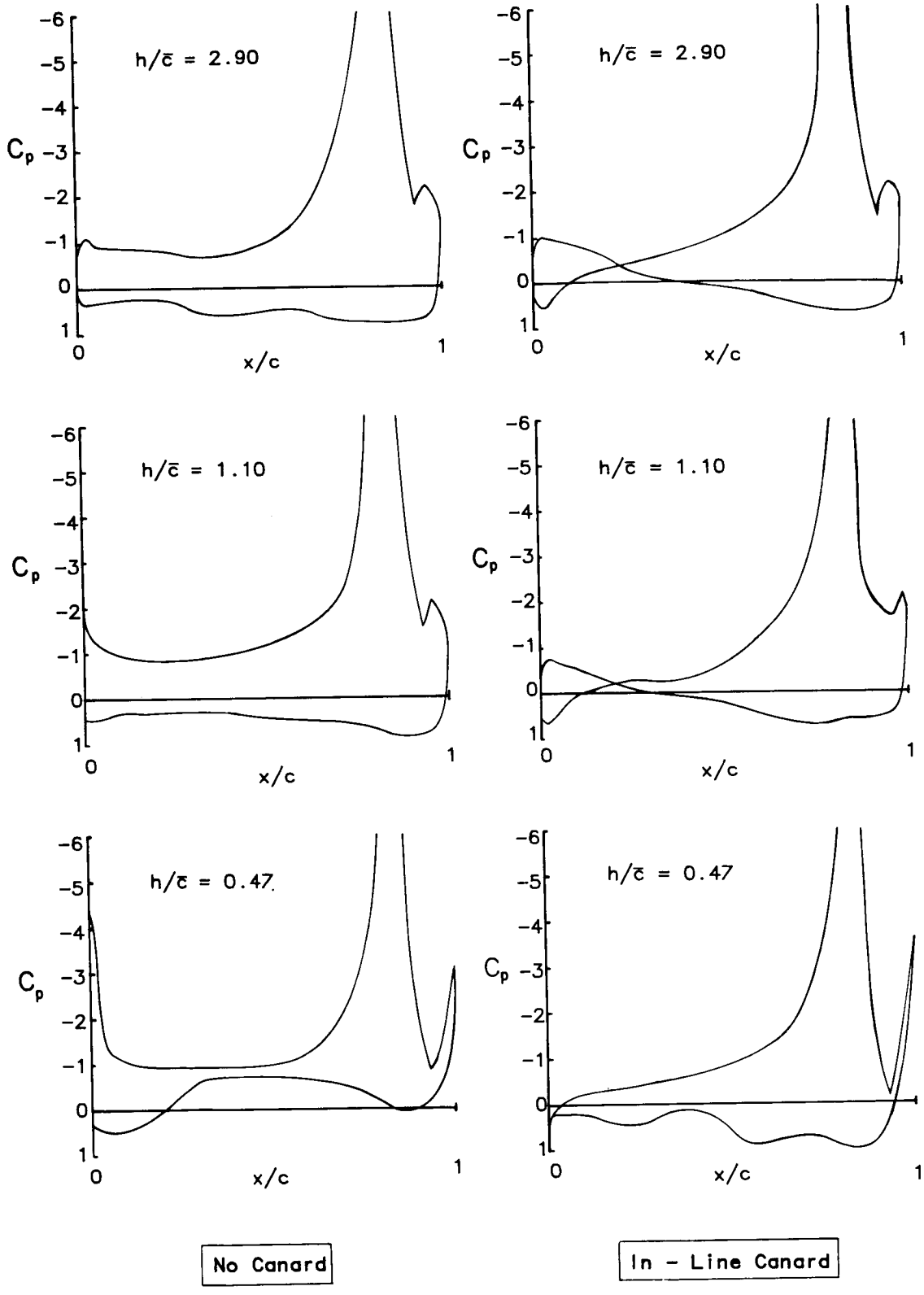

Figure 14. Canard effect on leading edge pressures in and out of ground effects. $\alpha = 0^{\circ}$, $\delta_f = 45^{\circ}$, $C\mu = 2$

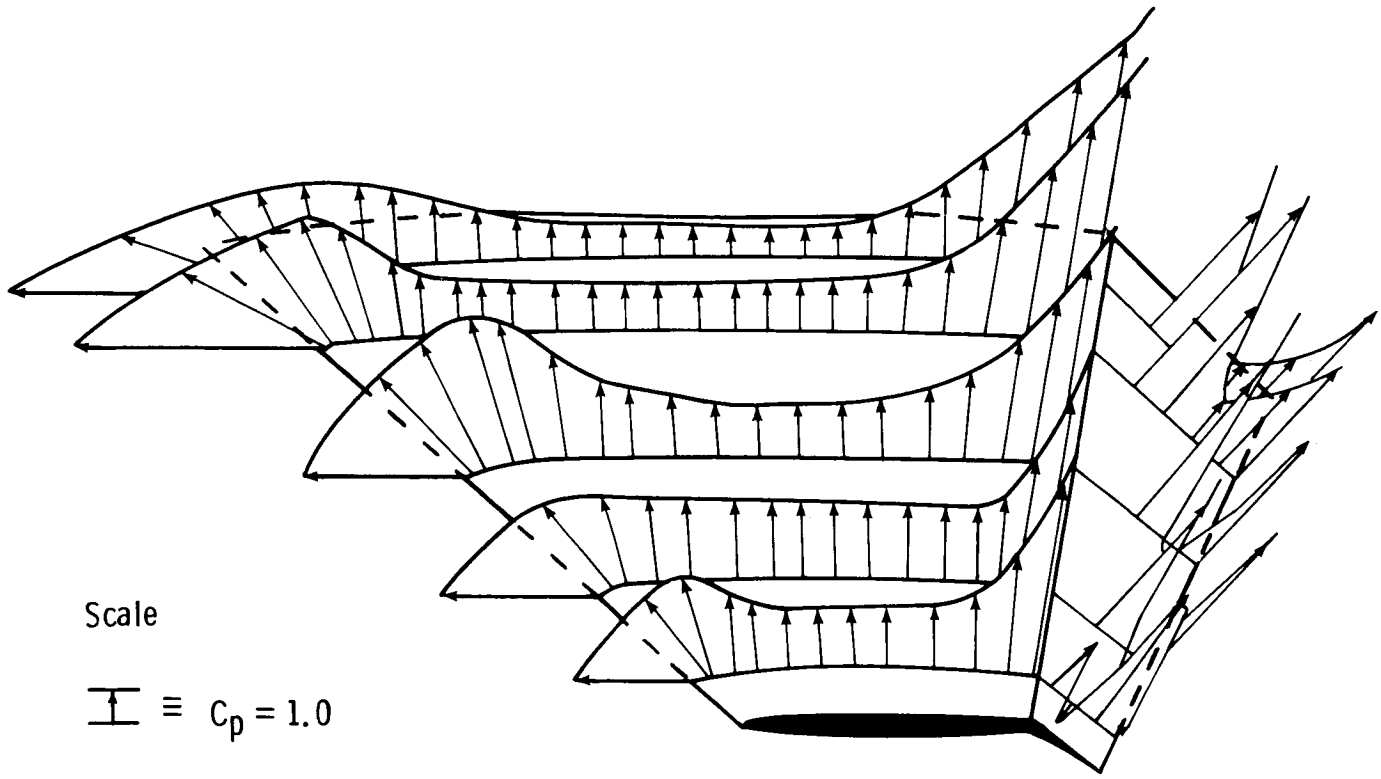

Figure 15. Upper surface pressures of a jet - flapped wing in ground effects with a separated upper surface.
$\alpha = 0^\circ$, $\delta_f = 45^\circ$, $C_\mu = 2$, $h/\bar{c} = 0.47$

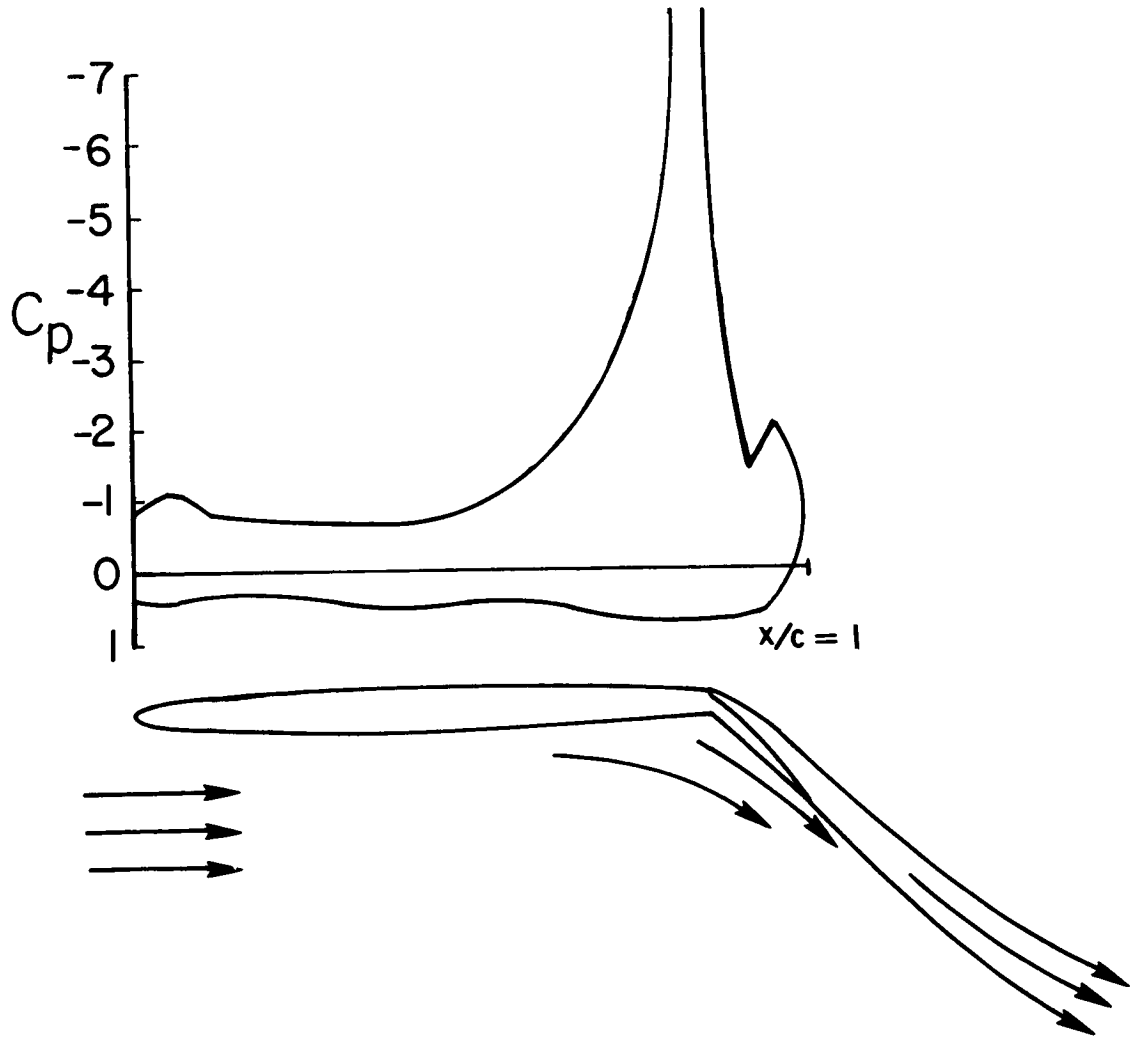

Figure 16. Pressure distribution on a jet - flapped wing out of ground effects. $C_\mu = 2$, $\alpha = 0^\circ$, $\delta_f = 45^\circ$, $h/\bar{c} = 2.90$

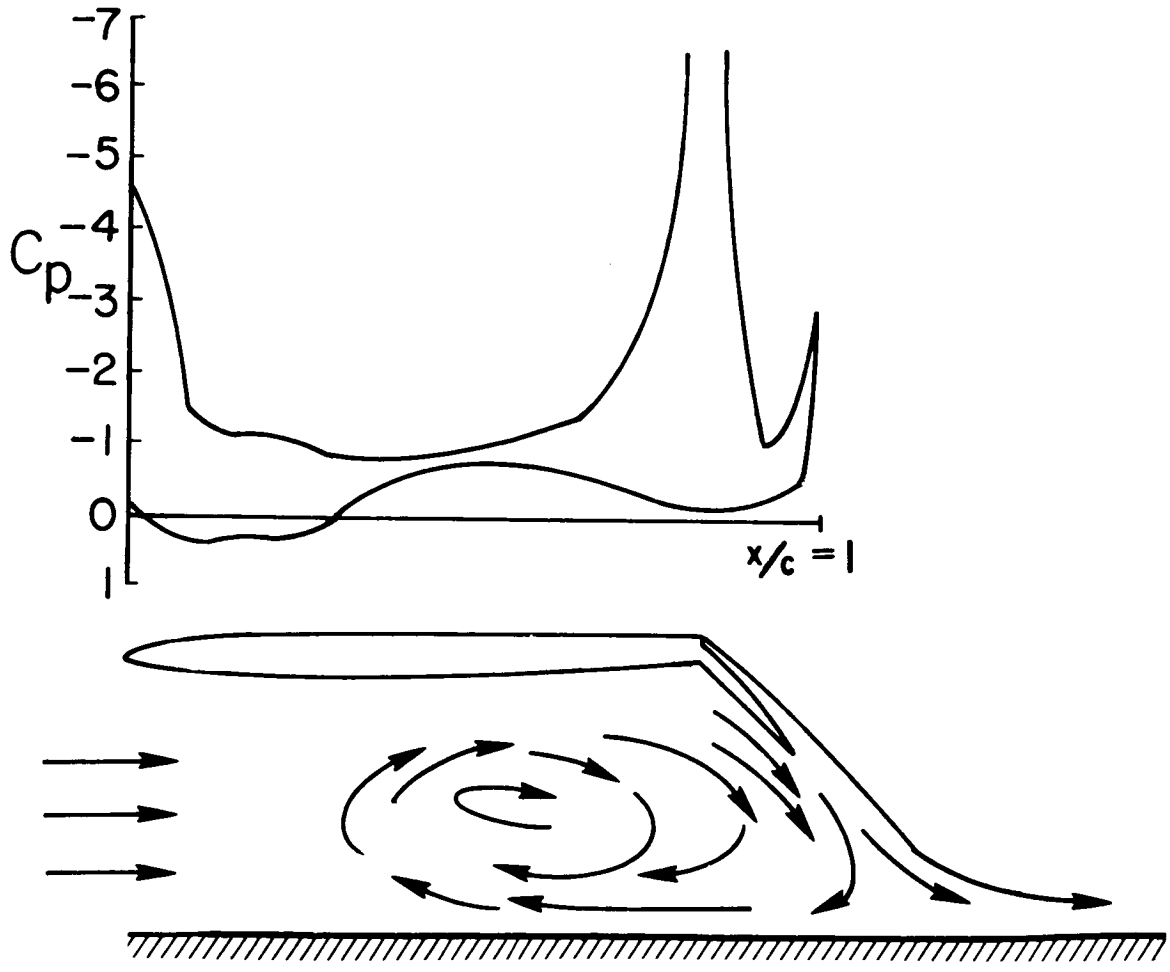

Figure 17. Pressure distribution on a jet - flapped wing with a ground vortex. $C_\mu = 2$, $\alpha = 0^\circ$, $\delta_f = 45^\circ$, $h/\bar{c} = 0.53$

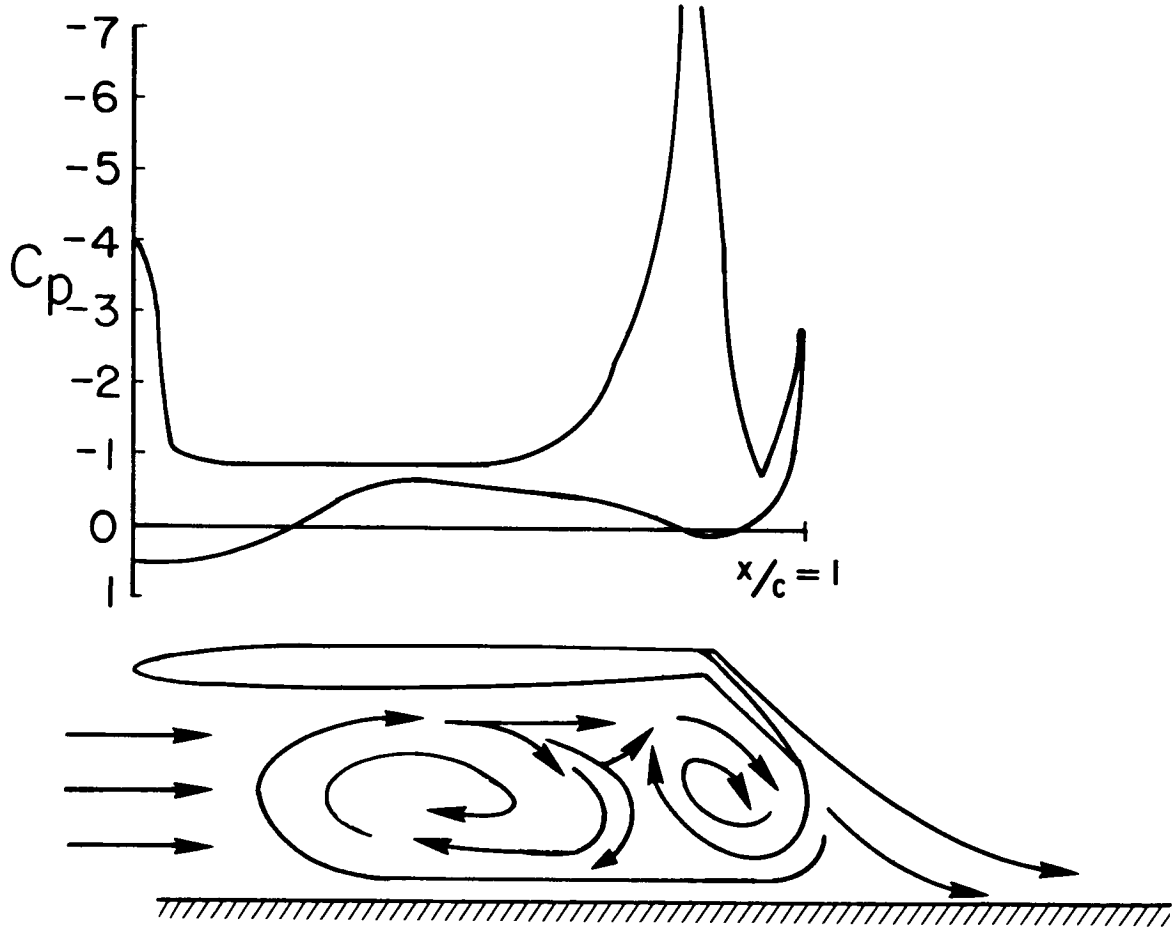

Figure 18. Pressure distribution on a jet - flapped wing with a trapped vortex pair. $C_\mu = 2$, $\alpha = 0^\circ$, $\delta_f = 45^\circ$, $h/\bar{c} = 0.47$

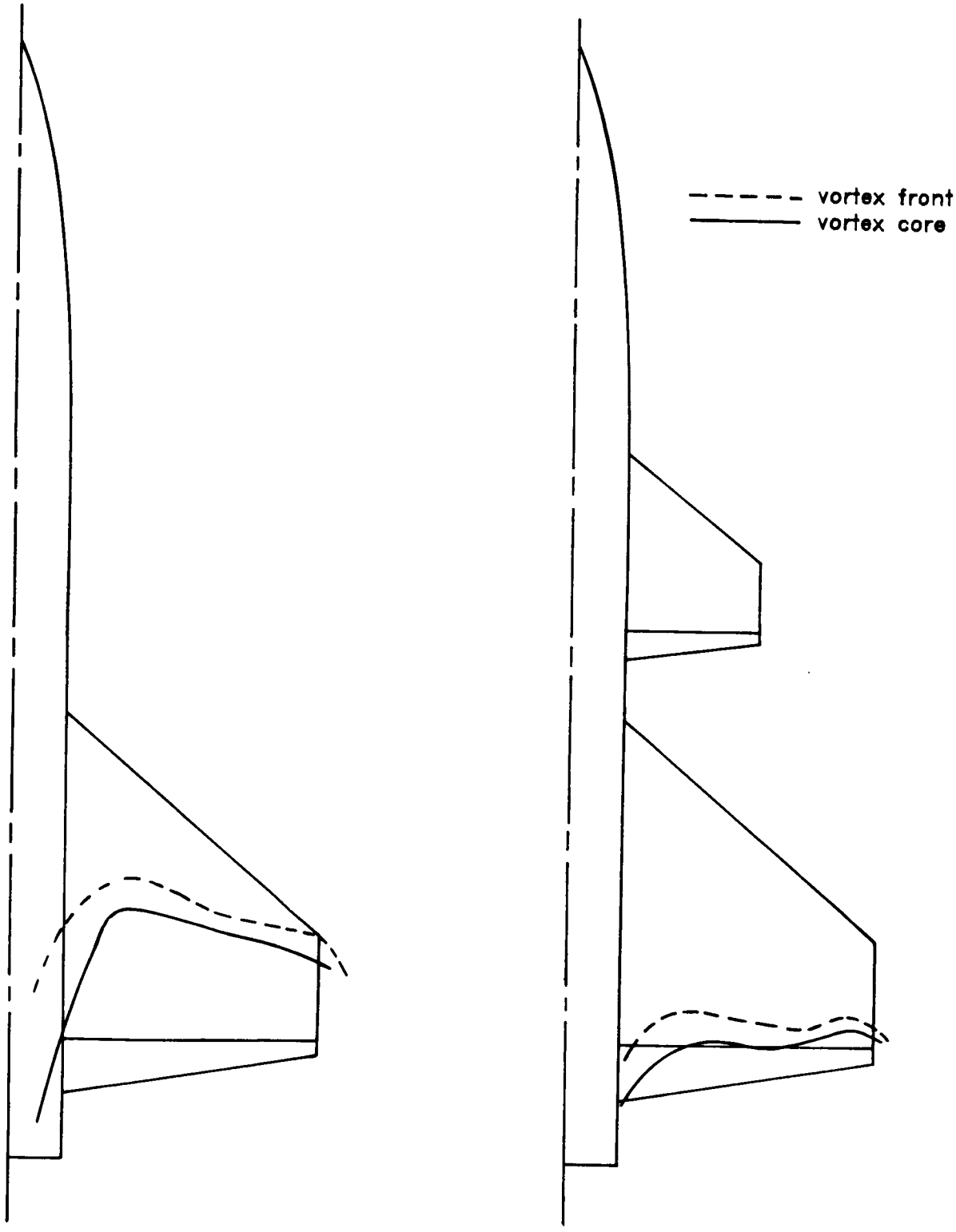

Figure 19. Blown – canard effect on ground vortex. $\alpha = 0^{\circ}$, $\delta_{f_w} = \delta_{f_c} = 45^{\circ}$, $C_{\mu} = 2$, $h/\bar{c} = 0.47$

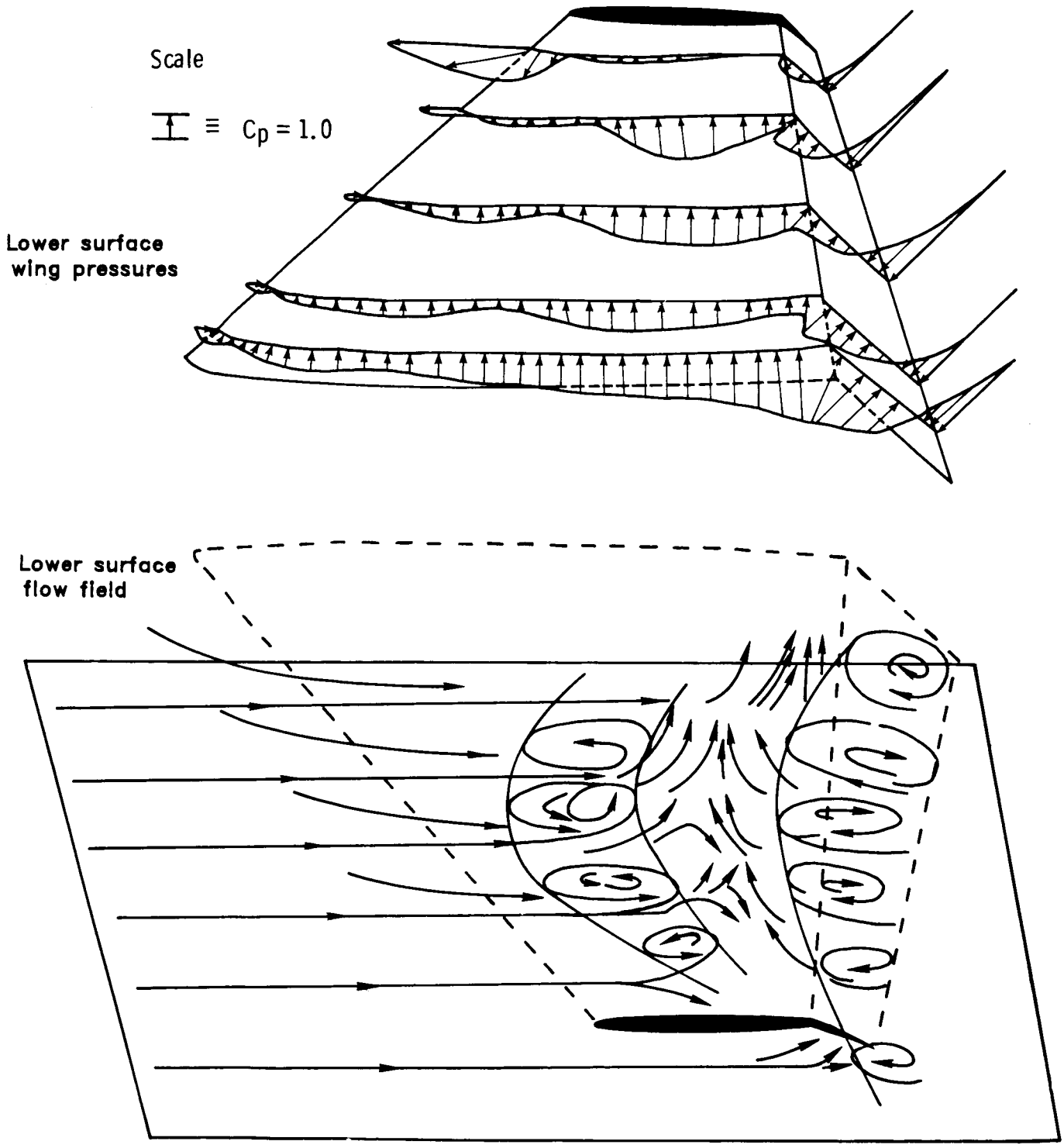

Figure 20. Resulting flow field when the canard jet interacts with the wing's wall jet. $\alpha = 0^\circ$, $\delta_{f_w} = \delta_{f_c} = 45^\circ$, $C_\mu = 2$, $h/\bar{c} = 0.47$

NASA
National Aeronautics and Space Administration

Report Documentation Page

1. Report No.	2. Government Accession No.	3. Recipient's Catalog No.
NASA CP 2462		

4. Title and Subtitle	5. Report Date
Proceedings of the 1985 NASA Ames Research Center's Ground-Effects Workshop	February 1987
	6. Performing Organization Code

7. Editor	8. Performing Organization Report No.
Kerry Mitchell	A-86391
	10. Work Unit No. 505-43-01

9. Performing Organization Name and Address	11. Contract or Grant No.
NASA Ames Research Center Moffett Field, CA 94035	

12. Sponsoring Agency Name and Address	13. Type of Report and Period Covered
National Aeronautics and Space Administration Washington, DC 20546	Conference Proceedings
	14. Sponsoring Agency Code

15. Supplementary Notes

Point of Contact: Kerry Mitchell, Ames Research Center, MS 247-2, Moffett Field, CA 94035, (415)694-6674 or FTS 464-6674

16. Abstract The NASA Ames Research Center's Ground-Effects Workshop was held on August 20-21, 1985; the proceedings are contained in this publication. The workshop was sponsored by the Powered-Lift Group of the Fixed-Wing Aerodynamics Branch at Ames Research Center.

The purpose of the workshop was to discuss the current technology base for aerodynamic ground effects and to establish directions for further research of advanced, high-performance aircraft designs, particularly those concepts utilizing powered-lift systems; e.g., V/STOL, ASTOVL, and STOL aircraft. To that end, 14 papers were presented in the following areas: suckdown and fountain effects in hover; STOL ground vortex and hot-gas ingestion; and vortex lift and jet flaps in ground effect. These subject areas were chosen with regard to current activities in the field of aircraft ground-effects research.

17. Key Words (Suggested by Author(s))	18. Distribution Statement
Ground effects V/STOL Powered lift	Unlimited/Unclassified Subject Category: 02

19. Security Classif. (of this report)	20. Security Classif. (of this page)	21. No. of pages	22. Price
Unclassified	Unclassified	457	A20

NASA FORM 1626 OCT 86

For sale by the National Technical Information Service, Springfield, Virginia 22161